Study of a C-wing Configuration for Passive Drag and Load Alleviation

Shaun N. Skinner

Submitted in fulfilment of the requirements for the
Degree of Doctor of Philosophy

Aerospace Sciences Research Division
School of Engineering
College of Science and Engineering
University of Glasgow

AUTHOR'S DECLARATION

"I herewith declare that, except where explicit reference is made to the contribution of others, that this dissertation is the result of my own work and has not been submitted for any other degree at the University of Glasgow or any other institution."

Printed Name: Shaun Neville Skinner

Date: 26/06/2018

"I am among those who think that science has great beauty. A scientist in his laboratory is not only a technician: he is also a child placed before natural phenomena which impress him like a fairy tale."

– Marie Curie (1867 – 1934)

ABSTRACT

Non-planar wing configurations are often hypothesised as a means for improving the aerodynamic efficiency of large transport aircraft; C-wings may have the ability to exploit and unify drag reduction, aeroelasticity, and dynamics and control but their capacity to do so is ambiguous. The aim of this work is to provide an experimental demonstration with the aim of verifying the C-wing configuration's potential application for drag and load alleviation.

The successful application of a C-wing system for improving the aerodynamic efficiency depends upon the ability to construct the wing system such that a sufficiently low root bending moment and parasitic drag is maintained, relative to an equivalent planar wing system. This was facilitated by the development of a structured genetic algorithm (sGA) optimisation architecture capable of utilising fundamental aerodynamic theory, design specifications, and experimental facility constraints to provide non-arbitrary wing topology designs. The optimisation procedure aided in the design of a planar wing analogous of a typical mid-sized transport commercial aircraft wing topology, representing a 10% scale model. From this baseline design the sGA reconfigured the outboard 26% of the wing to independently form a C-wing topology, increasing the planforms aerodynamic efficiency by 74.5%.

A modular wingtip semi-span model was designed to house the sGA planar and C-wing designs inside the University of Glasgow's de Havilland wind tunnel for tests at $Re = 1.5 \times 10^6$. A number of experimental techniques adopted, such as force/moment measurements, laser-Doppler vibrometry, PCB piezoelectric accelerometry, direct image correlation (DIC), surface flow visualizations, and stereoscopic particle image velocimetry (SPIV), provide insight into the semi-span model and wingtip arrangement structural dynamics and flow field physics. Aerodynamic performance metrics show that despite the C-wing operating with a 19.1% higher wing wetted area, a peak total drag reduction of 9.5% at $\alpha = 6^\circ$ is achieved in addition to a 1.1% reduction in the wing root bending moment for equivalent lift. Study of the near field wake indicated that this was achieved by the C-wing establishing a low vorticity spiral core vortex with accelerated vortex decay properties. The C-wing has also been found capable of passively attenuating buffet induced vibrations of the main-wing by up to 68.6%.

ACKNOWLEDGEMENTS

This dissertation, while the product of my efforts, has only been possible due to the support, patience, and encouragement of the people in my life. It is fitting that I first express my thanks to Dr. Daanish Maqbool whose extensive abilities and love for fluid dynamics is what inspired me to pursue a Ph.D. in the first place. It is also appropriate that I recognise the people who taught me, influenced me, and enabled me to get to this point in my life. For this I would like to thank Faye Restall, Cairan Bocquet, Paul Haig, Andrew Riddick, and Chris Clarke.

I would like to thank my supervisor, Dr. Hossein Zare-Betash, for giving me the opportunity to conduct research at the University of Glasgow. I would also like to express my gratitude to Dr. Richard Green and Dr. Euan McGookin for the continuous support of my Ph.D. research. Your patience, motivation, and immense knowledge helped guide me in my research ambitions and bring this dissertation to fruition. I could not have asked for better mentors. Furthermore, my thanks goes to Dr. Dougie Thompson for unrestricted access to your book collection; to Dr. Kiran Ramesh for unrestricted access to Turing; and to Dr. Angela Busse and Dr. Dave Anderson for meaningful and insightful discussion in my annual progression meetings.

For keeping me sane, for checking in on me when you knew I was having a difficult time, and for enduring the last few years with me, I would like to thank Jonathan McColgan. The process would have been much harder without you. I would also like to thank Andrew Russell, John Walker, Michea Giuni, Kevin Ferguson, David Pickles, Angel Zarev, and Sarah Fitzpatrick for our discussions (both work related and otherwise), your insightful comments, and encouragement.

I'm grateful for my little sister Georgia, my Grandmother Sheila, and my parents, Kirsty and George, for their unwavering belief in me. Thank you for supporting me, both emotionally and financially, and thank you for enabling me to pursue want I want in this life.

Finally, a special thank you to my girlfriend, Alice. Thank you for your continual support and love holding me up over the last few years. Thank you for always being there to steady me when I found life overwhelming, thank you for proofreading every last word I wrote, and thank you for listening to my incessant ramblings of algorithms

and wind tunnel testing. I also wish to thank Alice's parents, Esther and Hugh, for their support and kindness.

This work would not have been possible without my James Watt Scholarship funding from the Engineering and Physical Sciences Research Council (EPRSC); the de Havilland low speed National Wind Tunnel Facility (EPSRC grant number: EP/L024888/1); and Zephyr Business Solutions (grant number: 74603) and The Royal Aeronautical Society Centennial Scholarship (grant number: 21-657/A-SKI).

Dedicated to the memories of my Grandmother, Sheila Breckons (1934-2016).

"Straighten up and fly right..."

CONTENTS

Author's Declaration iii

Abstract vii

Acknowledgements ix

List of Figures xxiv

List of Tables xxvi

Nomenclature & Abbreviations xxvii

1 Introduction 1
- 1.1 Introduction 1
- 1.2 Research Motivation 2
- 1.3 Non-Planar Wing Design 5
  - 1.3.1 Review of Non-Planar Wingtip Development 5
  - 1.3.2 Unconventional Design: The C-wing 7
  - 1.3.3 The C-wing Arrangement 9
- 1.4 Aims and Objectives of Research 10
- 1.5 Structure of Thesis 11
- 1.6 Related Publications 12
- 1.7 Related Research Grants 13

2 Design Optimisation and Analysis of Wing Arrangements 15
- 2.1 Introduction 15
- 2.2 General Considerations for Aerodynamic Optimisation 16
  - 2.2.1 Basic Problem Formulation 16
  - 2.2.2 Review of Design Variables and Geometric Representation 18
  - 2.2.3 Definition of Design Variables and Geometric Representation Used 22
- 2.3 Genetic Algorithm Architecture 23
  - 2.3.1 Genotype-Phenotype Chromosome Mapping and Structure 24
  - 2.3.2 Population Size and Selection Methods 27

2.3.3 Crossover Operators 30
2.3.4 Mutation Operators 32
2.3.5 Constraint Management 33
2.3.6 Summary of Population Structured Genetic Algorithm (sGA) Algorithm 35
2.4 Vortex Ring Aerodynamic Analysis 36
2.4.1 Potential Flow Theory 37
2.4.2 Biot-Savart Law 37
2.4.3 Vortex Ring Method 38
2.4.4 Induced Drag Calculation 41
2.4.5 Viscous Drag Calculation 43
2.4.6 Stall Prediction 44
2.4.7 Experimental Validation 45
2.5 Aerodynamic Design Optimisation 48
2.5.1 Minimum Induced Drag 49
2.5.2 Minimise Induced and Parasitic Drag 53
2.5.3 Minimise Induced and Parasitic Drag with Root Bending Moment Constraint 54
2.5.4 Wind Tunnel Model Wing Design 57
2.6 Summary and Conclusions 65

3 Test Facility and Wind Tunnel Model Design 67
3.1 Introduction 67
3.2 The de Havilland National Wind Tunnel Facility 68
3.3 de Havilland Wind Tunnel Characterisation 69
3.3.1 Methods of Characterisation 69
3.3.2 Working Section Boundary Layer 71
3.3.3 Static Pressure Gradient 75
3.4 Wind Tunnel Model 76
3.4.1 Semi-Span Model Testing 76
3.4.2 Semi-Span Model Design 77
3.5 Wing Aeroelastic Considerations 81
3.5.1 Static Aeroelastics 82
3.5.2 Dynamic Aeroelastics 85
3.6 Structural Analysis: Static Loads 88
3.6.1 Finite Element Analysis 88
3.6.2 Planar Wing Static Load Results 92
3.6.3 Validation of FEA Results 93
3.7 Solid Body Blockage 95
3.8 Three Dimensional Boundary Corrections 96
3.8.1 Buoyancy Correction 97
3.8.2 Blockage Corrections 97

3.9 Experimental Apparatus and Procedure 98
3.9.1 Reference Systems 98
3.9.2 Force Platform 101
3.9.3 Stereoscopic Particle Imaging Velocimetry 101
3.9.4 Surface Flow Visualisations 111
3.9.5 Laser-Doppler Vibrometry 113
3.9.6 Accelerometer 115

4 Semi-Span Testing without Conventional Peniche 117
4.1 Introduction 117
4.2 Background into Semi-Span Model Testing 118
4.3 Force and Moment Measurements 121
4.4 Model Structural Dynamics and Inertial Loading 126
4.4.1 Model Bump Tests 127
4.4.2 Wind Tunnel Vibrations 128
4.4.3 Model Vibration During Wind Tunnel Operation 129
4.5 Stereoscopic Particle Image Velocimetry (SPIV) 131
4.5.1 Flow Field Velocities 131
4.5.2 Turbulence Quantities 135
4.6 Surface Flow Visualisations 139
4.6.1 Tuft Visualisation 139
4.6.2 Clay Flow Visualisation 142
4.7 Summary and Conclusions 145

5 C-wing Performance Relative to Planar Wing 149
5.1 Introduction 149
5.2 Force and Moment Measurements 150
5.3 Surface Flow Visualisations 155
5.4 Wingtip Deflection 158
5.5 Model Vibration and Structural Dynamics 159
5.5.1 Laser-Doppler Vibrometry Bump Tests: Wind Off 159
5.5.2 Model Vibration During Wind Tunnel Tests: Wind On 164
5.6 Summary and Conclusions 172

6 Wingtip vortex Development in the Early Wake 175
6.1 Introduction 175
6.2 Spatial Localisation of the Vortex Core Centre 176
6.2.1 Swirl Velocity Distribution 185
6.2.2 Axial Velocity Distribution 187
6.2.3 Vorticity Distribution 189
6.2.4 Turbulence Quantities 189
6.3 Planar Wing Trailing Vortex 197
6.3.1 Swirl Velocity Distribution 197

6.3.2 Vortex Core Shape 199
6.3.3 Axial Velocity Distribution 201
6.3.4 Vorticity Distribution 204
6.3.5 Turbulence in the Vortex Core 205
6.3.6 Summary of Planar Wing Vortex Core Structure 211
6.4 C-wing Vs. Planar Wing Trailing Vortex 212
6.4.1 Swirl Velocity Distribution 212
6.4.2 Vortex Core Shape 217
6.4.3 Axial Velocity Distribution 219
6.4.4 Vorticity Distribution 221
6.4.5 Turbulence in the Vortex Core 224
6.5 Summary and Conclusions 229

7 Conclusions and Future Work 233
7.1 Conclusions 233
7.1.1 Development of the sGA-VRM Optimisation Architecture 233
7.1.2 Semi-Span Testing Without Conventional Peniche 234
7.1.3 Analysis of the C-wing Design Relative to Equivalent Planar Wing 235
7.2 Future Work and Recommendations 236
7.2.1 C-wing Design Optimisation 236
7.2.2 Semi-Span Model Testing 237
7.2.3 Planar Wing Semi-Span Model Testing 237
7.2.4 C-wing Semi-Span Model Testing 238

Bibliography 239

Appendices 267

A: Vortex Ring Method Convergence Analysis 269

B: Considerations of SPIV Measurement Error 273

C: Statistical Convergence of Time-Averaged Vortex 277

D: Vortex Ring Method Planar Wing and C-wing Validation 283

E: Universal Behaviour of the Planar Wing Vortex Core 287

LIST OF FIGURES

1.1 Fuel efficiency improvement for long-range commercial transport aircraft. Data adapted from Arbritton et al. [1], Serrano-Bernardo et al. [2], and Bickerstaff [3]. 3
1.2 Somerville's biplane flying in Illinois, USA. Image credit: The Coal City Public Library. 5
1.3 Notable non-planar wingtip devices. 6
1.4 C-wing layout with positive direction of span-loading on each surface indicated. 10

2.1 Eight local optima found in blended wing optimisation [4]. 18
2.2 Global variables parametrising simple wing geometry [5]. 19
2.3 NURBS surfaces parametrising surface bland on fuselage [6]. 20
2.4 Image adapted from Lyu et al. [7] illustrating the free-form deformation of a wing with 720 control variables. Selected wing cross sections and associated C_P distributions are highlighted to show initial perturbed (red), and final optimised (blue) sections. 21
2.5 Design variables in wing topology optimisation. 22
2.6 Schematic illustrating typical genetic algorithm. 24
2.7 sGA dynamic chromosome structure. 26
2.8 Population of twelve solutions classified into four non-dominated Pareto-fronts. 29
2.9 The BLX-α operator acting on the i^{th} variable of parent chromosomes x^1 and x^2. 31
2.10 Two-point crossover. 32
2.11 Concept of parallel evaluation strategy of feasible and infeasable solutions to guide direction in a GA. 34
2.12 Schematic illustrating genetic algorithm strategy developed. 36
2.13 Three-dimensional vortex segment. 38
2.14 Vortex ring model of arbitrary wing with N_p spanwise, and N_c chordwise, vortex rings. 39
2.15 Experimental wind tunnel data from Sivells [8] and VRM calculated data. 45

2.16 Experimental wind tunnel and numerically calculated data for a 304CZ sailplane blended winglet wingtip. 47
2.17 Optimisation 1 - optimal induced drag solution. 50
2.18 Baseline wing Vs. Optimisation 1 solution. 50
2.19 Optimisation 2 - optimal induced drag solution. 52
2.20 Baseline wing Vs. Optimisation 2 solution. 52
2.21 Optimisation 3 Pareto-optimal solutions. 53
2.22 Optimisation 4 Pareto-optimal solutions; No RBM constraint: $m_{limit} \rightarrow \infty$ (Optimisation 3); RBM Constraint 1: $m_{limit} = 1.5$; RBM Constraint 2: $m_{limit} = 1$. 55
2.23 Illustration of aerodynamic coupling constraint. 58
2.24 Wind tunnel planar wing design Pareto-front. 59
2.25 Wind tunnel planar model. 60
2.26 sGA population optimisation. 61
2.27 Non-planar C-wing solution with lowest total drag. 63
2.28 Planar 'baseline' wing solution Vs. C-wing solution. 63
2.29 Percentage change of C-wing aerodynamic coefficients relative to planar arrangement. 64

3.1 de Havilland wind tunnel top view schematic. 68
3.2 Boundary pressure rake. 70
3.3 Schematic diagram of the dH working section illustrating pressure probe/rake sampling locations. 70
3.4 Boundary layer profiles from the dH working section floor centreline at $Re = 3.4 \times 10^6$. 72
3.5 Boundary layer thickness through working section. 73
3.6 Boundary layer static pressure and dH pitot probe freestream static pressure at x/L=0.2. 75
3.7 Static pressure gradient through working section with Reynolds number. 76
3.8 Semi-span model installed in the dH working section. 77
3.9 Schematic diagram of model with force platform reference frame indicated; dimensions in millimetres. 78
3.10 Exploded view of semi-span model. 79
3.11 NACA 63_1-412 aerofoil. 80
3.12 Aeroelastic phenomena; bold text indicates aeroelastic behaviours of interest in the present study. 81
3.13 Torsonal wing divergence. 82
3.14 Flutter oscillatory motion. 87
3.15 Semi-span model wing illustrating alignment of the inertial, elastic and aerodynamic axes. Note acceleration due to gravity is in $+z$. 88
3.16 Illustration of boundary conditions for planar wing arrangement static load finite element analysis. 90
3.17 Finite shell element mesh refinement. 91

3.18 Wing finite element discretisation convergence analysis. 92
3.19 von Mises stresses from finite element analysis of planar wing with constant static elliptic load. 93
3.20 Wingtip deflections from finite element analysis of planar wing with constant static elliptic load. Scale of deformation 1:1. 93
3.21 Visualisation of planar wing deformation under aerodynamic loading at $Re = 1.5 \times 10^6$ for several angles of attack. 94
3.22 Planar wing wingtip translations and rotations from finite element analysis compared to experimentally inferred translations and rotations from aerodynamic loading at angle of attack. 95
3.23 Solid body blockage of wing configurations and the percentage increase in blockage from planar to C-wing arrangement. 96
3.24 Schematic of semi-span model with relevant co-ordinate reference systems used in the present study. 99
3.25 SPIV experimental set up with laser sheet in wing wake at $x/\bar{c} = 1.35$. 103
3.26 Schematic of SPIV set-up shown in figure 3.25 with laser sheet in wing wake at $x/\bar{c} = 1.35$. Wind reference frame shown. 103
3.27 Schematic of SPIV set-up illustrating how the de-warping (correction) of images from camera 1 and 2 causes particles to be mapped to different locations in each image. The vector between these mapped positions is the disparity vector. 107
3.28 Tuft grid used over working section floor, fuselage and wing root. Pitch axes indicated. 111
3.29 Clay application sites prior to experiment start. 113
3.30 Laser vibrometer in Mach-Zehnder configuration schematic diagram. 114
3.31 Laser-Doppler vibrometer measurement sites. 115

4.1 Effect of stand-off gap height on aerodynamic coefficients for the planar wing arrangement. 121
4.2 Lift gradient as a function of stand-off gap height. 122
4.3 Illustration of additional circulation around fuselage with larger stand-off gap. 122
4.4 Difference in aerodynamic coefficients taking stand-off gap hieght $1.4\delta^*$ as baseline. 123
4.5 Vertical force and notional yaw moment acting on model as a function of stand-off height and angle of attack. 125
4.6 Frequencies of the semi-span model observed in bump tests with laser vibrometer (bump test measurement locations are indicated in respective figures). 127
4.7 Frequency response, detected by laser vibrometer, from the steel frame of the working section at Reynolds number based on the wing MAC. 128
4.8 Frequency response of planar wing detected by the laser vibrometer at $\alpha = 0^\circ$, 8°, and 14° at $Re = 1.5 \times 10^6$. Measurement location indicated. 129

4.9 Filtered and unfiltered drag coefficient (C_D) temporal data obtained from the force platform over 10s for $\alpha = 0°$, 8°, and 14° (left), with the frequency domain of the filtered and unfiltered data for $\alpha = 8°$ is also shown with the low-pass filter highlighted (right). 131
4.10 Time-averaged $|u|/U_\infty$ contour at the centreline of fuselage nose at $\alpha = 0°$ (dashed box in upper images illustrate location of enhanced view shown in lower images). 132
4.11 Tunnel wall boundary layer velocity magnitude profile development immediately upstream of fuselage nose/stand-off gap at $\alpha = 0°$. 133
4.12 Time-averaged u_z/U_∞ contour at the centreline of fuselage nose at $\alpha = 0°$. 134
4.13 Tunnel wall boundary layer u_z/U_∞ profile development immediately upstream of fuselage nose/stand-off gap at $\alpha = 0°$. 135
4.14 Velocity fluctuations over centreline of fuselage nose at $Re = 1.5 \times 10^6$, $\alpha = 0°$ for stand-off heights $1.4\delta^*$, $2\delta^*$, $3\delta^*$, $4\delta^*$, and $5\delta^*$. 137
4.15 Qualitative visualisation of the standard deviation of tuft fluctuations for stand-off gap heights $1.4\delta^*$, $3\delta^*$, and $4\delta^*$. 140
4.16 Clay flow around model at $\alpha = 0°$ at stand-off height $4\delta^*$; views of fuselage nose (a), and full fuselage, wing root and tunnel floor (b) are shown. 143
4.17 Clay flow around model at $\alpha = 14°$ at stand-off height $4\delta^*$; views of fuselage nose (a), wing root (b), and full fuselage, wing root and floor (c) are shown. 144

5.1 Aerodynamic coefficients for the planar wing and the C-wing. 150
5.2 $C_{M_{pitch}}$ vs. C_L for the planar and C-wing arrangements. 152
5.3 Percentage change of C-wing arrangement aerodynamic coefficients relative to planar arrangement. 152
5.4 Influence of the main-wing on the side-wing, and subsequently the side-wing on top-wing. The dashed red vectors indicate velocities and the solid blue vectors indicate forces. 153
5.5 Vertical (side) force and notional yaw moment acting on model for the planar and C-wing arrangements. 154
5.6 Surface clay flow visualisation over the planar and C-wing configurations at $Re = 1.5 \times 10^6$ for $\alpha = 0°$, 8°, and 14°. 155
5.7 Surface clay flow visualisation over outboard C-wing at $Re = 1.5 \times 10^6$ for $\alpha = 14°$ illustrating main-wing stall progression onto side-wing. 157
5.8 Planar and C-wing main-wing wingtip translation and elastic twist rotation with angle of attack at $Re = 1.5 \times 10^6$. 158
5.9 Bump test frequency response for the planar and C-wing main-wing; bump test location indicated. 159
5.10 Bump test frequency response the C-wing's top-wing; bump test location indicated. 160
5.11 System and dominant mode temporal responses of wing configurations undergoing bump tests. 161

5.12 Explanation of beating interference pattern observed from the interaction between the side and top-wing vibrations. 163
5.13 Frequency response observed in the longitudinal fuselage axis; bump test measurement location indicated. 164
5.14 Frequency response, detected by the laser vibrometer, for each wing arrangent at $\alpha = 0°$, $8°$, and $14°$, at $Re = 1.5 \times 10^6$; measurement locations indicated are identical to those used in figure 5.9. 165
5.15 Summary of peak vibrational velocity magnitudes observed for the planar and C-wing wing's; measurement locations identical to those designated in figure 5.9. 166
5.16 Simplified schematic of the C-wing vibrating system. 167
5.17 Frequency response, detected by the laser vibrometer, of the C-wing's top-wing at $\alpha = 0°$, $8°$, $14°$, at $Re = 1.5 \times 10^6$; measurement locations indicated are identical to those shown in figure 5.10. 168
5.18 Accelerometer arrangement 1 for $\alpha = 8°$. 170
5.19 Accelerometer arrangement 2 for the C-wing configuration at $\alpha = 14°$. 171
5.20 Drag coefficient filtered frequency response, detected by the force platform, for both planar and C-wing arrangements for $\alpha = 0°$, $8°$, $14°$. 172

6.1 Simple time-average and helicity centred time-average vorticity of the planar wing wingtip vortex at $\alpha = 8°$, for $x/\bar{c} = 1.5$ and 2.5. 177
6.2 Instantaneous seeding distribution at $x/\bar{c} = 2.5$, $Re = 1.5 \times 10^6$, and $\alpha = 8°$ for the planar wingtip. 178
6.3 Centring methods for an instantaneous realisation at $x/\bar{c} = 2.5$, $Re = 1.5 \times 10^6$, and $\alpha = 8°$ for the planar wing. 182
6.4 Instantaneous vortex centre locations based on different centring methods at $x/\bar{c} = 2.5$, $Re = 1.5 \times 10^6$, and $\alpha = 8°$ for the planar wing. 184
6.5 Probability density functions (PDF) of the vortex wander amplitudes recoded using the helicity centring method. 185
6.6 Simple averaged vorticity of the planar wing wingtip vortex at $\alpha = 8°$ for $x/\bar{c} = 2.5$, with schematic illustrating various slicing cuts made across the vortex to measure the mean flow characteristics. 186
6.7 Average swirl velocity profiles, and vortex mean swirl profile (red line), calculated with different centring methods at $x/\bar{c} = 2.5$, $Re = 1.5 \times 10^6$, and $\alpha = 8°$ for the planar wing. 187
6.8 Average axial velocity profiles, and vortex mean axial profile (red line), calculated with different centring methods at $x/\bar{c} = 2.5$, $Re = 1.5 \times 10^6$, and $\alpha = 8°$ for the planar wing. 188
6.9 Average vorticity profiles, and vortex mean vorticity profile (red line), calculated with different centring methods at $x/\bar{c} = 2.5$, $Re = 1.5 \times 10^6$, and $\alpha = 8°$ for the planar wing. 190
6.10 In-plane velocity fluctuations, σ_v/U_∞, for different centring methods at $x/\bar{c} = 2.5$ and $\alpha = 8°$ for the planar wing arrangement. 192

6.11 In-plane velocity fluctuations, σ_w/U_∞, for different centring methods at $x/\bar{c} = 2.5$ and $\alpha = 8^\circ$ for the planar wing arrangement. 192
6.12 Out-of-plane velocity fluctuations, σ_u/U_∞, for different centring methods at $x/\bar{c} = 2.5$ and $\alpha = 8^\circ$ for the planar wing arrangement. 193
6.13 Time-averaged turbulent kinetic energy, k/U_∞^2, for different centring methods at $x/\bar{c} = 2.5$ and $\alpha = 8^\circ$ for the planar wing arrangement. 194
6.14 Time-averaged vortex Reynolds stresses, $\overline{v'w'}/U_\infty^2$, for different centring methods at $x/\bar{c} = 2.5$ and $\alpha = 8^\circ$ for the planar wing arrangement. 195
6.15 Shear strain rate, $\varepsilon_{yz} \cdot U_\infty/\bar{c}$, for different centring methods at $x/\bar{c} = 2.5$ and $\alpha = 8^\circ$ for the planar wing arrangement. 195
6.16 Shear strain data profiles for different centring methods presented in figure 6.15; data cut taken along $z/\bar{c} = 0$. 196
6.17 Swirl velocity development with angle of attack and $x/\bar{c}$ plane. 198
6.18 Peak swirl velocity at different $x/\bar{c}$ planes as a function of α. 199
6.19 Development of vortex core shape for different angles of attack and $x/\bar{c}$ plane. 200
6.20 Mean vortex core radius at different $x/\bar{c}$ planes as a function of α. 200
6.21 Axial velocity development with angle of attack and $x/\bar{c}$ plane. 202
6.22 Peak axial velocity at different $x/\bar{c}$ planes as a function of α. 203
6.23 Axial velocity contours at $x/\bar{c} = 1.35$ for $\alpha = 4^\circ$, 8°, and 10°. 203
6.24 Vorticity development with angle of attack and $x/\bar{c}$ plane. 204
6.25 Peak core vorticity at different $x/\bar{c}$ planes as a function of α. 205
6.26 Turbulent kinetic energy data slice through the planar wing vortex core vertical plane (along $z/\bar{c}$ at $y/\bar{c} = 0$) for $\alpha = 0^\circ$, 4°, 8°, and 10° at $x/\bar{c} = 1.35$ and 5.418. 206
6.27 Richardson number as a function of distance from the core centre for the trailing vortex at $x/c = 1.35$ and 5.418 at $\alpha = 8^\circ$. 208
6.28 Streamwise development of in-plane Reynolds shear stresses ($\overline{v'w'}$) for $\alpha = 4^\circ$ and 8°. 209
6.29 Streamwise development of in-plane Reynolds shear stresses ($\overline{v'w'}$) for $\alpha = 4^\circ$ and 8°; data slices taken at 135° for data presented in figure 6.28. 209
6.30 Streamwise development of shear strain rate for $\alpha = 4^\circ$ and 8°. 210
6.31 Streamwise development of shear strain rate for $\alpha = 4^\circ$ and 8°; data slices taken along $y/\bar{c}$ at $z/\bar{c} = 0$ for data presented in figure 6.30. 211
6.32 Schematic of the planar wing trailing vortex core structure. 212
6.33 Planar wing trailing vortex swirl velocity contours at $x/\bar{c} = 2.5$ for $\alpha = 4^\circ$, 8°, and 10°. 213
6.34 C-wing trailing vortex swirl velocity contours at $x/\bar{c} = 2.5$ for $\alpha = 4^\circ$, 8°, and 10°. 213
6.35 Swirl velocity development comparison for $\alpha = 4^\circ$ and 8° at $x/\bar{c} = 2.5$ and 5.418 SPIV planes. 214

6.36 Vortex peak swirl velocity as a function of α and $x/\bar{c}$ for the planar wing and C-wing. 215
6.37 $|u_y|/U_\infty$ and $|u_z|/U_\infty$ data cuts from the planar and C-wing trailing vortex at $x/\bar{c} = 2.5$ for $\alpha = 4^\circ$, 6°, 8°, and 10°. 216
6.38 Development of vortex core shape for the C-wing for $\alpha = 4^\circ$ and 8° at $x/\bar{c} = 2.5$ and 5.418 SPIV planes. 218
6.39 Mean vortex core radius for the planar and C-wing as a function of α and downstream location $x/\bar{c}$. 219
6.40 C-wing axial velocity contours at $x/\bar{c} = 2.5$ for $\alpha = 0^\circ$, 4°, and 8°. 220
6.41 Axial velocity deficit development for $\alpha = 4^\circ$ and 8° at $x/\bar{c} = 2.5$ and 5.418 SPIV planes. 220
6.42 Vortex peak axial deficit velocity at $x/\bar{c} = 2.5$ and 5.418 as a function of α for the planar wing and C-wing. 221
6.43 Vorticity development comparison for $\alpha = 4^\circ$ and 8° at $x/\bar{c} = 2.5$ and 5.418 SPIV planes. 222
6.44 Vortex peak vorticity for the planar and C-wing as a function of α and downstream location $x/\bar{c}$. 223
6.45 Turbulent kinetic energy data slice through the C-wing vortex core vertical axis (along $z/\bar{c}$ at $y/\bar{c} = 0$) for $\alpha = 4^\circ$, 6°, 8°, and 10° at $x/\bar{c} = 2.5$ and 5.418. 224
6.46 Richardson Number as a function of distance from the centre for the C-wing trailing vortex at $x/\bar{c} = 2.5$ and 5.418 at $\alpha = 8^\circ$. Refer to figure 6.37a for clarification on upwash/downwash sides for vortex. 226
6.47 In-plane Reynolds shear stresses for $\alpha = 4^\circ$, 8°, and 10° at $x/\bar{c} = 2.5$ for the planar wing configuration. 227
6.48 In-plane Reynolds shear stresses for $\alpha = 4^\circ$, 8°, and 10° at $x/\bar{c} = 2.5$ for the C-wing configuration. 228
6.49 Shear strain rate for $\alpha = 4^\circ$, 8°, and 10° at $x/\bar{c} = 2.5$ for the planar wing configuration. 229
6.50 Shear strain rate for $\alpha = 4^\circ$, 8°, and 10° at $x/\bar{c} = 2.5$ for the C-wing configuration. 229

A.1 VRM spatial discretisation convergence analysis using validation case 1 at $\alpha = 7.48^\circ$. 269
A.2 VRM accuarcy Vs. speed. 270

B.1 Probability density function (PDF) histogram of velocity components for instantaneous vector grid realisation for the planar wing for $Re = 1.5 \times 10^6$, at $\alpha = 0^\circ$ at $x/\bar{c} = 2.5$. 274

C.1 Swirl velocity at $x/\bar{c} = 2.5$, $Re = 1.5 \times 10^6$, and $\alpha = 8^\circ$ for the planar wing. 278
C.2 Uncertainty for a confidence level of 95% for the helicity centred swirl velocity with different sample sizes of N instantaneous vortex realisations. 278

C.3 Uncertainty for a confidence level of 95% for the helicity centred axial velocity with different sample sizes of N instantaneous vortex realisations. 279
C.4 Convergence of the vortex peak swirl velocity, core radius, axial deficit, and vorticity, with maximum uncertainty for a confidence level of 95% for wingtip vortex of the planar wing at $\alpha = 8^\circ$, $x/\bar{c} = 2.5$. 280
C.5 Shear strain rate convergence at $x/\bar{c} = 2.5$, $Re = 1.5 \times 10^6$, and $\alpha = 8^\circ$ for the planar wing. 281
C.6 Convergence and peak uncertainty for the in-plane Reynolds shear stress, and shear strain rate for a confidence level of 95% for wingtip vortex of the planar wing at $\alpha = 8^\circ$, $x/\bar{c} = 2.5$. 281

D.1 Numerically predicted VRM and experimentally evaluated lift and drag coefficients for the planar wing and the C-wing. 283

E.1 Radial distribution of circulation: **I**, inner-core region; **II**, buffer region; **III**, logarithmic region; **IV**, outer region. 288

LIST OF TABLES

2.1 Typical variable description. 23
2.2 VRM validation case 1 drag polar RMSE. 46
2.3 VRM validation case 2 drag polar RMSE prior to stall onset ($-5^\circ \leq \alpha \leq 13^\circ$). 48
2.4 Test case specifications based on planar wing presented by Sivells [8]. 48
2.5 sGA-VRM settings. 49
2.6 Design specifications for model design. 57
2.7 Wing solution topology. 60
2.8 Summary for aerodynamic performance change and C-wing sGA design point ($\alpha = +6.04^\circ$). 65
2.9 Wing aerodynamic efficiency. 65

3.1 Summary of pitot probe and pressure rake sample locations through working section. Re based on $L = 1m$. 71
3.2 Summary of pitot probe and pressure rake sample locations through working section. 73
3.3 Summary of longitudinal static pressure gradients through the dH working section for with Reynolds number. 76
3.4 Wing parameters. 78
3.5 Polyurethane wing material physical properties. 89
3.6 Summary of force platform experiments; all experiments conducted at $Re = 1.5 \times 10^6$. 101
3.7 Summary of SPIV experiments; all experiments conducted at $Re = 1.5 \times 10^6$. 104
3.8 Capability of seeding particles for flow tracing,. 105
3.9 Summary of tuft visualisation experiments; all experiments conducted at $Re = 1.5 \times 10^6$. 112
3.10 Summary of clay flow visualisation experiments; all experiments conducted at $Re = 1.5 \times 10^6$. 113
3.11 Summary of laser vibrometer experiments; wind-off experiments signify bump tests, wind-on experiments conducted at $Re = 1.5 \times 10^6$. 115

4.1 Average lift coefficient deviation from $1.4\delta^*$ baseline with stand-off gap over range $0^\circ \leq \alpha \leq +10^\circ$; corresponding to data shown in figure 4.4a. 123
4.2 Average drag coefficient deviation from $1.4\delta^*$ baseline with stand-off gap over range $-5^\circ \leq \alpha \leq +7^\circ$; corresponding to data shown in figure 4.4b. 124
4.3 Summary comparing unfiltered and $38Hz$ low-pass filtered drag coefficient (C_D) temporal data for $\alpha = 0^\circ$, 8°, and 14° presented in figure 4.9. 131

5.1 Summary of frequencies associated with the C-wing in free vibration and the domain in which they are detectable. 163
5.2 Percentage change of the first two primary modes illustrating whether modal vibrations of the main-wing were attenuated or amplified by the C-wing relative to the planar wing. 165
5.3 Percentage difference of the dominant vibration magnitude observed in the C-wing's top-wing relative to the C-wing's main-wing. 169

D.1 Summary of numerically predicted (VRM) and experimentally evaluated (EXP) lift-curve-slope data. 284

NOMENCLATURE & ABBREVIATIONS

UNITS

All units of measurement throughout this thesis conform to the *Système Internationale*, with deviations from this rule noted where appropriate.

NOTATION

This section describes the general form of notation for properties such as scalars, vectors and matrices and their derivatives.

TIME DERIVATIVES

$\dot{x}$	first derivative of x with respect to time
$\ddot{x}$	second derivative of x with respect to time
$x^{(n)}$	nth derivative of x with respect to time

SCALARS, VECTORS AND MATRICES

x	scalar
$\mathbf{X}_i$	ith element of vector $\mathbf{X}$
$f(x)$	function of scalar x
L_f	Lie derivative in the direction of f

SYMBOLS

The following symbols are used throughout this thesis. Where a symbol is used only briefly, it is defined at the appropriate point in the text.

LATIN

$\boldsymbol{A}$	Aerodynamic influence matrix
AR	Aspect ratio
a	Non-dimensional distance between inertial axis and aerodynamic centre
a_{mm}	Aerodynamic influence coefficient
b	Wingspan
b_{mm}	Aerodynamic influence coefficient
$\boldsymbol{C}$	Damping matrix of system
C_D	Drag force coefficient (Three-dimensional)
C_{D_i}	Induced drag force coefficient (Three-dimensional)
C_{D_p}	Parasitic drag force coefficient (Three-dimensional)
C_d	Drag force coefficient (Two-dimensional)
C_{d_p}	Parasitic drag force coefficient (Two-dimensional)
C_{F_z}	Vertical force coefficient (Three-dimensional)
C_L	Lift force coefficient (Three-dimensional)
C_{L_α}	Lift curve slope (Three-dimensional)
C_l	Lift force coefficient (Two-dimensional)
C_{l_α}	Lift curve slope (Two-dimensional)
$C_{M_{pitch}}$	Model pitching moment (Around centre of gravity)
$C_{M_{RBM}}$	Model root bending moment (Around centre of gravity)
$C_{M_{yaw}}$	Model notional yawing moment (Around centre of gravity)
C_{m_o}	Local pitching moment coefficient (Around quarter-chord)
c	Aerofoil chord
$\bar{c}$	Mean aerodynamic chord

D	Drag
D_i	Induced drag
D_p	Parasitic drag
d_{ij}	Euclidean distance
d_{int}	Interrogation window dimension
d_L	Laser sheet thickness
e	Non-dimensional distance between elastic axis and aerodynamic centre
e_0	Aerodynamic efficiency (Oswald efficiency factor)
F	Force
f	Frequency/Objective function
g	Gravitational constant
H_x	Streamwise helicity
$h_{wingtip}$	Height of wingtip relative to wing root
$\boldsymbol{K}$	Stiffness matrix of system
k	Turbulent kinetic energy
L	Lift/Length of wind tunnel test section/Characteristic length
l	Wing segment span
$\boldsymbol{M}$	Mass matrix of system
M	Moment
M_∞	Freestream Mach number
m_{limit}	Non-dimensional root bending moment limit
N	GA population size
N_c	Number of chordwise vortex rings
N_p	Number of spanwise vortex rings
$\boldsymbol{n}$	Normal unit vector
n	Aerodynamic panel number ($1 \leq n \leq 5$)
p	Static pressure

Q	Discriminant of the characteristic equation of the velocity gradient
Re	Reynolds number, $= \frac{\rho_\infty U_\infty L}{\mu}$
Ri	Richardson number
$\vec{\boldsymbol{r}}$	Position vector
r	Local vortex core radius
r_c	Mean vortex core radius
r, θ, x	Cylindrical (polar) coordinates
S	Wing area
Sp	Bradshaw non-dimensional shape parameter
St	Stokes number
T_c	Convective time-scale
T_v	Viscous time-scale
t	Time
U_∞	Freestream flow speed
$\boldsymbol{u}$	Generic velocity vector
$\bar{\boldsymbol{u}}$	Mean velocity vector, $= \boldsymbol{u} - \boldsymbol{u}'$
$\boldsymbol{u}'$	Velocity vector fluctuation, $= \boldsymbol{u} - \bar{\boldsymbol{u}}$
u, v, w	Axial, lateral, vertical velocity components in Cartesian coordinates
$\overline{u'^2}, \overline{v'^2}, \overline{w'^2}$	Turbulent normal stresses in Cartesian coordinates
u_r, u_θ, u_x	Radial, tangential (swirl), and axial velocity in cylindrical coordinates
V_{ind}	Induced velocity
$\overline{v'w'}, \overline{u'v'}, \overline{u'w'}$	Reynolds stresses in Cartesian coordinates
x, y, z	Dimensionless Cartesian coordinates

GREEK

α_o	Zero lift angle of attack
α	Angle of attack/BLX-α crossover operator
α_{eff}	Effective angle of attack

α_{ind}	Induced angle of attack
α_r	Root angle of attack
β	Angle of camera offset from viewing plane
Γ	Dihedral angle/Circulation
γ	Vortex sheet strength/Crossover operator
$\Delta()$	$()_n - ()_{n-1}$
Δt	Laser pulse separation time/Time-step
ΔU	Slip velocity
Δx	Displacement of tracer particle
Δy	Vortex ring span
∇	Laplace operator
δ	Boundary layer disturbance thickness
δ^*	Boundary layer displacement thickness
ϵ	Wind tunnel correction factor
ε_{xx}	Normal strain
ε_{yy}, ε_{zz}	Elongation strain
ε_{yz}, ε_{zy}	Shear strain
ζ	Damping
θ	Wing twist
θ_E	Elastic wing twist
Λ	Sweep angle
λ	Taper ratio/Wavelength
λ_2	Eigenvalue of the tensor $\Sigma^2 + \Omega^2$
μ	Dynamic viscosity
v	Kinematic viscosity
ρ	Air density
ρ_p	Particle density
Σ	Strain Tensor

σ_1, σ_2, σ_3	Principal stresses
σ_u	Root mean square of the axial velocity fluctuation
σ_v, σ_w	Root mean square of the in-plane velocity fluctuations
$\sigma_{von\ Mises}$	von Mises stress
τ_{flow}	Flow time scale
τ_p	Relaxation time
Φ	Phase
ϕ	Velocity potential
Ω	Vorticity Tensor
$\boldsymbol{\omega}$	Vorticity vector
ω	Wing bending deflection
ω_d	Damped natural frequency
ω_{ind}	Induced downwash
ω_n	Natural frequency
ω_x	Streamwise vorticity

SUBSCRIPTS

∞	Freestream
o	Offset/Zero Value/Initial Value
av	Average
DV	Design Variable
max	Maximum
min	Minimum
mw	Main-Wing
RBM	Root Bending Moment
ref	Reference
$root$	Wing Root
Seg	Segment

sw	Side-Wing
TE	Trailing Edge
tw	Top-Wing
u, v, w	Axial, Lateral, Vertical Velocity Components
x, y, z	Axial, Lateral, Vertical Direction

SUPERSCRIPTS

L	Lower Limit
sb	Solid-Body Blockage
tb	Total Blockage
U	Upper Limit
wb	Wake Blockage

ABBREVIATIONS

ACARE	Advisory Council for Aeronautics Research in Europe
BLX	Blended Crossover
CCD	Charged Coupled Device
CFD	Computational Fluid Dynamics
CMOS	Complementary Metal-Oxide-Semiconductor
DIC	Direct Imaging Correlation
dH	de Havilland
FAA	Federal Aviation Administration
FEA	Finite Element Analysis
FFD	Free-Form Deformation
GA	Genetic Algorithm
ICAO	International Civil Organisation
IPCC	Intergovernmental Panel of Climate Change
LDA	Laser-Doppler Anemometry
LE	Leading Edge

LVV	Low Vorticity Vortex
MAC	Mean Aerodynamic Chord
MDI	Modulation Detection Interference
MW	Main-Wing
NACA	National Advisory Committee for Aeronautics
NASA	National Aeronautics and Space Administration
NI	National Instruments
NSGA	Non-dominated Sorting Genetic Algorithm
NURBS	Non-Uniform Rational Basis Spline
PCB	Printed Circuit Board
PDE	Partial Differential Equation
PIV	Particle Imaging Velocimetry
PLV	Pulsed Light Velocimetry
QDV	Quick Decay Vortex
RANS	Reynolds-Averaged Navier-Stokes
RBF	Radial Basis Functions
RBM	Root Bending Moment
RMS	Root Mean Square
RSME	Root Square Mean Error
SPIV	Stereoscopic Particle Imaging Velocimetry
STD	Standard Deviation
SW	Side-Wing
sGA	Structured Genetic Algorithm
TE	Trailing Edge
TW	Top-Wing
VRM	Vortex Ring Method

CHAPTER 1

INTRODUCTION

1.1 INTRODUCTION

Non-planar wing arrangements can offer significant gains in aerodynamic efficiency relative to conventional planar wing designs, of equivalent span and lift, by lowering the total induced drag. This is achieved via the redistribution of vorticity and manipulation of how it is shed into the wing wake. Numerous non-planar wing/wingtip concepts have been proposed since the late 1970s differing in general arrangement and aerodynamic characteristics. Of these designs, C-wings have been hypothesised to have the unique capability of exploiting and unifying induced drag reduction, aeroelasticity, and flight dynamics. However their capacity to do so is ambiguous. The purpose of this project is to provide an experimental demonstration verifying the C-wing configuration's practical application.

The position of this work in relation to modern aviation is expressly addressed in Section 1.2. A brief overview of non-planar wing design throughout the last century is then discussed in Section 1.3. Subsequently, a more focused discussion is given to outline state-of-the-art knowledge and understanding of the C-wing design. The scope and targeted contributions of this work are then presented in Section 1.4. It is anticipated that the wing design methodology and the wide ranging experimental diagnostic techniques employed make this research a deep contribution to the understanding of the C-wing aerodynamic performance metrics, structural dynamics, and extended effects into the wingtip vortex flow. The guideline of the presentation of the results in the following chapters is described in Section 1.5.

1.2 RESEARCH MOTIVATION

Between now and 2030, there is an estimated global demand for approximately 27,000 new passenger aircraft, potentially worth up to $3 trillion. These aircraft must comply with strategic research agendas developed by the Advisory Council for Aeronautics Research in Europe (ACARE) which aims to enforce strict emission targets by 2050—CO_2 emissions per passenger kilometre to be reduced by 75%, NO_x emissions by 90% and perceived noise by 65%, all relative to the year 2000 [9]. Similarly, the International Civil Aviation Organisation (ICAO) in conjunction with the Federal Aviation Administration (FAA) and the National Aeronautics and Space Administration (NASA) have goals to mature fuel efficient technologies by 2030 in order to meet the same targets as ACARE by 2050 [10]. The impact of aviation on the environment is now a main driving factor affecting the designs of future aircraft [11]. In recent years, the potential for hybrid electric, or even full electric, aircraft has received a great deal of attention with most indicating the need for a fundamental change in the aircraft configuration to drive greatly increased aerodynamic efficiency [12, 13, 14].

In the cruise phase of large transport aircraft, typically 90% of the total flight time, the induced drag is relatively lower than the parasitic drag but still contributes 40 to 45% of the total drag budget [15, 16]. At critical take-off conditions the induced drag typically accounts for 80 to 90% of total drag [17]. According to Airbus, a 1% reduction of the total drag for an A340 aircraft operating over long ranges saves 400,000 litres of fuel and consequently 5000kg of noxious emissions per year [18]. If this drag reduction were to be directly correlated to induced drag, lower noise emissions would also be achieved. In fact, the primary trend of wing design specification for commercial transport aircraft over the last 70 years has been to increase the aspect ratio and flexibility (reducing weight) such that more optimal lift distributions (and thus lift-to-drag ratios) could be achieved [19, 20]. In the same time period, commercial interest in non-planar wingtip devices (winglets), whether purpose designed or retrofitted to older fleets, to passively reduce the wing induced drag in take-off, climb, cruise, and descent phases (for a fixed wingspan) is evident [17, 21]. However, the lift distribution of today's modern aircraft are already tightly optimised for compromise between aerodynamic loading, structure, physical size, stability and control, safety, *etc.*, any significant reductions of induced drag cannot be easily obtained, and indeed, there have been several high-fidelity optimisation strategies that strive to further optimise conventional planar wings [22, 23, 24].

Albritton et al. [1] compiled Rolls-Royce plc data to show the steady improvement in fuel efficiency for long-range commercial aircraft between the late 1950s to the 1990s, which was published in the Intergovernmental Panel on Climate Change (IPCC) Special Report on Aviation and the Global Atmosphere [25]. Figure 1.1 presents this data, with post year 2000 data adapted from Serrano-Bernardo et al. [2], Bickerstaff

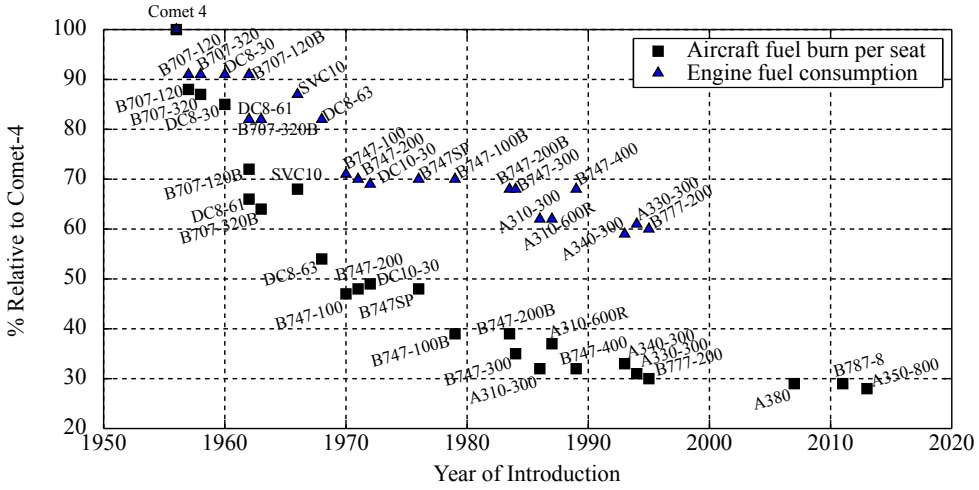

FIGURE 1.1: Fuel efficiency improvement for long-range commercial transport aircraft. Data adapted from Arbritton et al. [1], Serrano-Bernardo et al. [2], and Bickerstaff [3].

[3], and Peeters et al. [26]. With the Comet-4 used as a benchmark, it is claimed that modern aircraft of the mid 1990s have a 70% higher fuel efficiency (aircraft fuel burn per seat); 40% of which is due to the engine and 30% to the airframe [1]. It has been claimed by several studies that the trend of increasing aircraft fuel efficiency is plateauing because of two primary reasons: 1) aerodynamics of the traditional 'tube-wing' design and the already mature bypass engine technology is stagnating [1, 27, 28]; and 2) a combination of social and economic factors have left the aviation industry with low incentive to innovate, leading to slowed technological development [29].

Modern aircraft, at least aesthetically, appear relatively unchanged compared to their ancestors and although this similar appearance belies significant reductions in fuel usage (as shown in figure 1.1) and operational costs, certain measures of aerodynamic performance have seen little change in decades. Liebeck et al. [30] demonstrated that between 1960 to 1990 there was very little (or no) progress in the overall aerodynamic efficiency of commercial aircraft, although it would be somewhat naive to state that no aerodynamic advancements have been made since the 1950s. Advances in modern aircraft aerodynamics have actually served in the design stages where trade-offs for other disciplines have been made to improve the economics of the aircraft [31]. For example, the ability to increase the thickness-to-chord ratio of a wing while maintaining the lift-to-drag ratio reduces the structural weight of the wing, thus providing improved weight allowances for payload and/or additional fuel. However, such conclusions have raised concerns about the commercial aviation industry and its ability to keep up with new transportation systems and attract investment [32].

Sun et al. [33] recently presented a comprehensive study weighing continent-wide air travel verses high speed rail (HSR) transportation with focus on passenger demand, transit time, ticket price, frequency of use, environmental impact, and social welfare. Their results indicate that while the infrastructure of HSR systems are not as mature,

existing systems outperform air transportation, also demonstrating better resilience to disruption. Such studies emphasise the requirement for the aviation industry to innovate at a faster pace—especially with new and competitive transportation concepts such as the *Hyperloop* emerging which have the potential to be faster, safer, and cheaper [34, 35, 36, 37].

Commercial aviation is the most scrutinised and closely watched transportation system, and due to this heritage of technology has become important. This encourages low-risk innovations which result in small incremental changes to suit social attitudes and the integration new aircraft fleets into a fixed world-wide airport infrastructure. One of the major challenges faced today in aviation is the problem of improving flight safety in the airspace surrounding airports due to the combination of close proximity air traffic and subsequent wingtip vortices [38, 39, 40, 41, 42]. In particular, the encounter of an aeroplane during take-off or landing with the wake generated by a preceding aircraft can pose a serious hazard which is particularly dangerous because it occurs near the ground. Loss of control and altitude, and strong structural loads, are some of the dangers that the following aeroplane may suffer if subjected to the vortex wake of another aircraft; this interaction has led to the injury and deaths of passengers [42, 43, 44, 45]. As a result, regulations require aircraft to maintain set distances behind each other and set time intervals between landings and take-offs; this consequently leads to increased operating costs and airport congestion. For new aircraft fleets to be designed in such a way as to radically reduce the the wingtip vortex strength, and consequently lift induced drag, perceived aircraft noise, and overall environmental impact, technological advances in the aircraft aerodynamics must be leveraged.

A potential step forward in air transportation, addressing all of the aforementioned challenges faced by aviation today, is the introduction of disruptive technological advancements which may result in unconventional aircraft configurations [46, 47, 48]. Non-planar wing configurations have been widely recognised as a means of reducing total drag compared to conventional planar wing systems of the same span and lift [17]. A number of unconventional configurations have so far been proposed including the blended-wing-body [30, 49, 50], C-wings [51], polyplane, ring wings [52], box wings [53], and joined wings [54, 55, 56], including strut- and truss-braced wings [57, 58, 59]. However, very few exploratory experimental investigations have been conducted on such configurations. Among these non-planar wing arrangements, the C-wing is hypothesised to have an inherent ability to exploit and unify induced drag reduction and accelerate the vortex wake decay, aeroelastic control, and flight dynamics [51, 60].

1.3 NON-PLANAR WING DESIGN

1.3.1 REVIEW OF NON-PLANAR WINGTIP DEVELOPMENT

The first functional use of a non-planer wingtip geometry was achieved by Scottish engineer Somerville [61] in 1910. The wingtip geometry can be seen in figure 1.2, installed on Somerville's biplane design. Described as 'up-curled wing ends', the wingtip geometry was used to enhance the lateral stability of a biplane.

Fundamental investigations into non-planar wingtip geometries, which consisted of only simple end-plate attachments, did not begin until decades later [62, 63, 64]. These end plates were shown to increase the effective span of the wing. Whitcomb [21] found that carefully designed high aspect ratio end-plates were able to provide significant gains in efficiency compared to that of a planar wing of equivalent span and lift; improving the lift-to-drag ratio by nearly a factor of two when compared to a tip extension of equivalent root bending moment. A schematic illustration of the Whitcomb winglet is shown in figure 1.3.

At the same time, another study by Heyson et al. [65] considered the relative advantages of winglets and wingtip extensions. It was concluded that for an equivalent increase in root bending moment, winglets provided a greater induced drag reduction relative to a wingtip extension. Later, Jones and Lasinski [66] conducted a numerical study comparing winglets and tip extensions with different weight constraints. It was concluded that the winglet did not provide a definitive advantage over a tapered wing extension due to structural considerations. Kroo [67] also found that winglets provided no definite advantage over planar wings. Asai [68] concluded that the trade-off between the induced drag and the wing root bending moment alone was not enough to determine the effectiveness of winglets, stating that the reduction of induced drag achieved by winglets would be offset by the additional wetted area that did not contribute to lift: increasing parasitic drag. Thus, tip extensions were found to provide a slight improvement over winglets.

van Dam [69] investigated highly curved wing configurations inspired by fish

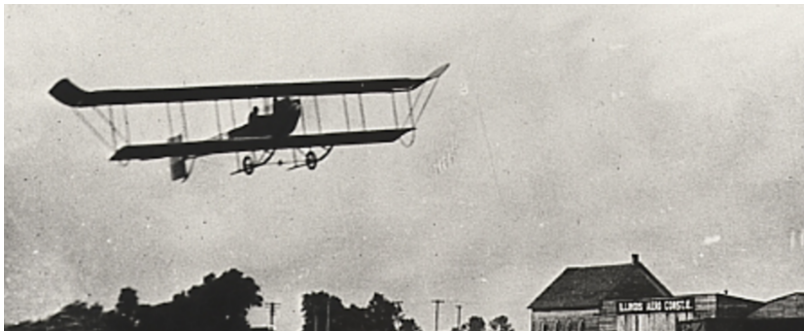

FIGURE 1.2: Somerville's biplane flying in Illinois, USA. Image credit: The Coal City Public Library.

caudal fins which produced non-planar wings at angle of attack, and suggested that these geometries could provide significant induced drag savings. Later studies identified that much of the optimistic improvement was attributed to numerical inaccuracies [70]. However, the idea of exploiting planform shape does hold merit. Smith [71] supported this in planar split-tip investigations showing up to 10% drag reductions relative to an optimally loaded planar wing.

More recently, the improvement and tailoring of non-planar wingtip geometry performance has become a primary research interest. Several studies exist, both numerical and experimental, which vary the winglet cant angle to investigate effects on the wing performance and the near field vortex wake structure [72, 73, 74, 75]. Similarly, the relative performance between different wingtip devices is of interest. Mostafa et al. [76] compared a planar wing with, and without, spiroid and simple winglets to compare performance metrics within a commercial CFD package. This study suggests that increased non-planar geometry complexity offers superior gains in terms of vortex suppression and overall drag reduction. Mann and Elsholz [77] came to a similar conclusions experimentally, comparing a wingtip fence, a large blended winglet and a Kuchemann tip in both high lift and cruise conditions.

Due to the vastly different flow conditions experienced at the wingtip under different flight conditions, achieving an optimal winglet shape for the entire flight envelope is unlikely. To compound this, recent work by Giuni [78] shows that despite the wide ranging studies conducted on the fundamental aspects of wingtip vortices, gaps in the literature remain in regard to vortex formation and early wake development for even simple wingtip (planar) geometries. Due to this, most wingtip device attempts are purely experimental in nature; ten of the most notable wingtip devices are shown in figure 1.3. Unfortunately, the general lack of the winglet local-flow-field understanding makes it challenging to explain experimental results, and uncover proper improvement directions for future designs.

The diversity of wingtip devices shown in figure 1.3 reflects the lack of consensus within the field, with each device differing in their general arrangement of lifting surface geometry, resulting in different aerodynamic characteristics. Additional

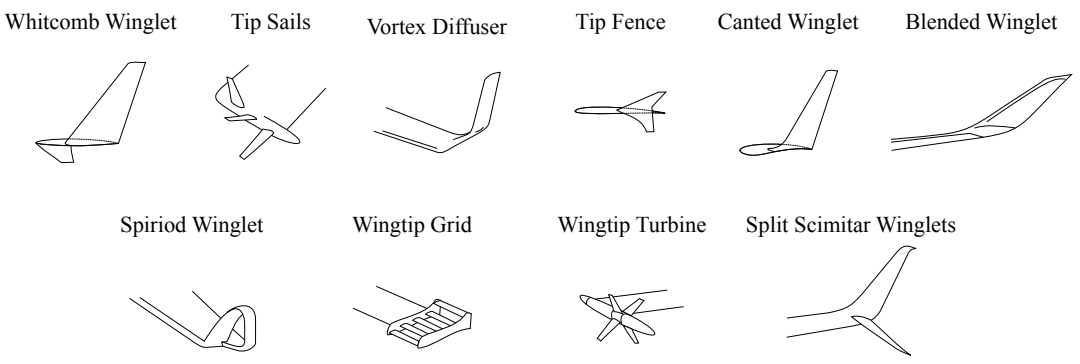

FIGURE 1.3: Notable non-planar wingtip devices.

information on each of the devices shown in figure 1.3 is provided here: Whitcomb winglet [21]; tip sails [79]; Lockheed Martin's vortex diffuser [80]; Airbus' A310 wingtip fence [81]; 'classic' canted winglets such as that on the A330/A340 or the Boeing 747/757/767; blended winglets such as Airbus' Sharklet [82, 83]; spiroid winglet [84, 85]; wingtip grid [86, 87]; wingtip turbine [88, 89]; and Boeing 737's split scimitar winglet [90, 91].

Optimisation of a winglet geometry is typically based on the results from a large population of samples, from either computational and/or wind tunnel experiments, from which statistical approaches, such as a Pareto-front, can help identify complex design trade-offs. This approach to modernise existing winglet designs enables multi-disciplinary design insight, however the results only enable the refinement of a predefined initial design rather than a novel one [92]. Recent winglet geometry optimisation studies over the last decade have mostly focused on cruise as a single-point design case for the wingtip device, resulting in solutions which are grossly sub-optimal in off-design conditions [92, 93, 94, 95, 96, 97, 98]. In order to compensate for wide sub-optimality, multi-point optimisation would have to be adopted to increase performance over a broader range of the flight envelope, however such studies to date have been limited to planar wing optimisations [22, 24, 50, 99, 100].

In an attempt to accommodate a broader flight envelope, several active winglet devices have been suggested including: winglets with integrated control surfaces [101]; morphing winglets which adapt their cant and/or twist distribution depending on the flight condition [102, 103, 104]; and oscillating winglets for active vortex wake manipulation [105, 106, 107]. Other studies have also suggested the implementation of plasma actuators as an active method to enhance, or entirely replace, passive winglet technology [108, 109]. Bio-inspired devices have also been investigated with multiple variable triangular leading-edge extensions [110]. With multiple elements, in which each element is set at a given angle contributing at a certain flight regime, overall efficiency can be sustained [111, 112]. To date, none of these solutions have found application on an operational airliner, due to their complexity and energy consumption which compromises reliability and involves a weight penalty. These factors combined are likely to cancel any potential aerodynamic efficiency gain.

1.3.2 UNCONVENTIONAL DESIGN: THE C-WING

Closed non-planar lifting surface arrangements include ring wings [52], box wings [53], and joint wings [54, 55, 56]. Such arrangements are often considered the most capable passive means of reducing the strength and associated influence of wingtip vortices [56, 113, 114]. C-wings have been considered a compromise between a box wing and a winglet; theoretically providing a reduction in the induced drag that approaches that of the closed box wing arrangement [48, 114, 115, 116] whilst additionally reducing the viscous drag penalty incurred by large wetted areas [5, 117]. In fact, the box wing

arrangement among all non-planar configurations was shown by Prandtl [118] to offer the *"best wing system"*, achieving the minimum possible induced drag for a given lift and height-to-span ratio [119].

The C-wing has also been recognised to have the potential to replace the conventional horizontal stabiliser to provide pitch control [51, 113]. However, owing to large and heavy wingtip extensions, the C-wing is inherently sensitive to structural and aeroelastic issues; they are not closed systems like box wing arrangements which are, by comparison, much stiffer as the upper wing is fixed. Despite the aeroelastic concerns that C-wings are seemingly prone to, conceptually the auxiliary lifting surface at the main-wing wingtip could be used to introduce substantial damping to modes of vibration [120].

In consideration of aerodynamic properties alone, Gage [115] identified the C-wing configuration as an optimal solution while attempting to minimise the induced drag of a planform with fixed lift, span and height. Slingerland and Verstraeten [121] used a low-fidelity potential flow model with a drag-free wake to conclude that with a constrained wingspan, winglets were able to provide drag reductions on the order of 5%, but no significant advantages were found using C-wing configurations. Ning and Kroo [94] conducted a similar investigation taking into account the area-dependant weight, effects of critical structural loading, and stall speed constraints. They concluded that C-wings achieved a lower net drag compared to winglets for a constant positive pitching moment about the aerodynamic centre, especially for wing planforms with span constraints and low sweep. Looking at aeroelastic design trade-offs, Jansen et al. [5] used a medium-fidelity aerostructural panel code approach to show that for maximum induced drag efficiency a box wing configuration was optimal. When compensating for viscous drag effects alone, the C-wing configuration was preferred. However, when structural considerations were taken into account, the C-wing and box wing configurations were found to add more structural weight than their respective drag reduction potential could compensate for; *i.e.* the reduction in induced drag was not worth the gain in structural weight.

Gagnon and Zingg [122] later performed high-fidelity aerodynamic shape optimisation for several non-planar aircraft concepts: a blended-wing-body with C-wings, a box wing, and a high-aspect ratio strut-braced wing. They identified that C-wings provided much greater span efficiencies under optimal loading, however encountered difficulties when optimising the C-wing. By only accounting for variation in the C-wing's horizontal extension span and dihedral, at a fixed height and stagger, the configuration could not be properly optimised. The optimiser attempted to unfold the C-wing in favour of a winglet of increased length. Therefore, the authors conclude that C-wings do not appear to offer any significant benefits over winglets but do point out that more research is needed to confirm this as C-wings offer the opportunity for tailless aircraft with substantially reduced total wetted areas.

Bauhaus Luftahrt [123, 124, 125] numerically investigated the development of a

C-wing configuration designed for a tailless electric passenger aircraft. The concept was suggested to be able to achieve pitch control and trimmed flight, but the ability to achieve induced drag reduction while maintaining pitch stability requires more evidence. Airbus [60] has also shown interest in the C-wing due to its ability to exploit and unify drag reduction, aeroelasticity, and flight dynamics and control. It is suggested that longitudinal stability requirements cannot be met if significant reductions in induced drag are pursued. The performance improvement due to induced drag reduction was lost due to the increased wing weight necessary to provide control authority. Aeroelastic design constraints of the C-wing, to avoid flutter and divergence, were able to be met in the optimisation design problems when provisions were made to not use the top-wing to provide longitudinal control authority. This reduced the weight of the outboard wing section.

Potential aerodynamic benefits of C-wings have also been realised by Suresh et al. [126], who used a commercial computational fluid dynamics (CFD) package to compare a planar wing with and without an arbitrary C-wing extension. Inviscid simulations with a Mach number of 0.85 and Reynolds number of $\approx 10^8$ conclude that the lift-to-drag ratio increased for low angles of attack, however this is the result of large increases in both lift and drag. Parasitic drag, wing loading and/or moments were not taken into account in this study. Following on from this work Gobpinaath et al. [127] present a combined numerical and experimental investigation of C-wings at low Reynolds numbers ($\approx 1.8 \times 10^5$). They observed that the C-wing can achieve improved lift-to-drag ratios in the range of $2 \leq \alpha \leq 6$ compared to an equivalent planar wing.

Most recently, Skinner and Zare-Behtash [120] presented a C-wing arrangement capable of total drag reductions of up to 9.5% while demonstrating the capability to simultaneously reduce the root bending moment by $\approx 1\%$. This is relative to a planar wing of equivalent lift and wingspan at $Re = 1.5 \times 10^6$. Furthermore, this work demonstrated the C-wing's ability to attenuate buffet induced vibration of the wing under high lift conditions by up to 68%.

1.3.3 THE C-WING ARRANGEMENT

The C-wing configuration is a three element wing system consisting of a side-wing and top-wing mounted at the wingtip of the main-wing, as shown in figure 1.4.

C-wings differ from other multi-element configurations (such as a biplane or canard) as the secondary surface is designed to produce a down-force, thereby acting against useful lift [48]. Typically non-planar wing configurations attempt to reduce induced drag contributions by scheduling the loading on each of the lifting surfaces. The C-wing theoretically achieves drag reduction via two mechanisms [123, 125]: 1) alteration of the main-wing load distribution by promoting a less pronounced decrease in local lift at the main-wing wingtip; and 2) forward tilting of the lift vector of the

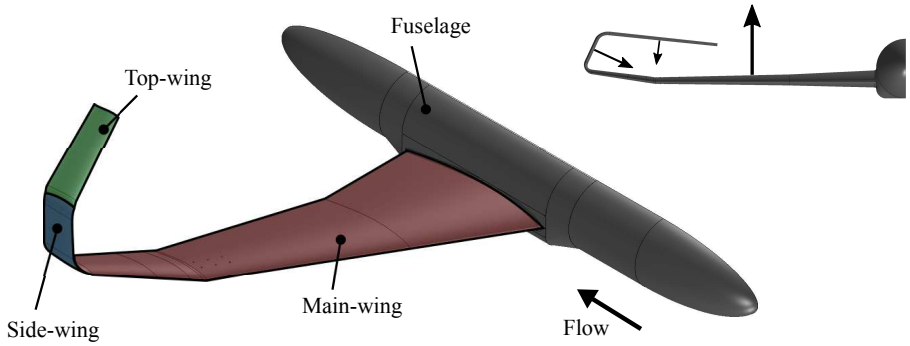

FIGURE 1.4: C-wing layout with positive direction of span-loading on each surface indicated.

top-wing where the main-wing's downwash is exploited to produce a thrusting effect. If designed appropriately, winglets, and non-planar wingtip variants, can be made to show aerodynamic advantages when compared to conventional designs but often fail as they usually lead to structurally heavier wings, due to increased root bending moment, with detrimental increases in parasitic drag. The C-wing is thought to be capable of overcoming these issues.

The optimal loading condition indicated in figure 1.4 indicates that the circulation of the main-wing is carried onto the side-wing, acting much like a winglet, thus loaded inward toward the fuselage [48]. The circulation is then further extended onto the top-wing producing a net down-loaded surface for minimum induced drag at a fixed total lift and wingspan. The goal of minimising the induced drag of the system requires the gradients of circulation, where possible, to be minimised [118]. Conventional planar wings shed strong vortices at the wingtips and the circulation tends to zero. Hence, distributing the vorticity in the wake over an effectively longer wingspan would reduce the wake sheet intensity, in addition to moving the wingtip vortices closer together than that for a conventional wing, accelerating the breakdown of the wake system [51]. The down-loading of the top-wing surface will naturally have an effect on the structural weight, performance and control, and may provide a means of stability that is less affected by the main-wing downwash such as conventional horizontal stabilisers.

1.4 AIMS AND OBJECTIVES OF RESEARCH

Conclusions and understanding of the performance of C-wing configurations, whether positive or negative, are conflicting. Numerical investigations vary depending on the specific design problem considered and the fidelity/scope of the physics models used. This is compounded by the distinct lack of experimental wind tunnel data for validation. Thus, the aim of this work is to provide an experimental demonstration to

quantify the C-wing's practical application through an exploratory proof-of-concept study.

The main objectives of this work are as follows:

1. Development a novel population structured genetic algorithm to facilitate the topological design optimisation candidate planar wing and C-wing designs for progression to wind tunnel tests. This required the establishment of a low fidelity aerodynamic model capable of capturing the flow physics with sufficient accuracy to guide design decisions.
2. Design and manufacture of a custom-built semi-span wing/fuselage wind tunnel model capable of housing alternative wing configurations while maintaining baseline structural dynamics. This objective required wind tunnel modification and benchmarking.
3. Quantify the flow field associated with the application of an unconventional peniche-less semi-span wind tunnel model. This details a systematic approach to assess how variation in the stand-off gap height alters the aerodynamic performance metrics of the semi-span model, and the fluid dynamic mechanisms that drive them.
4. Quantify the ability of the C-wing to provide drag reductions; this has not been studied within relevant literature.
5. Quantify how the C-wing alters the wing's structural dynamics and static aeroelastic behaviour.
6. Investigate the trailing vortex wake system produced from both the planar wing and C-wing arrangements, and subsequently examine the mechanisms for drag reduction and other associated advantages the C-wing may facilitate.

Both qualitative (surface flow visualisations) and quantitative (stereoscopic particle imaging velocimetry, force platform, pressure measurements, digital image correlation, laser-Doppler vibrometry, and accelerometry) techniques have been utilised to achieve the above objectives.

1.5 STRUCTURE OF THESIS

Following this introduction, the thesis is divided into the following sections:

Chapter 2 describes the development of an exploratory design optimisation architecture for the purpose of developing two wing designs: 1) a baseline planar wing; and 2) a non-planar C-wing. These wings are designed to have equivalent wingspan, lift, and root bending moment.

Chapter 3 presents a detailed account of both the de Havilland wind tunnel and the custom built semi-span wind tunnel model. The experimental apparatus and

techniques adopted to conduct this work are also described here.

Chapter 4 investigates how variations in the peniche-less semi-span model's stand-off gap height influences the aerodynamic behaviour of the model by altering the wind tunnel's boundary layer interaction with the stand-off gap.

Chapter 5 explores the C-wing performance relative to the planar wing of equivalent wingspan, lift, and root bending moment. Drag reduction capability and the C-wing's effect on the wing structural dynamics and aeroelastic behaviours are of primary focus.

Chapter 6 investigates the wingtip vortex development in the early wake for the planar and C-wing configurations. A comparison and critical discussion of methods for correcting the vortex meander is presented. Subsequently, the planar wing and C-wing early vortex wake systems are examined to understand the fluid dynamic mechanisms which drive the C-wing's induced drag reduction. Secondary benefits unique to the C-wing arrangement are also explored.

Chapter 7 presents the main conclusions of this study, along with recommendations for future work to be conducted.

Appendix A presents the numerical convergence analysis of the vortex ring method.

Appendix B presents a discussion on the accuracy and error of the SPIV measurements.

Appendix C includes details of the statistical convergence of the SPIV data, including errors involved in the current study. The degree of repeatability and random uncertainty of the experimental arrangement is also given.

Appendix D provides a comparison of the vortex ring method to the wind tunnel data for the planar wing and C-wing configurations.

Appendix E gives a description of the of the universal (or self-similar) behaviour of the radial distribution of circulation within the planar wing vortex core.

1.6 RELATED PUBLICATIONS

JOURNAL PUBLICATIONS

Skinner, S. N., and Zare-Behtash, H. (2017). Semi-span wind tunnel testing without conventional peniche. Experiments in Fluids, 58(163).

Skinner, S. N., and Zare-Behtash, H. (2018). State-of-the-art in aerodynamic shape optimisation methods. Applied Soft Computing Journal, 62, 933-962.

Skinner, S. N., and Zare-Behtash, H. (2018). Study of a C-wing configuration for passive drag and load alleviation. Journal of Fluids and Structures, 78, 175-196.

Skinner, S. N., and Zare-Behtash, H. Topological design optimisation of a C-wing arrangement. (Under preparation for submission). Numerical Methods in Fluids.

Skinner, S. N., and Zare-Behtash, H. Dissipation and rapid decay of wingtip vortex using a C-wing arrangement. (Under preparation for submission). Journal of Fluids and Structures.

Skinner, S. N., and Zare-Behtash, H. Spatial localisation methods for vortex meander. (Under preparation for submission). Experiments in Fluids.

Skinner, S. N., and Zare-Behtash, H. Investigation of the wingtip vortex development in the near field of a swept and tapered wing model. (Under preparation for submission). Experiments in Fluids.

CONFERENCE PUBLICATIONS

Skinner, S. N. and Zare-Behtash, H. (2014). Fluid structure interactions of non-planar wings. In: Greener Aeronautics Symposium, Glasgow, UK.

Skinner, S. N. and Zare-Behtash, H. (2015). Aerodynamic and stability optimisation of non-planar wings. In: The Aerospace Ecosystem, Glasgow, UK.

Skinner, S. N., and Zare-Behtash, H. (2016). Aerodynamic optimisation of non-planar lifting surfaces. In 57th AIAA/ASCE/AHS/ASC Structures, Structural Dynamics, and Materials Conference, AIAA 2016-0164 (pp. 1-21). San Diego, California.

1.7 RELATED RESEARCH GRANTS

1. July 2016: Private investment into this research from Zephyr Business Solutions through the UK National Wind Tunnel Facility consortium for the purpose of funding wind tunnel model manufacture; grant number: 74603.
2. November 2016: Royal Aeronautical Society Centennial Scholarship 2016 for the purpose of funding wind tunnel model manufacture; grant number: 21-657/A-SKI.

CHAPTER 2

DESIGN OPTIMISATION AND ANALYSIS OF WING ARRANGEMENTS

2.1 INTRODUCTION

This chapter describes the development of an exploratory design tool for the purpose of developing two wing designs: a baseline planar wing and a non-planar C-wing, to progress to a wind tunnel experimental campaign. The design tool applies fundamental aerodynamic theory to investigate potential wing design solutions that meet design specifications and experimental facility constraints. Thus, wing solutions are related in their design optimisation architecture, with the same design criteria and underlying physics, additionally facilitating that wing designs selected for the experimental campaign are not arbitrary.

Section 2.2 explores general considerations to be made for aerodynamic shape optimisations, the problem definition, identification of appropriate optimisation approach, and geometric representation of selected design variables. Following this, Section 2.3 discusses the development of the optimisation algorithm; specifically a population structured genetic algorithm. The aerodynamic analysis model used by the optimisation procedure to guide exploration and identification of superior wing solution topology, within a defined design space, is subsequently reported in Section 2.4. Section 2.4 also covers the theory, development, and experimental validation of a vortex ring potential flow analysis tool. Using the optimisation architecture developed, Section 2.5 presents four preliminary wing topology optimisations of increasing complexity. This led to the design optimisation of the planar wing and C-wing arrangements selected to be carried forward to wind tunnel testing. Section 2.6 summarises the main findings of the chapter.

2.2 GENERAL CONSIDERATIONS FOR AERODYNAMIC OPTIMISATION

The difficulty in any aerodynamic optimisation is the ability to define an analysis method that is sufficiently simple to operate numerous times within a parametrised search space, but is sophisticated enough to capture enough consideration that determines a local geometry that feeds into a globally optimal system [128]. The overall optimisation procedure, limited by computational resource, must be able to navigate the required design space with the ability to capture enough information from performance simulations to make 'good' design decisions. These design decisions should guide solutions toward feasible design spaces, defined by design constraints, while manipulating solutions to ensure the betterment of the optimisation objectives. Hence, before an appropriate simulation platform can be established, the scope, complexity, modality, dimensionality, and continuity of the design space and how it must be navigated via an optimisation algorithm must be considered.

2.2.1 BASIC PROBLEM FORMULATION

The field of optimisation is expansive, and the choice of a suitable algorithm is highly problem dependant [129]. A general optimisation problem can be presented mathematically as [130]:

$$
\begin{aligned}
&\textit{Minimise} \left\{ \begin{array}{lll} f(\mathbf{X}) & & \textit{Objective function} \end{array} \right. \\
&\textit{With respect to} \left\{ \begin{array}{lll} \mathbf{X} & & \textit{Design variables} \end{array} \right. \\
&\textit{Subject to} \left\{ \begin{array}{lll} g_i(\mathbf{X}) \leq 0 & i = 1, l & \textit{Inequality constraints} \\ h_j(\mathbf{X}) = 0 & j = 1, l & \textit{Equality constraints} \\ X_k^l \leq X_k \leq X_k^u & k = 1, N_{DV} & \textit{Parameterised constraints} \end{array} \right. \\
&\textit{where } \mathbf{X} = \left\{ \begin{array}{c} X_1 \\ X_2 \\ \vdots \\ X_{N_{DV}} \end{array} \right\}
\end{aligned}
$$

Most optimisation methods use an iterative procedure. The initial set $\mathbf{X}$ design variables, which in the context of aerodynamic optimisation is referred to as the baseline configuration, is updated until a minimum objective function, $f(\mathbf{X})$, is identified or the optimisation process runs out of allocated time/iterations. In the initial set-up of the optimisation problem consideration must be given to: 1) the level of information fidelity required from the flow solver, which is dependant on the type of problem; 2) scope of parametrised design space; 3) types of design variables, *i.e.* discrete and/or continuous; 4) single or multi-objective optimisation; 5) constraints handling; and 6) properties of the design space, e.g. number of local optima, discontinuities. It is important to acknowledge that no optimisation procedure guarantees that the global optima of the objective function will be found: the process may only converge towards a locally optimal solution. Typically in this situation there are three possibilities: 1)

restart the optimisation process to investigate whether the same solution is found; 2) approach the design problem with a different optimisation methodology to compare solution quality at a high computational expense; or 3) accept the optimum obtained knowing that while it is superior to the baseline configuration it may not be the optimal solution.

In the design case considered here, an optimisation algorithm is required to provide a design tool that ensures experimental constraints and design criteria are adhered to. For example, wing design specifications will be constrained by the test facility limitations which will limit the physical size of the wing (relative to the wind tunnel working section), and maximum allowable forces/moment dictated by mounting systems and diagnostic equipment. In addition, the design space for a C-wing configuration (while largely dictated by the physics solver employed) is not well understood, and consequently neither is the required design space properties. Furthermore, there is no way to select a suitable starting design of the wing arrangement—any user-defined starting design would be entirely suboptimal and arbitrary.

Based on the conclusions of a comprehensive review of 229 aerodynamic optimisation studies conducted by Skinner and Zare-Behtash [131], genetic algorithms (GA) have been identified as a suitable class of optimisation algorithm for the design task considered in this work. These algorithms are often praised for their ability to explore and exploit solutions simultaneously due to their inherent stochastic, population based, multi-start capability; thus no specific starting design point is required. This also provides a platform for parallel processing, enabling the optimisation of multiple designs simultaneously. They are also capable of constructing insightful design trade-off relationships, referred to as Pareto-fronts, between objective functions in a multi-objective design space. GAs are well-suited to complex optimisation tasks, as they can use both discrete and continuous design variables, and are insensitive to any non-linearity, non-convexity, and discontinuity present within the design space; unlike gradient-based methods which are completely dependant upon the existence of smooth and continuous mathematical relationships in the design and objective spaces.

The main drawbacks of GAs are associated with their high computational cost, placing limitations on their scalability and how many design variables are computationally feasible to handle, the fidelity of physics solvers employed, inherently poor constraint handling capabilities, and the requirement for problem specific tuning. Furthermore, studies have shown that GAs are very fast to identify design regions of optimality, but demonstrate rapidly slowing rates of convergence as solutions within the GA population become increasingly more optimal [129]. Some studies have tried to build on the classical GA to enhance its applications to aerodynamic optimisation, demonstrating that with architectural tailoring the classical GA can achieve mitigation of the aforementioned drawbacks [132, 133, 134].

2.2.2 REVIEW OF DESIGN VARIABLES AND GEOMETRIC REPRESENTATION

In general, it is necessary to implement geometric parametrisations in such a way that they reduce the complexity and cost of the optimisation process but do not restrict the communication of variables or the degree to which aerodynamic performance is optimised. Parametrisation aims to balance the fundamental compromise between computational speed of the optimisation run-time, favouring a tight parametrisation. Zhang et al. [135] shows that the defined dimensionality of a problem for shape optimisations can restrict the optimal design. Using too few variables may prove certain potential improvements impossible; for example, Gagnon and Zingg [122] conclude that limiting design variables to top-wing span and dihedral in the optimisation of C-wings considerably limits the optimisation procedure. Conversely, if too many design variables are used, particularly if variables are strongly coupled, the search landscape can become intractably complex to navigate. Increasing the dimensionality of a given problem excessively leads to a paradox, first addressed by Sobieszczanski-Sobieski [136, 137], in which increasing the number of design variables leads to a decrease in the number of variables that can be manipulated as a direct result of increased coupling. It is often desirable to limit the allowable design variables to avoid geometries that cannot be evaluated with sufficient accuracy by the flow solver: due to meshing (discretisation) limitations for example. Furthermore, this can help avoid geometries that are unacceptable in terms of some criteria, or similarly, restrict the optimisation to geometries that are necessary for other criteria. Regardless of the user defined parametrisation, the final design is most definitely suboptimal—often limited by parametrisation [138].

Chernukin and Zingg [4] conducted one of the few studies of how the number of variables used and the related modality can affect aerodynamic designs, highlighting that distinguishing between multi-modality and poor optimiser convergence can prove problematic. By increasing the dimensionality of a design space it can be expected, but not guaranteed, to increase the modality of the search space. Initialising 224 random starting geometrics with 368 design variables they demonstrated the presence of at least 8 local optima for a blended wing optimisation, shown in figure 2.1. All 8 solutions satisfied both optimality and feasibility tolerances with the objective value varying by approximately 5% between the local optima. The planform shapes are distinct and so demonstrate that geometric variation is significant between local optima which share similar performance characteristics.

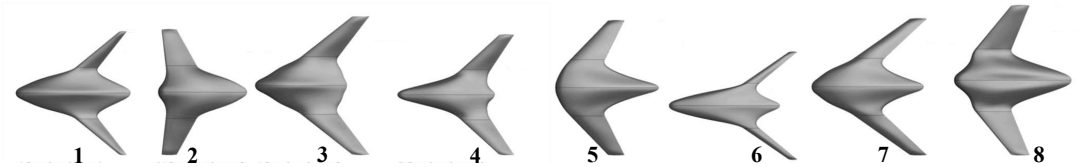

FIGURE 2.1: Eight local optima found in blended wing optimisation [4].

Furthermore, the method of geometric parametrisation used to communicate a set of variables plays an important role in identifying optimal aerodynamics. It determines which shapes and topologies can be represented, and how many design variables are necessary for sufficient representation of the geometry. Thus, parametrisation dictates particular geometric requirements and has a strong influence on the design landscape. Therefore it cannot be precluded that different geometric parametrisations will increase or decrease the degree of modality, linearity, or discontinuity observed. However, it is indicated that a complex geometry parametrisation may impose distinct computational costs. Representations of a geometry can be broken down into a number of categories, but in a more broad sense, they can be considered to be constructive, deformative, or volume based.

Constructive models include functions which define basic body shapes, spline methods (such as Bezier splines, basis splines (B-splines), non-uniform rational basis spline (NURBS)) and partial differential equations. Jansen et al. [5] used a medium-fidelity aerostructural panel code to perform optimisation of conceptual wing configurations, shown in figure 2.2. The basic wing topology was defined through a series of globally enforced geometric variables (*i.e.* sweep, span, taper, etc.) to manipulate a series of wing sections. Parametrising the entire geometry in this way typically allows for simplified global shape control with very few basic variables. This method is well suited to low-fidelity aerodynamic models if a wide allowable design scope of wing topology is necessary—there is no need for mesh deformations.

Constructive spline-based geometric parametrisations are used to represent two- or three-dimensional surfaces and are typically used in conjunction with higher-fidelity flow solvers, such as Euler and Navier-Stokes solvers, with the control points being the design variables. Bezier splines are most efficient to evaluate, requiring few variables and have been used for efficient aerofoil definition by Peigin and Epstein [139]. Modification of any single control point defining a Bezier spline will modify the entire curve, and thus is inherently effective for global shape definition, but has very limited local control. B-splines address this issue of local control, enabling single control point modifications to alter small portions of the overall curve. This allows for more complex aerofoil definitions, as demonstrated by Koziel at al. [140], and can enable the use of hinged control surfaces to an otherwise rigid body. NURBS increase the local deformation control over surface definitions further in order to have more complex geometric shapes such as fairings or wing-fuselage junctions. Vecchia and

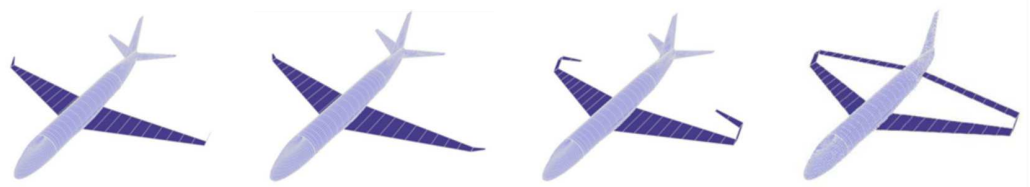

Figure 2.2: Global variables parametrising simple wing geometry [5].

Nicolosi [141] and Hashimoto et al. [142] adopt NURBS to parametrise the entire aircraft configuration in order to reduce the drag of the vehicle through streamlining fillets and fairings. Figure 2.3 shows an example of NURBS control points re-defining the surface over the upper section of the fuselage/wing juncture.

Geometry definition through the use of partial differential equations (PDEs) is not as commonly used as well-established spline-based methods, but is just as versatile for geometry surface definition. Athanasopoulos et al. [143] show that for equivalently complex surface construction PDEs require fewer design variables, resulting in a more compact design space. Due to the small set of design parameters required by the PDE method, the computational cost associated with the optimisation of a given aerodynamic surface can be reduced [144]. In a PDE-based method the parameters are boundary values to the PDE, hence the relationship between the value of the design parameter and the geometry can be unclear making methodical surface deformations tedious. This is likely why the aerodynamic definition of a body in an optimisation scheme does not use PDE representation, even though it may initially seem a more appropriate method. Comparatively, spline-based methods are conceptually simpler and will provide a more direct relationship between design parameters and the resulting geometry and thus allow better control over the range of geometries that can be generated.

If optimisation establishes performance metrics from computational fluid dynamics (CFD), the simplest methods for body surface definitions are deformative ones. In deformative methods the mesh points on the surface of the body are directly treated as design variables [145], and their position can be perturbed by the optimiser in order to generate new shapes. This approach has the significant advantage that any geometry the mesh generation algorithm is capable of generating can be evaluated, however it is likely to require many hundreds of design variables; deformations are therefore usually limited to single degree-of-freedom deformations. A common method used for aerodynamic optimisation is the free-form deformation (FFD) approach which is useful if the the geometry manipulations are particularly complex; FFD is covered in depth by Kenway and Martins [146]. This approach embeds the solid geometry within a FFD

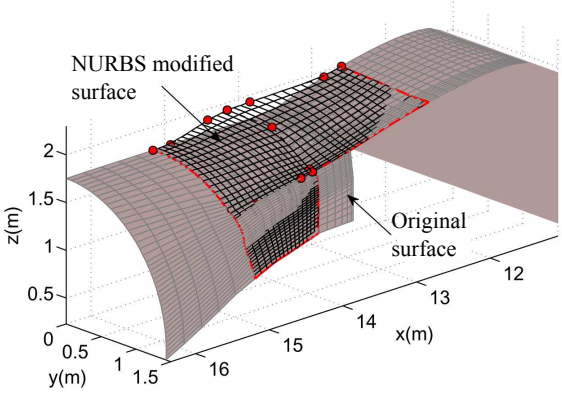

FIGURE 2.3: NURBS surfaces parametrising surface bland on fuselage [6].

hull volume (volumes are typically trivariate analogues of Bezier splines, B-splines of NURBS), which are parametrised by a series of control points. These control points deform the mesh volume which translate to geometric changes of the solid geometry rather than redefining the whole geometry itself (constructive parametrisation), giving a more efficient set of design variables for CFD based optimisation. A key assertion of the FFD approach, when applied within a CFD environment, is that a geometry has constant topology throughout the optimisation process [7]; this is typical of high-fidelity optimisations where the initial geometry considered is sufficiently close to the optimal solution. Figure 2.4 shows the FFD hull volume enclosing a wing with 720 geometric control points used by Lyu et al. [7] with shape deformation control in the vertical (z) axis. The initial random wing deformation and associated optimised wing cross sections at select locations are also shown.

A similar method is based on radial basis function (RBF) interpolation, which defines data sets of design variables and their global relationships. Fincham and Friswell [147] use radial basis functions to optimise morphing aerofoils, and report that they provide a means to deform both aerodynamic and structural meshes, and interpolate performance metrics between two non-coincident meshes.

Volumetric-based body representation has been used for optimisations, but rarely in the field of aerodynamics, a recent review of the applicability of volumetric parametrisation for aerodynamic optimisation is given by Hall et al. [148]. The authors point out the limitations of volumetric representations stating that black-box optimisers cannot be used and even gradient-based methods can often be impractical.

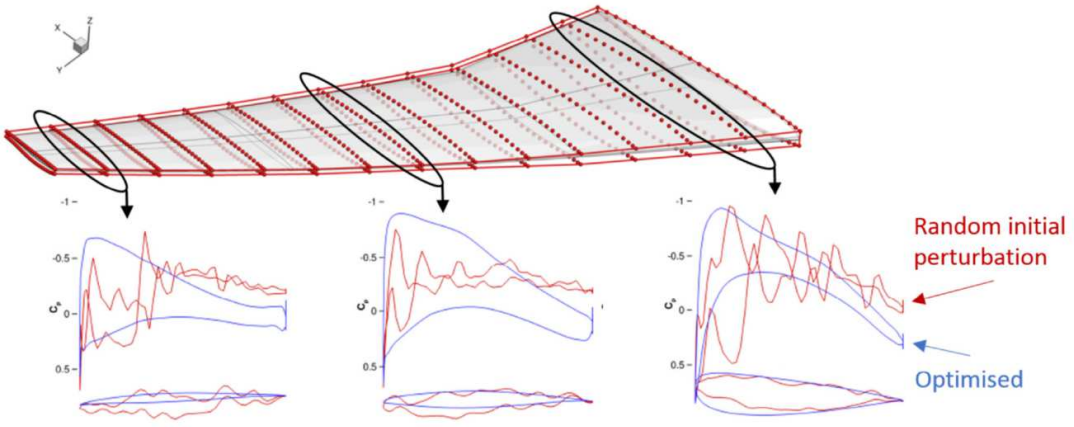

Figure 2.4: Image adapted from Lyu et al. [7] illustrating the free-form deformation of a wing with 720 control variables. Selected wing cross sections and associated C_P distributions are highlighted to show initial perturbed (red), and final optimised (blue) sections.

2.2.3 DEFINITION OF DESIGN VARIABLES AND GEOMETRIC REPRESENTATION USED

The purpose of the algorithm developed in this chapter is to design a non-planar wing topology, relative to some baseline, that is suitable for wind tunnel testing. Thus, to simplify the parametrisation of any single wing solution, an individual wing solution is represented by a series of trapezoidal wing segments. The constructive global geometry of each wing segment is described by a minimum of six design variables: sweep (Λ), span (l), taper (λ), twist (θ), dihedral (Γ), and aerofoil section. Additional variables considered include the root chord (c_{root}), the wing's angle of attack (α), and the outboard wing panel's ($n \geq 4$) ability to reverse the camber orientation of the aerofoil. The geometry description of any wing can be described by an infinite number of wing segments, however in the present study the wing description is limited to a maximum of 5 segments such that the maximum number of variables is limited to 35. The geometric variable description of such a wing is presented in figure 2.5, with variable type and the typical ranges considered summarised in table 2.1.

This geometric definition provides sufficient detail to be solved by either low-fidelity potential flow solvers, or high-fidelity CFD. Due to the nature of the optimisation at hand, coupled with the computational resources available, the defined wing geometries will be evaluated using a potential flow vortex ring panel method which is discussed in Section 2.4.

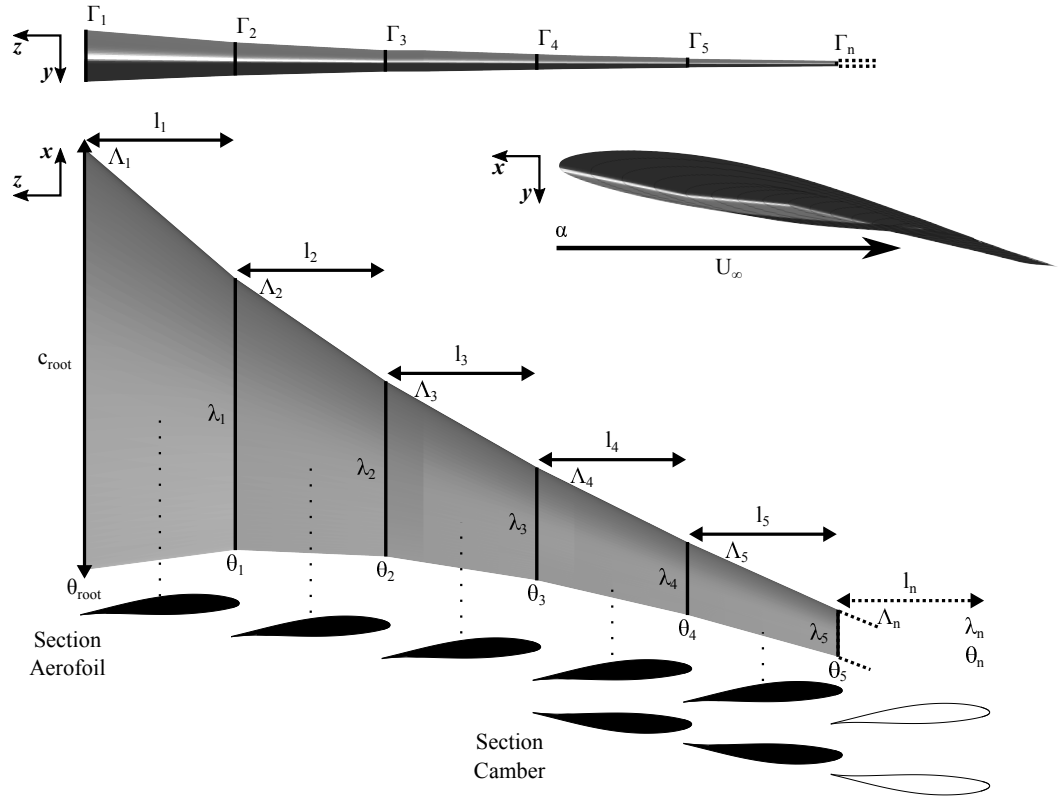

FIGURE 2.5: Design variables in wing topology optimisation.

Table 2.1: Typical variable description.

Variable	Max N$^{o\cdot}$ of inputs	Discrete or continuous	Typical range
Sweep	5	Continuous	$0 \leq \Lambda_n \leq 45$ [deg]
Span	5	Continuous	$0 \leq l_n \leq 2$ [m]
Taper	5	Continuous	$0.1 \leq \lambda_n \leq 1$
Twist	5	Continuous	$-10 \leq \theta_n \leq 10$ [deg]
Root twist	1	Continuous	$-5 \leq \theta_{root} \leq 5$ [deg]
Dihedral	5	Continuous	$0 \leq \Gamma_n \leq 195$ [deg]
Root chord	1	Continuous	$0.5 \leq c_{root} \leq 1$ [m]
Angle of attack	1	Continuous	$0 \leq \alpha \leq 15$ [deg]
Aerofoil	5	Discrete	-
Camber invert	2	Discrete	0, 1

The discretised description of each wing section's aerofoil is generated from a predefined database of aerofoil geometries created to enable the accurate prediction of parasitic drag. This database will be discussed further in Section 2.4.5. Both symmetric and cambered aerofoils are available for selection with a maximum chord to thickness ratio of 15%; a total of 10 aerofoil geometries are available.

2.3 GENETIC ALGORITHM ARCHITECTURE

Genetic Algorithms (GAs) are a population-based optimisation technique inspired by the Darwinian theory of survival of the fittest: a primary aspect of evolution [149]. GAs can be thought of as the propagation of a population of potential mathematical solutions which evolve generation-by-generation by means of natural selection and reproduction, along with the occasional modification though mutation [150].

A GA mimics this process by representing the candidate solutions as chromosomes, describing the individual's genotype, which is decoded to form the solution's phenotypes whose ability to perform is then evaluated via some fitness function determined in numerical simulation. The genotype represents the genetic blueprint (or DNA) of the solution within the design space dictating the rules and traits of that solution. The observable traits of that solution, determined by the genotype, are then reflected by the solution's phenotype; this is what feeds into the numerical analysis. Once the population is analysed, selection pressures drive the selection process of parent chromosomes for reproduction. During reproduction parent chromosomes are recombined to form child chromosomes which enables the propagation of useful schema from generation to generation; this process is referred to as crossover [151]. Child chromosomes are then mutated probabilistically perturbing the solution; this process is referred to as mutation [151, 152, 153]. At this point the population is then re-evaluated and the process repeats until some convergence criteria is met. Figure 2.6

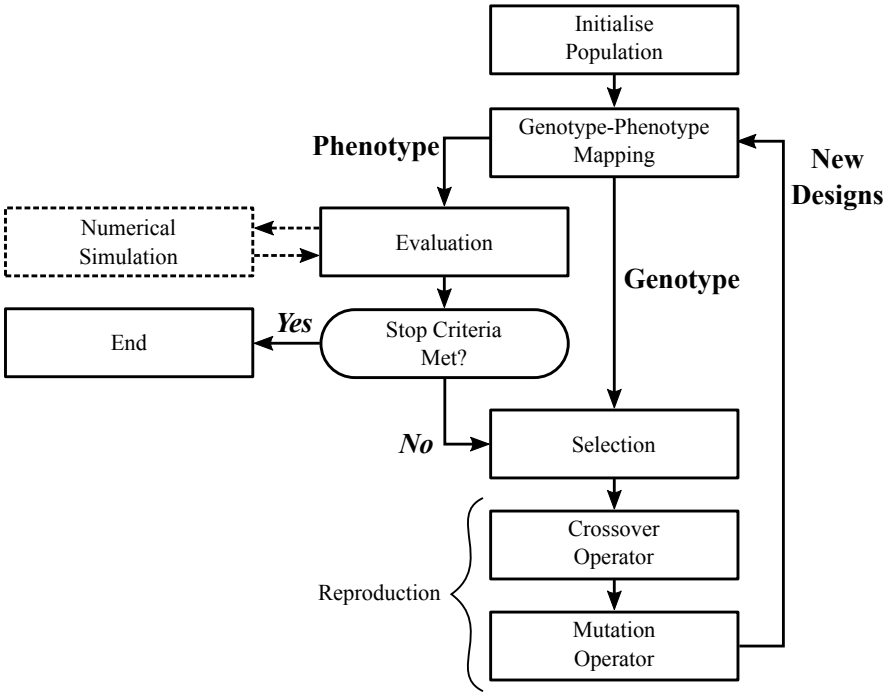

FIGURE 2.6: Schematic illustrating typical genetic algorithm.

illustrates this iterative process.

Key influencers, each posing characteristic difficulties, in the construction of GAs suitable for aerodynamic optimisation problems include: 1) GA population size; 2) selection methods; 3) genetic operations (namely crossover [154, 155] and mutation [151, 153, 154, 156]); 4) genotype-phenotype mapping; 6) sufficient design constraints for adequate problem definition; and 7) computational resource. Insufficient selection of these factors can delay, if not prohibit, the performance of a GA in finding optimal solutions.

2.3.1 GENOTYPE-PHENOTYPE CHROMOSOME MAPPING AND STRUCTURE

Genotype-phenotype mapping is a major influencer in a GAs performance. Traditional GAs use binary encoding [152] to describe the solution's genotype. In binary encoding, the number of exploitable schema is maximised [157] and the algorithm is able to converge quickly to a solution [158], but can yield low-quality solutions when applied with many variables. In binary encoded GAs, string length must be assigned *a priori* giving the algorithm discretised precision; thus, the higher the precision required, the longer the string length resulting in considerably slower performance with increased memory requirements [159, 160]. Avenues for decreasing the length of large binary chromosomes are discussed by McGookin [153].

A particular drawback of binary encoding, which is often overlooked, is the existence of Hamming cliffs in the genotypic search space [161]. This limitation is a consequence of discretising the variables in genotype space via binary chromosomes.

It requires the GA to simultaneously change the genotype bit representation in a very small and precise manner to achieve a more optimal solution. This is obviously an issue in consideration of aerodynamic optimisation, since small changes in a single variable can have a large impact on the overall performance. The probability that stochastic reproductive operators will achieve this is unlikely, while also the binary code does not preserve the locality of points in the phenotype space [162]. Additionally, binary GAs often suffer from bias towards superior solutions in the very early populations due to genetic drift. Genetic drift will encourage premature convergence to sub-optimal solutions and is discussed in detail by Lim [163]. Work towards maintaining a heightened population genetic diversity ensures avoiding premature convergence [164], where diversity is the volume of dissimilarity between individuals within a given population. Non-random mating has been shown to maintain genetic diversity [165]. Massaro and Benini [166] discuss a variety of relevant diversity preserving techniques and compare several binary encoded GA variants.

Real-number encoding is more commonly used to resolve limitations of binary encoding, and is widely confirmed to be more efficient than binary [167, 168, 169, 170]. In real-number encoding the genotype and phenotype spaces share an identical topological structure [160], and has the advantage of dynamic coding and floating point representation to tackle large design spaces that require a continuous design space that would otherwise be discretised [132]. Real-encoding gives a robust search while keeping the string length small and enables the candidate solutions to exist within a continuous design space. This allows the GA population to continuously move towards more promising regions within the design space [171]. The main issue with this is the requirement to have well defined search boundary limits for each variable through explicit constraint management.

Thus, with the design variables encoded as real numbers, the chromosome structure must be defined; in this work a genetic modelling technique called a Structured Genetic Algorithm (sGA), first introduced by Dasgupta and McGregor [172], is used. A sGA uses a multi-layered structure for the chromosomal representation of a solution's genotype, which enables dynamic behaviour of gene variability within the chromosomal description of the solution's phenotype. This leads to an increased design capability of the chromosome and inherently maintains genetic diversity by allowing alternative solution types of varying geometric complexity to exist simultaneously within the population. For example, a planar wing defined by 1 wing segment can exist in a population with a box wing defined by 5 wing segments and a planar wing with winglet defined by 3 wing segments; where each wing solution is described by a different number of design variables. To achieve this, a two-level chromosomal structure is used: Level 1 binary genes, regarded as high level genes, act as a switch that can activate (1) or deactivate (0) genes on the second level; Level 2 real-encoded genes provide the physical description of the solution. Figure 2.7a shows this two-level hierarchical chromosome structure, and figure 2.7b illustrates the chromosomal description of a solution where a change in high level genes facilitates multiple solution

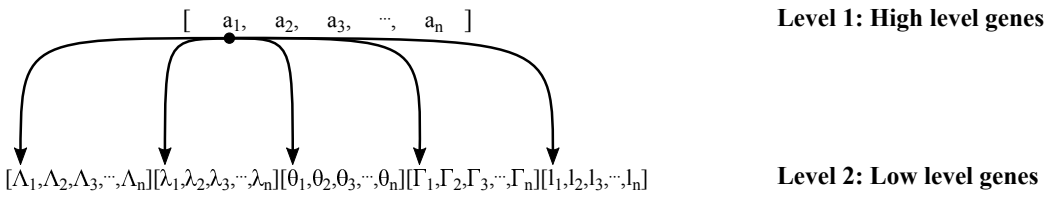

(a) The two-level structure of sGA chromosomes.

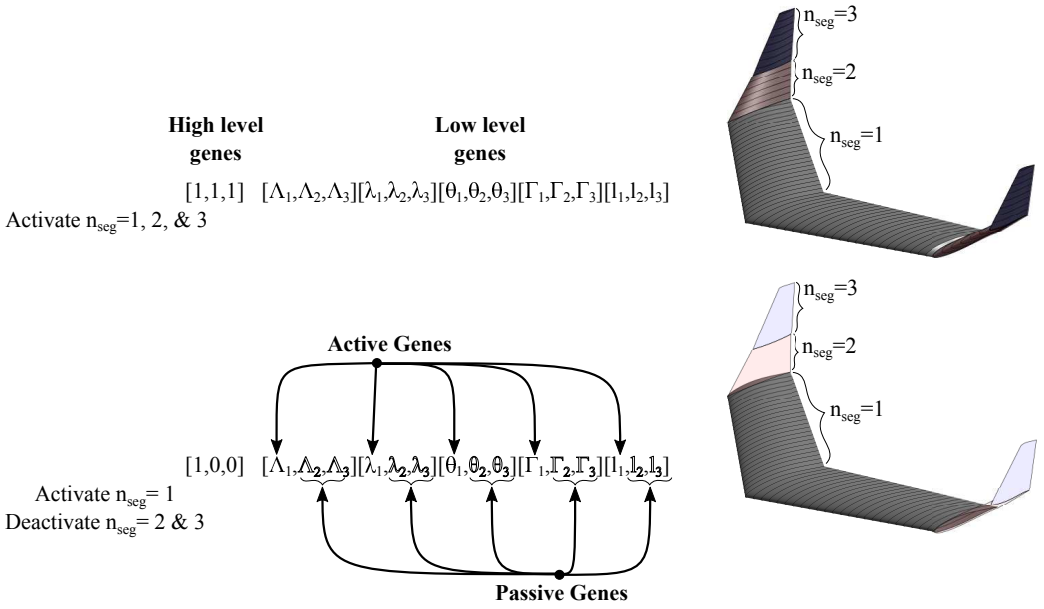

(b) The effect of active (dominant) and passive (recessive) low level genes in sGA chromosome.

FIGURE 2.7: sGA dynamic chromosome structure.

changes in terms of active/passive genes. In the genotype-phenotype mapping, only those genes which are active in the genotype contribute to the fitness of the phenotype. Passive genes are dormant and are carried as redundant genetic material through the evolutionary process.

Representing the chromosomes in this manner allows the GA to retain alternative solution possibilities as shown in figure 2.7b, where it is seen that wing segments, $n_{seg} = 2, 3$, are deactivated. As a population of solutions converge in phenotypic space, genotypic diversity will persist which is a unique characteristic for a GA. In other genetic models phenotypic convergence suggests genotypic stagnation and a lack of diversity. This is the main cause of trapping the algorithm at a local-optima and results in premature convergence of the design; methods for assessing whether the algorithm is becoming trapped at a local-optima is discussed in Section 2.2. In addition, the algorithm can naturally facilitate co-evolution of different solution types by simultaneously preserving different areas of the search space.

The biological inspiration for this genetic model, whereby genetic traits can be

turned 'on' (active) and 'off' (passive) but remain embedded within a solution's genotype description, comes from mechanism of dominant and recessive structural genes. Each candidate solution within a population must have the same chromosomal genotype structure (length) in order to apply reproduction between solutions; two parent solutions entering reproduction must contain the same total number of variables/properties. Genes which are not active (passive genes) remain in the genotype chromosome but remain neutral in an apparently redundant form but can be passed on to subsequent generations where they may be made active through reproduction.

2.3.2 Population Size and Selection Methods

Population size, N, is very much related to the complexity of the problem and the number of design variables considered; understanding how the population size influences a particular problem is not a trivial task. A good selection of population size will improve both computation time and solution quality. It is generally argued that small populations can lead to premature convergence and poor solution optimisation and that larger populations may unnecessarily expend computational resources. Various generalised guidelines exist regarding appropriate population size and methods for tuning can be found in the literature [173, 174, 175]. Pandey et al. [176] present a detailed comparative review of approaches to prevent premature convergence based on several different factors affecting the GA's behaviour: initial population; initial population diversity; fitness/objective function; search space scope Vs. selection pressure; problem complexity Vs. population size.

After the population of solutions have been evaluated (via some numerical simulation) and the fitness of each solution has been determined, selection methods can be implemented. These methods are used to structure the population in preparation for the creation of new candidate solutions. Selection methods are independent of the genotype-phenotype representation, simply presenting alternative methods to select candidate solutions for the recombination of their schema; *i.e.* how to choose solutions in the current population used to create new solutions for the next population. Typically, the population is structured with regard to each solution's fitness in order to emphasize the better solutions in the population with the aim of using the current best solutions to construct offspring with a higher fitness. However, the selection process is also key for maintaining diversity in the population which is required for solution progress away from sub-optimal solutions. There are no strict rules on how selection is implemented and is often down to user preferences. The most common selection methods for GAs include: elitism [153, 154, 177]; roulette wheel [154, 178]; and tournament selection [154, 178, 179, 180].

Elitist methods force the GA to retain the best few solutions from one generation to the next; *i.e.* the best x% of the population for example is passed to the next generation and mating pool for reproduction. The advantage of this is that the best few solutions

are never lost due to not being selected for reproduction, and removes the risk of them being altered/destroyed through mutation. Researchers have found that elitism significantly improves the GA's performance [181, 182], however there is evidence to indicate that this can drive premature convergence [153]. Mitigating this may require a high mutation rate to maintain sufficient genetic diversity [153].

Roulette Wheel selection [183] is a probabilistic method for selecting solutions for reproduction. It works by creating a biased selection pressure towards better solutions in the population [179, 184]. Therefore, probabilistically good solutions are more likely to be selected than poorer ones. This method allows both good and bad solutions to progress to the next generation with no guarantee of the 'best' solution(s) surviving. This helps maintain population diversity, and thus helps to preserve randomness which is essential for good exploration of the design space, but also has the effect of slowing the convergence rate [153].

Tournament selection involves holding 'tournaments,' in which the fitness of random solution pairs from the population are compared: the highest fitness solution progresses. When enough tournaments have been completed, the winners from each tournament progress to the reproduction stages [180]. This selection method provides a certain level of elitism where the single most fit solution will survive (but not all good solutions will), and helps to maintain a certain level or randomness in the selection process so that a lower mutation rate can be employed. Worrall [184] states that this is well suited for large populations.

In the current work, tournament selection is employed in conjunction with the non-dominated sorting of the entire parent and child populations. The strategy of non-domination organises the population into a hierarchy of sub-populations based on the ordering of Pareto-dominance, thus with two solutions entering a 'tournament' the solution with the lowest Pareto-dominance rank wins. Non-Dominated Sorting Genetic Algorithms (NSGA) are discussed in detail by Srinivas and Deb [185], and Deb [160, 186].

Figure 2.8 illustrates the non-domination organisation strategy used in this work with a population of twelve solutions, within a two-objective (f_1 and f_2) minimisation problem, ranked into four Pareto-fronts: the first solution sub-population (S_1, S_2, S_3, S_4, and S_5) is completely non-dominated and given a rank of 1; the second sub-population (S_6, S_7, and S_8) is dominated by the individuals in the first Pareto only and given a rank of 2; and so on. The shaded region indicates the feasible solution design space. The aim of creating these sub-populations is to improve the adaptive fit capability of the population of candidate solutions to a Pareto-optimal front constrained by some objective function(s).

Non-domination, by definition, indicates that any two solutions from the same Pareto-front cannot be considered to be better than one another with respect to all objectives as they have the same rank. This introduces the crowding comparison

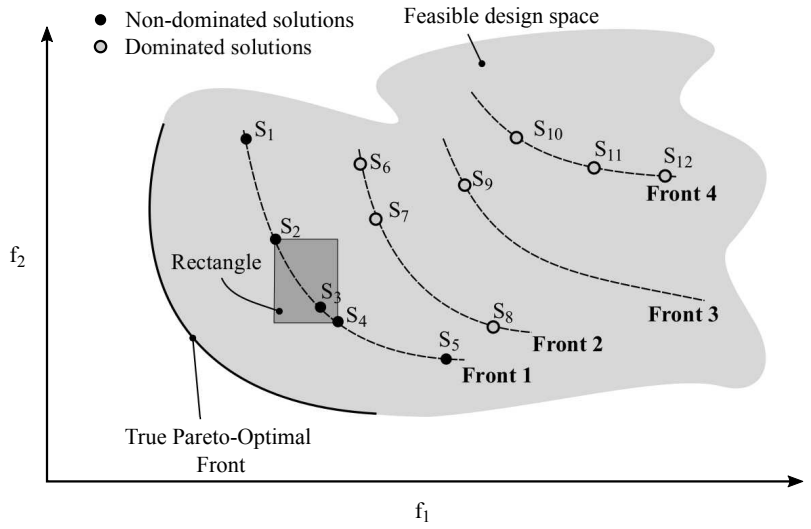

FIGURE 2.8: Population of twelve solutions classified into four non-dominated Pareto-fronts.

operator which is attributed to every individual within each Pareto-front and represents a measure of density of solutions in the vicinity of a particular design point. To gain an estimate of the density of solutions surrounding a particular solution in a certain front, the average distance to the neighbouring solutions, either side of the *i-th* solution, is calculated. The crowding comparison operator guides the selection process towards uniformly distributing solutions over Pareto-optimal fronts. Thus, if two solutions enter a tournament from the same Pareto-front then the algorithm will place preference on the solution which is located in a region of the design space with a lesser number of solutions nearby, *i.e.* the more isolated solution. To gain information about a solution's crowding distances, the euclidean distances of neighbouring solutions surrounding a particular design point in each objective space is calculated. This is shown in figure 2.8 by the rectangle, enclosing solution S_3 without including any other solution in the population, emphasizing the crowing distance for S_3. Hence, the sum of the individual normalised euclidean distance between any two solutions i and j, of the same Pareto-front (rank), in a population of N solutions is calculated as follows:

$$d_{ij} = \sqrt{\sum_{k=1}^{N} \left(\frac{f_k^{(i)} - f_k^{(j)}}{f_k^{(max)} - f_k^{(min)}} \right)^2} \tag{2.1}$$

where $f_k^{(max)}$ and $f_k^{(min)}$ are the maximum and minimum objective function values of the k^{th} objective. For solution i, d_{ij} is computed for each solution j of the same rank. Boundary solutions at the edge of a Pareto-front (*e.g.* S_1 and S_5 from front 1 in figure 2.8) are assigned an infinite crowding distance.

Although the crowding distance is calculated in the objective space here, it can also be implemented in the parameter design space. Deb [187] points out that while using the parameter-space to determine the crowing distance will vastly increase the

phenotypic diversity of the GA population, it may mask information about Pareto-optimal front. That is, evaluating objective-space crowding distances will provide solutions with more trade-off in design features. In the current study, as several diversity maintaining mechanisms have been employed, and there is an importance in understanding specific design trade-offs, objective-space crowding distances are used.

In order to maintain traits of elitism and enable a broad range of sub-Pareto-fronts to be assessed, the parent and child populations are combined for non-dominated sorting and tournament selection. Rudolph [181] adopts this strategy to perform a complete population sort including both parent and child solutions to identify all fronts whereby the allocation of fitness is carried forward accordingly. This doubles the size of the population ($2N$) which enters sorting and tournament selection, from which only N solutions are selected to proceed into the next generation. The other half of the population is discarded.

2.3.3 CROSSOVER OPERATORS

With parent solutions selected for the mating pool, the crossover operations breakdown and re-combination of schema of candidate variables to create child solutions. This represents the biological process of reproduction. Genetic operations are dependant on genotype-phenotype mapping and therefore some forms of crossover are more suitable than others. The exact combination of genetic operations is often omitted from literature, however common examples of crossover include: single-point crossover [151, 177]; two-point crossover [151, 153, 156]; multi-point crossover [188]; gene-lottery [189]; uniform crossover [151]; and blended crossover (BLX-α) [167]. In this work the primary method of crossover is blended crossover (BLX-α) with a probabilistic secondary two-point section crossover.

The blended crossover operator (BLX-α) was first introduced by Eshelman and Schaffer [167] for real encoded GAs. This operator generates two child/offspring solutions over a design space segment defined by two parent solutions and a user-defined parameter α as:

$$\begin{aligned} Child_1 &= \gamma \cdot Parent_1 + (1-\gamma) \cdot Parent_2 \\ Child_2 &= (1-\gamma) \cdot Parent_1 + \gamma \cdot Parent_2 \end{aligned} \tag{2.2}$$

where,

$$\gamma = (1+2\alpha) \cdot rand - \alpha \tag{2.3}$$

$Child_{1,2}$ and $Parent_{1,2}$ denote $\mathbf{X}$ encoded design variables of the children (new population solutions) and parents (a mated pair of solutions from the previous generation) respectively, and $rand$ is a random number between 0 and 1. γ is then uniformly distributed for a fixed value of α. A schematic view of the BLX-α operator is shown in figure 2.9, where x_i^U and x_i^L are the upper and lower search bounds of the

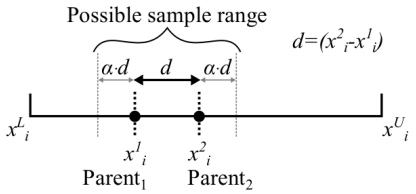

FIGURE 2.9: The BLX-α operator acting on the i^{th} variable of parent chromosomes x^1 and x^2.

i^{th} design variable of a given solution $\mathbf{X}$.

A number of investigations [160, 190, 191] have reported that BLX-0.5 ($\alpha = 0.5$) performs better than BLX operators with any other α value; if $\alpha = 0$ offspring variables cannot be outwith the variable range d as illustrated in figure 2.9 and rapid convergence will result. Oyama and Liou [191] indicate that BLX-0.5 helps to balance the conflict of exploiting good solutions while continuing to search for new ones. This is achieved as BLX-α produces offspring depending on the dissimilarity between the parent solutions. If the difference between the two parents is small, the difference between the offspring and parents is also small. This inherent property allows the search operator to establish an adaptive search. If diversity within the parent population is large, an offspring population with a large diversity can be expected, and vice versa. Hence, such an operator enables a good bias toward searching for solutions early on (especially with a random population initialisation through the design space), and then also allows an increasingly more focussed search as the population tends to converge in a certain region of the design space.

Following blended crossover operations, offspring solutions are subject to probabilistic two-point crossover, with an increased chance of occurrence in earlier generations. The advantage of this is that the search space can be even more broadly searched than the BLX-α method is capable of achieving alone. As a broad design space is to be considered, re-iterating the fact that multiple solution types can exist due to the structured GA chromosomal hierarchy, it is important to maximise the search early on. This also helps to define 'anchor points' in the design space that help to guide the optimisation as the constraints are progressively tightened over generations.

A schematic view of two-point crossover operations is shown in figure 2.10. The two-point crossover acts on the offspring chromosomal pair created by the BLX-α operation. The chromosomes are cut at two randomly selected locations, creating three chromosome sub-sections, of which one of the chromosomal sub-section are swapped between child solutions. This method leads to a bulk gene transfer between the solutions.

Work by Dejong [192] suggests that single- or two-point crossover, while perceived to be the most appropriate method of crossover due its popularity, increases the chance of disrupting fitter solutions. It is also concluded that any more than two crossover points will degrade the overall GA performance. Alfaro-Cid [179] indicates

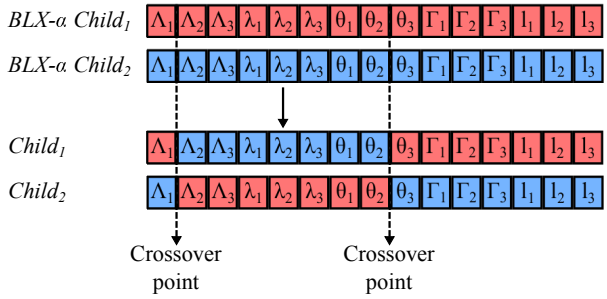

FIGURE 2.10: Two-point crossover.

that this is true, but only when conservative selection methods (elitism) are employed. With strong selection methods, or as a secondary crossover method, schemes using two-point or multi-point crossover have shown good performance [179]. A thorough study of how uniform single/two/multi-point crossover operations compare can be found in Khoo and Suganthan [151].

2.3.4 MUTATION OPERATORS

Goldberg [193] argued that in real-encoded GAs the action of selection is naturally driven to force above-average solutions to survive. Thus, it is suggested that after very few generations, a real-encoded GA will begin to treat continuous design variables in a discretised manner. In such an event, the search becomes restricted to specific sub-regions of the design space limiting the design capability. Mutation operators can help mitigate this through enabling a natural diffusion of solutions through the design space. In Holland's early work [152] the crucial genetic operator is crossover, with mutation playing only a secondary role.

Mutation operations are implemented to slightly perturb select offspring solutions generated by crossover [152, 153, 156, 179]. The basic principle of the mutation operator is to choose one or more genes of the selected solution chromosome and the *allele*, the value of that gene, is replaced with a randomly generated value [179]. The mutations occur with reference to a mutation rate [152, 153, 184]. The mutation rate is a value representing a percentage of the population that is to be mutated during a single iteration of the GA. There are various approaches to select the mutation rate. High mutation rates can help to fully exploit the full search domain but also increase the probability that mutations will destroy useful schema. Conversely, low mutation rates may not spread solutions out enough to successfully search the possible solution space and thus can reduce the chance of finding superior optimal solutions.

In traditional GAs, the mutation rate often remains constant until termination of the algorithm [160, 184]. Khoo and Sugantham [151] present methods experimenting with time varying mutation rates. It is argued that an initially high mutation rate leads to a diverse population, and a low mutation rate at the end means good solutions are not destroyed. Yaman and Yolmaz [194] have also shown that a fixed mutation rate

compared to a variable mutation rate can increase the overall performance for GAs.

In the present study, time varying mutation rates are employed which randomly update gene *alleles*; this value remains within the user defined variable limits. This operator is independent of the parent solutions and is equivalent to the random initialisation of that variable with a uniform probability distribution.

2.3.5 Constraint Management

Constraint handling in aerodynamic, and indeed any industrial optimisation problem, plays a consequential role in the quality and robustness of an optimised solution within the defined design space. Geometric parametrisation itself poses a constrained optimisation problem since, in addition to minimising the objective $f(\mathbf{X})$, the design variables must satisfy some geometric constraints. Constraint management techniques found in literature have been classified by Koziel and Michalewicz [195] and Sienz and Innocente [196] as: 1) strategies that preserve only feasible solutions with no constraint violations: infeasible solutions are deleted; 2) strategies that allow feasible and infeasible solutions to co-exist in a population, however penalty functions penalise the infeasible solutions (constraint based reasoning); 3) strategies that create feasible solutions only; 4) strategies that artificially modify solutions to boundary constraints if boundaries are exceeded; and 5) strategies that repair/modify infeasible solutions.

Most commonly, optimisations apply weighted penalties to the objective function if the constraints are violated. The reason for this is that penalty functions are often deemed to ease the optimisation process, and bring the advantage of transforming constrained problems into unconstrained ones by enforcing the penalties directly to the objective function. With this method, Pareto-optimal solutions with good diversity and reliable convergence for many algorithms can be obtained easily when the number of constraints are small; fewer than 20 constraints. It becomes more difficult to reach Pareto-optimal solutions efficiently as the number of constraints increase, and the number of analyses of objectives and constraints quickly becomes prohibitively expensive for many applications. This is because the selection pressure decreases due to the reduced region in which feasible solutions exist [197].

Kato et al. [198] suggest that in certain circumstances Pareto-optimal solutions may exist in-between regions of solution feasibility and infeasibility. This concept is illustrated in figure 2.11, where it is seen that feasible and infeasible solutions could be evaluated in parallel to guide the optimisation search direction towards feasible design spaces. This is intuitively true for single discipline aerodynamic optimisation problems where often small modifications to design variables can largely impact the performance, rendering designs infeasible. Algorithm understanding of infeasible solutions can help in the betterment of feasible solutions through algorithm learning/training and constraint based reasoning. Robinson et al. [199], comparing the performance of alternative trust-region constraint handling techniques, demonstrated

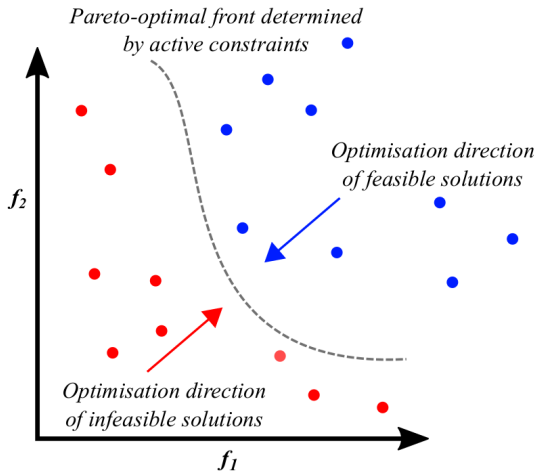

FIGURE 2.11: Concept of parallel evaluation strategy of feasible and infeasable solutions to guide direction in a GA.

that reapplying knowledge of constraint information to a variable complexity wing design optimisation problem reduced high-fidelity function calls by 58%.

Gemma and Mastroddi [200] demonstrated that for multi-objective aerodynamic optimisations, the objective space of feasible and infeasible design candidates are likely to share no such definitive boundary. With the adoption of flutter constraints, structural constraints, and mission constraints, the solutions defined as infeasible under certain conditions would otherwise be accepted, hence forming complex Pareto-fronts. Interdisciplinary considerations such as this help to develop and balance conflicting constraints. For example, structural properties which may be considered feasible, but are perhaps heavier than necessary and so inflict aeroelastic instabilities at lower frequencies.

In the present study, constraint based reasoning has been applied to the optimisation problems. This will enable both feasible and infeasible solutions to coexist without forcing the optimisation in a particular direction as artificial modification/correction to solutions or complete removal of inferior solutions would. This is important to consider as the variable complexity wing topology may create superior geometric arrangements in terms of the objective space, and achieve the performance constraints (root bending moment for example), but violate geometric constraints (such as maximum wingspan) by a small amount. Hence, if such a solution is found, if that solution is deleted or modified based on a small constraint violation then the schema and associated solution performance is lost.

Based on the fact that many of the geometric constraints are dictated by the wind tunnel test section, it is likely that many superior solutions will be on the cusp of violating geometric constraints such as that placed on the maximum allowable wingspan or root chord. In other words, optimal solutions are likely to lie on the intersection of constraint boundaries [159]. Infeasible solutions must be allowed to coexist with feasible solutions in the population, but the way in which they are infeasible, and the

severity of the constraint violation, must be realised by the algorithm.

Geometric, $g_j(\mathbf{X}^n)$, and performance, $h_k(\mathbf{X}^n)$, constraint violations of the solution $\mathbf{X}^n$ are accumulatively added via weighted penalties to the objective function, $f(\mathbf{X}^n)$, based on the total number of constraint violations. This is established by the function:

$$f(\mathbf{X}^n) = F(\mathbf{X}^n) + \underbrace{\sum_{j=1}^{J} R_j |g_j(\mathbf{X}^n)|}_{Geometric\ constraints} + \underbrace{\sum_{k=1}^{K} r_k |h_k(\mathbf{X}^n)|}_{Performance\ constraints} \tag{2.4}$$

where R_j and r_k are user defined penalty parameters. Geometric constraint violations are weighted based on the number of violations and the percentage of constraint overshoot. These violations are evaluated prior to numerical simulation to ensure that the geometry does not render the potential flow model unreliable. After simulation, each solution's performance metrics are compared to performance constraints (e.g. minimum lift, maximum root bending moment, etc.) which are variably weighted and scaled relative to the most inferior solution based on all performance requirements. This enables superior solutions in terms of objective function which may violate some geometric constraints to obtain a relatively high rank when the population is subjected to non-dominated sorting. However, such a solution cannot obtain a non-dominated rank 1 status within the population, and therefore can be dominated by objectively inferior solutions that meet the minimum design constraint criteria. This arrangement offers the schema of constraint violating superior solutions to evolve and propagate through generations towards solutions of similar performance that meet all design constraints. If a solution grossly violates geometric/performance constraints, its penalty weighting will force it to be ranked lower within the population, eventually leading to its replacement by a superior offspring solution through tournament selection.

2.3.6 Summary of Population Structured Genetic Algorithm (sGA) Algorithm

Based on the number of different encoding, selection, crossover and mutation methods, and innovative modifications available it is clear that there are a number of forms of genetic algorithms that can be implemented for any single problem. For practical reasons, not all of these variations can be tested, so the different constituent parts should be chosen sensibly. Thus, understanding how GAs work involves understanding the notion of *schemas*, which are the building blocks of chromosome solutions within the GA [201]. In this context good solutions will exhibit similar patterns of allele values (possible traits of a design variable) and thus will have common schema. Statistically, as the GA progresses, the number of good schemas are likely to increase, as the number of bad schemas are destroyed.

A schematic illustration of the sGA developed in this work is shown in figure

2.12. The evaluation of wing aerodynamic properties, used by the sGA to drive the exploration and identification of superior wing solutions within the defined search space, is reported in the following section.

2.4 VORTEX RING AERODYNAMIC ANALYSIS

The difficulty in any aerodynamic optimisation problem is the ability to define an analysis method that is sufficiently simple enough to operate repeatedly within a defined search space but sophisticated enough to capture enough consideration that determines a local geometry that feeds into a globally optimal system [128]. This includes the fact that the analysis method must additionally be integrated with the optimisation algorithm developed. Thus, the aerodynamic model must be computationally efficient while simultaneously maintaining reasonable accuracy. Overall design trends must be represented correctly in order to achieve a reliable optimisation architecture capable of assessing different wing configurations.

Panel methods, which are based on potential flow theory, meet these requirements and are utilised to model low-speed steady aerodynamic forces in this work. These are

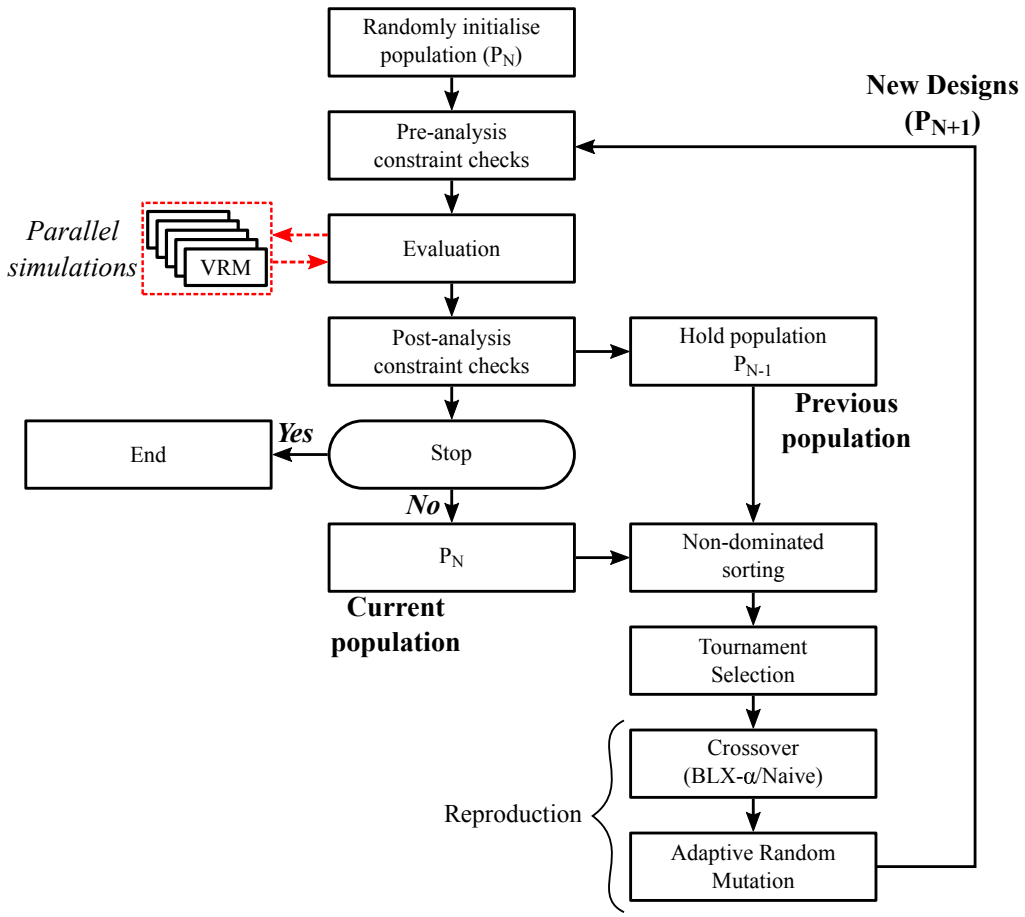

FIGURE 2.12: Schematic illustrating genetic algorithm strategy developed.

derived from the potential flow equations which describe a low-speed, incompressible ($M_\infty < 0.3$), inviscid, irrotational fluid flow. Rather than iteratively resolving the flow properties across a discretised volume/domain they predict aerodynamic loads from the analysis of fluidic singularities modelled on the surface of a body only; this approach is therefore accepted to be a computationally economic method of aerodynamic analysis [202].

Due to the low computational demand and ability to provide sufficient accuracy, within well-defined limitations, potential flow analysis has been broadly applied to conceptual wing design problems [60, 98, 203, 204, 205, 206]. Furthermore, the geometry of the wing configurations is not required to be known in great detail, which suits the purpose for designing un-conventional lifting configuration topologies. Specifically a Vortex Ring Method (VRM) has been developed. The VRM requires the panelling of the mean surface where only the camber and thickness distribution is required. Correction methods have been applied to improve the total drag computation through estimating the parasitic drag.

2.4.1 Potential Flow Theory

Panel methods are based on providing a solution to the potential flow problem. From potential flow theory, the flow of interest is assumed incompressible and irrotational by the continuity equation. The governing equation in terms of the velocity potential ϕ is expressed as [202]:

$$\nabla^2 \phi = 0 \tag{2.5}$$

This is Laplace's equation and presents a boundary-value problem. This solution of this Laplacian equation can be obtained by discretising the problem and applying elementary solutions, such as point sources, point sinks, doublets, and vortex lines to obtain the solution of a complex problem. The boundary condition of zero normal flow at surfaces needs to be satisfied at the wing's solid surface:

$$\nabla(\phi + \phi_\infty) \cdot \mathbf{n} = 0 \tag{2.6}$$

2.4.2 Biot-Savart Law

The continuous distribution of bound vorticity over the wing surface and of the trailing vorticity in the wing wake are approximated using a finite number of vortex ring elements. The advantages of this element, as opposed to the simpler horseshoe element, is that the exact boundary conditions will be satisfied on the actual wing's surface and is therefore better suited to coping with camber and twist distributions and various planform shapes [202].

The velocities induced by a straight vortex line segment at any arbitrary point in space, such as any of the four segments forming the vortex ring. Each vortex line

cannot start or end in a fluid and the contribution of a segment has to be considered as part of a continuous vortex line. The induced velocity, $\mathbf{V}_{ind}$, at an arbitrary point in space of a constant vortex line segment is given by the Biot-Savart formula [202, 205]:

$$\mathbf{V}_{ind} = \frac{\Gamma}{4\pi} \frac{\vec{\mathbf{r}_1} \times \vec{\mathbf{r}_2}}{|\vec{\mathbf{r}_1} \times \vec{\mathbf{r}_2}|^2} \vec{\mathbf{r}_0} \left(\frac{\vec{\mathbf{r}_1}}{\vec{\mathbf{r}_2}} - \frac{\vec{\mathbf{r}_2}}{\vec{\mathbf{r}_1}} \right) \tag{2.7}$$

In equation 2.7, Γ is the constant vortex strength of the vortex segment, $\vec{\mathbf{r}_1}$ and $\vec{\mathbf{r}_2}$ are the spatial vectors from the starting and ending points of the vortex segment, and $\vec{\mathbf{r}_0}$ is the spatial vector along the length of the vortex segment as illustrated in figure 2.13. The induced velocity of a horseshoe vortex is computed by applying the Biot-Savart law on each vortex element composing the vortex ring.

Referring to figure 2.13, it is noted that when point P lies on the vortex line then the vortex solution is singular. Hence, for numerical purposes, the vortex segment is assumed to have a small radius within which the net induced velocity is zero.

2.4.3 VORTEX RING METHOD

The vortex lattice, in this instance composed of vortex rings, divides the lifting surface planform into separate panels as shown in figure 2.14. The leading edge of each segment ring is placed on the quarter chord line of the associated wing panel and the collocation point, at the centre of the vortex ring, placed on the three-quarter chord line of the panel. This satisfies the two-dimensional Kutta-condition along the local chord. Additionally, along the wing trailing edge, the trailing vortex of the last panel row must be cancelled to satisfy the three-dimensional Kutta-condition at the trailing edge such that:

$$\gamma_{TE} = 0 \tag{2.8}$$

Both the vortex segments and collocation points are distributed over the aerofoil's camber line. A normal vector $\mathbf{n}$ is defined at each collocation point and a positive Γ is defined along each vortex segment according to the right-hand rule. The vortex

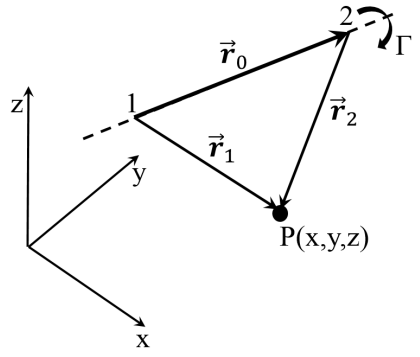

FIGURE 2.13: Three-dimensional vortex segment.

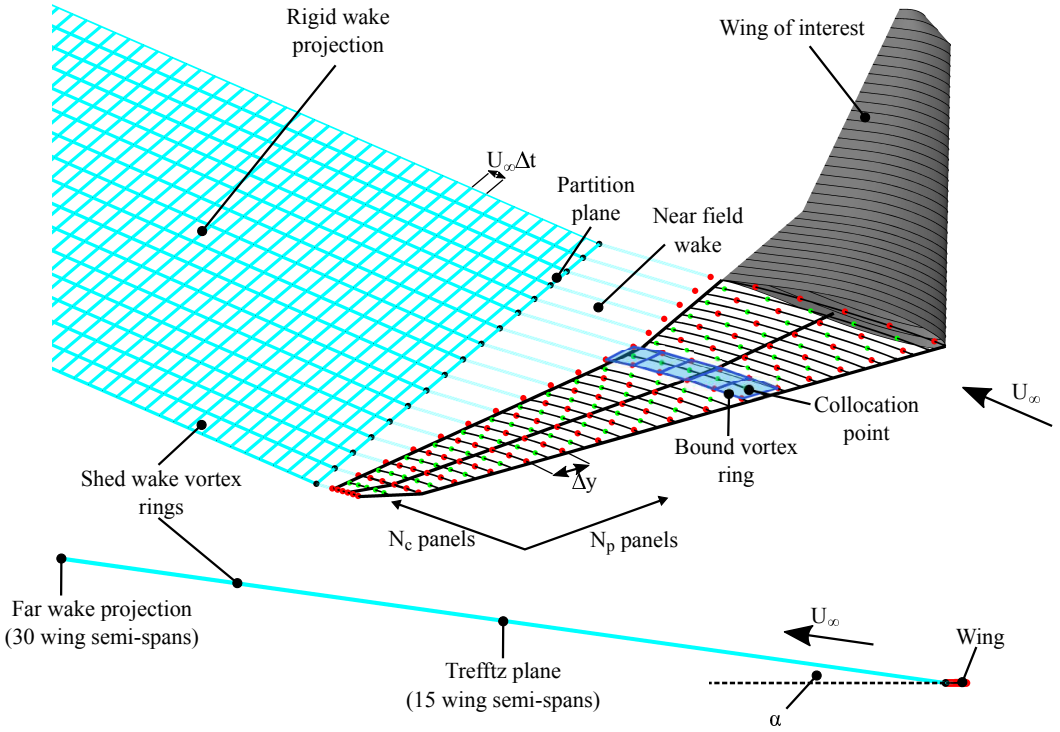

Figure 2.14: Vortex ring model of arbitrary wing with N_p spanwise, and N_c chordwise, vortex rings.

filaments of the vortex rings induce a velocity on each panel's collocation point, which is computed using the Biot-Savart law. Additionally, as geometry symmetry exists about the wing root chord, only the starboard wing is modelled, while the influence port wing is treated as a solid boundary reflection [202]. This halves the computational demand of any wing solution's performance computation.

A surface panel meshing algorithm automatically discretises each wing segment taking into account individual panel sweep, dihedral, taper, twist, and aerofoil camber. A subtlety in the meshing algorithm, with regard to the optimisation procedure, is how to discretise each wing segment where length is a continuous design variable. For numerical accuracy, the vortex ring span is held constant for each wing segment, and the joining vortex rings can vary continuously. Spatial discretisation is requested by the user but is modified by the meshing algorithm depending on the overall wing geometry to ensure fixed distribution of vortex rings and that biasing of vortex rings toward certain wing segments does not occur.

Once discretised, an aerodynamic influence coefficient matrix can be determined which represents the induced velocities from each vortex ring on all other panel collocation points. In order to determine the vorticities of the vortex rings a kinematic boundary condition is applied which forces the normal velocity at the collocation point of each panel to be zero; this is the so called no penetration boundary condition. The vortex strength distribution, Γ, for a given geometry can therefore be obtained by solving the linear equations:

$$\underbrace{\begin{pmatrix} a_{11} & a_{12} & \cdots & a_{1m} \\ a_{21} & a_{22} & \cdots & a_{2m} \\ \vdots & \vdots & \ddots & \vdots \\ a_{m1} & a_{m2} & \cdots & a_{mm} \end{pmatrix}}_{\text{Aerodynamic influence matrix}} \underbrace{\begin{pmatrix} \Gamma_1 \\ \Gamma_2 \\ \vdots \\ \Gamma_m \end{pmatrix}}_{\text{Vortex strength distrobution}} = \underbrace{-Q_\infty \cdot \mathbf{n}_m \begin{pmatrix} 1 \\ 1 \\ \vdots \\ 1 \end{pmatrix}}_{\text{Boundary condition vector}} \tag{2.9}$$

where a represents aerodynamic influence coefficients, m is the order of the matrix (number of spanwise $\times$ number of chordwise vortex rings), and Q_∞ are the normal velocity components of the freestream flow (U_∞, V_∞, W_∞). Typically, the solution of panel methods is based on solving the system of equations in equation 2.9 which is not an iterative solution technique and involves a simple projection of a drag-free wake aligned with the freestream to the far field (typically 30 wing semi-spans) [71]. The wake aligns with the freestream from the partition plane indicated in figure 2.14, which enables the near field wake projection to compensate for the shedding of a complex drag-free wake from a wing with variably swept segments [71]. Doing so simplifies the wake projection as it does not need to match the trailing edge sweep for far-field projections. This simplification removes the near field wake and its influence on the wing planform.

While unsteady aerodynamics over the wing are not of interest, the influence of induced velocities (downwash) generated by the vortex wake wake behind the wing is. Hence, for each time-step Δt the wing trailing edge vortex rings are propagated into the wake satisfying the Kelvin condition [202], which states that the circulation around a closed curve moving through a fluid remains constant with time. The influence coefficient matrices are separated into an influence coefficient matrix $\mathbf{A}_{wing,wing}$ to account for the self-induced velocities from the aerodynamic lifting surfaces, and an influence coefficient matrix $\mathbf{A}_{wake,wing}$ to account for the induced velocities from the wake on the aerodynamic lifting surface. Given these influence coefficient matrices, the bound vortex strength $\Gamma_{wing,t+\Delta t}$ for the time-step $t + \Delta t$ can be computed:

$$\Gamma_{wing,t+\Delta t} = \mathbf{A}^{-1}_{wing,wing}(-\mathbf{V}_{ind_{t+\Delta t}} - \mathbf{A}_{wake,wing}\Gamma_{wake,t+\Delta t}) \tag{2.10}$$

where Γ_{wing} denotes the vortex strength of the aerodynamic lifting surface panels, Γ_{wake} denotes the vortex strength of the wake panels, and $\mathbf{V}_{ind_{t+\Delta t}}$ denotes the induced velocities at the wing collocation points at time-step $t + \Delta t$.

A force-free wake model utilising a wake relaxation scheme has not been employed to align the wake everywhere with the local flow; *i.e.* the effect of the induced velocity on the wake is not determined and therefore wake roll-up due to vorticity shed from the wingtips is not modelled. Thus, for the purpose of improving optimisation run times, iteratively time-stepping vortex rings into the wake projection is not utilised. Neglecting these higher-order effects leads to the assumption of a rigid wake projection within which deflections and perturbations are small compared to the freestream

velocity. The primary reason of this simplification is to maintain a simpler analysis model for the purpose of integration with the optimiser. Smith [71] demonstrated that neglecting wake roll-up does not invalidate the shed trailing wake and that appropriate consideration (leading to a significant increase in computational cost) of these effects will ultimately account for a 1 to 2% change in the induced drag through slight redistribution of the wing downwash. Evidence also suggests that the bound circulation of the wing is unaffected. Furthermore, several other studies have shown effective use of drag-free rigid wake modelling [60, 94, 207].

The wake vortex strength for each subsequent time-step Δt is computed using a propagation matrix $\mathbf{P}_{wing}$, which is a binary matrix used to guide the trailing edge vortex rings into the wake, and $\mathbf{P}_{wake}$ which is also a binary matrix guides all vortices in the wake downstream with each iteration:

$$\Gamma_{wake,t+\Delta t} = \mathbf{P}_{wing}\Gamma_{wing,t+\Delta t} + \mathbf{P}_{wake}\Gamma_{wake,t} \tag{2.11}$$

Given the circulation of the vortex ring elements, the inviscid aerodynamic force ΔL per unit width Δy acting on the bound segment of each vortex ring strip over the lifting surface can be computed using the Kutta-Joukowsky theorem [202]:

$$\Delta L_m = \rho_\infty Q_\infty \Gamma_m \Delta y_m \tag{2.12}$$

The total aerodynamic load is the sum of the contributions of each of the individual panels.

To derive Laplace's equation (equation 2.5) the flow is assumed to be inviscid, irrotational, and incompressible. Thus potential flow models cannot properly model viscous drag effects, flow separation, or compressibility effects such as shock waves.

2.4.4 Induced Drag Calculation

On Wing Calculation: 'Near Field'

The 'near field' approximation of the induced drag poses a simple extension to the panel method, where the downwash over the wing is estimated directly on the wing at the distributed collocation points. Here, an aerodynamic influence matrix is computed in which only the trailing vortex segments are considered; the influence of the bound vortex segments are neglected. This procedure can be summarised by the matrix formulation in equation 2.13 where all influence coefficients and vorticity of the trailing edge segments responsible for the induced downwash are known:

$$\underbrace{\begin{pmatrix} \omega_{ind_1} \\ \omega_{ind_2} \\ \vdots \\ \omega_{ind_m} \end{pmatrix}}_{\text{Induced downwash}} = \underbrace{\begin{pmatrix} b_{11} & b_{12} & \cdots & b_{1m} \\ b_{21} & b_{22} & \cdots & b_{2m} \\ \vdots & \vdots & \ddots & \vdots \\ b_{m1} & b_{m2} & \cdots & b_{mm} \end{pmatrix}}_{\text{Aerodynamic influence matrix}} \underbrace{\begin{pmatrix} \Gamma_1 \\ \Gamma_2 \\ \vdots \\ \Gamma_m \end{pmatrix}}_{\text{Vortex strength distribution}} \tag{2.13}$$

The induced drag computation of each bound vortex segment arising from the trailing vortex segments are then obtained using the Kutta-Joukowsky theorem [202]:

$$\Delta D_m = -\rho_\infty \Gamma_m \omega_{ind_m} \Delta y_m \tag{2.14}$$

FAR FIELD: TREFFTZ PLANE ANALYSIS

Von Karman [208] developed a far field approach for determining the induced drag from properties in a traversed plane far downstream of a lifting system. When this plane is moved far enough away from the lifting system, the u-perturbations produced by the bound vorticity become diminishingly small, leaving only the perturbations produced by the trailing wake system. This plane is traditionally referred to as the Trefftz plane. For the case of a streamwise wake of wingspan b, the induced drag becomes:

$$D_i = -\frac{1}{2}\rho_\infty \int_{-b/2}^{b/2} \Delta\phi \frac{\partial \phi}{\partial z} dy \tag{2.15}$$

where $\Delta\phi$ is the potential jump from the upper side to the lower side of the wake in the far downstream Trefftz plane. Although the potential jump is discontinuous across the wake, the induced velocity, $\frac{\partial \phi}{\partial z}$ is continuous. More information on conducting Trefftz analysis is detailed by Drela [205]. In the present study the Trefftz plane is positioned fifteen wing semi-spans downstream of the lifting system as shown in figure 2.14 and suggested by Smith [71].

In applying this method the following assumptions are made:

- The flow is continuous, stationary, and inviscid.
- The flow is an isentropic perfect gas in the vicinity of the wake far away from the wing.
- In the Trefftz plane the flow is considered two-dimensional; u-perturbations are assumed negligible.
- The thin wake has a zero static pressure jump across it, and assuming that the total pressure does not vary either, the incompressible steady Bernoulli equation then implies a zero jump in velocity magnitude through the wake also. Thus, there are no wake deflections.

Smith [71] has shown that Trefftz plane analysis is a reliable computational method for estimating induced drag which is insensitive to vortex ring spatial density and numerical round off. Furthermore, this method does not suffer from pressure drag cancellation errors which can make near field induced drag calculations unreliable.

2.4.5 Viscous Drag Calculation

Consideration of a wing configuration's total drag, which includes contributions from both the induced and viscous drag, will alter the optimisation problem considerably. Inclusion of the viscous drag is a particularly important factor to address when comparing different wing configuration geometries including planar wing tip-extensions, addition of winglets, C-wings, and box wings as each will have very different wetted areas. Thus, the viscous drag is important for the comparison between design trade-offs and ensuring impractical gains in the viscous drag are not incurred. Simply fixing the wetted area between planar and non-planar configurations would not allow for a fair comparison as this would artificially drive maximum lift capability and lead to pseudo-optimal results.

There are several approaches to extend the linear aerodynamics of panel methods to include boundary layer effects, and hence viscous drag, such as coupling the potential flow solver with a boundary layer solver [202]. A computationally less-expensive method is to develop an analytical database of drag polar information for a given aerofoil over a broad range of Reynolds numbers [203]. In this study an analytical aerofoil database was developed and embedded into the panel method by performing two-dimensional calculations using XFOIL [209, 210]. The contribution of viscous drag is then introduced by embedding the two dimensional aerofoil data into the panel method calculations. It is assumed that the viscous two-dimensional drag coefficient of the local aerofoil over the wingspan varies quadratically with the sectional lift coefficient [5, 94, 121, 128]:

$$C_{d_p} = C_{d_{p2}}(Re)C_l^2 + C_{d_{p1}}(Re)C_l + C_{d_{p0}}(Re) \tag{2.16}$$

where C_{d_p} is the section viscous drag coefficient. The coefficients ($C_{d_{p2}}$, $C_{d_{p1}}$, $C_{d_{p0}}$) of the drag calculation in equation 2.16 depend upon the local Reynolds number at the mid-span of each aerodynamic panel and the pre-defined aerofoil characteristics. The viscous drag coefficients are determined by interpolating the results for the given aerofoil at different Reynolds numbers at different sectional lift coefficients. Thus, the upper and lower bounds for which this approximation is valid must not be exceeded at any wing cross section, while sufficient resolution for how the drag polar varies with the Reynolds number must also be provided.

2.4.6 STALL PREDICTION

Potential flow theory is only applicable to low angles of attack, providing a linear approximation of aerodynamic performance metrics for a given wing geometry. Flow separation, and subsequently wing stall, and its effects on the wing's performance cannot be predicted with such low fidelity models; flow separation is a highly three dimensional non-linear fluid dynamic viscous interaction. For a continual increase in angle of attack, the lift coefficient predicted via a potential flow model, for any wing, would increase constantly in a linear fashion.

This characteristic limitation of the potential flow model must be addressed and explicitly constrained within the optimisation protocol. The reason for this is that during the optimisation, if the presence of stall is not realised, one of two situations may arise: 1) the wing, or some portion of the wing, may take on too high an angle of attack, and 2) wing configurations may be optimised to have unrealistically small tip chords. With the latter, small sectional chords would result in high sectional lift coefficients. Therefore, stall constraints will indirectly apply constraints to the sectional chord and effective angle of attack, which is necessary as the optimisation procedure will consider numerous multi-element non-planar wing arrangements.

As with the viscous drag approximations, there are several approaches to extend the linear aerodynamics of panel methods to include boundary layer effects; namely the effects of boundary layer thickening and separation arising from adverse pressure gradients over the wing's upper surface. The approaches used to extend linear aerodynamic prediction models to include non-linear and post-stall lift-curve effects can generally be classified into three main categories: the α-correction approach [211], the Γ-distribution approach [212, 213], and the aerofoil de-cambering approach [214]. In the first approach, the deviation of the aerofoil non-linear lift-curve from the potential flow linear lift-curve is used to apply a correction to the sectional angle of attack. In the second, the wing lift distribution is assumed and then corrected to determine the effective sectional angle of attack for the non-linear aerofoil lift-curve. Lastly, the de-cambering approach reduces the sectional chordwise camber distribution to account for three dimensional flow separation effects at lift coefficients/angles of attack. All of these methodologies dictate an iterative aerodynamic analysis, and therefore a significantly increased computational demand.

For the optimisations conducted here the post stall performance for a given wing geometry is not of immediate interest, however ensuring that the wing's geometry remains within the limitations of the VRM model's predictive capability is. Hence, critical section theory, similar to that employed by Ning and Kroo [215], has been used to predict the onset of stall. This means that stall is predicted when any i^{th} wing section reaches a specified analytical section $C^i_{l_{max}}$. In a similar manner to the viscous drag approximations, an analytical aerofoil database was developed and embedded into the panel method by performing two-dimensional calculations using XFOIL

[209, 210]. Operating as a look-up table, the sectional C_l^i for the i^{th} wing section (which is a function of the sectional Reynolds number, Re, and sectional angle of attack, α, is compared to the two-dimensional lift coefficient from the embedded aerofoil database. Thus, the lift coefficient of each wing section is evaluated, where it must be less than or equal to a maximum allowable sectional lift coefficient, $C_{l_{max}}$, as shown in equation 2.17:

$$C_l^i(Re, \alpha)|_{VRM} \leq C_{l_{max}}^i(Re, \alpha)|_{XFOIL} \tag{2.17}$$

This obviously does not provide any information of when a given wing arrangement actually stalls, but does ensure that wing configurations will not stall at the given wing C_L.

Studies have used this method in a slightly different manner by considering the stall speed of a given wing, and so kept the maximum sectional lift coefficient, $C_{l_{max}}^i$, constant across the span of all wing segments [5, 94]. In the current work, the $C_{l_{max}}^i$ can vary over the span of each wing, from section to section, providing a more accurate approximation of stall onset. This is particularly important at the outboard wing section where the local Reynolds number and chord are, relative to the global wing, smaller.

2.4.7 EXPERIMENTAL VALIDATION

CASE 1

The vortex ring panel method approach with viscous drag corrections has been validated against wind tunnel tests for a planar wing with a NACA 65-210 aerofoil at a Reynolds number of 4.4×10^6, based on the wing mean aerodynamic chord. The wing geometry, experimental data, and test conditions are provided by Sivellis [8]. The calculated, using both near and far field induced drag models, and experimental lift-curve and drag polar is given in figure 2.15.

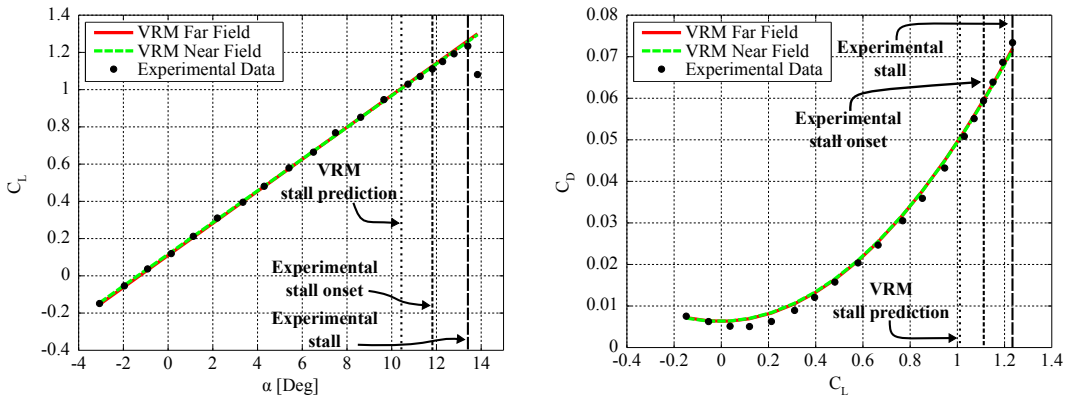

(a) C_L-α (b) C_D-C_L

FIGURE 2.15: Experimental wind tunnel data from Sivells [8] and VRM calculated data.

The wing has been discretised into panels 46 spanwise vortex rings ($\approx 0.05m$ in width), and 8 chordwise vortex rings. The computation time was ≈ 15 seconds per angle of attack. A convergence analysis for the vortex ring analysis considering spatial discretisation and computation time is given in Appendix A. The root mean square error (RMSE) between the experimental data and the numerical estimates are shown in table 2.2; the agreement between the experimental data and both computed results are deemed acceptable with the far field Trefftz analysis providing a marginally more accurate performance prediction.

The experimental and numerical computations match well. Figure 2.15a shows a limitation of the panel method where the most significant discrepancies occur at high angles of attack since no flow separation physics or stall characteristics are modelled. The experimental lift-curve-slope (per degree) of $C_{L\alpha} = 0.0850$ agrees with the lift-curve-slope of the near field model $C_{L\alpha} = 0.0861$, and the far field model $C_{L\alpha} = 0.0849$. The difference in the $C_{L\alpha}$ arises due to the different way in which the near field and far field Trefftz analysis computes the downwash over the wing. However in each instance, stall prediction was indicated at $\alpha = 10.4^{\circ}$. Sivellis [8] reports that evidence of stall onset began at $\approx 11.9^{o}$, with $C_{L_{max}}$ occurring at 13.5^{o}; under predicting stall onset by 12.6%.

The drag polars are shown in figure 2.15b. At low lift coefficients, the VRM model over predicts the total drag by up to 14.08% as the viscous drag model dominates. The simplifying assumption of a quadratic variance of viscous drag with sectional lift coefficient does not achieve consistent accuracy here. Discrepancies also exist at higher lift coefficients, as the wing begins to stall, since no flow separation is modelled.

Increased vortex ring discretisation in the spanwise direction of the wing was found to give a better prediction of C_{D_i}. A fundamental statement within this aerofoil theory is that the camber line is considered a streamline of the flow over which the vortex strength varies. Therefore, the nature of the panel method is devised to conceptually obtain values for the vortex strength which treat the modelled wing as a streamline of the flow; this also satisfies the Kutta condition. Increasing spanwise panels serves to better resolve the vortex strength per unit length across the span, but it does not sufficiently aid in the resolution of the induced velocities (i.e. downwash). Hence, increasing the number of chordwise panels serves to distribute more collocation points along the camber line at which the surface boundary conditions are applied; that is, at each control point the normal component of the velocity is zero. This velocity is the superposition of the uniform flow velocity and the velocity induced by the vortex

TABLE 2.2: VRM validation case 1 drag polar RMSE.

VRM model	RMSE [%]
Near field analysis	1.34
Trefftz plane analysis	1.23

panels. As a result, the induced velocity distribution over the wing is more accurately modelled (leading to a more accurate computation of the induced drag), and the Kutta condition is applied more precisely. Furthermore, increased chordwise panelling will also aid in resolving the effects of geometric twist and camber more effectively.

CASE 2

Additional experimental validation of the VRM analysis model has been carried out to ensure versatility and reliability in solving different wing geometries. Wind tunnel data was gathered in the de Havilland (dH) National Wind Tunnel Facility using a modified 304CZ sailplane wingtip winglet section, originally used by Anderle et al. [216, 217], at a Reynolds number of 8.6×10^5 based on the model's mean aerodynamic chord. The wing section had a constant NACA 63_2-514 aerofoil cross section. The numerical and experimental lift-curve, variation in the wing root bending moment, and drag polar is given in figure 2.16. The 304CZ sailplane is modelled with 25 spanwise vortex rings ($\approx 0.05m$ in width), and 8 chordwise vortex rings. The computation time was ≈ 7 seconds per angle of attack. Force and moment data has been calculated to a confidence level of 95% with a margin of error less than 1% for each datum.

Figure 2.16 further illustrates the limitations of the VRM panel method in dealing with stall; stall onset begins at $\alpha \approx 13^\circ$ after which the model becomes increasingly less accurate. For this reason, errors will only be considered over the pre-stall-onset region ($-5^\circ \leq \alpha \leq 13^\circ$); this is shown in table 2.3. The VRM stall prediction indicated the likelihood of stall at $\alpha = 11.4^\circ$; under-predicting stall onset by 12.3%.

Figure 2.16a shows good agreement between the numerical, both near and far field models, and experimental wind tunnel data. The experimental lift-curve-slope of $C_{L\alpha} = 0.0762$ agrees with the lift-curve-slope of the near field model $C_{L\alpha} = 0.0744$,

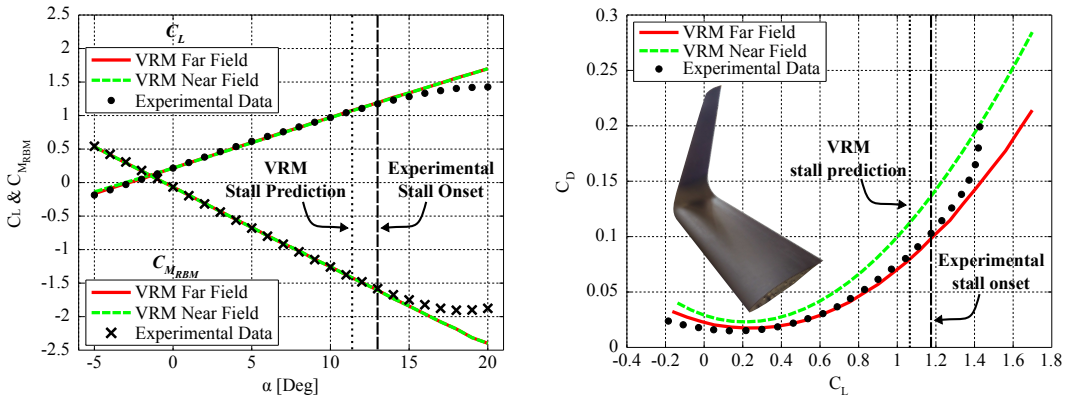

(a) α-C_L & $C_{M_{RBM}}$ (b) C_L-C_D

FIGURE 2.16: Experimental wind tunnel and numerically calculated data for a 304CZ sailplane blended winglet wingtip.

TABLE 2.3: VRM validation case 2 drag polar RMSE prior to stall onset ($-5^\circ \leq \alpha \leq 13^\circ$).

VRM model	RMSE [%]
Near field analysis	7.79
Trefftz plane analysis	1.39

and the far field Trefftz model $C_{L\alpha} = 0.0759$. Furthermore, validation of the capability to sufficiently predict the wing root bending moment is necessary so that it can be employed as a design constraint in the optimisation procedure. This is an important parameter to consider when trying to reduce the induced drag of a wing configuration.

Figure 2.16b shows a distinct difference in the drag polars predicted for the 304CZ sailplane wingtip winglet section, where it is seen that the near field prediction of the induced drag is consistently higher. This is due to the over prediction of the local downwash and thus an over-prediction in the local angle of attack. This result was also found by Smith [71] who highlights that the Trefftz plane analysis better accounts for the wake shape. Hence, it is concluded that the near field model is unsuitable for modelling arbitrary non-planar wing configurations.

2.5 AERODYNAMIC DESIGN OPTIMISATION

This section presents aerodynamic optimisation problems of increasing complexity, including both single and multi-objective optimisations of wing lifting surface arrangements working towards the design optimisation of the final wind tunnel models. Multi-objective design criteria and competing constraints are methodically added to investigate how they change the problem, and how the sGA copes with the changing feasible design space.

The specifications for these tests are listed in table 2.4, where the baseline wing is the same as that used in the **Case 1** experimental validation. As the angle of attack of each wing within the sGA population is allowed to vary continuously, according to lift-curve-slope data presented in figure 2.15, the lift constraint varies as a function of

TABLE 2.4: Test case specifications based on planar wing presented by Sivells [8].

Specification	
Freestream velocity	54.667 $[m/s]$
Mach number	0.17
Atmospheric pressure	$\approx$ 234422 $[Pa]$ ($\equiv 34 psi$)
Atmospheric density	≈ 2.754 $[kg/m^3]$
Max semi-span (b_{ref})	2.286 $[m]$ ($\equiv 7.5 ft$)
Max span-to-height ratio	0.2
Root Chord	0.725 $[m]$ ($\equiv 1.769 ft$)

angle of attack ($L_{ref}(\alpha)$). Therefore, for a specific angle of attack there is a fixed lift constraint, this enables better comparison between the different candidate solutions and the baseline planar configuration. The specific wing geometry and test conditions are provided by Sivellis [8].

All presented optimisation results shown in this work have been obtained by running the sGA-VRM algorithm on a Dual Intel Xeon (E5-2640 v3) parallel computing platform (RAM: 2133MHz DDR4, 4×8GB) using 15 cores via MATLAB's parallel computing toolbox suite. The sGA-VRM settings used for all optimisations in this work are given in table 2.5.

TABLE 2.5: sGA-VRM settings.

Parameter	Value
Population	150
Generations	600
Mutation rate	0.05 - 0.3
BLX-α	$\alpha = 0.5$
Secondary crossover operator	0.05
Spanwise discretisation (N_p)	≈ 0.01 [m]
Chordwise discretisation (N_c)	8

2.5.1 MINIMUM INDUCED DRAG

OPTIMISATION 1

The Optimisation 1 problem considers the aerodynamic optimisation of un-swept, and un-tapered rectangular lifting surface design space, for which only the induced drag of the system is minimised. The optimisation problem is presented as follows:

$$\textit{Minimise: } D_i$$

$$\textit{w.r.t. variables} \begin{cases} 1 \leq n \leq 5 & \\ 0 \leq \alpha \leq 15 & [deg] \\ 0 \leq \Gamma_n \leq 195 & [deg] \\ 0.25 \leq l_1 \leq 2.286 & [m] \\ 0 \leq l_n \leq 2.286 & [m] \\ -10 \leq \theta_n \leq 10 & [deg] \\ -5 \leq \theta_{root} \leq 5 & [deg] \\ Camber = 0, 1 & \end{cases} \qquad \textit{Subject to} \begin{cases} 1 - \frac{L}{L_{ref}} \leq 0 \\ \frac{h_{wingtip}}{b_{ref}} \leq 0.2 \\ b \leq b_{ref} \end{cases}$$

where n is the number of wing segments. The twist distribution, θ_n, varies linearly over each wing segment span, l_n. The lift constraint ensures that wing solutions must

maintain a required total lift, while the total wingspan, b, and wingtip height, $h_{wingtip}$, provide a maximum height-to-span ratio of 0.2.

As the posed optimisation problem is single objective, a single optimal solution is identified. The optimal solution obtained for rectangular (un-swept and un-tapered) lifting surfaces is shown in figure 2.17. This configuration is a closed box wing of maximum allowable span and height made up of three wing segments; this configuration is the optimal prediction given by lifting line theory [5, 118]. This provides validation of the sGA-VRM optimisation algorithm performing to identify anticipated optimal solutions.

The sGA designed the box wing arrangement to be optimal (i.e. have minimum induced drag) at $\alpha = +7.48°$ as indicated in figure 2.18a. At $\alpha = +7.48°$ the induced drag is 29.62% lower when compared to the planar baseline wing, with an average induced drag reduction of 27.51% over $0° \leq \alpha \leq +13°$. The drag polars in figure 2.18a also indicate that the much larger wetted area of the box wing results in an $\approx 48.2\%$ increase in the wing's parasitic drag. Hence, only small total drag savings are made over the range $+3.34° \leq \alpha \leq +6.49°$, and at all other angles of attack the net total drag actually increases despite the induced drag saving.

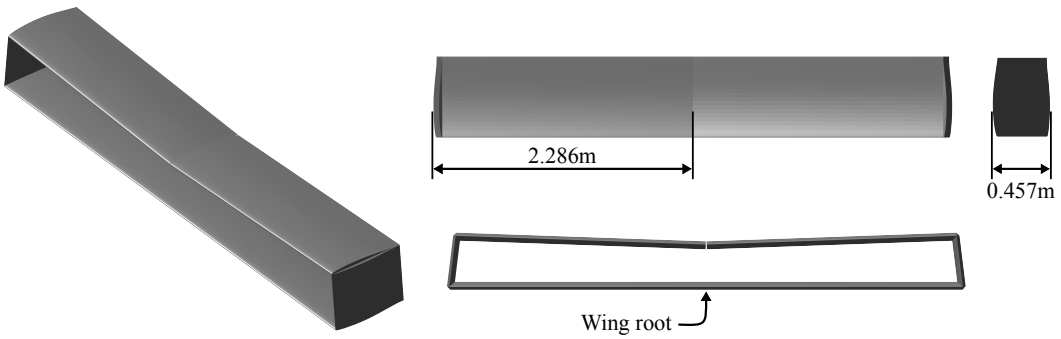

FIGURE 2.17: Optimisation 1 - optimal induced drag solution.

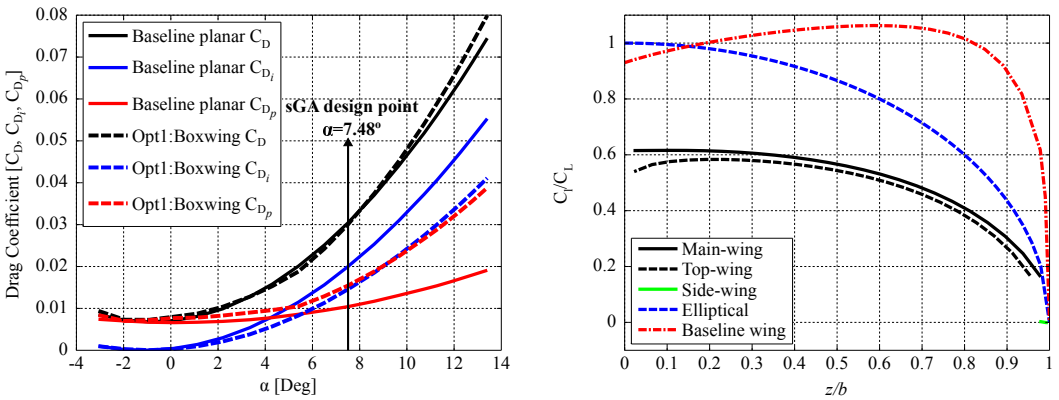

(a) C_D-α (b) Spanwise loading at $\alpha = 7.48°$.

FIGURE 2.18: Baseline wing Vs. Optimisation 1 solution.

The spanwise loading for the optimised box wing surface arrangement, the baseline wing, and its optimal elliptical distribution is shown in figure 2.18b. Both the upper (top-wing) and lower (main-wing) surfaces of the box wing are positively loaded, and carry approximately the same section-wise lift, while the side-wing element carries little load. Is it indicated that the side-wing is loaded inboard (positive loading). The elliptical spanwise distribution theoretically provides the minimum (optimal) induced drag for planar wings [202]. The baseline planar wing, described by Sivellis [8], presents a sub-optimal spanwise loading indicative of an untwisted tapered ($\lambda = 0.4$) wing. With taper, the outboard local lift coefficient increases due to the reducing chord.

OPTIMISATION 2

Optimisation 1 considered un-swept and un-tapered rectangular wing sections only, allowing the sGA to change the span, dihedral and twist of each segment. Including sweep and taper design variables for each wing segment enables a broader topological planform design space. The inclusion of taper can lead to unrealistically small sectional chord distributions at the wingtip resulting in high local lift coefficients and encourage wingtip stall, as previously discussed in Section 2.4.6. To prevent this, a sectional stall prediction constraint is added to the lift and geometry constraints. Thus, the optimisation problem is presented as follows:

$$
\begin{aligned}
&\textit{minimise: } D_i \\
&\textit{w.r.t. variables} \begin{cases}
1 \leq n \leq 5 & \\
0 \leq \alpha \leq 15 & [deg] \\
0 \leq \Gamma_n \leq 195 & [deg] \\
0.25 \leq l_1 \leq 2.286 & [m] \\
0 \leq l_n \leq 2.286 & [m] \\
-10 \leq \theta_n \leq 10 & [deg] \\
-5 \leq \theta_{root} \leq 5 & [deg] \\
Camber = 0, 1 & \\
0 \leq \Lambda_{0.5c} \leq 45 & [deg] \\
0 \leq \lambda \leq 1 &
\end{cases}
\qquad
\textit{Subject to} \begin{cases}
1 - \frac{L}{L_{ref}} \leq 0 \\
\frac{h_{wingtip}}{b_{ref}} \leq 0.2 \\
b \leq b_{ref} \\
C_l^i|_{VRM} \leq C_{l_{max}}^i|_{XFOIL}
\end{cases}
\end{aligned}
$$

The Optimisation 2 problem remains single objective, thus a single optimal solution is identified. The obtained optimal solution is shown in figure 2.19. This configuration is a closed box wing of maximum allowable span and height made up of five wing segments: two segments in the primary lifting wing, two segments in the side-wing, and one segment in the top-wing.

The wing drag polar and spanwise loading distribution are shown in figure 2.20. Allowing the main lifting surfaces to sweep further apart from each other improves the aerodynamic performance of the closed non-planar configuration because of

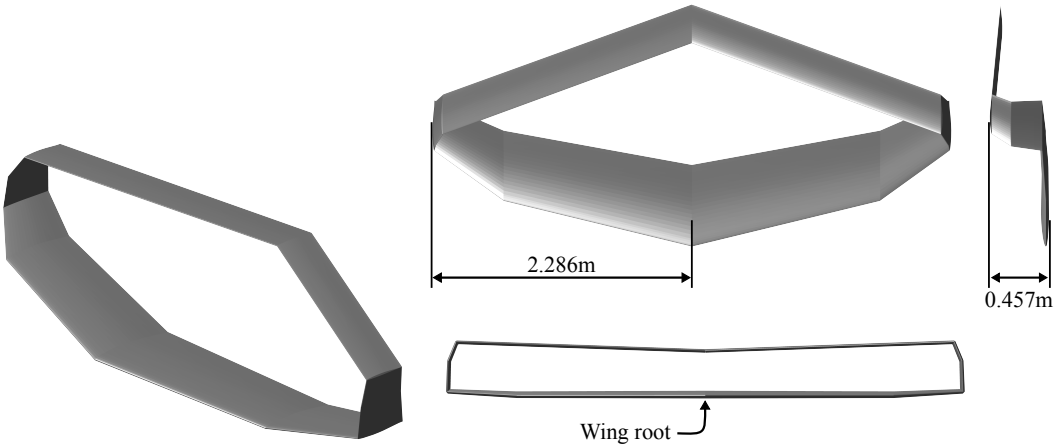

FIGURE 2.19: Optimisation 2 - optimal induced drag solution.

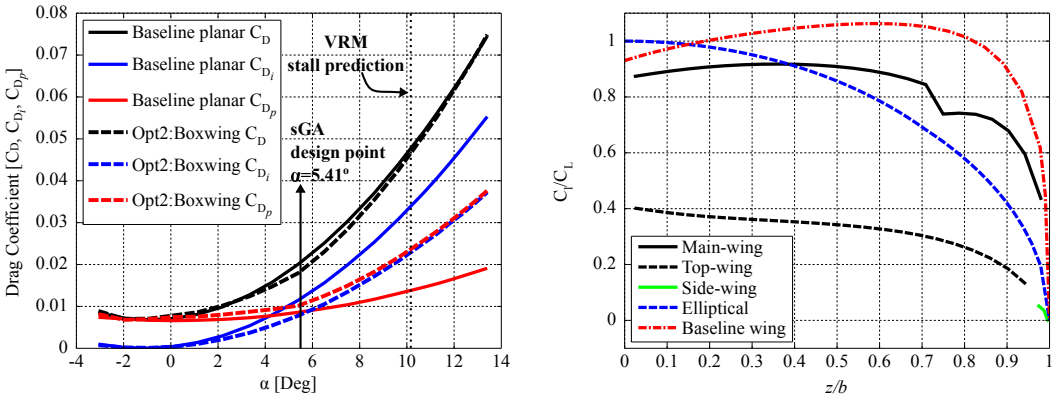

(a) C_D-α (b) Spanwise loading at $\alpha = +5.41°$.

FIGURE 2.20: Baseline wing Vs. Optimisation 2 solution.

the increased downwash over the wing. At $\alpha = +5.41°$, which denotes the sGA design point, the induced drag of the optimised wing is reduced by 32.38% when compared to the baseline wing, with an average induced drag reduction of 31.22% over $0° \leq \alpha \leq +13°$.

The drag polars in figure 2.20a indicate that the much larger wetted area of the optimised box wing results in an $\approx$ 43.7% increase of the wing's parasitic drag. The net total drag of the optimised wing, relative to the baseline planar wing, is seen to reduce in the angle of attack range $3.12° \leq \alpha \leq 13.41°$ by an average of 3%.

Figure 2.20b shows the spanwise loading of the wing swept box wing arrangement, indicating that the main-wing carries the bulk of the lift, while the top-wing carries less load, however retains positive loading. The variation of C_l over the top and main-wing is approximately flat, with the main-wing segment demonstrating high tip loading due to low wing taper. The spanwise loading of the baseline wing and an elliptically loaded planar wing are also shown.

2.5.2 MINIMISE INDUCED AND PARASITIC DRAG

OPTIMISATION 3

Both Optimisation 1 and Optimisation 2 have dealt with only the minimisation of the induced drag: a single objective. The inclusion of parasitic drag will have a pronounced impact on the optimisation of non-planar arrangements which will strongly influence the wing's wetted area. Thus, Optimisation 3 is presented as follows:

$$\textit{minimise: } D_i \text{ and } D_p$$

$$\textit{w.r.t. variables} \begin{cases} 1 \leq n \leq 5 & \\ 0 \leq \alpha \leq 15 & [deg] \\ 0 \leq \Gamma_n \leq 195 & [deg] \\ 0.25 \leq l_1 \leq 2.286 & [m] \\ 0 \leq l_n \leq 2.286 & [m] \\ -10 \leq \theta_n \leq 10 & [deg] \\ -5 \leq \theta_{root} \leq 5 & [deg] \\ 0 \leq \Lambda_{0.5c} \leq 45 & [deg] \\ 0 \leq \lambda \leq 1 & \\ Camber = 0, 1 & \end{cases} \qquad \textit{Subject to} \begin{cases} 1 - \frac{L}{L_{ref}} \leq 0 \\ \frac{h_{wingtip}}{b_{ref}} \leq 0.2 \\ b \leq b_{ref} \\ C_l^i|_{VRM} \leq C_{l_{max}}^i|_{XFOIL} \end{cases}$$

It is highlighted that Optimisation 3 is fundamentally identical to Optimisation 2, other than the inclusion of the parasitic drag objective. Due to the presence of two objectives, the sGA's final population is presented as a Pareto-front of solutions; this is shown in figure 2.21. It is found that solutions identified as achieving the best induced drag reduction are closed box wing arrangements with 5 wing sections active. Unsurprisingly the box wing solution from Optimisation 2 is identified within the Pareto-front, and is indicated in figure 2.21. Moving down the Pareto-front, the closed box wing arrangements open up to form C-wing configurations with large top-wings

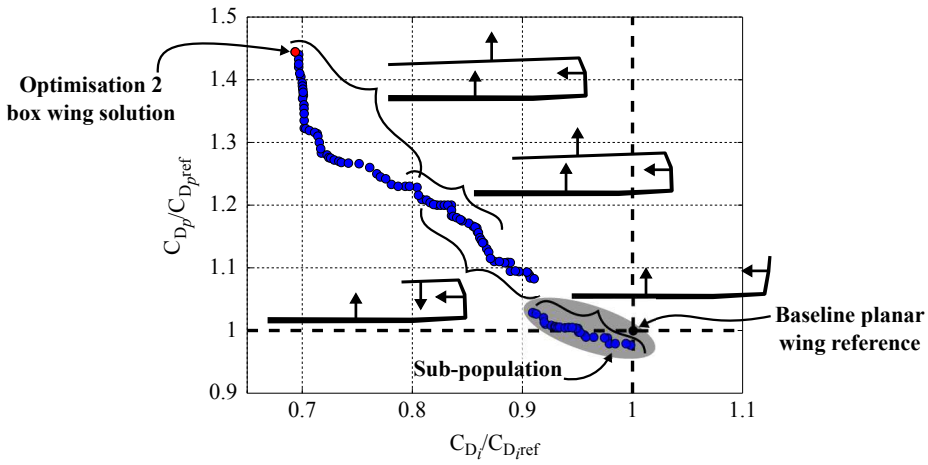

FIGURE 2.21: Optimisation 3 Pareto-optimal solutions.

which are positively loaded over the range $0.78 \leq C_{D_i}/C_{D_{iref}} \leq 0.85$. All C-wing solutions have 3 to 5 active wing segments. These wing arrangements also increase the wing root bending moment relative to the baseline case by up to 250%.

Moving further down the Pareto-front into the range $0.85 \leq C_{D_i}/C_{D_{iref}} \leq 0.91$, the C-wing configurations have smaller top-wings with inverted camber orientation in-order to maintain positive loading. Such top-wings produce a net down-force opposing useful lift. These solutions, achieving an $\approx$ 10 to 15% induced drag reduction, are noted to identify some configurations which only increase the root bending moment by 1 to 2% (facilitated by the down-loaded top-wing), while others increase the root bending moment by up to 85%. For the C-wing solutions there are still significant increases in parasitic drag of about 15%.

Along the Pareto-front, a discontinuity is observed in the parasitic drag variation of solutions from $C_{D_p}/C_{D_{pref}} = 1.08$ to $C_{D_p}/C_{D_{pref}} = 1.02$. This jump in the Pareto-front is caused by a sub-population within the sGA of different chromosomal structure. This sub-group of solutions are planar wings with highly swept wingtips and outboard canted winglets, as indicated in figure 2.21, which provide some induced drag savings without causing a significant increase in the parasitic drag. As no root bending moment constraints have been introduced but a constraint on the maximum wingspan has, the identification of such solutions is promising. Whitcomb [21] showed in 1976 that winglets could reduce the induced drag of wings with constrained wingspans, several studies since have confirmed this finding [5, 94]. Although wingletted solutions appear to provide savings of the induced drag with minimal increase of the parasitic drag, the wing root bending moments are seen to increase by $\approx$ 20% in order to meet the lift constraints.

2.5.3 MINIMISE INDUCED AND PARASITIC DRAG WITH ROOT BENDING MOMENT CONSTRAINT

OPTIMISATION 4

Further building on the optimisation procedure presented in Optimisation 3, Optimisation 4 introduces an extra constraint acting to limit the wing root bending moment via the root bending moment scaling factor m_{limit}. The lift produced by any wing surface, even a closed box wing, is taken to be carried as a bending moment through the main-wing root only. Optimisation 4 is presented as follows:

$$\textit{minimise: } D_i \text{ and } D_p$$

$$\textit{w.r.t. variables} \begin{cases} 1 \leq n \leq 5 & \\ 0 \leq \alpha \leq 15 & [deg] \\ 0 \leq \Gamma_n \leq 195 & [deg] \\ 0.25 \leq l_1 \leq 2.286 & [m] \\ 0 \leq l_n \leq 2.286 & [m] \\ -10 \leq \theta_n \leq 10 & [deg] \\ -5 \leq \theta_{root} \leq 5 & [deg] \\ 0 \leq \Lambda_{0.5c} \leq 45 & [deg] \\ 0 \leq \lambda \leq 1 & \\ Camber = 0, 1 & \end{cases} \quad \textit{Subject to} \begin{cases} 1 - \frac{L}{L_{ref}} \leq 0 \\ \frac{h_{wingtip}}{b_{ref}} \leq 0.2 \\ b \leq b_{ref} \\ C_l^i|_{VRM} \leq C_{l_{max}}^i|_{XFOIL} \\ M_{RBM} \leq m_{limit} M_{RBM_{ref}} \end{cases}$$

The addition of the root bending moment constraint will indirectly help the optimisation place a limit on the wing structural weight. The loading of non-planar wing arrangements without root bending moments, as previously observed, tend to be highly tip loaded. The addition of root bending moment constraints will try to move the main-wing's centre-of-pressure inboard, and is likely to encourage more heavily down-loaded top-wings. This constraint is expected to produced aerodynamically less efficient wing configurations. Non-planar wingtip arrangements encourage 'cleaner' flow over the outboard wing section, modifying the circulation at the main-wing wingtip, which has the effect of causing additional lift over the outboard wing. Even a small amount of additional lift can significantly increase the wing root bending moment due to the moment arm (wing semi-span). Limiting the root bending moment, while simple, has been shown to work for limiting the structural weight in conceptual wing design optimisations. [68, 98, 121, 218, 219]

Figure 2.22 presents three optimisation cases: No RBM constraint ($m_{limit} \to \infty$), which is represented by Optimisation 3; RBM Constraint 1 ($m_{limit} = 1.5$); and RBM

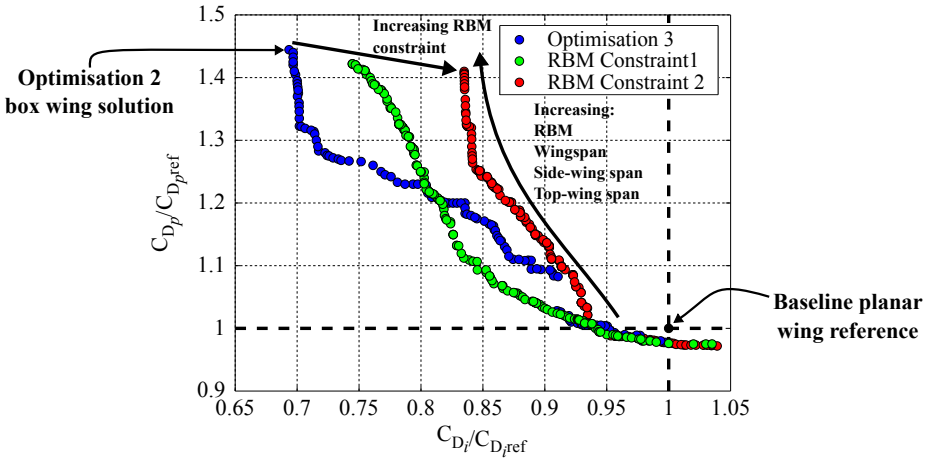

FIGURE 2.22: Optimisation 4 Pareto-optimal solutions; No RBM constraint: $m_{limit} \to \infty$ (Optimisation 3); RBM Constraint 1: $m_{limit} = 1.5$; RBM Constraint 2: $m_{limit} = 1$.

Constraint 2 ($m_{limit} = 1$). In the absence of any root bending moment constraint, the sGA solutions increase the root bending moment by up to $\approx$ 250% relative to the baseline planar wing. In this instance the identified box and C-wing solutions are found to add more structural weight than their respective induced drag reductions can compensate for. Therefore, these configurations cannot be justified.

It is observed that the addition of the RBM constraint modifies the Pareto-front. This is indicative of the feasible solution design space changing. With the application of RBM constraints the box wing is immediately removed, and consequentially peak parasitic drag gains reduce with tighter RBM constraints. This situation reflects a possible false optimisation design decision as the lift of the entire wing is considered to be carried as a bending moment through the main-wing root only. In reality, a closed box wing arrangement would share the wing root bending moment through the main and top-wing roots. Furthermore, is it observed in figure 2.22 that a portion of the converged 'RBM Constrain 1' Pareto falls bellow the converged 'Optimisation 3' Pareto. The reason for this is that in the absence of the RBM constraint the sGA identifies several optimal solution types in alternative design spaces, as discussed in Section 2.5.2. With the application of the RBM constraint, the sGA drives the solution types into the same design space, resulting in a smoother Pareto-front, and facilitates a more robust search guided by constraint based reasoning.

For RBM Constraint 1 ($m_{limit} = 1.5$), the wing configurations can exceed the planar wing reference RBM by 50% for the respective angle of attack and associated lift constraint. Some large aspect ratio top-wings persist for C-wing arrangements where most are positively loaded with lower angles of attack and lower wing sweep. C-wings with heavily down-loaded top-wings have slightly reduced total wingspans ($\approx$ 4%) and lower angles of attack. The top-wing segments are also noticed to have highly raked wingtips. The high sweep reduces the component of velocity that a certain wing section encounters ($U_\infty cos(\Lambda)$). Similar to the Optimisation 3 design case a few wingletted wings are identified, however a discontinuity in the Pareto-front is not seen as all wing segments are active. Thus, a smoother Pareto-front trade-off is obtained. The winglet solutions are found to slightly reduce the parasitic drag by 2 to 3% and the induced drag by 4 to 5%. The solutions in the Pareto that increase the induced drag relative to the baseline are wingletted wings with reduced total span and high angle of attack in order to meet lift constraints.

For RBM Constraint 2 ($m_{limit} = 1$), all wing arrangements in the Pareto-front meet the root bending moment of the baseline planar reference wing for the respective angle of attack and associated lift constraint. In this design case, top-wings reduce in surface area relative to those for RBM Constraint 1, all remain positively down-loaded. Peak induced drag reduction appears limited to 17%, with only very minor additional induced drag savings accompanied by an almost asymptotic increase in parasitic drag which begin to exceed 40%. These C-wings are of maximum span and height. It is also noticed that for this design case all side-wings are canted inboard.

2.5.4 Wind Tunnel Model Wing Design

With the design algorithm specified (sGA-VRM) this section describes the design of two wing arrangements, specifically a baseline planar wing and a C-wing, to be carried forward to manufacture and wind tunnel testing. The sGA-VRM provides an effective design tool to ensure experimental constraints and design criteria can be met while maintaining characteristics of each wing arrangement. Thus, the expected performance of the two wings are related in their design architecture with the same specifications and underlying physics to guide the topological design. The primary function of this is to ensure that the C-wing carried forward to the experimental stage is not arbitrary. The sGA is implemented with specifications provided in table 2.5.

Each wing's design specification is dictated by criteria adhering to the test facility limitations which place restrictions on the wing sizing (relative to the wind tunnel working section), and maximum feasible forces/moments which are dictated by diagnostic equipment measurement capabilities. The experimental conditions and facility limitations are summarised in table 2.6.

The planar wing, relative the the C-wing, has a very restrictive design space to ensure that the wing is analogous to a typical mid-size transport commercial aircraft wing topology, representing an approximately 10%-scale model. Thus, constraints have been implemented to force a specific quarter chord sweep angle and overall wing taper ratio. The C-wing design is given more flexibility in terms of variable accessibility, however the inboard 74% of the main-wing wingspan is held constant to the planar wing topology. The function of this is to reduce complexity and cost of the wing model manufacture. The C-wing designed is thus more representative of a C-wing wingtip retro-fit design. Furthermore, all wing sections remain untwisted with constant aerofoil section, NACA 63_1412. The design decision of using the NACA 63_1412 for the wind tunnel model is discussed further in Section 3.4, while the 12% thickness-to-chord ratio remains suitable for application of potential flow models [202]. Due to the lack of wing twist (washout), sub-optimal lift distribution over the wing

Table 2.6: Design specifications for model design.

Specification	Value
Freestream velocity	50 $[m/s]$
Mach number	0.14
Atmospheric pressure	$\approx$ 101325 $[Pa]$
Atmospheric density	$\approx$ 1.225 $[kg/m^3]$
Max semi-span ($b_{ref}/2$)	1.5 $[m]$
Max span-to-height ratio	0.2
Max lift	2225 $[N]$
Max root bending moment	1100 $[Nm]$

regardless of wingtip arrangement is expected. It is necessary to highlight that neither wing arrangements can be considered truly optimal, but can be considered optimal given the allowed design space and experimental constraints. While the C-wing may achieve a total drag reduction, it is unlikely that it will provide optimal reduction of induced drag relative to net increase of the parasitic drag.

No aerostructural design optimisations were made during the optimisation procedure, however additional geometric design constraints were enforced to reduce the aerodynamic coupling term. Theory covering the wind tunnel model wing aeroelastic design is covered in Section 3.5. The sGA facilitates the prerequisite design criteria required to enable the decoupling of each wing arrangement's bending and torsional modes through aeroelastic constant management. The local elastic and inertial axes are designed to coincide at 34% of the local chord line over the wingspan, thus the inertial coupling is assumed negligible. Illustrated in figure 2.23, an additional geometric constraint is implemented in which the distance between the elastic axis and the aerodynamic centre for each spanwise panel is monitored. The sGA then drives forward solutions which aligns the aerodynamic and elastic axes of the wing ($ec \rightarrow 0$).

BASELINE PLANAR WING

In the design optimisation of the baseline wing there is no reference design. This is one of the advantages of employing the genetic algorithm as no *a priori* knowledge of the design space is needed. As previously stated, the allowable design space is restrictive, however refinement of the design relative to the specified design constraints would be tedious and prone to human error if conducted manually via trial and error. Design optimisation of the planar wing is presented as follows:

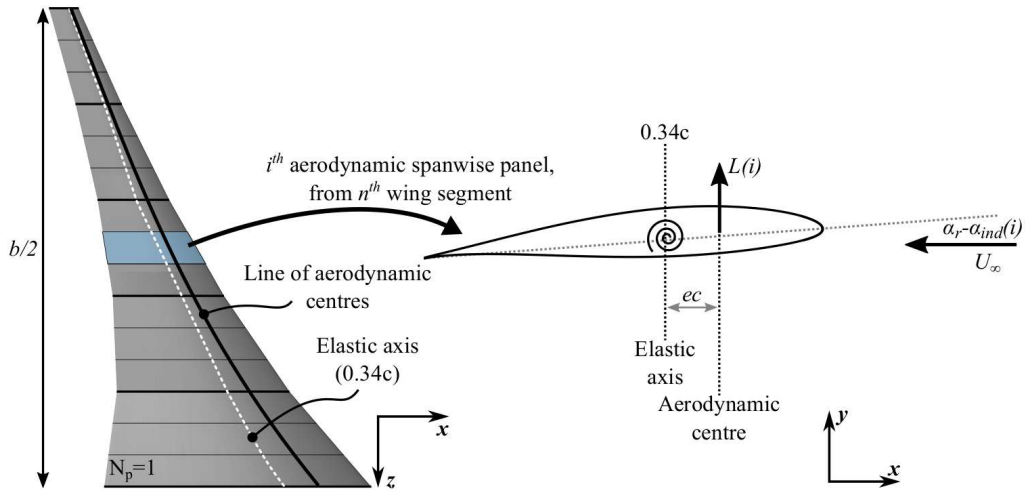

FIGURE 2.23: Illustration of aerodynamic coupling constraint.

$$
\begin{aligned}
&\textit{minimise}: D_i \text{ and } D_p;\\
&\textit{maximise}: L\\
&\textit{w.r.t. variables} \begin{cases}
1 \leq n \leq 3 & \\
0 \leq \alpha \leq 10 & [deg]\\
0.25 \leq l_1 \leq 1.5 & [m]\\
0 \leq l_n \leq 1 & [m]\\
0 \leq \Lambda_{0.5c} \leq 45 & [deg]\\
0 \leq \lambda \leq 1 & \\
0.5 \leq c_{root} \leq 0.8 & [m]
\end{cases}
\qquad
\textit{Subject to} \begin{cases}
b \leq b_{ref} & \\
C_l^i|_{VRM} \leq C_{l_{max}}^i|_{XFOIL} & \\
M_{RBM} \leq m_{limit} M_{RBM_{ref}} & \\
ec_{Np} \to 0 \quad (ec_{Np} \geq 0) & \\
\Lambda_{0.25c} \to 30^\circ & \\
\lambda_{wing} \to 0.2 &
\end{cases}
\end{aligned}
$$

The constraint to influence the main-wing quarter chord sweep ($\Lambda_{0.25c}$) to 30° forces the wing into the topology sought and, combined with the aerodynamic coupling constraint, will cause the elastic axis (or 34% local chord line) to be linear. The wing root bending moment is allowed to approach facility limitations (dictated by the force platform) within the optimisation ($m_{limit} = 1$). The resulting Pareto-optimal solutions from the sGA are presented in figure 2.24. All wing solutions have the same lift within 10%, where wings with the lowest root bending moment exist in the region of the Pareto-front nearest the utopia point; this region is highlighted in the figure. The solution selected to be used as the baseline planar wing for the wind tunnel model and C-wing optimisation is also indicated in figure 2.24.

The solutions with the highest induced drag are found to have slightly reduced wingspans (smallest wingspan $\approx 1.46m$—roughly 97% of the max allowable span) and increased angles of attack. Following this section over the range of $0.043 \leq C_{D_i} \leq 0.025$ wing solutions are observed to have a relatively constant parasitic drag coefficient of 0.0162. Over this range, solutions are found to have increasing wingtip sweep (raked wingtip) reducing the induced drag with minimal effect on the parasitic drag. The local parasitic drag at the wingtip actually increases slightly as the local chord decreases, leading to a reduction of the local Reynolds number. Wing solutions with

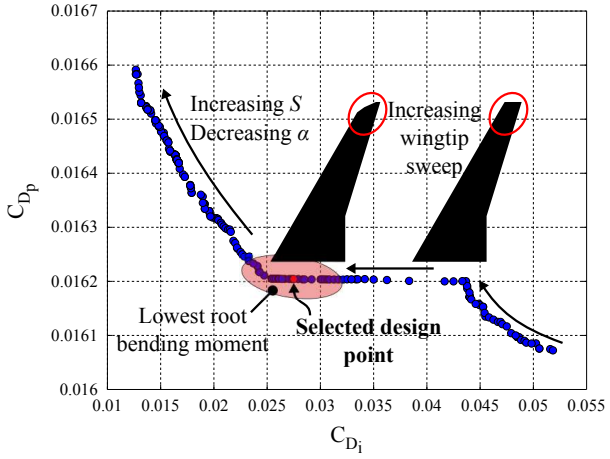

FIGURE 2.24: Wind tunnel planar wing design Pareto-front.

$C_{D_i} > 0.025$ continue to have swept wingtips at maximum allowable sweep (45°), but the overall wing area is seen to increase driven by an increase in the wing root chord length. The root bending moment constraint then drives these wings to take on a reduced angle of attack.

The planar wing solution selected (indicated at $C_{D_i} = 0.0265$, $C_{D_p} = 0.0162$ on the Pareto-front) meets all the design criteria with the best alignment of aerodynamic centres along the 34% local chord line. The planar wing solution topology is shown in figure 2.25, with a summary of the topology description presented in table 2.7.

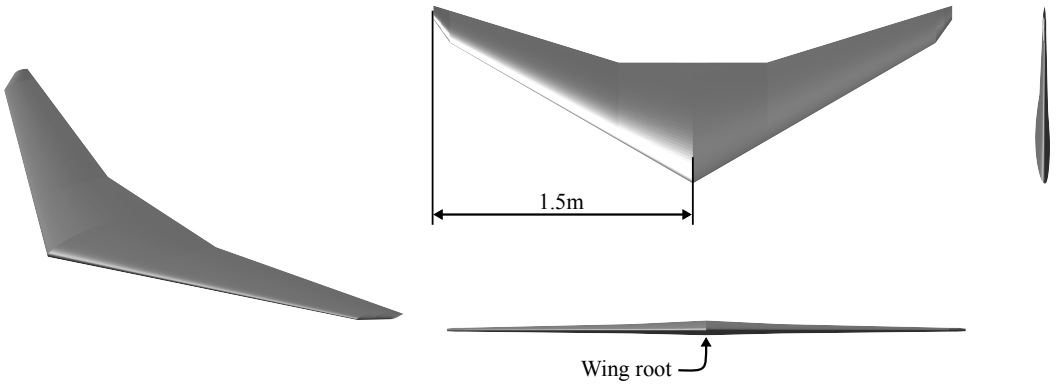

FIGURE 2.25: Wind tunnel planar model.

TABLE 2.7: Wing solution topology.

Geometric parameter	Value
Wing semi-span ($b/2$)	1.50 [m]
Wing root chord (c_{root})	0.70 [m]
Mean aerodynamic chord ($\bar{c}$)	0.44 [m]
Main wing sweep ($\Lambda_{0.25c}$)	30 [deg]
Wing taper ratio (λ_{wing})	0.21

C-WING

With the baseline wing defined, the sGA was tasked with modifying the outboard 26% of the wingspan to house a non-planar wingtip extension. The primary goal of the design optimisation is to identify wing solutions which reduced the wing system's total drag while maintaining equivalent (or smaller) wingspan and root bending moment for the same lift relative to the baseline planar wing system. This enables a confident comparison between the two arrangements with regards to the aerodynamic performance of the overall wing system [21]. The successful application of any non-planar wing system for improving the aerodynamic efficiency depends entirely upon the ability to construct the wing system such that a sufficiently low root bending moment and parasitic drag is maintained, relevant to the equivalent planar wing system [46].

The non-planar wingtip optimisation is presented as follows:

$$\textit{minimise: } D_i \text{ and } D_p$$

$$\textit{w.r.t. variables} \begin{cases} 1 \leq n \leq 5 \\ 0 \leq \Gamma_n \leq 195 \quad [deg] \\ 0 \leq \alpha \leq 10 \quad [deg] \\ 0 \leq l_n \leq 1.5 \quad [m] \\ 0 \leq \Lambda_{0.5c} \leq 45 \quad [deg] \\ 0 \leq \lambda \leq 1 \end{cases} \qquad \textit{Subject to} \begin{cases} 1 - \frac{L}{L_{ref}} \leq 0 \\ b \leq b_{ref} \\ C_l^i|_{VRM} \leq C_{l_{max}}^i|_{XFOIL} \\ M_{RBM} \leq m_{limit} M_{RBM_{ref}} \\ ec_{Np} \to 0 \quad (ec_{Np} \geq 0) \end{cases}$$

The wing root bending moment should be equivalent to the planar solution, therefore $m_{limit} = 1$. It is emphasised that with the variables presented, a broad design scope is provided to ensure that any C-wing design is not an artificially forced solution. While a box wing design is infeasible given the wing section of fixed topology, planar wing arrangements (other than a span extension) and wingletted designs are obtainable. Figure 2.26 presents the sGA solution population over 600 generations.

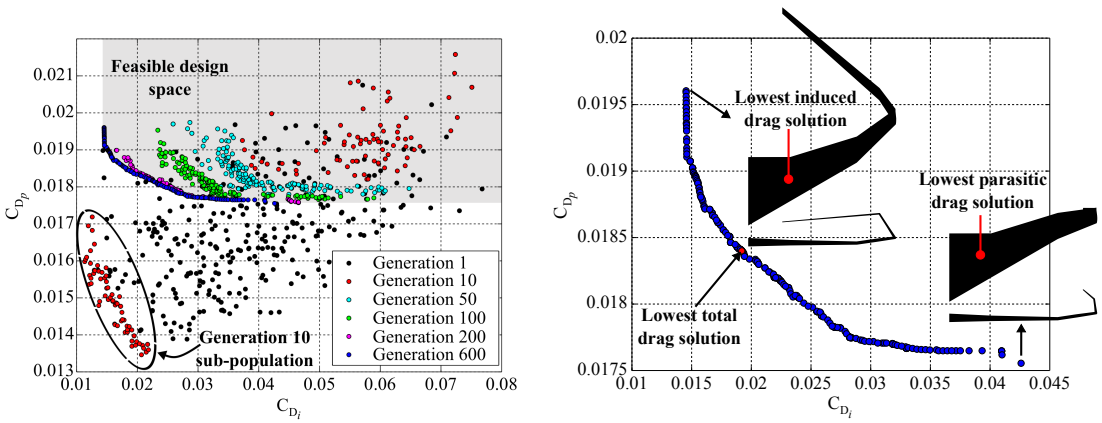

(a) sGA population evolution.

(b) sGA 600^{th} generation Pareto-front.

FIGURE 2.26: sGA population optimisation.

Predictably, the majority of initialised solutions in the 1^{st} generation exist within the infeasible design space, as indicated by figure 2.26a. By the 10^{th} generation, the solution population is split between an infeasible and feasible range of solutions. The reason for this is that a sub-population, indicated in figure 2.26a, of very low total drag solutions exist. These solutions are composed of wingletted wings (with outboard cant angle of 20° to 45°) of maximum allowable span and height, thus meeting geometric constraints, however they exceed the root bending moment constraint by up to 24%. The sGA explores these solutions, suggested by the apparent movement of the sub-population towards a Pareto-front. However, by the 50^{th} generation all wing solutions enter the feasible design space, and all outboard cant winglet designs are abandoned by the sGA. Since the 1970s, outboard winglet cant angles have been recognised as more aerodynamically efficient than inboard cant, at the expense of increased root bending moment [21, 220]. Hence, the sGA is following physical phenomena that is well understood by the aeronautic community in the pursuit of a reduced total drag wing.

Typical of any genetic algorithm performance, the rate of solution betterment slows as more optimal solution populations are found. The first 50 generations show much faster solution development than the subsequent 550 generations, progressing toward the final Pareto-front at generation 600. By the 200^{th} generation, 83 of the 150 solutions form a non-dominated solution Pareto-front. From the 200^{th} to the 600^{th} generation, the 'best' solutions only improve by a few percent with regards to their objective however, by the 600^{th} generation all solutions are non-dominated and are spread over the Pareto-optimal front. The Pareto-front from the 600^{th} generation is shown in figure 2.26b.

The solution topological planforms from the Pareto extremes are illustrated in figure 2.26b, *i.e.* lowest induced drag solution and lowest parasitic drag solution. The location of the lowest total drag solution in the Pareto-front is also shown. All wing solutions have approximately the same lift. The lowest parasitic drag/highest induced drag solution is observed to have a large compound winglet with positive loading. Moving along the front towards the highest parasitic drag/lowest induced drag solution, the design trend is for the winglet to fold back on itself toward the main-wing root to form a top-wing, which then increases in span between solutions. The top-wing maintains positive loading for all solutions in figure 2.26b. The lowest induced drag solutions have the highest root bending moments, some exceeding the root bending moment constraint by 6%. Furthermore, the solutions at the extremes of the Pareto-front meet the maximum wingspan and height constraints, whereas the solutions in the centre (near the knee point) have maximum wingspans and heights within the defined geometric constraint limits by up to 2%. Within this region the lowest total drag solution is determined, the geometry of which is presented in figure 2.27.

Relative to the baseline planar wing, the C-wing solution shown in figure 2.27 has

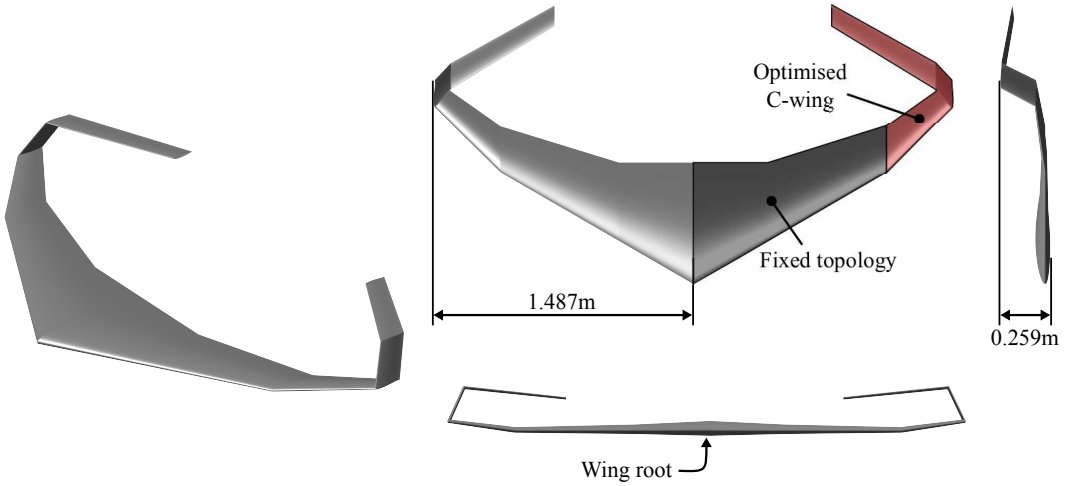

FIGURE 2.27: Non-planar C-wing solution with lowest total drag.

a 0.87% reduced wingspan which reduces the aspect ratio of the main-wing surface by 1.42%, and an increased wing wetted area of 19.1%. A study by Ning and Kroo [94] also found root bending moment constrained C-wing solution designs to have reduced maximum wingspans relative to a planar baseline.

Considering the relative performance between these two wings, consider the total, induced, and parasitic drag polars presented in figure 2.28a. The trend in the total drag polars (C_D) shows that for $\alpha < +3°$ the C-wing will result in a relative increase of total drag. This is due to the increase of the wing parasitic drag, because of the increased wing wetted area. As the induced drag component dominates the net drag ($\alpha > +3°$), the C-wing performance is seen to reduce the total drag of the wing. As discussed, post stall wing performance is expected to deviate away from predicted values. Stall onset is predicted to start at $\approx 8.5°$ for the planar wing, and $\approx 8.9°$ for the C-wing. A similar stall angle is expected due to the overall main-wing similarity. The C-wing stall angle is slightly higher due to the increased chord and the main-wing

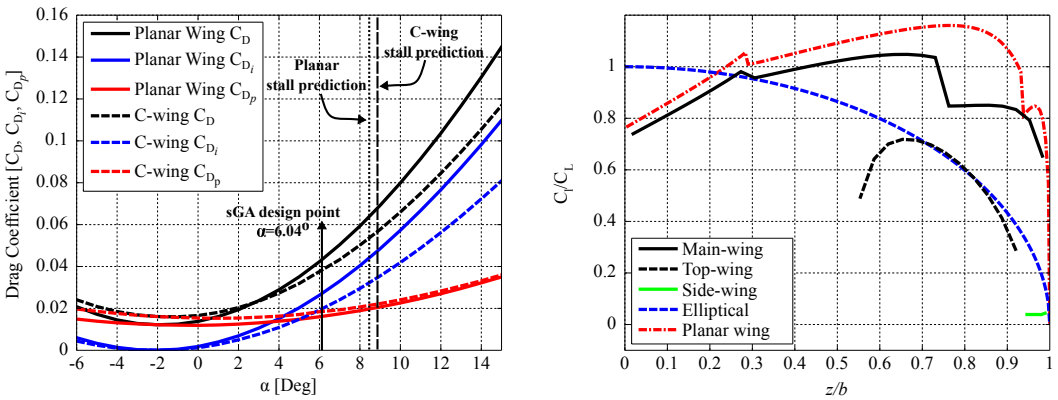

(a) C_D-α. (b) Spanwise loading.

FIGURE 2.28: Planar 'baseline' wing solution Vs. C-wing solution.

wingtip. Both configurations indicate stall onset starting at the wingtip. From figure 2.28b the spanwise loading of each wing shows higher local lift coefficients at the wingtip. Limitations of the VRM analysis is also noticed where neighbouring wing segments have instantaneous variations in sweep angle creating non-physical 'kinks' in the load distribution; such as that seen at $z/b = 0.27$ and 0.95 for the planar wing. These discontinuities are small confined variations within the overall trend, and so are not deemed able to drive pseudo-optimisation [131].

The side-wing and top-wing of the C-wing are positively loaded, with the side-wing loaded inward towards the wing root, and the C-wing down-loaded (acting against useful lift). This result has been observed previously. Elsewhere, studies [48, 121, 221, 222] have shown that this characteristic is physically necessary for such a non-planar arrangement to reduce the induced drag, and so is a promising result.

To further compare the performance of the sGA baseline planar and C-wing solutions, figure 2.29 presents the percentage change in the C-wing's aerodynamic performance metrics as a function of angle of attack, α, relative to the baseline planar wing solution. Figure 2.29a shows the trend previously discussed in which a total drag saving is observed for $\alpha > +3^\circ$. With increasing angle of attack the induced drag saving is suggested to dominate the parasitic drag increase.

Figure 2.29b illustrates the change in lift and root bending moment coefficients. The VRM analysis tool indicates that the lift-curve-slope (C_{L_α}) is 0.100, and 0.102 for the planar and C-wing respectively. It is also identified that the zero-lift angle of attack (α_0) is -2.28° for the planar wing, and -2.02° for the C-wing. Around the zero-lift angle of attack, the top-wing of the C-wing will experience a positive angle of attack producing a down-force. While this force is small it is not present for the baseline planar wing, hence the seemingly dramatic reduction of lift (by almost 100%) and root bending moment at $\alpha \approx -2^\circ$. Table 2.8 summarises the aerodynamic coefficient deviations at the C-wing design point angles of attack ($\alpha = 6.04^\circ$).

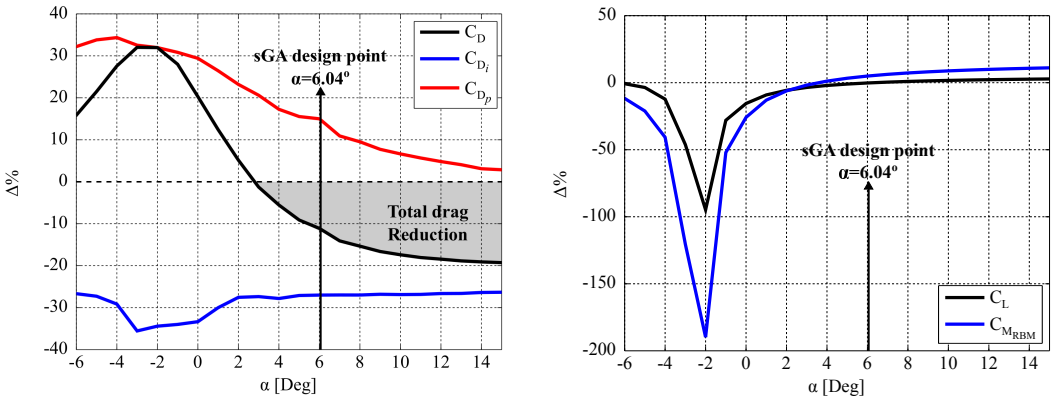

(a) ΔC_D, C_{D_i}, C_{D_p}-α. (b) ΔC_L, $C_{M_{RBM}}$-α.

FIGURE 2.29: Percentage change of C-wing aerodynamic coefficients relative to planar arrangement.

Table 2.8: Summary for aerodynamic performance change and C-wing sGA design point ($\alpha = +6.04^{\circ}$).

Parameter	$\Delta\%$
C_L	-0.21
$C_{M_{RBM}}$	$+3.4$
C_D	-11.11
C_{D_i}	-27.09
C_{D_p}	$+15.54$

As the VRM analysis indicates the C-wing reduces the induced drag, it is appropriate here to also consider the span (or aerodynamic) efficiency, e_0, of each wing configuration. For a planar wing, e_0 is always less than one but for optimal elliptical loading can be equal to one. For non-planar arrangements, the induced drag can be less than the equivalent ideal planar wing, such that e_0 can achieve a value greater than 1 [223]. Kroo [17] indicates that the span efficiency for an optimally loaded C-wing system (for $h/b = 0.2$) can theoretically obtain a span efficiency, e_0, of 1.45. In the same study, an optimally loaded box wing of same span and height achieved $e_0 = 1.46$. Takahashi and Donovan [224], Schirra at al. [225], and Nita and Scholz [226] also present studies in which non-planar wing aerodynamic efficiencies are calculated. Table 2.9 summarises the aerodynamic efficiencies for the planar and C-wing solutions selected from the sGA optimisations. As previously discussed neither wing system is optimally loaded (but are equivalently loaded), nevertheless the increased aerodynamic efficiency of the C-wing is evident. If both the planar and C-wing topologies presented in this work were optimally loaded, and then potentially no longer equivalently loaded, it is necessary to indicate that their relative aerodynamic efficiency would change greatly.

Table 2.9: Wing aerodynamic efficiency.

Wing solution	e_0
Planar	0.729
C-wing	1.272

2.6 SUMMARY AND CONCLUSIONS

A design optimisation architecture consisting of a population structured genetic algorithm combined with a vortex ring potential aerodynamic analysis tool has been developed. The objective of establishing such a capability is necessary to explore a multitude of possible wing topologies within a feasible design space dictated by experimental wind tunnel facility constraints. This permits the definition of a non-arbitrary baseline planar and an optimised non-planar wing to progress to wind tunnel testing. It is necessary to acknowledge that these wing solutions cannot be

considered optimal, but are optimal given the enabled design space and experimental constraints.

Preliminary aerodynamic optimisations of a wing planform relative to a planar wing were first used to optimise wing topology by solving a series of wing design problems. The problems differed in complexity, design consideration, and design objectives. For the minimisation of induced drag, only box wing configurations of maximum allowable span and height were found optimal, reducing the induced drag by up to 32.38%. When parasitic drag was added as an objective, the sGA identified a Pareto-optimal set of solutions ranging from box wings, to an assortment of C-wing arrangements, reducing wingtip geometry to winglet configurations. Due to the existence of span constraints, planar wingtip extensions were not identified in the Pareto-optimal set of solutions. All but a few of the C-wing arrangements, due to positive loading at the wingtip, were observed to dramatically increase the wing root bending moment. Consequently, the root bending moment was added as a constraint to indirectly limit the wing's structural weight requirements. Doing so was found to change the contour of the Pareto-front, indicative of the feasible design space changing. Furthermore, box wings were also no longer deemed optimal due to the root bending moment increase at the main wing root. The ability to decrease the induced drag relative to the associated increase in parasitic drag quickly diminishes as root bending moment constraints are tightened.

In the design of a planar baseline wing, the approximate planform shape was artificially forced through constraint management and a restrictive design space. This was to ensure the planar wing design was analogous of a typical mid-size transport commercial aircraft wing topology, representing an $\approx 10\%$ scale model. Although the analysis of wing geometries did not make any aeroelastic considerations, constraints were enforced to facilitate a wing model which, theoretically, would not be susceptible to divergence or flutter. This was achieved by aligning the aerodynamic, elastic and inertial axes of the wing. The following chapter will discuss this wing design feature in greater detail when considering the physical wind tunnel model.

With the definition of a planar baseline wing, the sGA-VRM re-designed the outboard 26% of the planar wing in order to reduce the induced drag without incurring an unacceptable increase of parasitic drag, and maintaining an equivalent root bending moment and lift relative to the baseline planar wing. At the sGA design point angle of attack ($\alpha = 6.04^\circ$), the C-wing's expected performance was found to reduce the total drag by 11.11% (decreasing the induced drag by 27.09%, and increasing the parasitic drag by 15.54%). The VRM suggests that the aerodynamic efficiency, e, of the C-wing is 74.5% higher than that of the planar wing design.

CHAPTER 3

TEST FACILITY AND WIND TUNNEL MODEL DESIGN

3.1 INTRODUCTION

A series of experiments using several experimental techniques have been conducted with the objective of qualitatively and quantitatively investigating a semi-span wind tunnel model. The semi-span model has been designed to house the baseline planar and C-wing developed in Chapter 2 using the population structured genetic algorithm. In this chapter the experimental facility, semi-span model design and experimental diagnostic techniques used are discussed.

Firstly, in Section 3.2, a description of the de Havilland (dH) National Wind Tunnel Facility at the University of Glasgow is given. Following which, Section 3.3 provides a study characterising the wind tunnel's working section boundary layer profile and growth in addition to the horizontal static pressure gradient. This information is required in the design and boundary corrections for the semi-span wing wind tunnel model described in Section 3.4. Subsequently, the model wing aeroelastic design, structural considerations, solid body blockage and wind tunnel corrections are discussed in Sections 3.5, 3.6, 3.7, and 3.8, respectively. With the model and test facility established, reference systems and experimental techniques/procedures, including force platform, stereoscopic particle imaging velocimetry, surface flow visualisations, laser-Doppler vibrometry, and accelerometry, are detailed in Section 3.9.

3.2 THE DE HAVILLAND NATIONAL WIND TUNNEL FACILITY

The de Havilland (dH) National Wind Tunnel Facility is a sub-sonic closed return wind tunnel circuit capable of reaching a Reynolds number of 4.4×10^6 a meter ($\approx 70ms^{-1}$). A top view schematic diagram of the circuit is shown in figure 3.1.

The working section has an octagonal cross section of $2.65m$ width, $2.04m$ height, and $5.64m$ length and has a contraction ratio of 5:1 relative to the settling chamber. Fillets are arranged to enable the working section's cross sectional area to increase from inlet to outlet by $\approx$ 2%. The purpose of this expansion is to alleviate the longitudinal static pressure gradient through the working section due to boundary layer growth and subsequent horizontal buoyancy effects. The air is driven by a three meter diameter fan located after the second set of turning vanes in the return leg of the circuit. The test section is vented to atmosphere by a breather vent of $0.05m$ around the wall perimeter at the down-stream side of the test section. This vent ensures that the internal pressure of the tunnel does not increase as the air heats due to friction during operation. It is common to have the breather vent at the downstream side of the test section so that the back of the test section is close to atmospheric pressure in order to reduce the effects of leaks through any holes in the test section; these are typically caused by mounting holes.

A pitot tube and a thermocouple are positioned just aft of the test section inlet. The test section is also equipped with several windows to allow for a wide optical access from both the port and starboard sides as well as the roof. The turbulence intensity, evaluated by Giuni [78] using hot wire anemometry, along the centre line of the working section length is $\approx$ 0.4%.

The working section is installed with an Ate Aerotech $2m$ diameter turntable with a stow away arc sector system for model positioning capable of providing roll (360° range), pitch (60° range), and yaw (360° range) motion. Pitch and yaw speed up to three degrees per second, roll speed up to 0.5 degrees per second with position

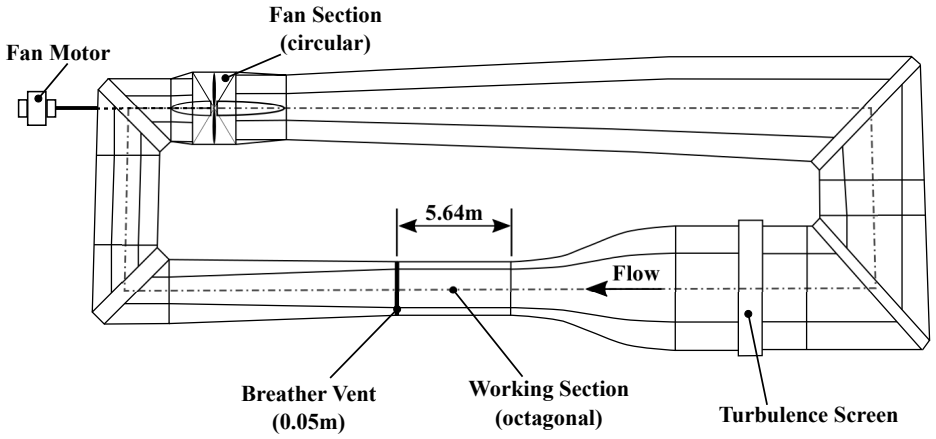

FIGURE 3.1: de Havilland wind tunnel top view schematic.

accuracy of $\pm 0.005^{\circ}$. In this study, the yaw of the turntable is used to control the incidence angle/angle of attack of the wind tunnel model.

3.3 DE HAVILLAND WIND TUNNEL CHARACTERISATION

An understanding of the dH's boundary layer development and consequential horizontal static pressure gradient through the working section is necessary in this work. The semi-span wind tunnel model, described in Section 3.4, will interact with the boundary layer, and will also require corrections to force platform data to account for the effect of any static pressure gradient through the working section.

The working section utilises expanding fillets which facilitate a $\approx 2\%$ increase in cross sectional area from inlet to outlet. This design feature is typical of low-speed close return wind tunnels in order to reduce the need for an excessively long diffuser while making efforts to counteract a thickening boundary layer [227]. The action of the progressive boundary layer thickening over the length of the working section reduces the effective area of the freestream jet from that of the physical dimensions of the test section. Thus, by conservation of mass, this causes an increase in the dynamic pressure (freestream flow speed) outside of the boundary layer; the streamlines are effectively squeezed by a contracting tube. If the geometric cross sectional area was constant, the speed increase would be more significant resulting in a more aggressive static pressure gradient through the test section. This would act to draw the test body downstream, and so artificially increase the total drag felt by that body. This extra drag is commonly referred to a 'horizontal buoyancy' and is analogous to hydrostatic forces (buoyancy) due to vertical pressure gradients acting on bodies submerged under water. The increase in cross sectional area of the dH working section passively attempts to minimise the effects of the boundary layer growth and maintain a constant static pressure (freestream velocity) through the section.

3.3.1 Methods of Characterisation

The working section boundary thickness and static pressure through the test section was sampled at several longitudinal locations using the $80mm$ pressure rake (with 2 static and 13 total pressure ports) and a series of pitot static probes through the working section length, as shown in figure 3.2. Boundary layer profiles were sampled at five locations over the working section length. Figure 3.3 presents a floor plan schematic diagram of the working section indicating the rake positions tested; at position x/L=0.3 the boundary layer was also sampled off-centre towards the starboard of the tunnel and roof centre line to assess the boundary layer thickness uniformity. This location is also where the leading edge of the semi-span model fuselage nose will be.

The static pressure was monitored using four pitot static probes, including the de

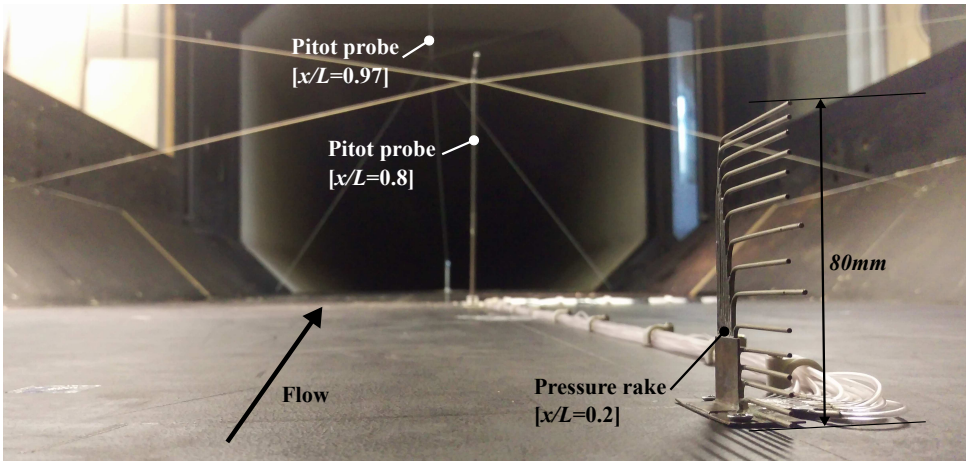

FIGURE 3.2: Boundary pressure rake.

Havilland's own dedicated pitot probe at x/L=0.2. Figure 3.2 shows the pressure rake installed at x/L=0.2 (floor mounted), with pitot probes at x/L=0.8 (floor mounted), and x/L=0.97 (roof mounted) visible in the background (pitot probe at x/L=0.3 is roof mounted). Each pitot probe reached 600mm into the freestream. Tethers were installed on the pitot probes to minimise vibration at higher velocities, which helped reduce the root mean square of the data sampled. Table 3.1 summarises the benchmarking plan. At positions x/L= 0.8 and 0.97 it was necessary to overlap the two pressure rake data sets in-order to capture the full boundary layer profile; at these test locations the boundary layer thickness was comparable to the height of the rake. Hence, additional measurements were taken at these locations but with the rake mounted on 30mm spacers lifting it partially out of the boundary layer.

The pressure rake and probes were connected to a Scanivalve Corporation temperature compensated electronic pressure scanning module. This system was composed of an ERAD4000 A/D base with 16-bit resolution and two module connections: 1) a ZOC22b pressure scanner (32 channels, $\pm$1psi differential pressure range); and 2) a ZOC23b pressure scanner (32 channels, $\pm$10inches H_20 differential pressure range).

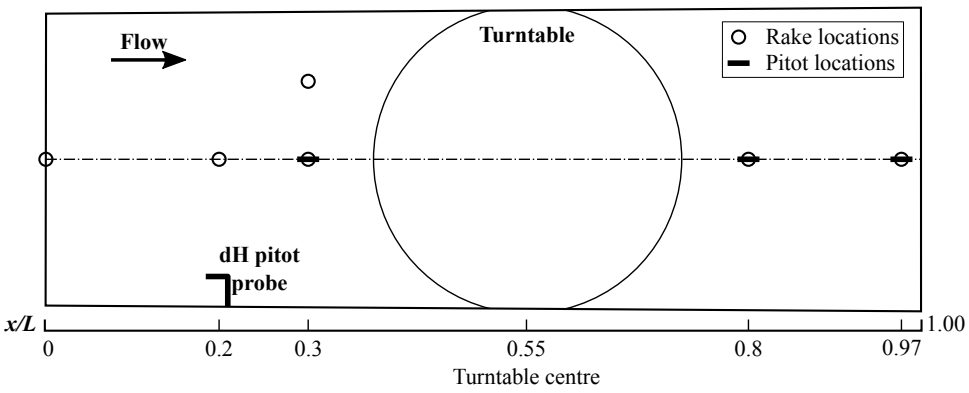

FIGURE 3.3: Schematic diagram of the dH working section illustrating pressure probe/rake sampling locations.

TABLE 3.1: Summary of pitot probe and pressure rake sample locations through working section. Re based on $L = 1m$.

x/L	Freestream Static Pressure	Pressure Rake	$Re[\times 10^6]$
0	-	✓	0.7, 1.4, 2.1, 2.7, 3.4, 4.1
0.2	✓ (dH wall pitot)	✓	0.7, 1.4, 2.1, 2.7, 3.4, 4.1
0.3	✓ (roof mounted)	✓	0.7, 1.4, 2.1, 2.7, 3.4, 4.1
0.8	✓ (floor mounted)	✓	0.7, 1.4, 2.1, 2.7, 3.4, 4.1
0.97	✓ (roof mounted)	✓	0.7, 1.4, 2.1, 2.7, 3.4, 4.1

All pressure measurements were taken relative to ambient atmosphere away from wind tunnel interference. Each channel was sampled at $250Hz$ over 60 seconds. This provided enough samples to time-average all pressure data, for all Reynolds numbers, to a confidence level of 98% with a margin of error (random uncertainty) consistently less than 3%.

In assessment of the boundary layer profiles the following assumptions were made:

- Steady incompressible flow.
- No body forces in the streamwise direction.
- No viscous forces outside of the boundary layer.
- Uniform flow outside of the boundary layer.
- Boundary layer is the same on all walls.
- Constant floor/roof elevation.

The pressure data from the rake was converted to boundary layer velocity profiles using the governing Bernoulli equation:

$$\underbrace{1/2\rho U^2}_{\textit{Dynamic pressure}} + \underbrace{p}_{\textit{Static pressure}} + \underbrace{\rho g z}_{\textit{Gravitational acceleration}} = constant \tag{3.1}$$

3.3.2 WORKING SECTION BOUNDARY LAYER

In this section, the boundary layer profiles through the working section for a Reynolds number of 3.4×10^6 (based on $L = 1m$) are presented as this condition matches the experimental conditions used throughout this study (1.5×10^6 based on the model's MAC). The disturbance thickness of the boundary layer is described as the distance from the surface to the point in the boundary layer velocity profile that reaches 99% of the freestream velocity [227]. In order to approximate this point, while accommodating for the coarse resolution of the pressure rake, cubic interpolation of the pressure rake data provided boundary layer velocity profiles. From this interpolated velocity profile, an estimation of the boundary layer thickness, δ, from the pressure rake data could

be made. Subsequently, the pressure rake velocity profile data (and boundary layer thickness) was verified using the empirical $1/7^{th}$ power law turbulent boundary layer velocity profile, defined as [228]:

$$\frac{u}{U_\infty} = \eta^{\frac{1}{7}}, \quad where\ \eta = \frac{z}{\delta} \tag{3.2}$$

The $1/7^{th}$ power law velocity profile is well-known to predict a valid solution for turbulent boundary layer profiles for $Re < 6 \times 10^6$ [229, 230]. Figure 3.4 presents the time-averaged pressure rake boundary layer velocity profile compared to the power law velocity profile at the three streamwise locations through the working section. The comparative agreement of the pressure rake data sampled at $Re = 3.4 \times 10^6$ to the empirical $1/7^{th}$ law profile across the five centreline position tests (see figure 3.3) have a root mean square error of 0.83%. The root mean square error in the agreement between the pressure rake and the $1/7^{th}$ power law across all Reynolds numbers tested is 4.10%. From figure 3.4 it is seen that the boundary layer thickness approximately doubles from inlet to outlet (from $\approx 35mm$ to $\approx 74mm$ respectively) at $Re = 3.4 \times 10^6$.

An important parameter to be considered in relation to the wind tunnel model used in this work is the displacement thickness of the wind tunnel boundary layer. The displacement thickness is the mass flux deficit inside the boundary layer near the wall. In this region, the flow is heavily retarded such that streamlines are displaced outward by the displacement thickness, δ^* to satisfy continuity. The displacement thickness can be approximated easily if the $1/7th$ power law is adopted for its computation, such that:

$$\delta^* \equiv \int_0^\delta (1 - \frac{u}{U_\infty})dz = \delta \int_0^1 (1 - \eta^{\frac{1}{7}})d\eta = \frac{1}{8}\delta \tag{3.3}$$

Illustrating the boundary layer growth rate, figure 3.5 presents the boundary layer thickness' through the working section along the centre line of the tunnel floor;

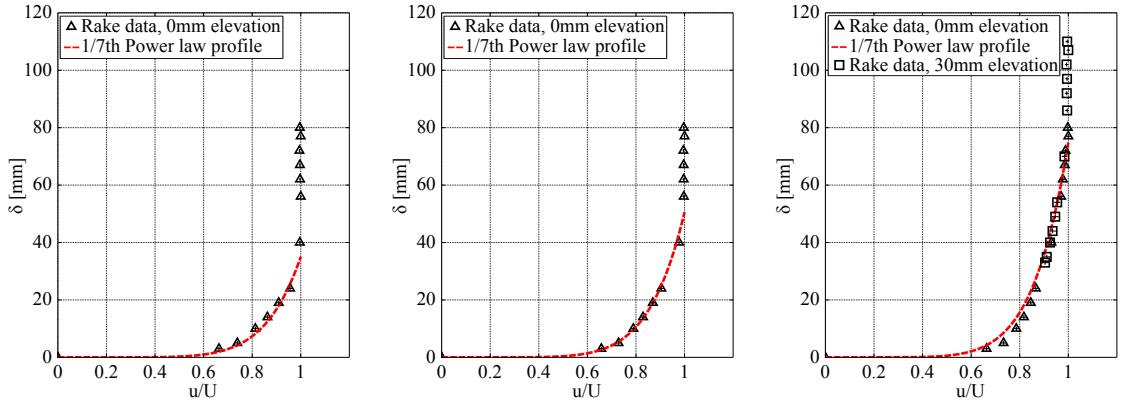

(a) $x/L = 0$ [dH inlet] (b) $x/L = 0.3$ (c) $x/L = 0.97$ [dH outlet]

FIGURE 3.4: Boundary layer profiles from the dH working section floor centreline at $Re = 3.4 \times 10^6$.

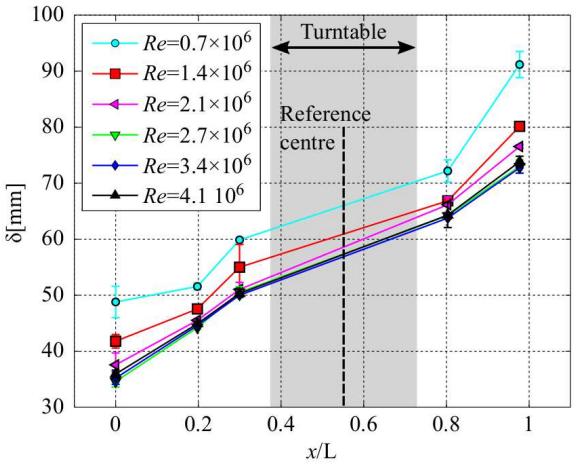

FIGURE 3.5: Boundary layer thickness through working section.

error bars indicated the standard deviation in the boundary thickness' measured. The turntable and its moment centre are indicated. The boundary layer thickness through the tunnel (and growth rate) appear to converge at $Re \geq 2.7 \times 10^6$ into a somewhat linear relationship. Additionally, the results presented in figure 3.5 provide confidence that the lip of the turntable does not appear to significantly interfere with the boundary layer thickening over the working section length.

Taking a best-fit line approximation of the data presented in figure 3.5, for each Reynolds number separately, the boundary layer growth rate appears independent of increases in Reynolds number. Boundary layer growth rate for each Reynolds number is summarised in table 3.2.

To understand the mechanism of boundary layer growth, the time history of the vorticity within the boundary layer is considered. Stokes' theorem states that the area integral of the vorticity vector, $\boldsymbol{\omega}$, bounded by a closed contour, is equal to the line integral of the velocity vector around the bounding contour; this is called the circulation which is mathematically expressed as:

$$\iint \boldsymbol{\omega} \cdot d\mathbf{a} = \oint \mathbf{V} \cdot d\mathbf{s} = \Gamma \tag{3.4}$$

TABLE 3.2: Summary of pitot probe and pressure rake sample locations through working section.

Re[$\times 10^6$]	Growth rate [mm/m]
0.7	7.130
1.4	6.456
2.1	6.701
2.7	6.497
3.4	6.358
4.1	6.430

This expression demonstrates that the circulation around a closed contour is the sum of the vorticity enclosed within it. It follows that the total amount of vorticity contained within the boundary layer per unit length over a flat surface is constant; the distribution of the vorticity normal to the surface does not change along its length. Vorticity within the boundary layer is introduced through the so called no-slip boundary condition arising from the viscous properties of the fluid. Physically, the velocity gradient through the boundary layer arises from viscous shear stresses acting on the fluid giving rise to friction which resists the relative fluid motion. Viscosity acts through the mechanism of molecular diffusion to spread vorticity transversely as it convects downstream. Thus, the local boundary layer thickness can be considered to be a measure of the distance vorticity has diffused away from the solid surface.

To relate the factors controlling the boundary layer growth rate consider the Reynolds number as a ratio of time scales, instead of a ratio of inertial to viscous forces. At time t, the thickness of the boundary layer is of the order of $\sqrt{\nu t}$, where ν is the kinematic viscosity and t is the time of diffusion [231]. In consideration of some characteristic length scale, L, the time taken for viscous and convective effects to travel distance L is:

Viscous time scale:

$$T_v = \frac{L^2}{\nu} \tag{3.5}$$

Convective time scale:

$$T_c = \frac{L}{U_\infty} \tag{3.6}$$

Hence, the ratio of viscous to convective time scales is:

$$\frac{T_v}{T_c} = \frac{(L^2/\nu)}{(L/U_\infty)} = \frac{U_\infty L}{\nu} = Re \tag{3.7}$$

Therefore, a large Reynolds number the viscous effects will propagate more slowly into the fluid from a body surface due to a longer viscous time scale. This is why, in figure 3.5, an initial decrease in boundary layer thickness at a given station is noticed as the Reynolds number increases; the fluid is being convected in the flow direction at a much faster rate than the thickening of the boundary layer which is normal to the flow direction. The growth rate remains independent of the Reynolds number as it is a mechanism of molecular diffusion acting through the fluid viscosity. In other words, at higher Reynolds numbers, at any position over a flat surface the boundary layer thickness is less because it has less time to grow but the rate of growth experienced over length L is constant, such that the growth rate is approximately constant.

3.3.3 Static Pressure Gradient

Within an attached boundary layer, the static pressure will remain relatively constant at a cross section of the working section while the total pressure is able to vary [227]. To verify this assumption, the cross sectional uniformity of the static pressure at x/L=0.2 was checked. The pressure rake was positioned at the centre of the tunnel floor, in line with the wind tunnel's dedicated pitot probe, and the gauge static pressure was monitored over the Reynolds numbers of interest and are presented in figure 3.6.

In figure 3.6 errorbars signify standard deviations in the pressure. The static pressure in the boundary layer in the centre of the floor is seen to agree well with the static pressure of the freestream over the Reynolds numbers shown. The standard deviation of the pitot probe readings are seen to increase with increasing Reynolds number, with increased probe vibration as the primary reason. The stiffer and smaller pitot rake does not experience the same structural vibration.

As a pitot probe could not easily be mounted at the working section inlet [x/L=0], the pressure rake was relied upon to provide static pressure at this location. Figure 3.7 shows the gauge static pressure through the wind tunnel working section over several Reynolds numbers. As expected with a closed return wind tunnel, there is a tendency for a static pressure drop through the working section (horizontal buoyancy). Additionally, the gradient of the static pressure drop the section is seen to increase with Reynolds number. Using a line of best fit, the longitudinal static pressure gradients, given in Pa/m through the working section at each Reynolds number is summarised in table 3.3.

The wind tunnel working section makes use of expanding fillet corners, which aim to offset the static pressure drop though the working section due to boundary layer thickening. While their efficiency cannot be quantified in the present study, the indicated pressure gradients through the working section at the Reynolds numbers

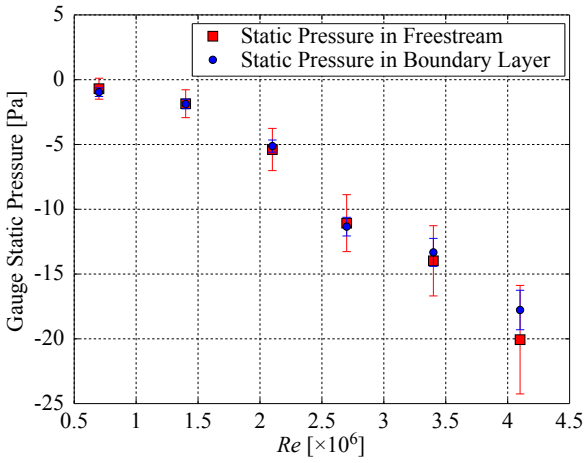

Figure 3.6: Boundary layer static pressure and dH pitot probe freestream static pressure at x/L=0.2.

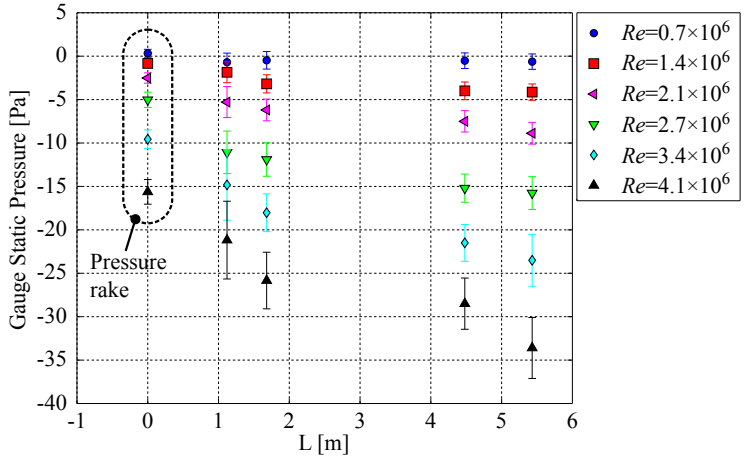

FIGURE 3.7: Static pressure gradient through working section with Reynolds number.

TABLE 3.3: Summary of longitudinal static pressure gradients through the dH working section for with Reynolds number.

Re[$\times 10^6$]	Longitudinal static pressure gradient $[Pa/m]$
0.7	-0.1068
1.4	-0.5708
2.1	-0.9813
2.7	-1.6975
3.4	-2.2797
4.1	-2.8208

tested are slight. This suggests that test article/model mounted within the dH working section will have very small, perhaps negligible, artificial drag increase arising from horizontal buoyancy effects. However, these static pressure variations through the test section will be modified in the presence of a test article, where large static pressure variations can arise in cases of sufficiently large test articles with significant blockage [227]. If solid body blockage can be maintained around (or below) 5%, and no significant lateral flow is induced by the model, deviation away from the static pressure gradients of the empty working section is minimal [227].

3.4 WIND TUNNEL MODEL

3.4.1 SEMI-SPAN MODEL TESTING

Semi-span testing techniques have been widely adopted as a tool to provide state-of-the-art wind tunnel research capabilities [232, 233, 234, 235]. Semi-span models are typically employed to double the maximum usable Reynolds number and enhance the quality of measurement data owing to improved model strength, stiffness, and overall fidelity [236]. Model construction costs are also significantly reduced [227]. However, semi-span models also have inherent difficulties associated with the quality

of flow over the model, and are vulnerable to increased interference effects from interaction with the wind tunnel. The basic principle of semi-span testing is to treat the mid-plane cross section of the body as a plane of symmetry. This is generally achieved by mounting the mid-plane of the body to some planar surface (such as the wind tunnel floor, wall, or ceiling) enabling the surface to act as a plane of symmetry. The wind tunnel walls however, provide poor symmetry planes due to the growth of respective boundary layers which begin to develop far upstream of the model. Interactions between the working section boundary layer and the model can introduce three-dimensional vortical structures (horseshoe vortices), which are recognised to have strong influences on the semi-span model's aerodynamic behaviours, especially over the inboard wing [237], which varies as a function of the angle of attack.

With the semi-span wind tunnel model designed in this study, efforts are made to minimise the effects of the wind tunnel boundary layer (which is discussed in depth in Chapter 4) and allow the main-wing section to house alternative wingtip configurations.

3.4.2 Semi-Span Model Design

The planar baseline wing semi-span configuration of the model is shown in figure 3.8a. This configuration is analogous of a typical mid-size transport commercial aircraft wing topology of 10% scale. The modular design enables the outboard wing section to be freely changed, with the secondary C-wing wingtip arrangement shown in figure 3.8b.

The topological design of these arrangements has been discussed in Chapter 2. A schematic diagram of the semi-span model with both tip configurations is presented in

(a) Planar 'baseline' wing (b) sGA designed C-wing.

Figure 3.8: Semi-span model installed in the dH working section.

TABLE 3.4: Wing parameters.

	Conventional full-scale	Planar	C-wing
Mach number (M_∞)	$\approx$ 0.78-0.8	0.145	0.145
Reynolds number (Re)	$\approx 10^9$	1.5×10^6	1.5×10^6
Altitude (h) $[m]$	$\approx 10972.8(36,000ft)$	0	0
Dynamic pressure (q_∞) $[Pa]$	$\approx$ 10107.04	$\approx$ 1531.25	$\approx$ 1531.25
(Main) Wing area (S) $[m^2]$	$\approx$ 65-90	0.5717	0.5726
MAC ($\bar{c}$) $[m]$	$\approx$ 4-5	0.44	0.44
Wing semi-span ($b/2$) $[m]$	$\approx$ 17-19	1.50	1.487
Taper ratio (λ)	$\approx$ 0.2	0.21	0.174
Aspect ratio (AR)	$\approx$ 4-4.5	4.12	4.06

figure 3.9, with relevant wing specifications and scaling information listed in table 3.4. The Reynolds number (Re) is based on the wing's mean aerodynamic chord (MAC) with atmospheric properties taken from Anderson [238]. Evident from figure 3.9 the semi-span model does not utilise the traditional peniche extrusion at the fuselage's symmetry plane, and instead a stand-off gap is employed at the fuselage symmetry plane. Skinner and Zare-Behtash [239] discuss the benefits of this. The model stand-off gap can be adjusted such that the model can be mounted with a continuously variable $10mm$ to $50mm$ stand-off gap; the size and scaling effects of which are discussed in detail in Chapter 4. Figure 3.9 additionally indicates that the position of the model's centre of gravity is aligned with the mounting shaft.

Relative to the planar arrangement, the C-wing has a 0.87% reduced wingspan, 0.16% main-wing area, and an increased wing wetted area of 19.1%. Using design criteria and insight outlined by Barlow et al. [227], the ratio of the model wingspan should be less than 0.8 of the wind tunnel height (for closed test sections) due to effects of the tunnel wall. Hence, the ratio of the wingspan to the tunnel height is 0.73.

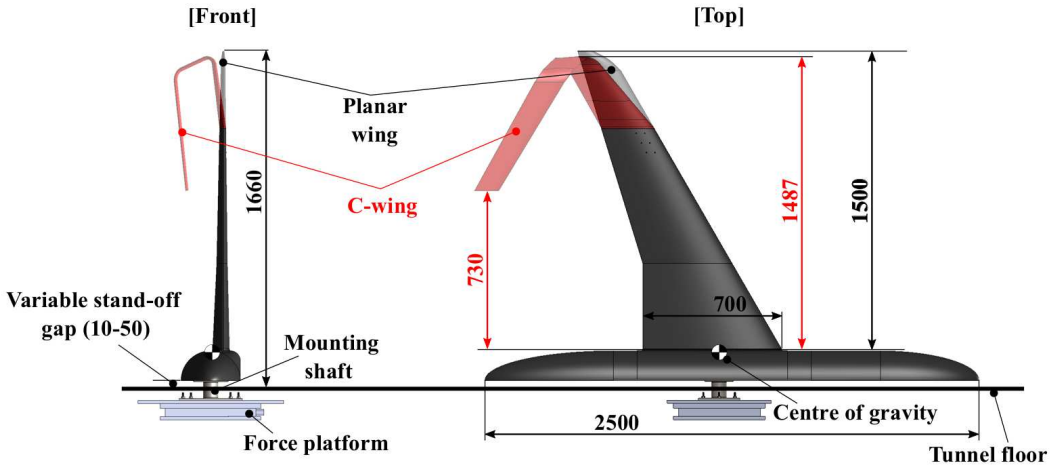

FIGURE 3.9: Schematic diagram of model with force platform reference frame indicated; dimensions in millimetres.

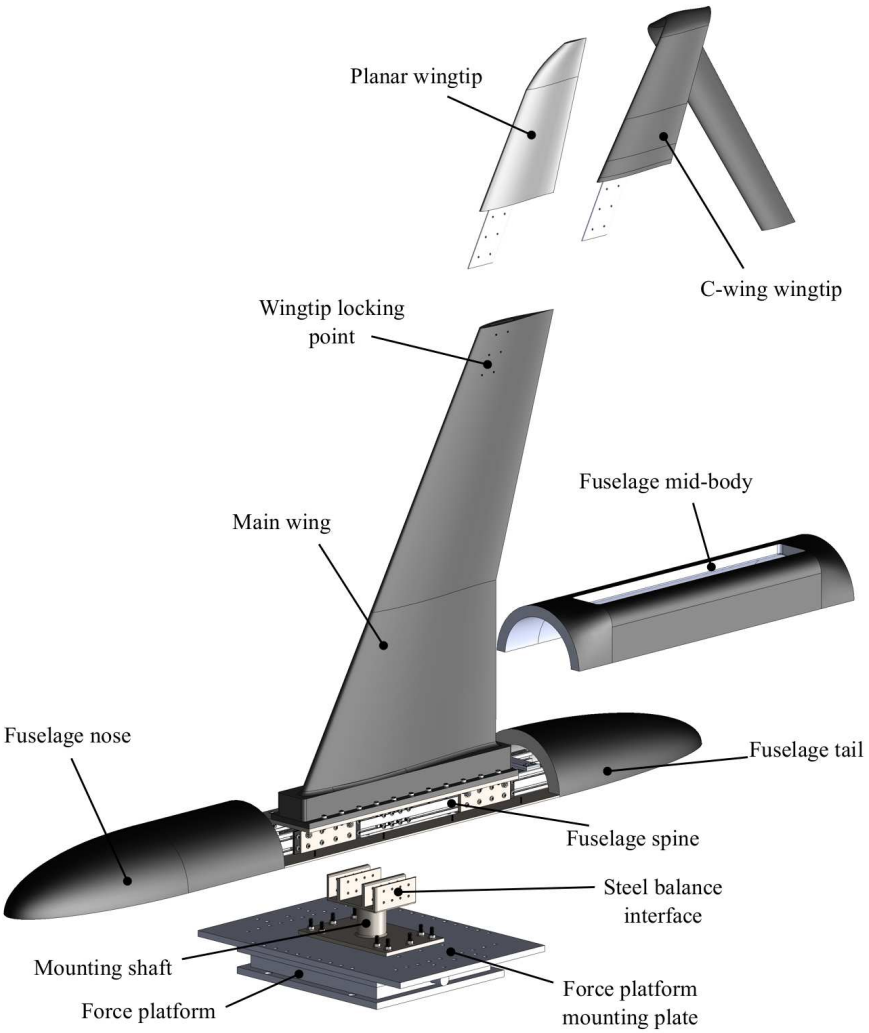

Figure 3.10: Exploded view of semi-span model.

Figure 3.10 illustrates an exploded view of the model and how it interfaces with the force platform. The model wing and fuselage are constructed from polyurethane foams with an aerodynamically smooth finish of surface roughness $< 0.1\mu m$ (surface roughness grade $N3$ provided by manufacturer); the surface finish is also matte-back to minimise laser reflections. The main-wing section connects through the fuselage's extruded aluminium spine to the steel balance interface. The fuselage spine provides longitudinal rigidity for the fuselage; mounting points for the main-wing's base; and interfaces with the steel balance which translates model body forces to the force platform. The steel balance interface is mounted centrally to the force platform's electromechanical centre, which is located at the centre of the turntable. Thus the electromechanical centre and the model mounting shaft of the steel balance interface are fixed to the pitch axis. However, the pitch axis is not geometrically fixed to the model and can be adjusted by the user. The steel balance interface connects to the fuselage spine in such a way that allows $210mm$ longitudinal continuous translation of the model. This capability serves two purposes: 1) re-positioning of the model's centre

of gravity/aerodynamic centre relative to the pitch axis; and 2) model translation to accommodate limitations in optical access and/or maximise SPIV data acquisition with minimised calibration planes. It is highlighted that changing between the wingtip arrangements alone does not effect the model's centre of gravity.

Each interchangeable wingtip extension connects to the main-wing via locking points around the main-wing's elastic axis, as shown in figure 3.10; secondary location pins provide alignment and support of the trailing edge. Grub screws are used to lock the desired wingtip directly to the elastic axis of the main-wing at the wingtip locking point. The fuselage mid-body slides over the wing and locks into the fuselage creating and airtight seal with no exposed screw heads. The main-wing section and both wingtip attachments are untwisted with a NACA 63_1-412 cross section, the profile of which is shown in figure 3.11. The constant untwisted profile reduces the complexity of the model for both simulation and manufacturing purposes. However, due to the lack of wing twist (washout), sub-optimal lift distribution over the wing, regardless of arrangement, is expected. The 63_1-412 aerofoil provided a sufficient distribution of thickness over the chord length (with a maximum thickness of 12% at 34.9% chord) which provides confidence in the wings structural integrity while maintaining good numerical predictability (thin aerofoil assumption $\leq$ 15% [202, 205]).

6-series aerofoil sections are designed to maintain a favourable pressure gradient on both sides of the profile and low drag characteristics over a broad range of angles of attack; additionally providing shallow stall characteristics above $Re = 0.5 \times 10^6$ [240]. Shallow and predictable stall characteristics are deemed particularly important in this study as buffet induced vibrations may become amplified (or attenuated) by the C-wing configuration, either due to C-wing aerodynamics or the extra mass (inertia) at the wingtip. In addition, tip stall is expected due to the high sweep and lack of washout (wing twist). The low-profile drag characteristics offered by the 63_1-412 aerofoil are also essential to enable the total drag of the wing to be more easily dominated by the induced drag component. Thus establishing a strong foundation for investigating how the C-wing will effect the total drag of the model. The C-wing's primary function is to attempt the reduction of induced drag but will inherently increase the parasitic drag due to the increased wetted area. In this study only the total drag on the model is available, hence the independent variations of the parasitic drag and induced drag cannot be assessed. Furthermore, while the aim of the C-wing

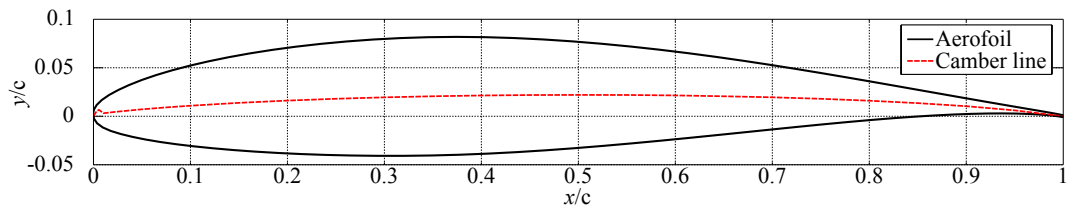

FIGURE 3.11: NACA 63_1-412 aerofoil.

arrangement it to reduced the total drag, it is unlikely that it will provide the optimal reduction of induced drag.

3.5 WING AEROELASTIC CONSIDERATIONS

Wind tunnel models (even wings in general) are prone to distortion when exposed to aerodynamic loads. These aerodynamic forces, themselves, depend on the physical geometry of the structure (also dictating polar and second moments of inertia), and the orientation of structural supports relative to the freestream direction. Thus, structural distortion results in a modification to the aerodynamic loading, leading to a change in structural distortion, and so on. This interaction of aerodynamics and structural forces in known as aeroelasticity.

In the design and subsequent operation of the semi-span model two distinct aeroelastic cases require consideration: 1) static, and 2) dynamic aeroelastic response. If the wing structure is too flexible, the interaction of aerodynamic and elastic forces may exhibit divergent tenancies leading to structural failure; such aeroelastic phenomena include divergence and control reversal. Dynamic aeroelastics involves the inertia of the structure in addition to the aerodynamic and elastic forces, the interactions of which induce oscillations of the structure. If the natural frequency of the structure in the the region of the frequency of the loading then the amplitude of oscillations may become unstable leading to structural failure. Typical examples of these oscillations include flutter, buffeting, and dynamic response. Aeroelastic phenomena have been summarised in figure 3.12.

Control reversal and dynamic response of the wing (to gusts, for example) do not require consideration, as the model will not interact with such phenomena in the present study. In order to protect both the model and the wind tunnel, steps have been taken to ensure structural failure from wing divergence, or flutter, will not occur within the experimental test envelope by attempting the to design the wing such that it is not vulnerable to either phenomena. The main-wing section, indicated in figures 3.9 and 3.10, has been designed to provide, as closely as possible, pure bending deformation in order to simplify the wing analysis. This is typically achieved though passive aeroelastic tailoring [241, 242]. However, in the present study aeroelastic tailoring of

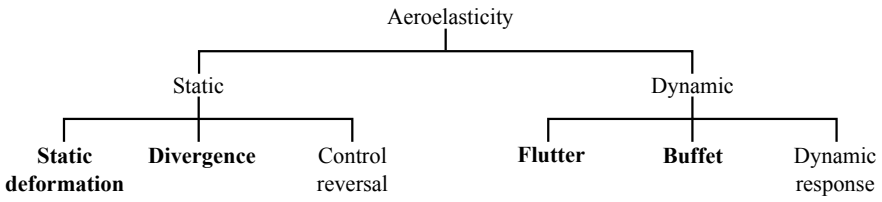

Figure 3.12: Aeroelastic phenomena; bold text indicates aeroelastic behaviours of interest in the present study.

the wing structure has not been adopted as the wing components are manufactured from polyurethane foam, an isotropic material. Thus, to achieve decoupled bend-twist deformation, the moments acting around the main-wing's elastic axis have been balanced. Furthermore, this approach inherently provides confidence that structural failure from torsional divergence or flutter will not occur.

3.5.1 STATIC AEROELASTICS

Distribution of the aerodynamic loading relative to the elastic axis leads to static deformation of the wing. As the wing is deformed in steady flight, an aerodynamic moment will generally be induced which causes the wing to twist. This twisting is resisted by the wings elastic moment reaction. However, the elastic stiffness of the wing is fixed and independent of the freestream velocity whereas the aerodynamic loads are proportional to the square of the freestream velocity. Hence, there may be a case in which a critical velocity is reached at which point the elastic stiffness is no longer sufficient to hold the wing in an elastically deformed state. Above this critical velocity, termed the divergent velocity, the wing is considered torsionally divergent at which point structural failure is likely [243].

To understand the steady-state aeroelastic deformation of a finite wing, consider figure 3.13. Typically the elastic axis of a finite wing lies distance *ec* behind the line of aerodynamic centres as presented from wing section **A-A**.

The wing cross section **A-A** illustrates the aerodynamic coupling term, *ec*, which drives static aeroelastic deformation. To observe the static aeroelastic characteristics of such a wing configuration, a distributed aerodynamic loading would act as a distributed load through, and a distributed twisting moment about, the elastic axis. Thus, the total translation at elemental section, δz, can be described as the combination

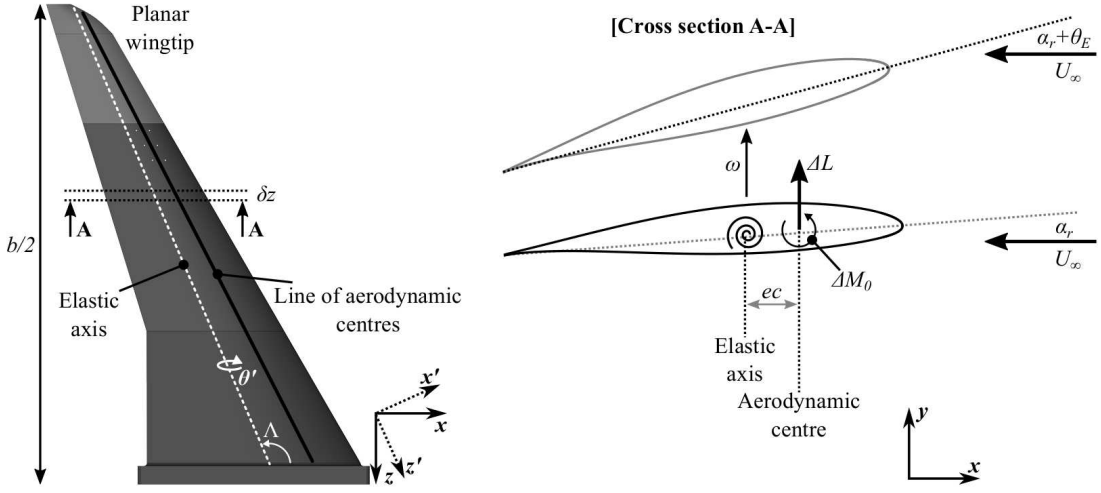

FIGURE 3.13: Torsonal wing divergence.

of rotations caused by elastic twist, θ' from torsion about the z' axis, and the wing bending $\frac{d\omega}{dz'}$, where ω is the wing's bending about axis x'. The effect of elastic deformation, θ_E, over the wingspan thereby modifies the wing root angle of attack, α_r, across the wingspan. Thus, the effective angle of attack α_{eff} along the span of a swept wing is described as:

$$\alpha_{eff}(z) = \alpha_r + \underbrace{\theta'(z')cos\Lambda - \frac{d\omega(z')}{dz'}sin\Lambda}_{\theta_E=\text{Elastic deformation}} \tag{3.8}$$

From this understanding it is possible to consider the finite wing torsional divergence through elementary aeroelastic theory by application of strip theory. Thus, treating a wing of span $\frac{b}{2}$ as a series of small elements of chord c and spanwise width δz, the moment about the elastic axis can be expressed as:

$$K\theta_E = M_0 + Lec \tag{3.9}$$

where K the torsional stiffness of the wing resisting the moment lift vector L and the wing pitching moment M_0, resulting in wing elastic twist θ_E. Assuming equilibrium and expressing the twisting moment around the elastic axis in terms of torque T at spanwise station z, and ΔL and ΔM_0 as the sectional lift and pitching moment respectively acting on elemental strips, δz, of infinitesimal thickness, equation 3.9 becomes [243]:

$$\frac{dT}{dz} + ec\frac{dL}{dz} + \frac{dM_0}{dz} = 0 \tag{3.10}$$

where the sectional lift, moment and torque acting on elemental strips can be expressed as:

$$\begin{aligned} \Delta L &= \frac{1}{2}\rho U^2 c\delta z \frac{\partial c_l}{\partial \alpha}(\alpha_r + \theta_E) \\ \Delta M_0 &= \frac{1}{2}\rho U^2 c^2 \delta z c_{m0} \\ T &= GJ\frac{d\theta_E}{dz} \end{aligned} \tag{3.11}$$

where $\frac{\partial c_l}{\partial \alpha}$ is the local two-dimensional lift-curve-slope, c_{m0} is the local pitching moment coefficient about the aerodynamic centre, and GJ is the torsional rigidity of the wing. Thus, substituting for L, M_0, and T in equation 3.10 and rearranging:

$$\frac{d^2\theta}{dz^2} + \frac{\frac{1}{2}\rho U^2 ec^2 \frac{\partial c_l}{\partial \alpha}\theta_E}{GJ} = -\frac{\frac{1}{2}\rho U^2 ec^2 \frac{\partial c_l}{\partial \alpha}\alpha_r}{GJ} - \frac{\frac{1}{2}\rho U^2 c^2 c_{m0}}{GJ} \tag{3.12}$$

Equation 3.12 is a second-order differential equation in θ_E, with a solution of the standard form:

$$\theta_E = Asin\lambda z + Bcos\lambda z - \left(\frac{c_{m0}}{e\frac{\partial c_l}{\partial \alpha}} + \alpha_r\right) \tag{3.13}$$

where,

$$\lambda^2 = \frac{\frac{1}{2}\rho U^2 e c^2 \frac{\partial c_l}{\partial \alpha}}{GJ} \tag{3.14}$$

A and B are unknown constants, but can be obtained for certain boundary conditions; specifically when $\theta_E = 0$ when $z = 0$ at the wing root, and $\frac{d\theta_E}{dz} = 0$ at $z = \frac{b}{2}$ as the torque is zero at the wingtip. Hence, taking $\theta_E = 0$ at $z = 0$:

$$B = \frac{c_{m0}}{e\frac{\partial c_l}{\partial \alpha}} + \alpha_r \tag{3.15}$$

and, taking $\frac{d\theta_E}{dz} = 0$ at $z = \frac{b}{2}$:

$$A = \left(\frac{c_{m0}}{e\frac{\partial c_l}{\partial \alpha}} + \alpha_r\right) tan\lambda\frac{b}{2} \tag{3.16}$$

Hence, substituting A and B into equation 3.13,

$$\theta_E = \left(\frac{c_{m0}}{e\frac{\partial c_l}{\partial \alpha}} + \alpha_r\right) \cdot (tan\lambda\frac{b}{2} sin\lambda z + cos\lambda z - 1) \tag{3.17}$$

Rearranging 3.17,

$$\theta_E = \left(\frac{c_{m0}}{e\frac{\partial c_l}{\partial \alpha}} + \alpha_r\right)\left(\frac{cos\lambda(\frac{b}{2} - z)}{cos\lambda\frac{b}{2}} - 1\right) \tag{3.18}$$

At the divergence condition the elastic twist α_E becomes infinite, such that $cos\lambda\frac{b}{2} = 0$, hence:

$$\lambda\frac{b}{2} = (2n+1)\frac{\pi}{2} \tag{3.19}$$

where $n = 0, 1, 2, ..., \infty$. In this instance the smallest value corresponding to the divergence speed U_d occurs when $n = 0$, such that,

$$\lambda\frac{b}{2} = \frac{\pi}{2} \tag{3.20}$$

or,

$$\lambda^2 = \frac{\pi^2}{4(\frac{b}{2})^2} \tag{3.21}$$

from which, substituting back in to equation 3.14,

$$U_d = \sqrt{\frac{\pi^2 GJ}{2\rho e c^2 (\frac{b}{2})^2 \frac{\partial c_l}{\partial \alpha}}} \tag{3.22}$$

Thus, a mathematical expression for the critical divergence velocity is shown in equation 3.22. Mathematical solutions such as this rarely apply with accuracy to real wing configurations, however it does accurately indicate the fundamental relationships between design parameters [244]. From equation 3.22 it is immediately evident that the divergence speed can be increased by either stiffening the wing's torsional rigidity,

or by decreasing the distance between the aerodynamic centre and the elastic axis, *ec*, referred to as the *aerodynamic coupling*. Furthermore, as only positive velocities relate to the divergence condition are physically meaningful, if $ec \leq 0$ this mathematically suggests that the wing will not reach a torsionally divergent condition. In other words, if the aerodynamic centre coincides with or is aft of the elastic axis then the wing will remain statically-stable at all speeds [243, 244, 245]. If the aerodynamic centre coincides with the elastic axis this would mean that the wing experienced pure bending with no elastic twist acting along the span as the aerodynamic loads would not impose a moment about the elastic axis. Inherently this would additionally be true for the wing at constant velocities at higher angles of attack; there would be no moment induced about the elastic axis [246].

This line of reasoning has led to the design of the main-wing section to have the elastic axis and the line aerodynamic centres positioned as closely as possible, with the aim of them coinciding to mitigate aerodynamic coupling. This minimises torsional divergence as a source of structural failure and additionally simplifies the deformed wing geometry. Skinner and Zare-Behtash [120] have demonstrated this analytically and experimentally. This design feature was facilitated by the genetic algorithm design optimisation algorithm discussed in Chapter 2.

In addition to the above considerations, the semi-span model has an aft swept wing whose elastic axis is therefore at an oblique angle to the oncoming freestream. Torsional divergence is inherently less liable to be serious for flexible aft-swept wings, as the wing bending provides a stabilising effect [247, 248]. A reduction in the streamwise incidence of the outboard wing sections due to bending deformation causes a movement of the centre of pressure inboard towards the wing root.

3.5.2 Dynamic Aeroelastics

Flutter is a complex phenomenon in which structural modes of vibration are simultaneously coupled and excited by aerodynamic loads. In other words, flutter is a condition in which a body, or components of that body, exhibit a self-sustained oscillatory behaviour at some critical velocity [218]. This dynamic aeroelastic phenomenon results from interactions between the aerodynamic, elastic, and inertial loading acting on the body. When the body structure is exposed to a critical freestream velocity, structural deformations induce additional aerodynamic loads which in turn produce additional structural deformations. Thus, flutter is an oscillation induced by the aerodynamic loading without any external force other than the freestream; the inertial and the elastic loads are both conservative and do not contribute to the net gain/loss of the oscillatory cycle [243]. Oscillations are regarded as unstable if the oscillations gain energy from the freestream from each subsequent cycle.

Considering a system with two degrees-of-freedom it is possible to explain the fundamentals of wing flutter behaviour. Figure 3.14a presents a finite wing with

defined elastic, inertial and aerodynamic axes, with cross section **A-A** illustrating the wing translation and rotation as aerodynamic forces excite the structure. The plunge (downward translation) is resisted by the wings bending stiffness, while the pitching is resisted by the torsional stiffness. A full cycle (of period T) of the pitch-plunge oscillation is presented in figure 3.14b, from which it is clear to see how the plunge mode (bending mode) and the and the pitch (torsional mode) drive one another. At $t = 0$ an initial increase in the effective angle of attack causing the lift to increase. As this lift force causes the wing to bend upward, the torsional stiffness reduces the effective angle of attack to neutral rotation at $t = T/4$. The bending stiffness then reacts to return the wing to the neutral bending position at $t = T/2$, but the wing simultaneously twists nose down reducing the effective angle of attack further. This increased down-force plunges the wing down and the torsional stiffness returns the wing to neutral twist at $t = 3T/4$. The cycle then completes. Notice this in this scenario the maximum forced torsion and maximum forced bending are out of phase by 90°, as are the neutral positions of the torsion and bending. If we consider only the plunging motion, when the wing section translates down it experiences an increased angle of attack helping the decelerated the wing and restore neutral twist. Thus, the fundamental cause of flutter becomes clear. When the critical freestream velocity is reached, disturbances are imposed on the wing which phase shift the bending mode and torsional mode amplitudes 90° out-of-phase.

From figure 3.14a typical locations for the inertial, elastic and aerodynamic centres have been indicated. The distance/moment arms which can drive flutter of the wing semi-span model are *ec*, termed the *aerodynamic coupling*, and *ac* termed the *inertial coupling*. It is indicated here that gravity would conventionally acts in the negative y direction relative to the wing presented in figure 3.14a, but for the experimental set-up employed gravity acts in the positive z direction. It is observed analytically that when $g = 0$, $ac \to 0$, and contributions from inertial coupling are almost entirely mitigated. However, it is acknowledged that even though gravity (weight) is not acting in the conventional direction relative to the wing orientation, the wing's inertial axis will persist as the wing has mass, but the effects of which will be negligible.

It follows that there are combinations of the aerodynamic and inertial couplings that aeroelastic theory would analytically indicate decoupled bend-twist deformation, reducing flutter sensitivity. If the inertial axis coincides with the elastic axis, $ac \to 0$, and simultaneously, if the aerodynamic centres coincide with the elastic axis, $ec \to 0$, then bending and torsion deformation will be decoupled [249]. With the line of aerodynamic centres aligned with, or aft of, the elastic axis the wing will remain statically stable at all speeds and a torsionally divergent state will not be reached [243, 244, 245]. Furthermore, if both coupling terms tend to zero, indicating coincidence of the three axes, flutter (due to the 90° phase shifted bend-twist coupled oscillation) cannot occur at any velocity [250].

Thus, alignment of the aerodynamic centres along the wingspan with the elastic

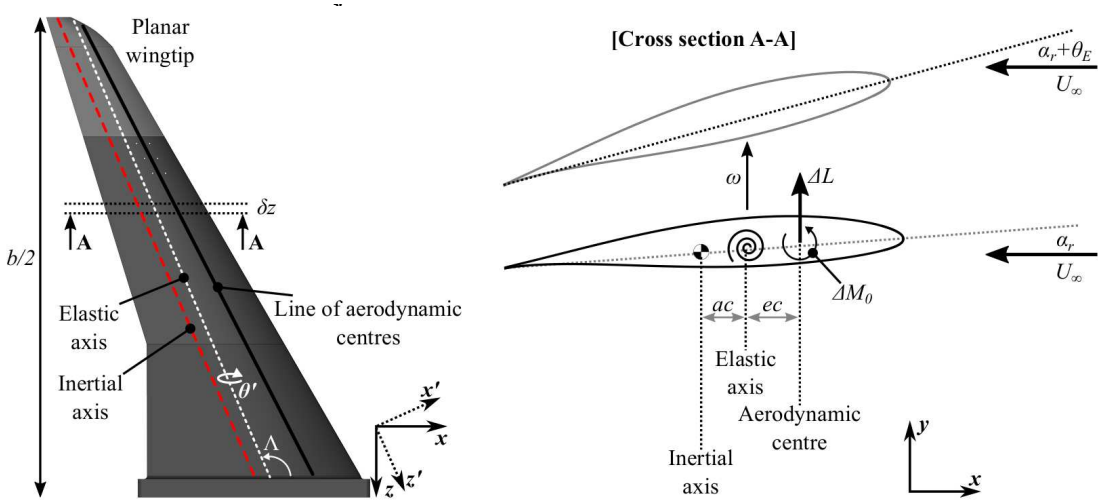

(a) Typical aerodynamic, elastic and inertial axes.

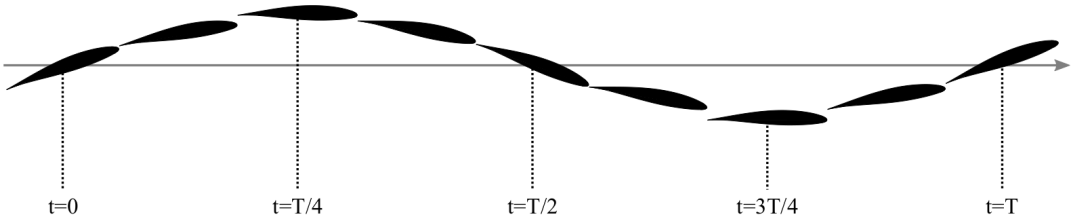

(b) Pitch and plunge motion of wing section **A-A** exhibiting flutter.

FIGURE 3.14: Flutter oscillatory motion.

and inertial axis result in pure bending elastic deformation, ω, with aerodynamic loading as indicated in figure 3.15. Fung [243] indicates that if this is achieved, oscillatory bending modes of the wing will remain aerodynamically stable and that purely translational flutter is impossible without the phase relationship with torsional modes. Figure 3.15 also shows the alignment of the three axes for each wingtip arrangement; each wingtip connects to the main-wing such that no discontinuities in the axes alignment arise. In this study wing sections have been designed and manufactured such that the aerodynamic centre of the wing, and the elastic and inertial axes coincide along the wingspan at 34% of the local chord. The inertial and elastic axis are linear over the wingspan, and the line of aerodynamic centres is assumed linear over the wingspan for fully attached flow over the wing.

Even though design mechanisms have been employed to minimise sensitivity of the wing to flutter, each wing arrangement will remain vulnerable to buffet induced vibrations. Buffeting of the cantilevered flexible wing will arise from unsteady separation over a wing surface facilitating vibrations in the wing structure. These vibrations are induced by aero-elastic coupling between a constant source of excitation (the freestream) which can persist for long periods and has a stable and reproducible response. Previous studies [251] have shown that the predominant buffet frequencies

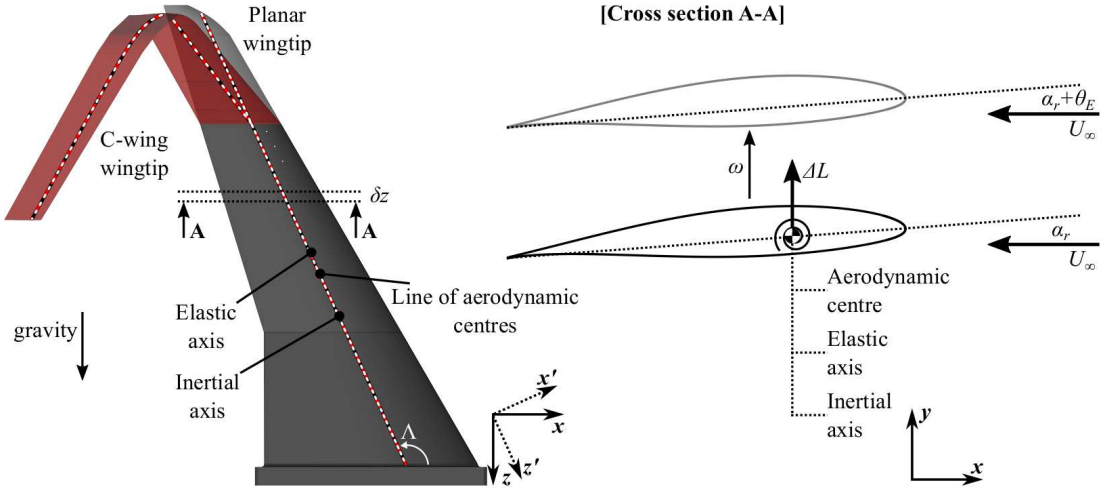

FIGURE 3.15: Semi-span model wing illustrating alignment of the inertial, elastic and aerodynamic axes. Note acceleration due to gravity is in $+z$.

typically correspond to the fundamental bending mode.

3.6 STRUCTURAL ANALYSIS: STATIC LOADS

3.6.1 FINITE ELEMENT ANALYSIS

Finite element analysis (FEA), of the planar wing arrangement only, has been carried out using the SOLIDWORKS simulation static load analysis tool box. The main objective of the FEA study is to conduct an analysis of the statically loaded wing structure to provide understanding of wing deflections and the progression of material stress prior to wind tunnel tests to ensure safety. In recent years the SOLIDWORKS FEA analysis package has been proven to be a useful analysis tool for solving complex three-dimensional problems including analysis of heterogeneous structures [252], structural analysis of large solar panel structures under wind loading [253], and vehicle chassis [254].

The governing equation of motion of a system under an external load may be expressed as:

$$[\mathbf{M}]\{\ddot{X}(t)\} + [\mathbf{C}]\{\dot{X}(t)\} + [\mathbf{K}]\{X(t)\} = \{f(t)\} \tag{3.23}$$

where $\{X\}$, $\{\dot{X}\}$, $\{\ddot{X}\}$ are the displacement, velocity and acceleration vectors, respectively. $[\mathbf{M}]$, $[\mathbf{C}]$, and $[\mathbf{K}]$ are the mass, damping and stiffness matrices of the structural system, respectively and $\{f(t)\}$ is the load vector.

In the static analysis, the loads are applied to the structure gradually, ramping up to the full magnitude. Once the full force magnitude is reached the force remains constant such that the analysis is time-invariant; *i.e.* static. Hence, accelerations and

velocities of the exited system are negligible and so no inertial or damping forces are considered, thus reducing equation 3.23 to equation 3.24 [255]:

$$[\mathbf{K}]\{X(t)\} \;=\; \{f(t)\} \tag{3.24}$$

In this analysis, materials are assumed to be isotropically linear elastic and homogeneous. With a linearly elastic material, stress is linearly proportional to the strain, therefore materials with non-linear properties/ranges will not be appropriately represented. Furthermore, material yielding and plastic deformation is not modelled, but expected material yielding can be determined based on the stress magnitudes reported as yield strength is exceeded [255]. In the FEA analysis the von Mises stress criterion provides this information.

The von Mises stress, also referred to as the Huber stress or maximum stress distortion theory, is a stress measure that accounts for all six stress components of a general three-dimensional state of stress [255]. According to the principle stress σ_1, σ_2, and σ_3, the von Mises stress is expressed as [255]:

$$\sigma_{von\ Mises} = \sqrt{\frac{1}{2}[(\sigma_1 - \sigma_2)^2 + (\sigma_2 - \sigma_3)^2 + (\sigma_3 - \sigma_1)^2]} \tag{3.25}$$

von Mises stress is commonly used to present results for structural integrity to indicate elastic or plastic deformation. The von Mises theory states that a ductile material will start to yield at a location on the structure where the von Mises stress becomes equal to or greater than the yield strength of the material.

The main-wing structure and planar wing attachment is made from polyurethane composite while the structural connection between the two was a aluminium plate. Each of these materials are homogeneous in their material properties. The physical properties of the materials in the wing structure are summarised in table 3.5 [256, 257].

The wing has been modelled in isolation of the fuselage and mounting system

Table 3.5: Polyurethane wing material physical properties.

	Property	Value
Polyurethane [Sika M945]	Density	$1300 kgm^{-3}$
	Tensile strength	$8.5 \times 10^5 Nm^{-2}\ [Pa]$
	Yield strength	$100 \times 10^6 Nm^{-2}\ [Pa]$
	Elastic modulus	$3400 \times 10^6 Nm^{-2}\ [Pa]$
	Compressive strength	$95 \times 10^6 Nm^{-2}\ [Pa]$
6061 Aluminium	Density	$2700 kgm^{-3}$
	Tensile strength	$310 \times 10^6 Nm^{-2}\ [Pa]$
	Yield strength	$276 \times 10^6 Nm^{-2}\ [Pa]$
	Elastic modulus	$69 \times 10^9 Nm^{-2}\ [Pa]$
	Compressive strength	$316 \times 10^6 Nm^{-2}\ [Pa]$

(including bolts, dowels, and grub screws), and replaced by appropriate connection fixtures and boundary conditions, as illustrated in figure 3.16. The wing base mounting bolts have fixed boundary conditions, meaning that nodal displacements will not be allowed. The aluminium plate connecting the main-wing to the wingtip has been given several rigid connections. In order to mimic the physical wing the internal aluminium plate is rigidly connected to the wingtip but not in entirety to the main-wing. Rigid connections are assumed for the wingtip locking pins fixing the aluminium plate in position as shown in figure 3.16. The overall wing structure is then able to flex (in a cantilever fashion) fixed at the wing base bolt locations. Force magnitudes of $220N$, $580N$, $920N$ and $1165N$ are representative of the normal force acting on the wing at $\alpha = 0°$, $4°$, $8°$, and $12°$. These forces have been estimated using the VRM aerodynamic analysis tool developed in Chapter 2. An additional loading case, determined by trail and error, of $\approx 8000N$ corresponded to the loading which first causes the von Mises stress to exceed the material yield strength; thus indicating the location material yielding (plastic deformation) is expected to be encountered first. It is important to highlight here that the load distribution over the wingspan has been assumed to follow that of the spanwise loading predicted by the VRM model from the planar wing shown in figure 2.28b.

With boundary conditions, material properties, and loads defined (characterising the mathematical model), the CAD geometry must then be discretised into *finite elements*. These elements are referred to as finite to emphasise that they are not infinitesimally small, but small in comparison to the physical geometry of the model. The loads and boundary conditions are also discretised at this stage. This entire process inherently induces three sources of error: 1) formulation or the mathematical

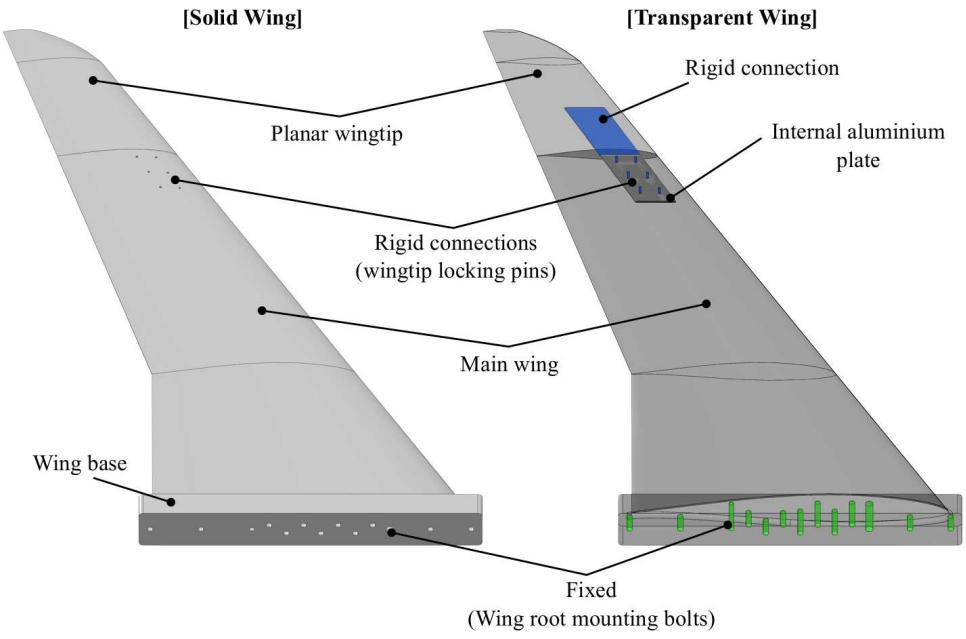

FIGURE 3.16: Illustration of boundary conditions for planar wing arrangement static load finite element analysis.

model, or idealisation/modelling errors (an accumulation of errors/assumptions made in material properties, boundary conditions and loads); 2) discretisation errors (a direct impact of mesh density); 3) solution errors (caused by an accumulation of round-off errors).

Assuming that the description of the mathematical model is sufficiently accurate, discretisation error and solution error can be minimised by subjecting the problem to a convergence analysis. Round-off errors of the discrete solution are not typically considered significant relative to other error sources, but can be minimised by high/finer discretisation of the geometry. Discretisation error is directly related to the discretisation quality (mesh quality). These errors occur from the representation of the governing equations and physical geometry description as algebraic expressions in a discrete spatial domain. A consistent numerical method to approach the continuum representation of the equations and zero discretisation error is to systematically increase the number of mesh points (nodes) to reduced the length of the finite elements; thereby increasing the number of elements in the discretisation. This process is illustrated in figure 3.17. As the mesh is refined, the solution will become less sensitive to grid spacing and approach the continuum solution. Figure 3.18 presents the mesh convergence analysis of the wing structural model under several static load conditions.

In figure 3.18a it is seen that the maximum von Mises stress identified is sensitive to the number of shell elements present in wing geometry discretisation. Convergence of the solution is found with $\geq$ 1264473 elements in the mesh. With further mesh refinements the von Mises stress over the entire structure varies by $< 1\%$. Figure 3.18b shows that the maximum wingtip deflection remains insensitive with mesh refinement, with wingtip deflections varying $\leq 0.2\%$. Nodes (connecting the elements) define the ability to perform translation and rotation six degrees-of-freedom [255]. This signifies the convergence of model rotations and translations, and suggests the efficient distribution of spatial element patterns [258]. All FEA results beyond this point use a geometry discretisation with 1264473 shell elements.

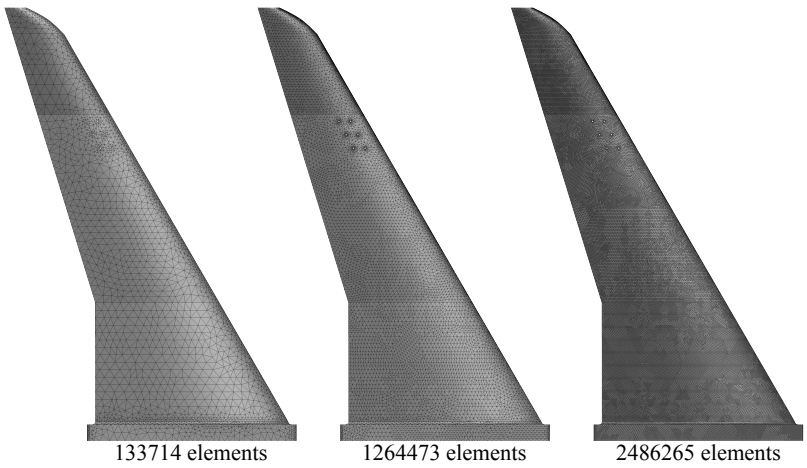

Figure 3.17: Finite shell element mesh refinement.

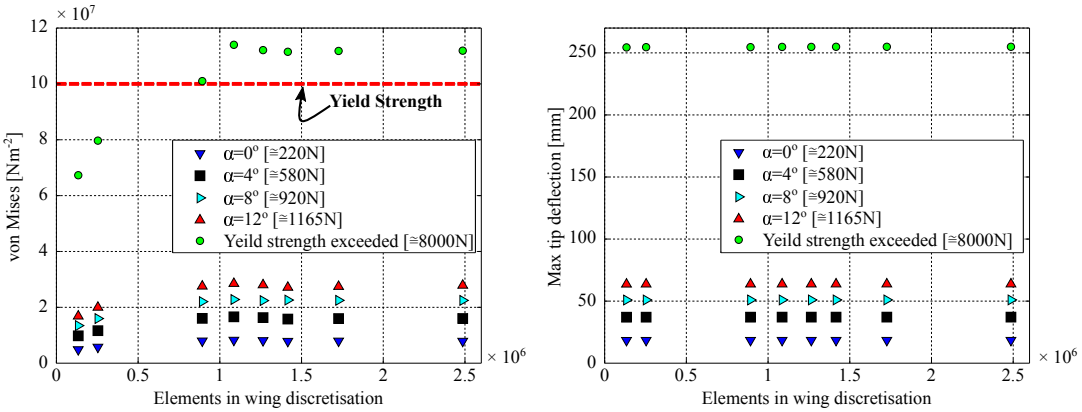

(a) Elements - von Mises stress (b) Elements - Maximum wingtip deflection

FIGURE 3.18: Wing finite element discretisation convergence analysis.

3.6.2 PLANAR WING STATIC LOAD RESULTS

With the results from figure 3.18a, figure 3.19 gives a visual representation of the von Mises stresses over the wing structure at the elastic deformation limit (load magnitude of $\approx$ 8000N) compared to the load magnitude expected at $\alpha = 12°$ ($\approx$ 1165N)—a load difference of 587%. This implies that the wing will operate within its elastic deformation potential; operation within broad elastic deformation ranges typically suggest that repeated compression–tension cycles will not lead to elastic softening/material fatigue [259]. Thus, it is anticipated that the model wing will not plastically deform within its designated experimental performance envelope or life span. In figure 3.19 both upper and lower sides of the wing are shown with no wing deflection, and the position of the internal aluminium plate connecting the wingtip to the main-wing indicated. It is clear that loading at $\alpha = 12°$ does not produce any concerning von Mises stress, this is also evident from figure 3.18a. There is a peak von Mises stress in the main-wing's polyurethane structure at the most inboard, wing leading edge, wingtip locking pin as indicated.

With the elastic limit case the von Mises stresses are seen to exceed the yield strength of the polyurethane of the main-wing at the most inboard wingtip locking pins; indicated as points of plastic deformation in figure 3.19. The main-wing structure as a whole is seen to carry the distributed load well with no concerning stress concentrations in the main structure. The internal aluminium insert is seen to support and strengthen the wing structure over the length of the plate, causing the von Mises stresses drop to a minimum relative to the rest of the loaded wing. The structural discontinuity of the aluminium plate is what eventually causes plastic deformation at the wing locking pins as it creates a focal point of material stress. This is, however, of no concern considering the experimental envelope of the model and the resulting forces expected to act on the wing.

Resulting wing deformation (translation and rotation) from the structural analysis of $\alpha = 4°$, 12°, and the elastic limit case are shown in figure 3.20. The rate of wing

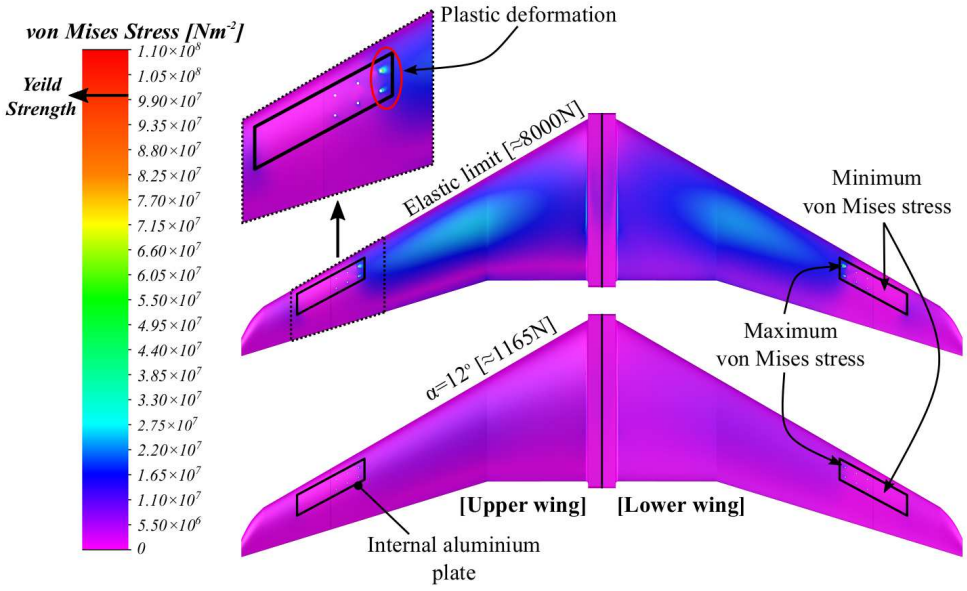

FIGURE 3.19: von Mises stresses from finite element analysis of planar wing with constant static elliptic load.

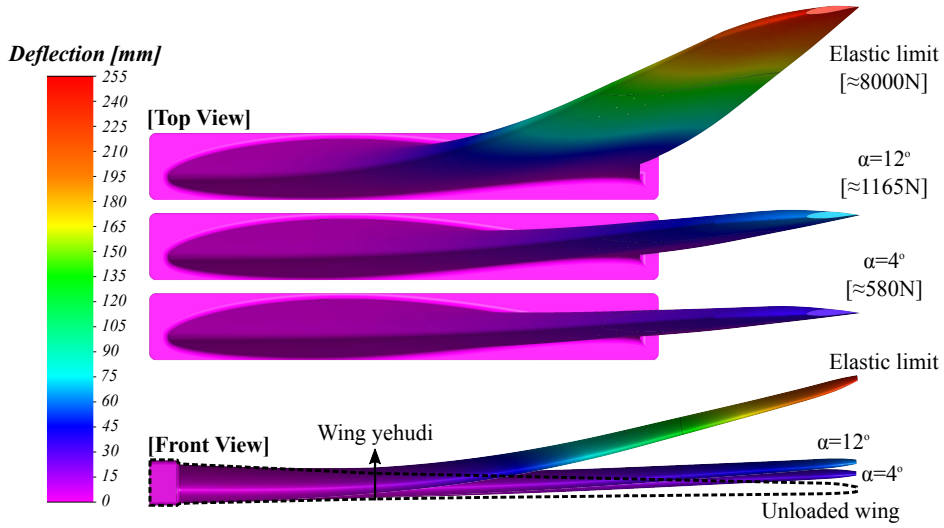

FIGURE 3.20: Wingtip deflections from finite element analysis of planar wing with constant static elliptic load. Scale of deformation 1:1.

bending increases immediately outboard of the wing trailing edge extension (yehudi). This may be an effect of the compound wing and the increased taper ratio outboard of the yehudi (material per unit length decreases faster, i.e. wing cross section reduces, thus reducing stiffness).

3.6.3 VALIDATION OF FEA RESULTS

Planar wing wingtip rotation and translation from aerodynamic loading in the wind tunnel at $Re = 1.5 \times 10^6$ at several angles of attack have been inferred using a

rudimentary two-dimensional direct image correlation (DIC) technique via point tracking at the wingtip. DIC is a non-intrusive optical approach for measuring displacement/strain, in which digital photographs (provided by a Phantom $v341$ digital high speed, 4 Megapixel camera with 2560×1600 pixel) of a structure at different stages of deformation are compared. MATLAB scripts have been developed to analyse digital images of the unloaded and loaded wing structure, such as those shown in figure 3.21 presenting a global visualisation of the planar wing deformation. Calibration images were also captured in order to relate the camera CMOS chip co-ordinate system with the spatial co-ordinates of the deformation field plane of interest. This provides the necessary transfer functions required to convert pixel displacements to physical structural deformations.

From the DIC results presented in figure 3.21, the wing bending is distinct. The resulting wingtip movement monitored with the DIC have been compared to finite element analysis of the statically loaded wing. This comparison is given in figure 3.22.

With the FEA wingtip translation summarised in figure 3.22a, a linear trend in the wingtip deflection with load is observed (compounded by the assumption of linearly elastic material properties). The experimentally inferred wingtip deflections demonstrate a non-linear variation of wingtip deflection with load, with a maximum difference from FEA of 23.93% at $\alpha = 8°$; root mean square error between the FEA and experimental results over the fours angles of attack tested is 10.56%. The standard deviation of each experimentally inferred datum is $< 1.4mm$.

As discussed in the Section 3.5, care was taken to align the line of aerodynamic

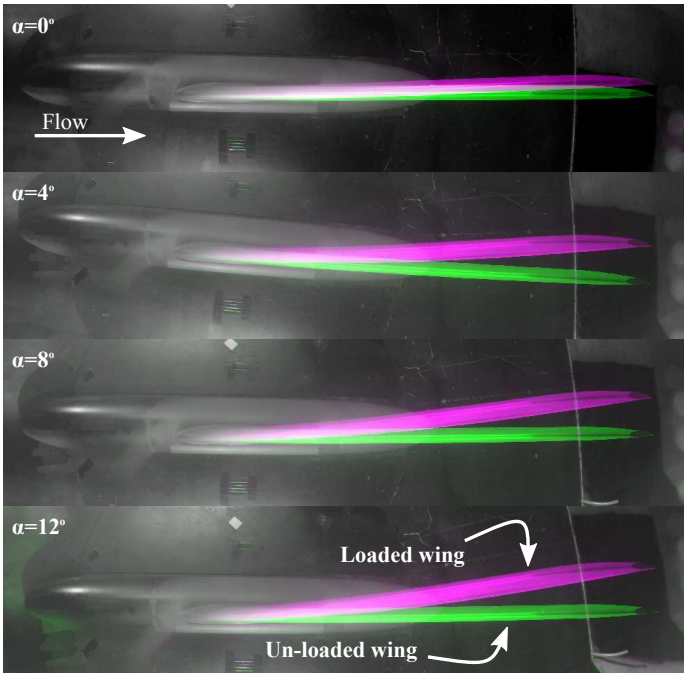

FIGURE 3.21: Visualisation of planar wing deformation under aerodynamic loading at $Re = 1.5 \times 10^6$ for several angles of attack.

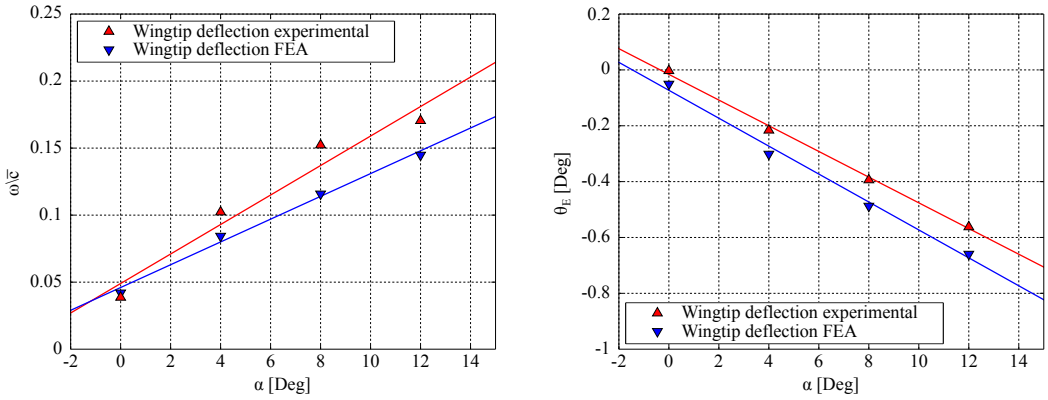

(a) Wingtip translation.

(b) Wingtip elastic twist.

FIGURE 3.22: Planar wing wingtip translations and rotations from finite element analysis compared to experimentally inferred translations and rotations from aerodynamic loading at angle of attack.

centres along the wing with the inertial and elastic axis. Doing so, attempts to decouple the bending and torsion of the wing when aerodynamically loaded such that the wing is inherently protected from aeroelastic instabilities. This also reduces the complexity of the model when loaded ensuring simulation and experiments are simplified. If the three axes are correctly aligned, zero twisting of the wing and pure bending will occur. Figure 3.22b compares the wingtip elastic twist rotation from the DIC experiments and the FEA analysis. Negative elastic twist indicate a leading edge down rotation, the magnitudes of which are small relative to the wingtip deflections. An approximately constant offset of 0.09° is observed between the DIC and FEA results; root mean square error between the FEA and experimental results over the angles of attack tested is 8.33%. The standard deviation of each experimentally inferred datum is $< 0.02^\circ$, which is too small to observe in figure 3.22b. These results provide validation that the finite element analyses captures the wing deformation trends and approximate magnitudes despite the FEA assumptions and simplifications. Unfortunately, this gives no validation of the von Mises stresses but does provide confidence that plastic deformation of the wing structure will not occur.

The negative gradient (wing twisting leading edge down) from the experimental DIC and FEA structural analysis, suggesting that the aerodynamic centre of the wing actually lies aft of the elastic axis. However, the relatively small wingtip rotation (in comparison with the wingspan and the wing bending) implies that the distribution of aerodynamic centres is very close the elastic axis.

3.7 SOLID BODY BLOCKAGE

The solid body blockage of a wind tunnel model is the ratio of the frontal area of the model to the stream cross sectional area of the working section. In wind tunnel tests, this ratio reflects the relative size of the model to the working section. Models are

typically designed to keep solid blockage bellow 10%, with most correction methods confidently applied with a solid blockage ratio of 5% or less [227]. With closed working section wind tunnels, and due to the conservation of mass flow, the effects of blockage produces an effective increase in the oncoming flow speed/dynamic pressure.

The solid body blockage percentage is given in figure 3.23 as a function of the angle of attack for each wing arrangement; the percentage increase between the wing arrangements from planar to C-wing is also given. For the planar wing arrangement the blockage does not exceed 5% at any angle of attack. The C-wing reaches a maximum blockage of 5.24% at $\alpha = 14^{\circ}$.

$$Blockage[\%] = \frac{(frontal\ area)}{(stream\ cross\ sectional\ area)} \cdot 100 \tag{3.26}$$

The effects of the mounting shaft are not included in figure 3.23. At the shaft's maximum extension ($5\delta^*$), the shaft increases the frontal area of the planar and C-wing configurations by 1.83% and 1.66%, respectively. These increases in frontal area equate to an additional solid body blockage of 0.73% for the planar wing, and 0.66% for the C-wing. Regardless, when considering wind tunnel corrections, the shaft at its respective extension is included in the frontal area of the model arrangement.

3.8 THREE DIMENSIONAL BOUNDARY CORRECTIONS

With design criteria outlined by Barlow et al. [227] closely adhered to, three-dimensional boundary correction can be applied with confidence; even though the corrections are small. Horizontal buoyancy drag, solid blockage, and wake blockage corrections have been applied. As the lifting surface wingspan is $< 0.8\%$ of the tunnel width coupled with the associated Reynolds number (10^6), downwash corrections and streamline

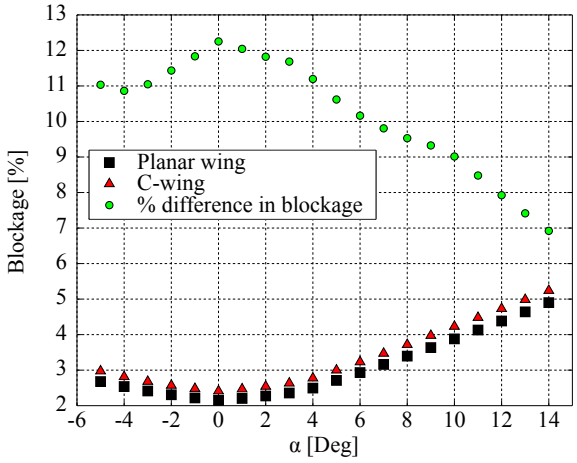

FIGURE 3.23: Solid body blockage of wing configurations and the percentage increase in blockage from planar to C-wing arrangement.

curvature corrections have been assumed to induce negligible error [227].

3.8.1 BUOYANCY CORRECTION

The wind tunnel, along with most other closed return wind tunnels, has a static pressure gradient long the longitudinal axis of the working section resulting from the thickening boundary layer progressing through it. The static pressure gradient is evaluated in Section 3.3 for several of Reynolds numbers. In this work, the semi-span model operated at a Reynolds number of 1.5×10^6 based on the wing MAC; this is equivalent to a Reynolds number of 3.4×10^6 per meter. At this Reynolds number the wind tunnel was found to have a horizontal static pressure gradient of $\frac{dp}{dx} = -2.2797\ Pa/m$ (taken from table 3.3). While buoyancy drag is less significant for wings, it is considered important for bluff bodies such as the model half fuselage [227]. Hence, according to Barlow et al. [227] the expression for the total buoyancy drag acting on a body is given by:

$$D_B = \frac{dp}{dx} \int_0^1 S(x).dx = \frac{dp}{dx} \cdot (model\ volume) \tag{3.27}$$

where $S(x)$ is the model cross sectional area at station x. Integrating over the length of the model results in the model volume ($model\ volume = 0.0974m^3$). From figure 3.23, the solid blockage for each arrangement is $\leq 5\%$ (maximum blockage $= 5.24\%$) regardless of angle of attack, thus deviation in the longitudinal static pressure from the empty wind tunnel gradient is very small [227]. Additional drag due to the buoyancy drag is $\approx 0.222N$.

3.8.2 BLOCKAGE CORRECTIONS

Three-dimensional wind tunnel blockage corrections described in detail by Barlow et al. [227] have been applied in this work, and have also been applied to similar semi-span models with success [260].

Summing the model components (wing + fuselage + mounting shaft), it is appropriate to determine the solid blockage velocity effects by:

$$\epsilon^{sb} = \frac{\Delta U^{sb}}{U_\infty} = \frac{K\tau(model\ volume)}{C^{\frac{3}{2}}} \tag{3.28}$$

where $K \approx 0.52$ for the semi-span model shape factor spanning in the vertical direction [260]; $\tau \approx 0.86$ and is an empirically derived factor from Barlow et al. [227] depending on the tunnel working section shape and the model span-to-tunnel height ratio; and C is the stream cross sectional area taken at the moment centre in the working section. Hence, $\epsilon^{sb} = 0.003919$.

The correction for wake blockage at each angle of attack is calculated by:

$$\epsilon^{wb} = \frac{\Delta U^{wb}}{U_\infty} = \frac{S(\alpha)}{4C} C_{Du}(\alpha) \tag{3.29}$$

where, $S(\alpha)$ is the frontal area of the model at angle of attack α; C is the stream cross sectional area taken at the moment centre in the working section; and $C_{Du}(\alpha)$ is the uncorrected drag coefficient evaluated from the force platform at α. The drag data must first have the buoyancy drag due to the horizontal static pressure gradient removed in the determination of C_{Du} [227]. Taking the planar wing arrangement at $\alpha = 14^\circ$, as an example, results $\epsilon^{wb} = 0.001712$. Hence, the total velocity increment is described by summing the solid and wake blockage corrections according to:

$$\begin{aligned} \epsilon^{tb} &= \epsilon^{sb} + \epsilon^{wb} \\ \epsilon^{tb} &= 0.005631 \end{aligned} \tag{3.30}$$

This correction factor can then be applied to the uncorrected freestream velocity, U_∞, or the freestream dynamic pressure, q_∞ as follows [261, 262, 263]:

$$\begin{aligned} U_\infty^{corrected} &= U_\infty(1 + \epsilon^{tb}) \\ U_\infty^{corrected} &= 1.005631 U_\infty \end{aligned} \tag{3.31}$$

$$\begin{aligned} q_\infty^{corrected} &= q_\infty(1 + 2\epsilon^{tb}) \\ q_\infty^{corrected} &= 1.01126 q_\infty \end{aligned} \tag{3.32}$$

3.9 EXPERIMENTAL APPARATUS AND PROCEDURE

3.9.1 REFERENCE SYSTEMS

Due to the nature of the different experiments conducted, the natural co-ordinate reference systems for each experiment were preferred. Therefore several co-ordinate reference systems are adopted during the discussion of experimental procedures and their associated results. Illustrations and description of the different reference systems used are introduced in figure 3.24, where all co-ordinate systems, with the exception of the polar vortex reference system, are normalised by the wing mean aerodynamic chord. Reference systems are identical between planar wing and C-wing arrangement with the flow direction fixed to the positive x_0 wind reference ($\equiv x_w$). Note that model reference systems are based of the force platform's frame of reference, while wind reference systems are based on the SPIV system's calibrated frame of reference.

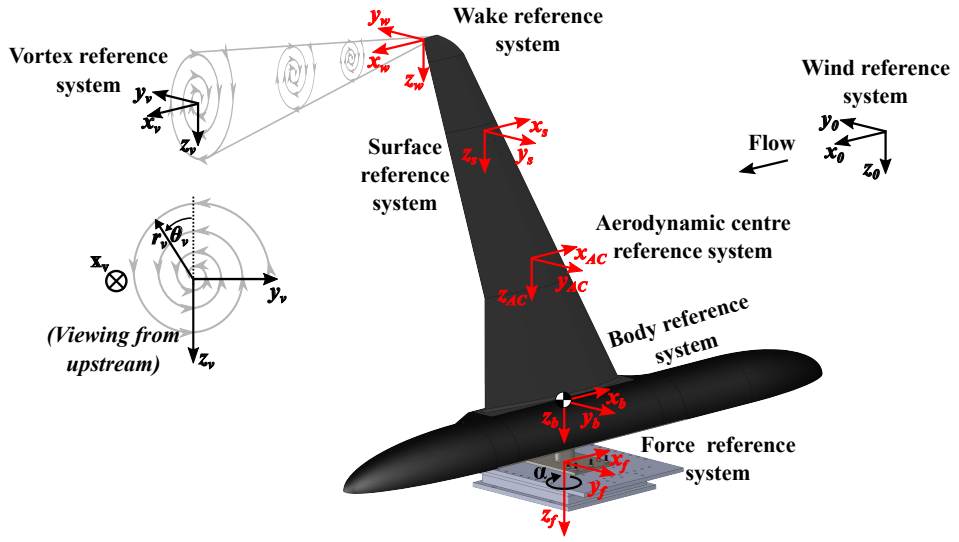

FIGURE 3.24: Schematic of semi-span model with relevant co-ordinate reference systems used in the present study.

FORCE AND BODY REFERENCE SYSTEM

Forces and moments produced by the model body are recorded about the electromechanical centre of the force platform indicated by the force reference system in figure 3.24. The force platform's natural reference system has been used as the standard to orientate all other body reference systems.

The force reference system is rigidly fixed in space to the body reference system of the model and rotates around the z_f ($\equiv z_b$) axis to change the model's angle of incidence relative to the wind reference system. Thus, the force platform provides normal force to the model body reference ($y_f \equiv y_b$), and axial force to the body reference ($x_f \equiv x_b$). In order to obtain lift, L, and drag, D, of the model at angle of attack, α, the normal and axial forces must be related to the wind reference system via the following trigonometric relationship:

$$\begin{aligned} L = F_{y_0} &= F_{y_f} cos\alpha + F_{x_f} sin\alpha \\ D = F_{x_0} &= F_{y_f} sin\alpha - F_{x_f} cos\alpha \end{aligned} \tag{3.33}$$

Additionally, it is often required that resultant moments about the force reference system at the electromechanical centre of the force platform can be related to suitable reference points of the model. In this instance the body reference system is positioned on the model centre of gravity located at the wing root, where $[\Delta x, \Delta y, \Delta z]$ is the spatial vector from the force reference system to the body reference system. Hence, obtaining the moments around the chosen body reference system is obtained from the following moment transfer:

$$\begin{aligned} M_{x_b} &= M_{x_f} + F_{y_f}\Delta z + F_{z_f}\Delta y \\ M_{y_b} &= M_{y_f} + F_{x_f}\Delta z - F_{z_f}\Delta x \\ M_{z_b} &= M_{z_f} - F_{x_f}\Delta y - F_{y_f}\Delta x \end{aligned} \tag{3.34}$$

WAKE AND VORTEX REFERENCE SYSTEM

The natural/convenient reference system for particle image velocimetry measurements of the wing wake aligns the x_w axis with the freestream direction, x_0, the y_w axis aligned with the in the direction of the model lift vector, y_0, and the z_w axis aligned with the wingspan, z_0. However, the vortex axis in general will not be aligned with the freestream, where the vortex will also move upward (in the direction of lift) and inboard when shed and translated downstream away from the wing. These natural vortex translations are also prone to meander amplitudes which is linearly proportional to levels of freestream turbulence [264]. Thus, the vortex y_v-z_v plane (*i.e.* particle imaging velocimetry plane) can not be assumed parallel to the y_w-z_w plane of the wake.

Utilising the trend suggested by Ramaprian and Zheng [265] and treating the arbitrary origin of the vortex system at the edge of the wingtip trailing edge, as shown in figure 3.24, the maximum misalignment of the the vortex reference x_v axis to the wake reference x_w axis over the range $x_w = -0.25$ to $4\bar{c}$ is $\pm 5.5^\circ$ around y_w, and $\pm 5.1^\circ$ around z_w. Thus, on the vortex measurement plane y_v-z_v geometrically perpendicular to the freestream leads to an estimation of the maximum plane misalignment of 3.7%. Assuming an axisymmetric vortex with an axis which follows analytical trends, this misalignment error corresponds to assume velocity vectors of $0.016\bar{c}$ length in the freestream direction as they were on the same plane (this length decreases moving downstream). This distance is small relative to the length scales of the axial evolution of an analytical vortex, therefore deeming the misalignment error negligible. Reference planes in the wake (y_v-z_v) used within this work are located at distances aft of the wing aerodynamic centre based on the wing mean aerodynamic chord: $x_{AC} = -1.35\bar{c}$, $-1.5\bar{c}$, $-2\bar{c}$, $-2.5\bar{c}$, and $-5.418\bar{c}$. For convenience these planes will simply be referred to as $x/\bar{c} = 1.35$, 1.5, 2, 2.5, 5.418.

With origin of the wake reference system at the trailing edge of the wingtip, intuitively as the model changes angle of attack the true distance from the wingtip trailing edge to the wake measurement plane (y_v-z_v) will increase. The maximum increase in the model angle of attack, from $\alpha = 0^\circ$ to 14°, represents a distance separation increase of 1.24% of the mean aerodynamic chord ($\approx 5.45mm$).

The vortex itself can be described in either Cartesian or polar co-ordinates (see figure 3.24); where the assumption that local Cartesian co-ordinates of the vortex reference aligns with the wind reference (based on negligible misalignment error), such that $x_v \equiv x_0$, $y_v \equiv y_0$, $z_v \equiv z_0$. The polar co-ordinate r_v is the radial co-ordinate

with origin at the centre of the vortex structure, and θ_v is the angular co-ordinate which is zero on the positive z_v axis, rotating anti-clockwise around x_v. All vortex visualisation in this work are presented with the vortex rotating anti-clockwise.

WING SURFACE REFERENCE SYSTEM

For measurement planes perpendicular to the wing local surface, x_s is the curvilinear reference which follows the surface (see figure 3.24). The y_s axis is aligned normal to the wing surface, and z_s is aligned with the wingspan. This provides a convenience reference system for one-dimensional vibration measurements of the finite wing.

3.9.2 FORCE PLATFORM

Aerodynamic coefficients have been assessed using an AMTI OR6-7 1000 series force platform which was housed beneath the tunnel floor in the centre of the turntable such that the electromechanical centre of the platform is centred with the yaw axis of the turntable. In this study, the yaw axis of the turntable is described as the pitch axis of the model. All force platform measurements have been taken with the model positioned so that its centre of gravity is aligned with the pitch axis. The force platform measures the three orthogonal force components along the X, Y, and Z axes, and the resulting moments about each axis. Measurement accuracy is $\pm 0.25\%$ of the applied load on the respective output. Each output datum was recorded at $2kHz$ over $20s$ for static conditions only, with each case repeated 5 times; this provides sufficient data to assess random uncertainty (margin of error) based on a given confidence level. Table 3.6 presents a summary of force platform experiments.

TABLE 3.6: Summary of force platform experiments; all experiments conducted at $Re = 1.5 \times 10^6$.

Wing	α range [$^\circ$]	Stand-off gap [δ^*]
Planar	-5 to $+14$	1.4, 2, 3, 4, 5
C-wing	-5 to $+14$	4

3.9.3 STEREOSCOPIC PARTICLE IMAGING VELOCIMETRY

Particle Image Velocimetry (PIV) is a laser optical measurement technique that yields non-intrusive global flow diagnostics of instantaneous velocity field within a planar cross section of flow. PIV is part of a broader class of velocity measurement techniques called pulse-light velocimetry (PLV). These methods measure the displacements of tracers in a fluid by comparing the location of each tracer within an image over some time, or a series of time-steps [266]. Such techniques vary in the type, size, and density of tracer; type, duration, and number of light pulses; type, frame rate, and number

of imaging devices; and processing technique of images. However, in each technique the estimation of the local velocity vector **u** is based on the first-order definition of velocity [267]:

$$\mathbf{u}(x,t) \doteq \frac{\Delta \mathbf{x}(x,t)}{\Delta t} \tag{3.35}$$

where $\Delta \mathbf{x}$ is the displacement of some tracer, located at **x** at time t, and Δt is the time interval separating two observed states of that tracer. As Δt approaches zero, the limit of **u** is the instantaneous local velocity.

The PIV technique is typically based on three components: 1) a pulsed laser light sheet; 2) tracer particles; and 3) camera. The pulsed laser light sheet illuminates the tracer particles with each pulse (separated by Δt) and simultaneously the camera captures images in order to determine the displacement of the tracer particles in the flow. If the flow is highly three-dimensional, the velocity component perpendicular to the laser sheet can be a source of error in the measured velocity up to more than 15% of the mean flow velocity [267]. This error is due to the dependence of the in-plane velocity vectors being subjected to a comparable, or dominating, out-of-plane velocity component. Hinsh [268] discusses a variety of approaches for recovering the complete set of velocity components.

Stereoscopic particle imaging velocimetry (SPIV), while based on the same fundamental principle of PIV, is capable of evaluating three mutually–orthogonal velocity components of a velocity vector from a two-dimensional plane of the flow field. The SPIV method typically uses a minimum of two camera systems to record distinct off-axis views of the region of interest simultaneously. Each camera system records an image pair with the laser light pulse, where each pair is then analysed independently to generate two in-plane velocity fields. Then, as the perspective of the camera orientations relative to the region of interest measurement plane in known (through calibration), the out-of-plane velocity can be derived; see Lawson and Wu [269] for more information. Furthermore, SPIV is known to result in more accurate flow diagnostics on the in-plane velocity components relative to PIV. SPIV also gives more experimental flexibility if optical access it limited as the cameras do not need to be perpendicular to the laser light sheet as with PIV.

A commercial LaVision SPIV system was used for experiments on the semi-span model in the wind tunnel; a detailed description of each component follows. The arrangement of a typical experimental set-up is shown in figure 3.25, with a detailed schematic illustration of the experimental set-up presented in figure 3.26. It is highlighted that the laser sheet can be freely rotated around z_0, and translated longitudinally in x_0, and laterally in y_0. In this dissertation not all of the configurational arrangements of the SPIV are discussed, though all of them are analysed and compared with a summary of all SPIV experiments summarised in table 3.7.

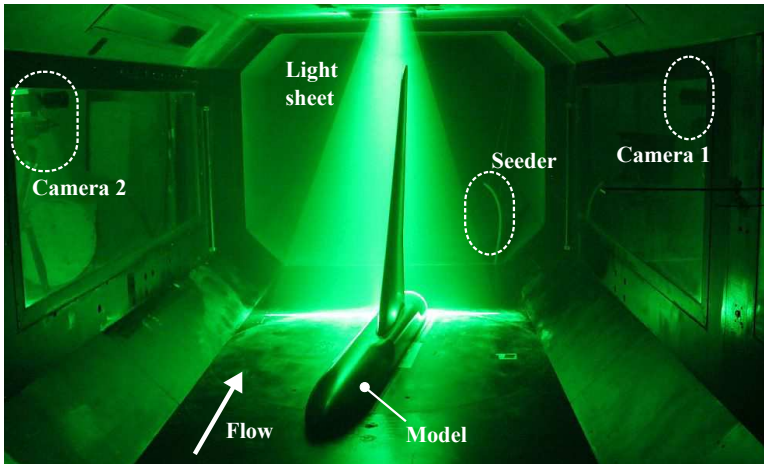

FIGURE 3.25: SPIV experimental set up with laser sheet in wing wake at $x/\bar{c} = 1.35$.

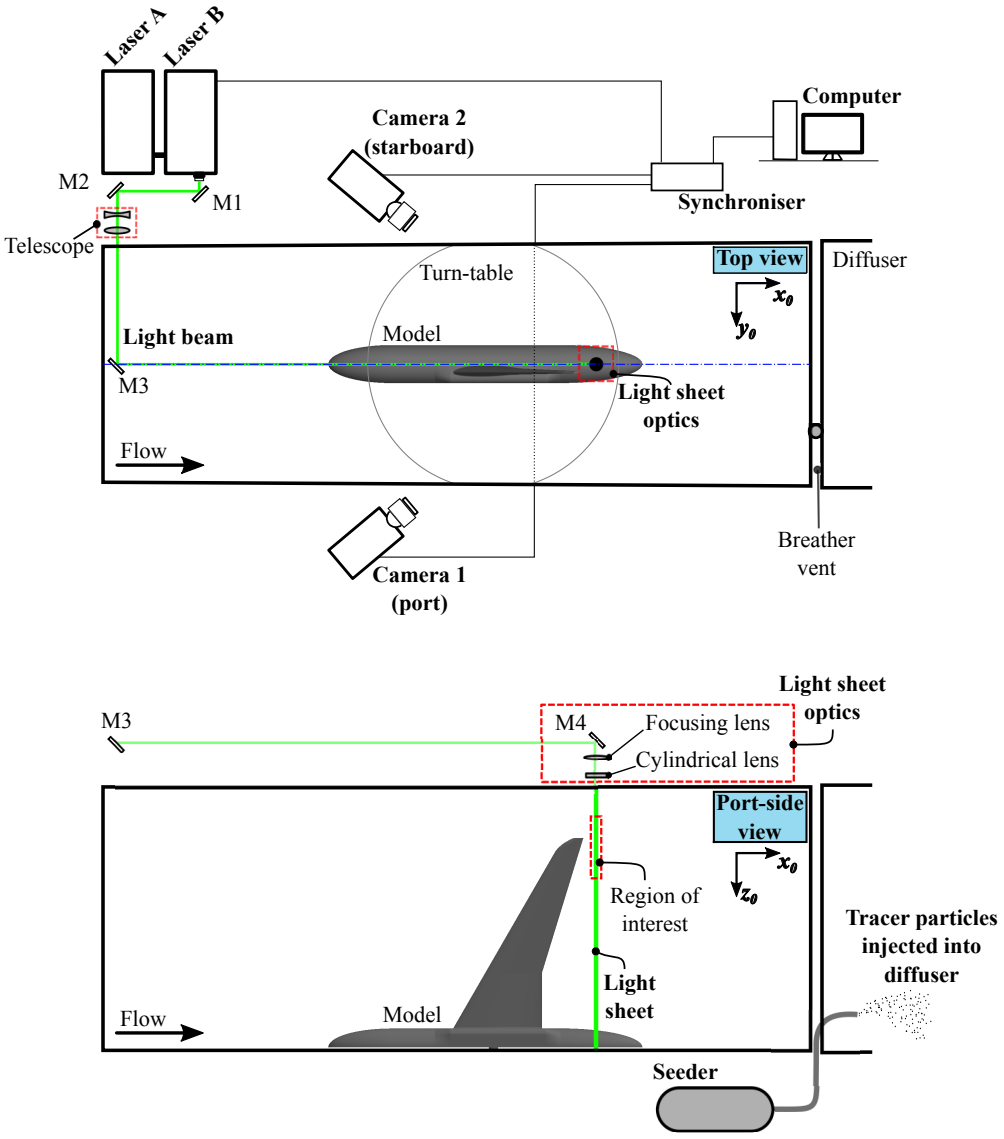

FIGURE 3.26: Schematic of SPIV set-up shown in figure 3.25 with laser sheet in wing wake at $x/\bar{c} = 1.35$. Wind reference frame shown.

TABLE 3.7: Summary of SPIV experiments; all experiments conducted at $Re = 1.5 \times 10^6$.

Wing	Laser plane position	α [°]	Stand-off gap [δ^*]
Planar	Centre-line of fuselage nose	0	1.4, 2, 3, 4, 5
Planar	In wake: $^x/_{\bar{c}} = 1.35, 1.5, 2, 2.5, 5.418$	0 to 14	4
C-wing	In wake: $^x/_{\bar{c}} = 2.5, 5.418$	0 to 10	4

LASER

A Litron double cavity (laser A and laser B) oscillator amplified, Nd:YAG laser (wavelength $532nm$) with an output energy of $100mJ$ per pulse, of duration $8ns$, was used to deliver the laser light sheet. The laser frequency, corresponding to the acquisition frequency of the recorded images remains constant at $200Hz$ for this study.

Figure 3.26 illustrates the series of mirrors and light optics for delivering the beam to the light sheet optic head. This arrangement allows two-dimensional translation (in x_0 and y_0) and a single axis of rotation of the laser sheet (around z_0) covering a broad range of the working section. Depending on the field of view required, the cylindrical lens in the light sheet optic of different focal length could be installed. For investigations with the light sheet parallel to the freestream (in-plane velocities dominate) flow a light sheet thickness of $\approx 1.5mm$ was used; for investigations with the light sheet perpendicular to the flow a light sheet thickness of $\approx 4mm$ was used (significant out-of-plane velocity). The former arrangement minimises tracking out-of-plane velocities, while the latter ensures the measurement of in-plane velocities while accommodating the dominant out-of-plane velocity.

Matte-black paint is used on the model and the working section walls to minimise surface glare that may exceed the scattered signal of the seeding particles.

TRACER

As PIV methods measure the flow velocity indirectly, measuring the displacements of seeded tracer particles, the dynamics of the seeding must be considered. The basic assumptions of tracer particles are:

- Particles follow the flow exactly.
- The particles are non-intrusive (i.e. they do not alter flow).
- The particles do not interact with each other.

In order to validate these assumptions, the seeding must be assessed to avoid significant errors in the velocity evaluation, and to ensure that the seeded tracer particles follow the fluid motion faithfully [270]. In addition to this, consideration must be given to the light scattering properties of the tracer particle and consequently

how much signal the camera receives. Raffel et al. [267] indicate that a sufficient trade-off must be found between a particle small enough (low enough mass) to ensure effective tracking of the fluid motion, and a particle physically large enough to scatter sufficient light to be seen by the camera.

In this study, the flow was seeded through a pipe mounted downstream of the working section through the breather vent, as shown in figure 3.26. Olive oil seeding was generated by a Pivtec-GmbH Aerosol Generator PivPart160 series device. The nominal peak in the probability density function of the olive oil particles diameter size distribution is $1\mu m$ [271]. Hence, the flow tracing capability of a particles of diameter d_p and density ρ_p (where $\rho_{olive\ oil} \approx 912 kgm^{-3}$, between 6-35$^\circ C$ [272]) in a fluid of viscosity μ_f, can be quantified through the particle relaxation time τ_p:

$$\tau_p = \frac{d_p^2 \rho_p}{18\mu_f} \tag{3.36}$$

The particle relaxation time is a measure for the tendency of the particles to attain velocity equilibrium with the surrounding fluid. Furthermore, if the flow time scale of the fluid motion is considered, described by [273]:

$$\tau_{flow} = 10\frac{\delta}{\Delta U} \tag{3.37}$$

where δ is the characteristic dimension (typically taken as boundary layer thickness), and ΔU is the flow slip velocity, then the theoretical behaviour of the tracing particles can then be reduced to the modified Stokes drag law for small spherical particles [274]. Hence the particle dynamic effects when suspended in a specific flow field may be quantified by the Stokes number:

$$St = \frac{\tau_p}{\tau_{flow}} \tag{3.38}$$

This is the ratio of particle aerodynamic response time to the flow time scale. In order to be confident in the assumption that the tracer particles follow the fluid motion accurately, $St << 1$ must be be satisfied. Table 3.8 summarises the associated time scales demonstrating that $St << 1$ is satisfied. The characteristic dimension, δ, has been taken as the wind tunnel boundary layer thickness at the moments centre indicated on figure 3.5.

Table 3.8: Capability of seeding particles for flow tracing,.

$\delta\ [m]$	$\tau_p\ [\mu s]$	$\tau_{flow}\ [\mu s]$	St
0.0503	2.7992	10060	2.78×10^{-4}

Raffel et al. [267] have demonstrated that if a Stokes number of $St \leq 0.06$ can be achieved, then the root mean square tracing error will be $< 1\%$.

Due to camera hardware limitations, the effective digital particle diameter on the image plane as viewed by the camera is a function of the physical particle size; the intensity, and wavelength of the scattered laser light; the magnification/physical distance between the camera and light sheet; the point response function of the lens; and the lens f-number [266]. With experimental set-up and calibration process used in this study, the particle size on the image plane as viewed by the camera is equal to $\approx 0.1mm$, which corresponds to a value between one and two pixels on the laser light sheet plane.

Another important aspect to consider is the seeding particle image density. Keane and Adrian [275] demonstrated that to achieve a valid detection probability of at least 90%, the density of particles should be at least 15 per interrogation window. Hence, the detection of a correct displacement evaluation increases with the number of particles, as the signal strength of the correlation peaks increase. However, if the seeding particle density per interrogation window begins to exceed the contrast of the camera system, leading to overexposure, individual particles become difficult to identify and peak-locking can occur as individual particles loose definition. A discussion of peak-locking and related SPIV measurement errors are discussed in Appendix B.

CAMERAS

Two Phantom $v341$ digital high speed, 4 Megapixel cameras with 2560×1600 pixel CMOS sensors, of $10\mu m$ pixel size, each equipped with automatic Scheimpflug mounts have been used. The Scheimpflug mounts ensure uniform magnification gradients, and good image focus over entire field of view. A range of Canon lenses, from $85mm$ to $200mm$ focal lengths and f-numbers between 2.5 to 5.6 were used to obtain the required depth of field and focus to provide suitable particle size during each test, with a maximum field of view of up to $600mm \times 400mm$. The system was controlled using LaVision DaVis 8 software.

The cameras were mounted outside of the working section; with camera 1 on the tunnel port side, and camera 2 on the starboard side as shown in figure 3.26. This set-up is true for all SPIV tests conducted in this work. Depending on the orientation and the positioning of the laser plane, the cameras were positioned to maintain an angle separation of 30 to 45 degrees from the laser light sheet plane. This angular displacement arrangement maintained measurement accuracy of the velocity components, ensuring low errors in the evaluation of both in-plane and out-of-plane components [269, 276]. The camera angular displacements in all three axes, between the camera and the light sheet plane, were determined in the DaVis 8 system during the calibration procedure.

CALIBRATION PROCEDURE

The calibration procedure uses a calibration plate with known geometric properties to relate the camera chip co-ordinate system with the spatial co-ordinates of the flow field plane of interest (*i.e.* laser light sheet plane). This process provides the necessary transfer functions required to convert pixel displacements of tracer particles to the physical particle displacements. LaVision FlowMaster software was used to perfrom the SPIV calibration based on a three-dimensional pinhole calibration [277].

The accuracy of the calibration is improved by taking several calibration images at the laser sheet plane, where the calibration plate is slightly rotated or translated between images. The average deviation of the de-warped marker positions to the ideal regular grid was < 0.3 pixels for each calibration with no trend/bias/gradient of the de-warped marker positions observed for either camera; *i.e.* uniform de-warping observed. This suggests that an accurate calibration has been achieved [277]. The camera distances and perspective angles to the laser light sheet are calculated during the calibration process.

In the calibration process a calibration plate is used which is aligned as closely as possible with the laser sheet. However due to the cameras being positioned wide apart, by distance D (shown in figure 3.27) in the SPIV set-up, the calibration requires correction due to the introduction of the so called 'disparity vector.' This disparity vector arises due to misalignment between the calibration plate and the laser sheet, and must be corrected accordingly from particle images from the laser sheet plane. This enhances the calibration accuracy as particle images themselves are used for the final stage of calibration.

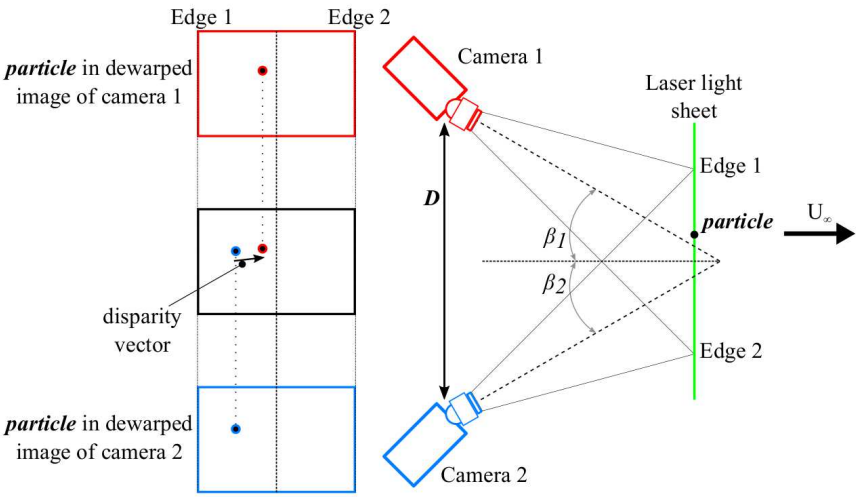

FIGURE 3.27: Schematic of SPIV set-up illustrating how the de-warping (correction) of images from camera 1 and 2 causes particles to be mapped to different locations in each image. The vector between these mapped positions is the disparity vector.

Figure 3.27 illustrates how the disparity vector is caused by the calibration procedure itself when de-warping (correcting) the images of each camera based on spatial information provided by the calibration plate. As the distance D between the cameras increase, angles β_1 and β_2 will also increase. With each camera focused on the laser sheet plane/calibration plane, the camera images are transformed in a manner as if they had been captured with the respective camera viewing perpendicular to the laser light sheet [277]. With large separation distances D, and by aligning the each camera's field of view, the centre of each camera's field of view will not co-inside.

LASER PULSE SEPARATION

The successive laser light sheet pulse separation time (Δt) is a key parameter that has to be optimised for the specific PIV experiment in question, and thus requires special consideration. The experimental conditions must be accounted for as minimum and maximum velocities, velocity gradients, and flow direction will dictate certain influence into the determination of the laser pulse separation time. Fundamentally, the laser pulse separation time must be long enough to allow sufficient movement of the slowest particles within the interrogation window, but short enough in order to not lose too many particles from each interrogation window. Additional factors that effect the separation time include the laser sheet thickness, interrogation window size, and the correlation process. There are several methods for calculating the separation time in the literature [267, 278, 279, 280]. In the current study a preliminary estimation of the pulse separation time was made and then adjusted by experimental observation of the resulting vector fields.

Keane and Adrian [275] showed that to achieve a validation detection probability of at least 90%, the mean number of particles per interrogation window should be greater than 15 and that the average particle displacement of the particles over the pulse separation, Δt, must be limited to less than 30% of the interrogation window size. Thus, it is possible to relate Δt directly to the geometric dimension of the interrogation window d_{int}, and *a priori* knowledge of the flow (*i.e.* freestream velocity). If the dominant velocity is parallel to the laser light sheet, referred to as the in-plane velocity, Δt can be approximated by:

$$\Delta t < \frac{0.3 d_{int}}{max|U_{in-plane}|} \tag{3.39}$$

When the dominant velocity is perpendicular to the light sheet, referred to as the out-of-plane velocity, the chance of particles clearing the light sheet and not being detected by the second light pulse at all is high. Hence, a second light pulse separation relationship related to the laser light sheet thickness d_L must be considered too:

$$\Delta t < \frac{0.3 d_L}{max|U_{out-of-plane}|} \tag{3.40}$$

The evaluation of the pulse separation for a reference wingtip vortex is now presented. The trailing vortex at $x/\bar{c} = 2.5$, at $\alpha = 8^\circ$ and $Re = 1.5 \times 10^6$ is adopted as the reference case. The corresponding freestream velocity is $\approx 50m/s$. For such experimental conditions, the maximum swirl velocity (maximum tangential velocity) of $0.8U_\infty$ and a maximum axial velocity deficit of $0.6U_\infty$ ($max|U_{out-of-plane}| = U_\infty$) is identified [264].

Equation 3.39 can be applied in assessment of both the object plane and the image plane (on CMOS camera chip). In the first case, the interrogation window size will use a scale factor of 0.1002mm/pixel (determined during calibration process), where as the latter case will use the pixel dimension 0.01mm/pixel (determined from camera specifications) and the magnification of the lens, 10.57 (determined from calibration process).

Therefore, for an interrogation window size of 32×32 pixels, equation 3.39 becomes:

$$\Delta t_{object\ plane} < \frac{0.3 \cdot (32 \cdot 0.1002 \cdot 10^{-3})}{0.8 \cdot 50} = 24.0\mu s \tag{3.41}$$

$$\Delta t_{image\ plane} < \frac{0.3 \cdot (32 \cdot 0.01 \cdot 10^{-3})}{(0.8 \cdot 50)} \cdot 10.57 = 25.4\mu s \tag{3.42}$$

The thickness of the laser sheet along the object plane is constant and equal to $4mm$. The laser pulse separation from equation 3.40 can then be evaluated on the object plane as:

$$\Delta t_{object\ plane} < \frac{0.3 \cdot 0.004}{50} = 24\mu s \tag{3.43}$$

The separation times from equations 3.41, 3.42, and 3.43 yield similar values which implies a good experimental arrangement and accurate results for both the in-plane and out-of-plane components. The in-plane separation is affected by the interrogation window size chosen during the image processing when the out-of-plane separation is dictated by the laser sheet thickness.

A laser pulse separation of $\Delta t = 45\mu s$ was used for the SPIV data provided in Chapter 4, while a pulse separation of $\Delta t = 25\mu s$ was used for the data presented in Chapter 5; the latter corresponds to the separation time calculation provided in this section. Each of these separation pulse times were found to yield best results in consideration flow features, peak velocities, and turbulent properties detected. In-plane and out-of-plane velocity histograms were calculated for all experimental set-ups, each showing no peak-locking effects, which indicates a well-conditioned experiment and analysis. Peak-locking, histograms, and additional considerations of the SPIV measurement accuracy and error have been discussed in Appendix B.

IMAGE PROCESSING PROCEDURE

DaVis 8 was used for the processing of the images and the calculation of vector fields. Analysis was conducted by purpose written MATLAB codes. The typical procedure for a stereo cross-correlation process is briefly described here.

Each data acquisition consisted of four images: two single frames with a time interval of Δt from each camera. Each frame is de-warped through the mapping functions developed in the calibration process and appropriately segmented into interrogation windows with set initial size, weighting, and overlap. Each interrogation window is cross-correlated with the corresponding region, shifting based off a reference vector field, from the first image to the second for each camera. The highest peak identified in the cross-correlation image is taken as the displacement vector and is used to calculate the corresponding velocity vector for that interrogation window. On completion of this process for each camera image pair, two two-dimensional vector fields are obtained. From the two planar vector fields stereoscopic reconstruction of a two-dimensional three-component vector field is established. The vectors are then subjected to a validation process and then projected onto a planar vector field which is used as the reference vector field for the next cross-correlation pass of different interrogation window size and overlap. This loop is repeated to the multi-pass criteria set and procedure adopted. At this point, post-processing, filtering, and bad vector handling can be implemented.

In the current study good quality seeding and imaging provided a high level of reliability to the experiments. Hence, no vector post-processing was conducted; no vector filtering, vector removal, or interpolation was enforced. Only a 3×3 point kernel smoothing filter was applied between each step of the multi-pass process. More details on the functions involved in the image processing can be found in the LaVision Manual [277].

In each SPIV test case, the stereo cross-correlation of the image pairs composed of a double step process on an interrogation window of 32×32 pixels with 25% overlap, followed by another two steps with interrogation window of 16×16 pixels with 50% overlap. Exact spatial resolution will be presented with results, however it is typically $\approx 1mm$.

The SPIV hardware recorded images at the maximum acquisition rate of $200Hz$. The internal memory of the cameras limited the maximum number of images that each camera could record in any one experiment to 600; experiments were repeated a minimum of three times to ensure statistical convergence could be reached. Appendix C presents the example investigation of the statistical convergence of different quantities (e.g. velocity, vorticity, turbulence qualities) for the planar wing trailing vortex system; consideration to the errors associated with SPIV have been discussed with their respective results.

3.9.4 SURFACE FLOW VISUALISATIONS

TUFTS

The simplest, cheapest, and most frequently used method for low speed surface flow visualisations is to attach tufts over the surface of interest. Tufts can very easily show flow patterns but must be light and flexible such that they easily align with the local flow field as a result of aerodynamic force. Hence, tufts can readily show where flow is steady and where it is unsteady; regions of complete separation are easily identified. Spatial resolution of the tufts should be close enough to sufficiently resolve local flow fields, but when tufts are in close proximity their influence on the flow and each other is very high and must be considered at all times.

To ensure that the tufts have minimal effect on the flow, the tufts used in this study are mono-filament nylon with size 3 denier (0.02mm diameter), and have been attached to the surfaces using a small amount of water soluble glue. Treatment of the tufts with fluorescent dye was not necessary as the fluorescent yellow tufts contrasted well with the black surface of the model and wind tunnel floor. All tufts used on the model were 25mm long and positioned on the tunnel floor and on the model in a grid pattern of 20mm laterally by 50mm longitudinally, as indicated in figure 3.28. The movement of the tufts was recorded at 100Hz for a period of 10 seconds using a Phantom v341 camera. A summary of tuft visualisation experiments and test conditions are given in table 3.9.

CLAY FLOW

A clay flow mixture consisting of fine white Kaolin clay suspended in paraffin is used to visualise the characteristics of the flow near/over the model and wind tunnel floor.

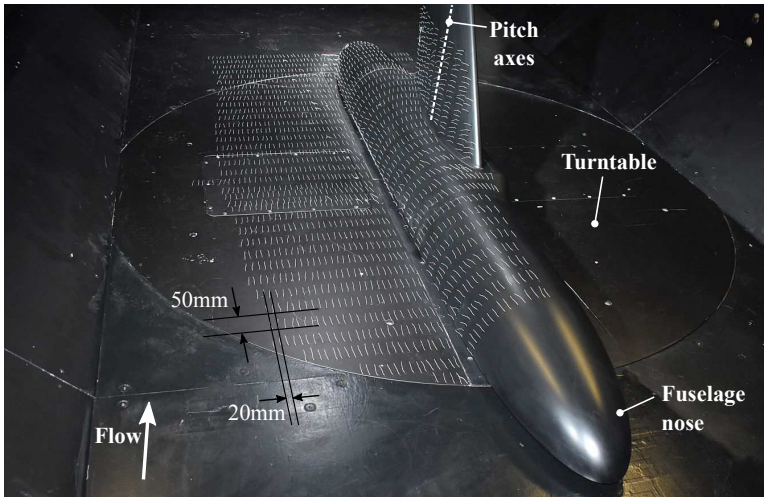

FIGURE 3.28: Tuft grid used over working section floor, fuselage and wing root. Pitch axes indicated.

TABLE 3.9: Summary of tuft visualisation experiments; all experiments conducted at $Re = 1.5 \times 10^6$.

Wing	Tuft locations	α [°]	Stand-off gap [δ^*]
Planar	Tunnel floor & fuselage	0 to 14	1.4, 3, 4, 5
Planar	Wing	0 to 14	4
C-wing	Wing	0 to 14	4

It performs in a very similar manner to oil flow surface visualisations but with a few advantages: 1) clay flow dries over the model and so can be photographed once the wind tunnel is turned off. Oil flow must be photographed with the wind tunnel on otherwise it will begin to run with the affect of gravity; 2) oil flow is more strongly effected by gravity which makes it difficult to use on inclined or vertical surfaces [227]; 3) oil flow can make the wind tunnel dirty and clog up turbulence screens which strongly impedes the performance of the wind tunnel.

Clay flow visualisation moves in the local flow direction, spreading out over a surface driven by the frictional shear force from the freestream air. From the patterns of clay accumulations over the surface, qualitative conclusions can be drawn in regards to the location and direction of streamlines, separation lines, and relative magnitudes of frictional shear stresses [281, 282, 283]. These frictional shear stresses are defined as the spatial derivative normal to the surface of the velocity field at the surface. The integral curve lines of the velocity in this vector field are often referred to as limiting streamlines, or skin friction lines. It is this vector field which produces the clay flow patterns during wind tunnel experiments [284].

Surface clay flow visualisations have been used to provide insight into the time-averaged flow features over the semi-span fuselage and floor as well as over each wing arrangement. Results have been obtained by the following procedure: 1) set the model angle of attack; 2) even application of the clay mixture to the surface; 3) operating the wind tunnel from zero velocity to the operational flow regime in a relatively short time ($\approx$ 4 seconds), and recording continuously (with a Phantom $v341$ at $50Hz$ over 30 seconds) to monitor the progressive movement of the clay; 4) sustained operation of the wind tunnel until clay mixture is dry ($\approx$ 12 minutes). Colour images were taken using a Canon SLR camera, model EOS-450D with 12 mega-pixel resolution.

Where and how the clay is placed before turning the wind tunnel on, as well as viscosity, strongly affects the final results. The viscosity of clay was maintained through batch making the clay mixture adhering to strict measurements, and thorough mixing to avoid the clay clumping. Sites for clay application are indicated in figure 3.29. Sites **A** and **B**, on the tunnel floor and fuselage nose respectively, were applied simultaneously, and site **C**, along the wing leading edge (for either planar or C-wing case) was applied on separate wind tunnel runs. These sites, found through trial and error, allowed the clay to flow over the floor and fuselage indicating points of interest. Experiments conducted using the clay fow visualisation have been summarised in

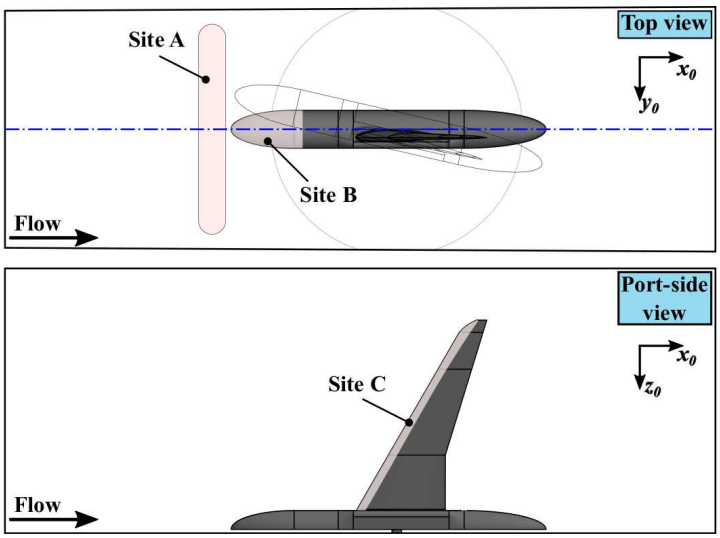

FIGURE 3.29: Clay application sites prior to experiment start.

TABLE 3.10: Summary of clay flow visualisation experiments; all experiments conducted at $Re = 1.5 \times 10^6$.

Wing	clay locations	α [°]	Stand-off gap height [δ^*]
Planar	Sites **A** & **B**	0, 8, 14	4
Planar	Site **C**	0, 8, 14	4
C-wing	Site **C**	0, 8, 14	4

table 3.10.

3.9.5 LASER-DOPPLER VIBROMETRY

Laser-Doppler vibrometry has been used to determine wind tunnel forcing frequencies, model natural frequency data, and monitor vibration of the model wing arrangements under different conditions. This gives a deeper understanding of the wing vibration and loads under different test conditions, and also how the wind tunnel influences the model.

The laser vibrometer used in this work is a Polytec PDV-100 portable digital laser-Doppler vibrometer, which provides a single degree-of-freedom point measurement with peak velocity detection of $500mm/s$ and a frequency range of 0-22kHz with 24-bit resolution. The laser vibrometer offers a non-intrusive optical means of measuring vibration from a distance with no contact. In addition, relative accuracy of vibration measurements is independent of the vibration frequency, and is immune from electrical noise, unlike mechanical based accelerometers, for example.

The PDV-100 vibrometer uses the heterodyne interferometer principle to determine the phase (and thus the optical path length) reflected back from the surface of some vibrating test article [285]. In a heterodyne vibrometer, an acousto-optic modulator, or Bragg cell, is used to frequency shift either the test signal or the reference signal;

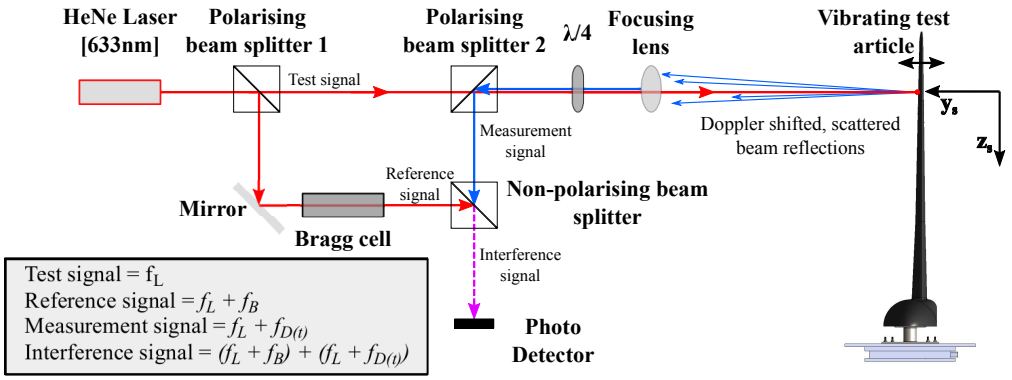

FIGURE 3.30: Laser vibrometer in Mach-Zehnder configuration schematic diagram.

figure 3.30 presents a schematic layout of the vibrometer using a Mach-Zehnder heterodyne interferometer configuration [286], in which the Bragg cell frequency shifts the reference signal.

With the configuration illustrated in figure 3.30, the test signal/laser frequency, f_L, is $4.7 \times 10^8 MHz$ to which the Bragg cell provides a frequency shift, f_B, of $+70MHz$ to form the heterodyne frequency reference signal. The vibrating test article causes a Doppler shift of the test signal to form the measurement signal described by:

$$f_L + f_D(t) = f_L + \frac{2v(t)}{\lambda_L} \tag{3.44}$$

where $v(t)$ is the test article velocity component with time in the direction of the laser beam and λ_L is the laser wavelength ($633nm$).

The reference signal (frequency shifted by the Bragg cell) and the measurement signal (frequency shifted by Doppler shift) are re-combined at beam splitter 3 as shown in figure 3.30. This creates a frequency and amplitude modulated interference signal through wave superposition, creating a pattern of constructive and destructing interference which is detected and demodulated by the photo detector. The polarising beam splitters and the $\lambda/4$ (quarter-wavelength) plate ensure that the superimposed beams are of the same polarisation state, otherwise the beams would not coherently align with the photo detector.

In operation, the laser vibrometer beam is positioned normal to the test article surface along y_s (single degree-of-freedom measurements) which is pre-treated with high gain industrial grade retroflective film. This helps maximise the scattered beam reflections detected, thus improving the measurement signal. Vibrations (velocities) are recorded at a sampling frequency of $10kHz$ over a 26.5 second period per test, achieving a resolution of $39\mu Hz$. No filtering was applied upon data acquisition; any post-processing filters will be specified with results. As the vibrometer only provides a single point measurement phased vibration between two points cannot be assessed. Other means have been used for this (piezo-accelerometers).

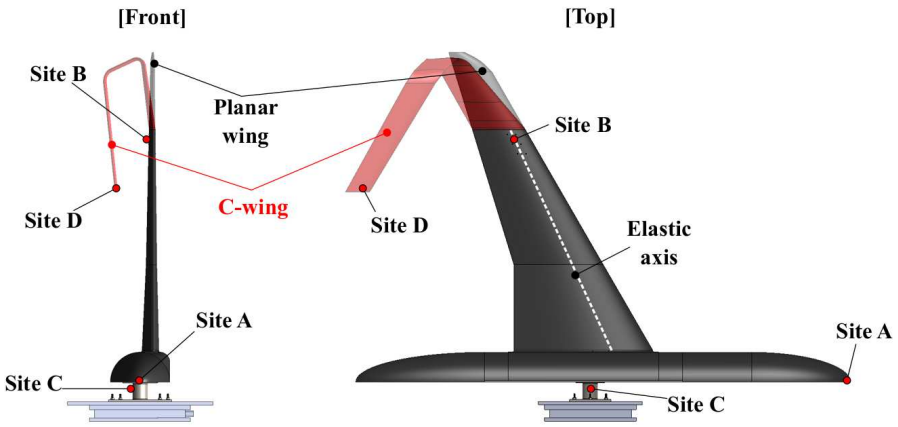

FIGURE 3.31: Laser-Doppler vibrometer measurement sites.

Measurement locations for laser-Doppler vibrometry are indicated in figure 3.31. A series of 'wind-off' and 'wind-on' experiments conducted at these specific measurement locations have been summarised in table 3.11. Preliminary 'wind-off' experiments indicate bump tests. In bump tests, the transient response of the model arrangement can be analysed to understand the fundamental vibrational characteristics of the model without influence of the aerodynamic loading, or forced wind tunnel structural vibration. By focusing the vibrometer to different measurement sites, and bump testing the model, thereby exciting all natural frequencies of the model, natural frequencies and structural damping can be assessed. 'Wind-on' experiments then employ the same measurement sites but with aerodynamic loading and wind tunnel vibration, at $Re = 1.5 \times 10^6$, at a series of angles of attack. The vibrometer moves with the body axis of the model such that measurements remain normal to the test surface.

TABLE 3.11: Summary of laser vibrometer experiments; wind-off experiments signify bump tests, wind-on experiments conducted at $Re = 1.5 \times 10^6$.

	Wing	Measurement location	α [°]	Stand-off gap height [δ^*]
Wind-off				
	Planar	Sites A, B, & C	0°	4
	C-wing	Sites A, B, C, & D	0°	4
Wind-on				
	Planar	Sites A, B, & C	0° to 14°	4
	C-wing	Sites A, B, C, & D	0° to 10°	4

3.9.6 ACCELEROMETER

Printed circuit board (PCB) accelerometers have been used to supplement findings of the laser-Doppler vibrometer. The three accelerometers used in this work are PCB Piezotronics^{inc} ceramic shear accelerometers (model No.352C22), each providing a single degree-of-freedom point measurement with peak acceleration detection of

$\pm 500g$ (m/s^2) with a frequency range of 1-10kHz. The voltage signals from the accelerometers are passed through a PCB Piezotronics^{inc} signal conditioner (model 482C series) and then recorded via a National Instruments dynamic signal acquisition module (NI 9234) capable of sampling all three sensors at rates up to 51kHz simultaneously with 24-bit resolution. It is also indicated that the acquisition model is specified to be unable to recognise frequencies $\approx< 0.5Hz$.

It is well known that accelerometers perform poorly at low frequencies ($\approx 1Hz$) due to acceleration amplitudes becoming very low [287]; accelerometers measure absolute measures of acceleration whereas laser-Doppler vibrometer systems detect relative displacements. In addition, if the frequency domain is considered, the data acquisition module provides a resolution of $\approx 1.3mHz$. The laser-Doppler system provides three orders of magnitude greater resolution by comparison. However, in addition to the accelerometers collaborating with the laser vibrometer (an optical measurement vs. a mechanical measurement) data, the accelerometers enable vibrations at independent points to be investigated. This enables the phased relationships of vibration within a structure to be examined such as torsional modes or separate components of the model; a single point laser vibrometer cannot provide this information. Arrangement of the accelerometer sensors on the model structure is presented with the results for clarity.

In operation, the accelerometers were mounted to the wing surface such that they are normal to the surface using adhesive wax. Adhesive wax was suitable due to the low mass of the sensors ($< 0.5g$) and relatively low accelerations ($< 6g$) are expected [288]. Accelerations (vibrations) are recoreded at a sample frequency of 10kHz over a 20 second period per test. Filtering of any perceived electrical noise was achieved by the signal conditioning box, with no cut-off filters applied. Only the results for the accelerometer sensors employed for 'wind-on' experiments with aerodynamic loading and wind tunnel vibration, at $Re = 1.5 \times 10^6$, have been discussed.

CHAPTER 4

SEMI-SPAN TESTING WITHOUT CONVENTIONAL PENICHE

4.1 INTRODUCTION

This chapter investigates the effect of varying the stand-off gap height of the penicheless semi-span model (described in Section 3.4) to enlighten flow field/stand-off gap interactions and how this influences the aerodynamic metrics of the model. The goal is to characterise how the stand-off gap height affects the flow over the model in order to select an appropriate stand-off gap as a constant for further experiments. In this study, no comparisons are made to any full span-models, thus only experimental trends of varying the stand-off gap and its effects on the aerodynamic behaviour of the model are of primary interest. Only the planar wing model is used in this study.

Section 4.2 presents a detailed background of semi-span model testing identifying general considerations, advantages, and inherent disadvantages of the traditional peniche extrusion. An initial study providing a quantitative description of how the aerodynamic performance metrics of the model vary with angle of attack and stand-off height, determined using the force platform, is presented in Section 4.3. In Section 4.4 structural dynamics of the model are considered in order to understand how the wind tunnel and model vibrations interact. This provides the justification for the post-processing of force platform data such that background experimental noise can be filtered out of the signal. Afterwards, the flow field around the semi-span fuselage nose at different stand-off gap heights is examined using stereoscopic particle imaging velocimetry (SPIV) in Section 4.5. Subsequently surface flow visualisations using tufts and clay flow methods are discussed in Section 4.6. These methods provide a deeper understanding of how flow features propagate around the fuselage by highlighting regions of flow unsteadiness, local flow directions, attached and separated flows, and reveal wake structures and associated shear flows moving over a surface. Section 4.7 summarises the main findings of this chapter.

4.2 BACKGROUND INTO SEMI-SPAN MODEL TESTING

Semi-span testing techniques have been widely adopted as a tool to provide state-of-the-art wind tunnel research capabilities [232, 233, 234, 235]. Semi-span models are typically employed to double the maximum usable Reynolds number and enhance the quality of measurement data owing to improved model strength, stiffness, and overall fidelity [236]. Additionally, the semi-span model arrangement for this study offers convenient integration of the model with the test facility model positioning system and diagnostic equipment.

The drawback of semi-span models is the inherent difficulties associated with the quality of flow over the model; they are vulnerable to increased interference effects within the wind tunnel. The basic principle of semi-span testing is to treat the mid-plane cross section of the body as a plane of symmetry. This is generally achieved by mounting the mid-plane of the body to some planar surface (such as the wind tunnel floor, wall, or ceiling) enabling the surface to act as a plane of symmetry. The wind tunnel walls however, provide poor symmetry planes due to the growth of respective boundary layers which begin to develop far upstream of the model. Interactions between the working section boundary layer and the model can introduce three-dimensional vortical structures (horseshoe vortices), which are recognised to have strong influences on the semi-span model's aerodynamic behaviours, especially over the inboard wing section [237].

To reduce the aforementioned interactions with the tunnel boundary layer/wall, and achieve near free-air conditions, semi-span models traditionally use the peniche technique. The traditional peniche is a two-dimensional profile extrusion identical to the model's mid-plane cross section to create a stand-off distance between the mid-plane and the tunnel wall. The stand-off distance is typically scaled to the boundary layer displacement thickness (δ^*) at the wind tunnel wall at the pitch axis/moment reference centre of the model. Unfortunately, studies are generally ambiguous in quantifying the complex interactions between the wall boundary layer and the peniche; including the resulting effects and sensitivity on wing aerodynamics. Generally the peniche is scaled through a trial and error approach forcing the semi-span model to mimic the full-span model's aerodynamic coefficients for a small range of angles of attack at a given Reynolds number. Variations in the peniche height are often seen to reflect variations in the lift-curve-slope, measured drag, stall characteristics and body moments as local flow phenomena governed by the peniche are not well understood.

Studies by NASA Langley [289, 290, 291] have reported that the influence of the peniche is to accelerate the flow over the entire upper surface of the wing, and simultaneously increase the cross flow observed over the inboard upper surface area of the wing. Conclusions suggest that a stand-off height equal to twice the displacement thickness of the empty tunnel boundary layer works best to mitigate this, and that modifications by filleting or undercutting the peniche (a three-dimensional peniche)

can alleviate separation at the fuselage nose, and weaken the development of vortical structures in this region. However, is has been shown that a standard 2-D peniche will produce data which correlates better with full-span data relative to other peniche configurations [291].

Eliasson [292] reports a reduction in the drag and maximum lift in semi-span wind tunnel experiments relative to the expected free-flight values. It was concluded that the discrepancy is a consequence of the peniche enforcing a redistribution of the velocity field and increasing cross-flow components in the plane of symmetry of the half model. The peniche's effect on the model enforces additional flow displacement leading to additional velocity gradients around the fuselage and inboard wing compared to a full-span model. Hence, the peniche is not able to supply a velocity field sufficiently parallel to the symmetry plane—especially at higher angles of incidence. Eliasson [292] suggests that changing the peniche height only redistributes the strength of the flow displacement and cannot be avoided, but that the shape of the peniche may alleviate this feature. Other studies have tried to reduce the flow displacement, and resulting vortical structures, through leading edge suction thereby reducing mass flow and velocity gradients [293]. There is little evidence to suggest however, that suction ahead of the peniche can produce a significant improvement in the aerodynamic characteristics of semi-span models.

Doerffer and Szukc [237] performed a numerical study of the wing-body configuration of the DLR F11 high-lift model in order to compare free-flight conditions to the semi-span model. Computations of the semi-span model placed directly at the wall and mounted using a standard peniche (at approximately $3\delta^*$) are presented. With the application of the peniche, the strength and size of the horseshoe vortex around the fuselage nose increased. It was found that the introduction of the peniche to the semi-span model led to poorer agreement with full-span data; this was based on comparisons between pressure distributions over the wing and aerodynamic coefficients C_L, C_D, and $C_{M_{pitch}}$. While it is concluded that the best results were found for the semi-span model mounted directly to the wall without the addition of a peniche, the authors speculate that a different factor, other than the peniche, is responsible for the lift break-down of the DLR F11 semi-span model in the experiment but no conclusion is reached. No attempts were made to vary the stand-off height of the peniche.

Yokokawa et al. [294] conducted a comprehensive experimental–numerical study focused on how the aerodynamic influence of a semi-span model changes with a peniche in an attempt to strategise the appropriate selection of the peniche stand-off height. While they observed no changes in surface flow patterns (using oil flow visualisations) with increasing peniche heights, strong changes in the aerodynamic coefficients and pressure distributions are noted. Lift-curve-slope gradients were observed to increase with a larger peniche height. The inconsistency of data for different peniche heights indicated changes in the local flow physics over the wing. Furthermore, the drag at a given angle of attack decreases as the peniche height

increases, however they show that the inboard wing local drag increases. The pressure distribution over the wing shows that only the leading edge of the wing is significantly affected by changes in peniche height. Yokokawa et al. [294] suggest that different peniche installations have the effect of changing the model's effective aspect ratio; thus strongly influencing the induced drag. To test this hypothesis, they implement numerical simulations to predict optimal peniche heights to best resemble free-flight conditions. It is found that two-to-three times the displacement thickness of the empty wind tunnel boundary layer is optimal for matching effective aspect ratios.

It is common to find studies which pay little attention to the appropriate sizing of the peniche. Ujang et al. [260] neglect investigation of the peniche's influence entirely, and opt to simply maximise the stand-off height in an attempt to raise the model out of the wall boundary layer. In doing so, the solid body blockage of the model was significantly increased. It can also be expected that the vortical structures around the fuselage nose are not mitigated but in-fact amplified as the peniche reaches into the freestream. In a similar manner, Kafyeke et al. [295] use a boundary layer spacer plate to isolate the model from the wall boundary layer. They conclude that the aerodynamic coefficients were comparable to flight test data, however pitching moment data across most of the test range and post stall behaviour correlated poorly. Kuo and Lin [296] demonstrated the application of a boundary layer spacer successfully integrated with a semi-span delta wing model. It was found that the boundary layer spacer reduced the influence of the tunnel wall boundary layer on the vortical structures over the wing. Elsewhere [297], semi-span delta wing models have been mounted on very long slender two-dimensional peniche extrusions.

The peniche attempts to reduce flow interference with the tunnel wall boundary layer and achieve a flow field representative of the equivalent full-span model in free-air. However, studies suggest that the application of the peniche appears to introduce more flow complexity and measurement uncertainty than it offsets. A solution, or at least a simple alternative, is to remove the peniche entirely and leave a stand-off gap as suggested by Eder et al. [298]. The two-dimensional peniche and resulting vortical structures modify the behaviour of the model, this is difficult to quantify and to correct. Eder et al. [298] show that changing the peniche height introduces varying discrepancies between full-span and semi-span aerodynamic coefficients and moments, and that these discrepancies also change with angle of attack. This suggests significant changes in the local flow fields over the model. Without a peniche, *i.e.* placing a gap between the fuselage and the wall, deviations in aerodynamic coefficients and moments were found independent of the angle of attack. A stand-off gap height of $4\delta^*$ was found to achieve constant deviation of the aerodynamic coefficients from the equivalent full-span model over a range of angles of attack.

To date there is no universally accepted method on how best to conduct semi-span testing despite the widespread use and recognised benefits of such models. A significant limitation is that it is difficult to draw comparisons between different

investigations due to lack of continuity and the various approaches adopted. Efforts are made here to investigate the effect the stand-off gap height has on aerodynamic behaviours while also understanding the local flow around the semi-span model and how it changes with both stand-off gap height and angle of attack.

4.3 FORCE AND MOMENT MEASUREMENTS

Variation of the lift, drag, and pitching-moment coefficients about the model's centre of gravity/pitch axis are presented in figure 4.1, illustrating the behaviour of the aerodynamic coefficients with stand-off gap height and angle of attack. Corrections for blockage and horizontal buoyancy, as discussed in Section 3.8, have been applied. The force and moment data presented have been post-processed using a $38Hz$ low-pass filter (justification for which is given in Section 4.4) and have been calculated to a confidence level of 98% with a margin of error (random uncertainty) of less than 1% for each datum. It is indicated that the model has only been operated in the pre-stall region so that the risk of damaging the model, and the wind tunnel, was avoided.

At all five stand-off heights, the lift coefficient, shown in figure 5.1a demonstrates

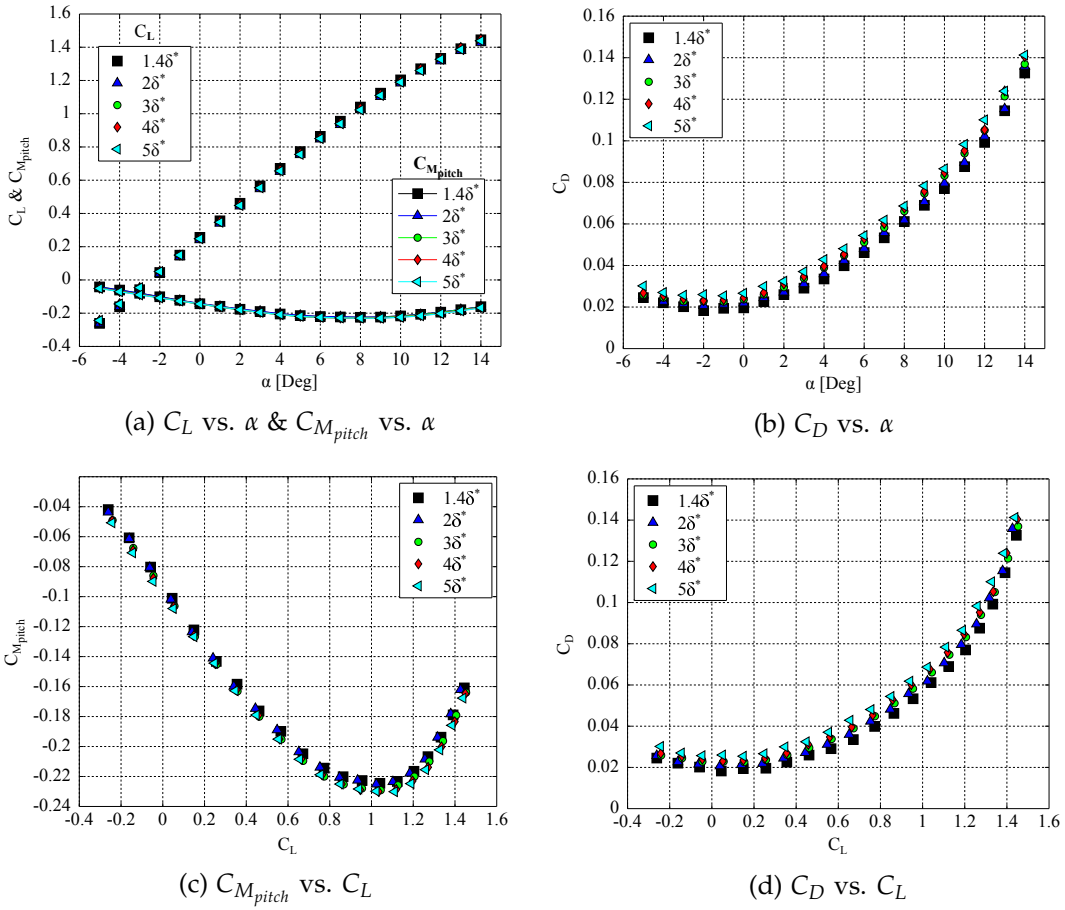

(a) C_L vs. α & $C_{M_{pitch}}$ vs. α

(b) C_D vs. α

(c) $C_{M_{pitch}}$ vs. C_L

(d) C_D vs. C_L

FIGURE 4.1: Effect of stand-off gap height on aerodynamic coefficients for the planar wing arrangement.

a linear relationship between -5° and $+7^\circ$, with the maximum lift for each case occurring at $+14^\circ$. This indicates that wing stall onset begins between $+7^\circ \leq \alpha \leq +8^\circ$, which is supported by the plateauing negative gradient of $\frac{\partial C_{M_{pitch}}}{\partial \alpha}$ over the same range to a positive gradient for $\alpha > 8$. The C_{L_α} gradient is noted to decrease with increasing gap size. This trend is independent of Reynolds number as shown by data presented in figure 4.2. The reducing gradient is caused by an increased mass flow though the gap between the tunnel wall and the model. This flow adds additional circulation around the fuselage which increases the induced angle of attack at the wing; this effect is illustrated in figure 4.3.

Figure 4.4a shows the deviation of the lift coefficient as a function of the angle of attack, taking the $1.4\delta^*$ case as the baseline. The general trend of ΔC_L with angle of attack is consistent for all cases. It is evident from figure 4.4a that for a given positive angle of attack the C_L of the model decreases with increasing gap size. For the range $0^\circ \leq \alpha \leq +10^\circ$, an approximately constant offset exists for ΔC_L from the baseline stand-off height $1.4\delta^*$, with relatively significant drops in C_L occurring when increasing from $3\delta^*$ to $4\delta^*$, and then again to $5\delta^*$. It is also observed that the initial

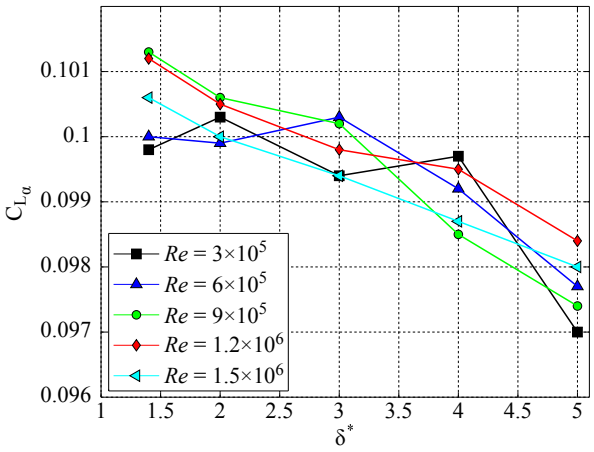

FIGURE 4.2: Lift gradient as a function of stand-off gap height.

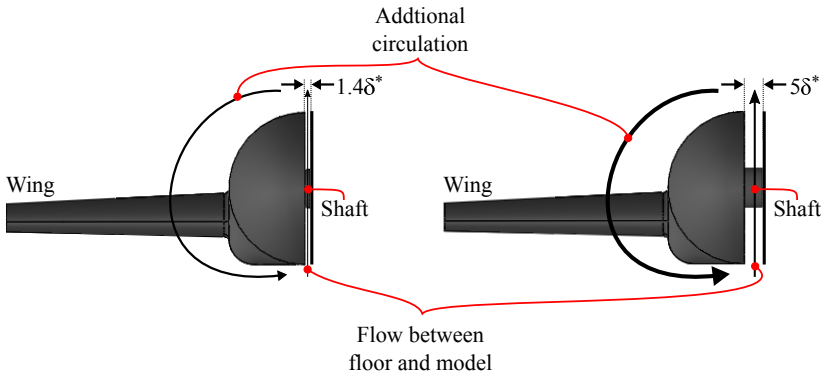

FIGURE 4.3: Illustration of additional circulation around fuselage with larger stand-off gap.

increase in stand-off height from $1.4\delta^*$, to $2\delta^*$, and again to $3\delta^*$ has little influence on ΔC_L. These deviations are summarised in table 4.1. For this α range, the deviation of lift coefficient is a function of the distance between the fuselage symmetry plane and the tunnel wall, and not a direct function of angle of attack. This result was also identified by Eder et al. [298] who used tuft visualisations to show that lower stand-off gap heights led to higher turbulence over the inboard wing, resulting in an increased interaction with the tunnel boundary layer leading to delayed separation at higher lift coefficients.

For $\alpha < 0$ and $\alpha > +10$ the lift coefficient is a function of the angle of attack as well as the gap height; both instances are under direct influence of the wake from the mounting shaft extending from the fuselage symmetry plane. At negative angles, the low-wing model configuration blocks incoming flow such that the shaft wake moves further over the fuselage afterbody than for equivalent positive angles of attack. With high angles of attack the shaft wake spreads more to the upper side of the fuselage. The influence of the shaft wake is less for smaller stand-off gap heights. Additionally, as the angle of attack increases above $\alpha = 7°$, and stall onset over the wing spreads, the ΔC_L becomes increasingly more irregular.

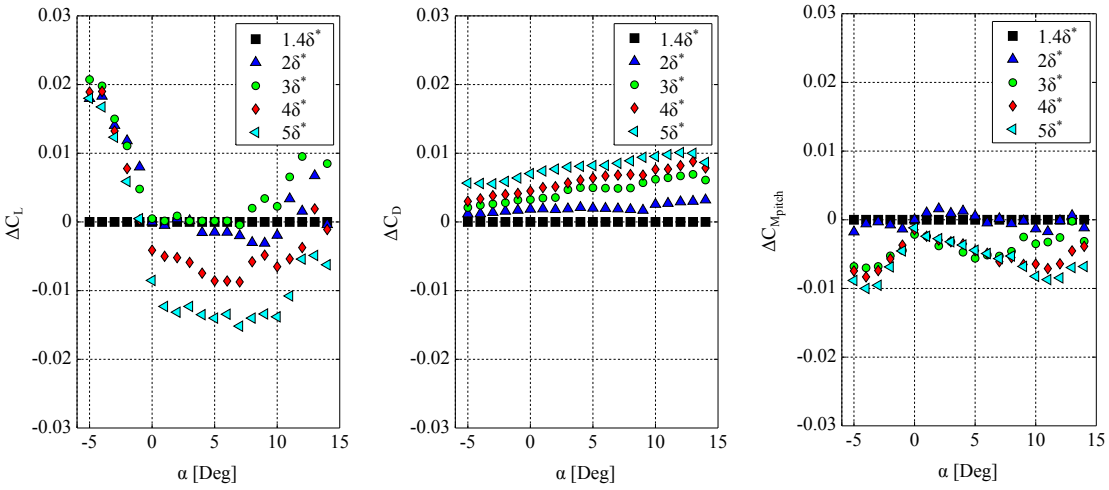

(a) ΔC_L vs. α (b) ΔC_D vs. α (c) $\Delta C_{M_{pitch}}$ vs. α

FIGURE 4.4: Difference in aerodynamic coefficients taking stand-off gap hieght $1.4\delta^*$ as baseline.

TABLE 4.1: Average lift coefficient deviation from $1.4\delta^*$ baseline with stand-off gap over range $0° \leq \alpha \leq +10°$; corresponding to data shown in figure 4.4a.

Test Case	ΔC_L Offset
$1.4\delta^*$	-
$2\delta^*$	-0.0013
$3\delta^*$	+0.0008
$4\delta^*$	-0.0064
$5\delta^*$	-0.0131

Figure 4.4b shows the deviation of the drag coefficient as a function of the angle of attack, taking the $1.4\delta^*$ case as the baseline. It is clearly visible that with increasing stand-off gap height the drag coefficient increases. Between angles of attack $-5^\circ \leq \alpha \leq +7^\circ$ (the linear portion of the lift-curve) the difference in drag coefficient is almost a constant offset from the baseline case, where this offset increases with gap height. These ΔC_D offsets have been summarised in table 4.2.

TABLE 4.2: Average drag coefficient deviation from $1.4\delta^*$ baseline with stand-off gap over range $-5^\circ \leq \alpha \leq +7^\circ$; corresponding to data shown in figure 4.4b.

Test Case	ΔC_D Offset
$1.4\delta^*$	-
$2\delta^*$	+0.0017
$3\delta^*$	+0.0038
$4\delta^*$	+0.0051
$5\delta^*$	+0.0072

Thus, the deviation in the drag coefficient is a function of the distance between the fuselage symmetry plane and the tunnel wall, and not a direct function of angle of attack. At angles of attack $\alpha > +7^\circ$, with the onset of wing separation, the deviation in the drag coefficient remains approximately constant, but a slight variation with angle of attack is noted.

The drag increase between the different stand-off heights is not associated with variations in the induced drag, but only those of the parasitic drag. The main increase of the drag is caused by the flow past the symmetry plane of the fuselage. As the gap height increases, illustrated in figure 4.3, the flow into the gap increases. The symmetry plane of the model, which is connected to the fuselage, will thus experience higher parasitic skin friction. Additionally, with increasing gap height the shaft beneath the model incrementally extends, increasing the shaft's wetted area. Despite the disadvantage of the increased drag, the deviation of the drag coefficient is not a direct function of the angle of attack; as it would be with a traditional peniche. As the shaft is connected to the steel balance interface (shown in figure 3.10) and the flow interaction between the tunnel wall and model symmetry plane will vary as a function of the model incidence angle, a drag tare cannot be accurately applied to remove the effect of the mounting shaft.

Figure 4.4c shows the deviation of the pitching moment coefficient as a function of the angle of attack from the baseline case, $1.4\delta^*$. The deviation in the pitching moment for the $2\delta^*$ stand-off height is very small, however at higher stand-off gap heights larger deviations occur which are a sensitive to the angle of attack. A significant decrease in the moment coefficient occurs between $2\delta^*$ and $3\delta^*$, which may suggest the longitudinally aft movement of the aerodynamic centre possibly caused by the shaft wake interfering with the flow over the fuselage afterbody. Stand-off heights $3\delta^*$, $4\delta^*$, and $5\delta^*$ demonstrate a similar behaviour (*i.e.* no further shifts of the aerodynamic

centre) over the linear portion of the lift-curve ($-5° \leq \alpha \leq +7°$). The pitching moment coefficient is particularly stable over the range $0° \leq \alpha \leq +7°$. At higher angles of attack ($\alpha > +7°$), as stall onset over the wing spreads, the deviations vary more strongly.

It is also interesting to note that the side (vertical) force and associated notional yaw moment acting on the model, which is suggestive of the flow behaviour between the tunnel floor and fuselage symmetry plane, changes with stand-off height and angle of attack. This information is presented in figure 4.5. Figure 4.5a shows the upward force C_{Fz} (opposing the direction of gravity) acting on the model, the magnitude of which is seen to decrease with increasing stand-off height, but increases as a function of the angle of attack for a given stand-off height. Understanding of the trends shown in figure 4.5a can be found if the results are compared to those found by Eder et al. [298].

Eder et al. [298] showed that increasing the distance between the tunnel wall and the fuselage symmetry plane caused the static pressure difference between the upper and lower sides of the fuselage to decrease. Thus, the C_{Fz} is a function of the pressure difference between the upper (wing side) and lower (between fuselage symmetry plane and tunnel floor) sides of the fuselage which is driven by the subsequent static pressure under the model. As the stand-off height of the model is increased, the mass flow under the model increases which causes an increase in the dynamic pressure and a drop in the static pressure under the model. Therefore the pressure differential between the upper and lower sides of the fuselage reduces. However, this also leads to an increased influence of the wake behind the mounting shaft between the wall and the model. Eder et al. [298] found that in the presence of the shaft wake the fuselage will experience an increased pressure differential between the upper and lower sides of the fuselage afterbody downstream of the shaft. The mounting shaft wake influence was shown to be a function of stand-off gap height and angle of attack.

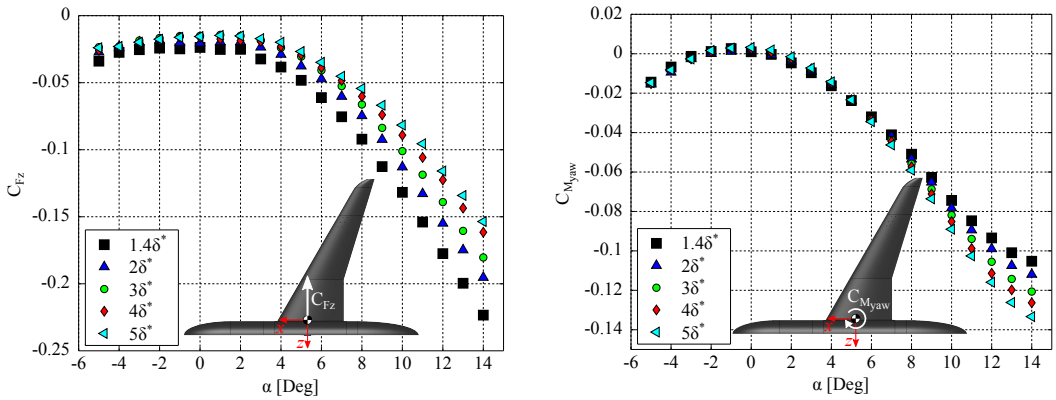

(a) C_{Fz} vs. α (b) $C_{M_{yaw}}$ vs. α

FIGURE 4.5: Vertical force and notional yaw moment acting on model as a function of stand-off height and angle of attack.

Figure 4.5b shows the trend in the notional model yawing moment with stand-off gap heights and angle of attack. Over the range $-2^\circ \leq \alpha \leq +1^\circ$ a positive (nose up) moment is observed as the model drag force dominates the moment contributions. Over the range $-5^\circ \leq \alpha \leq +5^\circ$ similar moments are noticed for all stand-off heights and angles of attack. For $\alpha > +5^\circ$, the nose down moment is seen to increase with increasing stand-off gap height and angle of attack. From figure 4.5a it is concluded that the magnitude of C_{Fz} reduces with stand-off height, and figure 4.5b shows that the notional nose down yawing moment increases with stand-off height at higher angles of attack. This indicates that as the flow under the model increases, reducing the magnitude of C_{Fz}, the C_{Fz} force centre must move aft increasing the moment arm to the model's centre of gravity. This may be caused by the shaft wake's path changing due to both the model incidence angle and effective Reynolds number, propagating downstream and remaining under the model for extended distances with increased stand-off gap height.

As the stand-off gap height increases, the velocity of the flow through the gap increases thereby reducing the magnitude of C_{Fz} as the pressure difference between the wing side and symmetry plane side of the model is reduced. This has the consequence of the cylindrical mounting shaft experiencing a greater velocity magnitude, a higher Reynolds number flow, through the gap which will alter the separation and profile of the turbulent shaft wake. Figures 4.5a and 4.5b show that increasing the stand-off gap from $4\delta^*$ to $5\delta^*$ results in little change relative to variations between other stand-off heights. This may indicate a 'plateauing' effect of the flow under the model as further increases in stand-off height have a reduced effect. However, to prove this conjecture further increases in stand-off height ($> 5\delta^*$) would have to be investigated, but this cannot be facilitated due to model/facility limitations.

4.4 MODEL STRUCTURAL DYNAMICS AND INERTIAL LOADING

In this section the structural dynamics of the planar wing semi-span configuration are discussed in order to provide clarity and justification for employing a $38Hz$ low-pass filter to the force platform data. The structural dynamics of the planar wing are examined and compared to the C-wing arrangement in detail in Section 5.5.

The natural frequencies of the model are identified by monitoring the transient response at different locations on the model surface which are subjected to bump testing. In performing bump tests the fundamental vibrational characteristics without the influence of aerodynamic loading (vibrations from freestream turbulence), and forced vibration from the wind tunnel (related to the wind tunnel physical structure) can be examined. Hence, by understanding the model and the wind tunnel vibrational characteristics in isolation of one another the force platform data can be post-processed to improve the quality of the data and reduce background noise. The wind tunnel vibrations have been monitored using the laser-Doppler vibrometer, which was also

used to monitor the planar wing vibrations under aerodynamic loading at angle of attack. These results are compared to the frequencies present in the data signals obtained from the force platform. It is emphasised here that the force platform is mounted below the tunnel floor on an independent structure, and thus does not make direct contact with the wind tunnel structure.

The stand-off gap height does not have any effect on the structural dynamics of the model as the model does not change in any physical/structural manner between stand-off gap height installations. Therefore, vibrational frequencies present within the model will not change with stand-off height. For the following vibration tests a stand-off gap height of $4\delta^*$ was used.

4.4.1 MODEL BUMP TESTS

The bump test frequency response evaluated from the planar wing and semi-span fuselage are shown in figure 4.6. The lateral bump test location shown in figure 4.6a, is located at 74% wingspan on the elastic axis (34% of the local chord). Two bending modes are detected; the first at $7.2Hz$, and the second at $33.5Hz$. Figure 4.6b presents the bump test frequency response evaluated along the longitudinal axis of the semi-span fuselage. From the frequency spectra observed the $9.3Hz$ registered is anticipated to be related to the fundamental bending mode of the main-wing structure, identified as $7.2Hz$ previously. It is logical that there is a frequency separation of the wing's fundamental mode observed between the two measurement points as they are structurally separated by several mechanical components of various material. Each mechanical component will resonate at its own natural frequency which will influence the system bump test measurement (note: the fuselage is more mechanically complex than than wing). The $39.9Hz$ frequency is identified as the longitudinal frequency of the half-body fuselage. Also note that the magnitude of vibrations detected from the fuselage are significantly smaller than that examined for the wing; this is due to the

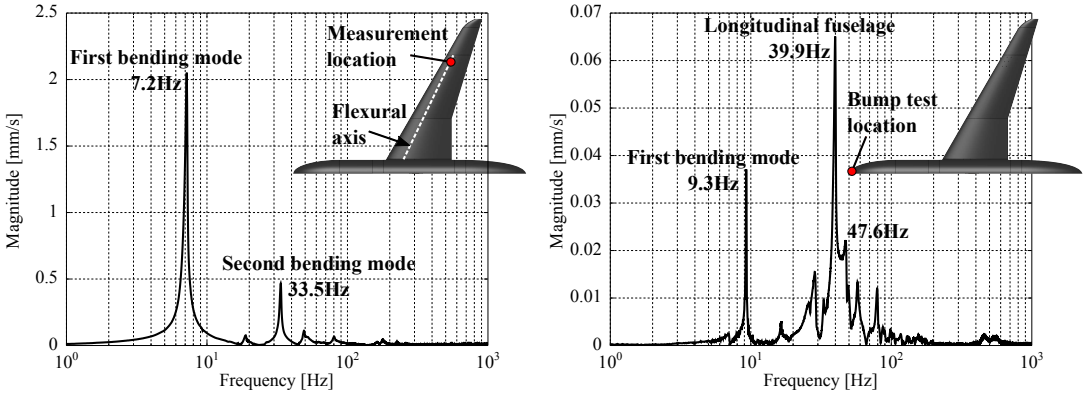

(a) Lateral wing bump test.

(b) Longitudinal fuselage bump test.

FIGURE 4.6: Frequencies of the semi-span model observed in bump tests with laser vibrometer (bump test measurement locations are indicated in respective figures).

fuselage being much stiffer than the wing.

4.4.2 WIND TUNNEL VIBRATIONS

In the previous section bump tests enabled the identification of dominant frequencies related to the planar wing semi-span model in isolation of the wind tunnel influence. Similarly, it is imperative that the wind tunnel frequencies are understood in order to consider their effect on the model. Figure 4.7 shows the vibrational frequencies detected in the working section steel structure of the wind tunnel. The wind tunnel operating conditions considered are two Reynolds numbers based on the wing's mean aerodynamic chord. $Re = 1.5 \times 10^6$ ($\approx 50ms^{-1}$) is the operating condition of interest, whereas $Re = 0.9 \times 10^6$ ($\approx 30ms^{-1}$) is an off experimental design condition presented to support the identification and analysis of wind tunnel frequencies.

Figure 4.7a shows that with the working section freestream at $Re = 0.9 \times 10^6$ the fan operates at $\approx 379.4rpm$ (monitored and logged via the wind tunnel health monitoring system). This was detected by the vibrometer on the working section structure indicted by the peak at $6.32Hz$. Consequently, two further peaks are detected at $25.28Hz$, and $50.56Hz$ which relate to the four fan blades and the eight stators (therefore a fan blade passing frequency of eight times the rpm), respectively. The same vibrational characteristics are observed when the fan speed is increased to $\approx 615rpm$, corresponding to the fan frequency of $10.25Hz$ and two subsequent peaks detected as a result of the fan blades and stators. Note that as the fan speed is increased the vibrations experienced by the wind tunnel frame also become stronger.

With both fan speeds shown in figure 4.7, the vibrational frequencies related to the stators are dominant. This is due to the stators imposing a direct structural vibration on the wind tunnel's frame, while the vibrations related to the fan are transmitted to the wind tunnel frame via air turbulence (the fan is mounted to a shaft bearing in the

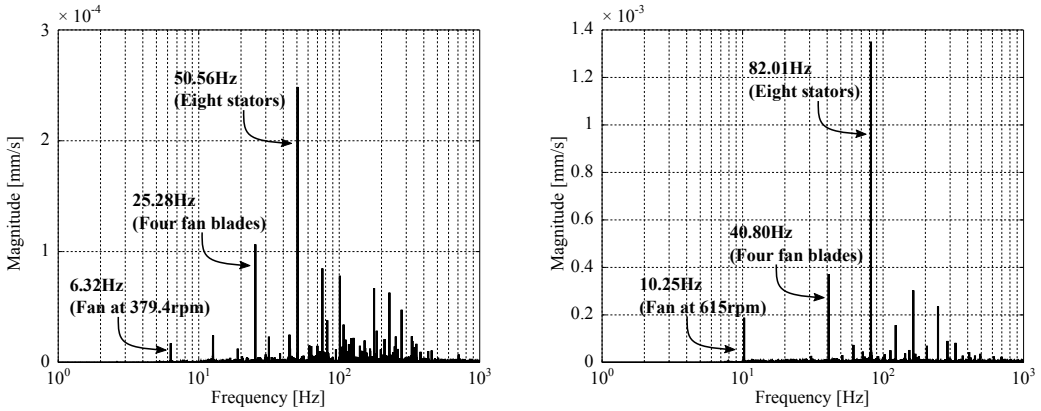

(a) $Re = 0.9 \times 10^6$ (b) $Re = 1.5 \times 10^6$

FIGURE 4.7: Frequency response, detected by laser vibrometer, from the steel frame of the working section at Reynolds number based on the wing MAC.

fan section and is not physically connected to the wind tunnel structure).

4.4.3 MODEL VIBRATION DURING WIND TUNNEL OPERATION

Here only static test conditions are considered. However, even under static conditions, wing deformation combined with both natural and forced vibrations will inevitably contribute towards a more dynamic loading to be detected by the force platform. If the interplaying vibrations influencing the model's body forces and aerodynamic performance metrics are understood at their source, they can be treated as background noise and filtered from the temporal force platform data.

Considering first the wing vibrations during live wind tunnel operations at $Re = 1.5 \times 10^6$, figure 4.8 presents the vibrational frequencies of the wing at $\alpha = 0°$, $8°$, and $14°$ detected by the laser vibrometer. The measurement location is identical to that used for bump tests with results presented in figure 4.6a. For the three angles of attack presented in figure 4.8 the first and second wind bending modes of frequency $7.2Hz$ and $33.5Hz$ are clear. For the $\alpha = 14°$ case, a tertiary peak is also observed at $50.2Hz$; it has been identified that for $\alpha \geq 10°$ a frequency peak of $\approx 50Hz$ is detected. As the wing begins to stall, initiating buffet induced vibration and incorporating the fact that the fuselage itself is at an oblique angle to the oncoming flow, the entire model will experience vibrations of greater amplitude at these higher angles of attack. Based on the knowledge of frequencies related to the fuselage it is anticipated that the $\approx 50Hz$ peak observed is related to fuselage vibrations being transferred to the wing. The wing mounts to the fuselage via a steel interface. Hence, the $\approx 50Hz$ frequency is a vibrational consequence of the fuselage structure excitation and not of the wing or a forced frequency.

Referring to the same angles of attack ($\alpha = 0°$, $8°$, and $14°$), and experimentally static conditions, the raw and filtered temporal signals for the drag coefficient mon-

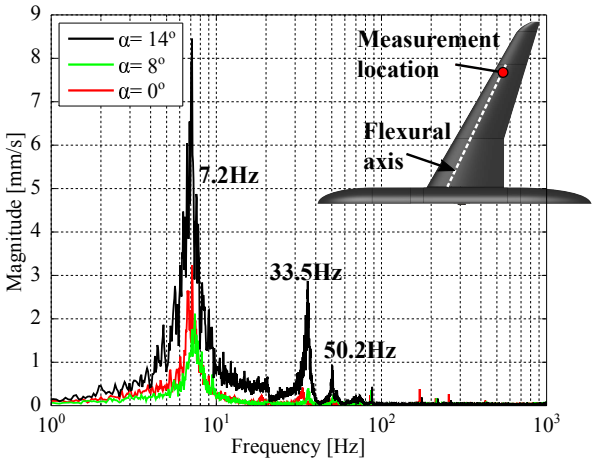

FIGURE 4.8: Frequency response of planar wing detected by the laser vibrometer at $\alpha = 0°$, $8°$, and $14°$ at $Re = 1.5 \times 10^6$. Measurement location indicated.

itored via the force platform is presented in figure 4.9. The noise within the raw signal is considerable. Taking the $\alpha = 8^\circ$ case as an example, the signal is also presented in the frequency domain in figure 4.9. Frequency peaks within the signal indicate the wing bending modes also detected from the laser vibrometer, alongside several other dominant frequencies of comparable magnitude. In fact, two frequencies detected at $44.2Hz$ and $253.2Hz$ are seen to dominate over that of the wing's primary vibrations.

Coincidently, the fuselage longitudinal natural resonant frequency of $39.9Hz$ (determined by bump tests shown in figure 4.6b) is within proximity of the $40.8Hz$ produced by the wind tunnel fan during operation at $Re = 1.5 \times 10^6$ (as shown in figure 4.7b). The effect of this is the excitation of the fuselage's longitudinal frequency, thus significantly contributing to the noise detected on the x-axis channel of the force platform which is fixed to the longitudinal axis of the model. This results in the dominant $44.2Hz$ peak seen in the frequency domain of $\alpha = 8^\circ$ shown in figure 4.9. An additional fuselage related frequency of $52.8Hz$ is also detected. This frequency has been seen to translate to the wing at increased angles of attack, detected by the laser vibrometer with results presented in figure 4.8, while the longitudinal fuselage frequency is not. This leads to the conclusion that the $\approx 50Hz$ frequency is related to a lateral natural frequency of the fuselage. This provides sufficient explanation as to why it is detected within the wing vibration while the far more dominant $\approx 40Hz$ frequency is not; the longitudinal fuselage frequency acts along the wing plane while the lateral fuselage frequency acts normal to the wing plane.

The secondary dominant vibrations at $253.2Hz$ detected within the unfiltered force platform data have been identified to relate to the fuselage-force platform mounting interface as indicated in figure 4.9. These vibrations are present on all six channels of the force platform while remaining undetectable to the laser vibrometer unless measured directly at the mounting shaft. As a consequence of not employing a semi-span model with a peniche, which would give the full model a larger ground footprint and broader structural support over the whole fuselage symmetry plane, the single stiff support point induces high frequency vibrations to the force platform. The fact that this high frequency is not detectable on the model by the laser vibrometer indicates high structural damping between the mounting interface and the model itself.

Consequently, in order to negate the 'noise' related to the excited fuselage frequencies and steel mounting interface, which are not deemed to interfere with the aerodynamic performance metrics, the force platform data was post-processed using a 10^{th} order $38Hz$ elliptical low-pass filter. The resulting filtered temporal data for $\alpha = 0^\circ$, 8°, and 14° is shown in figure 4.9. The benefit of filtering the data is to produce a much cleaner signal, and reduce random uncertainty of the measurement. A summary of how the filter affected the data, comparing the signal mean, root mean square (RMS), and standard deviation (STD) is given in table 4.3. Here it is seen that the mean values between the filtered and unfiltered data remain unaffected while the

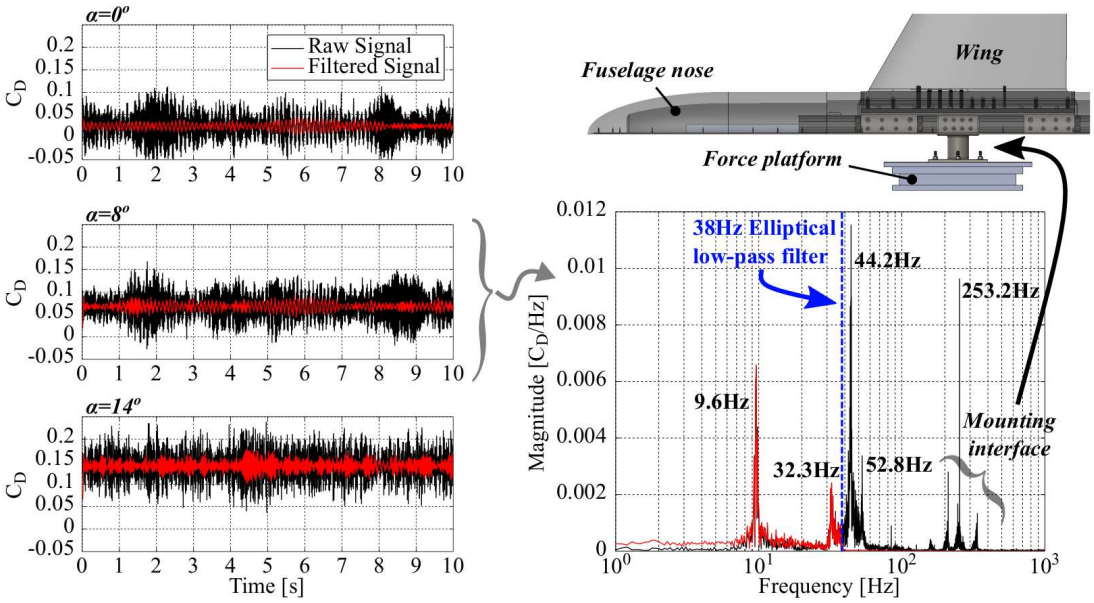

FIGURE 4.9: Filtered and unfiltered drag coefficient (C_D) temporal data obtained from the force platform over 10s for $\alpha = 0°$, 8°, and 14° (left), with the frequency domain of the filtered and unfiltered data for $\alpha = 8°$ is also shown with the low-pass filter highlighted (right).

RMS and STD of the signals are reduced. The reduction percentage is shown in red. Furthermore, the fact that the filter is less effective at reducing the signal RMS and STD with increased angle of attack is justified as natural frequencies of the wing are increasingly excited by buffet induced oscillations, for example.

TABLE 4.3: Summary comparing unfiltered and 38Hz low-pass filtered drag coefficient (C_D) temporal data for $\alpha = 0°$, 8°, and 14° presented in figure 4.9.

	Unfiltered Signal			Filtered Signal		
	mean	RMS	STD	mean	RMS	STD
$\alpha = 0°$	0.0245	0.0349	0.0249	0.0245	0.0253 (−27.5%)	0.0064 (−74.3%)
$\alpha = 8°$	0.0677	0.0721	0.0250	0.0677	0.0681 (−5.5%)	0.0079 (−68.4%)
$\alpha = 14°$	0.1405	0.1435	0.0292	0.1405	0.1410 (−1.7%)	0.0119 (−59.2%)

4.5 STEREOSCOPIC PARTICLE IMAGE VELOCIMETRY (SPIV)

4.5.1 FLOW FIELD VELOCITIES

Stereoscopic particle image velocimetry (SPIV) has been conducted along the centreline of the fuselage nose at $\alpha = 0°$ for the Reynolds number 1.5×10^6. The results presented in this thesis used a configuration with a laser light sheet thickness of $\approx 1.5mm$ and a laser pulse separation time of $\Delta t = 45\mu s$. The methodology used for calculating the separation time, Δt, is presented in Section 3.9. The results have been processed initially dividing the recoded images into 64×64 pixel interrogation windows with

25% overlap, and then refined to 32×32 pixel interrogation windows with 50% overlap. With this arrangement the spatial resolution is $3.4mm$, where the adjacent vector spacing is $1.7mm$. It must be highlighted that no vector post-processing has been conducted and data sets have been time-averaged over 1200 images (recorded at $200Hz$) to ensure statistical convergence. Time-averaging over 1200 images provided statistical convergence of the flow field, while maintaining a maximum random uncertainty of $< 3\%$ for a 95% confidence level. The procedure for assessing statistical convergence has been discussed in Appendix C.

The time-averaged flow fields showing normalised velocity magnitude and streamlines for stand-off heights of $1.4\delta^*$, $3\delta^*$, and $5\delta^*$ are presented in figure 4.10. The white dashed box in the top row of images illustrates the location of the lower images which provide an enhanced view of the flow around the model nose for each test case shown. The spatial co-ordinates have been normalised by the displacement thickness (δ^*) of the empty wind tunnel boundary layer at the moment reference centre (pitch axis) of the model, shown in figure 3.5.

The results presented in figure 4.10 show no formation of a horseshoe vortex at any gap height. Thus, in the absence of the peniche a more stable flow field is achieved. Additionally, as the stand-off height increases, the velocity gradients around the stagnation point at the fuselage nose become more axisymmetric. Considering the streamlines indicating the local flow direction, it is possible to qualitatively assess the effect that changing the stand-off gap height has on the incoming flow/respective boundary layer. At $1.4\delta^*$ stand-off height, shown in figure 4.10a, the streamlines in the boundary layer are deflected upwards as they approach the model, away from

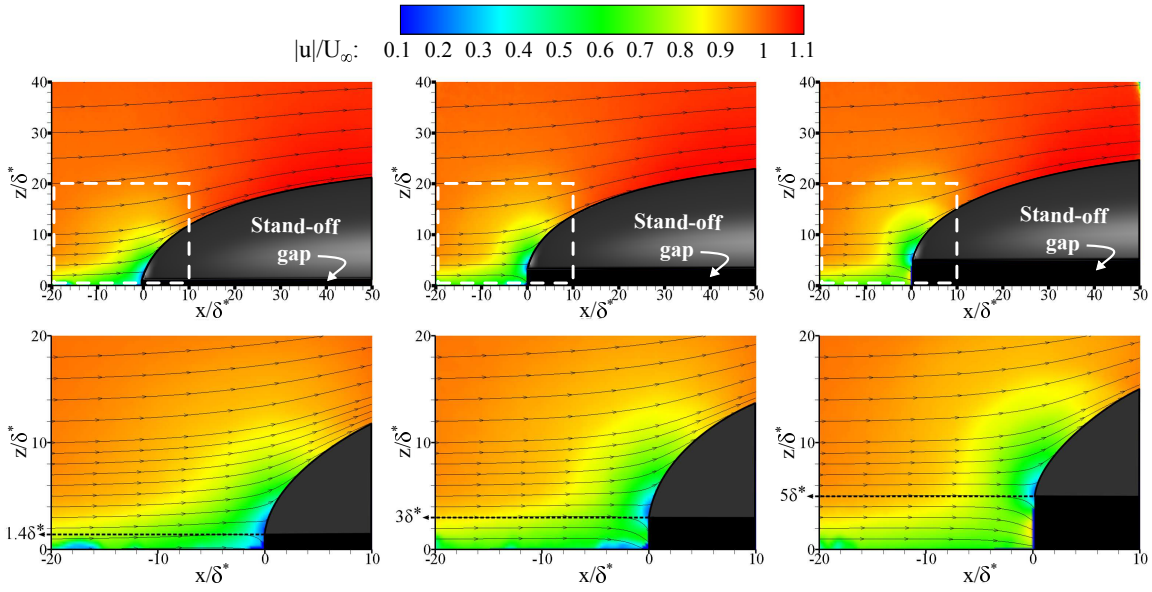

(a) $1.4\delta^*$ (b) $3\delta^*$ (c) $5\delta^*$

FIGURE 4.10: Time-averaged $|u|/U_\infty$ contour at the centreline of fuselage nose at $\alpha = 0°$ (dashed box in upper images illustrate location of enhanced view shown in lower images).

the tunnel floor boundary layer. Increasing the stand-off gap alleviates this effect as more of the boundary layer is drawn into the gap under the model, as evident in figures 4.10b and 4.10c. At $5\delta^*$ (figure 4.10c) the flow field around the symmetry plane of the model begins to closely resemble what could be expected for an equivalent full-span configuration at the symmetry plane. The flow near the tunnel wall is accelerated under the model, indicated by the increase in velocity magnitude, hence the flow does not separate away from the wall and no horseshoe vortex is formed. The streamlines above the symmetry plane of the model remain undeflected. Thus, as the stand-off height increases, the peak velocity deficit corresponding to the centre of the stagnation point moves closer to the symmetry plane.

Normalised velocity magnitude profiles of the boundary layer at streamwise stations $x/\delta^* = -20$, -10, -5, and -0.5 are presented in figure 4.11. The empty tunnel benchmark boundary layer profile from position $x/L = 0.3$ (taken from figure 3.4b) coincides with the leading edge of the fuselage nose. At $x/\delta^* = -20$, figure 4.11a, the velocity profiles at all stand-off conditions are similar to the empty tunnel velocity profile. At this station, there is a quantity deficit in the u_x component due to the presence of the model. Increases in the u_z component at this station are of the order of 3%. The u_z increase is stronger for lower gap heights forcing more aggressive fluid

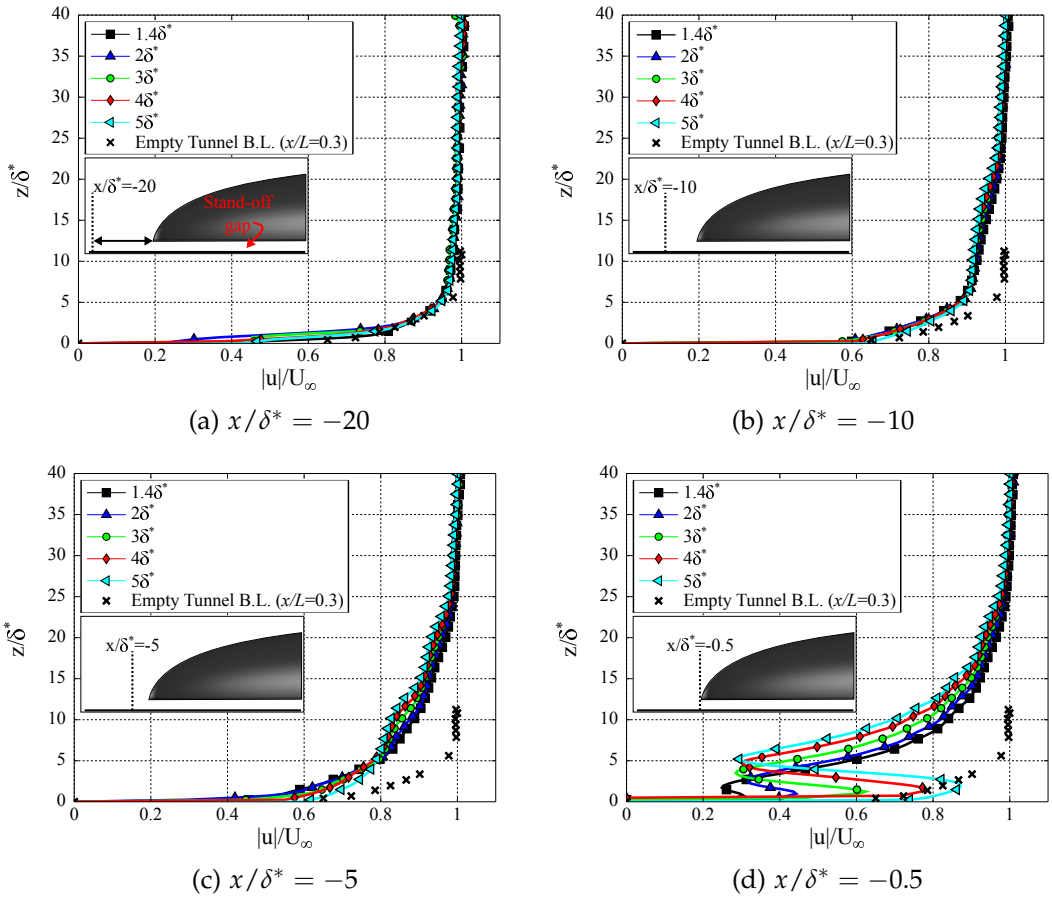

(a) $x/\delta^* = -20$ (b) $x/\delta^* = -10$

(c) $x/\delta^* = -5$ (d) $x/\delta^* = -0.5$

FIGURE 4.11: Tunnel wall boundary layer velocity magnitude profile development immediately upstream of fuselage nose/stand-off gap at $\alpha = 0°$.

displacement and lifting of the boundary layer.

As the flow approaches the fuselage nose ($x/\delta^* = 0$) a point of inflection in the velocity profiles develops which corresponds to the stand-off gap height. This is shown in figures 4.11b and 4.11c, illustrating the velocity profiles at $x/\delta^* = -10$ and $x/\delta^* = -5$, respectively. With increasing stand-off height, the approaching airflow below the stand-off gap height is drawn more strongly downstream towards the gap; the flow above the stand-off gap experiences a greater velocity deficit moving over the fuselage nose. The velocity profile immediately upstream of the fuselage nose at $x/\delta^* = -0.5$ (figure 4.11d) shows the peak velocity deficit indicating the stagnation point and the jet-like profile of the flow entering the stand-off gap. As the gap further increases, the respective stagnation point moves closer to the symmetry plane and the flow velocity into the gap increases at $4\delta^*$ and $5\delta^*$, resulting in an excess velocity relative to the empty tunnel boundary layer. As previously mentioned, the lower stand-off height causes an upward deflection of the flow, this is seen here to move the stagnation point away from the symmetry plane of the fuselage. At stand-off heights greater than $3\delta^*$ the stagnation point moves towards the symmetry plane. The velocity profiles above the corresponding stand-off height is lifted further away from the tunnel wall due to the model's increased distance from the wall.

Acceleration of the flow under the model, seen in figure 4.11d, is largely attributed to an increase of the u_z component of the flow field below the fuselage symmetry plane, as the flow approaches the stand-off gap. The time-averaged u_z/U_∞ component of the flow field and streamlines for all stand-off gap heights tested are presented in figure 4.12, with accompanying u_z/U_∞ velocity profiles shown in figure 4.13. It

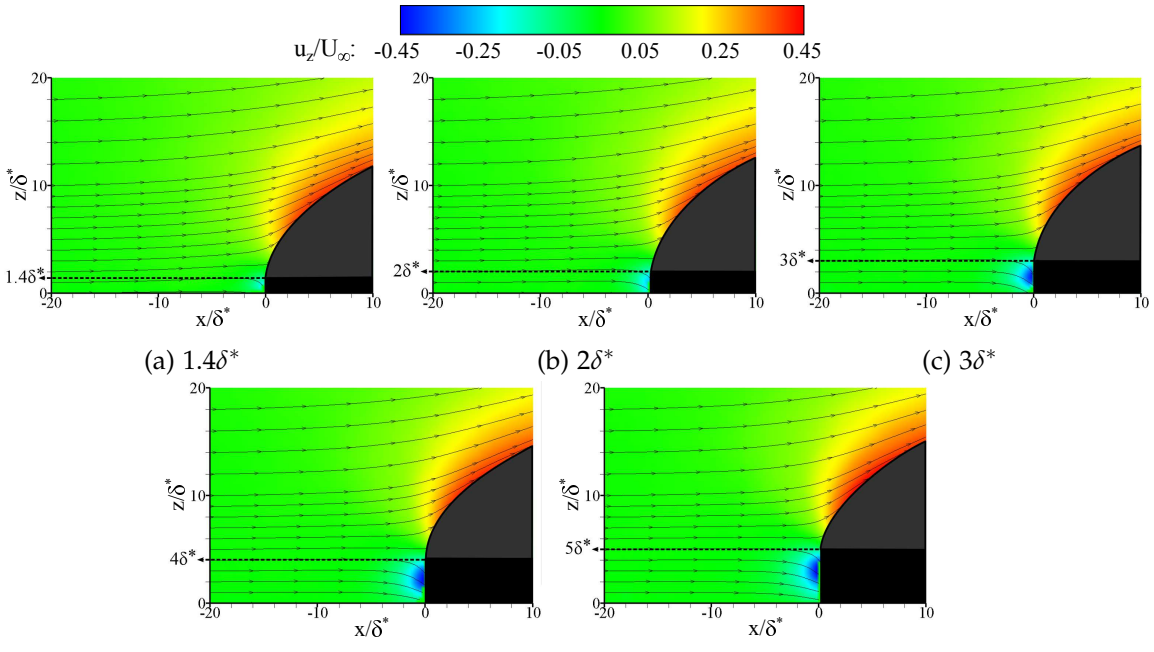

(a) $1.4\delta^*$ (b) $2\delta^*$ (c) $3\delta^*$

(d) $4\delta^*$ (e) $5\delta^*$

FIGURE 4.12: Time-averaged u_z/U_∞ contour at the centreline of fuselage nose at $\alpha = 0°$.

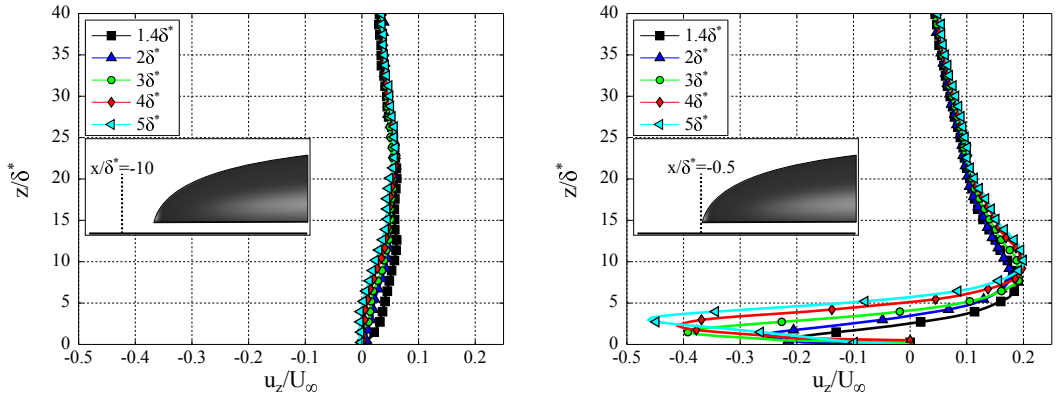

(a) $x/\delta^* = -10$ (b) $x/\delta^* = -0.5$

FIGURE 4.13: Tunnel wall boundary layer u_z/U_∞ profile development immediately upstream of fuselage nose/stand-off gap at $\alpha = 0°$.

is clear from figure 4.12 that as the stand-off gap height is increased the incoming boundary layer is deflected/accelerated downward under the model symmetry plane more strongly. The flow over the upper side of the fuselage does not experience significant changes with the stand-off height other than the position of the stagnation point as previously mentioned. The most significant change of the flow field occurs between $2\delta^*$ and $3\delta^*$. At $3\delta^*$ the stand-off gap height at the fuselage nose reaches approximately 40% of the empty wind tunnel's boundary layer thickness at the same location ($x/L = 0.3$).

Upstream from the fuselage nose at location $x/\delta^* = -10$ the u_z/U_∞ velocity profile, shown figure 4.13a, shows that with the model in closer proximity to the tunnel wall the flow deflection away from the tunnel wall is stronger. Moving nearer the model at $x/\delta^* = -0.5$, figure 4.13b, a peak downward u_z/U_∞ velocity located centrally to the respective stand-off gap is observed. The u_z/U_∞ velocity profiles over the top of the model match closely, the apparent discrepancies above the model symmetry plane arise due to the model having different mounting heights depending on the stand-off gap.

4.5.2 TURBULENCE QUANTITIES

Some of the turbulent quantities have been compared for different stand-off gap heights. The purpose of this is to provide some quantitative assessment of how varying the stand-off gap alters the propagation of turbulence over the model, which subsequently effects aerodynamic performance metrics. Previous studies have only considered this in a qualitative manner using surface flow visualisations [290, 291, 298].

The root mean square of the velocity fluctuations (square root of turbulent normal stresses) defined as follows is scaled by the freestream velocity U_∞:

$$\begin{aligned}\sigma_u &= \sqrt{\overline{u'^2}} = \sqrt{\overline{(u_i - \overline{u})^2}} \\ \sigma_v &= \sqrt{\overline{v'^2}} = \sqrt{\overline{(v_i - \overline{v})^2}} \\ \sigma_w &= \sqrt{\overline{w'^2}} = \sqrt{\overline{(w_i - \overline{w})^2}}\end{aligned} \tag{4.1}$$

In figure 4.14 the turbulent fluctuations of the three velocity components from the flow field around the half-body fuselage nose are compared for stand-off gap heights $1.4\delta^*$ to $5\delta^*$. In-plane velocity fluctuations in the freestream direction, σ_u, reflect the velocity profile streamlines in figure 4.10 indicating that with lower stand-off gap heights the boundary layer is deflected upward over the top of the fuselage. Figure 4.14a shows that at a stand-off height of $1.4\delta^*$, σ_u fluctuations from the oncoming boundary layer are seen to clearly propagate over the top of the fuselage nose. This is facilitated by the upward deflection/thickening of the wind tunnel floor boundary layer as it approaches the model. This indicates, at the very least, that the flow over the whole fuselage forebody will exhibit increased unsteadiness.

Comparing the change in σ_u as a function of stand-off gap height, it is noticed that higher stand-off gaps alleviate the unsteadiness transferred from the tunnel boundary layer to the flow enveloping the forebody. Figures 4.14d and 4.14g, illustrating σ_u for stand-off heights $2\delta^*$ and $3\delta^*$, respectively, indicate the transition of the downward deflection of the boundary layer under the model symmetry plane; as previously discussed, increasing the stand-off gap height is observed to accelerate the wind tunnel boundary layer flow underneath the model. Increasing the stand-off height to $3\delta^*$, presented in figure 4.14g, shows the σ_u fluctuations within the boundary layer flow diverging with the highest fluctuations of the inner boundary layer being drawn underneath the model, and lower fluctuations of the upper boundary layer moving slightly up and over the nose leading edge. This would seem to indicate that turbulent fluctuations translating from the tunnel boundary layer to the flow over the fuselage do not envelope the whole fuselage forebody as observed with the $1.4\delta^*$ case. Instead, increased unsteadiness transmitted from the tunnel boundary layer moves around the fuselage, remaining relatively low close to the fuselage symmetry plane. As these SPIV images illustrate the flow over the fuselage centreline at $\alpha = 0^\circ$, this is a reasonable explanation of the flow behaviour which will be discussed further in Section 4.6.

Progressing on to higher stand-off gap heights $4\delta^*$ and $5\delta^*$, shown in figures 4.14j and 4.14m, respectively, no boundary layer thickening or upward deflection is noticed upstream of the fuselage; this is in agreement with the streamline data presented in figure 4.10, and 4.12. In both instances, most of the tunnel boundary layer is seen to be drawn under the model symmetry plane with no significant σ_u fluctuations transferred to the flow over the fuselage forebody.

Now, consider the other components of the turbulent velocity fluctuations, σ_w, the in-plane fluctuation normal to the freestream direction, and σ_v, the out-of-plane fluctuation. The intention of the stand-off gap is to attempt to isolate the model

from the tunnel boundary layer as much as possible in order to maintain a flow field without any significant increase in cross flow velocity components. In achieving this, the flow field would more closely mimic that around the equivalent whole body. In the vicinity of the stagnation point on the fuselage nose there is a region of increased cross flow fluctuations σ_w and σ_v, indicated in figures 4.14b and 4.14c. In this region cross flow fluctuations reach up to about 12% of the freestream velocity regardless of stand-off gap height. With lower stand-off gap heights, this unsteady region around the stagnation point is observed to be larger with higher fluctuations also present within the upstream boundary layer region.

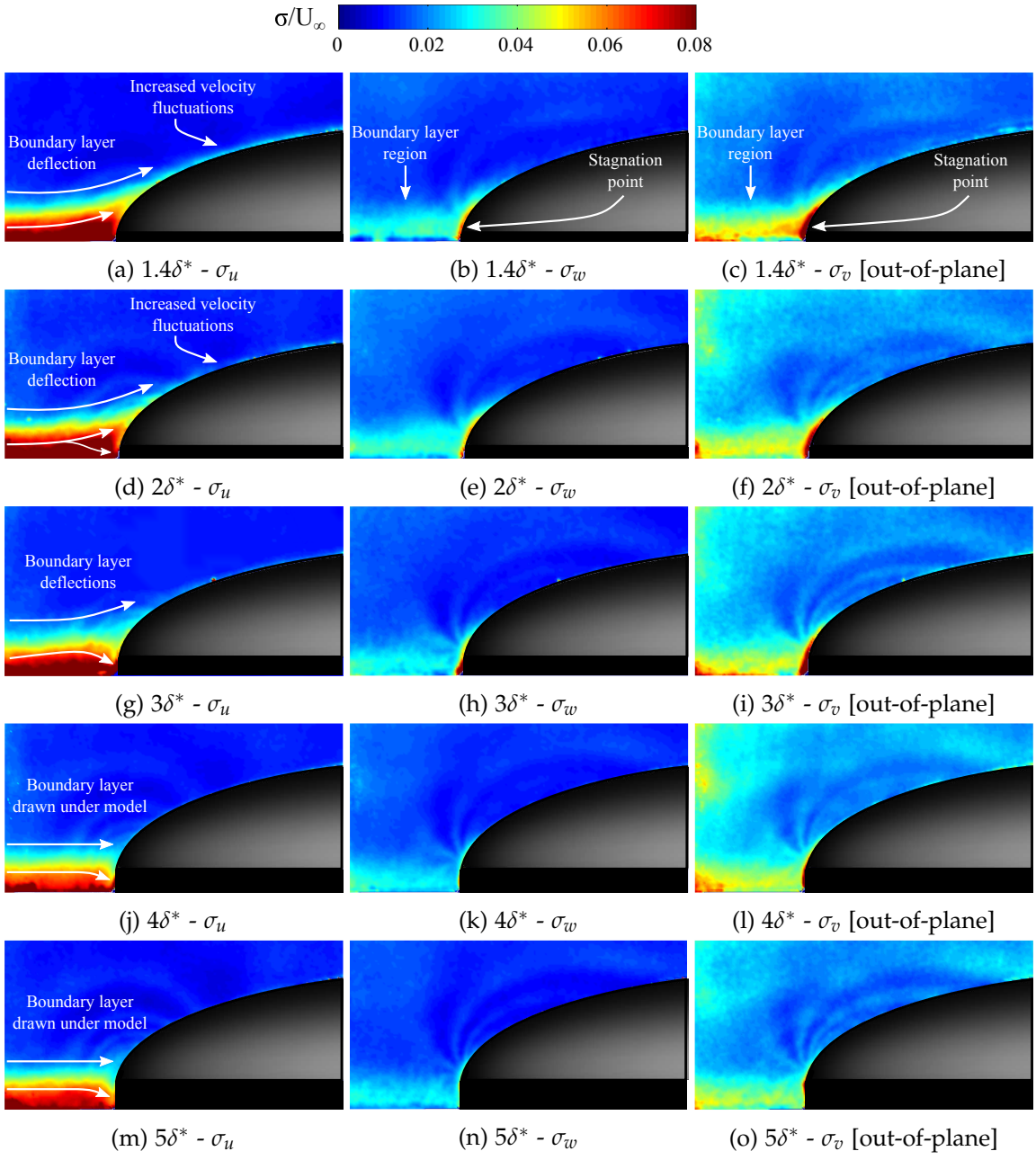

(a) $1.4\delta^*$ - σ_u (b) $1.4\delta^*$ - σ_w (c) $1.4\delta^*$ - σ_v [out-of-plane]

(d) $2\delta^*$ - σ_u (e) $2\delta^*$ - σ_w (f) $2\delta^*$ - σ_v [out-of-plane]

(g) $3\delta^*$ - σ_u (h) $3\delta^*$ - σ_w (i) $3\delta^*$ - σ_v [out-of-plane]

(j) $4\delta^*$ - σ_u (k) $4\delta^*$ - σ_w (l) $4\delta^*$ - σ_v [out-of-plane]

(m) $5\delta^*$ - σ_u (n) $5\delta^*$ - σ_w (o) $5\delta^*$ - σ_v [out-of-plane]

FIGURE 4.14: Velocity fluctuations over centreline of fuselage nose at $Re = 1.5 \times 10^6$, $\alpha = 0^\circ$ for stand-off heights $1.4\delta^*$, $2\delta^*$, $3\delta^*$, $4\delta^*$, and $5\delta^*$.

In assessment of the in-plane σ_w fluctuations presented in figure 4.14, from a stand-off gap height of 1.4 to $5\delta^*$, the turbulent region at the stagnation point can be seen to reduce in size and move closer to the fuselage symmetry plane with increasing stand-off height. The same trend is also observed for the out-of-plane σ_v fluctuations. With lower stand-off heights the boundary layer is largely blocked from flowing under the model such that the oncoming air must be more aggressively displaced around the fuselage nose. In this subsonic flow field, the effects of this are felt upstream which cause upward deflection/thickening of the tunnel boundary layer and results in the higher fluctuations noticed. As the stand-off gap size is increased through $3\delta^*$ to $4\delta^*$ and $5\delta^*$, the region of strong cross flow fluctuations is reduced as a result of achieving a velocity field that remains sufficiently parallel to the fuselages plane of symmetry. It is necessary to indicate here that increased out-of-plane fluctuations at the top left corner of the σ_v field of view, in the freestream, is suggestive of pixel-locking. This may have been caused by thinning of the laser sheet in this region and is not detected in any histogram.

As shown previously in figures 4.10 and 4.11, increasing the stand-off gap height causes the tunnel boundary layer to accelerate into the gap. This quantitative flow acceleration indicates that a favourable pressure gradient is achieved (defined as a negative pressure gradient), therefore achieving a net pressure drop between the tunnel wall and the fuselage forebody symmetry plane; this result was also identified by Eder et al. [298]. This mechanism draws the wind tunnel floor's turbulent boundary layer underneath the model and subsequently alleviates large cross flow displacement of the relatively slower air of the tunnel boundary layer. Thus, the data presented shows that lower stand-off gap heights will result in higher flow unsteadiness of the fuselage forebody. Increasing the stand-off gap height to $4\delta^*/5\delta^*$ reduces the flow unsteadiness over the upper side of the fuselage forebody.

Referring back to the force and moment measurements in Section 4.3, trends of how the aerodynamic coefficients of the model changed with stand-off gap height were investigated. The lift coefficient was seen to decrease by approximately constant offsets with increasing stand-off height. This indicates that for certain α ranges the deviation in the lift coefficient is a function of the stand-off gap, and not a direct function of the angle of attack. The SPIV data presented here demonstrates that lower stand-off gap heights enable the propagation of turbulent flow over the forebody of the fuselage. This in turn leads to increased turbulence of the inboard wing section, leading to higher lift coefficients and delayed separation as speculated by Eder et al. [298] who used tufts to visualise this phenomenon. Changes to the local lift coefficients/lift distribution will also play a role in modifying the pitching moment coefficient.

Furthermore, the SPIV reveals the acceleration of the inner region of wind tunnel boundary layer into the stand-off gap. The fact that the flow velocity into the stand-off gap region increases as the stand-off gap height is increased, aids in the explanation of

the almost incremental drag rise experienced by the model. The deviation in the drag coefficient was shown to be a function of the distance between the fuselage symmetry plane and the tunnel wall, and not a direct function of the angle of attack. This drag rise is associated with the higher parasitic drag acting on the fuselage symmetry plane which increases with the square of the velocity.

4.6 SURFACE FLOW VISUALISATIONS

SPIV measurements, shown in figure 4.10, demonstrated the absence of a horseshoe vortex at the nose of the fuselage and the acceleration of the flow under the model. The results, shown in figure 4.14, also indicated the reduction of turbulent velocity fluctuations over the fuselage forebody centreline at $\alpha = 0^\circ$. While informative, this does not provide information away from the centre-line of the fuselage forebody, or at increased angles of attack. Regions of interest around the model on the floor, along the upper side of the fuselage, and the wing root region are logistically challenging to investigate with SPIV due to restricted optical access. Consequently, these areas have been qualitatively investigated in order to enhance the local flow field understanding. Tuft and clay surface flow visualisation methods can highlight regions of flow unsteadiness, indicate local flow direction, reveal regions of attached/separated flow, infer pressure gradients and boundary layer development, and display behaviour of wakes and associated shear flows moving over the surface under analysis. Each method will however have intrusive influences on the local flow field, however these effects have been deemed negligible. Results shown here can be considered time-averaged.

4.6.1 Tuft Visualisation

Surface flow visualisation using the tufts method is presented in figure 4.15. Information regarding the tuft visualisation experiments has been provided in Section 3.9. The standard deviation of the intensity fluctuations of the tufts with the model at three stand-off heights ($1.4\delta^*$, $3\delta^*$, and $4\delta^*$), for two angles of attack ($\alpha = 0^\circ$ and 14°) are shown. It should be noted that the $4\delta^*$ and $5\delta^*$ show similar tuft patterns. The model geometry is outlined by dashed lines, with the pitch axis and freestream flow direction shown. Local flow streamlines interpreted from the tuft patterns are also indicated. The tufts were attached to the tunnel floor, the main fuselage body, and the wing root. Regions observed to have increased unsteadiness have been highlighted both on the model and the wind tunnel floor where the bounding solid lines indicate local shear flows.

Observations from the tuft visualisations agree with the information provided by the SPIV in Section 4.5; the cases with the model at $\alpha = 0^\circ$ are identical to those presented for SPIV. Both experimental techniques demonstrate a correlation between increased stand-off gap height and reduced flow instability over the fuselage.

Furthermore, the SPIV data presented in figures 4.14b and 4.14c illustrate the region of fluctuating cross flow components orthonormal to the freestream direction of σ_w and σ_v, respectively. It is observed here that ahead of the fuselage nose cross flow fluctuations are higher for lower stand-off gap heights. With a lower stand-off height, the oncoming flow is more aggressively displaced around and over the fuselage nose, whereas with increased stand-off height the oncoming boundary layer is drawn into the gap (under the model). This aids in achieving a velocity field around the forebody that remains sufficiently parallel to the fuselage symmetry plane, the downstream effects of which can be examined in the tuft visualisations.

At $\alpha = 0°$, the stand-off gap is increased from $1.4\delta^*$, to $3\delta^*$, to $4\delta^*$ (figures 4.15a, 4.15c, and 4.15e respectively). With increasing stand-off gap height the region of heightened tuft activity over the fuselage length is seen to reduce, moving aft towards

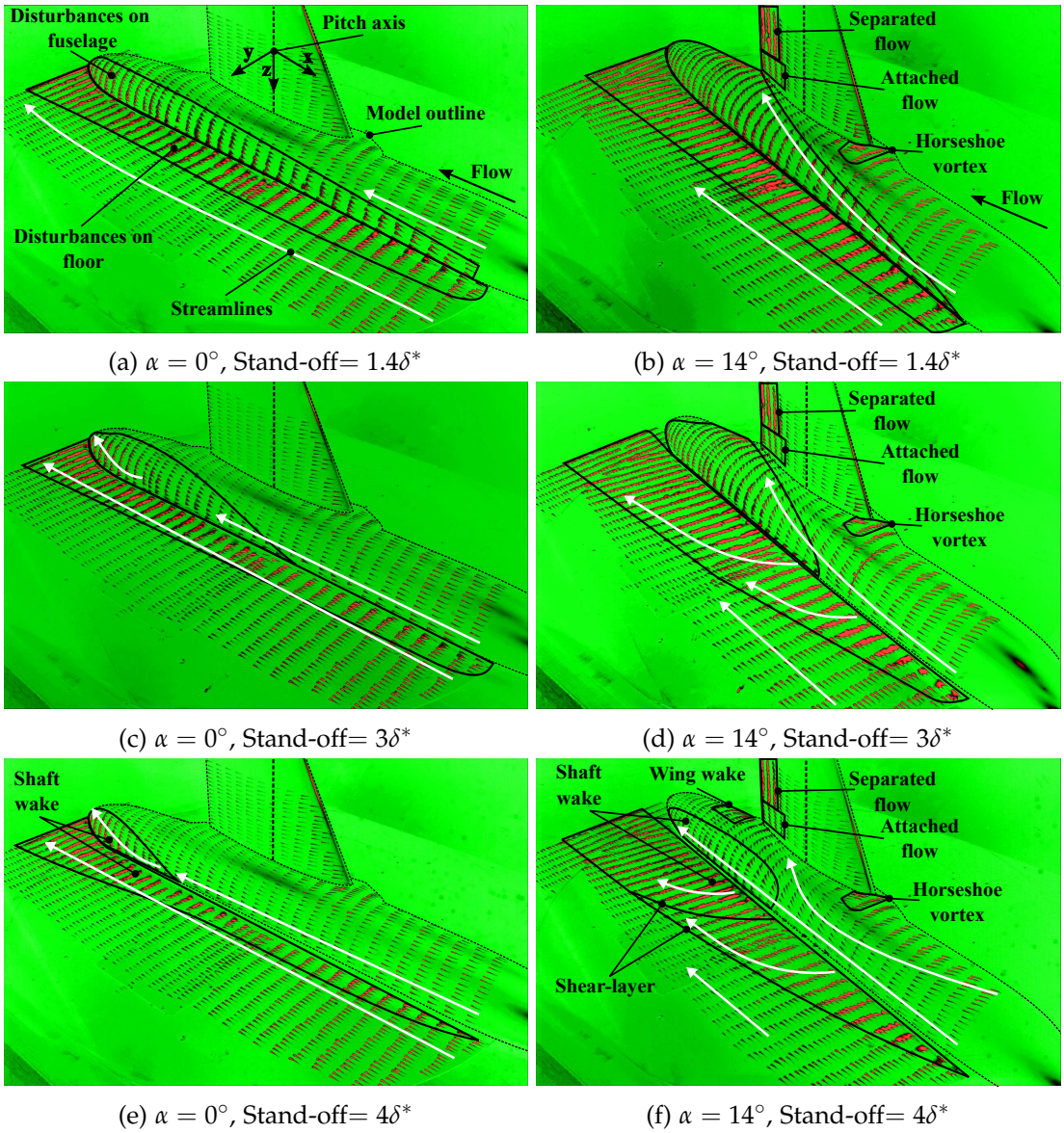

(a) $\alpha = 0°$, Stand-off= $1.4\delta^*$

(b) $\alpha = 14°$, Stand-off= $1.4\delta^*$

(c) $\alpha = 0°$, Stand-off= $3\delta^*$

(d) $\alpha = 14°$, Stand-off= $3\delta^*$

(e) $\alpha = 0°$, Stand-off= $4\delta^*$

(f) $\alpha = 14°$, Stand-off= $4\delta^*$

FIGURE 4.15: Qualitative visualisation of the standard deviation of tuft fluctuations for stand-off gap heights $1.4\delta^*$, $3\delta^*$, and $4\delta^*$.

the tail section. There are two sources of flow instability here: 1) the mass of fluid being displaced around and over the half-body fuselage forebody; and 2) the mounting shaft's turbulent wake interacting with the flow over the half-body fuselage afterbody. There are no observed regions of unsteadiness over the wing root, at any stand-off height at $\alpha = 0^\circ$.

The general shape of the disturbed region over the fuselage length at $\alpha = 0^\circ$ does not change. The extent and strength of the tuft fluctuations is largely dominated by the velocity fluctuations and displacement of the fluid around the nose. At $1.4\delta^*$, figure 4.15a, the displaced turbulent flow propagates over the fuselage forebody, with the highest flow instabilities travelling around the fuselage symmetry plane near the floor. With increasing stand-off gap height, to $3\delta^*$ and $4\delta^*$ shown in figure 4.15c and 4.15e, respectively, less fluid is displaced around the nose as the wind tunnel boundary layer is drawn underneath the model into the gap. While this is shown to be the case with SPIV, the reduced tuft excitation and parallel uniformity over the fuselage with increasing stand-off height indicates a more stable velocity field is achieved over the entire fuselage length.

The area of tuft instability on the fuselage afterbody, near the tail section, visible in figure 4.15e, is caused by the mounting shaft wake escaping from under the model and impinging over the upper surface. This wake effect is noted to still be present in the other two stand-off heights, $1.4\delta^*$ and $3\delta^*$, but is weaker (less air mass under model) and also combined with unsteadiness from upstream. It is also seen that in each case the disturbance patterns over the floor is narrower towards the nose of the fuselage and diffuses away from the fuselage body moving downstream with the lateral rate of growth increasing aft of the pitch axis due to the introduction of the shaft wake.

At $\alpha = 14^\circ$, as the stand-off gap is increased from $1.4\delta^*$ to $3\delta^*$ and then to $4\delta^*$ (figures 4.15b, 4.15d, and 4.15f respectively), the region of high fluctuations over the fuselage length reduces in size. However, unlike the cases at $\alpha = 0^\circ$ (see figures 4.15a, 4.15c, and 4.15e), the region and patterns of tuft activity change with stand-off height. The changing flow structures arise as secondary cross flow from between the model's symmetry plane, and the tunnel floor becomes more influential as the model's angle of attack is increased; the fuselage is no longer parallel to the flow. With increased stand-off height, at $\alpha = 14^\circ$, the flow from under the fuselage is noticed to become more stable as the tuft fluctuations reduce. At the same time, the shaft wake becomes more noticeable. The tufts over the floor indicate that the secondary cross flow through the stand-off gap from under the fuselage forebody, forward of the pitch axis, is more stable than the flow aft of the pitch axis from under the afterbody. This is due to the presence of the shaft wake.

For the stand-off height of $1.4\delta^*$ at $\alpha = 14^\circ$ (figure 4.15b) tuft fluctuations are present over most of the fuselage, enveloping all of the visible fuselage afterbody. The floor shows high tuft activity along the entire length of the fuselage with no

clear flow direction, which is indicative of the high flow instability. This indicates the likelihood of a longitudinal vortex along the back of the fuselage at the stand-off gap. Tuft fluctuations increase immediately downstream of the shaft (the model pitch axis). As the stand-off height is increased from to $3\delta^*$ and $4\delta^*$, figures 4.15d and 4.15f respectively, the cross flow from under the nose of the fuselage appears to becomes more stable. This increase in flow stability reduces the tuft oscillations and shows the local flow direction more clearly. Further downstream of the pitch axis, the wake of the shaft is observed in the increased tuft activity on the floor.

Figure 4.15f shows an approximately mirrored disturbance over the floor and fuselage due to the shaft wake. At the stand-off heights of $4\delta^*$ and 5δ, with a high angle of attack, the shaft wake encounters a relatively faster cross flow emerging from under the model forebody. There is a bounding shear-layer, indicated in figure 4.15f, between the cross flow from under the semi-span model's nose and the shaft wake. The cross flow from under the fuselage nose excites the tufts, but the flow direction is still clear. Downstream of the pitch axis, where the shaft wake is present, the turbulent wake excites the tufts enough that a definitive local flow direction is not clear.

At higher angles of attack, and higher stand-off gap heights, the shaft's wake encroaches further over the upper side of the fuselage's after-body. However, this increased influence from the shaft's wake is outweighed by the clear reduction of flow instability along the entire length of the fuselage as gap height is increased. This encourages the wind tunnel boundary layer to be drawn underneath, and not over/around the fuselage. Moving the fuselage symmetry plane away from the proximity of the tunnel floor moves the fuselage higher into the wind tunnel floor's turbulent boundary layer. From the SPIV results it was clear that at stand-off heights $3\delta^*$, $4\delta^*$, and $5\delta^*$, the wind tunnel's boundary layer is drawn underneath the model with systematically increasing effectiveness.

Furthermore, at the increased angle of attack, the interference noticed ahead of the wing root leading edge is attributed to the presence of a horseshoe vortex formation. This is present for each stand-off case shown in figures 4.15b, 4.15d, and 4.15f, where the tuft patterns in each instance appear identical. Towards the trailing edge of the inboard wing, shown in each figure, there is a region of separation indicated by the high fluctuation and local flow directions of the tufts. The horseshoe vortex forming at the leading edge of the wing root causes the flow to remain attached at the wing root trailing edge for each stand-off height.

4.6.2 CLAY FLOW VISUALISATION

Figures 4.16 and 4.17 show the surface flow clay patterns on the tunnel floor around the model at a gap height of $4\delta^*$ at $\alpha = 0^\circ$ and 14°, respectively. This enables observations of the interaction between the boundary layer flow on the fuselage and the inboard wing area and also how disturbances propagate and develop over the model at this

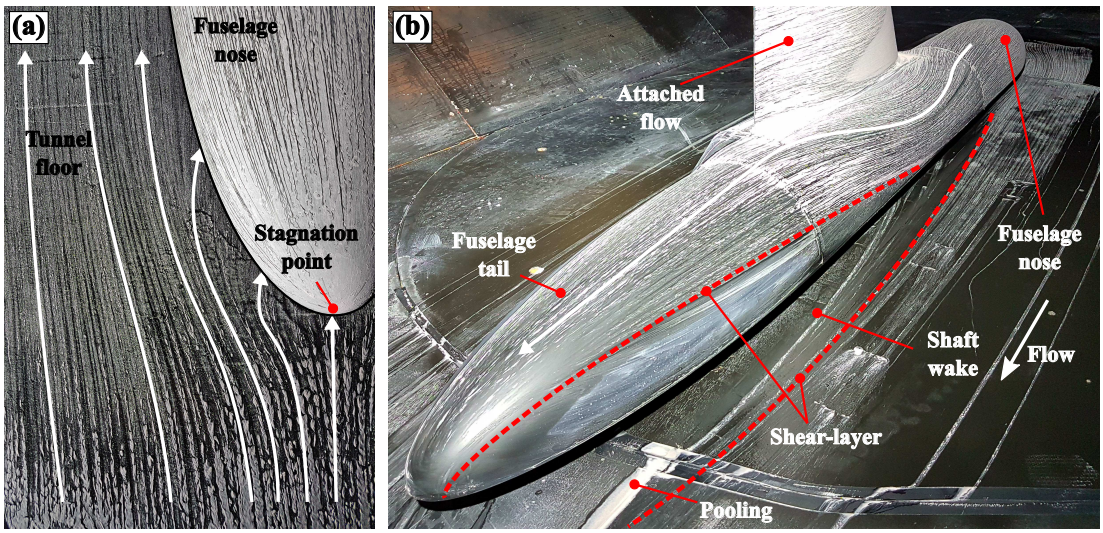

FIGURE 4.16: Clay flow around model at $\alpha = 0°$ at stand-off height $4\delta^*$; views of fuselage nose (a), and full fuselage, wing root and tunnel floor (b) are shown.

stand-off height. From the SPIV results in figure 4.11d it is evident that the inner tunnel boundary layer flow accelerates into the stand-off gap under the model. Without a peniche there is a velocity gradient at the wall in front of the fuselage nose. Therefore, due to the acceleration of the flow into the gap under the model, the flow does not separate from the wind tunnel wall. Hence, no horseshoe vortex is formed. This effect is visualised using the clay flow method at $\alpha = 0°$ in figure 4.16a. The streamlines formed by the clay around the fuselage nose, in figure 4.16a, indicate the flow turning and being drawn under the fuselage. This corresponds well to the SPIV data in figure 4.10 illustrating the flow accelerating into the stand-off gap. Figure 4.16 was conducted under identical conditions as the tuft visualisation in figure 4.15e, and SPIV data for $4\delta^*$ presented in figure 4.11d. Comparing figures 4.16b and 4.15e, the influence of the shaft wake is visible in both instances. In the tuft visualisations the shaft wake increased the flow instability indicated by the tufts, however the clay flow results in 'clean' patches over the same region following the shear-layer formed between the shaft wake and the surrounding flow. The clay/paraffin mixture was pushed around the shaft's wake due to the wake's relatively higher static pressure. The overall wake pattern outlined by the clay (figure 4.16b) corresponds closely to regions of heightened tuft fluctuations in figure 4.15e.

Furthermore, it is noted that the clay flow mixture progressively accumulates (pooling) near the fuselage tail inside the shaft wake region, as indicated in figure 4.16b. The build up of clay in this location suggests that the relative magnitude of the frictional shear forces acting on the clay is reduced. This intuitively indicates a drop in the dynamic pressure (velocity) within the shaft wake region.

Applying the clay mixture to the model at $\alpha = 14°$ results in the surface flow patterns shown in figure 4.17. The absence of the horseshoe vortex is again illustrated by the clay flow patterns, with the flow streamlines being drawn under the model as

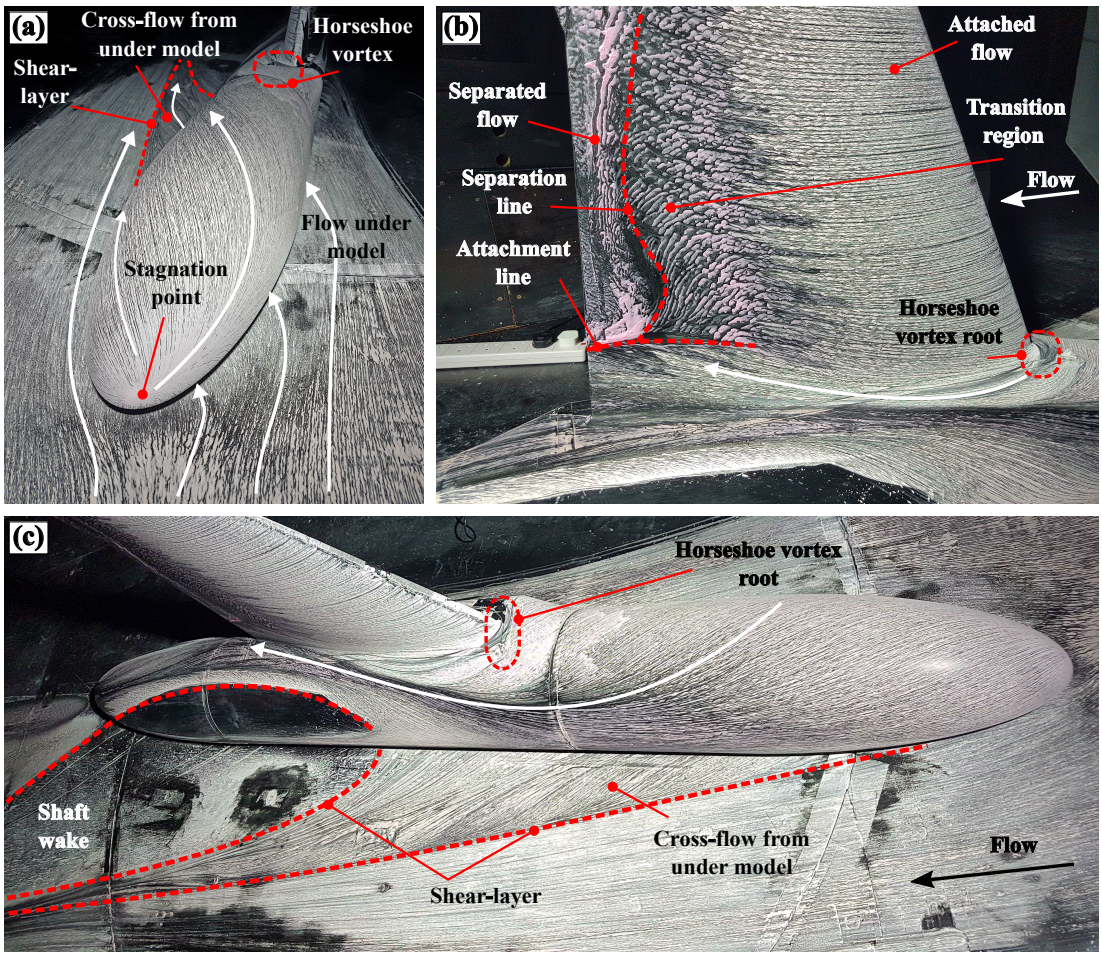

FIGURE 4.17: Clay flow around model at $\alpha = 14^\circ$ at stand-off height $4\delta^*$; views of fuselage nose (a), wing root (b), and full fuselage, wing root and floor (c) are shown.

previously seen at $\alpha = 0^\circ$ in figure 4.16a. The streamline curvature over the fuselage length is shown in figures 4.17a and 4.17c, which is strongly influenced by the induced velocity over the wing root and also the shaft wake. Importantly, the streamlines show an attached flow over the entire fuselage at this high angle of attack.

Figure 4.17b shows the flow patterns arising from the induced velocity over the wing root. Due to the tuft visualisations at the wing root and consistent absence of the horseshoe vortex at the fuselage nose, it is expected that the flow over the inboard wing is similar for all stand-off heights. Akin to the tuft visualisations, with comparison made to figure 4.15f, the horseshoe vortex ahead of the wing root leading edge and the regions of separated and attached flow towards the wing trailing edge are observed. The wing leading edge horseshoe vortex is responsible for the flow reattachment toward the wing root in figure 4.17b with the reattachment and separation lines highlighted. Attached flow over the inboard section of the wing and transitional flow, suggesting boundary layer thickening, is also indicated. It is necessary to bring to attention the possible influence of gravity on the surface patterns in this region. As the boundary layer thickens and develops in the transitional region, indicative of the local wall shear stresses weakening, gravitational forces may become

influential (note that the wing is mounted vertically) and draw the clay mixture down towards the fuselage. However, from experimental observations and the development of the surface streamlines over time, it is found that forces due to gravity are negligible, and that fluid dynamic shear forces from the flow on the clay remain dominant.

As the angle of attack increases, the shaft wake impinges more onto the top side of the fuselage, the effect of this is clear when comparing figures 4.16b and 4.17c. However, from the tuft visualisations it is understood that the instabilities over the entire fuselage would be greater at lower gap heights.

4.7 SUMMARY AND CONCLUSIONS

The use of a stand-off gap for a peniche-less semi-span wind tunnel model at $Re = 1.5 \times 10^6$ based on the wing mean aerodynamic chord has been investigated; only the planar wing arrangement is considered here. The model stand-off gap is scaled to the displacement thickness (δ^*) of the wind tunnel at the pitch axis of the model such that stand-off gap heights $1.4\delta^*$, $2\delta^*$, $3\delta^*$, $4\delta^*$ and $5\delta^*$ are considered. The main findings of this chapter have been published by Skinner and Zare-Behtash [239].

Assessment of how the aerodynamic performance metrics of the semi-span model vary with changes in the stand-off gap height demonstrated low sensitivity. This itself is an appealing result as the conventionally applied two-dimensional peniche extrusion has been widely confirmed to enforce flow displacement around the fuselage nose leading to the formation of a horseshoe vortex and increased velocity gradients over the model [291]. This subsequently has been shown to dramatically affect the aerodynamic performance metrics of the model as both a function of stand-off height and angle of attack [292, 294, 298]. Some studies [237] identified that the larger the peniche installed the stronger the interactions with the respective horseshoe vortex became. Consequentially the application of no peniche with the model mounted directly to the wall was suggested to perform better and minimise the horseshoe vortex influence.

In this study, it has been observed that deviations in aerodynamic coefficient between stand-off gap height installations are approximately constant over the tested linear lift region of the model ($-5^\circ \leq \alpha \leq +7^\circ$). This demonstrates that over this region, deviations of aerodynamic coefficients are a function of the distance between the fuselage symmetry plane and the tunnel wall, and not a function of the angle of attack. Raising the stand-off gap height from $1.4\delta^*$ to $5\delta^*$ is noticed to increase the drag by $\Delta C_D = +0.0072$ ($\approx 26\%$ increase) over the linear lift region. The lift-curve-slope is noticed to decrease with increasing stand-off gap size in a linear fashion; this trend is shown independent of the Reynolds number.

Assessment of the model structural dynamics and dynamic loading due to vibrations indicate that the model is perhaps more vulnerable to forced vibration due

to the single structural support via the mounting shaft. This however is shown to be of no great importance as post-processing of the force platform signals with a $38Hz$ low-pass filter mitigates vibrations resulting in increased signal noise. Any data acquired from the force platform will be subjected to post-processing with the $38Hz$ low-pass filter.

The oncoming wind tunnel boundary layer velocity gradients and fluctuations around the semi-span fuselage forebody have been measured using stereoscopic particle imaging velocimetry. Investigation of velocity profiles and gradients demonstrate that no horseshoe vortex is formed at any stand-off gap height. Increasing the gap height to $4\delta^*$ or $5\delta^*$ is shown to alleviate the displacement of boundary layer flow around the fuselage nose, encouraging the tunnel boundary layer under the model, where the inner region of the boundary layer experiences a favourable pressure gradient thus accelerating under the model. This is seen to reduce the upward deflection of the wind tunnel boundary layer as it approaches the fuselage nose and helps to maintain a velocity field that is sufficiently parallel to the fuselage plane of symmetry. A knock-on effect of this is that turbulent velocity fluctuations from the boundary layer, which propagate over the model forebody at lower stand-off gaps, are drawn underneath the model symmetry plane.

In addition, cross flow velocity fluctuations at the fuselage stagnation point reduce in intensity with increasing stand-off gap height. It is suggested that with a stand-off heights of $4\delta^*$ or $5\delta^*$ the upper side of the semi-span model is sufficiently isolated from the wind tunnel boundary layer. This is concluded as the flow field demonstrates no significant increase in cross flow velocity fluctuations that reach above the symmetry plane of the fuselage. Achieving this flow field is vital to closely mimic what would be expected around an equivalent full-span model in the freestream.

Moreover, how the flow then translates over, around, and under the fuselage as well as the inboard wing section has been investigated using qualitative surface flow visualisation techniques. Observations from tuft visualisations enabled regions of unsteadiness over the model to be highlighted, where results agreed with those of the SPIV; higher stand-off gap height leads to reduced unsteadiness over the fuselage forebody. The tufts also give insight into how the flow behaves as it emerges from the stand-off gap where the extent of the mounting shaft wake over the fuselage afterbody is evident, with results presented for $1.4\delta^*$, $3\delta^*$, and $4\delta^*$. The $4\delta^*$ stand-off gap results are also accompanied by clay flow visualisations. The clay flow enhanced the understanding of flow structure from underneath the model symmetry plane, and gave insight into the extent and influence of the mounting shaft's wake over the model afterbody and tunnel floor.

Variations in the flow field caused by changing the stand-off gap height, while seemingly not as severe as those experienced for a peniche extrusion, are seen to modify the flow around the fuselage with associate effects which modify the aerodynamic metrics of the model. Thus, all experimental results presented from this point

forwards are conducted with the semi-span model installation using a stand-off gap height of $4\delta^*$. While $4\delta^*$ and $5\delta^*$ are shown to create flow fields with ultimately the same outcome in terms of model performance, and flow features, a stand-off height of $4\delta^*$ ensures longevity of the model mounting interface. Eder et al. [298], conducting experiments with similar flow conditions and model installation, also identified $4\delta^*$ as a optimal stand-off gap distance between the fuselage and wall.

CHAPTER 5

C-WING PERFORMANCE RELATIVE TO PLANAR WING

5.1 INTRODUCTION

With the development of a semi-span wind tunnel model, and identification of a suitable stand-off gap height ($4\delta^*$), the present chapter explores the performance of the C-wing configuration developed in Chapter 2. Therefore, the objective of this chapter is to provide an experimental demonstration of the sGA designed C-wing configuration with the aim of verifying potential practical application.

The wind tunnel tests presented in this work are designed to be an exploratory *'proof-of-concept'* study. This is achieved by considering aerodynamic performance metrics of the C-wing relative to a planar wing of equivalent wingspan, lift, and root bending moment, the results of which are presented in Section 5.2. Subsequently, Section 5.3 features the use of clay flow visualisations to qualitatively examine how the global flow over the main-wing is effected by the addition of the C-wing. Furthermore, efforts have been made to design the wing configurations such that bend-twist deformations were decoupled when aerodynamically loaded, resulting in near pure bending of the wing as shown in Section 5.4. This characteristic has enabled the assessment of buffet induced vibrations by simplifying the dominant vibrations of the main-wing to bending modes alone. Section 5.5 presents an in-depth analysis of each of the semi-span model's wing configurations vibrations in which the structural dynamics of the C-wing are compared to that of the planar wing. Section 5.6 summarises the main findings of this chapter.

5.2 FORCE AND MOMENT MEASUREMENTS

Changes in lift, drag, pitching moment about the model's centre-of-gravity/pitch axis, and the wing's notional root bending moment are presented in figure 5.1, comparing the behaviour of the C-wing relative to the planar wing. All measurements have been corrected for solid-body blockage (Planar wing: 4.9% at $\alpha = 14°$; C-wing: 5.2% at $\alpha = 14°$), wake blockage, and horizontal buoyancy using methods presented by Barlow et al. [227]. The force and moment data has been post-processed using a $38Hz$ low-pass filter (justification for which is provided in Section 4.4). The force and moment data presented have been calculated with a confidence level of 98% with a margin of error less than 1% for each datum. The model has only been operated in the pre-stall region to prevent damage to the wing due to high flexibility in bending.

To draw comparisons between the two equivalent wing configurations, where one is anticipated to achieve a lower induced drag, it is common practice to maintain equivalent wing lift coefficient without any gain in root bending moment [21]. Typically, any reductions of induced drag are offset by the increase in the root bending moment; Takenaka et al. [92] showed a linear correlation between winglet span length, induced drag reduction, and increases in root bending moment. This implies that

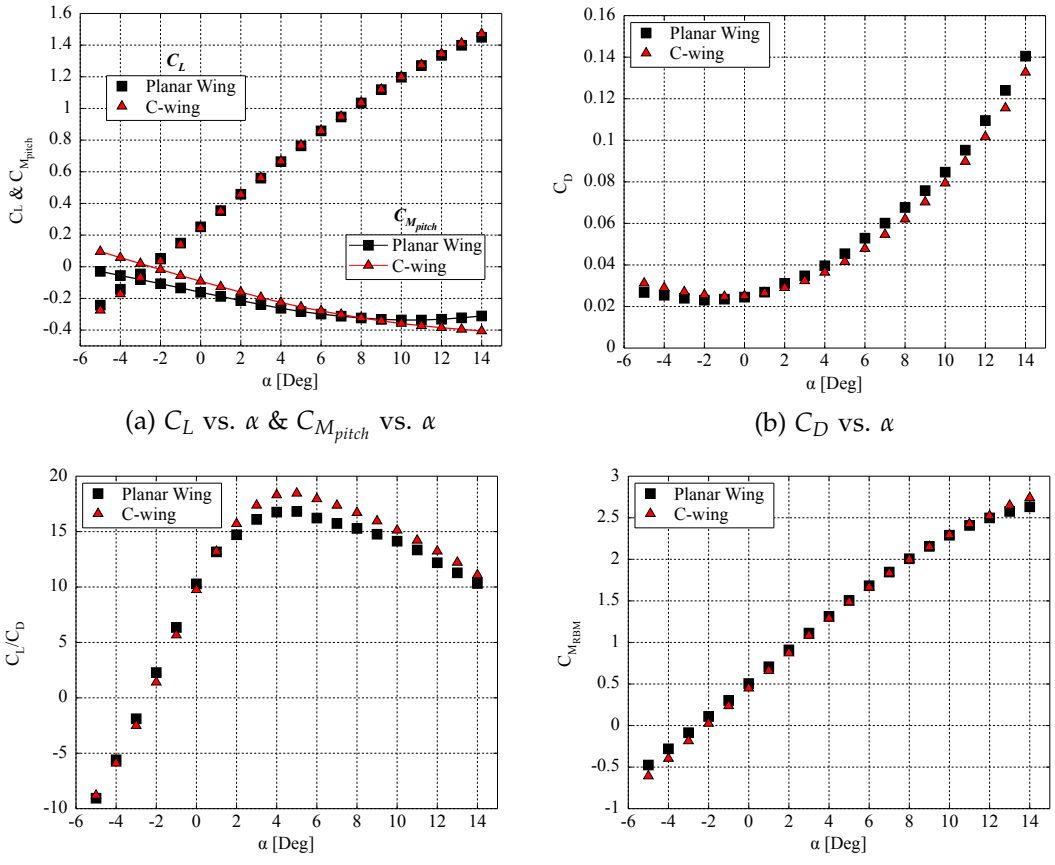

(a) C_L vs. α & $C_{M_{pitch}}$ vs. α

(b) C_D vs. α

(c) C_L/C_D vs . α

(d) $C_{M_{RBM}}$ vs. α

FIGURE 5.1: Aerodynamic coefficients for the planar wing and the C-wing.

wing systems such as this are often found to add more structural weight than their respective drag reduction potential can compensate for; i.e. typically any induced drag reduction achieved cannot be justified due to the gain structural weight.

For the C-wing tested, figures 5.1a and 5.1d show that the lift coefficient and notional root bending moment coefficients match the baseline planar wing closely for the angles of attack range tested. For both wings a slight drop in the lift coefficient gradient is noticed at higher angles of attack, signalling the on-set of stall. This small loss in lift coincides with a reduction of the root bending moment at higher angles of attack, shown in figure 5.1d. This trend is suggestive of tip-stall.

The linear portion of the lift-curve-slope for the planar wing is $-5^\circ \leq \alpha \leq +7^\circ$, while the linear portion of the C-wing is $-5^\circ \leq \alpha \leq +5^\circ$; the resulting lift-curve-slope, C_{L_α}, is 0.100 and 0.104 respectively. At negative angles of attack, the C-wing's top-wing angle of attack becomes increasingly more positive, and thus more strongly down-loaded. Hence, the increasingly down-loaded top-wing reduces the wing's net lift relative to the planar wing, as shown in figure 5.1a, also resulting in the reduced root bending moment seen in figure 5.1d. The down-loaded top-wing also affects the model's pitching moment as shown in figure 5.1a. The top-wing not only provides a restoring nose-up pitching moment for angles of attack lower than the C-wing model's zero-lift angle of attack ($\alpha_o = -2.36^\circ$), but is also seen to maintain a negative pitch stiffness derivative, C_{m_α}, thus implying longitudinal static stability.

Further explanation of how the C-wing modifies the static pitching moment of the semi-span model is provided in figure 5.2. Before stall onset over the main-wing, $\approx 7^\circ$ ($C_{L_{planar}} = 0.946$ or $C_{L_{C-wing}} = 0.949$), the C-wing's top-wing is down-loaded. As stall onset over the main-wing deepens ($\alpha > 7^\circ$), it appears that the top-wing loading changes direction to act in the direction of useful lift creating a restoring nose-down pitching moment. While this is detrimental to the C-wing's ability to reduce the induced drag, it compensates for loss of nose-down pitching moment due to the loss of the main-wing lift from separated flow. Additionally, this is what causes the root bending moment of the wing to increase (relative to the planar wing for $\alpha > 11^\circ$).

Figure 5.1b shows the total drag variation with angle of attack for the planar and C-wing configurations. For angles of attack $\alpha \leq 0^\circ$ the drag of the C-wing is higher with a maximum total drag increase of 16.6% at $\alpha = -5^\circ$. This is due to the C-wing having a 19.1% increased wetted area resulting in a parasitic drag increase. However, the induced drag reduction of the C-wing across the positive angle of attack range is evident; i.e. the induced drag reduction is greater than the parasitic drag increase over this range. Despite this increased wetted area, the C-wing achieves an average total drag reduction of 7.4% over the $0^\circ \leq \alpha \leq +14^\circ$ range. Peak drag reduction is reached at $\alpha = 6^\circ$, with a 9.5% saving. With further increases in the model's angle of attack, the C-wing begins to enter a condition analogous of T-tail aircraft approaching deep stall. In this condition the main-wing's wake begins to impinge on the top-wing reducing its effectiveness.

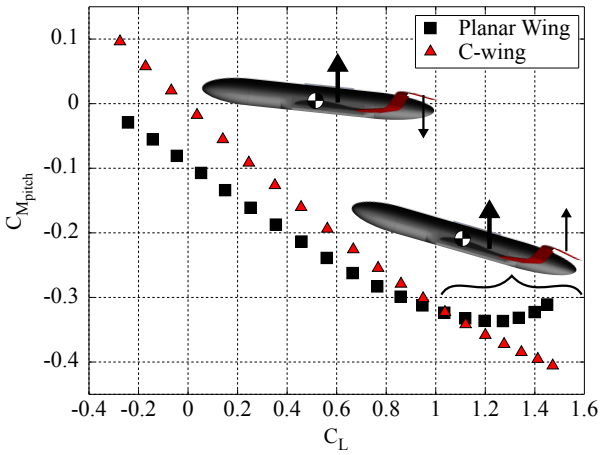

FIGURE 5.2: $C_{M_{pitch}}$ vs. C_L for the planar and C-wing arrangements.

To summarise the trends discussed in the aerodynamic coefficients, figure 5.3 presents the percentage increase/decrease of the C-wing's aerodynamic coefficients as a function of angle of attack relative to the planar wing arrangement. It is evident that at negative angles of attack, the down-force produced by the top-wing causes a reduction in lift and root bending moment, while increasing total drag. This has the combined effect of also reducing the lift-to-drag ratio. Over positive angles of attack ($0° \leq \alpha \leq +14°$), the lift-to-drag ratio increases by an average of 8.5%, with a peak increase of 10.67% at $\alpha = 6°$.

Referring back to figure 2.29 in Section 2.5.4, the VRM aerodynamic predictive model utilised by the genetic algorithm optimisation procedure is observed to accurately predict the relative performance of the C-wing illustrated in figure 5.3. A peak total drag reduction of 11.11% at $\alpha = 6.04°$ was suggested by the VRM. A more direct comparison of the VRM prediction of the wind tunnel semi-span model arrangements is provided in Appendix D.

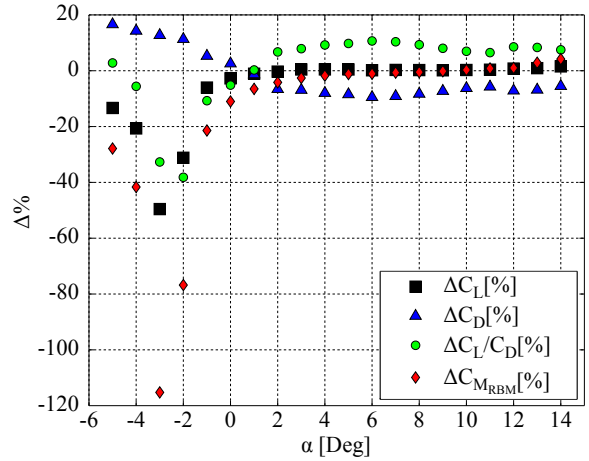

FIGURE 5.3: Percentage change of C-wing arrangement aerodynamic coefficients relative to planar arrangement.

The C-wing theoretically achieves an induced drag reduction via two primary mechanisms: 1) alteration of the main-wing load distribution through promoting a less pronounced decrease in local lift at the main-wing tip; and 2) forward tilting of the side-wing and top-wing lift vectors where the main-wing's downwash is exploited to produce a thrusting effect. The former achieves induced drag reduction through decreasing the downwash of the flow approaching the wing; the downwash caused by circulation at the tip is spread over a larger (longer) surface. The Biot-Savart law indicates that induced velocity (downwash) is proportional to circulation strength and inversely proportional to distance over which the circulation is distributed [238]. This acts to reduced the gradients of circulation [118]. The latter is achieved through loading the side and top-wing in such a way that the C-wing operates as a quasi-closed system of continuous circulation [48]. Due to the induced velocities created by the pressure difference from the main-wing's production of lift, the side and top-wing produce thrust components acting to reduce the induced drag. This effect is illustrated in figure 5.4, where the side-wing's thrust, T_{sw}, is created due to induced velocity U_{mw}, and the top-wing's load vector is tilted forward due to the influence of the flow component U_{sw} caused by the pressure difference at the side-wing, creating the thrust component T_{tw}.

Though the drag reduction is clear, the responsible forces acting on the side and top-wing are not easily isolated from the wing system. The direction of top-wing loading can be inferred due to the lift coefficients observed and resulting pitching moment. Similarly, the net side-force acting on the model is detected via the force platform; the change in side-force between wing arrangements will be dominated by the side-wing contribution. Hence, the side-wing forces and notional model yaw moment for both the planar and C-wing configurations are shown in figure 5.5. It is necessary here to recall the inherent influence of the model mounting shaft wake,

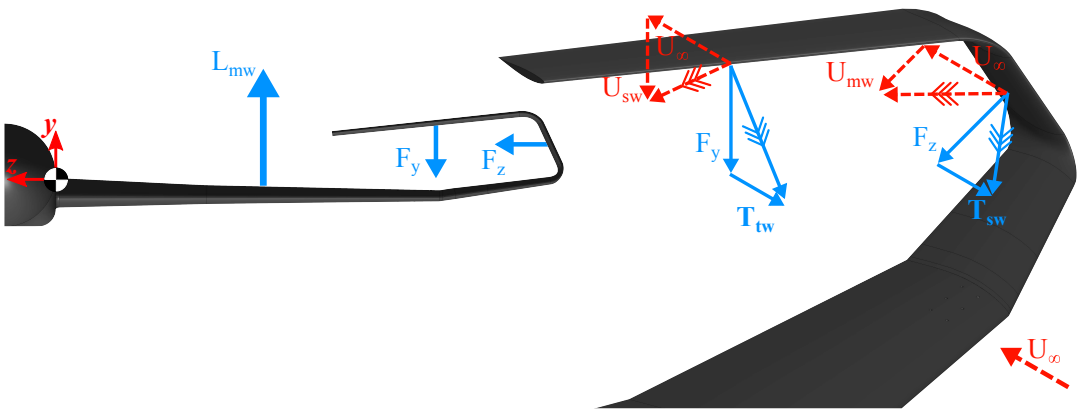

Figure 5.4: Influence of the main-wing on the side-wing, and subsequently the side-wing on top-wing. The dashed red vectors indicate velocities and the solid blue vectors indicate forces.

discussed in Chapter 4. The semi-span model has been mounted with a stand-off gap height $4\delta^*$ in-order to offset the influence of the wind tunnel boundary layer over the model forebody and inboard wing. The mounting shaft between the model symmetry plane and floor has been shown to create a wake which interacts with the flow over the fuselage afterbody whose influence is a function of the stand-off height. The shaft's wake influence on the semi-span model is assumed to be unchanged between the planar and C-wing arrangements, therefore deviations in the side-force and notional yawing moment from planar to C-wing configurations have been assumed to be caused solely by the change in geometry at the wingtip.

Figure 5.5a shows that the side-wing is loaded inboard toward the fuselage for all angles of attack; with highest gains in side-force achieved for the range $-1^\circ \leq \alpha \leq +1^\circ$. This is logical as the side-wing is aft swept at 25°, and therefore, unlike the main-wing or top-wing, will experience an effective increase in sweep relative to the freestream direction as the angle of attack is increased. Additionally, as the wing's angle of attack is increased, consequently increasing the circulation and induced velocities, the resultant force vector will become inclined more into the flow, transferring a component of the side-force from C_{Fz} to C_D. For angles of attack $\alpha > 8^\circ$, a rapid decline in the side-force is noticed. This coincides with stall-onset of the main-wing as indicated by the lift-curve-slope shown figure 5.1a.

Furthermore, due to the inboard loading of the side-wing, in addition to its positioning aft of the model centre of gravity/pitch axis, an increase in the notional model yawing moment occurs, as shown in figure 5.5b. The peak increase in $C_{M_{yaw}}$ occurs over the range $-3^\circ \leq \alpha \leq +2^\circ$.

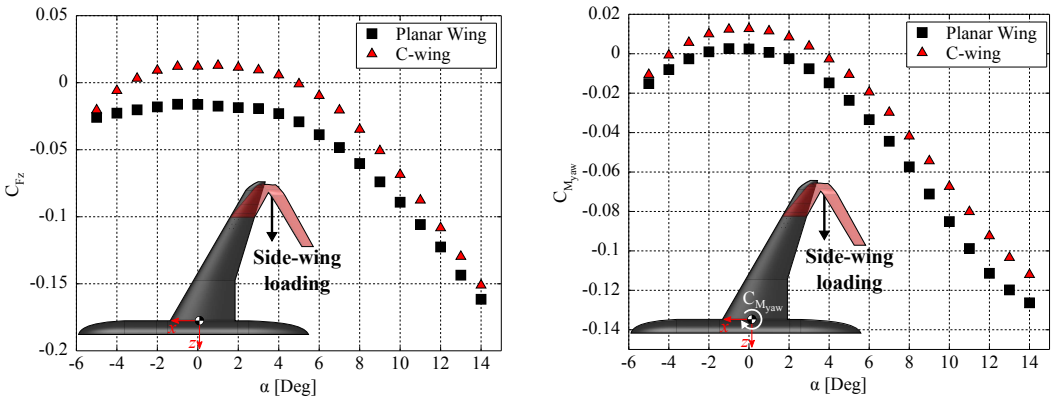

(a) C_{Fz} vs. α (b) $C_{M_{yaw}}$ vs. α

FIGURE 5.5: Vertical (side) force and notional yaw moment acting on model for the planar and C-wing arrangements.

5.3 SURFACE FLOW VISUALISATIONS

Surface clay flow visualisations for the planar and C-wing main-wing at $\alpha = 0°$, 8°, and 14° are shown in figures 5.6a and 5.6b, respectively; the freestream and gravitational force directions are indicated. Qualitatively, structures arising from attached/separated flows, stall cell formations, surface imperfections, and horseshoe vortex interactions can be examined. The flow over each wing's surface at $\alpha = 0°$, shown in figure 5.6a and 5.6b for the planar and C-wing main-wing respectively, is fully attached with no inexplicable deviations from the freestream direction. Vortical wake structures in the order of 4 to 5mm are visible downstream of all six wingtip locking pins in addition to some flow disturbances caused by the wingtip joint; such features have been deemed to have a negligible effect on the global flow field.

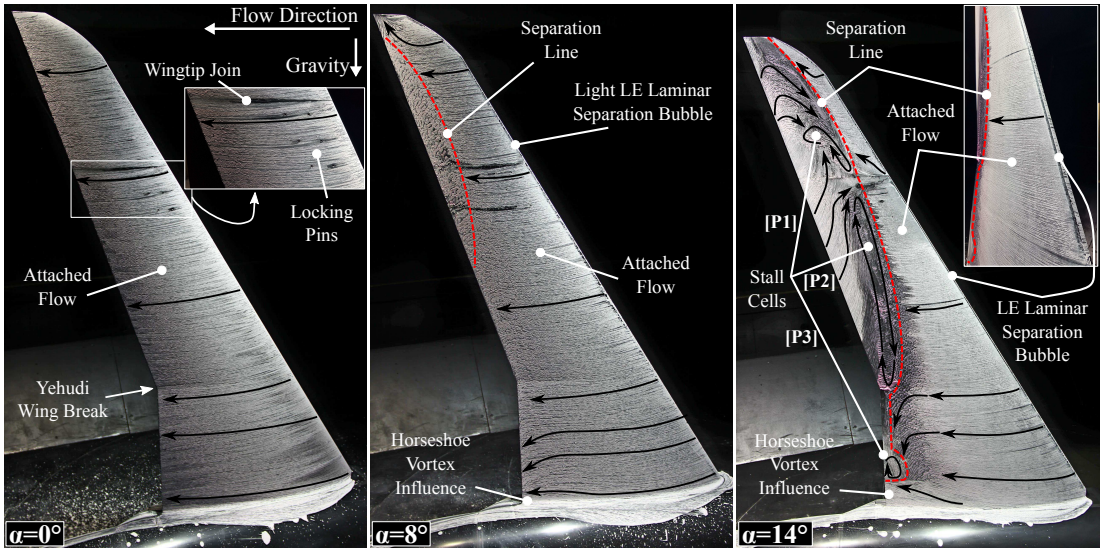

(a) Planar wing.

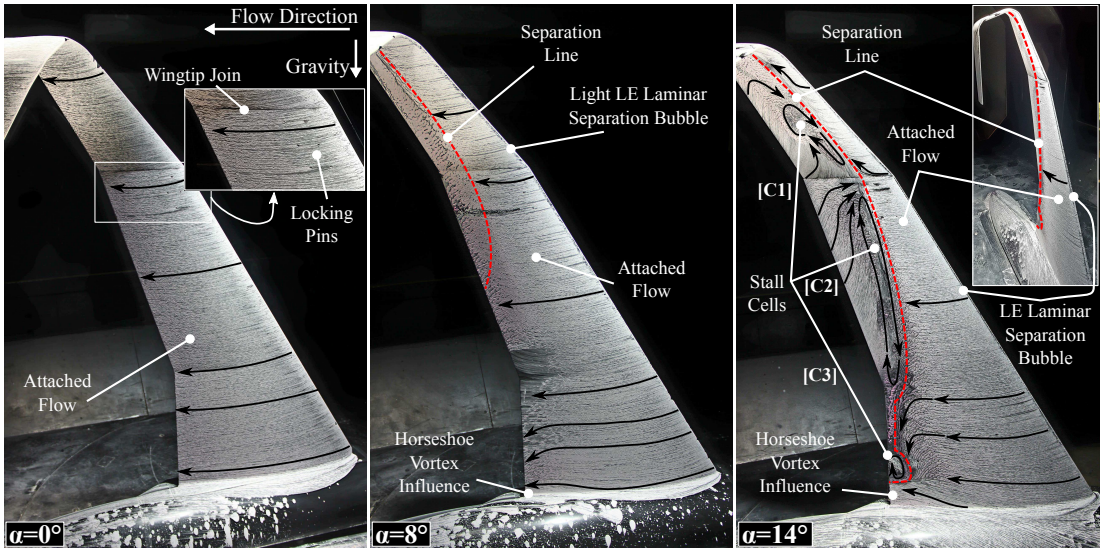

(b) C-wing main-wing.

FIGURE 5.6: Surface clay flow visualisation over the planar and C-wing configurations at $Re = 1.5 \times 10^6$ for $\alpha = 0°$, 8°, and 14°.

For both wing configurations, the clay flow indicates the flow is attached over all surfaces at $\alpha = 0^\circ$. Increasing the model's angle of incidence to $\alpha = 8^\circ$, clear outboard separation is noted for both the planar and C-wing. Outboard stall of the untwisted swept wing, while detrimental to performance, is expected. In addition, this result agrees with lift-curve-slope results from figure 5.1a indicating the onset of stall from $\alpha \approx 7^\circ$. The stall lines in each wing configuration share similar profiles; the only distinctive difference is that the C-wing's stalled region progresses onto the side-wing. Interference patterns due to the locking pins and wingtip joint are indistinguishable from the $\alpha = 0^\circ$ case. At the wing root/fuselage juncture, streamline deviations show evidence of induced flow from a horseshoe vortex; the horseshoe vortex root is located at the leading edge (LE) of the wing root. Furthermore, both wing arrangements show evidence of light LE separation bubbles over the span of the wing.

At $\alpha = 14^\circ$ there are consistent stall characteristics between the planar wing and C-wing's main-wing. Surface flow visualisations for both configurations show the development of three stall cells; these have been labelled P1, P2, and P3 for the planar wing at $\alpha = 14^\circ$ shown in figure 5.6a, and C1, C2, and C3 for the C-wing at $\alpha = 14^\circ$ shown in figure 5.6b. Soon after the wind tunnel reaches stable operating conditions, the progressive accumulation of the clay flow mixture is observed to form along the stall front, and begins collecting in these stall cells. The immediate build-up of clay in the location of the stall cells suggests that the stall cell locations are immediately realised in explicit locations with no large spacial fluctuations. The abundance of the clay in the stall cell is translated from the recirculation region formed by the buckling of the separation front. This is determined from experimental observation and is not explicitly shown in figure 5.6. However, it is noticed that a consistent modification of the clay flow streamlines from their otherwise straight path is seen upstream of the separation as they blend together into the separation front.

The wing-to-wingtip joint appears to act in a similar manner to a vortex generator, in that the resulting turbulence promotes attached flow which appears to divide a larger stall cell into two as seen in figure 5.6a and 5.6b at $\alpha = 14^\circ$. This moves a smaller stall cell towards the wingtip, labelled P1 and C1, from a much larger stall cell extending from the wingtip joint down to the yehudi wing break, P2 and C2, which are indistinguishable from one another. This phenomenon occurs for both the planar and C-wing, however the stall cell C1 located towards the C-wing main-wing tip appears larger relative to P1. This is likely caused by the stall progressing onto the C-wing's side-wing, which has the effect of elongating stall cell C1.

Stall cell P3 for the planar wing and C3 for the C-wing, located at the wing TE near the wing root at $\alpha = 14^\circ$, show similar interactions with the wing root horseshoe vortex which forces reattachment inboard of P3/C3. The induced flow from the horseshoe vortex, coupled with boundary layer thickening inboard of the yehudi, is seen to have the effect of sharply turning the inboard wing flow down towards stall cell P3/C3 as suggested by the streamlines and the build-up of clay. From the

experimental observations and the development of the surface streamlines with time, it is assumed that forces due to gravity are negligible, and that fluid dynamic shear forces from the flow on the clay are dominant.

Additionally, common between both configurations at $\alpha = 14^\circ$ is the formation of a LE separation bubble over most of the wingspan as indicated in figures 5.6a and 5.6b. As the wing is untwisted, the separation bubble forms a straight line along the LE. At the operational Reynolds number regime of 10^6 a short separation bubble is expected to occur as the very initial flow in contact with the wing is laminar. Since a laminar boundary layer is incapable of coping with anything but a very slight adverse pressure gradient, the flow almost immediately separates. The separated flow then transitions to turbulence, entraining fluid and re-attaching, forming a turbulent boundary layer. In other words, the laminar separation bubble represents the transition-forcing tripping mechanism to a turbulent boundary layer. At the operational Reynolds number, and angles of attack of interest, this separation bubble will remain 1 to 2% of the local chord and will not greatly affect performance. The formation and structure of a laminar separation bubble at the wing LE is described in detail by Wallis [299] and Lissaman [300].

In consideration of the force and moment data presented in Section 5.2, it is realised that the angle of attack range with peak drag reduction coincides with strong side-wing loading. The aerodynamic coefficients evaluated suggest that a drop-off in the C-wing's ability to reduce the induced drag diminishes as the main-wing exceeds $\alpha = 8^\circ$. As previously mentioned, figure 5.6b appears to indicate the progression of stall from the main-wing onto the C-wing's side-wing at $\alpha = 8^\circ$ and 14°. Figure 5.7 presents the progression of this stalled region from the main-wing on to the side-wing for the $\alpha = 14^\circ$ case.

Stall cells C1 and C2 are identified in addition to the stall line advancing from the main-wing to the side-wing, unhindered by the connecting blend. Identification of this feature supports the conjecture made previously regarding the rapid decline in the production of side-force, which also coincides with the deterioration of the

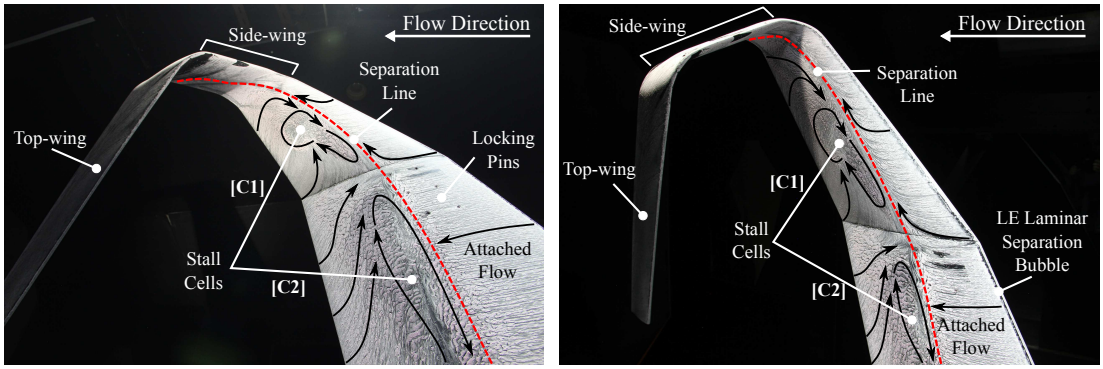

Figure 5.7: Surface clay flow visualisation over outboard C-wing at $Re = 1.5 \times 10^6$ for $\alpha = 14^\circ$ illustrating main-wing stall progression onto side-wing.

C-wing's drag reduction capability.

5.4 WINGTIP DEFLECTION

The planar and C-wing arrangement wingtip translation and rotation from aerodynamic loading at $Re = 1.5 \times 10^6$ for several angles of attack have been inferred using an in-house two-dimensional direct imaging correlation (DIC) technique. Wingtip translation and rotations are presented in figure 5.8.

Figure 5.8 indicates that each wing arrangement shows a similar bend-twist behaviour at the wingtip; negative elastic twist angles indicate leading edge down rotation. Peak wingtip deflections of $\omega/\bar{c} = 0.2065$ and 0.2259, for the planar and C-wing respectively, occur at $\alpha = 14°$. The effect of the C-wing's top-wing is seen to be responsible for modifying the wingtip translation. At lower angles of attack ($\alpha < 8°$), the top-wing is down-loaded (opposing main-wing lift) and therefore reduces the wingtip translation, as shown in figure 5.8a. Similarly, figure 5.8b illustrates that the top-wing down-loading enforces a nose up pitching moment which increases the wingtip twist angle. The negative trend of the wingtip rotation with angle of attack suggests that the aerodynamic centres along the wing lie slightly aft of the elastic axis. At angles of attack $\alpha > 8°$, figures 5.8a and 5.8b suggest that the C-wing becomes up-loaded (contributing to main-wing lift) therefore increasing the wingtip translation, and now imposing a nose down pitching moment at the wingtip relative to the planar wing. This result is in agreement with the aerodynamic coefficient trends observed in figure 5.1.

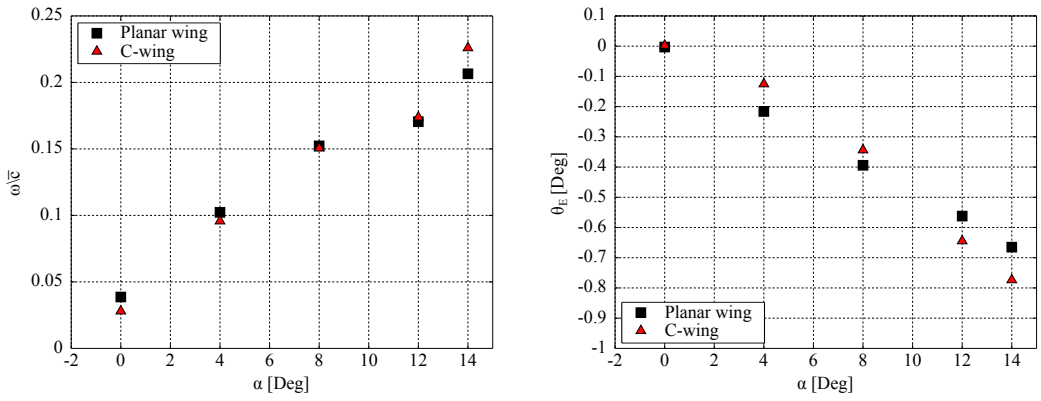

(a) Mean wingtip translation.

(b) Mean wingtip elastic twist.

FIGURE 5.8: Planar and C-wing main-wing wingtip translation and elastic twist rotation with angle of attack at $Re = 1.5 \times 10^6$.

5.5 MODEL VIBRATION AND STRUCTURAL DYNAMICS

5.5.1 Laser-Doppler Vibrometry Bump Tests: Wind Off

The transient response from bump tests for both the planar wing and C-wing arrangements has been analysed to better understand fundamental vibrational characteristics without the influence of wind loading (vibrations from wind tunnel turbulence) and forced wind tunnel vibrations (vibrations related to natural frequencies of the wind tunnel structure). By focusing the laser-Doppler vibrometer to different measurement locations and bump testing the model, thereby exciting all natural frequencies of the model, measurements of the associated natural frequencies and system damping can be identified. The excitation 'bump' is applied via a pendulum at the test locations indicated, where the impact force is perpendicular to the surface and consistent to within 4%. Since the measurements are one-dimensional, the bending and torsional modes cannot be definitively differentiated. However, from the experimental observations the dominant modes are anticipated to be the bending modes, which is typical of swept wings.

The frequency response evaluated from the main-wing for both wing configurations are shown in figure 5.9. The bump test location indicated in figure 5.9 is $z/b = 74\%$ of the wingspan on the wing flexural axis; the flexural axis along the wing is located at 34% of the local chord. The C-wing demonstrates a more complex vibrational system, however there is a clear attenuation of the vibration of the main-wing structure. The bump tests show a 41.2% attenuation of the first mode (7.2Hz planar and 5Hz C-wing), and a 45.8% attenuation of the second mode (33.5Hz planar and 32.1Hz C-wing) in figure 5.9. The C-wing is also observed to introduce a unique low magnitude split-peak within the frequency domain at 8.45Hz and 8.98Hz.

The top-wing extension is suitably positioned for passive vibration absorbency as

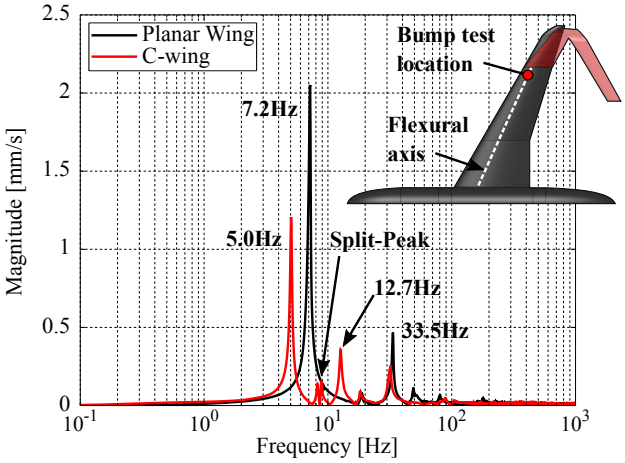

Figure 5.9: Bump test frequency response for the planar and C-wing main-wing; bump test location indicated.

is it connected via wingtip which will experience the main-wing's greatest amplitude deflections [301]. In this situation it will perform as an axillary mass within a tuned mass-damper system. Such a design is expected to introduce other peak response frequencies in the structure, typically one below and the other above the excitation frequency it suppresses [302, 303]. The dominant $7.2Hz$ peak present in the planar wing has been broken down into two reduced magnitude frequency shifted peaks in the C-wing configuration ($5.0Hz$ and $12.7Hz$). This behaviour is indicative of the C-wing acting as a dynamic vibration absorber [304, 305, 306], absorbing the vibrational energy within a certain frequency interval thereby reducing the dynamic response of the system. The sharpness of the frequency peaks implies that the vibration absorber has very low damping [304]; a damped/tuned vibration absorber would have characteristically softer peaks.

Examination of the bump tests performed directly on the C-wing's top-wing is presented in figure 5.10. The characteristic split-peak of the C-wing is noticed to be more predominant; the bump test location shown in figure 5.10 is located on the C-wing's top-wing wingtip at 34% local chord. The $5Hz$ main-wing mode persists in the C-wing top-wing bump test, while the $12.7Hz$ mode is barely registered. Relative to the $5Hz$ peak, the split peak is approximately three times the magnitude. Also shown in figure 5.10 is the results of applying full wave rectification (taking the absolute values of the raw signal) to the vibrational signal recorded from the C-wing top-wing bump test. This reveals a 'hidden' frequency at $0.27Hz$, referred to as the amplitude modulating frequency, f_{AM}.

The temporal response of the bump tests are shown in figure 5.11, and can be used to gain further insight into this amplitude modulating frequency and it's role within the observed split-peak phenomena. Main-wing vibrations under bump testing for both the planar and C-wing cases (indicated in figure 5.9) give temporal responses shown in figures 5.11a and 5.11b, respectively. Perceptual segregation of the modal

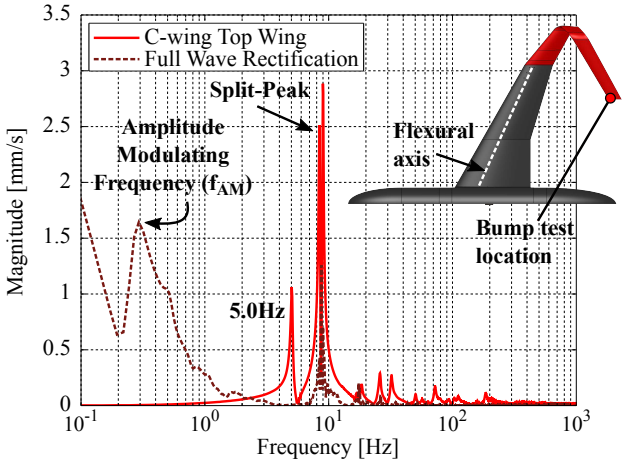

FIGURE 5.10: Bump test frequency response the C-wing's top-wing; bump test location indicated.

frequencies has been achieved through applications of elliptic bandpass filters which can provide sharp roll-off, helping to isolate frequencies that are close to one another. The overall system reaction to bump tests characteristically resembles the response of an under-damped 2^{nd} order system. This free vibration, due to an initial displacement X_o, is theoretically described by:

$$X(t) = X_o e^{-\zeta\omega_n t}\left\{cos\omega_d t + \frac{\zeta}{\sqrt{1-\zeta^2}} sin\omega_d t\right\} \tag{5.1}$$

Within the C-wing's response, an amplitude modulated vibrational mode with a frequency of $8.72Hz$ is observed in figure 5.11b; this frequency is the average of the split-peak. The amplitude modulated response is clearer if the C-wing top-wing is considered directly, this is shown in figure 5.11c. This temporal response is, at first glance, made up of two frequencies: 1) an $8.72Hz$ wave, analogous of a carrier wave; and 2) an amplitude modulating wave enveloping the carrier wave at $0.27Hz$. Referring back to figure 5.10, illustrating the bump test of the C-wing top-wing in the frequency domain, it appears that no information concerning the amplitude

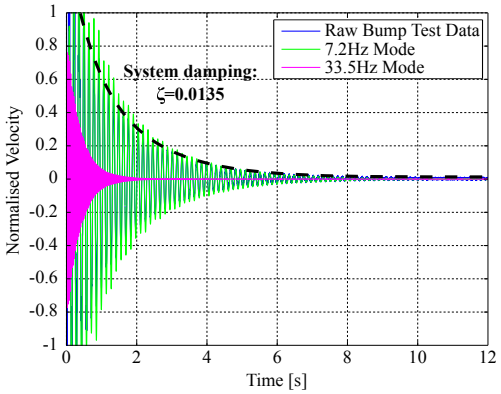

(a) Temporal response of planar wing; bump test indicated in figure 5.9

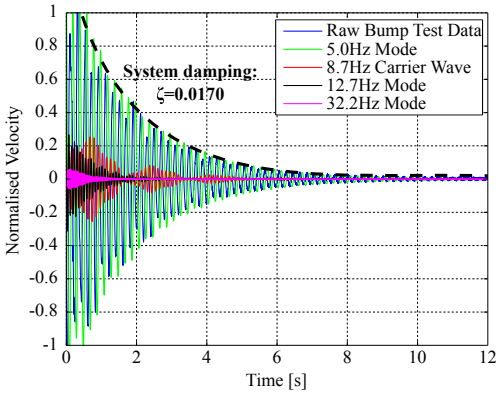

(b) Temporal response of C-wing main-wing; bump test indicated in figure 5.9

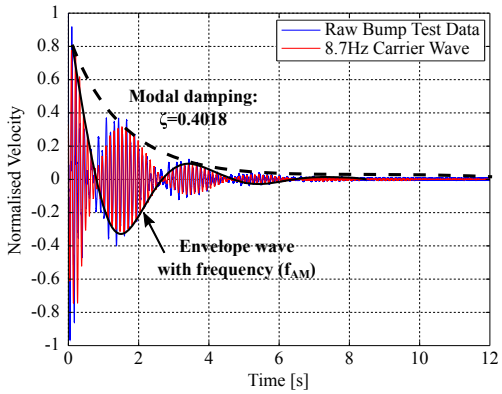

(c) Temporal response of C-wing top-wing; bump test indicated in figure 5.10

Figure 5.11: System and dominant mode temporal responses of wing configurations undergoing bump tests.

modulating signal is immediately obvious. In the presence of amplitude fluctuations, the ability to detect the modulation of the signal can be masked by the presence of multiple carrier waves. This effect is known as modulation detection interference (MDI), and by applying full-wave rectification to the signal (taking the absolute signal values), it is possible to detect the amplitude modulation frequency. Furthermore, as pointed out by Hall and Grose [307], MDI occurs when two or more carrier waves are superimposed into a singular waveform, which brings attention back to the split-peak observed in figures 5.9 and 5.10.

The two carrier waves, with frequencies of $8.45Hz$ and $8.98Hz$, are identified to be the natural frequencies of the side-wing and top-wing respectively. Considering the physical vibration and interaction between these two components, they are inherently mechanically coupled. Thus with the two vibrations excited simultaneously, the law of superposition states that the total amplitude is the sum of the vibrational amplitudes at time t. Figure 5.12a and 5.12b simulate the undamped vibration of the side-wing and top-wing with frequencies f_{sw} and f_{tw}, respectively; where f_{mw} is the fundamental bending mode frequency of the main-wing. Figure 5.12c shows the superposition of the side and top-wing vibrations resulting in an interference pattern with amplitude oscillations of $0.27Hz$, and a carrier frequency equal to the average of the interfering waves $f_{av} = 8.72$. This phenomenon is called beating. The beating pattern is the result of two waves with similar frequencies which merge creating points of constructive and destructive interference as labelled in figure 5.12. When local maxima of the two waves are 180° $(\pi \ radians)$ out-of-phase, the maxima of one wave cancels the minima of the other (destructive interference). When the local maxima of the two waves have no phase difference, and are therefore in-phase, the interference pattern shows increased amplitude (constructive interference). The beating pattern can be assessed through consideration of trigonometric identities, leading to equation 5.2, to aid in the explanation of the beating observed.

$$cos(2\pi f_{tw}t) + cos(2\pi f_{sw}t) = 2cos\Big(2\pi \underbrace{\frac{f_{tw} + f_{sw}}{2}}_{f_{av}} t\Big) cos\Big(2\pi \underbrace{\frac{f_{tw} - f_{sw}}{2}}_{f_{AM}} t\Big) \tag{5.2}$$

Equation 5.2 characterises the interference pattern created as the periodic variation in the amplitude (amplitude modulation) of a single carrier wave with frequency f_{av}, where the function modulating the amplitude is occurring at frequency f_{AM}. Intuitively beats occur at twice the amplitude modulating frequency, thus the number of beats per second is the difference in frequency between the two interfering waves:

$$f_{beat} = |f_{tw} - f_{sw}| \tag{5.3}$$

A summary of the vibrational frequencies associated with the C-wing bump tests and the domain in which they are detectable is summarised in table 5.1.

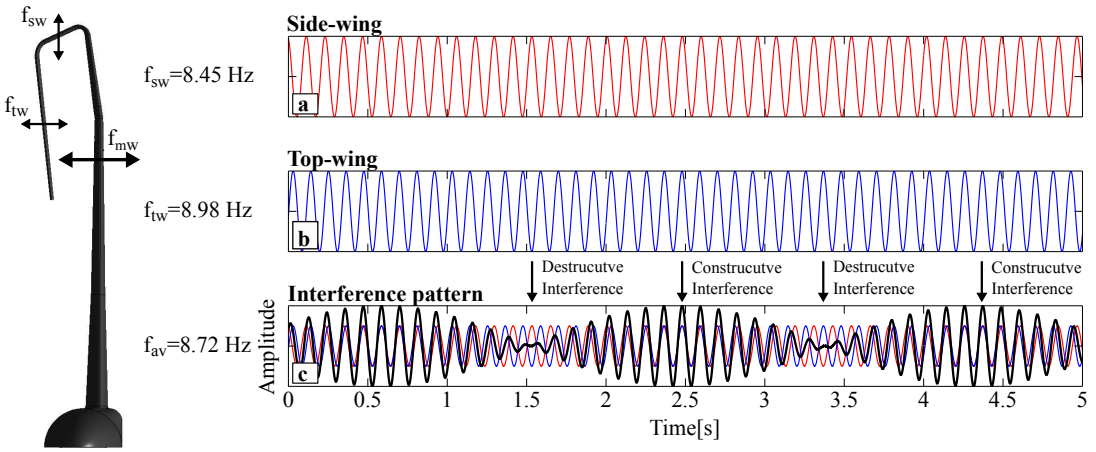

Figure 5.12: Explanation of beating interference pattern observed from the interaction between the side and top-wing vibrations.

	Observed Frequencies				
Detection	f_{sw}	f_{tw}	f_{av}	f_{AM}	f_{beat}
Frequency Domain	✓	✓		✓	
Temporal Domain			✓	✓	✓

Table 5.1: Summary of frequencies associated with the C-wing in free vibration and the domain in which they are detectable.

Table 5.1 serves to emphasise the complexity of the C-wing structural dynamics. Bump tests undergoing free vibration have enabled the observation of a temporally modulated interference pattern embedded within the dynamic noise of the C-wing vibration. This will provide a deeper understanding of the wing vibrational behaviour when aerodynamically loaded, and exposed to aeroelastic phenomena.

Briefly considered in Section 4.4, the force platform is connected via a steal mounting interface through the fuselage symmetry plane, hence the natural frequencies relating to the fuselage must also be examined with the exclusion of the wind tunnel vibrations. This is necessary to fully understand and explain the frequencies of the forces and moments monitored by the force platform under live experiments. Figure 5.13 shows the bump test responses observed in the longitudinal axis of the fuselage for both the planar and C-wing arrangements. Examination of the figure shows that the effect of different wing configurations is negligible on the frequency spectra where there are two distinct frequencies; the low magnitude of the vibrations are due to the high stiffness of the fuselage. The registered $9.3Hz$ is anticipated to be related to the fundamental bending mode of the main-wing structure, previously identified at $7.2Hz$ for the planar wing, and $5Hz$ for the C-wing. It is logical that a frequency shift in the wings fundamental mode is observed between the two measurement locations as they structurally separated by several components of varying material. The $39.9Hz$ frequency is only excited through longitudinal bump tests of the fuselage.

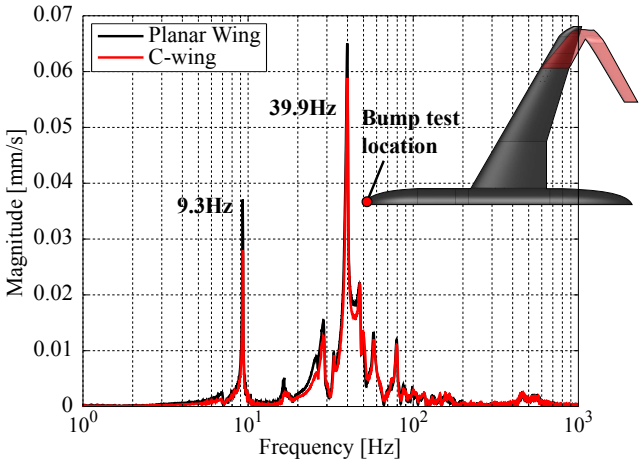

FIGURE 5.13: Frequency response observed in the longitudinal fuselage axis; bump test measurement location indicated.

5.5.2 MODEL VIBRATION DURING WIND TUNNEL TESTS: WIND ON

LASER-DOPPLER VIBROMETRY

The measurement locations with the laser vibrometer during live wind tunnel experiments are identical to those considered for the bump tests. Figures 5.14a and 5.14b show the frequency response of the planar and C-wing configurations respectively at three angles of attack ($\alpha = 0°$, $8°$, and $14°$). The frequency responses displayed have been averaged over five repeat experiments, each 25.6 seconds in duration sampling at $10kHz$ providing a resolution of $39\mu Hz$. Measurement locations are identical to those taken for bump tests in figure 5.9.

The frequency responses for each wing arrangement, shown in figure 5.14, identify the same modal frequencies as the bump test results presented in figures 5.9. Confirming the findings obtained from the bump tests which suggested that the C-wing would operate as a dynamic vibration absorber, figure 5.14 shows a remarkable attenuation of all fundamental wing vibrations. The $7.2Hz$ peak present in the planar wing has been split into two frequency shifted peaks in the C-wing configuration, at $5.3Hz$ and $11.8Hz$ respectively, under static wind tunnel tests. The split-peak arising from the side and top-wing vibration is noticeable but could have been over looked and regarded as mechanical noise had the bump tests not highlighted its existence.

It is noticed that when transitioning from $\alpha = 0°$ to $8°$ the vibration magnitude for each wing arrangement decreases. The reason for this is that as the wing becomes more heavily loaded, and separation does not yet impose an oscillation of the lift, the structural vibrations are attenuated. This will be discussed further later. Considering the first two dominant modes of each wing configuration (1^{st} mode: $7.2Hz$ for planar; $5.3Hz$ for C-wing; and 2^{nd} mode: $33.5Hz$ for planar; $32.2Hz$ for C-wing), table 5.2 gives a summary of attenuation or amplification of the C-wing's main-wing vibrations

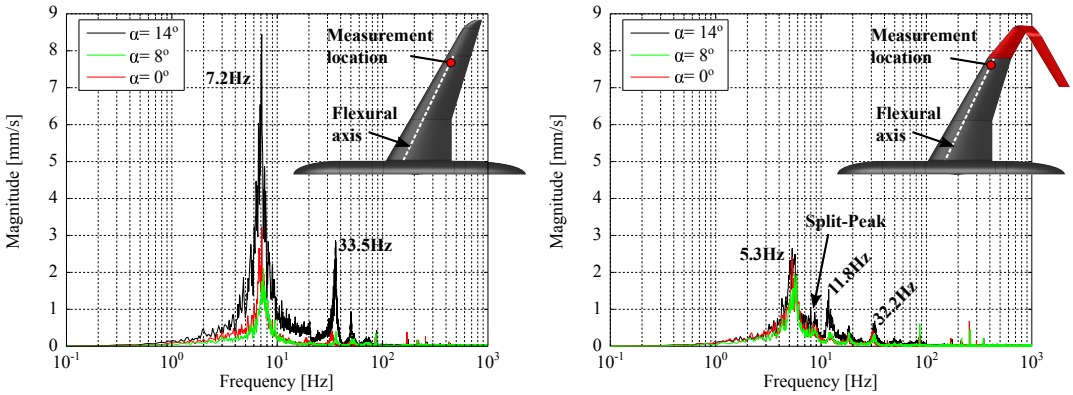

(a) Planar wing.

(b) C-wing main-wing.

Figure 5.14: Frequency response, detected by the laser vibrometer, for each wing arrangent at $\alpha = 0°$, 8°, and 14°, at $Re = 1.5 \times 10^6$; measurement locations indicated are identical to those used in figure 5.9.

Table 5.2: Percentage change of the first two primary modes illustrating whether modal vibrations of the main-wing were attenuated or amplified by the C-wing relative to the planar wing.

α	1^{st} Mode [Δ%]	2^{nd} Mode [Δ%]
0°	-25.22	+3.98
8°	-7.46	-20.55
14°	-68.63	-76.01

relative to the planar wing.

While there is a slight amplification of the second dominant mode at $\alpha = 0°$ in table 5.2, all other cases show attenuation of the vibration amplitude. As separation over the upper side of the wing spreads, the wing will begin to buffet, the strength of which will increase with angle of attack. Notably, the C-wings ability to attenuate the main-wing vibrations improves as buffeting/separation deepens; 68.63% attenuation of the fundamental mode is achieved at $\alpha = 14°$. This is made clearer if the peak magnitudes of the two primary modes from each wing are examined across the entire angle of attack range. Figure 5.15 summarises this by presenting the peak velocity magnitude vibration response detected from the main-wing vibrations, including the data shown in figure 5.14, for both the planar and C-wing configurations.

Examining the 1^{st} mode peak vibration magnitude of the planar wing, it is observed that the wing vibrations gradually increase between $\alpha = -5°$ and $+2°$. This is due to the wing being lightly loaded, with natural frequencies of the wing excited by the freestream turbulence [308]. The peak vibration amplitude is then observed to decrease between $\alpha = 2°$ and 10° before rapidly increasing due to buffeting; over this range the wing loading will increase with angle of attack. Some studies [309] have suggested that increased wing loading will impose a stress distribution through the wing structure increasing its effective stiffness. This would only be possible

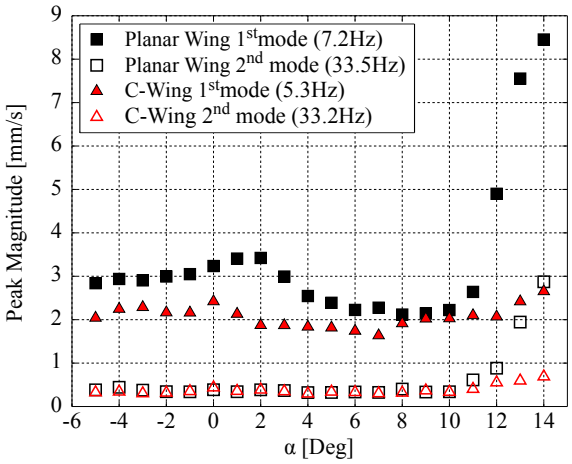

FIGURE 5.15: Summary of peak vibrational velocity magnitudes observed for the planar and C-wing wing's; measurement locations identical to those designated in figure 5.9.

due to structural non-linearities, imposing an increase in the vibration's frequency while reducing the vibration's amplitude. The vibrational frequencies of the wing arrangements in the current work (manufactured from polyurethane foam—a linearly elastic material) do not experience any frequency shift under increasing aerodynamic load. From Section 5.4 it is also understood that each wing arrangement deforms under increasing aerodynamic loads in a linear manner. Thus, a reasonable explanation of the reduction of vibration peak amplitude is provided by Whalley [310], who indicates that as aerodynamic loading increases transient oscillations of the wing structure will subside as the lift distribution holds the wing's statically deformed shape under higher tension. The 2^{nd} mode of vibration for each wing arrangement is observed to be relatively insensitive to the wing loading, only increasing due to buffeting for $\alpha > 10^{\circ}$.

Peak vibration magnitudes for the C-wing structure are shown to consistently attenuate mode vibrations relative the planar wing, while also demonstrating reduced sensitivity to angle of attack. The 1^{st} mode exhibits similar behaviour to that of the planar wing. Vibration of the main-wing structure is noticed to increase slightly at 8°, before buffet onset, due to the top-wing impinging on the main-wing's wake. For $\alpha > 10^{\circ}$, with the main-wing exposed to buffet induced oscillation, the C-wing's ability to attenuate the main-wing vibration in clear from figure 5.15.

From surface clay flow visualisations in Section 5.3 it is shown that the planar and C-wing have similar stall characteristics. Buffeting results from a particular form of unsteady separation arising over a wing facilitating vibrations in the wing structure. Previous studies [251] have shown that the predominant buffet frequencies are expected to correspond to the fundamental bending frequency. This phenomenon is not critical for aircraft but does limit the flight envelope of commercial aircraft as the maximum allowable intensity of buffet is limited by regulations for passenger comfort and safety. Buffeting can become detrimental to the flying performance and

manoeuvrability of the aircraft. If a reduction in the intensity of buffeting could be achieved for a typical commercial aircraft this would allow flight at higher altitudes, enable the aircraft to cope better with high angle of attack manoeuvres, and increase the maximum allowable take-off weight [24, 251]. In other words, the wing would be able to perform better scenarios of high-wing loading and increased sectional lift coefficient.

Modern attempts to reduce buffeting are typically approached in one of two ways: 1) applying small static actions to control surfaces to slightly increase lift; 2) modifying the wing aerodynamics to avoid flow separation by adapting the wing profile or using mechanical vortex generators. The latter can be difficult to implement while only delaying buffet occurrence and does not reduce its intensity. In addition, aerodynamic modifications (such as mechanical vortex generators) are only effective in respect of buffeting of a specific nature and have been shown to increase drag in nominal cruise conditions [311]. There have been some attempts to actively reduce buffeting of swept wings in view of addressing a broad frequency spectrum, but these methods are complex, require instrumentation, feedback control systems, power supply, and will add significant weight to the wing [312, 313]. The findings of this study have shown that the C-wing passively attenuates the main-wing vibration, whilst simultaneously reducing total drag without a significant increase in the weight or root bending moment.

In its simplest form, the dynamics of the C-wing operating as a passive vibration absorber consists of an axillary mass (the top-wing) coupled to the main vibrating mass (the main-wing) via a spring–damping element (the side-wing). This is illustrated in figure 5.16.

Thus, the C-wing dynamic vibration absorbency provided by the auxiliary mass (top-wing) to the main vibrating system (main-wing) can be described by the differential equations 5.4 and 5.5.

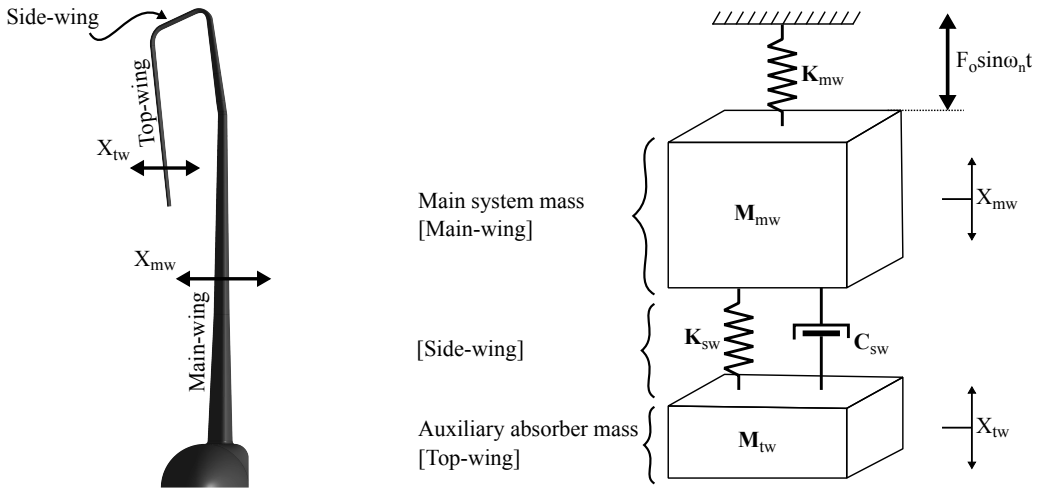

Figure 5.16: Simplified schematic of the C-wing vibrating system.

$$\mathbf{M}_{mw}\ddot{X}_{mw} + \mathbf{C}_{sw}(\dot{X}_{mw} - \dot{X}_{tw}) + \mathbf{K}_{mw}X_{mw} + \mathbf{K}_{sw}(X_{mw} - X_{tw}) = F_o sin\omega_n t \tag{5.4}$$

$$\mathbf{M}_{tw}\ddot{X}_{tw} + \mathbf{C}_{sw}(\dot{X}_{tw} - \dot{X}_{mw}) + \mathbf{K}_{sw}(X_{tw} - X_{mw}) = 0 \tag{5.5}$$

At frequencies well below resonance of the auxiliary mass, both masses can be expected to move in phase with little/no vibration absorbency observed. This is indeed the case for the C-wing tested here; table 5.2 indicates that the C-wing's vibration attenuation capability becomes more effective as stall progression (and subsequent buffet) spreads. Above the resonant frequency, the auxiliary mass provides an apparent fixed point in space which results in an opposing force being transmitted to the main-system. Through conservation of energy, the amplitude of displacement/velocity of vibration of the main system is reduced as kinetic energy is transferred to the auxiliary mass, thereby increasing the amplitude of displacement/velocity of vibration of the auxiliary mass [314]. The vibration of the auxiliary mass (the top-wing) will move out-of-phase with the main-wing. Therefore, the elastic deformation of the side-wing is not only key for the transfer of forcing/kinetic energy, but also plays an important role in the mechanical impedance of the system and could be an expected point of structural failure manifested through material fatigue over time.

Figure 5.17 shows the frequency response of the C-wing's top-wing at three angles of attack ($\alpha = 0°$, $8°$, and $14°$) under the same test conditions for the results shown in figure 5.14, with the same measurement location for bump tests of figure 5.10. The relative magnitude between the top-wing's peak vibrations relative to the main-wing's peak vibrations, shown in figures 5.17 and 5.14b respectively, have been summarised in table 5.3.

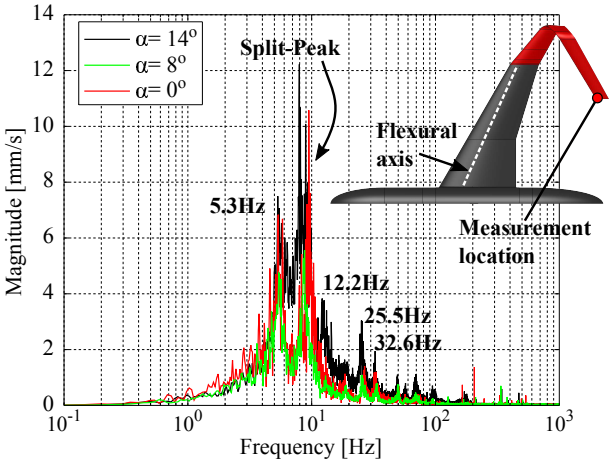

FIGURE 5.17: Frequency response, detected by the laser vibrometer, of the C-wing's top-wing at $\alpha = 0°$, $8°$, $14°$, at $Re = 1.5 \times 10^6$; measurement locations indicated are identical to those shown in figure 5.10.

Table 5.3: Percentage difference of the dominant vibration magnitude observed in the C-wing's top-wing relative to the C-wing's main-wing.

α	Change in peak vibration magnitude [Δ%]
0°	+337.19
8°	+183.83
14°	+361.16

Due to the nature of the top-wing acting as a vibration absorber, and therefore absorbing kinetic energy from the main-wing, the dominant velocity magnitudes of the top-wing are significantly higher than that for the main-wing. This characteristic was also observed in bump tests comparing the C-wing main-wing response from figure 5.9, to the C-wing top-wing response in figure 5.10. For $Re = 1.5 \times 10^6$ at $\alpha = 14°$, the velocity magnitude of the top-wing is noted to be 361.16% higher than that detected for main-wing structural vibrations.

It is appreciated that the induced vibrations from buffeting are entirely different from gust loading and violent manoeuvres in a turbulent atmosphere with unsteady transient phenomena of short duration. Buffeting is induced by aeroelastic coupling between a constant source of excitation which can persist for long periods and has a stable and reproducible response. Consequently, particular flight conditions such as gusts do not occur under the same conditions, therefore the C-wing's structural vibration absorbency may not achieve the same level of attenuation when exposed to transient external stimulus.

Accelerometry: Phased Wing Vibration

Supplementary to the laser-Doppler vibrometry measurements, PCB piezoelectric accelerometers have also been employed. This enhances the understanding of the wing's structural dynamics by enabling a vibrational phase analysis which cannot be performed with the single point laser vibrometer. Three accelerometers have been fixed to the wing surface in various arrangements in order to ascertain certain vibrational phase relationships.

Figure 5.18 presents data for the accelerometers applied to both the planar and C-wing configurations, in the so-called *'arrangement 1'*: all sensors at $z/b = 74\%$ wingspan, with sensor 1, 2, and 3 placed 5%, 34% (elastic axis), and 95% of the local chord, respectively. The test condition presented in figure 5.18 is with the wing at $\alpha = 8°$ for $Re = 1.5 \times 10^6$.

The results in figure 5.18 support those provided through the vibrometry measurements. Frequency responses of the two configurations, with the planar shown in figure 5.18a and the C-wing in figure 5.18c, indicate the attenuation and frequency shift of the primary mode, indicative of vibration absorbency characteristics. The split-peak

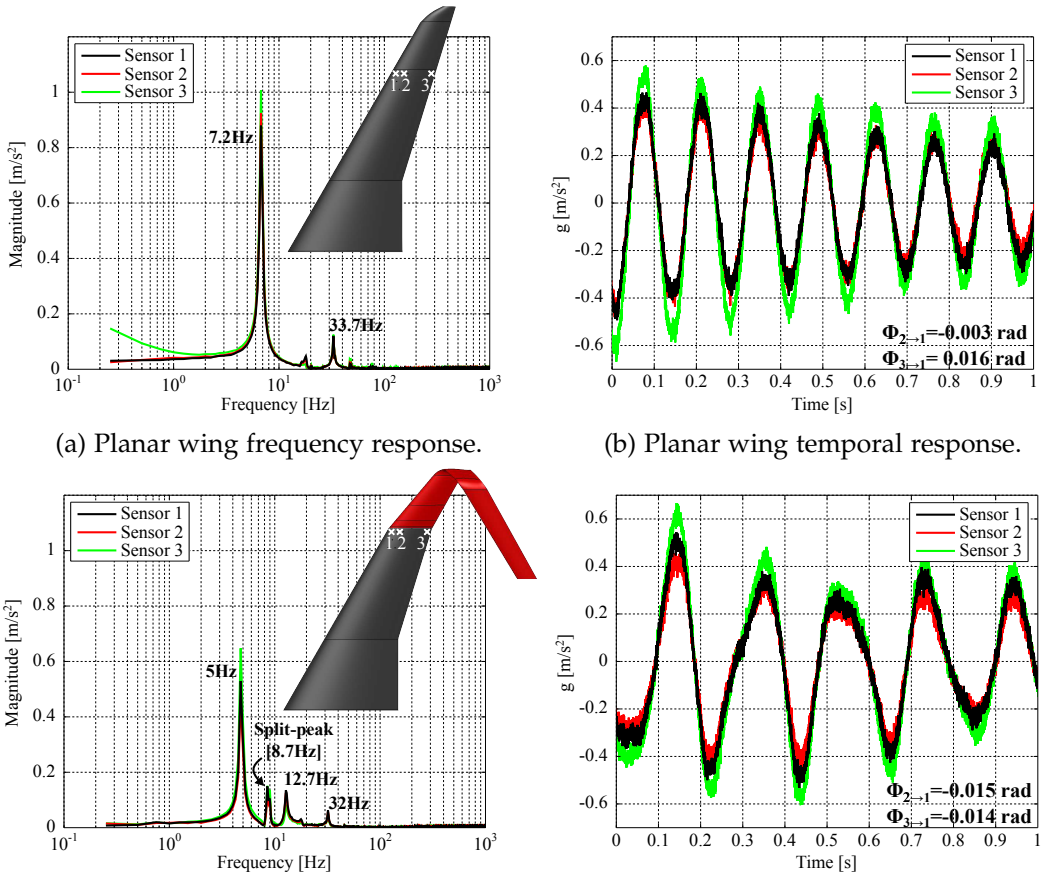

(a) Planar wing frequency response.

(b) Planar wing temporal response.

(c) C-wing frequency response.

(d) C-wing temporal response.

FIGURE 5.18: Accelerometer arrangement 1 for $\alpha = 8°$.

caused by the side and top-wing beating interference is also observed. Considering the temporal domain of the vibration shown in figures 5.18b and 5.18d, for the planar and C-wing respectively, it is evident that the vibrations detected across the chord at the $z/b = 74\%$ wingspan are in-phase: $\approx 0rad$). This implies that there are no dominant torsional modes, confirming that all frequencies detected are indeed bending modes. Furthermore, the phased vibration between two sensors, *i.e.* the torsional modes, can be address directly by subtracting the signal from any two sensors. Doing so cancels each signal leaving broadband noise of the order of $0.04g$. As there is no detected phase relationship over the chord length of the wing, this further supports the conclusion of no dominant torsional modes in either wing arrangement. This result is found for all angles of attack. It is necessary to acknowledge that torsional modes $<< 1Hz$ may exist as the accelerometers are unable to register such frequencies. Similarly, torsional modes of higher frequency and very low amplitude may be present, however such modes will remain undetected due to low acceleration amplitudes.

Regarding the general vibrational patterns of each wing, the planar wing's temporal vibration waveform appears smooth and sinusoidal whereas the C-wing's oscillatory motions are more irregular. This is due to the C-wing operating with a more complex vibrational signature (indicated by comparing the frequency domain responses), from which constructive and destructive interference patterns warp the

dominant sinusoidal motion.

Rearranging the accelerometers into the so-called *'arrangement 2'* for the C-wing places sensor 1 at $z/b = 74\%$ wingspan placed at 34% (elastic axis) of the local chord, and sensors 2 and 3 at $z/b = 54\%$ wingspan on the C-wing's top-wing wingtip placed at 5% and 95% of the local chord, respectively. The results for the C-wing with this accelerometer arrangement at $\alpha = 14^\circ$ at $Re = 1.5 \times 10^6$ is shown in figure 5.19.

From both the frequency and temporal domains, presented in figures 5.19a and 5.19b respectively, it is clear that the relative magnitude of acceleration between the top-wing wingtip and the main-wing is considerable. This finding agrees with the laser vibrometry data indicating that the top-wing, acting as the auxiliary mass of a vibration absorber, is 'absorbing' the vibrational kinetic energy of the main-wing. Considering the temporal domain shown in figure 5.19b, it is seen that the vibrational phase analysis shows that signals from sensors 2 and 3 lag the signal from sensor 1 by $-3.0826rad$ ($\approx -\pi rad$) and $-3.1035rad$ ($\approx -\pi rad$) respectively. Therefore, this provides evidence that the top-wing vibrations are out-of-phase with the main-wing, as previously speculated. In addition, it is noted that sensors 2 and 3 signals are in phase ($\approx 0rad$), indicating the absence of any dominant torsional modes present in the top-wing structure.

Force Platform: Model Inertial Loading from Wing Vibration

With evidence of the attenuation of wing vibration, it is necessary to consider how the interplaying vibrations influence the model's body forces and aerodynamic performance. Buffeting results in lift and drag variations that greatly affect an operational aircraft's aerodynamics and impose limitations to the flight envelope. The frequency response for each wing arrangement's drag coefficient under experimentally static conditions at $\alpha = 0^\circ$, 8°, and 14° are presented in figure 5.20. To negate the wind tunnel vibrations, the excited longitudinal fuselage natural frequency, and steel mounting

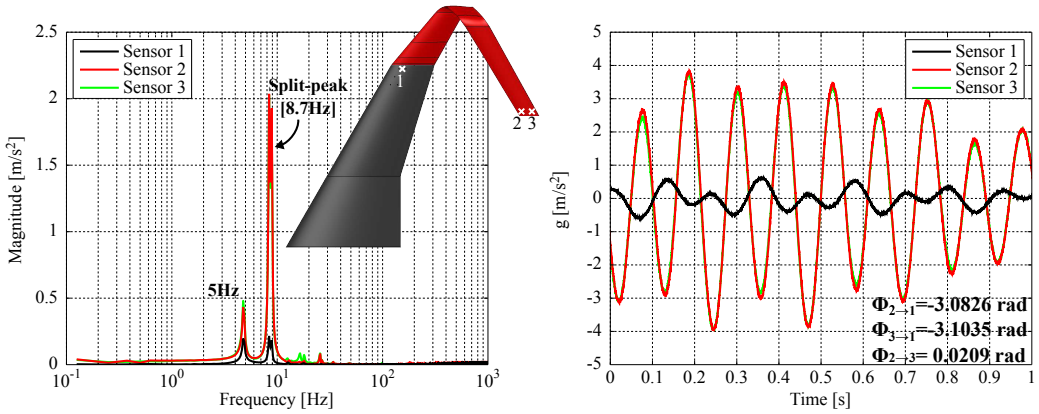

(a) Frequency response.

(b) Temporal response.

Figure 5.19: Accelerometer arrangement 2 for the C-wing configuration at $\alpha = 14^\circ$.

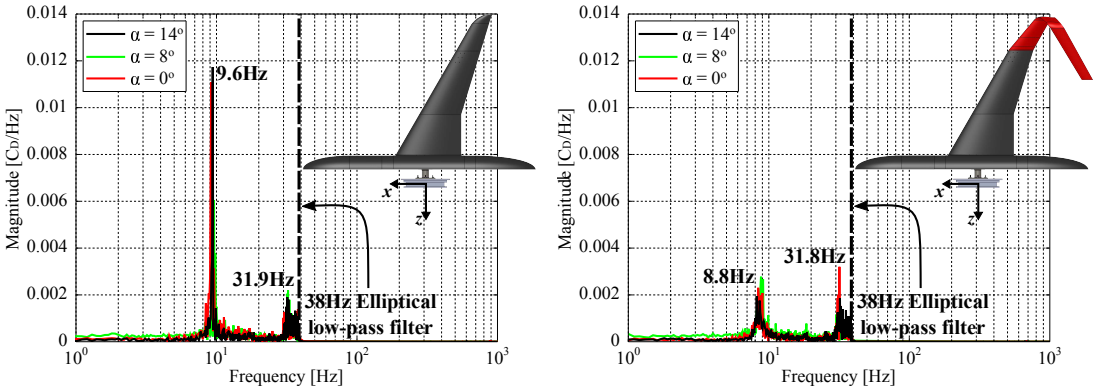

(a) Planar wing.

(b) C-wing.

FIGURE 5.20: Drag coefficient filtered frequency response, detected by the force platform, for both planar and C-wing arrangements for $\alpha = 0°, 8°, 14°$.

interface vibrations, the force platform data has been post-processed with a 10^{th} order $38Hz$ elliptical low-pass filter. These vibrations, detected on all six force platform channels, represent a consequence of utilising a peniche-less semi-span model. This is deemed to not outweigh the aerodynamic interference benefits of removing the semi-span model's peniche; justifications and effects of this have been discussed in Chapter 4. The $38Hz$ low-pass filter cut-off has been indicated in figure 5.20.

The results presented in figure 5.20, which measured mechanically, are consistent with the optical laser-Doppler vibrometry results presented previously in figure 5.14. The significance of this result irrefutably indicates that attenuation of the wing's natural modes have the knock-on effect of attenuating vibrations felt by the fuselage. In other words, the C-wing's ability to operate as a vibration absorber acts as a form of suspension system for the fuselage via the main-wing. While it is clear that the relative motion between the wing system and the fuselage is limited, the practical application of this, other than improving aircraft handling and performance, would be to improve ride quality for on-board passengers.

5.6 SUMMARY AND CONCLUSIONS

An experimental investigation has been conducted to compare the performance of a semi-span planar wing and a non-planar C-wing configuration at $Re = 1.5 \times 10^6$, including a detailed understanding of the model vibrations. Surface clay flow visualisations were used to compare flow over the wing and identify regions of attached/separated flows, stall fronts, stall cells, model surface imperfections, and horseshoe vortex interactions at the wing root. Aerodynamic performance metrics of each configuration were assessed using a force platform. The main findings of this chapter have been published by Skinner and Zare-Behtash [315].

Assessment of each configuration's aerodynamic performance metrics (via the

force platform) showed that, despite the C-wings 19.1% increase in wing wetted area, an average total drag reduction of 7.4% over a $0^\circ \leq \alpha \leq 14^\circ$ angle of attack range was achieved, *i.e.* where induced drag contribution to the total drag dominated over parasitic drag. A peak total drag reduction of 9.5% was reached at $\alpha = 6^\circ$. This is accomplished with the C-wing maintaining lift and root bending moment equivalent to that of the planar wing configuration over the same angle of attack range. At negative angles of attack the total drag is seen to increase by up to 16.6% as parasitic drag dominates. Forced vibrations due to the wind tunnel excitation of the fuselage's longitudinal natural frequency, which translates to noisy interpretation of aerodynamic performance metrics, was mitigated through application of a $38Hz$ low-pass filter. This is somewhat a consequence of a peniche-less, semi-span model having less structural support and stiffness.

The surface clay flow visualisations identified similarities in each wing configuration's stall characteristics, indicating that the C-wing's effects on stall over the main-wing are negligible. In addition to highlighting the progression of stall over each wing, clay visualisations supported force data indicating that peak drag reduction coincided with strong inboard side-wing forces. At higher angles of attack, the drag reduction capability drops off, as does the side-wing inboard loading. Clay visualisation indicates that this was caused by the main-wing stall propagating onto the side-wing.

Furthermore, laser-Doppler vibrometry was used to examine the C-wing's ability to act as a passive undamped vibration absorber. This examination is supported by accelerometer results and the force platform. The accelerometers also indicate that all mode frequencies detected are bending modes, with no evidence of dominant torsional modes observed as envisioned from the wing aeroelastic design methodology discussed in Section 3.5. Furthermore, it is found that the C-wing top-wing vibrations are out-of-phase with the main-wing. This achieves an 68.63% attenuation of the excited primary bending mode due to buffet at $\alpha = 14^\circ$, relative to the planar wing.

The C-wing's ability to maintain passive drag reduction and vibration damping without significant increases in wing weight or root bending moment are promising. There are however, foreseeable structural limitations to the C-wing configuration which have not been examined in this study, the primary limitations being: 1) inertial loading coupled with wing weight distribution; and 2) the possibility of side-wing failure through material fatigue/inertial loading. The former was not an issue in this study as the wing was mounted vertically; however, it is necessary to highlight that this does understate the effect of gravity on the relatively heavier C-wing wingtip. The latter is a bi-product of the C-wing acting as an effective vibration absorber where the top-wing's dominant vibrational velocity magnitude is up to 361.16% higher than that experienced by the main-wing.

CHAPTER 6

WINGTIP VORTEX DEVELOPMENT IN THE EARLY WAKE

6.1 INTRODUCTION

Having assessed the relative performance of the C-wing to the planar wing in Chapter 5, the aim of this chapter is to elucidate the link between how the C-wing alters the wingtip vortex wake and how this plays a role in reducing the induced drag. The vortex system develops quickly after leaving the wing trailing edge, and understanding the mechanisms driving the development of the vortex in the near field region is crucial for understanding performance implications and how the vortex is expected to behave in the far field. The physics of the vortex flow in the early wake are very complex and are directly linked to the vortex formation process over the wingtip geometry. The wingtip geometry, the distribution of the wing circulation, and the roll up of the wake sheet characteristically determine the early evolution of the vortex.

A comprehensive understanding of both the planar wing and C-wing near field trailing vortex system is achieved in this study through comparing several angles of attack at various downstream distances at a fixed Reynolds number ($Re = 1.5 \times 10^6$). The relationships between the wingtip geometry and the resulting vortex wake velocity fields, vortex core shape development, and the low frequency ($\leq 100Hz$) turbulent properties inside the vortex core have been studied. SPIV was used to provide instantaneous and time-averaged global flow field measurements.

In Section 6.2 the phenomenon of vortex wander and its implications on the time-averaged SPIV data have been defined. Additionally, the problem of establishing an appropriate vortex spatial localisation algorithm for centring and averaging the instantaneous velocity fields is addressed by providing a critical discussion for the adoption of different centring methods. Subsequently, Section 6.3 investigates the properties of the planar wing vortex wake and how these develop as a function of both angle of attack and downstream distance. Thus, with a detailed understanding of the planar wing vortex wake, the C-wing vortex system and how it compares to

the planar wing vortex system is investigated in Section 6.4. Specifically, the fluid dynamic mechanisms adopted by the C-wing and how they manifest as a reduction of the induced drag is examined. Secondary benefits of the C-wing's unique capability to simultaneously provide a low vorticity vortex (LVV) and a quick decay vortex (QDV) system with reduced turbulence levels is also explored. A summary of the main findings is finally presented in Section 6.5.

6.2 SPATIAL LOCALISATION OF THE VORTEX CORE CENTRE

Wingtip vortices are non-stationary flows that exhibit small random motions normal to the vortex axis. This phenomenon is referred to as vortex wander (or meander), referring to the aperiodic motions which scatter the vortex centre location over time [316]. Spatially adjusting instantaneous PIV images to accommodate vortex meander provides better knowledge of the flow properties of the trailing vortex structure. Birch [317] demonstrated that the averaging of a wandering vortex, if not corrected appropriately, can blur and distort the data forcing convergence upon a universal (or self-similar) circulation profile obtained for the case of a Batchelor q-vortex.

In practice, vortex wandering produces an artificial spreading effect in the time-averaged flow field measurements, which vary in both magnitude and frequency over time. Artificial spreading results in a larger apparent vortex core size and smaller peak magnitudes of the vortex flow properties (*e.g.* swirl velocity) compared to any instantaneous measurement. It is common practice to acknowledge the presence of vortex wander but assume its affects, without quantification, are negligible [318]. Analysis of the effects of wandering is necessary to accurately reveal flow structures inside the core region, and to give confidence in the measurements made outside the core [319]. Whatever the source of the wandering (wing vibration, freestream turbulence, *etc.*), the vortex core translation and mean flow properties must be acknowledged.

Figure 6.1 presents streamwise vorticity contours for the wingtip vortex produced by the planar wing at $\alpha = 8^\circ$ at $x/\bar{c} = 1.5$ and 2.5. For the simple averaged examples, the vortex core is blurred for both figures 6.1a and 6.1c, relative to figures 6.1b and 6.1d in which the instantaneous SPIV flow realisations have been spatiality corrected using helicity centring. Furthermore, figure 6.1a implies an asymmetric vortex structure, whereas the wander corrected vortex structure presented in 6.1b presents a more symmetric vortex with a well defined core. The wing vortex sheet is also found to become better defined with the application of vortex centring corrections.

Although the vortex wandering phenomenon has a more pronounced effect on the mid-field for finite wings, correcting for wandering effects is essential when the objective is to accurately quantify flow structures and turbulent properties in the wake and inside the wingtip vortex core [320]. The mid-field is defined as $10 \leq x/\bar{c} \leq 2000$ [321].

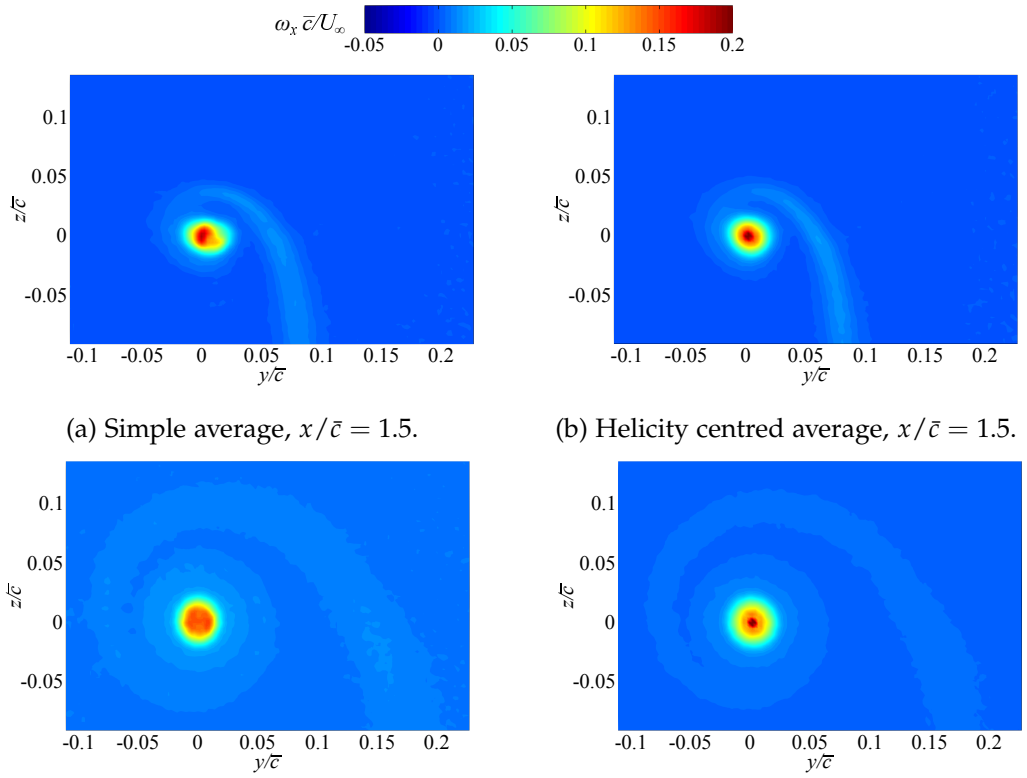

(a) Simple average, $x/\bar{c} = 1.5$.

(b) Helicity centred average, $x/\bar{c} = 1.5$.

(c) Simple average, $x/\bar{c} = 2.5$.

(d) Helicity centred average, $x/\bar{c} = 2.5$.

FIGURE 6.1: Simple time-average and helicity centred time-average vorticity of the planar wing wingtip vortex at $\alpha = 8°$, for $x/\bar{c} = 1.5$ and 2.5.

The spatial centring of instantaneous realisations of the vortex can be considered as a post processing procedure in which the solid-body translation of the vortex and the turbulent fluctuation within the vortex are separated. The solid translation of the vortex is what is experimentally observed and referred to as vortex meander. Hence, the implementation of a methodology which is capable of extracting vortex wander information to spatially adjust the time-average vortex flow field requires close consideration. Birch [317] showed that for isotropic and Gaussian vortex wandering amplitudes, any flow field with zero in-plane velocity at $r = 0$ and $r \to \infty$ converges towards the circulation profile obtained for a Batchelor q-vortex. This implies that strong agreement between time-averaged vortex velocity profiles and the Batchelor q-vortex does not mean that the instantaneous profiles will also agree well with the q-vortex model.

Averaging procedures which align the instantaneous realisations of the vortex, therefore localising their centres, assumes that the wandering is a solid translation of the vortex on the plane perpendicular to its axis. The velocities associated with the wandering movement of the vortex itself are negligible compared to those generated by the vortex [319]. Thus, the challenge is to identify a robust methodology that can be used to define the instantaneous vortex centre. Two approaches are available from the literature: 1) identification of the vortex centre through identification of flow field

properties in the region of the vortex core [316, 320, 322]; or 2) the application of a discrete mask to the data assuming the behaviour of an analytical vortex model [323, 324]. The first approach is dependant upon the accuracy and spatial resolution of the measurements around the vortex core, the fidelity of which is particularly affected by the lack of seeding particles in the vortex core. The latter is based on an appropriate least square fit on a number of variables (such as the vortex centre position, velocity, orientation, core radius, and circulation) to a reasonable analytical model.

For wing trailing vortices, peak magnitudes of vorticity and swirl velocity properties are well defined within the vortex centre, in contrast to, for example, the tip vortices generated by lightly loaded rotors in forward flight, especially those on the advancing side, which are often very small and weak, hard to detect, and coexist in the vicinity of similar magnitude secondary vortices [323]. Also, in the early wake ($x/\bar{c} \leq 10$ [321]), the vortex may not be symmetric, and therefore poorly described by analytical models. It was found that enough seeding particles were present within the vortex core, and the SPIV measurements resulted in a sufficiently high vector spatial resolution ($\approx 1mm$) and reliability to track flow properties within the core; approximately 20 vectors over the vortex core diameter. Therefore, in this study, the first approach is adopted for the instantaneous vortex centre identification. A reference case of the planar wing trailing vortex at $x/\bar{c} = 2.5$ aft of the wing mean aerodynamic chord, at $\alpha = 8^\circ$ and $Re = 1.5 \times 10^6$, has been used to demonstrate the application of vortex centring methods. It is highlighted at this stage, with reference to figure 6.1, that all vortices shown in this work are viewed from upstream and are therefore rotating anti-clockwise.

Pre-processing of the raw images was necessary to facilitate the high spatial accuracy within the vortex core. Figure 6.2a presents the instantaneous seeding distribution for the reference case. A core diameter of $\approx 15mm$ is indicated ($\approx 3.4\%$ of the mean aerodynamic chord). The dark region observed at the vortex core is

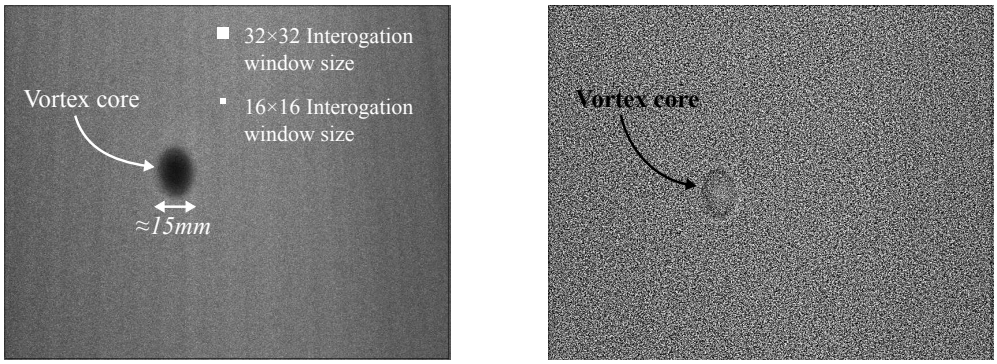

(a) Raw instantaneous seeding image.

(b) Particle intensity normalisation filter applied to figure 6.2a.

FIGURE 6.2: Instantaneous seeding distribution at $x/\bar{c} = 2.5$, $Re = 1.5 \times 10^6$, and $\alpha = 8^\circ$ for the planar wingtip.

approximately 75% of the vortex core diameter. This seemingly empty void in the seeded flow exists due to the centrifugal force of the swirling flow accelerating the mass of the seeding particles radially out of the vortex core [270, 325]. Relatively, there are fewer particles within the vortex core because of this, however, there remains a sufficient number for cross-correlation. To compensate for the fluctuation in seeding density, a particle intensity normalisation filter is applied to all raw data; the effect of applying such a filter to the raw data shown in figure 6.2a, is presented in figure 6.2b. It is emphasised here that applying this filter only manipulates the relative particle intensity, and not particle position. It also removes the need for post-processing of the instantaneous images. With this, a reliable and accurate description of the flow inside the core is achieved with a measurement grid spacing of $\approx 5\%$ of the core radius.

Methods for the detection of the vortex centre from measurements in the core can be based on several different properties of the vortex. Analytically, all of these methods would indicate the same location of the vortex core. A discussion of the most suitable vortex centre localisation methods is presented as follows.

1. *Centroid of the seed void*. The dark region formed by centrifugal forces acting on the seeding particles (shown in figure 6.2a) provides a simple qualitative method for vortex centre estimation. The shape is not usually circular or repeatable in any of the instantaneous SPIV images. Several factors including the image contrast, seeding distribution, particle size and mass, bit resolution of the camera, and vortex size and strength, make the utilisation of this method for establishing an automatic and robust instantaneous vortex centring method unreliable compared to tracking quantitative flow properties [316].

2. *Zero in-plane velocity (or swirl centre)*. Swirl centre is represented by the spatial location at which the in-plane velocity component is zero, as described by equation 6.1:

$$\sqrt{v^2 + w^2} = 0 \tag{6.1}$$

   For an isolated vortex (such as for a finite wing) this method will indicate the geometric centre of the vortex. However, this method can lead to false meander results if the vortex axis is not straight or when axis curvature is high (such as rotor vortices). Additionally, this method becomes increasingly more unreliable for large vortex translations, or if the PIV measurement plane is misaligned.

3. *Peak axial velocity perturbation,* $(u_x - U_\infty)$. Either a velocity perturbation deficit or excess, depending on tip loading and roll-up of the wake sheet, can be identified as the vortex centre. When the perturbation is strong, the vortex centre can be identified as the point of peak axial velocity.

4. *Peak vorticity*. Vorticity is a three-dimensional pseudo-vector defined as the curl of the velocity field. SPIV measurements on a single plane can only provide the velocity gradients in the in-plane directions (*i.e.* $\partial/\partial y$ and $\partial/\partial z$). As a result,

only a single component (the streamwise component) can be estimated, which is given by equation 6.2:

$$\omega_x = \frac{\partial w}{\partial y} - \frac{\partial v}{\partial z} \tag{6.2}$$

In this work, the streamwise vorticity is calculated with the eight-node circulation method described by Raffel et al. [267] which is shown to perform better than other schemes in terms of error and smoothness of the results. This method can be employed due to the sufficiently high spatial resolution, where the location of the peak vorticity can be taken as the vortex centre.

5. *Peak of helicity*. Helicity is a conserved quantity which measures the helical motion of a vortex. It is defined as the dot product of the velocity and vorticity such that the result indicates the inclination between the vorticity vector and the velocity vector. In this work only the streamwise vorticity is available. As the wingtip vortex convects downstream with the freestream flow, a more appropriate definition is the scalar product of the axial velocity perturbation and the vorticity [320], as presented by equation 6.3:

$$H_x = |u_x - U_\infty| \cdot \omega_x \tag{6.3}$$

Peak helicity identifies the vortex core.

6. *Q-criterion (peak swirl strength)*. Singular points typical of vortical features of spiral or close streamlines can be mathematically described by complex eigenvalues of the velocity gradient tensor, This description is composed of the strain tensor Σ and the vorticity tensor Ω, and is expressed as follows:

$$\begin{aligned} \frac{d\mathbf{V}}{dx} = \Sigma + \Omega &= \begin{bmatrix} \varepsilon_{yy} & \varepsilon_{yz} \\ \varepsilon_{zy} & \varepsilon_{zz} \end{bmatrix} + \frac{1}{2}\begin{bmatrix} 0 & -\omega_x \\ \omega_x & 0 \end{bmatrix} \\ &= \begin{bmatrix} \frac{\partial v}{\partial y} & \frac{1}{2}\left(\frac{\partial v}{\partial z} + \frac{\partial w}{\partial y}\right) \\ \frac{1}{2}\left(\frac{\partial w}{\partial y} + \frac{\partial v}{\partial z}\right) & \frac{\partial w}{\partial z} \end{bmatrix} + \begin{bmatrix} 0 & \frac{1}{2}\left(\frac{\partial v}{\partial z} - \frac{\partial w}{\partial y}\right) \\ \frac{1}{2}\left(\frac{\partial w}{\partial y} - \frac{\partial v}{\partial z}\right) & 0 \end{bmatrix} \end{aligned} \tag{6.4}$$

A vortex characterised by the invariance of the velocity gradient tensor requires the discriminant Q of the characteristic equation of the velocity tensor gradient to be below zero [326]. Hence, the centre of the vortex can be defined as the point of minimum Q, defined as [316]:

$$Q = \frac{(\frac{\partial v}{\partial y} + \frac{\partial w}{\partial z})^2}{4} + \frac{\partial v}{\partial z}\frac{\partial w}{\partial y} - \frac{\partial w}{\partial z}\frac{\partial v}{\partial y} \tag{6.5}$$

As this method uses velocity gradients to identify the vortex core, the measurement spatial resolution will greatly influence the accuracy and reliability, especially in the presence of high gradients.

7. *Peak of the eigenvalues of the velocity gradient tensor, λ_2.* Starting from the gradient operator applied to the Navier-Stokes equations, Jeong and Hussain [326] found a definition of a vortex that leads to the eigenvalues of the tensor $\Sigma^2 + \Omega^2$, which must be negative. This method leads to the identification of the vortex centre as the point of minimum λ_2, defined as:

$$\lambda_2 = \frac{(\frac{\partial v}{\partial y})^2 + (\frac{\partial w}{\partial z})^2}{2} + \frac{\partial v}{\partial z}\frac{\partial w}{\partial y} \tag{6.6}$$

As this method uses velocity gradients to identify the vortex core, the measurement spatial resolution will greatly influence the accuracy and reliability, especially in the presence of high gradients.

In the centre of an analytical vortex, the following relation is true [327]:

$$\omega_x^2 = |Q| = |\lambda_2| \tag{6.7}$$

Among the seven aforementioned vortex centre identification methods, only the method of tracking the centroid of the seed void is excluded. This method is only qualitative in nature, and may not be axisymmetric, or in any repeatable shape, in the acquired instantaneous flow images due to seeding density, and several other previously discussed factors. It is necessary to indicate that the vortex centre tracking methods described in this work reflect only a few methods available from the literature. Jiang et al. [328], among others [316, 329, 330, 331, 332], provide discussion on various vortex centre identification methods.

Figure 6.3 illustrates the vortex properties reported for identifying the vortex centre within instantaneous realisations. The calculation of the in-plane velocity and the axial velocity perturbation, shown in figures 6.3a and 6.3b respectively, involve the local velocity vectors only. It is assumed that the vortex axis is aligned with the freestream (as described in Section 3.9) so that the out-of-plane component measured by the SPIV is the true vortex axial velocity. While the axial perturbation velocity (figure 6.3b) appears axisymmetric, the in-plane velocity (figure 6.3a) appears to be slightly asymmetric. This is caused by the spiral roll-up of the wing wake sheet. Within the region of the vortex core, an axial velocity deficit with distinct peaks of $\approx 0.22U_\infty$, is observed as the vortex is fully developed. Less developed wingtip vortices in the very early wake are known to exhibit high asymmetry and a jet-like core structure with a velocity excess [333, 334].

The streamwise vorticity, shown in figure 6.3c, is calculated with the eight-node circulation method described by Raffel et al. [267] which is shown to perform better than other schemes in terms of error and smoothness of the results. A region of high vorticity is observed within the core. A similar result is observed in figure 6.3d where a concentration of helicity is observed within the core. The helicity highlights the vorticity peak when an axial velocity perturbation is present within the vortex core;

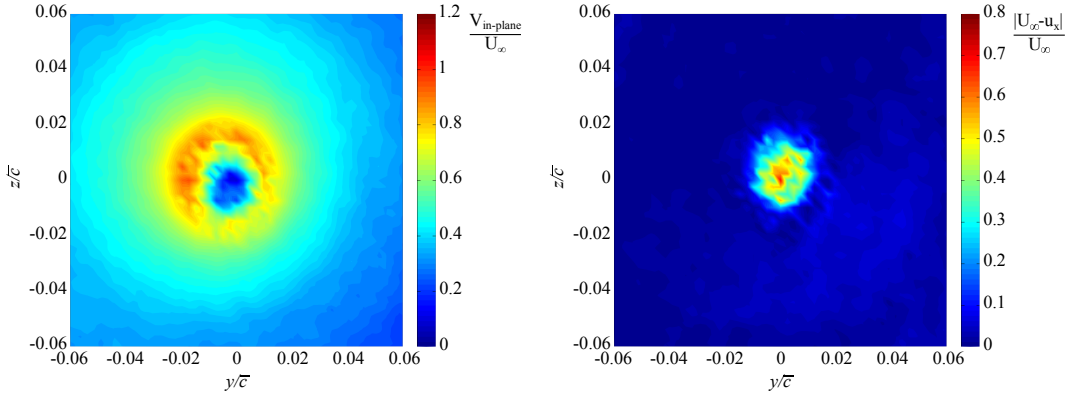

(a) In-plane velocity.

(b) Axial velocity perturbation.

(c) Peak streamwise vorticity.

(d) Peak streamwise helicity.

(e) Q.

(f) λ_2.

FIGURE 6.3: Centring methods for an instantaneous realisation at $x/\bar{c} = 2.5$, $Re = 1.5 \times 10^6$, and $\alpha = 8^\circ$ for the planar wing.

this exists in most trailing vortex structures. Additionally, helicity is the only vortex property which includes, in its calculation, all three velocity components available from the SPIV.

The derivatives used for the calculation of Q and λ_2 (shown in figures 6.3e and 6.3f) are calculated with the 4-point centred least-square approach [267]. The two contours appear very similar, with identical peaks marking the vortex centre. This occurs since in the vortex core, the planar elongational strains ε_{yy} and ε_{zz} are negligible

when compared to the shear strains ε_{yz}, ε_{zy}, and at the vortex notional centre:

$$\left(\frac{\partial v}{\partial y}\right)^2, \quad \left(\frac{\partial w}{\partial z}\right)^2, \quad \frac{\partial v}{\partial y}\frac{\partial w}{\partial z} \quad << \quad \frac{\partial v}{\partial z}\frac{\partial w}{\partial y} \tag{6.8}$$

which leads to an approximately identical definition of Q and λ_2 from equations 6.5 and 6.6 in the vicinity of the vortex centre.

Each data set presented in this work is time-averaged over 1800 vortex SPIV vector fields (at $200Hz$); figure 6.4 illustrates the 1800 instantaneous vortex centre positions recorded by each centring method for the reference case (planar wing arrangement at $Re = 1.5 \times 10^6$ and $\alpha = 8^\circ$, for $x/\bar{c} = 2.5$). The spatial centroid of the vortex meander is indicated by the red marker, the perimeter around this marker is the *rms*-perimeter indicating the azimuthal magnitude of the notional vortex centre fluctuation.

From figure 6.4, two characteristics of the distribution patterns of the instantaneous centres are apparent. Firstly, the distribution of instantaneous centres, regardless of the centring methodology, is strongly affected by the grid spatial resolution of the vector field. The vector grid spatial resolution for all SPIV data presented in this work is $\approx 1mm$, which is of the order of one tenth of the movement of the core centres. The grid resolution is also considered small relative to the size of the vortex core radius ($\approx 5\%$), thus the alignment of each instantaneous centre based on the closest grid node does not incur significant error. In essence, this will result in a residual observational systematic error in vortex wandering measurements which is less that one half of the diagonal grid spacing ($\approx 0.7mm$). Referring to an analysis by Devenport et al. [319], this would result in less than a 0.8% error in the measured peak swirl velocity and core radius. Therefore, vortex realisations have been aligned based on the grid node closest to the vortex centre in the present work.

The second characteristic observed from the centring methods is the general distribution. Scattering of the vortex centres between the centring methods indicate azimuthally equivalent ranges of dispersion; illustrated by the *rms*-perimeter. For each centring method, the peak vortex meander amplitude is $\approx 2\%$ of the wing mean aerodynamic chord for the reference case shown, where the distribution of centres appears to have no particular bias or orientation of vortex wander. Observations here would thus indicate an isotropic wander amplitude.

Figure 6.5 shows probability density functions (PDF) of the vortex wander amplitude for different angles of attack and different downstream stations. Figure 6.5a suggests insensitivity of vortex wander amplitude to angle of attack; results for meander are presented in the $y/\bar{c}$ and $z/\bar{c}$ axes separately, again indicating isotropic wander. This behaviour is observed at all downstream $x/\bar{c}$ planes. However, for a given angle of attack, the vortex wander amplitude increases with downstream convection away from the wing as illustrated in figure 6.5b. Devenport et al. [319] suggests that this trend occurs as the dominant source of vortex wander is from wind tunnel unsteadiness. Isotropic wander amplitudes are also observed with downstream

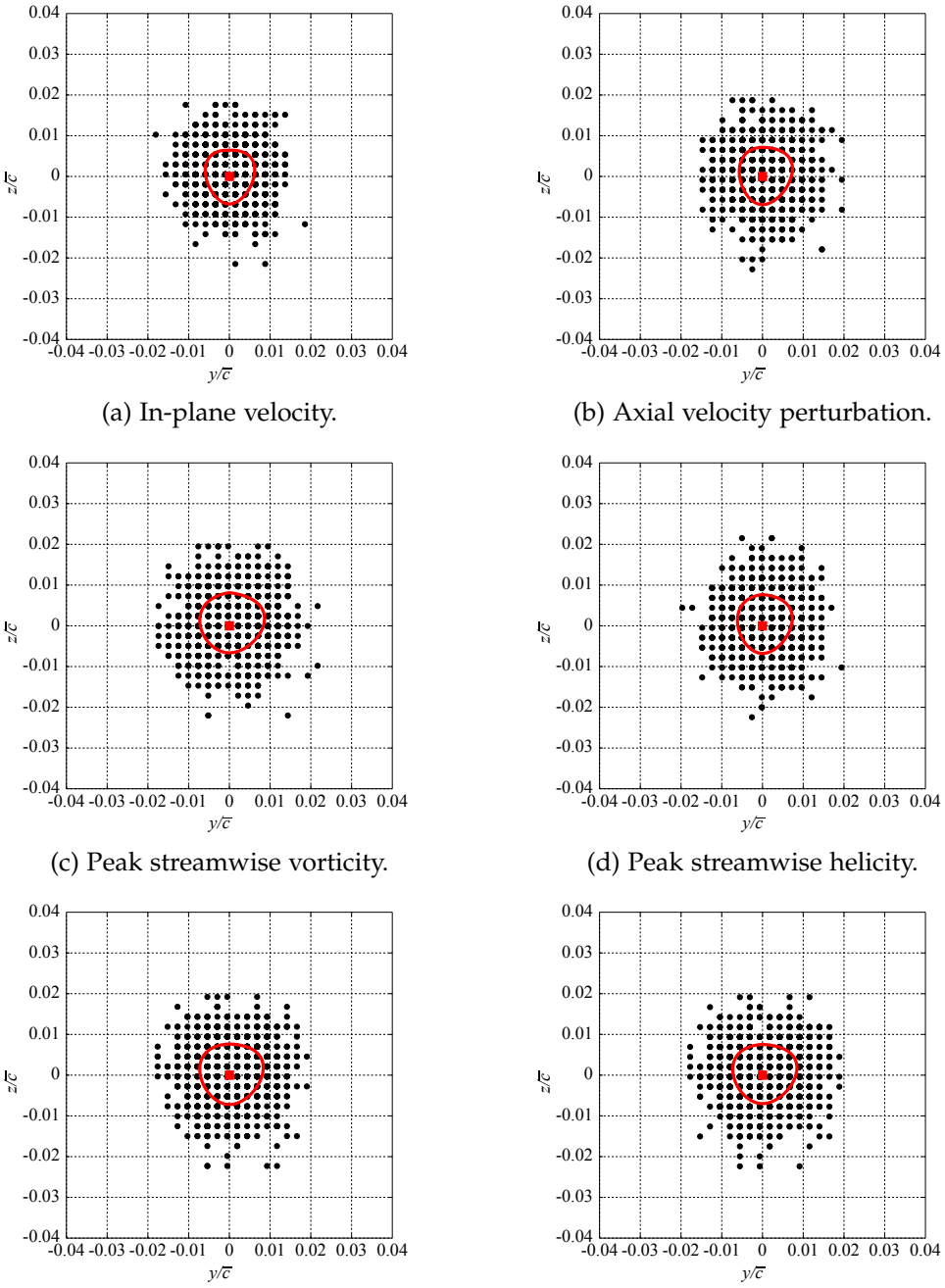

(a) In-plane velocity.

(b) Axial velocity perturbation.

(c) Peak streamwise vorticity.

(d) Peak streamwise helicity.

(e) Q.

(f) λ_2.

FIGURE 6.4: Instantaneous vortex centre locations based on different centring methods at $x/\bar{c} = 2.5$, $Re = 1.5 \times 10^6$, and $\alpha = 8^\circ$ for the planar wing.

translation (see figure 6.5b), however, at $x/\bar{c} = 5.418$ the PDF distribution indicates that vortex wander becomes slightly biased in the $z/\bar{c}$ axis.

The effects of the vortex centre localisation method adopted for the correction of the wandering is discussed in this work with particular attention paid to the swirl velocity distribution, the axial velocity distribution, the vorticity distribution, and turbulent quantities. As the centring methods are effectively filtering and time-averaging the SPIV data differently, dictating different vortex structures, each must be closely

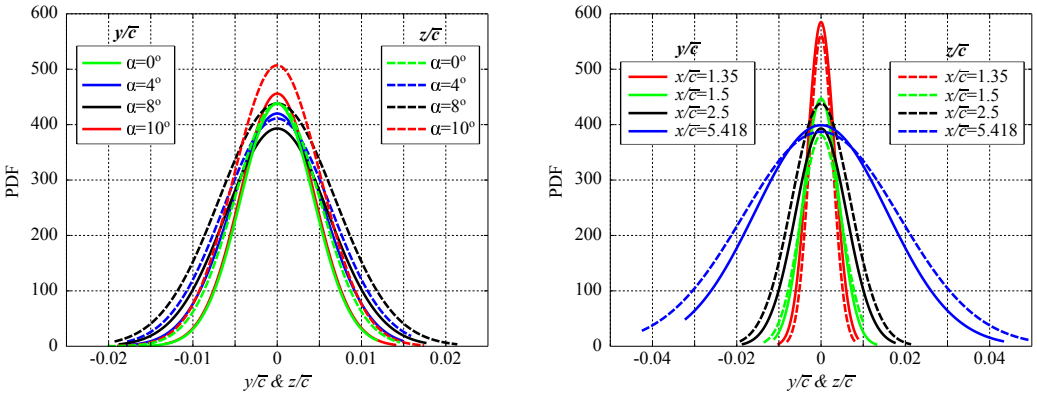

(a) Varying α at constant $x/\bar{c} = 2.5$.

(b) Varying $x/\bar{c}$ at constant $\alpha = 8°$.

FIGURE 6.5: Probability density functions (PDF) of the vortex wander amplitudes recoded using the helicity centring method.

scrutinised. The average of the 1800 instantaneous vector fields is calculated for each vortex centring localisation method, involving the centring of each vortex realisation. The average of the instantaneous vector field without any centring methodology applied is referred to as the *simple average* case. Vortex centring results for λ_2 are not shown as they yield similar results to those provided by the Q-criterion.

6.2.1 SWIRL VELOCITY DISTRIBUTION

Typically, without centring each instantaneous flow field measurement, the vortex wander causes the mean vortex to show a larger core radius and a reduced maximum swirl velocity due to artificial spreading. Application of centring methods tends to result in a smaller core radius realisation and higher peak swirl velocities [316]. All wingtip vortices considered in this work are within the early wake ($x/\bar{c} < 10$ [321]).

All circumferentially averaged vortex data profiles presented in this work are calculated by a cubic interpolation of the respective data field (swirl velocity, axial velocity, vorticity, etc.) along 36 radii equispaced around the respective notional centre, adopting a cubic interpolation from the Cartesian grid of the original velocity vectors. Figure 6.6 illustrates this process utilising a vorticity contour to additionally illustrate the wake sheet roll-up.

Figure 6.7 presents the swirl velocity profiles for the different centring methods; the circumferentially averaged profile is shown by the red line. In figure 6.7a the swirl velocity profiles from the simple averaged vector field are shown. An asymmetry between the swirl velocity peaks on the suction and pressure sides of the vortex is observed. This is due to the flow interaction of the vortex with the wake sheet roll-up spiralling around the it. Both **Region A** and **Region B** are indicative of momentum transfer from the turbulent free shear-layer to the wingtip vortex [319, 335]; these regions have been indicated in figure 6.6. From figure 6.7, it is observed that there is no significant change in the swirl velocity differential with the application of different

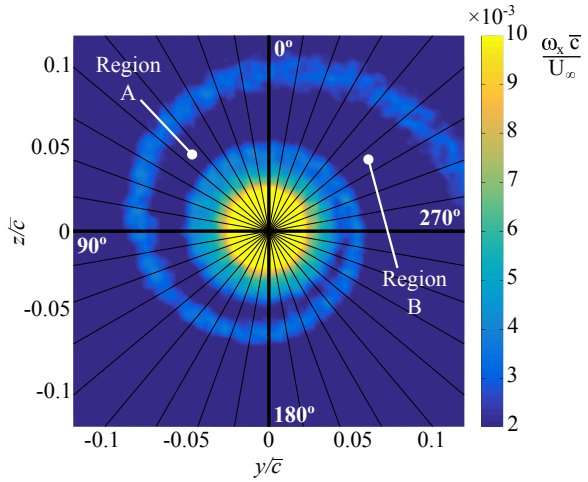

FIGURE 6.6: Simple averaged vorticity of the planar wing wingtip vortex at $\alpha = 8^\circ$ for $x/\bar{c} = 2.5$, with schematic illustrating various slicing cuts made across the vortex to measure the mean flow characteristics.

centring methods.

The swirl velocity profile embodies the three-layered description of a turbulent trailing vortex during roll-up presented by Phillips [336]: 1) the viscous core which linearly decreases the swirl velocity to zero as $r \to 0$, and rotation is close to solid-body; 2) the fluid region bounding the vortex core, defined by maximum swirl velocity (vortex core radius r_c); and 3) the outer vortex region in which the swirl velocity decays. Regardless of the centring method applied, figure 6.7 indicates that the swirl velocity profile remains largely unaffected, with peak swirl velocities increasing by less than 2%.

Considering the swirl velocity at the centre of the core ($y/\bar{c} = 0$), the swirl velocities are seen to converge to $u_\theta/U_\infty = -0.012$ for the zero in-plane centring methods shown in figure 6.7b; the swirl velocities at the centre of the simple average case and the axial velocity perturbation centring methods both show a scatter of $u_\theta/U_\infty \pm 0.085$ in figures 6.7a and 6.7c respectively. The vorticity, helicity, and Q-criterion centring methods show similar scatter patterns at the vortex core, each converging to $u_\theta/U_\infty \approx -0.03$. Additionally, the mean swirl velocity profiles for the vorticity, helicity, and Q-criterion centring methods each indicate a subtle double gradient structure near the core centre at $y/\bar{c} \approx \pm 0.0035$ ($\approx 0.18 r_c$).

As previously mentioned, the vortex core radius r_c is defined as the distance between the vortex centre ($y/\bar{c} = 0$) and the point of maximum swirl velocity. The mean vortex core radius is evaluated by averaging the 36 radii swirl velocity peaks determined for each centring method, the values of which are presented (in mm) in figure 6.7 for each centring method. The average vortex core radius, regardless of centring method, is $0.019\bar{c}$ to $0.022\bar{c}$ and is therefore comparable to the maximum vortex meander amplitudes detected in figure 6.4. For the reference case shown, all centring methods are recorded to reduce the size of the vortex core radius, relative to

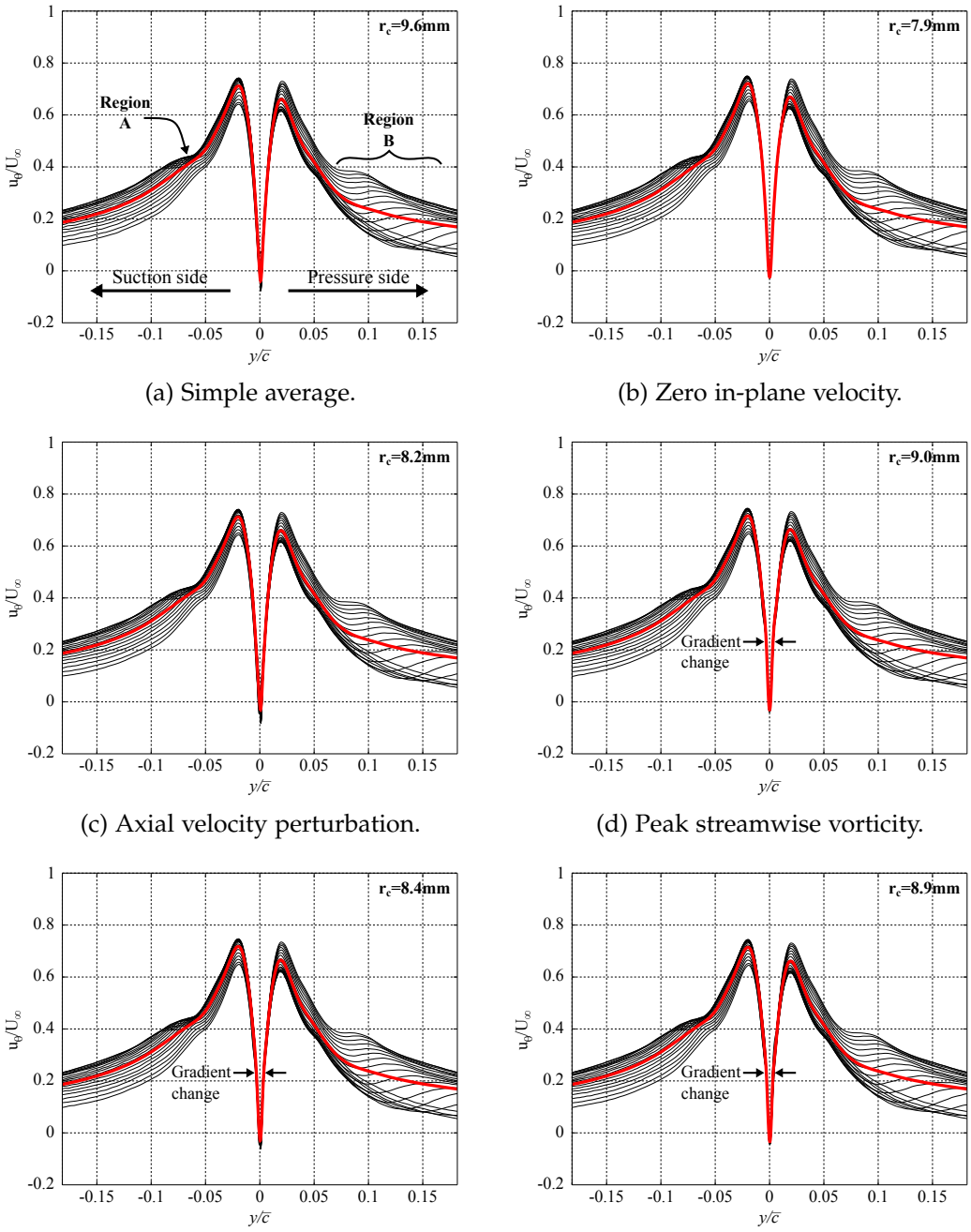

(a) Simple average.

(b) Zero in-plane velocity.

(c) Axial velocity perturbation.

(d) Peak streamwise vorticity.

(e) Peak streamwise helicity.

(f) Minimum Q.

FIGURE 6.7: Average swirl velocity profiles, and vortex mean swirl profile (red line), calculated with different centring methods at $x/\bar{c} = 2.5$, $Re = 1.5 \times 10^6$, and $\alpha = 8^\circ$ for the planar wing.

the simple average case, with the zero in-plane velocity centring method resulting in the greatest reduction of 17.7%, as shown in figure 6.7b.

6.2.2 AXIAL VELOCITY DISTRIBUTION

While variation of the in-plane swirl velocity description is subtle when comparing the vortex centring methods to the simple averaged vortex, more obvious variations

arise when the axial velocity (out-of-plane) profiles are viewed. In figure 6.9, the axial velocity profile of the simple average and vortex centred averages are reported along 36 radii equispaced around the notional centre, with mean velocity profiles also given.

All velocity profiles reveal an axial velocity deficit contained to the vortex core, with a region of velocity excess induced by the wingtip/wake sheet roll-up interaction previously referred to as **Region B**, indicated in figure 6.6. The velocity excess region is unaffected by the applied centring method; $u_z/U_\infty \approx 1.051$ for all cases. The zero

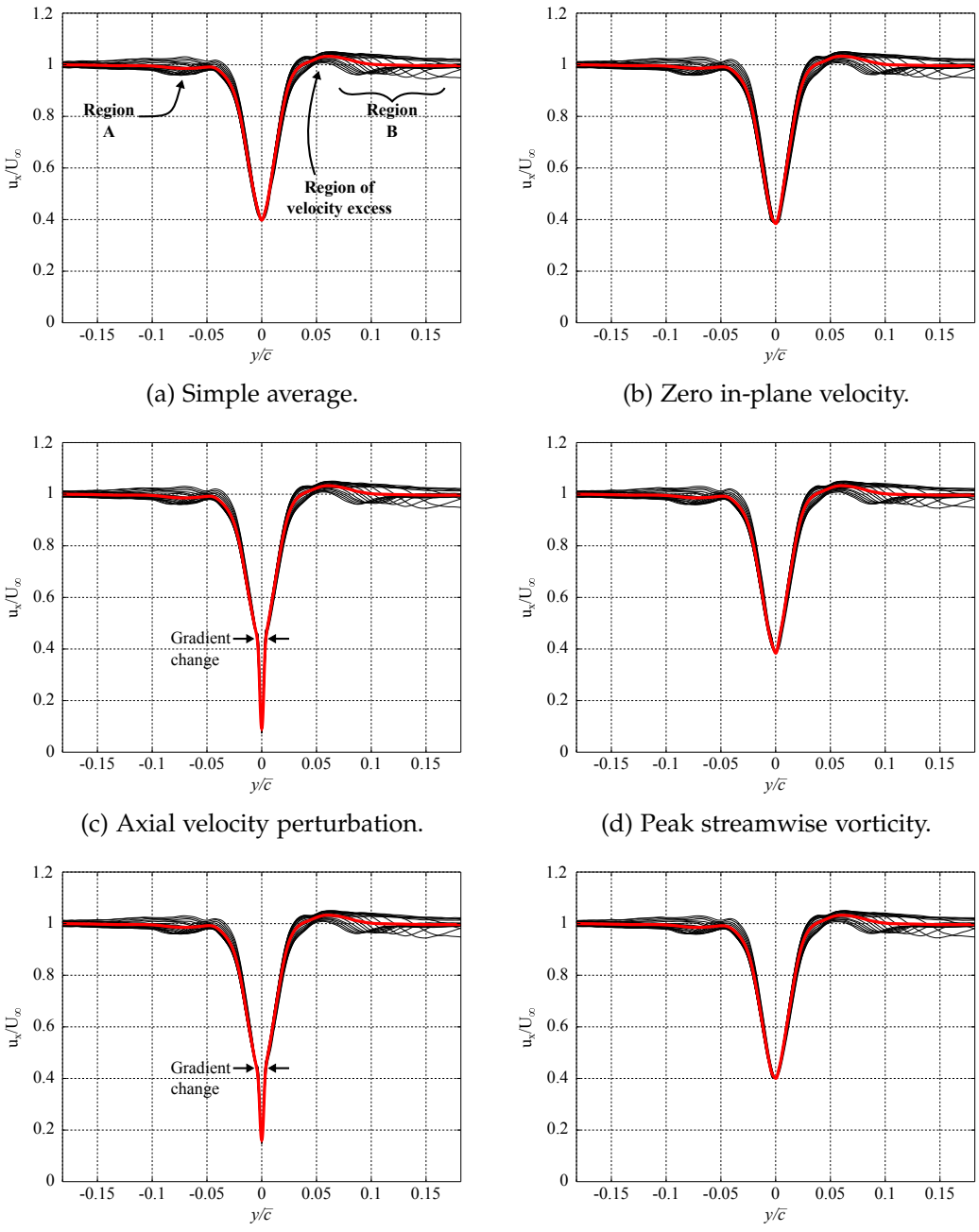

(a) Simple average.

(b) Zero in-plane velocity.

(c) Axial velocity perturbation.

(d) Peak streamwise vorticity.

(e) Peak streamwise helicity.

(f) Minimum Q.

FIGURE 6.8: Average axial velocity profiles, and vortex mean axial profile (red line), calculated with different centring methods at $x/\bar{c} = 2.5$, $Re = 1.5 \times 10^6$, and $\alpha = 8°$ for the planar wing.

in-plane, vorticity, and Q-criterion centring methods, shown in figures 6.8b, 6.8d, and 6.8f respectively, have little effect on the peak axial deficit. It is seen that the zero in-plane and vorticity based methods increase the peak axial velocity deficit at $y/\bar{c} = 0$ by $\approx 3\%$, while the Q-criterion centring method actually reduced the deficit by 6.5% relative to the simple averaged case.

It is observed that the axial perturbation (figure 6.8b) and helicity (figure 6.8e) based centring methods have a remarkable influence on the velocity deficit recorded, increasing the peak axial velocity deficit by 76.9%, and 75.7% respectively, relative to the simple averaged vortex. Referring back to figure 6.3b, the instantaneous vortex realisation of the vortex indicated a core axial velocity of $\approx 0.22U_\infty$. The axial perturbation and helicity centring methods provide comparable time-averaged results. Furthermore, for both of these cases, a double gradient structure is observed near the vortex core centre at $y/\bar{c} \approx \pm 0.0035$ ($\approx 0.18r_c$). This coincides with the double gradient observed for the swirl velocity field.

6.2.3 VORTICITY DISTRIBUTION

Figure 6.9 presents the normalised vorticity profiles of the simple average and vortex centred averages, reported along 36 radii equispaced around the notional centre, with mean vorticity profiles also illustrated.

The peak vorticity at the core centre is found to vary with the application of instantaneous vortex centring methods while, similar to the swirl and axial velocity components, the overall profile remains largely unchanged. All centring methods are recorded to increase the peak vorticity, relative to the simple averaged case, with the axial perturbation centring proving least effective in this instance with a peak vorticity increase of 0.2%. The zero in-plane, vorticity, helicity, and Q-criterion centring methods increase the peak vorticity at the core centre by 14.6%, 41.0%, 27.9%, and 35.2%, respectively.

A double gradient structure is observed in the vicinity of the vortex centre for the vorticity, helicity, and Q-criterion centring methods at $y/\bar{c} \approx \pm 0.007$ ($\approx 0.37r_c$). The structure of the inner vortex core will be discussed in detail in Section 6.3.

6.2.4 TURBULENCE QUANTITIES

The fluctuating turbulent properties of the vortex core have been compared for different vortex centring methods; a detailed analysis of the turbulence in the planar wing vortex core is presented in Section 6.3. The instantaneous velocity at one point of the flow field is expressed as the sum of the average velocity at that point and its fluctuating component:

$$\mathbf{u} = \overline{\mathbf{u}} + \mathbf{u}' \tag{6.9}$$

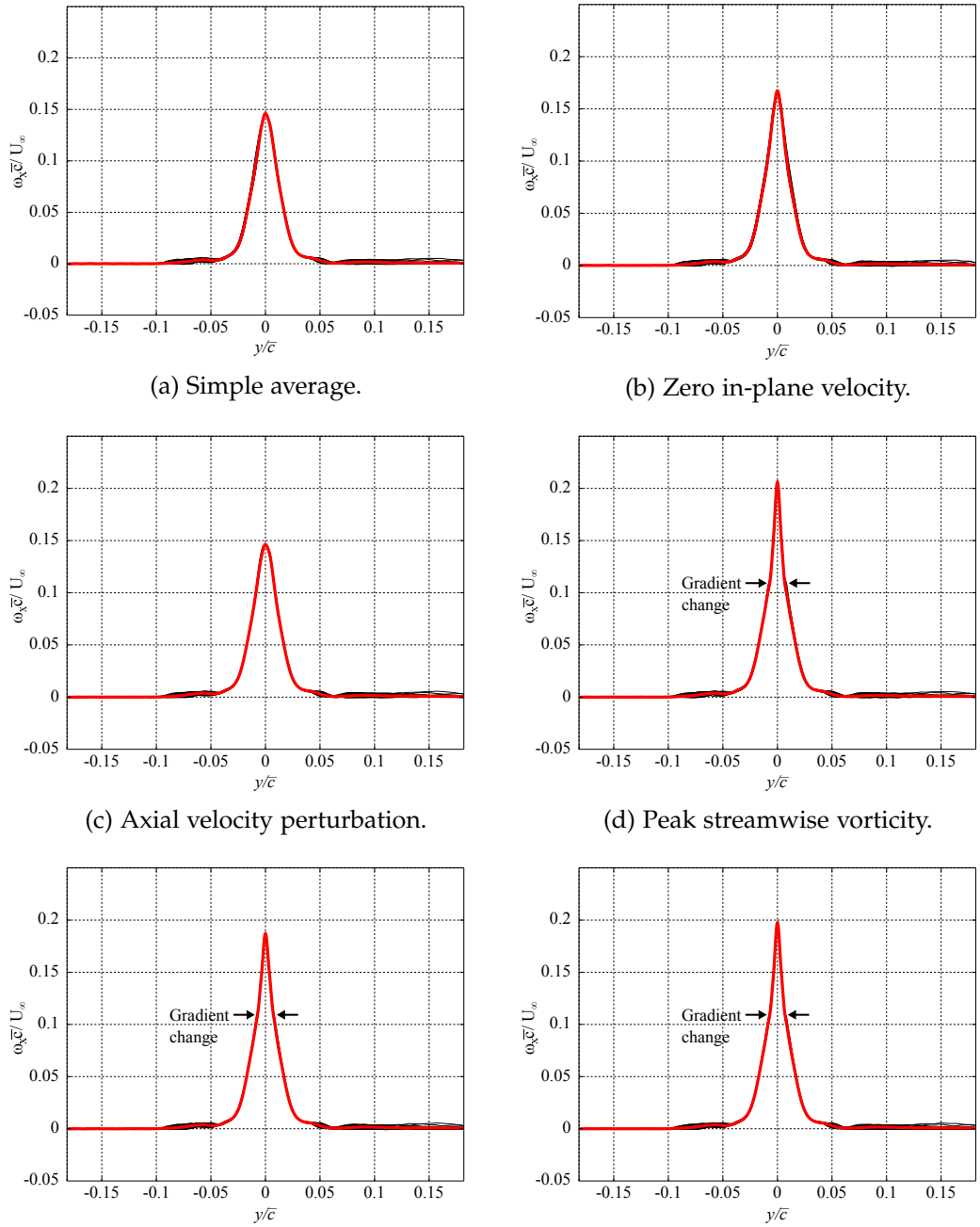

(a) Simple average.

(b) Zero in-plane velocity.

(c) Axial velocity perturbation.

(d) Peak streamwise vorticity.

(e) Peak streamwise helicity.

(f) Minimum Q.

FIGURE 6.9: Average vorticity profiles, and vortex mean vorticity profile (red line), calculated with different centring methods at $x/\bar{c} = 2.5$, $Re = 1.5 \times 10^6$, and $\alpha = 8^\circ$ for the planar wing.

The root mean square of velocity fluctuations (square root of turbulent normal stresses) is defined as follows and is scaled by the freestream velocity U_∞:

$$\begin{aligned} \sigma_u &= \sqrt{\overline{u'^2}} = \sqrt{(\overline{u_i - \overline{u}})^2} \\ \sigma_v &= \sqrt{\overline{v'^2}} = \sqrt{(\overline{v_i - \overline{v}})^2} \\ \sigma_w &= \sqrt{\overline{w'^2}} = \sqrt{(\overline{w_i - \overline{w}})^2} \end{aligned} \tag{6.10}$$

The turbulent kinetic energy (TKE) is also calculated, characterised by the measured root mean square of the velocity fluctuations. The TKE can be quantified by the mean of the turbulence normal stresses (half the sum of the variance of the velocity fluctuations):

$$k = \frac{1}{2}\left(\overline{u'^2} + \overline{v'^2} + \overline{w'^2}\right) \tag{6.11}$$

The TKE is scaled by U_∞^2.

The Reynolds stresses (a second order term), also scaled by U_∞^2, are defined as follows:

$$\begin{aligned} \overline{v'w'} &= \overline{(v_i - \overline{v})(w_i - \overline{w})} \\ \overline{u'v'} &= \overline{(u_i - \overline{u})(v_i - \overline{v})} \\ \overline{u'w'} &= \overline{(u_i - \overline{u})(w_i - \overline{w})} \end{aligned} \tag{6.12}$$

where the $\overline{v'w'}$ are the stresses on the SPIV plane.

The shear strain rate ε_{yz} and the normal strain rate ε_{xx} are calculated with an eight point scheme as described by Raffel at el. [267] where, for the latter, incompressibility is assumed:

$$\begin{aligned} \varepsilon_{yz} = \varepsilon_{zy} &= \frac{1}{2}\left(\frac{\partial v}{\partial z} + \frac{\partial w}{\partial y}\right) \\ \varepsilon_{xx} &= \frac{\partial u}{\partial x} = -\left(\frac{\partial v}{\partial y} + \frac{\partial w}{\partial z}\right) \end{aligned} \tag{6.13}$$

The maximum Mach number found in the flow field of the trailing vortex is of the order of $M = 0.14$, thus the assumption of $\nabla \cdot \mathbf{u} = 0$ is reasonable. The normalisation of the shear strain rate is scaled by $U_\infty / \bar{c}$.

Figures 6.10 and 6.11 present the in-plane turbulent velocity fluctuation components, while figure 6.12 presents the out-of-plane fluctuations. In each figure, the simple average and vortex centred flow field are compared. High fluctuations are observed within the vortex core for all components. Both in-plane fluctuations, σ_v, and σ_w, exhibit elliptical profiles aligned with the y- and z- major axis respectively, whereas the axial fluctuations, σ_u show a more axisymmetric profile. This behaviour was also observed by Ramasamy et al. [320].

Chow et al. [337] have discussed the biasing effect on the in-plane fluctuations in detail, where the results shown in figures 6.10 and 6.11 agree with the results of Chow et al. [337] in that the turbulence distribution inside a trailing vortex is anisotropic. Furthermore, it is clear that for the in-plane centring method, viewed in figures 6.10b and 6.11b, very low in-plane fluctuations are observed in the centre of the vortex core of the same order of the in-plane velocity fluctuations recorded in the freestream ($\approx 0.08\sigma$). Conversely, the axial velocity perturbation, peak vorticity, and Q-criterion centring methods increase the in-plane velocity fluctuations at the core centre.

The out-of-plane velocity fluctuations show an axisymmetric distribution around the vortex core. Both zero in-plane and helicity based centring methods, figures 6.12b

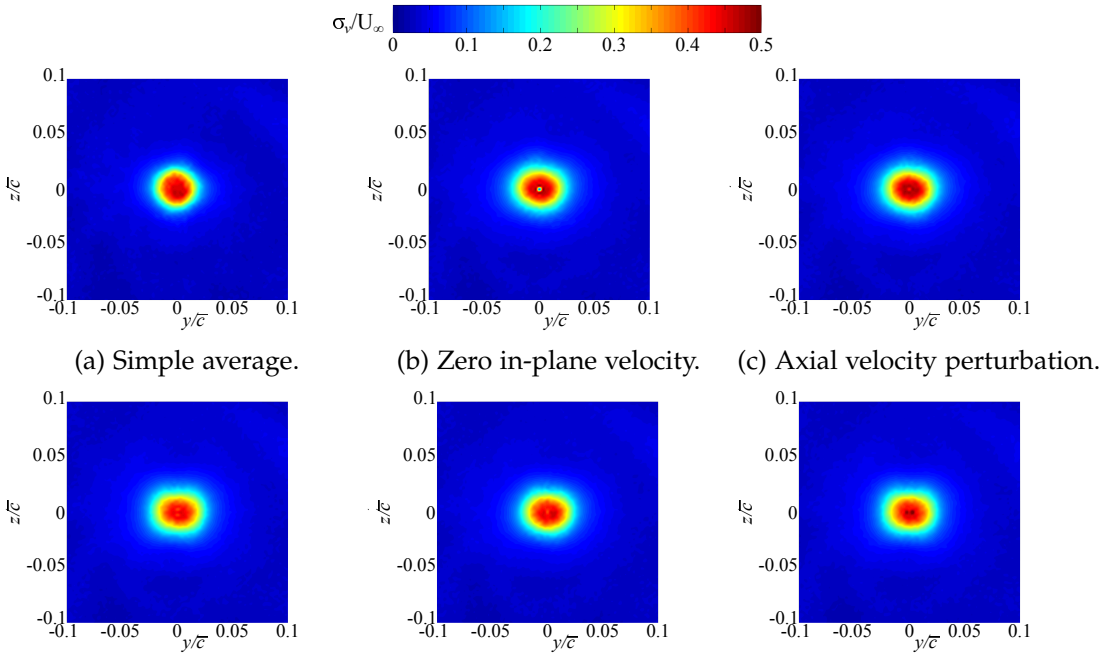

(a) Simple average. (b) Zero in-plane velocity. (c) Axial velocity perturbation.

(d) Peak streamwise vorticity. (e) Peak streamwise helicity. (f) Minimum Q.

FIGURE 6.10: In-plane velocity fluctuations, σ_v/U_∞, for different centring methods at $x/\bar{c} = 2.5$ and $\alpha = 8°$ for the planar wing arrangement.

and 6.12e respectively, show a decrease of σ_u fluctuations at the centre of the vortex surrounded by peak turbulent fluctuations. The axial velocity perturbation, peak vorticity and Q-criterion centring methods are observed to increase the the out-of-

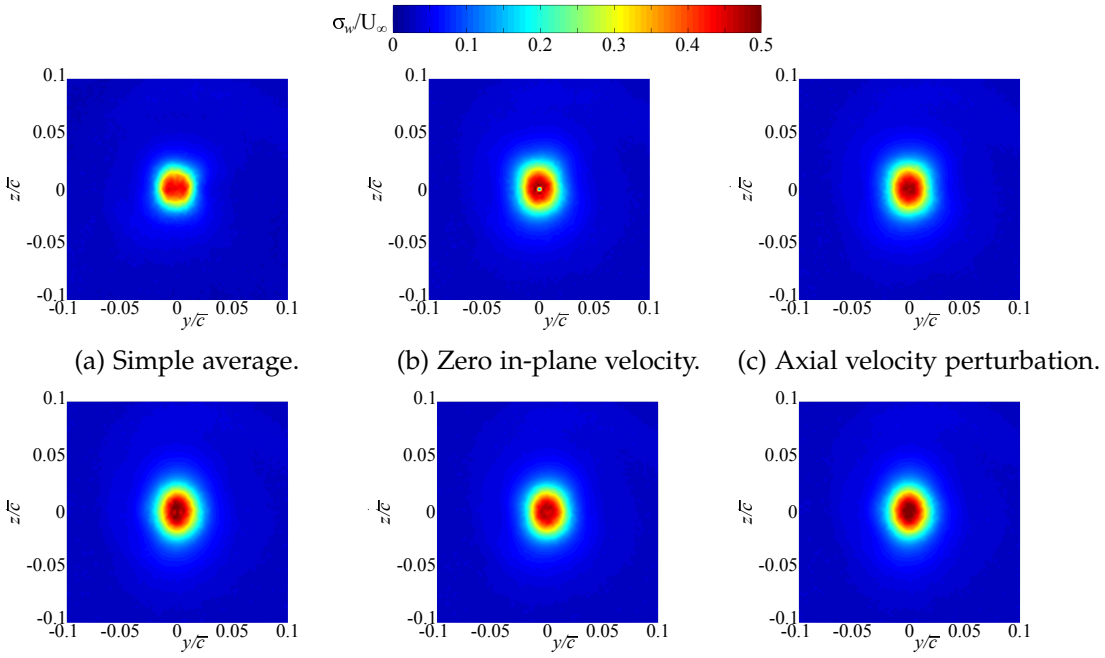

(a) Simple average. (b) Zero in-plane velocity. (c) Axial velocity perturbation.

(d) Peak streamwise vorticity. (e) Peak streamwise helicity. (f) Minimum Q.

FIGURE 6.11: In-plane velocity fluctuations, σ_w/U_∞, for different centring methods at $x/\bar{c} = 2.5$ and $\alpha = 8°$ for the planar wing arrangement.

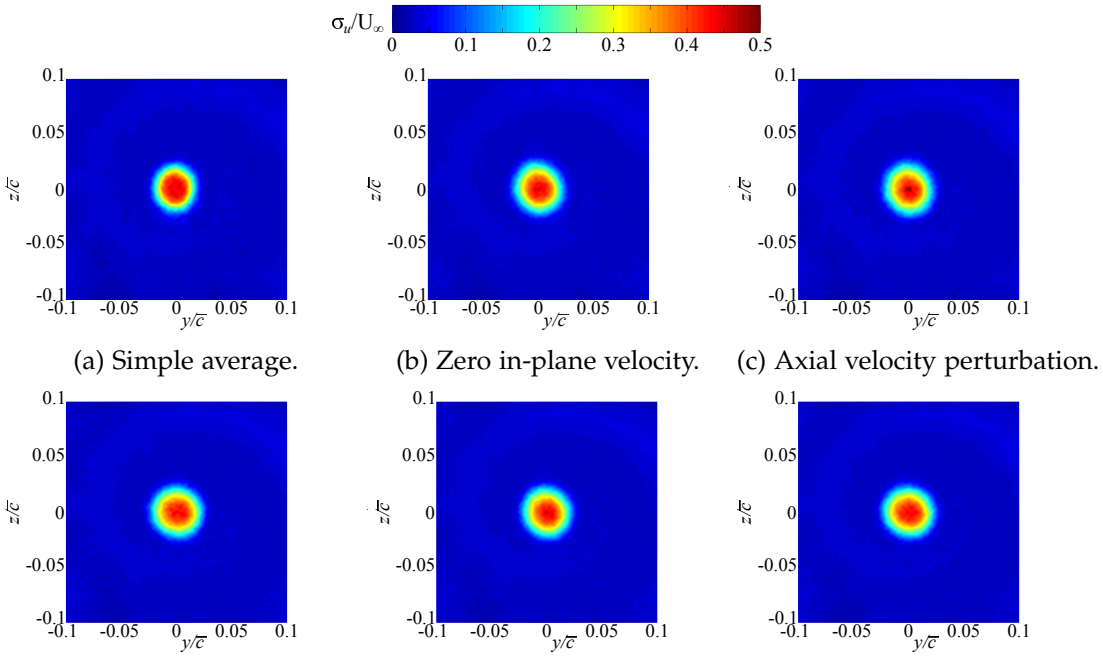

(a) Simple average. (b) Zero in-plane velocity. (c) Axial velocity perturbation.

(d) Peak streamwise vorticity. (e) Peak streamwise helicity. (f) Minimum Q.

FIGURE 6.12: Out-of-plane velocity fluctuations, σ_u / U_∞, for different centring methods at $x/\bar{c} = 2.5$ and $\alpha = 8^\circ$ for the planar wing arrangement.

plane velocity fluctuations in the core centre. It is appropriate to indicate that strong turbulent velocity fluctuations inside the vortex core do not necessarily correspond to the vortex centre velocity fluctuations, but instead refer to a point within the vortex core. Only the peak axial perturbation centring method, by definition, would correspond to the vortex centre. Therefore, the fluctuations of the out-of-plane velocity are not directly related to the vortex wander, but only to its instantaneous intensity. Due to this, Ramasamy et al. [320] and Han et al. [338] indicate that the out-of-plane fluctuation component will dominate any characteristic estimation (such as TKE, shear strain rates, or Reynolds stresses) within the vortex core, and thus can be expected to show similar characteristics to that indicated by the out-of-plane fluctuating velocity component.

Compiling the velocity components in the three axes the TKE is obtained; contours of which are presented in figure 6.13. For all methods the TKE is observed to be axisymmetric. The axial perturbation and vorticity centring methods, shown in figures 6.13c and 6.13d, suggest an increase of turbulence in the centre of the core, while the zero in-plane, helicity, and Q-criterion centring methods illustrate a drop in TKE at the vortex centre. Regardless of the centring method adopted, peak turbulence is located in the vicinity of the core. The peak TKE at the centre is dictated by the high turbulence level of all the velocity components within the core. The application of the zero in-plane, helicity, and Q-criterion centring methods indicate that relaminarisation of the vortex core has occurred. More details of relaminarisation in the planar wing vortex core is discussed in Section 6.3.5.

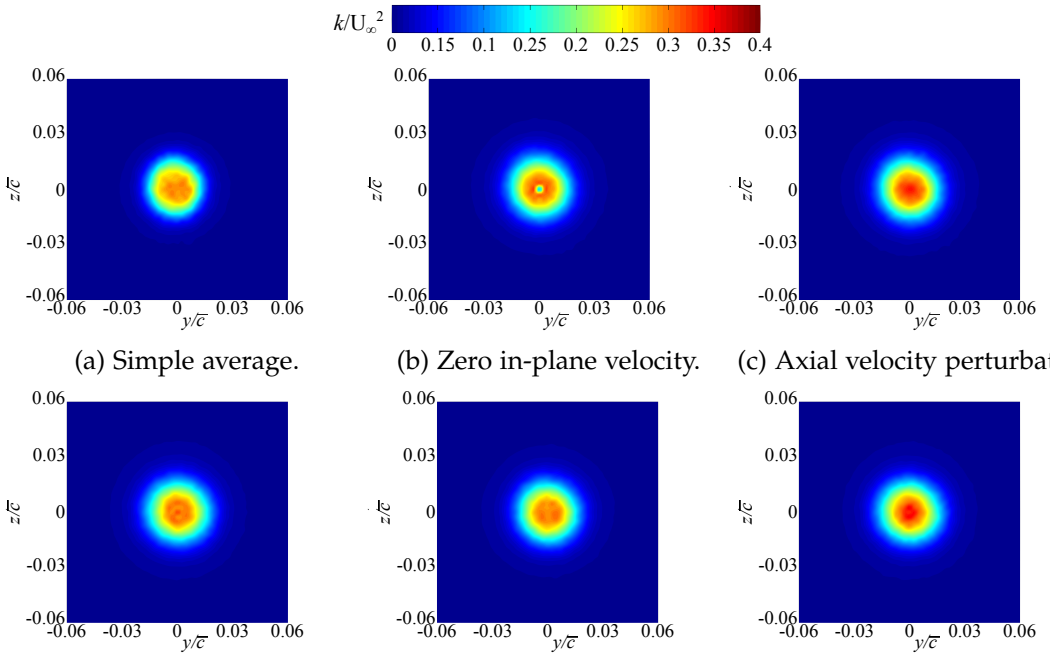

(a) Simple average. (b) Zero in-plane velocity. (c) Axial velocity perturbation.

(d) Peak streamwise vorticity. (e) Peak streamwise helicity. (f) Minimum Q.

FIGURE 6.13: Time-averaged turbulent kinetic energy, k/U_∞^2, for different centring methods at $x/\bar{c} = 2.5$ and $\alpha = 8°$ for the planar wing arrangement.

The Reynolds shear stress in the SPIV plane, and the corresponding shear strain are shown in figures 6.14 and 6.15 for the different averaging methods. The four-lobed pattern observed, with alternative positive and negative signs for both the $\overline{v'w'}$ and the strain rate components has physical meaning; especially when the relative orientation between the $\overline{v'w'}$ and the strain rate is 45°. Both Chow et al. [337] and Ramasamy [320] observe this result, indicating that this reveals the anisotropic eddy viscosity within the vortex core. Both the shear strain rates and the Reynolds stresses are seen to change in pattern and magnitude when adopting different centring methods. Understanding the variation of strain rates and Reynolds stresses is crucial for understanding the production of turbulence inside the vortex.

Application of any of the centring methods is seen to vastly improve the realisation of the Reynolds stresses within the vortex core relative to the simple averaged case, as shown in figure 6.14. Regardless of centring method used, the Reynolds stresses, $\overline{v'w'}$, are seen to reach a maximum at $\approx$ 95% of the core radius, with a maxima also observed at $\approx$ 24% of the core radius; both of which are particularly clear in the vorticity and helicity centring methods shown in figures 6.14d and 6.14e. Following the maxima at $\approx$ 95% of the core radius, the Reynolds stresses reduce rapidly to zero within two core radii of the vortex axis. The magnitude of the shear stresses is found to reach its minimum value at the vortex axis.

With reference to figure 6.15a, the shear strain rates are observed to show the same four-lobed pattern outside of the vortex core independent of the averaging method used. Of the four large lobes present in each case, a maximum shear strain

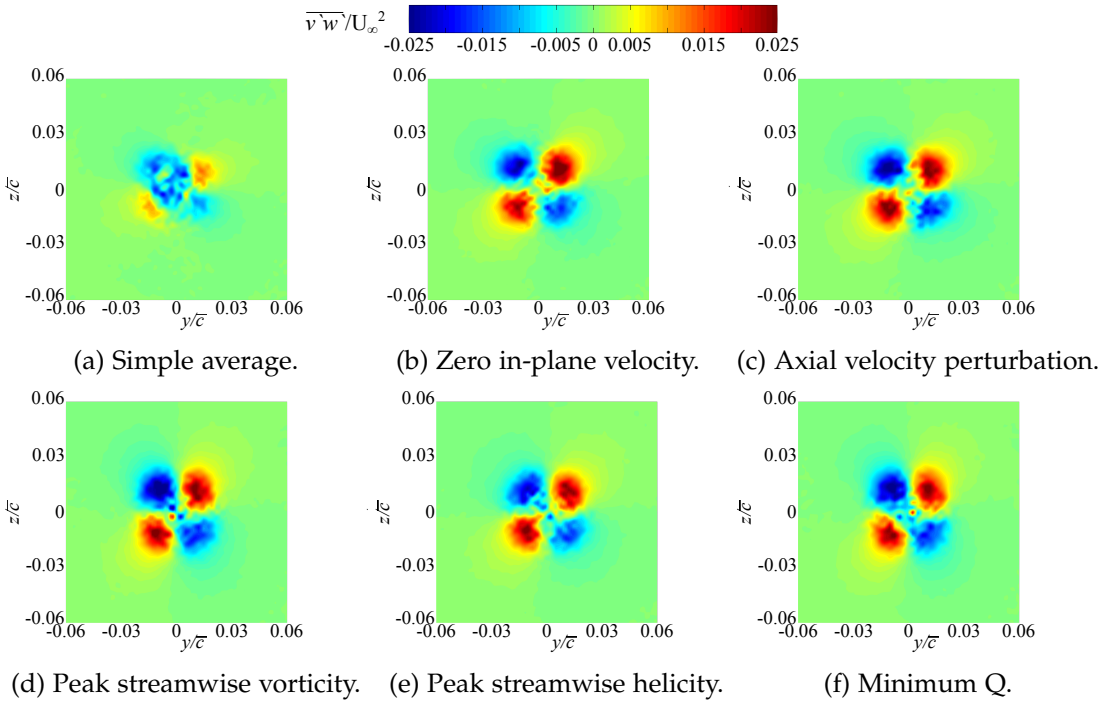

(a) Simple average. (b) Zero in-plane velocity. (c) Axial velocity perturbation.

(d) Peak streamwise vorticity. (e) Peak streamwise helicity. (f) Minimum Q.

FIGURE 6.14: Time-averaged vortex Reynolds stresses, $\overline{v'w'}/U_\infty^2$, for different centring methods at $x/\bar{c} = 2.5$ and $\alpha = 8^\circ$ for the planar wing arrangement.

is indicated outside the vortex core at $\approx 1.22r_c$. The zero in-plane and axial velocity perturbation methods are found to reduce the magnitude of the shear strains observed, while unable to provide any shear strain information from within the vortex core. A remarkable realisation of the shear strain rates within the vortex core is found with

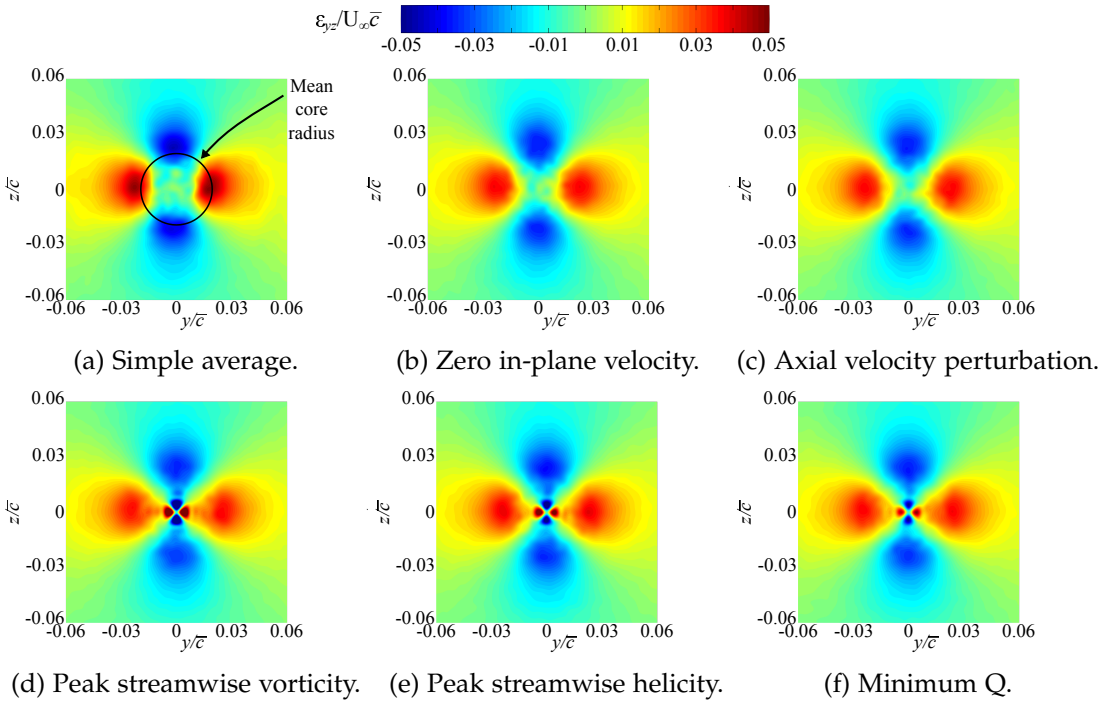

(a) Simple average. (b) Zero in-plane velocity. (c) Axial velocity perturbation.

(d) Peak streamwise vorticity. (e) Peak streamwise helicity. (f) Minimum Q.

FIGURE 6.15: Shear strain rate, $\varepsilon_{yz} \cdot U_\infty/\bar{c}$, for different centring methods at $x/\bar{c} = 2.5$ and $\alpha = 8^\circ$ for the planar wing arrangement.

the application of the vorticity, helicity, and the Q-criterion centring methods, each of which defining a double lobed structure. Shear strain peaks are identified at $\approx 30\%$ of the core radius, with a minimum shear strain inside the vortex core occurring at $\approx 50\%$ of the core radius. Figure 6.16 illustrates this trend taking a data cut along the horizontal ($z/\bar{c} = 0$) for each averaging method.

Figure 6.16 highlights the double lobe structure with maximum shear strain near the centre of the core ($\approx 0.30r_c$). This is followed by a minima at half the core radius ($\approx 0.5r_c$), and a second shear strain maxima just beyond the core radius ($\approx 1.22r_c$). The wingtip vortex flow, in the very early stages of the wake, is dominated by secondary vortex structures and the roll up of the vortex sheet. The vortex meandering spatial correction is observed, in this case, to not strongly affect the macro vortex structure, but instead reveals the flow structures within the core and provides confidence in the measurements made outside of the core region.

The helicity based correction method is the only method discussed in this work which uses all available velocity components, and provides consistent description of the inner vortex core structure. The vorticity and Q-criterion methods have also proven reasonably robust with the exception of sufficiently describing the inner core axial velocity. The Q-criterion (and the λ_2) centring method is complex, computationally expensive, and introduces errors from the calculation of the flow field gradients while not providing any clear benefits [267]. The zero in-plane and axial velocity perturbations cannot accurately account for the whole vortex structure, particularly when considering turbulence analysis. Therefore, unless explicitly indicated otherwise, the helicity centring method will be used for correcting for vortex wander, having been found to be the most appropriate in describing the swirl and axial velocity distributions, vorticity profiles, and turbulent properties of the vortex core, including Reynolds stress and shear strain rates. Ramasamy et al. [316] arrived at the same conclusion in a study for rotor blade tip vortices.

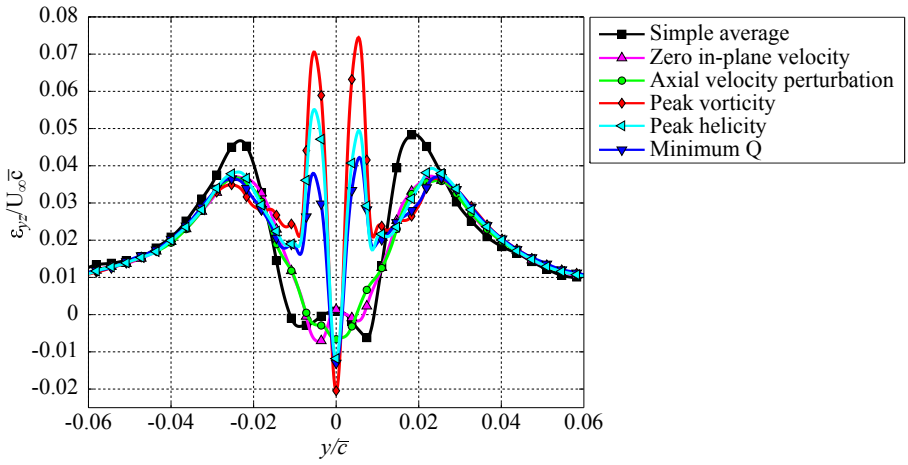

FIGURE 6.16: Shear strain data profiles for different centring methods presented in figure 6.15; data cut taken along $z/\bar{c} = 0$.

Assessment of the statistical convergence and random uncertainty for several vortex properties with the application of the helicity based centring method is presented in Appendix C. Based on this analysis all SPIV data presented from this point forward has been averaged over 1800 samples to provide statistical convergence with a peak random uncertainly of less than 3% for all velocity components.

6.3 PLANAR WING TRAILING VORTEX

The planar wing trailing wingtip vortex is discussed in this section. The planar wing arrangement and its near field vortex wake must be understood before it is compared to the C-wing trailing vortex. The C-wing trailing vortex is compared to the planar wing vortex system as a benchmark in Section 6.4.

6.3.1 SWIRL VELOCITY DISTRIBUTION

Figure 6.17 shows the averaged swirl velocity distributions for a range of α and $x/\bar{c}$, where the suction and pressure sides of the vortex relative to the wing have been indicated. Distributions have been averaged over 36 radii equispaced around the vortex centre. The vortex core radius is defined as the distance between the vortex centre ($r/\bar{c} = 0$) and peak swirl velocity. Inside the core, the swirl flow varies approximately linearly, while outside of the vortex core the swirl velocity varies inversely with the radial distance asymptotically approaching zero.

Within the vortex core, a secondary structure is observed consistently at 18 to 22% of the core radius, indicated by a point of inflection in the otherwise linear profile. This inflection is particularly clear for $x/\bar{c} > 2.5$ for all angles of attack. Such double-core, or layered-core, structures have been observed by Devenport et al. [319], who argues that the double-core is a remnant of the vortex initial conditions imposed by a blunt or squared wingtip. Engel [339] showed the formation of the main wingtip vortex on the suction side of the wing, accompanied by the development of strong secondary vortices from the pressure side of a squared wingtip. Devenport et al. [319] suggested that the vorticity associated from the pressure side vortices become wrapped up into an annulus around the main vortex core. This diffusive merging of primary and secondary wingtip vortices, leading to a multi-structured core, has also been discussed by Phillips [336]. While multi-structured core structures are theorised and discussed, with few experimental observations, little information regarding the actual structure or behaviour has been explored in the literature.

Independent of angle of attack, the early vortex peak swirl velocity on the suction side, relative to the pressure side, of the wing is up to 14% higher at $x/\bar{c} = 1.35$; implying an ever-developing vortex. This differential decreases with downstream distance as the vortex rolls up further circumferentially, distributing the swirl velocity around the core and becoming increasingly more isolated from the vortex sheet. Figure

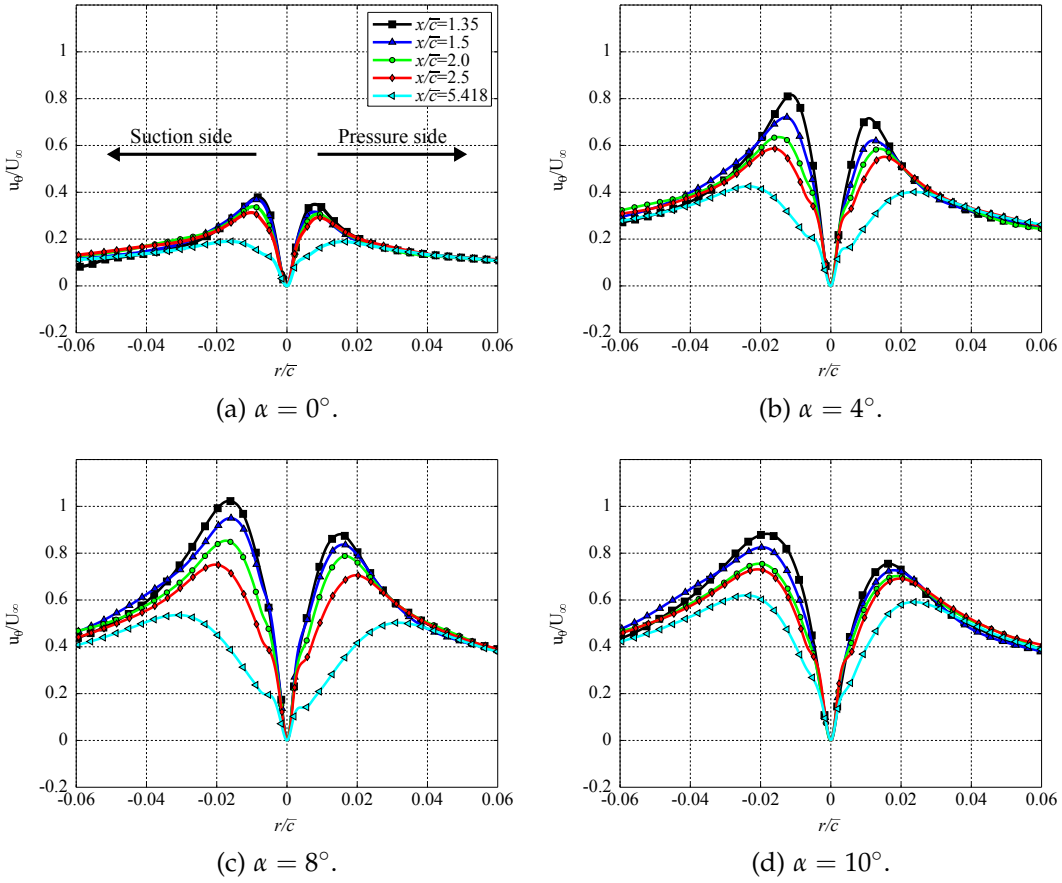

(a) $\alpha = 0°$. (b) $\alpha = 4°$.

(c) $\alpha = 8°$. (d) $\alpha = 10°$.

FIGURE 6.17: Swirl velocity development with angle of attack and $x/\bar{c}$ plane.

6.17 shows that for the angles of attack presented, the peak swirl velocities on the pressure side begin to reach an equivalent magnitude to those observed of the suction side as $x/\bar{c} = 2.5$ is approached, and an axisymmetric swirl velocity distribution, unhindered by the vortex sheet, is reached.

Variation in the vortex peak swirl velocity with downstream distance as a function of the wing angle of attack is presented in figure 6.18. Over $0° \leq \alpha \leq 6°$ (linear lift region) a linear relationship is observed between the peak swirl velocity and angle of attack. This is indicative of a laminar rate of growth. As the wing enters light stall at approximately $\alpha = 8°$ to $9°$, the swirl velocities for any given $x/\bar{c}$ plateaus. Further increases in the angle of attack, leading into deeper wingtip stall, leads to the transport/convection of separated flow into the wingtip vortex and a rapid decay of peak swirl velocity is recorded. This trend was also observed by Birch et al. [340]. Peak swirl velocities are also observed to reduce with $x/\bar{c}$ for any given angle of attack.

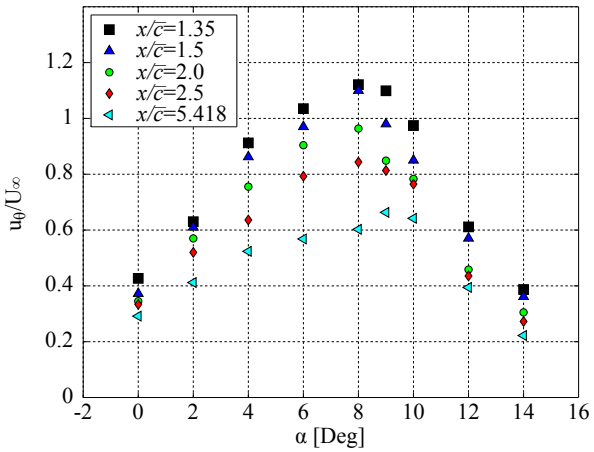

FIGURE 6.18: Peak swirl velocity at different $x/\bar{c}$ planes as a function of α.

6.3.2 VORTEX CORE SHAPE

As previously stated, the vortex core radius, r, is defined as the distance between the vortex centre ($r/\bar{c} = 0$) and the point of maximum peak swirl velocity. In this section, the vortex core shape is presented as the locus of the points of maximum swirl velocity around the vortex centre. Thus, the vortex core edge has been defined from 36 radii equispaced around the vortex centre. From this, different values of the core radius are found depending on the orientation (with θ_v as the azimuthal coordinate) of the cut along which the swirl velocity is measured. Ramasamy et al. [316] found that two data slices across the tip vortex (producing four profiles) provided an acceptable measurement of the vortex core dimension.

In figure 6.19, the radius values at each $x/\bar{c}$ downstream plane are plotted on polar plots as a function of θ_v for different angles of attack. In the present reference system the vortex rotates anti-clockwise. For each angle of attack presented the vortex core shape is observed to be axisymmetric, and grows in size with both angle of attack and downstream convection. Comparing figures 6.19c and 6.19d, for $\alpha = 8^\circ$ and 10° respectively, it is intriguing to note that the rate of vortex core growth is lower for $\alpha = 10^\circ$ than for $\alpha = 8^\circ$. This is clear when comparing the farthest downstream location $x/\bar{c} = 5.418$. It is also noticed that at the upstream locations (such as $x/\bar{c} = 1.35$), the vortex for $\alpha = 8^\circ$ is smaller than that for $\alpha = 10^\circ$. The only explanation that can currently be attributed to this is that between $\alpha = 8^\circ$ and 10° the progression of the stall front over the outboard wing alters the load distribution such that at $\alpha = 10^\circ$ the way in which the vortex forms changes.

Variation in the mean vortex core radius with downstream distance as a function of the wing angle of attack is presented in figure 6.20a, with an enhanced view of the lower angle of attack range shown in figure 6.20b. Over the range $0^\circ \leq \alpha \leq 8^\circ$ (which mostly coincides with the linear lift region of the wing), a linear rate of growth is observed in the vortex core radius with angle of attack at any given downstream

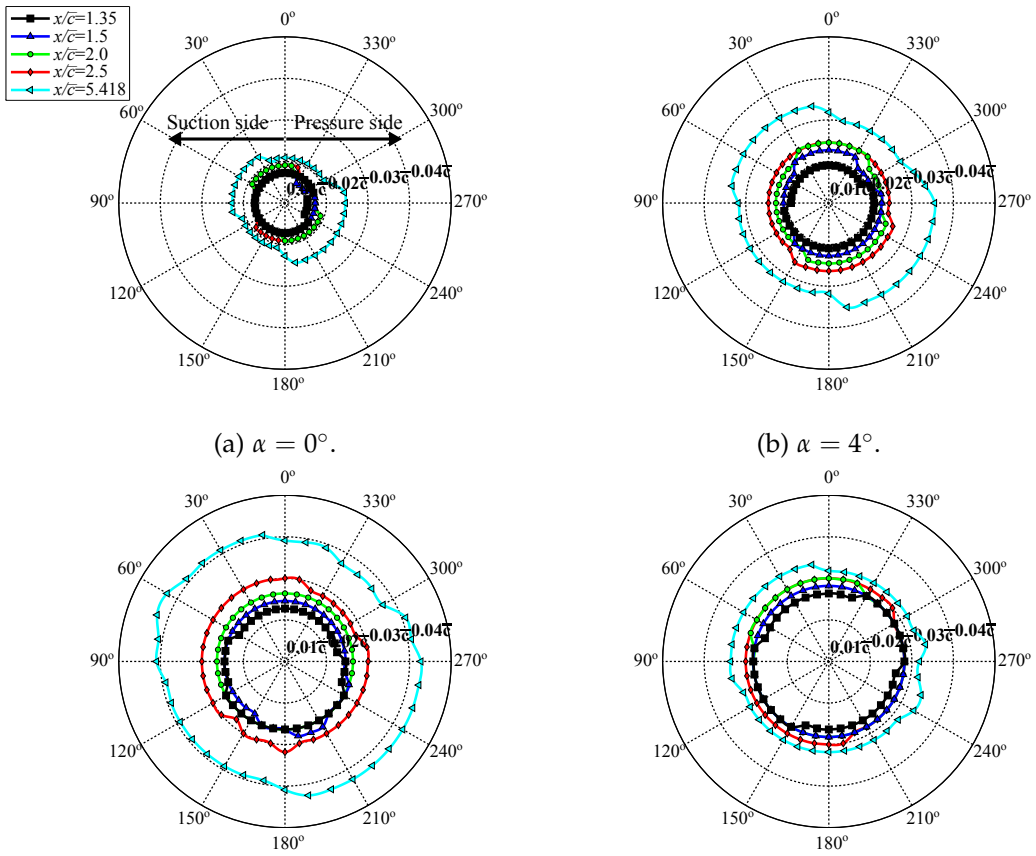

(a) $\alpha = 0°$.

(b) $\alpha = 4°$.

(c) $\alpha = 8°$.

(d) $\alpha = 10°$.

FIGURE 6.19: Development of vortex core shape for different angles of attack and $x/\bar{c}$ plane.

plane. Figure 6.20b illustrates that the core radius reduces in size for all downstream locations for both $\alpha = 9°$ and $10°$ relative to $\alpha = 8°$. For angles of attack $\alpha < 10°$, rapid vortex growth is observed as wingtip stall deepens, and a less well defined and subsequently weaker vortex forms with an increased radius.

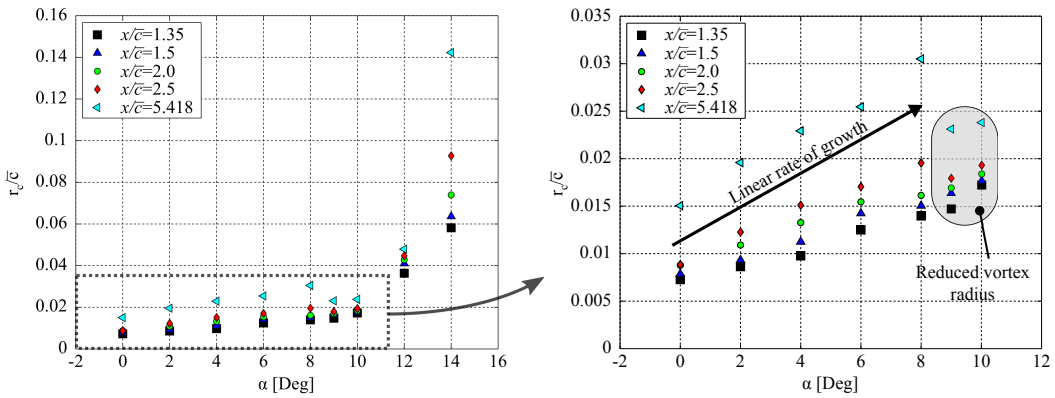

(a) $0° \leq \alpha \leq 14°$.

(b) $0° \leq \alpha \leq 10°$.

FIGURE 6.20: Mean vortex core radius at different $x/\bar{c}$ planes as a function of α.

6.3.3 AXIAL VELOCITY DISTRIBUTION

The axial flow associated with trailing tip vortices has been studied in great depth over the years and has been shown to be either directed towards the wing (wake-like or velocity deficit), or away from the wing (jet-like or velocity excess), however a unique solution, to date, has not yet been found.

The fact that experiments identify either an excess of a deficit in the axial velocity was explained by Spalart [333] as the result of the acceleration of the flow described by inviscid theory and the total pressure losses by viscosity of the boundary layer fluid layered around the vortex core. Axial velocity excess at the vortex centre can be explained in two mathematically equivalent ways: 1) from consideration of the helical shape of the vortex lines; and 2) from equating the pressure at different points of the vortex. Both approaches lead to the following relationship:

$$\frac{d(u_x^2 + u_\theta^2)}{dr} + 2\frac{u_\theta^2}{r} = 0 \tag{6.14}$$

The circulation profile can be expressed as $\Gamma(r) = 2\pi r u_\theta$, hence re-arranging and substituting for u_θ into equation 6.14:

$$2\pi^2 r^2 \frac{du_x^2}{dr} + \frac{d\Gamma(r)^2}{dr} = 0 \tag{6.15}$$

As it is generally observed that Γ increases with r, it is clear that u_x increases as the vortex axis is approached ($r \to 0$) resulting in a velocity excess. In a physical flow, the fluid surrounding the vortex core is layered with the boundary layer fluid entrained from the wake sheet from the wing surface. This introduces strong shear-layers and viscous losses that contribute to the deceleration of the flow. Spalart [333] indicates that there must be a balance between viscous effects and inviscid acceleration of the axial flow. Thus, large values of the circulation will result in an excess velocity, while low values will result in a velocity deficit of the axial flow field.

Bailey et al. [334] demonstrated that in the very early stages of the vortex formation, the pressure in the vortex core gradually decreases along the vortex axis generating a favourable axial pressure gradient which in turn accelerates the core fluid in the streamwise direction. This results in a jet-like core having an axial velocity excess [319]. Farther downstream, viscous effects decelerate the flow, acting to convert the core to wake-like. It has also been observed that axial velocity gradients introduce a possible mechanism for the production of turbulence within the core [337, 341]. All trailing vortices examined in this study exhibit a wake-like structure, and are considered too far downstream ($x/\bar{c} \geq 1.35$) to exhibit a jet-like vortex core.

Figure 6.21 shows the averaged axial velocity distributions for a range of α and $x/\bar{c}$, where the suction and pressure sides of the vortex relative to the wing have been indicated. Distributions have been averaged over 36 radii equispaced around the

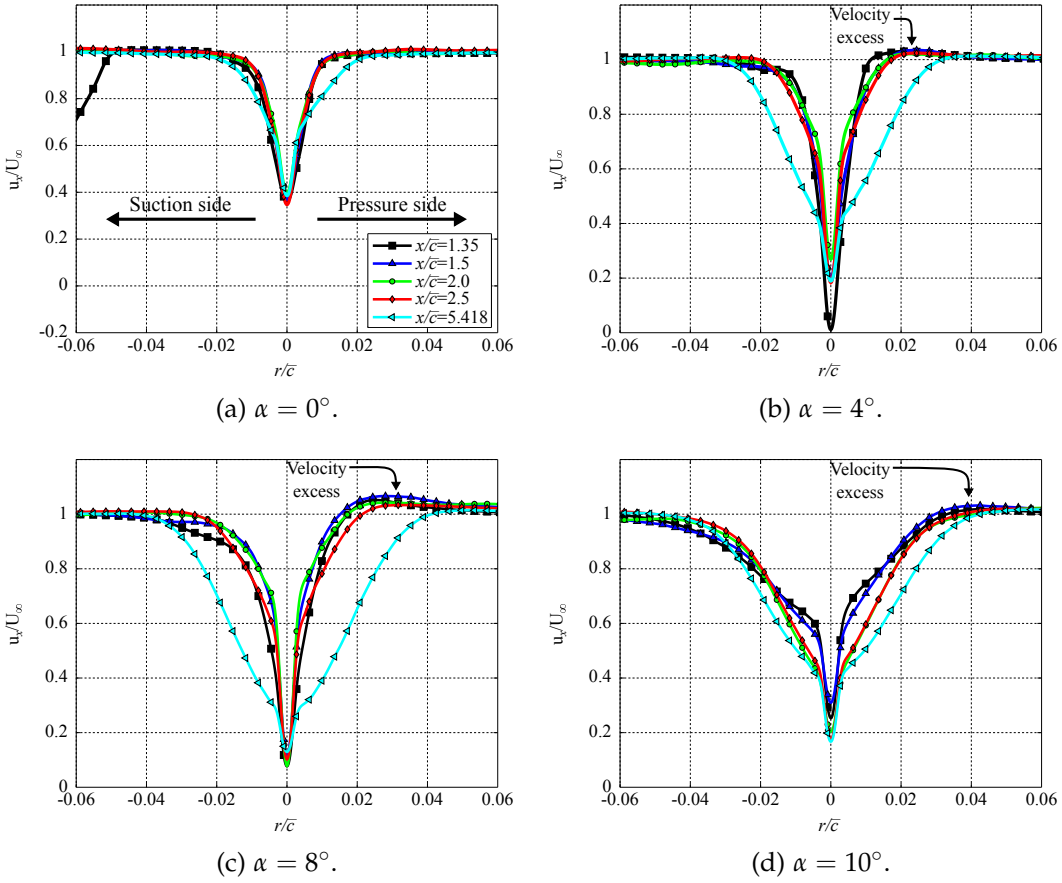

(a) $\alpha = 0°$. (b) $\alpha = 4°$.

(c) $\alpha = 8°$. (d) $\alpha = 10°$.

FIGURE 6.21: Axial velocity development with angle of attack and $x/\bar{c}$ plane.

vortex centre. Inside the core, the axial flow shows a velocity deficit, however, outside the vortex core on the pressure side of the vortex a velocity excess is noticed. This velocity excess is located in a pocket of flow between the vortex and the trailing wake sheet, and is observed to be stronger nearer to the wing for moderate angles of attack.

Variation in the vortex peak axial velocity with downstream distance as function of the wing angle of attack is presented in figure 6.22. Over the linear lift region the peak axial deficit increases until stall onset is approached at which point the peak velocity deficit in the core is shown to decrease. This result was also observed by Gerontakon and Lee [264]. Additionally, peak core deficit is observed to show a general decreasing trend as the vortex travels downstream, indicative of a favourable pressure gradient ($\partial p/\partial x < 0$) along the vortex axis. The mild decay of the velocity deficit at the centre of the vortex core evolves approximately as $x^{-1}log(x)$, which coincides with the asymptotic variation proposed by Batchelor [342] for a fully developed trailing vortex. At $\alpha = 10°$, this relationship appears to reverse such that the peak axial deficit increases with downstream distance. This is indicative of an adverse pressure gradient ($\partial p/\partial x > 0$) along the vortex axis. Similar observations have been made by Phillips and Graham [343], and Sousa and Pereira [318], who indicate that the development of axial pressure gradients along the vortex axis in a trailing vortex system is driven by the axial variation of the swirl velocity, which in turn gives rise to the core axial

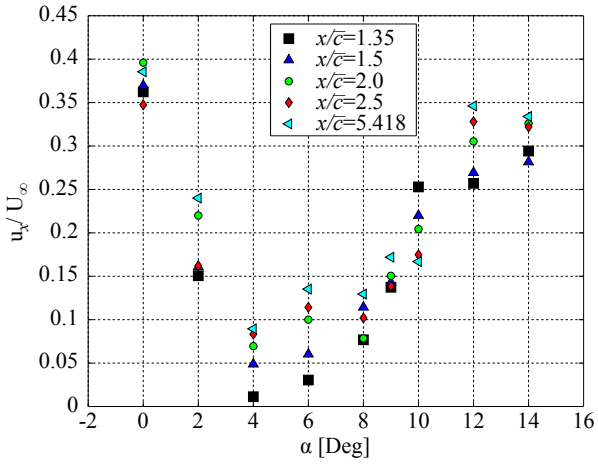

FIGURE 6.22: Peak axial velocity at different $x/\bar{c}$ planes as a function of α.

velocity gradient. These mechanisms provide a balance between inertial and pressure gradient forces.

Considering the aforementioned balance, such a pressure distribution can be responsible for the appearance of axial velocity excess outside of the vortex core on the pressure side of the vortex ($+y/\bar{c}$) as shown in figure 6.23. Similar regions of velocity excess have been identified in other experimental campaigns [265, 318, 344]. The region indicated to exhibit velocity excess is subject to a favourable pressure gradient.

Based on Bernoulli's theorem (derived from the principle of conservation of energy), Batchelor [342] predicted the existence of axial velocity excess trailing vortex systems, both inside and outside of the core, capable of exceeding the freestream velocity [345]. In the three-dimensional vortex, the swirling mass of air is accelerated axially as it is compressed between the highly viscous regions of the wake sheet and the vortex core roll-up. With stronger vortices, and higher swirl velocities, the region of excess velocity is seen to grow while the magnitude remains fairly constant at $u_x/U_\infty \approx 1.05$. As the vortex convects downstream and continues to roll-up, the vortex core becomes increasingly more isolated from the wake sheet, and the velocity excess decreases, tending to U_∞.

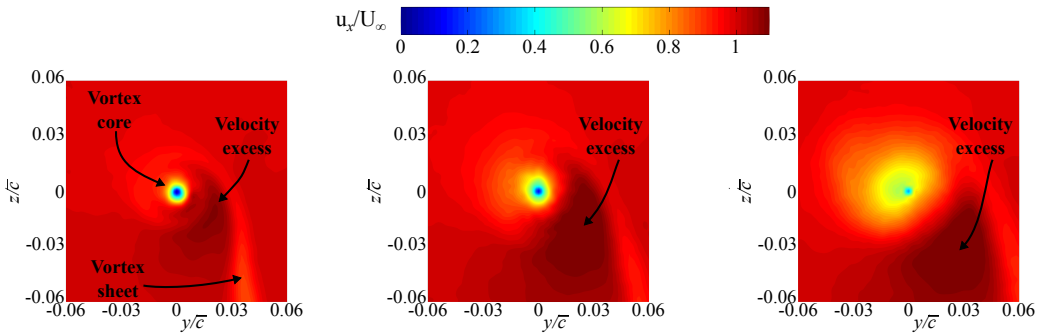

(a) $\alpha = 4°$, at $x/\bar{c} = 1.35$. (b) $\alpha = 8°$, at $x/\bar{c} = 1.35$. (c) $\alpha = 10°$, at $x/\bar{c} = 1.35$.

FIGURE 6.23: Axial velocity contours at $x/\bar{c} = 1.35$ for $\alpha = 4°$, $8°$, and $10°$.

6.3.4 VORTICITY DISTRIBUTION

The vorticity distributions for $\alpha = 0°$, $4°$, $8°$, and $10°$ at all streamwise ($x/\bar{c}$) stations are shown in figure 6.24. For all angles of attack, the peak vorticity at the centre of the vortex core is observed to persist as the vortex translates downstream with only very slight rates of decay over the $1.35 \leq x/\bar{c} \leq 5.418$ range. However, with downstream propagation of the wingtip vortex, the vortex core develops into two distinct structures meeting at $\approx 38\%$ of the core radius, with the outer core vorticity dissipating. The inner core structure (at approximately $\leq 0.38r_c$) appears insulated by the outer vortex core structure, acting as a 'buffer' region which disperses with downstream distance via viscous/turbulent diffusion mechanisms. This explanation helps to clarify why the peak vorticity does not reveal any significant rate of decay with downstream distance for any angle of attack. The persistence and stability of peak streamwise vorticity with downstream position in the near field has also been observed by Ramaprian and Zheng [265] and Yang and Shengjin [346] for planar wings.

Variation in the peak vorticity at the vortex core centre with downstream distance is presented in figure 6.25 as a function of the wing angle of attack. Over the range $0° \leq \alpha \leq 6°$ (which coincides with the linear lift region of the wing) a linear increase of the peak vorticity is observed for each angle of attack for any given downstream

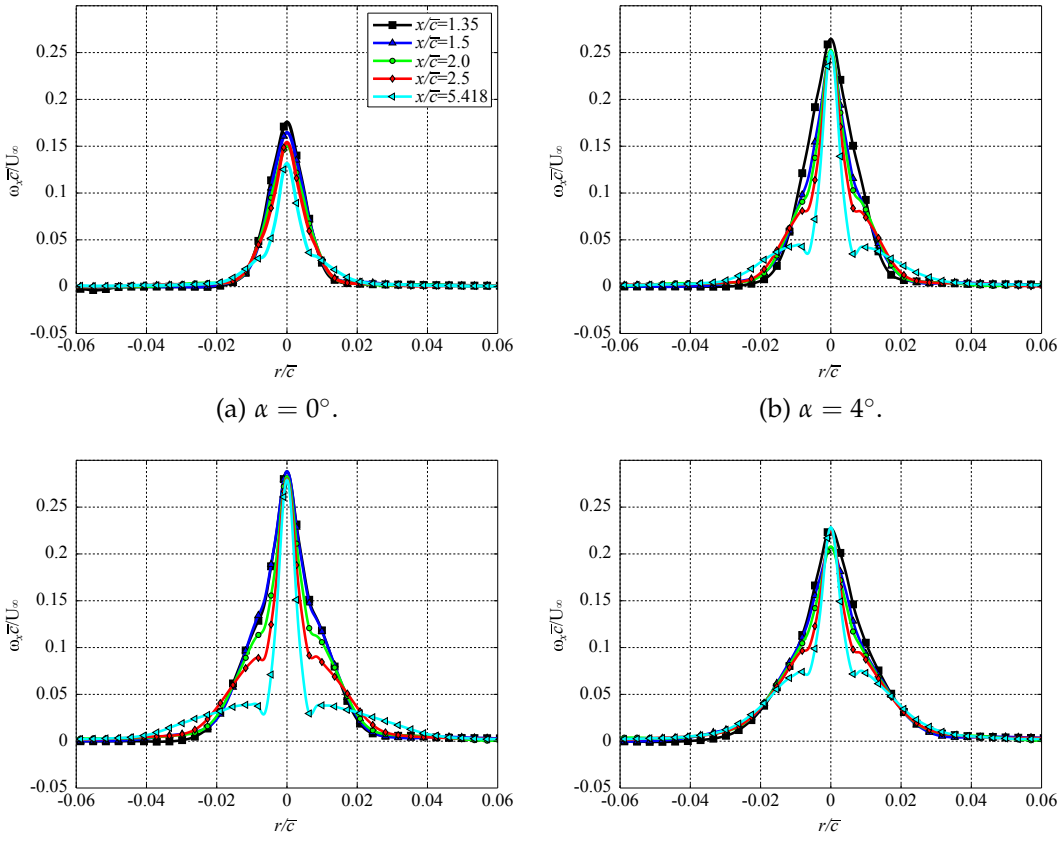

(a) $\alpha = 0°$. (b) $\alpha = 4°$.

(c) $\alpha = 8°$. (d) $\alpha = 10°$.

FIGURE 6.24: Vorticity development with angle of attack and $x/\bar{c}$ plane.

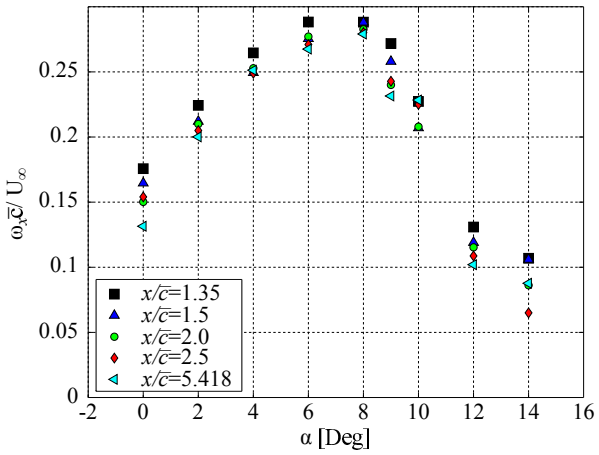

FIGURE 6.25: Peak core vorticity at different $x/\bar{c}$ planes as a function of α.

plane. Progressing into stall $\alpha > 7°$, the peak vorticity is recoded to plateau and then steeply drop off as the wing stall deepens and a weaker wingtip vortex is formed.

6.3.5 TURBULENCE IN THE VORTEX CORE

TURBULENT KINETIC ENERGY EVOLUTION

Despite the high Reynolds numbers encountered in flight conditions of conventional mid-size commercial aircraft (in the order of 10^9), vortices grow with rates typical of laminar flows. This explains the persistence and strength of vortices in the far field. The dissipation rates also follow that of a laminar flow, which is comparably much slower and less dissipative than that found in turbulent flows [347]. Rotations within the vortex core can strongly inhibit turbulence transport of the fluid leading to a stratified flow [348]. Trailing vortices, and in particular vortex cores, are examples of relaminarisation of the flow induced by the fluid rotation in which the contribution of the turbulent fluctuations to the mean flow dynamics become negligible, and a laminar flow is developed [349].

Contours of in-plane velocity fluctuations σ_v and σ_w are roughly elliptical in shape and aligned with the respective major axis and maxima occurring at the vortex centre; examples of this have previously been shown in figures 6.10e and 6.11e, respectively. This shape, observed in all instances, illustrates anisotropy in the radial fluctuations. This is explained by Chow et al. [337] as a consequence of the production of Reynolds shear stress within the vortex core. The out-of-plane velocity fluctuations show an isotropic distribution, such as that shown previously in figure 6.12e, with a reduction of turbulent fluctuations within the core centre. This is found for all test cases. Ramasamy et al. [320] and Han et al. [338] indicate that the out-of-plane fluctuation component will dominate any characteristic estimation (such as TKE, shear strain rates, or Reynolds stresses) within the vortex core, and thus can be expected to

show similar characteristics to that shown by the out-of-plane fluctuating velocity component. Consequently, the TKE also presents a dip in magnitude at the vortex centre.

The turbulent kinetic energy (TKE) development for $\alpha = 0°$, $4°$, $8°$, and $10°$ are presented in figure 6.26 in order to provide a concise description of how the TKE varies with both angle of attack and downstream distance for the planar wing vortex. The dip the in TKE at the vortex centre indicates that relaminarisation of the inner vortex core has occurred, such that the trailing vortex has, at least partially, a laminar core [320, 337]. Work by Martin [350, 351] has shown evidence that the trailing vortex core structure is neither fully laminar or fully turbulent, but is instead in a continuous state of dynamic evolution with an inner core of relatively slow laminar diffusion surrounded by a region of accelerated turbulent diffusion. This is seen in figure 6.26 where the dip signifies a laminar inner core structure, while the peaks at either side indicate an annulus of relatively higher turbulent flow completely enveloping it. Thus, the vortex core propagates downstream away from the wing trailing edge, with the major diffusion mechanism driven by viscosity rather than turbulence [352]. The mechanism for this will be discussed.

Figure 6.26a shows the increase of TKE with angle of attack at $x/\bar{c} = 1.35$, the closest SPIV plane to the wing trailing edge. At $\alpha = 10°$ the relatively shallower dip in TKE at the vortex centre is attributed to the increased interaction of the primary core with secondary vortices generated by the squared wingtip which are stronger and more persistent at higher angles of attack [78]. This induces higher disturbances into the primary vortex core and increases the TKE. At the downstream plane, $x/\bar{c} = 5.418$ shown in figure 6.26b, the peak turbulence levels are seen to persist for each angle of attack, the radial diffusion turbulent annulus grows significantly while the laminar inner core shows little radial growth. The behaviour matches observations made by Martin [350, 351].

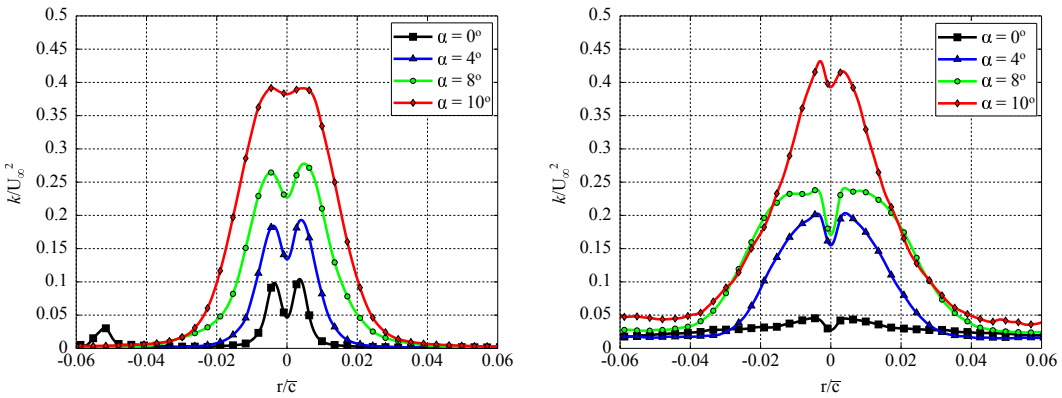

(a) $x/\bar{c} = 1.35$. (b) $x/\bar{c} = 5.418$.

FIGURE 6.26: Turbulent kinetic energy data slice through the planar wing vortex core vertical plane (along $z/\bar{c}$ at $y/\bar{c} = 0$) for $\alpha = 0°$, $4°$, $8°$, and $10°$ at $x/\bar{c} = 1.35$ and 5.418.

The turbulent dissipation of trailing vortices can be broadly explained as a fluidic system tending towards a state of lower kinetic energy by dissipating TKE while conserving angular momentum [348]. Bradshaw [353] quantified this analogy between rotation and stratification. Using energy arguments, he developed an expression for the local strength of the analogous stratification in a rotating flow, expressed as an equivalent gradient Richardson number. This analogy, formulated in terms of a Richardson number, can be applied to further the understanding of viscous turbulent vortices. The Richardson number is the ratio of the potential to kinetic energy in the stratified flow. The local gradient Richardson number is defined as [348]:

$$Ri = 2S_p(S_p + 1) \tag{6.16}$$

where the Bradshaw non-dimensional shape parameter S_p is given in terms of the swirl velocity and its gradient [353]:

$$S_p = \left(\frac{u_\theta}{r}\right) / \left(\frac{du_\theta}{dr}\right) \tag{6.17}$$

The measured distribution of Ri as a function of r/r_c is shown in figure 6.27. The result simply states that the high streamline curvature around the vortex core prevents the formation of large scale turbulent eddies. The existence of such eddies would contribute to the turbulent diffusion of vorticity away from an otherwise laminar core. As the Richardson number falls bellow a critical value, based on the vortex Reynolds number ($Re_\nu^{1/4}$), where the vortex Reynolds number is defined as:

$$Re_\nu = \Gamma_o \nu^{-1} \tag{6.18}$$

required to prevent the formation and/or transport of large scale turbulent eddies (see figure 6.27). In other words, where $Ri > Re_\nu^{1/4}$, the flow is so strongly stratified and smooth, the turbulence is heavily damped [348]. At $r/r_c = 1$ large-scale high energy eddies have insufficient kinetic energy to entrain fluid across the boundary, while at $r/r_c = 0$ Kolmogorov micro-scale eddies are unable to engulf fluid and increase mixing [347]. Hence, for $r/r_c < 1$ diffusion is the only possible transport mechanism. According to this theoretical model, the diffusive flux is determined by a surface renewal frequency of either large-scale or small-scale eddies [354]. These two eddy sizes in turn correspond to the two possible limits of vortex persistence. If the large-scale eddies are not persistent with respect to the surface, the flux is determined by the smallest eddies. At this condition, the radial momentum transport would be proportional to $Re_v^{1/4}$.

This result supports the suggestion that core relaminarisation has occurred. Over the range $1.35 \leq x/\bar{c} \leq 5.418$, the planar wing vortex core is expected to be subjected to only viscous diffusion due to the results presented in figure 6.27. This is why the vortex core grows at a slow, viscous, laminar rate, as previously illustrated in figure 6.20, unaffected or perturbed by the surrounding turbulent flow exhibiting persistent

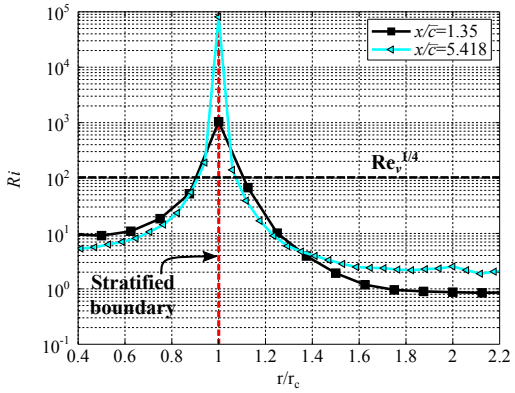

FIGURE 6.27: Richardson number as a function of distance from the core centre for the trailing vortex at $x/c = 1.35$ and 5.418 at $\alpha = 8°$.

behaviour. Similar profiles to that shown in figure 6.27, for the local Richardson number, are obtained for all α, at all $x/\bar{c}$ planes, and any azimuthal orientation of data cut through the respective vortex core for the planar wing vortex. From figure 6.27 the value of Ri at r/r_c is noticed to increase as the vortex propagates downstream, indicating increased stratification. This suggests that the laminar core, over the $x/\bar{c}$ range investigated, becomes increasingly less vulnerable to turbulent dissipation.

REYNOLDS SHEAR STRESS AND SHEAR STRAIN RATES

The evolution of the in-plane Reynolds shear stress $\overline{v'w'}$ for $\alpha = 4°$ and $8°$ is shown in figure 6.28; the respective mean core radii have been superimposed. The shear stress intensity is observed to increase for planes closer to the wing trailing edge and with increasing angle of attack. For planes $x/\bar{c} \leq 2.5$ the axisymmetry of the vortex is visible, while further downstream at $x/\bar{c} = 5.418$ shear stresses exhibit strong decay and asymmetry. The shear stress shows peak values at two different vortex core radii, which are clearer for planes $x/\bar{c} \leq 2.5$: an inner peak occurring at $\approx 0.24r_c$, and an outer peak occurring at $\approx 0.94r_c$. Considering that shear stress is primarily caused by friction between fluid particles due to viscosity, it is interesting that peak stresses occur near the vortex core substructure, and the vortex core boundary itself.

Figure 6.29 illustrates the evolution of the in-plane Reynolds shear stresses with downstream distance for $\alpha = 4°$ and $8°$, taking data slices at 135° from the SPIV data presented in figure 6.28. The shear stress intensity is observed to decay moving away from the wing trailing edge for the angle of attack shown. The shear stress reaches its maximum at $\approx 0.94r_c$, and then reduce rapidly to zero within 1.5 core radii of the vortex axis.

The eddy viscosity distribution (the production of turbulence) is dependant upon the Reynolds shear stress $\overline{v'w'}$, and not explicitly on the turbulence intensities [320]. As a result, even though the in-plane turbulent fluctuations both reach a maximum at the centre of the vortex, their product ($\overline{v'w'}$) is found to reach a minimum, this is

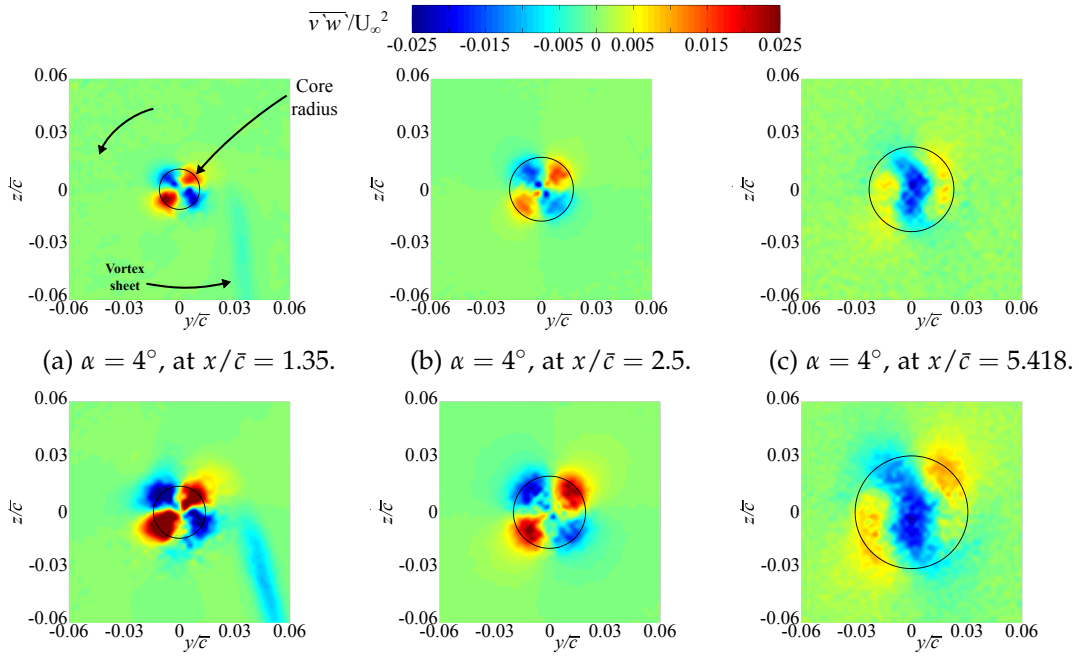

(a) $\alpha = 4°$, at $x/\bar{c} = 1.35$. (b) $\alpha = 4°$, at $x/\bar{c} = 2.5$. (c) $\alpha = 4°$, at $x/\bar{c} = 5.418$.

(d) $\alpha = 8°$, at $x/\bar{c} = 1.35$. (e) $\alpha = 8°$, at $x/\bar{c} = 2.5$. (f) $\alpha = 8°$, at $x/\bar{c} = 5.418$.

FIGURE 6.28: Streamwise development of in-plane Reynolds shear stresses ($\overline{v'w'}$) for $\alpha = 4°$ and $8°$.

consistent with other studies [320, 337].

The shear stresses drive the shear strain rates and thus contribute to the viscous dissipation of the fluid kinetic energy to heat. The shear strain rate is the deformation of the fluid caused by elongation, compression, volume change, or angular distortion due to an external force (shear stress), and thus expresses how the relative velocity of the medium changes (*i.e.* velocity gradient). The contours of the shear strain rates, corresponding to the Reynolds shear stresses presented in figure 6.28, are reported in figure 6.30.

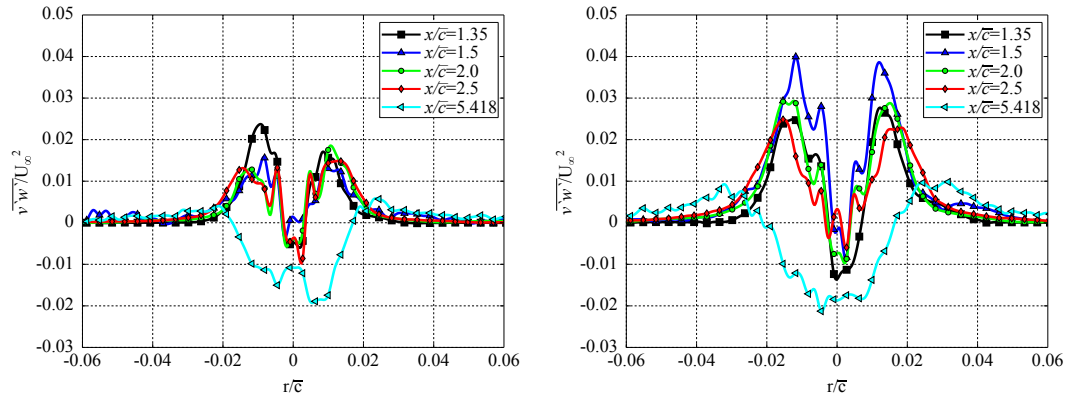

(a) $\alpha = 4°$. (b) $\alpha = 8°$.

FIGURE 6.29: Streamwise development of in-plane Reynolds shear stresses ($\overline{v'w'}$) for $\alpha = 4°$ and $8°$; data slices taken at 135° for data presented in figure 6.28.

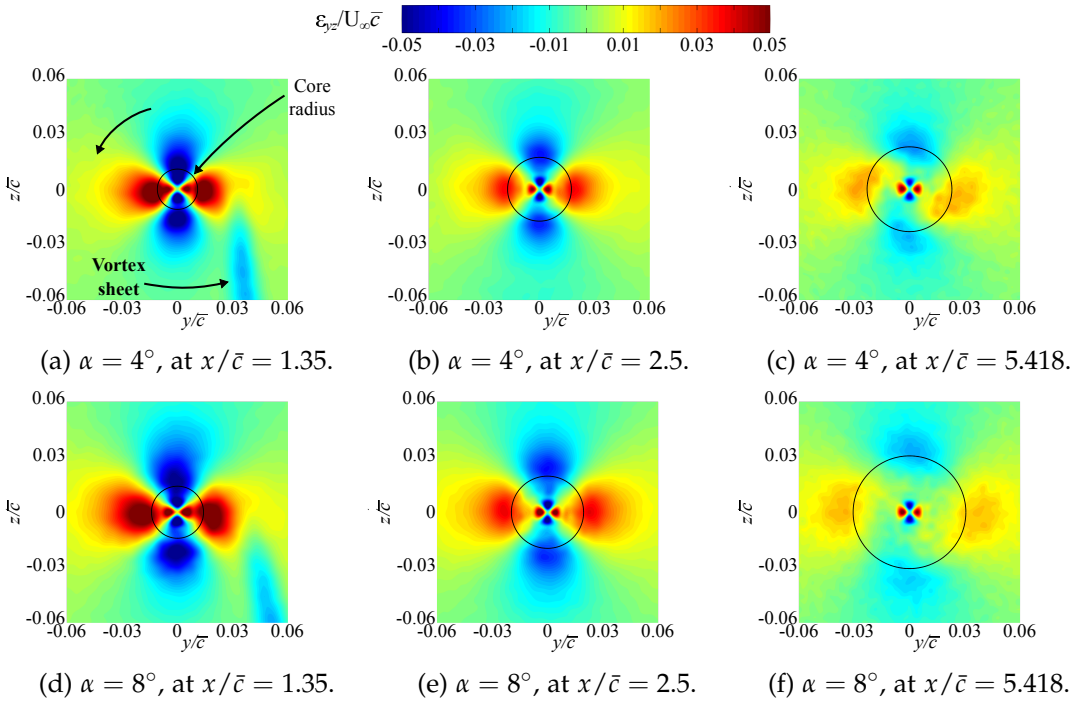

(a) $\alpha = 4°$, at $x/\bar{c} = 1.35$. (b) $\alpha = 4°$, at $x/\bar{c} = 2.5$. (c) $\alpha = 4°$, at $x/\bar{c} = 5.418$.

(d) $\alpha = 8°$, at $x/\bar{c} = 1.35$. (e) $\alpha = 8°$, at $x/\bar{c} = 2.5$. (f) $\alpha = 8°$, at $x/\bar{c} = 5.418$.

FIGURE 6.30: Streamwise development of shear strain rate for $\alpha = 4°$ and $8°$.

The Reynolds shear stresses (shown in figure 6.28), and their associated shear strains (see figure 6.30), each exhibit a bimodal four-lobed pattern with alternative positive/negative signs which has physical meaning, especially when orientated in different directions. In the case of the $\overline{v'w'}$ components, the lobes are at approximately 45° to the $y/\bar{c}$ and $z/\bar{c}$ axes, whereas the lobes in the stress rate are aligned with these axes. The difference in orientation between the stress and strain indicates that a linear eddy viscosity assumption is invalid. An interesting point in view of this, is that linear eddy viscosity models used in Reynolds Averaged Navier-Stokes (RANS) solutions assume an isotropic distribution of eddy viscosity by representing the entire stress tensor using a scalar (*e.g.* with k-ε and k-ω models). Simulation modelling can be misleading concerning the turbulence measurements inside the vortex core, as demonstrated by Churchfield and Blaisdell [355]. Thus models which assume linear eddy viscosity, and express the Reynolds shear stresses as linear functions of the shear strain rates thereby aligning their axes, are expected to be unable to describe the vortex evolution in the near wake observed in this work. However, features of the mean flow, such as the formation of the vortex system, axial and swirl velocities and vortex centreline static pressure can be correctly described. Therefore, non-linear eddy viscosity models of Reynolds stress models have to be adopted when an accurate description of the vortex core evolution is required [352, 356].

Another observation from the shear strain rates is that two radii of local peaks can be detected, forming the double-lobed pattern visible in figure 6.30. Additionally, higher angles of attack, and downstream distance, generate vortices with a broader distribution of high shear strain rates. Symmetry of the vortex is maintained at all

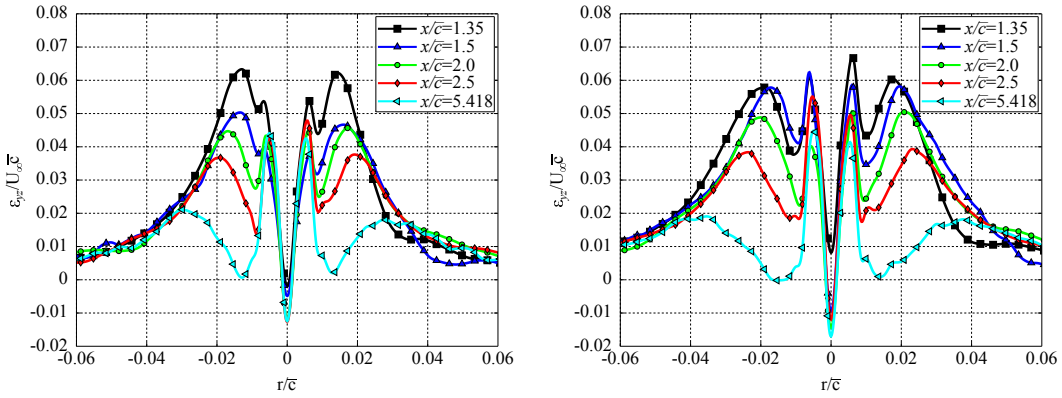

(a) $\alpha = 4°$. (b) $\alpha = 8°$.

FIGURE 6.31: Streamwise development of shear strain rate for $\alpha = 4°$ and $8°$; data slices taken along $y/\bar{c}$ at $z/\bar{c} = 0$ for data presented in figure 6.30.

conditions. The inner peak occurs at $\approx 0.30r_c$, and the outer occurs outside of the vortex core at $\approx 1.22r_c$ consistently for all angles of attack and all planes. This is summarised in figure 6.31, which illustrates a data slice taken horizontally through the positive lobes of the shear strain rate. From figure 6.31, the outer region of shear strain dissipates and weakens with downstream distance as the vortex core grows. The inner-lobe shear strain rates are seen to persist with downstream distance.

6.3.6 SUMMARY OF PLANAR WING VORTEX CORE STRUCTURE

The overall structure of the vortex core and its properties, which are consistent with all angles of attack and downstream location, is summarised in figure 6.32. Similar structures are noted to have been observed by Devenport [319]. This description agrees with the work of Phillips [336] who studied the turbulent roll up of a vortex sheet. This work divided the vortex region into three concentric regions, however stated that multi-structured cores could be expected to reach a state of equilibrium. The three dominant regions of the vortex are:

1. The innermost part dominated by viscous effects within which the swirl velocity decreases linearly to zero in correspondence to the vortex centre. In addition, approaching the centre, the rotation is close to solid-body rotation and the Reynolds stresses will tend to zero with the square of the distance from the centre.

2. The second region is located around the point of maximum swirl velocity (at the vortex core radius r_c). Here, the viscous effects are small and in this highly strained turbulent region a logarithmic law for the circulation applies [357].

3. In the outer region, the flow is turbulent, the swirl velocity decays as a potential vortex (as $1/r$) and the Reynolds stress goes to zero as $1/r^2$.

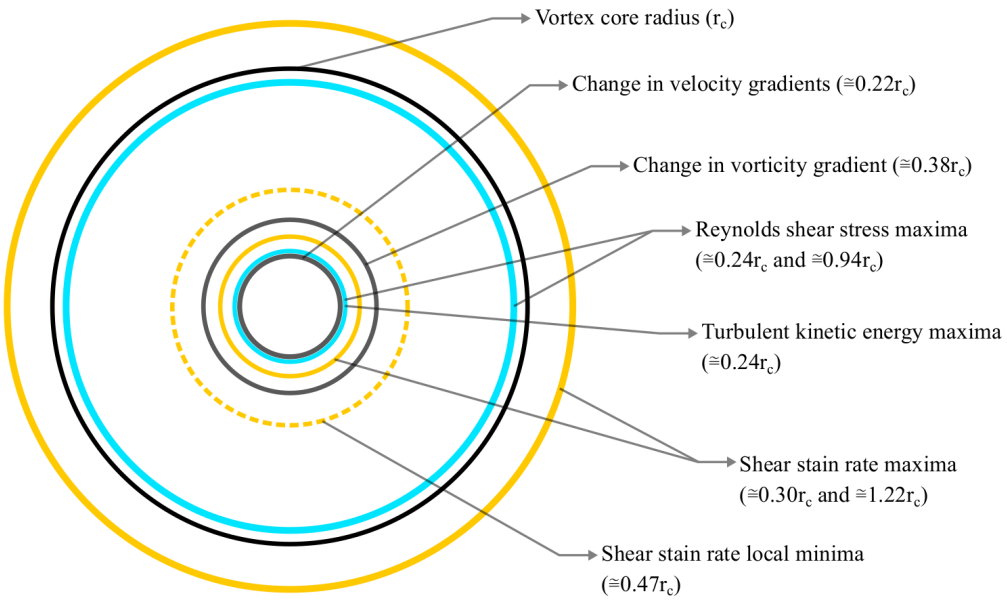

FIGURE 6.32: Schematic of the planar wing trailing vortex core structure.

Investigations [265, 340] of axisymmetric turbulent vortex structures, such as that produced by the planar wing, have demonstrated that the circulation distribution of the first two regions should follow universal behaviour in the near field, described by semi-empirical laws. Appendix E provides analysis of the self-similar behaviour of the planar wing vortex core.

6.4 C-WING VS. PLANAR WING TRAILING VORTEX

6.4.1 SWIRL VELOCITY DISTRIBUTION

As previously discussed in Section 6.2, the planar wing trailing vortex was observed to produce a seeding void at the centre of the vortex core due to high swirl velocities and subsequent centrifugal forces. This void, for the planar wing, is visible in all raw SPIV data for all $x/\bar{c}$ planes for the range $0^\circ \leq \alpha \leq 10^\circ$, beyond which stall at the wingtip forces a weaker vortex. Over the same α range no seeding void is observed for the C-wing vortex, thus qualitatively implying a weaker vortex system with lower swirl velocities.

Figures 6.33 and 6.34 present the swirl velocity around the wingtip vortex at $x/\bar{c} = 2.5$ for $\alpha = 4^\circ$, 8°, and 10° for the planar wing and C-wing respectively. Emphasis is made to the different u_θ/U_∞ ranges used to present the data. Initial observations indicate that the planar wing swirl velocities around the vortex core are $\approx 60\%$ higher. Furthermore, the planar wing's vortex is axisymmetric while the C-wing's vortex system is asymmetric in both shape and swirl velocity distribution, while also distinctly larger.

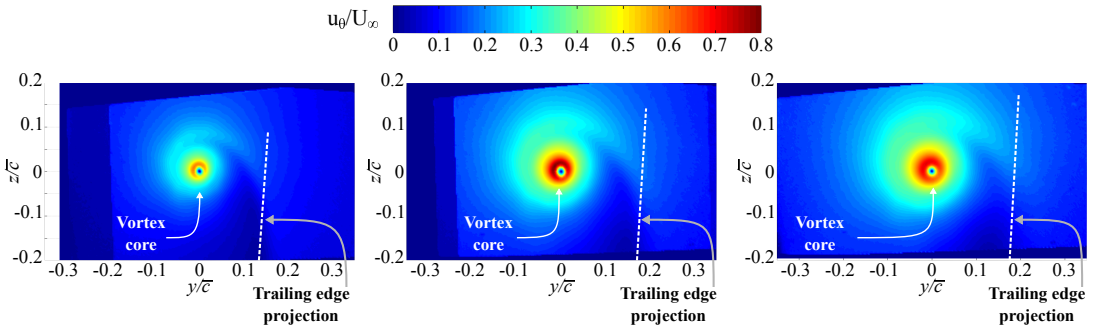

(a) $\alpha = 4°$, at $x/\bar{c} = 2.5$. (b) $\alpha = 8°$, at $x/\bar{c} = 2.5$. (c) $\alpha = 10°$, at $x/\bar{c} = 2.5$.

FIGURE 6.33: Planar wing trailing vortex swirl velocity contours at $x/\bar{c} = 2.5$ for $\alpha = 4°$, $8°$, and $10°$.

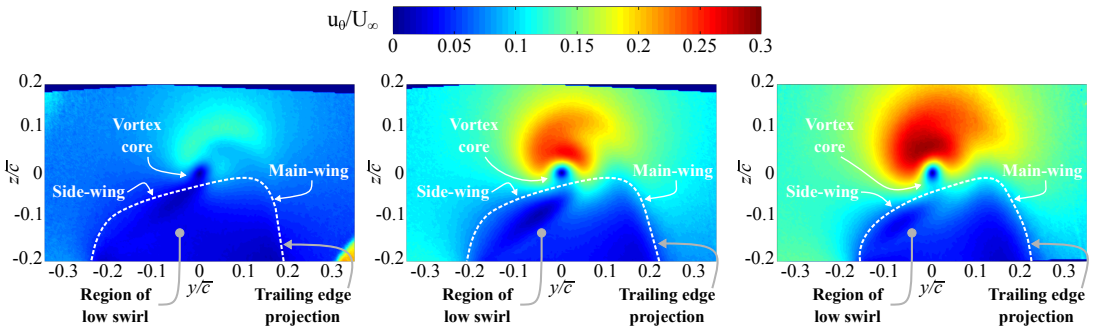

(a) $\alpha = 4°$, at $x/\bar{c} = 2.5$. (b) $\alpha = 8°$, at $x/\bar{c} = 2.5$. (c) $\alpha = 10°$, at $x/\bar{c} = 2.5$.

FIGURE 6.34: C-wing trailing vortex swirl velocity contours at $x/\bar{c} = 2.5$ for $\alpha = 4°$, $8°$, and $10°$.

Examining the planar wing vortex position relative to the projected wing TE (figure 6.33), the core moves inboard as α increases. This is also observed as a function of downstream station $x/\bar{c}$. The C-wing vortex does not behave in the same manner, instead the core appears to have a spatially locked trajectory insensitive to angle of attack or the downstream position. Figure 6.34 shows that the C-wing vortex core is fixed relative to the side-wing's free shear-layer, sitting at $\approx$ 30% to 40% of the side-wing's span. The vortex is not observed to translate toward the upper half of the side-wing free shear-layer. Few studies [72, 77, 358] have examined the structure of the vortex system behind a winglet (side-wing). However, Gerontakos and Lee [72] have shown that in the wake of a near vertical winglet ($\Gamma \geq 67°$), a junction vortex forms at the base of the winglet with a smaller vortex at the winglet tip. While the core shape is not investigated, the reduction in swirl velocity was shown, with the junction vortex remaining outboard of the winglet's wake sheet for some distance downstream.

Between $x/\bar{c} = 2.5$ and the downstream station $x/\bar{c} = 5.418$, the decay of swirl velocity is noticed while the vortex core maintains its position on the side-wing wake sheet with the vortex shape not losing definition. This will be discussed further in Section 6.4.2. In referring to figure 6.34, the C-wing's wake sheet is observed to create a perimeter (similar to the TE projection) within which low swirl velocities are found.

The driving mechanism for this will be discussed later.

Compiling the vortex structures for $\alpha = 4°$ and $8°$ in figures 6.33 and 6.34, figure 6.35 shows the averaged swirl velocity distribution at $x/\bar{c} = 2.5$ and 5.418. This illustrates the reduction in average swirl magnitude achieved by the C-wing. It is more informative to also consider how the relative peak swirl velocities vary as a function of α and $x/\bar{c}$. Figure 6.36a presents the peak swirl velocities recorded for each wing arrangement over the range of $0° \leq \alpha \leq 10°$ at $x/\bar{c} = 2.5$ and 5.418; the planar wing data is adapted from figure 6.18. Figure 6.36b presents the decay of the peak swirl velocity with downstream distance, $x/\bar{c}$, for both wing arrangements.

From figure 6.36a both wing arrangements show a linear increase in peak swirl velocity with angle of attack for $0° \leq \alpha \leq 8°$. Over this range, the C-wing peak swirl velocities are of the order of 75% lower relative to those produced by the planar wing. For $\alpha > 8°$, and the progression of stall over the outboard wing, the planar wing shows a dip in the peak swirl velocity while the C-wing demonstrates a continued, but lessened, increase in swirl with α; this behaviour is also noticed in figure 6.36b.

As previously discussed, the drop in peak swirl velocity for the planar wing arises due to the wingtip stall forcing the transport of separated flow into the very early vortex development. While this remains true for the C-wing, (recalling that force and moment data and surface clay flow visualisations demonstrate equivalent stall front/cell progression over the main-wing, discussed in Chapter 5) the blend juncture between the main-wing and side-wing are thought to smooth out the initial flow interaction at the main-wing wingtip where the flow from the suction and pressure sides of the main-wing would otherwise abruptly meet. There is also the existence of the C-wing free shear-layer, initially separating the suction and pressure sides. For the planar wing, only a discontinuous termination of the wingspan exists.

Figure 6.36a also indicates that the rate of swirl velocity decay is slower for the C-wing trailing vortex. This is further shown by referring to figure 6.36b, considering

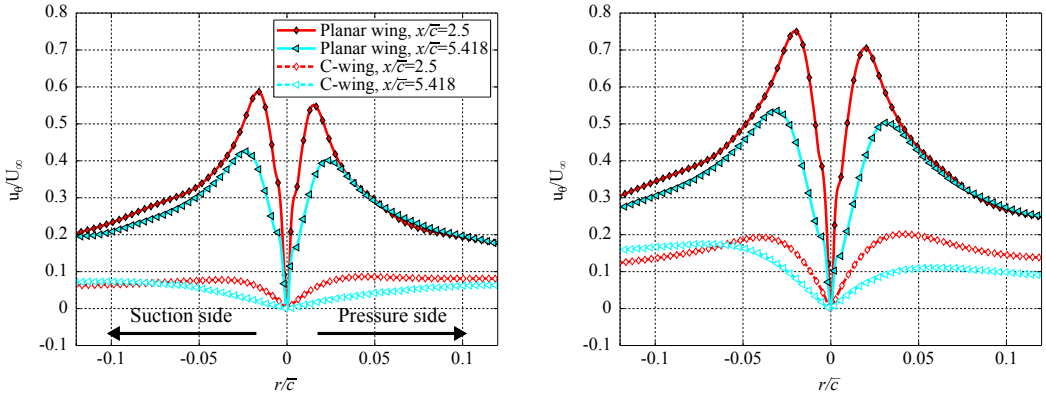

(a) $\alpha = 4°$. (b) $\alpha = 8°$.

FIGURE 6.35: Swirl velocity development comparison for $\alpha = 4°$ and $8°$ at $x/\bar{c} = 2.5$ and 5.418 SPIV planes.

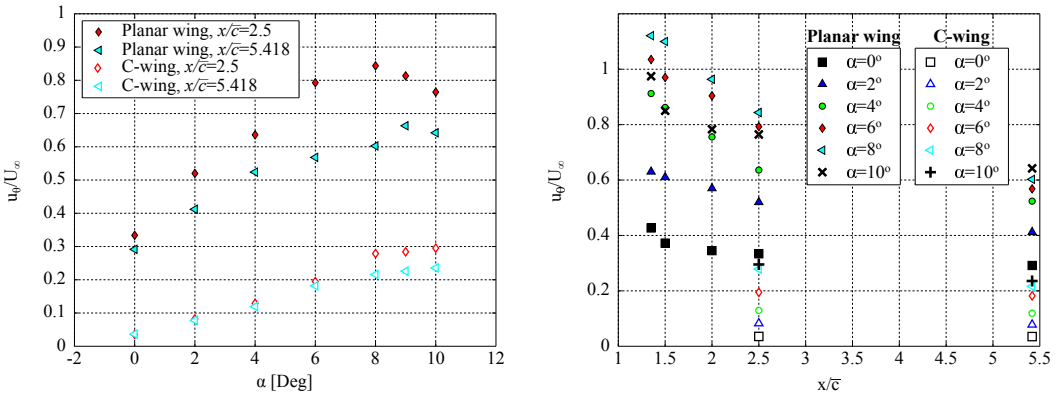

(a) Peak swirl Vs. α.

(b) Peak swirl Vs. $x/\bar{c}$.

FIGURE 6.36: Vortex peak swirl velocity as a function of α and $x/\bar{c}$ for the planar wing and C-wing.

the peak swirl velocity as a function of $x/\bar{c}$. The rate of decay ($(u_\theta/U_\infty)/(x/\bar{c})$) of the peak swirl velocity is noticed in figure 6.36b to increase with angle of attack, and reduce with downstream distance $x/\bar{c}$. Considering the two planes $x/\bar{c} = 2.5$ and 5.418, between which the decay of peak swirl as a function of streamwise distance can be compared for the two wings, it is observed that the rate of peak swirl decay is consistently higher for the planar wing by a factor of ≈ 2. Additionally, it is important to note that figure 6.36b illustrates that for all α, the C-wing trailing vortex peak swirl velocity remains lower than the peak swirl velocity recorded for the planar wing vortex at $\alpha = 0°$. In other words, for the range of angles of attack tested, the C-wing's strongest vortex remains weaker than the planar wing's weakest vortex for $2.5 \leq x/\bar{c} \leq 5.418$.

Decomposition of the in-plane swirl (tangential) velocity components can be used provide insight into the mechanisms driving the C-wing's induced drag reduction capability. Figure 6.37 presents the time-averaged in-plane velocities u_y and u_z for both the planar wing (figures 6.37a and 6.37b) and the C-wing (figures 6.37c and 6.37d), illustrating the downwash, outboard, upwash, and inboard flows at $x/\bar{c} = 2.5$; a schematic diagram indicating the relative flow directions is given in figure 6.37a. Emphasis is made to the relative magnitude of the velocity components for the planar wing and C-wing. For the angles of attack shown, the planar wing demonstrates an axisymmetric distribution of induced velocities, but the upwash and inboard components consistently have a slightly higher peak velocity at the vortex core edge. Kinks, such as those indicated in figure 6.37b, are caused by the vortex induced velocities interacting with the wing wake sheet rolling up around the vortex. The drop-off in the data profile in figure 6.37a for $\alpha = 4°$ and $6°$ for $z/\bar{c} > 0.15$ is due to reaching the edge of the SPIV plane (outside of the calibrated field of view), and is not a physical feature of the flow.

The C-wing induced circumferential velocities illustrate the aforementioned asymmetry of the trailing vortex, but similar to the planar wing vortex the upwash and

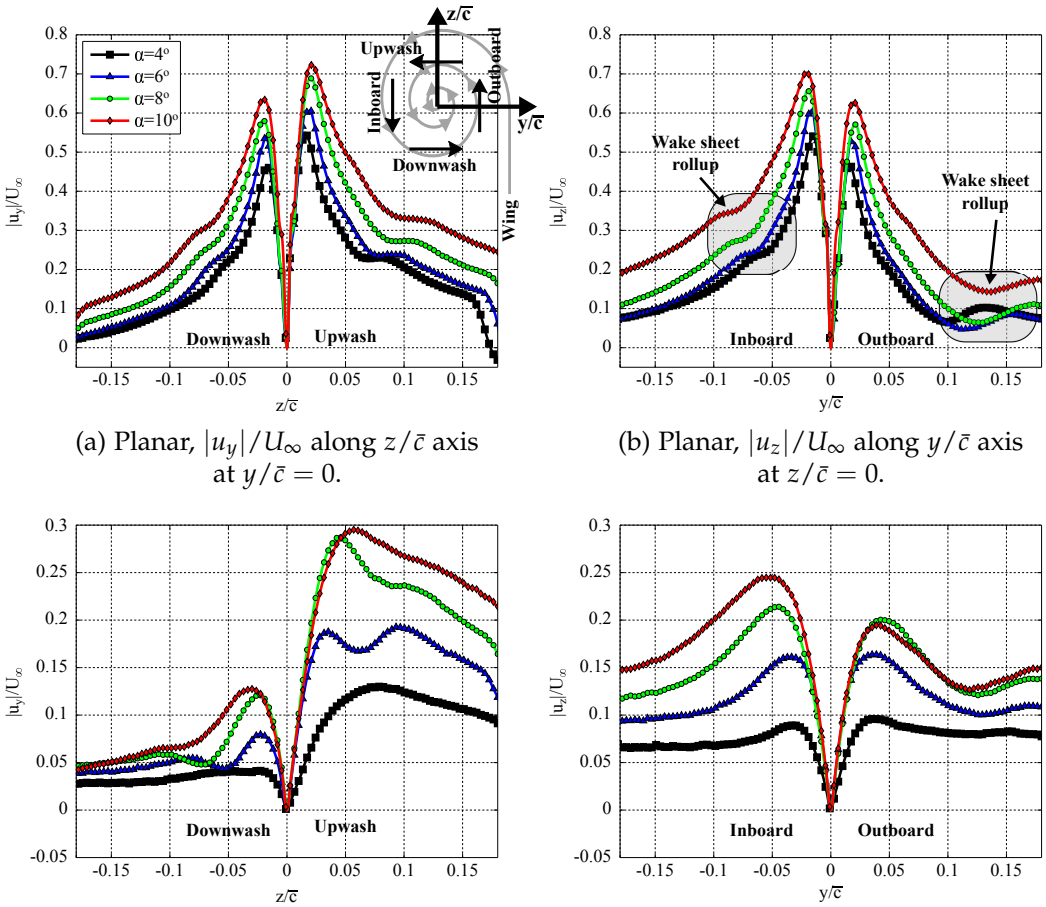

(a) Planar, $|u_y|/U_\infty$ along $z/\bar{c}$ axis at $y/\bar{c} = 0$.

(b) Planar, $|u_z|/U_\infty$ along $y/\bar{c}$ axis at $z/\bar{c} = 0$.

(c) C-wing, $|u_y|/U_\infty$ along $z/\bar{c}$ axis at $y/\bar{c} = 0$.

(d) C-wing, $|u_z|/U_\infty$ along $y/\bar{c}$ axis at $z/\bar{c} = 0$.

FIGURE 6.37: $|u_y|/U_\infty$ and $|u_z|/U_\infty$ data cuts from the planar and C-wing trailing vortex at $x/\bar{c} = 2.5$ for $\alpha = 4°$, $6°$, $8°$, and $10°$.

inboard flow components are seen to dominate their counterpart. While all induced velocities of the vortex are reduced relative to the planar wing, the most remarkable observation is that of the local downwash (shown in figure 6.37c) in the vicinity of the C-wing vortex core. This is the main driving factor contributing to the region of low swirl velocity indicated in figure 6.34.

Further investigation would be required to quantify the downwash distribution over the main-wing span, and how the C-wing affects this, however the wingtip vortex is the primary source of induced velocity. Therefore, it is reasonable to assume that, based on the SPIV data obtained, the C-wing reduces the downwash acting over the main-wing span. The effect of this on the wing's performance is the driving mechanism behind the induced drag reduction. Downwash modifies the wing's effective angle of attack across the wingspan tilting the lift vector aft, a component of which then acts in the direction of drag: lift induced drag. The C-wing disperses the concentration of vorticity at the wingtip into a large asymmetric vortex, forcing an overall weaker vortex system which achieves a large reduction of the induced velocities. The vortex is also observed to remain outboard of the main-wing wingtip,

unable to pass through or roll-up the side-wing wake sheet for $x/\bar{c} \leq 5.418$. This vortex behaviour is thought to be primarily driven by the blend juncture and the lower side-wing. The upper side-wing and top-wing convected wake sheets are subsequently responsible for further reducing the induced downwash component, by acting as a turbulent barrier through which circumferential velocity components are damped. This provides an explanation for the lower induced downwash leading to the region of low swirl indicated in figure 6.34.

6.4.2 VORTEX CORE SHAPE

The C-wing vortex core shape is presented as a locus of points of maximum swirl velocity around the vortex core centre. The vortex core edge has been defined from 36 radii equispaced around the vortex core centre. From this, different values of the core radius are found depending on the orientation (with θ_v as the azimuthal coordinate), along which the swirl velocity is evaluated. The planar wing vortex core shape for a range of α and $x/\bar{c}$ has previously been reported in Section 6.3.2, and so will not be re-illustrated here, however will be referred to.

In Section 6.3.2 the trailing wingtip vortex for the planar wing was shown to be axisymmetric for $0^\circ \leq \alpha \leq 10^\circ$ over the $1.35 \leq x/\bar{c} \leq 5.418$ experimental range. For $\alpha \leq 10^\circ$, the planar wing vortex core radius was not observed to exceed $0.035\bar{c}$ at any stage, as illustrated in figures 6.19 and 6.20b.

Referring to swirl velocity contours for the planar wing and C-wing, (shown in figures 6.33 and 6.34 respectively) the planar wing vortex core shape is well defined, whereas the C-wing core shape, while distinctly larger, is more elusive. Figure 6.38 presents the vortex core shape for the C-wing for planes $x/\bar{c} = 2.5$ and 5.418, at $\alpha = 4^\circ$ and 8°. In the present reference system the vortex rotates anti-clockwise. At $\alpha = 4^\circ$ (figure 6.38a), a clockwise spiral shaped core structure is observed at both $x/\bar{c}$ planes, characterised by a discontinuous jump of the core radius at $\theta_v = 300^\circ$ at $x/\bar{c} = 2.5$, and $\theta_v = 200^\circ$ at $x/\bar{c} = 5.418$. Furthermore, considering the relative locations of the spiral shaped core discontinuity, the relative locations would suggest a minimum of $\approx 260^\circ$ anti-clockwise core rotation between the two $x/\bar{c}$ stations. The same core structure and behaviour is observed for both $\alpha = 2^\circ$ and 6°, while no vortex core is viewed at $\alpha = 0^\circ$. Comparing figure 6.38a to figure 6.19b, other than the dissimilarity in general shape and structure, the C-wing wingtip vortex is noticed to be larger by an order of magnitude. This is true for $\alpha \leq 6$. When the flow is fully attached, the main-wing to side-wing juncture promotes diffusion of the vortex, while interaction with the side-wing wake sheet drives the clockwise spiral vortex structure.

For $\alpha = 8^\circ$ and 10° a closed core profile nearing a more axisymmetric vortex structure is found, as shown in figure 6.38b. With stall progressing around the main-wing to side-wing juncture, the vortex core is pushed farther outboard, away from the side-wing wake sheet. This behaviour is noticed when comparing the swirl velocity

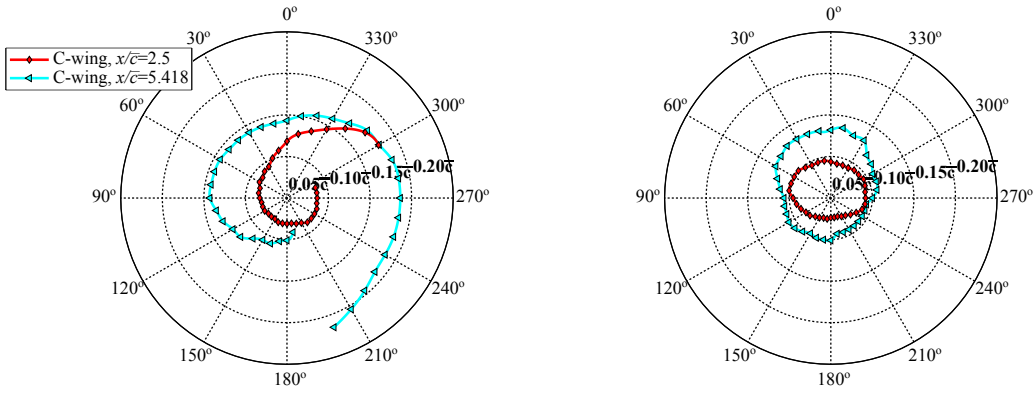

(a) $\alpha = 4°$. (b) $\alpha = 8°$.

FIGURE 6.38: Development of vortex core shape for the C-wing for $\alpha = 4°$ and $8°$ at $x/\bar{c} = 2.5$ and 5.418 SPIV planes.

contours in figure 6.34. This enables the swirl distribution around the core to become more circumferentially balanced, allowing the discontinuity in the spiral core structure to close. The wake sheet continues to interact with the vortex core causing a horizontal elongation of the core at $x/\bar{c} = 2.5$, as seen in figure 6.38b. The core radii at both $x/\bar{c} = 2.5$ and 5.418 are smaller relative to those for $\alpha \leq 6°$, however they remain larger relative to the planar wing's vortex core for the same conditions (shown in figure 6.19c).

Variation in the mean vortex core radius at downstream positions $x/\bar{c} = 2.5$ and 5.418 as a function of angle of attack is presented in figure 6.39a for each wing arrangement. The planar wing, previously discussed in Section 6.3.2, demonstrates a linear increase of the vortex core radius over $0° \leq \alpha \leq 8°$; after which, outboard wing stall forces weaker swirl velocities and an apparent reduction of the mean core radius. For the C-wing, no vortex is realised at $\alpha = 0°$, a spiral core vortex is found for $2° \leq \alpha \leq 6°$, and a more axisymmetric profile for the core is found for $8° \leq \alpha \leq 10°$. While already physically larger in size, the spiral core vortex is recorded to grow in size at a much faster rate relative to any other experimental arrangement.

Figure 6.39b illustrates how the trailing vortex mean radius varies as a function of downstream location. For all planar wing angles of attack shown, the rate of the vortex growth varies linearly with downstream location driven by relaminarisation of the core. The planar wing stall onset does not drive a smaller vortex radius, but reduces the rate of growth of the vortex. Figure 6.39a shows that for $\alpha > 8°$ there is a reduction in the size of the planar wing vortex for $x/\bar{c} > 2.5$. Figure 6.39b further indicates that for $x/\bar{c} < 2.5$ all incrementally higher angles of attack result in a linearly larger vortex core, however the downstream rate of core growth lessens for $\alpha > 8°$. This behaviour is also realised when comparing the planar wing vortex core shape as a function of downstream distance for $\alpha = 8°$ and $10°$, as shown in figures 6.19c and 6.19d, respectively.

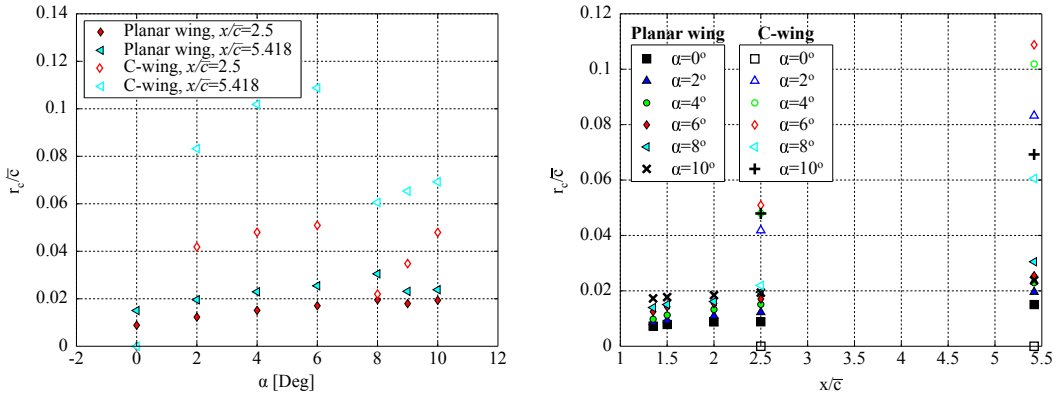

(a) Mean radii Vs. α. (b) Mean radii Vs. $x/\bar{c}$.

FIGURE 6.39: Mean vortex core radius for the planar and C-wing as a function of α and downstream location $x/\bar{c}$.

For the C-wing, it is clear from figure 6.39b that the spiral vortex core causes an increased rate of core growth between $x/\bar{c} = 2.5$ and 5.418. The relative extent of this growth is evident when comparing figures 6.19b and 6.38a. It is indicated that $\alpha = 6^\circ$ results in the largest core structure with the greatest rate of growth; this corresponds to the angle of attack which achieves the largest induced drag reduction, as examined in Section 5.2. As discussed, it is observed that for the C-wing at $\alpha \geq 8$ the vortex core changes structure. Figure 6.39b indicates that this change in structure reduces the core radius and lowers the rate of core growth with downstream position.

6.4.3 AXIAL VELOCITY DISTRIBUTION

Having discussed the planar wing's axial velocity behaviours in Section 6.3.3, the C-wing's axial velocity deficit will be analysed here. Figure 6.40 presents the axial velocity contour at the C-wing's main-wing wingtip at $x/\bar{c} = 2.5$. Figure 6.40a illustrates the absence of any vortex core while showing the vortex wake sheet of the main-wing wingtip and side-wing. Due to the absence of any detectable vortex core, figure 6.40a has been averaged using the simple averaging method; *i.e.* no centring method has been applied. In figures 6.40b and 6.40c, the vortex core at 4° and 8° is distinct, as is its positioning relative to the C-wing wake sheet. Comparing figures 6.40b and 6.40c for the C-wing to the equivalent planar wing vortex axial velocity contours, shown in figures 6.23a and 6.23b, it is realised that the axial deficit in the vortex core is greatly reduced for the C-wing. The difference in the u_x/U_∞ contour range is emphasised. The C-wing vortex core is not accompanied by the velocity excess observed with the formation of the planar wing vortex. The vortex core for the planar wing rolls up in closer proximity to the wake sheet of the wing which drives the velocity excess as discussed in Section 6.3.3. Referring to figures 6.40b and 6.40c, the C-wing vortex core is seen to form at the base of the side-wing, but is lifted away from the main-wing vortex sheet by the blend juncture; which has been labelled

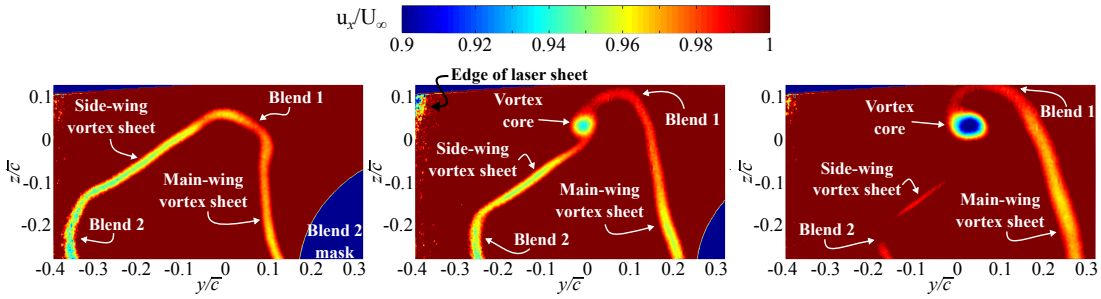

(a) $\alpha = 0°$, at $x/\bar{c} = 2.5$. (b) $\alpha = 4°$, at $x/\bar{c} = 2.5$. (c) $\alpha = 8°$, at $x/\bar{c} = 2.5$.

FIGURE 6.40: C-wing axial velocity contours at $x/\bar{c} = 2.5$ for $\alpha = 0°$, $4°$, and $8°$.

Blend 1. *Blend 2* refers to the blend junction from the side-wing to the top-wing. With increased angle of attack, the velocity deficit of the side-wing wake sheet reduces.

Compiling the planar axial velocity contours for $\alpha = 4°$ and $8°$, from figures 6.23a and 6.23b, and the C-wing axial velocity contours shown in 6.40b and 6.40c, figure 6.41 shows the circumferentially averaged axial velocity distribution at $x/\bar{c} = 2.5$ and 5.418. This illustrates the reduction in averaged velocity deficit achieved by the C-wing relative to the planar wing under the same experimental conditions. Furthermore, it is noticed that the planar wing vortex core adopts a distinct conical structure, whereas the C-wing deficit profiles illustrate a more diffused vortex which imposes shallower axial flow velocity gradients.The peak deficit remains at the centre of the vortex core.

The peak axial deficit velocity as a function of α, for each wing arrangement, over the range of $0° \leq \alpha \leq 10°$ at $x/\bar{c} = 2.5$ and 5.418 is presented in figure 6.42. The planar wing data has been adapted from figure 6.22. For the planar wing, the peak deficit increases with α over the linear lift region of the wing until stall onset is approached ($\approx 7°$), after which the peak deficit at the core centre begins to decrease with α.

The peak axial deficit of the C-wing core behaves differently. There is a very

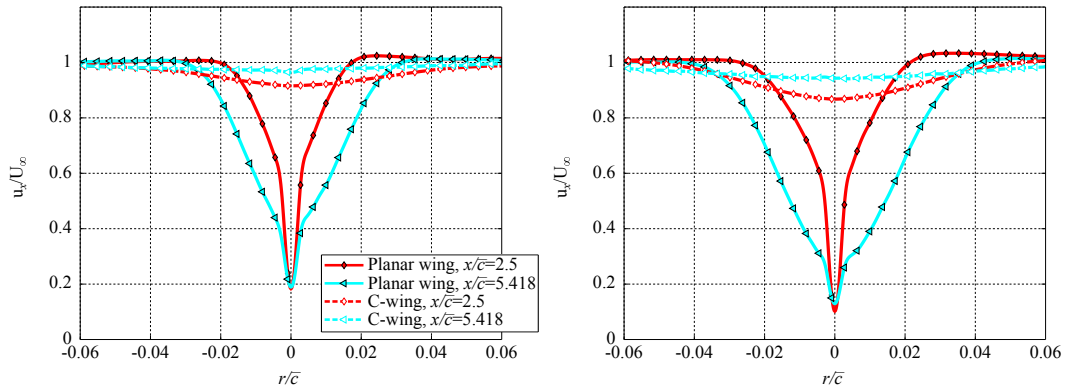

(a) $\alpha = 4°$. (b) $\alpha = 8°$.

FIGURE 6.41: Axial velocity deficit development for $\alpha = 4°$ and $8°$ at $x/\bar{c} = 2.5$ and 5.418 SPIV planes.

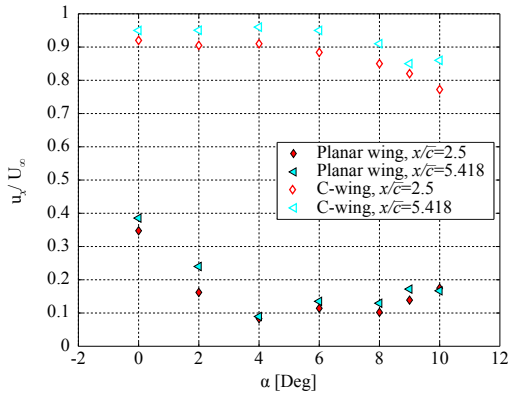

FIGURE 6.42: Vortex peak axial deficit velocity at $x/\bar{c} = 2.5$ and 5.418 as a function of α for the planar wing and C-wing.

gradual increase in the peak axial deficit over the linear lift range of the wing ($\alpha \leq 6°$); this coincides with the vortex core having a spiral structure. For $\alpha \geq 8°$, and with the transition of the spiral core structure into a more axisymmetric core, the velocity deficit begins to increase more sharply. It has been previously indicted that at this condition ($\alpha \geq 8°$) the peak swirl velocities also increase. Observations by Batchelor [342] and Phillips and Graham [343] indicated that the effect of an increased swirl motion acts to increase the static pressure in the vortex core and consequently decrease the axial velocity there; the axial deficit arises from the conservation of azimuthal fluid motion. As the swirl velocity decays with downstream position, the static pressure in the core falls and the dynamic pressure increases, thereby decreasing the axial deficit. Hence, a favourable axial pressure gradient exists along the axis of the vortex core. Considering figure 6.42, the C-wing vortex at all α can be considered to have a stronger favourable pressure gradient along the vortex axis as the axial deficit decrease between $x/\bar{c} = 2.5$ and 5.418 is larger relative to that for the planar wing at any respective angles of attack. This relatively stronger favourable pressure gradient is facilitated by the much weaker swirling motion of the C-wing vortex.

6.4.4 VORTICITY DISTRIBUTION

The circumferentially averaged streamwise vorticity distributions at $\alpha = 4°$ and 8° and stations $x/\bar{c} = 2.5$ and 5.418, for both the planar wing and C-wing arrangements, are presented in figures 6.43a and 6.43b, respectively. It is observed that for all angles of attack, and for each configuration, the peak vorticity occurs at the centre of the vortex core. As previously discussed in Section 6.3.4, the planar wing peak vorticity persists as the vortex translates downstream with only very slight rates of decay over the $1.35 \leq x/\bar{c} \leq 5.418$ range. For the C-wing, the vortex peak vorticity is observed to be an order of magnitude lower; achieving a reduction of $\approx 80\%$. The dispersion of the vorticity field is driven by the larger vortex core size and the reduction of circumferential velocities produced by the C-wing. Figure 6.43 additionally indicates a much more rapid decay of vorticity between $x/\bar{c} = 2.5$ and 5.418 for the C-wing

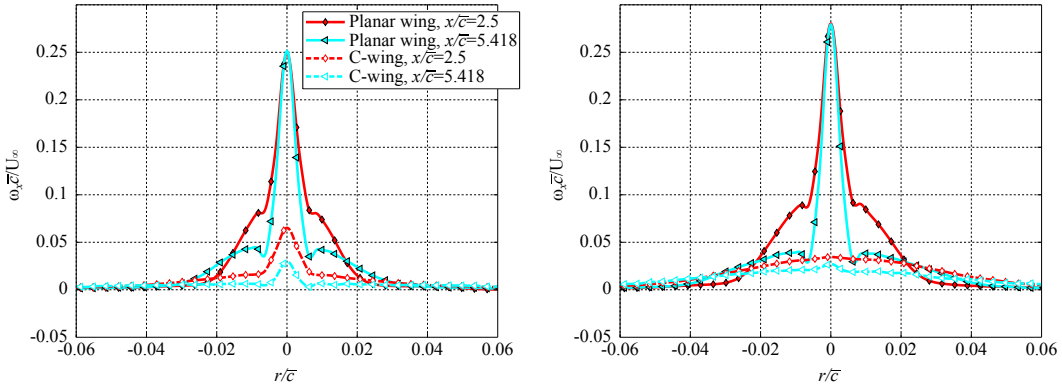

(a) $\alpha = 4°$. (b) $\alpha = 8°$.

FIGURE 6.43: Vorticity development comparison for $\alpha = 4°$ and $8°$ at $x/\bar{c} = 2.5$ and 5.418 SPIV planes.

trailing vortex.

Akin to the two-layer core structure observed in the plane wing vortex, the circumferential averaging of the spiral vortex core structure for the C-wing for $2° \leq \alpha \leq 6°$ suggests a similar structure such as that shown in figure 6.43a. This is however, an artefact of circumferentially averaging the spiral core. Unaveraged data cuts through the vortex show comparable profiles, however each would be biased toward the inner side of the spiral core.

Variation of the peak vorticity in the vortex core as a function of angle of attack and downstream position is presented in figure 6.44. In figure 6.44a, the planar wing demonstrates a linear increase in peak vorticity over the linear lift range of the wing, beyond which ($\alpha > 7°$) the effects of stall onset decays the vortex strength. The peak vorticity from the C-wing vortex is much lower over the full α range, as previously indicated. At $x/\bar{c} = 2.5$ the C-wing exhibits a rise in the peak vorticity as the spiral vortex core gets stronger. With transition to the closed core structure for $\alpha \geq 8°$, a drop in peak vorticity is noticed. A fairly constant peak vorticity is observed over $2° \leq \alpha \leq 10°$ at $x/\bar{c} = 5.418$. Over the same range of α the rate of decay of vorticity is suggested to vary, with maximum decay occurring for the spiral core vortices. Figure 6.44b illustrates the very slow vorticity decay for the planar wing with downstream distance for all angles of attack. Similarly, the increased rate of decay for $2° \leq \alpha \leq 6°$ between $x/\bar{c} = 2.5$ and 5.418 for the C-wing is clear.

Gerz at al. [45] and Breitsamter [359] each present comprehensive reviews of the wake vortex characteristics of large transport aircraft, in which fundamental aspects of trailing vortex alleviation strategies are discussed. Each indicate that strategies for minimising the strength of the wingtip vortex can be divided into two categories: 1) the generation of a low vorticity vortex (LVV) by enhancing the dispersion of the vorticity field; and 2) the generation of a quickly decay vortex (QDV) system through the promotion of three-dimensional instabilities. Both properties, LVV and QDV,

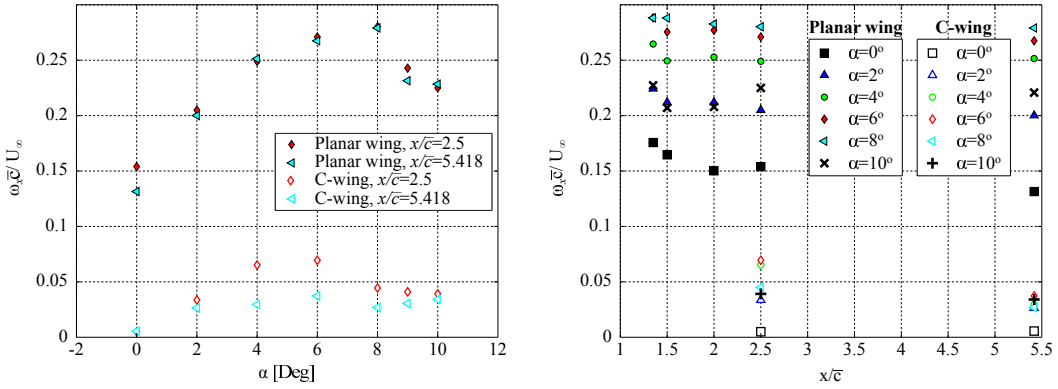

(a) Peak vorticity Vs. α.

(b) Peak vorticity Vs. $x/\bar{c}$.

FIGURE 6.44: Vortex peak vorticity for the planar and C-wing as a function of α and downstream location $x/\bar{c}$.

define strategies toward less impactful wingtip vortices in terms of induced drag and the wake vortex hazard imposed on a following aircraft [359].

With the data presented in figure 6.44, the C-wing appears to promote a LVV. The objective of a LLV design is to disperse the vorticity field over a wider spatial area via the generation of wingtip vortices with larger core sizes and lower swirl velocities around the core radius after roll-up is completed. On the other hand, the QDV designs promote rapid growth rates of the vortex core via turbulent diffusion. The radial transport of vorticity, and thus the rapid expansion of the vortex core, is supported by the relative increase of turbulence in the vortex core. This can be achieved by disrupting the primary core by forced interference from multiple secondary vortex systems (passive), or by active excitation of the core. Passive QDV interference can be introduced by using wing control surfaces, such as spoilers, flap edge elements, or the tail plane, to create zones of turbulent vortical flows to interact and expand the core size of the wingtip vortex [359, 360, 361]. Notable examples of active QDV which have been successfully applied include: application of periodic motions to control surfaces to perturb secondary vortex cores and excite wake instabilities [362, 363]; oscillating winglets at reduced frequencies which concentrate narrowband turbulent kinetic energy which distort and disperse the near-field wingtip vortex resulting in an amplification of inherent far-field instabilities [107, 364]; and blowing/suction devices to manipulate very early wake swirl velocities and pressure gradients to modify the vortex location, strength and structure [365].

With reference to both passive and active attempts to achieve LVV and QDV systems, the C-wing arrangement designed in this work meets criteria to achieve both a LVV and promote a QDV system in a mechanically simpler, passive, and reliable manner.

6.4.5 TURBULENCE IN THE VORTEX CORE

TURBULENT KINETIC ENERGY EVOLUTION

Having examined the turbulent kinetic energy (TKE) evolution of the planar wing vortex core in Section 6.3.5, it was found that relaminarisation of the inner core at all α and $x/\bar{c}$ planes had occurred. Additionally, independent consideration of the streamline curvature around the core via the Richardson number indicated a laminar core structure, within which large scale turbulent eddies could not contribute to the turbulent diffusion of vorticity away from the core. This behaviour is typical of conventional planar wing trailing vortices [364].

Figure 6.45 presents select SPIV data sets to provide a concise description of the TKE behaviour of the C-wing vortex core. Equivalent data for TKE evolution in the planar wing vortex core has previously been presented in figure 6.26. The fundamental observation here is that the TKE within the C-wing vortex core is one to two orders of magnitude lower (depending on α) than that observed in the planar wing vortex core. This indicates a much lower turbulent vortex wake within which relaminarisation of the core is not observed.

Figure 6.45a illustrates a Gaussian distribution for the TKE for all α shown with peak turbulence at the vortex core centre. A data profile for $\alpha = 0°$ is not given as no vortex core can be identified. Between profiles for $\alpha = 6°$ and 8° there appears to be a rapid rise in the TKE—this is due to the onset of light stall at the main-wing wingtip. Furthermore, each profile is noticed to be biased slightly toward the upwash side of the vortex ($r/\bar{c} > 0$), which corresponds to the vortex region of highest swirl as illustrated previously in figure 6.34. Farther downstream at $x/\bar{c} = 5.418$, figure 6.45b indicates the rapid diffusion of the TKE for $\alpha = 4°$ and 6° as the outer regions of the vortex increase in turbulence level, and the Gaussian distribution of the TKE is lost. Data profiles for $\alpha = 8°$ and 10° also demonstrate increased turbulence levels

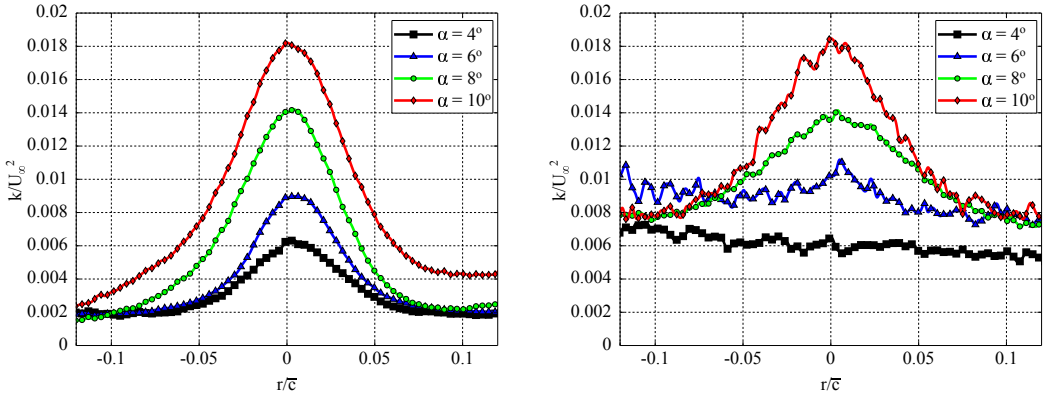

(a) $x/\bar{c} = 2.5$. (b) $x/\bar{c} = 5.418$.

FIGURE 6.45: Turbulent kinetic energy data slice through the C-wing vortex core vertical axis (along $z/\bar{c}$ at $y/\bar{c} = 0$) for $\alpha = 4°$, 6°, 8°, and 10° at $x/\bar{c} = 2.5$ and 5.418.

in the outer vortex, but the Gaussian distribution is maintained due to the structural change in the vortex core into a more stable axisymmetric core.

Wingtip geometry is known to strongly affect the vortex formation process and characteristics of the developed vortex, however the identification and understanding of the governing phenomena taking place in this region is poor. Consequently, very few studies exist in the literature which consider how the vortex wake turbulence is affected by the application of wingtip devices. However, those which do comprehend this subject matter provide results which are in agreement with those found in this work, and aid in providing a deeper understanding of the mechanisms which drive reduced turbulence in the vortex wake. Marchman et al. [366], investigating the application of the Whitcomb winglet [21] for general aviation aircraft, found that a by-product of reducing the strength of the wingtip vortex was the reduction of the vortex wake turbulence due to the smoothing and distribution of vorticity concentrations. Similar results have also been observed for spiroid winglets [367]. Gerontakon and Lee [72] found that as a result of the reduced turbulence, the wingtip vortex from a wingletted swept wing was more resistant to diffusion due to the increased lack of turbulent dissipation. As a result some wingtip devices, such as the vortex dissipater [368], are designed to specifically increase the turbulence within the vortex wake with the aim of forcing a faster decay (QDV), but compromises the optimal induced drag reduction capability of the device.

Both Airbus [82] and Boeing [369] have released articles acknowledging that winglet devices provide a reduction in perceived aircraft noise by reducing the vortex wake turbulence. Recent developments in commercial aircraft have resulted in the emergence of increasingly blended winglets, such as the so called 'Sharklet' winglet [83]. Discontinuous junctions, sharp edges, and rapid changes in chord between the wingtip device and the main-wing contribute to shed concentrations of vorticity and turbulence production from flow interactions with the wing-juncture [73]. This produces higher turbulent kinetic energy levels in the vortex wake and is suboptimal for drag reduction [370]. Blended junctions (such as that utilised on the C-wing) consist of a smooth curved geometric transition between surfaces. This design feature reduces turbulence levels in the vortex by shedding the trailing vorticity sheet over a larger trailing edge distance, removing the possibility of shedding vorticity concentrations at the intersection [370].

In Section 6.4.4, it was indicated that the C-wing trailing vortex, relative to the planar wing vortex, met criteria to achieve both a LVV and promote a QDV system. With having established that the C-wing drives a lower turbulence level in the vortex wake, it may appear ambiguous as to how the C-wing promotes a QDV between $x/\bar{c} = 2.5$ and 5.418. A QDV system promotes rapid growth of the vortex core by increasing the relative turbulence level within the vortex to excite wake instabilities which distort the core structure [359]. With fully attached flow, the C-wing distributes shed vorticity in such a way that the wingtip vortex is forced to take on an inherently

distorted spiral shape. This is maintained via interaction with the side-wing wake sheet. Hence, even through the global turbulence in the vortex wake is lower, the vortex core is no longer shielded from the mechanisms of turbulent diffusion and relaminarisation of the core cannot occur.

The Richardson number (defined in equation 6.16) can be used to determine if the streamline curvature around the vortex core is high enough to prevent the formation and transport of large scale turbulent eddies. The existence of such eddies would contribute to the turbulent diffusion of vorticity away from the core. The local Richardson number, Ri, plotted as a function of r/r_c, for both the upwash (strongest) and downwash (weakest) sides of the vortex are shown in figure 6.46 for $\alpha = 8°$ at $x/\bar{c} = 2.5$ and 5.418. The trailing vortex at $\alpha = 8°$ has been used here as it is more resistive to turbulent diffusion than the that seen for $\alpha \leq 6°$ with the spiral core structure, thereby presenting a *'worst case'* scenario. It also provides suitable comparison of the planar wing's Ri profiles at $\alpha = 8°$ shown in figure 6.27.

At the core edge, if the Richardson number falls bellow a critical value, based on the vortex Reynolds number, the damping of large scale turbulent eddies no longer occurs [348]. In other words, where $Ri > Re_v^{1/4}$, the core boundary r/r_c is so strongly stratified that the flow is smooth and the turbulence is heavily damped. Even Kolmogorov micro-scale eddies would not be able to entrain fluid across the boundary. Hence, for strong axisymmetric vortices one would typically expect that for $r/r_c < 1$ laminar diffusion of the core is the only possible transport mechanism [350, 351], which is what is observed in Section 6.3.5 for the planar wing.

In figure 6.46a it is noticed that only the upwash side of the vortex presents sufficiently high streamline curvature to provide the strong stratification of the flow required to damp large scale turbulence. The downwash side of the vortex (approximately 1/3 of the vortex circumference) does not indicate the same behaviour. Hence,

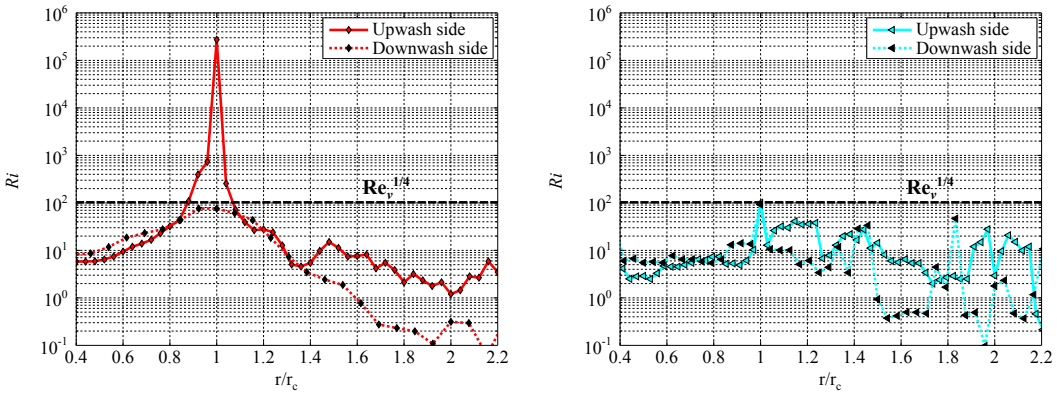

(a) $x/\bar{c} = 2.5$. (b) $x/\bar{c} = 5.418$.

FIGURE 6.46: Richardson Number as a function of distance from the centre for the C-wing trailing vortex at $x/\bar{c} = 2.5$ and 5.418 at $\alpha = 8°$. Refer to figure 6.37a for clarification on upwash/downwash sides for vortex.

this would imply that the vortex core is not circumferentially protected from the mechanism of turbulent diffusion. This characteristic is exaggerated with the spiral vortex core due to the discontinuity in the core structure.

With the clear growth and rate of dissipation of the C-wing vortex, it is seen that from figure 6.46b that $Ri < Re_v^{1/4}$ at the core edge ($r/r_c = 1$) at $x/\bar{c} = 5.418$. Both the upwash and the relatively weaker downwash side of the vortex indicate comparable Ri peaks at the vortex core edge which almost match the $Re_v^{1/4}$ threshold. This suggests that the entire vortex core is weak and dissipated enough to be entirely susceptible to turbulent diffusion. While the vortex wake turbulence is greatly reduced for the C-wing, the vortex core structure is vulnerable to turbulent dissipation which is thought to be primarily driven by interaction with the side-wing wake sheet.

REYNOLDS SHEAR STRESS AND SHEAR STRAIN RATES

Figures 6.47 and 6.48 present the in-plane Reynolds shear stresses ($\overline{v'w'}$) in the vicinity of the wingtip vortex at $x/\bar{c} = 2.5$ for $\alpha = 4°$, $8°$ and $10°$, for the planar wing and C-wing, respectively. Emphasis is made to the different $\overline{v'w'}/U_\infty^2$ scaling ranges used to present each data set, and that the edge of the calibrated field of view is visible at $z/\bar{c} \approx 0.18$ beyond which a non-physical signal is observed. The planar wing shear stresses around the vortex core are an order of magnitude higher than that of the C-wing. Furthermore, the planar wing vortex stresses are more concentrated around the smaller and focused vorticity field, relative to that of the C-wing vortex shear stresses which cover a vastly larger spatial region. In Section 6.4.2 it was shown that the planar wing's average vortex core radius was consistently smaller by an order of magnitude.

The planar wing vortex shear stresses are seen to be much stronger relative to the planar wing's wake sheet. Conversely, due to the dispersion of the vorticity field, and lower induced velocity gradients, the C-wing's trailing vortex stresses are seen to be comparable in magnitude to that of the side-wing's wake sheet at all angles of

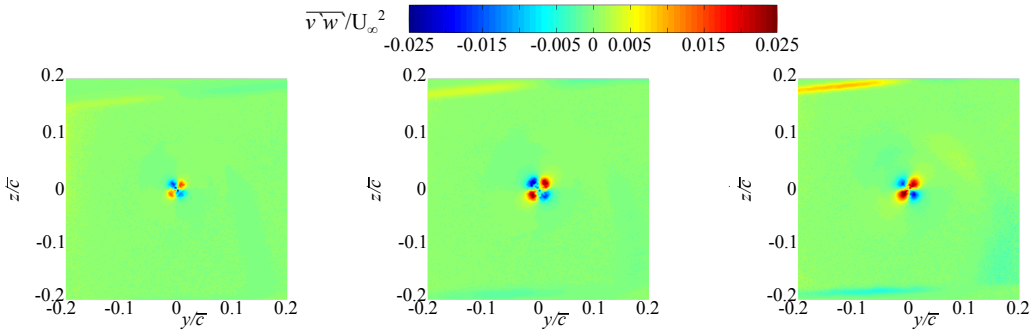

(a) $\alpha = 4°$, at $x/\bar{c} = 2.5$. (b) $\alpha = 8°$, at $x/\bar{c} = 2.5$. (c) $\alpha = 10°$, at $x/\bar{c} = 2.5$.

FIGURE 6.47: In-plane Reynolds shear stresses for $\alpha = 4°$, $8°$, and $10°$ at $x/\bar{c} = 2.5$ for the planar wing configuration.

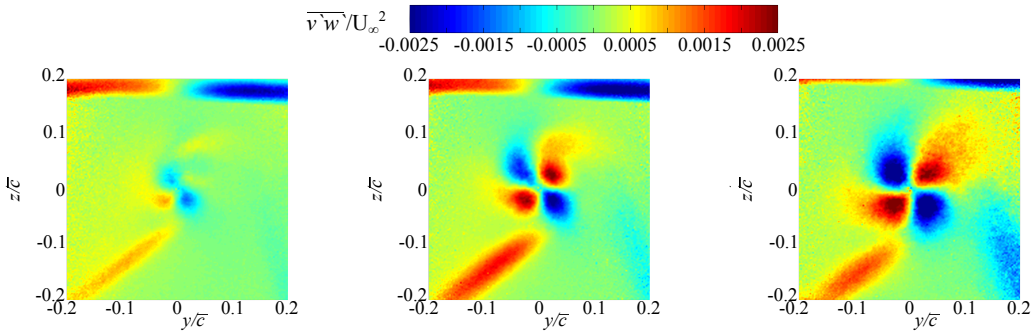

(a) $\alpha = 4°$, at $x/\bar{c} = 2.5$. (b) $\alpha = 8°$, at $x/\bar{c} = 2.5$. (c) $\alpha = 10°$, at $x/\bar{c} = 2.5$.

FIGURE 6.48: In-plane Reynolds shear stresses for $\alpha = 4°$, $8°$, and $10°$ at $x/\bar{c} = 2.5$ for the C-wing configuration.

attack shown. At $10°$, the stresses from the wake sheet of the main-wing are noticed to increase, tending towards similar magnitudes for that recorded in the C-wing vortex and side-wing wake sheet.

The reduction in the Reynolds shear stresses, produced by the C-wing relative to the planar wing, occurs as the turbulent fluctuating terms of the velocity field are lower. The C-wing's vortex has been shown to be dispersed and of lower turbulence relative to the planar wing vortex.

Each vortex structure shown in figure 6.48 exhibits a bimodal lobed structure of the same orientation, however the radial positions at which the Reynolds shear stress reaches maximum values are found to be different. Discussed in Section 6.3.5, the planar wing vortex constantly presented a double-lobed structure with local stress maxima at $\approx 0.24r_c$ and $\approx 0.94r_c$. These stress peaks occurred in the vicinity of rapid gradient changes in the local velocity field. The C-wing vortex on the other hand, reached a peak value at $\approx 0.5r_c$, and reduced rapidly to zero within two mean core radii of the vortex axis. This is a typical result found in weaker vortex systems [320]. In both the planar wing and C-wing cases, the magnitude for the Reynolds shear stresses were found to reach a minimum at the vortex axis ($r_c = 0$).

The contours of the shear strain rates, corresponding to the Reynolds shear stress presented in figures 6.47 and 6.48, are reported in figures 6.49 and 6.50, respectively. Emphasis is made to the different $\varepsilon_{yz}/U_\infty\bar{c}$ scaling ranges used to present each data set.

The shear strain rates for the C-wing vortex are noticed to be an order of magnitude lower than that for the respective planar wing vortex. Similar to the shear stress, the planar wing vortex shear strain distribution is more focused within the strong axisymmetric vortex core, while the C-wing presents a weaker and more dispersed strain rate contour. This result is expected, as the shear strain rates are derived from the mean in-plane velocity gradients, which the C-wing has shown to decrease relative to the planar wing while illustrating a much larger vortex core. Discussed in Section 6.3.5, the planar wing vortex constantly presented a double-lobed structure with local

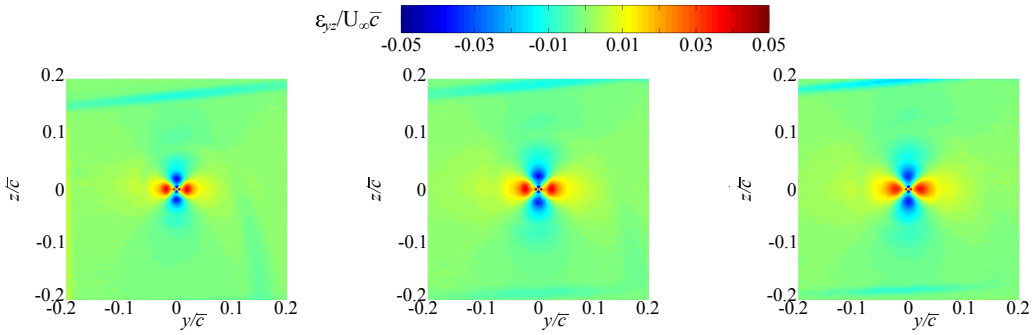

(a) $\alpha = 4°$, at $x/\bar{c} = 2.5$. (b) $\alpha = 8°$, at $x/\bar{c} = 2.5$. (c) $\alpha = 10°$, at $x/\bar{c} = 2.5$.

FIGURE 6.49: Shear strain rate for $\alpha = 4°$, $8°$, and $10°$ at $x/\bar{c} = 2.5$ for the planar wing configuration.

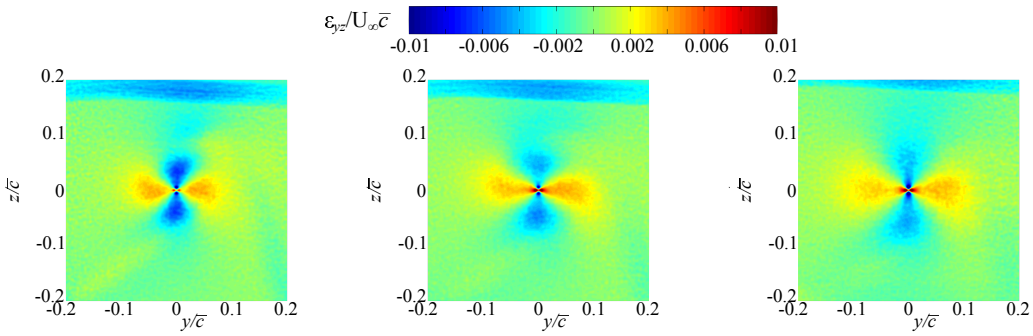

(a) $\alpha = 4°$, at $x/\bar{c} = 2.5$. (b) $\alpha = 8°$, at $x/\bar{c} = 2.5$. (c) $\alpha = 10°$, at $x/\bar{c} = 2.5$.

FIGURE 6.50: Shear strain rate for $\alpha = 4°$, $8°$, and $10°$ at $x/\bar{c} = 2.5$ for the C-wing configuration.

strain maxima at $\approx 0.30r_c$ and $\approx 1.22r_c$. These strain peaks occur due to deformation in the fluid (velocity gradients), driven by shear stresses. The C-wing vortex on the other hand, reaches a peak value within $0.12r_c$ of the mean core radius. In both cases, the magnitude for the shear strain rates were found to reach a minimum at the vortex axis ($r_c = 0$).

Furthermore, previously discussed in Section 6.3.5 was the physical meaning of bimodal pattern of the Reynolds shear stress (planar wing in figure 6.47 and C-wing in figure 6.48) and shear strain rates (planar wing in figure 6.49 and C-wing in figure 6.50) and the relative 45° orientation; the shear stress aligned approximately 45° to the $y/\bar{c}$ and $z/\bar{c}$ major axes, whereas the strain rates are aligned with the major axes. The difference in the orientation of the stress and strain indicates that eddy viscosity is non-linear. This behaviour is consistent between each wing arrangement; the implications of which are discussed in Section 6.3.5.

6.5 SUMMARY AND CONCLUSIONS

SPIV has been used to conduct an investigation into the early wingtip vortex structure of a planar wing and C-wing arrangement of equivalent wingspan, lift, and root

bending moment, having previously demonstrated the performance benefits of the C-wing in Chapter 5.

The selection of an appropriate vortex centring procedure to spatially localise the instantaneous vector fields is found in the clarification of a robust vortex centre definition, which can be taken in various forms. From the comparative study presented which considered several vortex properties such as vortex translation, swirl velocity, axial velocity, vorticity, and turbulent qualities, the identification of the vortex core centre with the peak streamwise helicity was found to provide the highest reliability. In conjunction with the centring methods examined, SPIV hardware constraints and the limitations of the vector grid spatial resolution have also been also addressed.

Examination of the planar wing trailing vortex system over the downstream range $1.35 \leq x/\bar{c} \leq 5.418$ produced an axisymmetric vortex core for which the peak swirl velocity, mean core radius, peak axial deficit, and peak vorticity increased linearly with angle of attack over the linear lift range of the wing. The turbulent kinetic energy (TKE) evolution of the planar wing vortex core demonstrated that relaminarisation of the inner core at all α and $x/\bar{c}$ planes had occurred. Additionally, independent consideration of the streamline curvature around the core via the Richardson number indicated a laminar core structure, within which large scale turbulent eddies could not contribute to the turbulent diffusion of vorticity away from the core. This behaviour is typical of conventional planar wing trailing vortices [364], and explains the persistence of the vortex core observed and its laminar growth rates.

The planar wing configuration was also seen to display a double-layered core structure, the likes of which have been previously observed by Devenport [319]. Due to the sufficient resolution provided by the SPIV, the layers within the core structure and how vortex properties vary within the core have been examined. Based on observations and analysis from the literature, the formation of such a core structure is hypothesised to be caused by the planar wing's squared wingtip. Further analysis beyond the scope of this work would be required to confirm this.

Evaluation of the of the C-wing trailing vortex, relative to the planar wing vortex, shows that the vortex has an asymmetric clockwise spiral core structure with peak swirl velocities $\approx 75\%$ lower than that observed in the planar wing vortex. In addition, the asymmetric distribution of swirl velocity is maintained by the C-wing's wake sheet which also stops inboard translation of the vortex. Consequently, this facilitates a significant reduction of $\approx 80\%$ of the peak induced downwash in the vicinity of the vortex core. This is intrinsically linked to the reduction of the induced drag achieved by the C-wing.

Further benefits of the C-wing, relative to the planar arrangement in this work, have also been identified. Owing to the dramatic reduction of the swirl velocities and the much larger vortex core, the C-wing achieves a low vorticity vortex (LVV) due to the dispersal of the vorticity field; peak vorticity in the core centre is recorded to be an

order of magnitude smaller than that for the planar wing vortex. As a by-product of this, a reduction of the vortex wake turbulent kinetic energy was also found due to the smoothing and distribution of the vorticity field. In terms of commercial application this would imply that the C-wing could also achieve a reduction in the perceived aircraft noise [82, 369].

Induced drag reductions accomplished by means of implementing a LVV generally imply that, due to the reduced wake turbulence, the wingtip vortex will become more resistant to diffusion due to lack of turbulent dissipation [72, 359]. This is compounded by typical wingletted wings as they are are likely to continue to produce an axisymmetric vortex system susceptible to core relaminarisation. However, the C-wing has been shown able to produce a vortex core structure which promotes turbulent diffusion of the trailing vortex system, increasing dispersion rates of the vortex by a factor of ≈ 2 relative to the planar wing vortex. Examination of the Richardson number suggests that the core is vulnerable to the mechanisms of turbulent diffusion.

CHAPTER 7

CONCLUSIONS AND FUTURE WORK

The findings of this investigation can be summarised into three categories: (i) the development and implementation of a population structured genetic algorithm (sGA) and vortex ring method (VRM) design-optimisation architecture; ii) semi-span wind tunnel testing without the use of a conventional peniche; and iii) experimental findings related to the sGA-VRM designed planar wing and C-wing arrangements. The findings of the aforementioned categories are summarised below.

7.1 CONCLUSIONS

7.1.1 DEVELOPMENT OF THE SGA-VRM OPTIMISATION ARCHITECTURE

Considering the different design specifications and constraints, the sGA-VRM algorithm was found capable of identifying theoretically optimal solutions while unveiling design trade-off Pareto-fronts. This was facilitated by the navigation of complex design spaces, utilising both feasible and infeasible designs via constraint based reasoning, to find superior wing solutions. Subsequently, the sGA-VRM re-configured the outboard 26% wingspan of the planar baseline wing (analogous of a typical mid-size commercial aircraft wing topology) to independently form a C-wing topology and increase the aerodynamic efficiency by 74.5%. At the sGA design point angle of attack ($\alpha = 6.04^{\circ}$), the C-wing's predicted performance was found to reduce the total drag by 11.11% (decreasing the induced drag by 27.09%, and increasing the parasitic drag by 15.54%).

It is important to emphasise that neither configuration (planar or C-wing) in this study are truly optimal, but are optimal given the allowable design space and experimental constraints explicitly given to the sGA.

7.1.2 SEMI-SPAN TESTING WITHOUT CONVENTIONAL PENICHE

The application of the traditional peniche attempts to reduce flow interference with the tunnel wall boundary layer and achieve, as closely as possible, a flow field representative of that expected around the equivalent full-span model in free-air. However, the introduction of the peniche is known to introduce the formation of a horseshoe vortex around the nose of the model which adds more complexity and uncertainty to measurements than it offsets. This is primarily due to the horseshoe vortex varying with the model angle of attack. Adopting scaling methods to selected the 'best' peniche stand-off height is typically ineffective.

Removal of the conventional peniche extrusion, thereby placing a gap between the fuselage symmetry plane and tunnel wall, for stand-off gap heights $1.4\delta^*$, $2\delta^*$, $3\delta^*$, $4\delta^*$, and $5\delta^*$ have been shown to prevent the formation of a horseshoe vortex at the fuselage nose. Furthermore, variation in the aerodynamic performance metrics of the semi-span model demonstrated low sensitivity to changes in the stand-off gap height. Deviations in aerodynamic coefficients between stand-off gap heights are approximately constant over the linear lift range of the model ($-5^\circ \leq \alpha \leq +7^\circ$). This demonstrates that over this region, deviations in aerodynamic coefficients are a function of the distance between the fuselage symmetry plane and tunnel wall, and not a direct function of the angle of attack. General trends show that with increasing stand-off gap height the lift coefficient decreases and the drag coefficient increases.

Increasing the stand-off gap height to $4\delta^*$ and $5\delta^*$ was observed to encourage acceleration of the wind tunnel boundary layer into the stand-off gap, under the model symmetry plane. This reduced the upward deflection of the wind tunnel boundary layer as it approached the the fuselage nose, maintaining a velocity field sufficiently parallel to the fuselage symmetry plane. The velocity fluctuations over the fuselage forebody reduced in intensity with increasing stand-off gap height. Results show that for stand-off gaps heights $4\delta^*$ and $5\delta^*$, the upper side of the semi-span model is sufficiently isolated from the wind tunnel boundary layer and a flow field closely mimicking what would be expected around an equivalent full-span model in freestream air is achieved. The aforementioned drag coefficient increase with stand-off gap height is caused by the accelerated flow through the stand-off gap causing an increase in the parasitic drag acting on the fuselage symmetry plane. The lift coefficient decrease with stand-off gap height is caused by the increased circulation around the fuselage, increasing the induced angle of attack. While $4\delta^*$ and $5\delta^*$ create equivalent outcomes in terms of flow features and model performance, $4\delta^*$ ensures longevity of the mounting interface.

The removal of the peniche introduces two primary limitations depending on the nature of the experimental set up. These are: 1) vulnerability to forced vibration; and 2) the mounting shaft wake flow over the fuselage after body. In this work the former was mitigated via a detailed understanding of the model structural dynamics,

inertial loading, and interactions with the wind tunnel natural frequencies enabling the post-processing and filtering of force platform data. The latter was not an issue in the current work but was observed to influence the flow over the fuselage after body, which could become problematic if the model incorporated a horizontal tail plane unit. As the model angle of attack is increased, the mounting shaft wake impinges more onto the top side of the fuselage, however surface flow visualisations suggest that instabilities over the entire fuselage reduce with increased stand-off gap height. Regions of persistent instability are shown to be confined with no obvious spatial translations over the body at a gap height of $4\delta^*$. Shaft wake interactions with the model are observed to affect the model's pitching moment and notional yawing moment as a function of stand-off gap height.

7.1.3 ANALYSIS OF THE C-WING DESIGN RELATIVE TO EQUIVALENT PLANAR WING

Assessment of each wing arrangement's aerodynamic performance metrics at $Re = 1.5 \times 10^6$ showed that despite the C-wing operating with a 19.1% higher wing wetter area, an average total drag reduction of 7.4% over a $0^\circ \leq \alpha \leq 14^\circ$ range was achieved. A peak total drag reduction of 9.5% (or a lift-to-drag ratio increase of 10.67%) was reached at $\alpha = 6^\circ$ while maintaining equivalent lift and root bending moment relative to the planar wing; this was accurately predicted by the sGA-VRM algorithm. Drag reduction capability correlates to high side-wing loading, thus at higher lift conditions ($\alpha > 8^\circ$) the main-wing wingtip stall develops and spreads onto the side-wing reducing the C-wing's effectiveness. The top-wing has been observed to maintain the wing's longitudinal static stability post stall on-set, and reduce the main-wing static aeroelastic deflections for $\alpha < 8^\circ$.

The structural dynamics of the C-wing, relative to the planar wing, is identified to have a more complex vibrational signature. Structurally, the primary effect of the C-wing is to act as a dynamic vibration absorber with very low damping, promoted by the top-wing vibrating out-of-phase with the main-wing. In addition, the side- and top-wing natural frequencies interact, causing a mechanically coupled amplitude modulated beating interference pattern masked by modulation detection interference. The C-wing's ability to passively attenuate the main-wing buffet induced oscillation has been observed, with the C-wing attenuating the fundamental bending mode of the main-wing by 68.63% at $\alpha = 14^\circ$ relative to the planar wing. Under such conditions, the vibrations of the top-wing increase significantly; at $\alpha = 14^\circ$, the velocity magnitude of the top-wing is recorded to be 361.16% higher than that detected for the main-wing structural vibrations.

The early wake trailing vortex behind each wing configuration has been studied using SPIV. The importance of spatially centring each instantaneous vector field realisation before averaging has been demonstrated, particularly for the evaluation of

the axial flow, vorticity, and turbulence properties within the core. Several definitions found in the literature have been compared, from which the peak of the streamwise helicity component was found the most satisfactory.

The planar wing configuration demonstrated a vortex wake with properties analogous to that of a typical commercial aircraft; the trailing vortex system was axisymmetric over the $1.35 \leq x/\bar{c} \leq 5.418$ downstream range, with the peak swirl velocity, mean core radius, peak axial deficit, and peak vorticity increasing linearly with angle of attack. Examination of the turbulent kinetic energy of the vortex indicated that relaminarisation of the inner core at all α and $x/\bar{c}$ had occurred. Additionally, independent consideration of the streamline curvature around the core edge via the Richardson number indicated a laminar core structure, within which the stratified flow damped large scale turbulent eddies. This is typical behaviour of planar wing vortices and explains the persistence and slow growth of the vortex core as it propagates downstream, as diffusion is the only possible transport mechanism.

Investigation of the C-wing trailing vortex shows that the vortex structure has an asymmetric clockwise spiral core structure with peak swirl velocities $\approx 75\%$ lower than that observed for the planar wing vortex. This is what drives the induced drag reduction. The vortex core structure also decreases the peak axial deficit by $\approx 350\%$, the peak core vorticity by $\approx 80\%$, and increases the dispersion rate of the vortex by a factor of 2 relative to the planar wing vortex. Thus, the C-wing arrangement designed in this work meets criteria to passively achieve both a low vorticity vortex and a quick decay vortex system. Assessment of the turbulence within the vortex core indicated that the spiral core shape prevents relaminarisation of the core. Furthermore, streamline curvature around the core indicates that the flow is not strongly stratified implying radial diffusive flux of the core is increased due to mechanisms of turbulent dissipation.

7.2 FUTURE WORK AND RECOMMENDATIONS

7.2.1 C-WING DESIGN OPTIMISATION

1. Investigate the application of other optimisation approaches, for example: particle swarm optimisation, simulated annealing, adjoint gradient based optimisation, surrogate modelling, *etc*.

2. Incorporate fuselage, fuselage-wing integration, and control surfaces into aerodynamic optimisation procedure.

3. Incorporate an equivalent non-linear finite element beam model into the sGA-VRM algorithm to explore non-planar configurations taking into account the coupling between aerodynamics and structures. Structural model should account for gravitational forces (inertial loading/relief), fuel masses, non-structural

masses of control surfaces and actuators, as well as engine thrust and mass.

4. Investigate optimisation of full aircraft arrangements: engine position, blended wing body, canard, *etc.*.

5. Investigate the inclusion of more complex inter-disciplinary optimisation objectives/constraints, such as: i) using the C-wing for longitudinal and lateral control and stability; ii) flutter analysis; iii) wing loading under high manoeuvre loads.

6. With a well defined starting design point defined, and computational resource permitting, high fidelity CFD utilising free-form deformation and adjoint-based gradient optimisation could be implemented to investigate C-wing arrangements at transonic speeds. Aerostructural optimisation could be conducted using coupled-adjoint formulations.

7.2.2 SEMI-SPAN MODEL TESTING

1. Modify mounting interface to increase stand-off gap height above $5\delta^*$. This would allow investigations into very high stand-off gaps ($> 10\delta^*$), and investigate if increasing the stand-off gap past a certain point plateaus model performance.

2. Investigate the differences between full-span and semi-span wind tunnel testing. This would require the development of a purpose built aircraft arrangement capable of both arrangements: *i.e.* a full span model that can be split in half. This would enable stand-off gap heights to be compared to two-dimensional and three-dimensional peniche extrusions as well as the true equivalent full span model. Hence, scaling factors between the different semi-span arrangements and equivalent full span could be determined.

7.2.3 PLANAR WING SEMI-SPAN MODEL TESTING

1. Modify the existing planar wing's squared wingtip to enable a modular rounded wingtip. This would enable the investigation of the double-core structure by altering the vortex initial considerations imposed by the wingtip.

2. Manufacture a new planar wingtip insert without a raked tip. This would enable the investigation of how raked wingtip geometry affects early vortex formation.

3. Redesign the planar wing to incorporate an optimal twist distribution to provide stall behaviour analogous to commercial aircraft.

4. Redesign the planar wing to be manufactured out of carbon-fibre to enable the incorporation of surface mounted pressure transducers. This would enable: i) quantitative surface pressure data; ii) lift distribution data; iii) evaluation of induced and parasitic drag contributions (total drag provided by force platform).

7.2.4 C-WING SEMI-SPAN MODEL TESTING

1. Manufacture a winglet model identical to the C-wing without the top-wing extension. This will help investigate mechanisms for enhanced induced drag reduction which separate winglets and C-wings.
2. Use SPIV, or laser-Doppler anemometry (LDA), to investigate the iteration of the main-wing's wake with the top-wing at high angles of attack.
3. Obtain SPIV data for downstream positions closer than $x/\bar{c} = 1.35$, and further downstream than $x/\bar{c} = 5.418$.
4. Use SPIV, or LDA, to investigate the C-wing junction flows: main-wing to side-wing, and side-wing top-wing junctions. The main-wing to side-wing junction facilities the dispersion of the vorticity field facilitating a weaker trailing vortex. The side-wing to top-wing junction creates a region of further reduced swirl velocity inboard of the wingtip. The mechanisms and early formation of these structures is crucial to induced drag reduction. Making the C-wing from carbon fibre and using surface mounted pressure transducers would help in this endeavour.
5. Redesign the C-wing to be manufactured out of carbon-fibre to enable the incorporation of surface mounted pressure transducers. This would enable: i) quantitative surface pressure data; ii) lift distribution data; iii) evaluation of induced and parasitic drag contributions (total drag provided by force platform).
6. Investigation of aeroelastic response of the C-wing to transient gusts.
7. Redesign of the C-wing to: i) allow the wing to be mounted horizontally so that effects of inertial loading and the heavy C-wing wingtip become more predominant; ii) incorporate control surfaces for high lift configurations and scheduling of loads on each lifting surface; iii) to schedule the top-wing loading only to investigate the manipulation of the bending and torsion deflections and modes, and the applicability of this to controlling flutter characteristics of the wing.

BIBLIOGRAPHY

[1] D. Abritton, G. Amanatidis, G. Angeletti, J. Crayston, D. Lister, M. McFarland, J. Miller, A. Ravishankara, N. Sabogal, N. Sundararaman, and H. Wesoky, "Global Atmospheric Effects of Aviation: Report of the Proceedings of the Symposium," in *NASA CP-3351*, NASA, Washington, 1996.

[2] F. Serrano-Bernardo, L. Bruzzi, E. Toscano, and J. Rosúa-Campos, "Pollutants and Greenhouse Gases Emissions Produced by Tourism Life Cycle: Possible Solutions to Reduce Emissions and to Introduce Adaptation Measures," *Air Pollution - A Comprehensive Perspective*, 2012.

[3] C. Bickerstaff, "Aircraft Technological Developments," in *AERONET III Workshop on Air Transportation Systems*, (Stockholm), 2005.

[4] O. Chernukhin and D. Zingg, "Multimodality and Global Optimization in Aerodynamic Design," *AIAA Journal*, vol. 51, no. 6, pp. 1342–1354, 2013.

[5] P. Jansen, R. Perez, and J. Martins, "Aerostructural Optimization of Nonplanar Lifting Surfaces," *Journal of Aircraft*, vol. 47, no. 5, pp. 1490–1503, 2010.

[6] P. Della Vecchia, *Development of Methodologies for the Aerodynamic Design and Optimization of New Regional Turboprop Aircraft*. PhD thesis, University of Naples, 2013.

[7] Z. Lyu, G. Kenway, and J. Martins, "Aerodynamic Shape Optimization Investigations of the Common Research Model Wing Benchmark," *AIAA Journal*, vol. 53, no. 4, pp. 968–985, 2014.

[8] J. Sivells, "Experimental and Calculated Charactaristics of Three Wings of NACA 64-210 and 65-210 Airfoil Sections with and without 2 Degrees Washout," *NACA TN-1422*, 1947.

[9] "Flightpath 2050 Europe's Vision for Aviation," in *European Commission Report of the High Level Group on Aviation Research*, 2011.

[10] "United States Aviation Greenhouse Gas Emissions Reduction Plan," 2015.

[11] J. Green, "Civil Aviation and the Environment - The Next Frontier for the Aerodynamicist," *Aeronautical Journal*, pp. 469–486, 2006.

[12] A. Gohardani, G. Doulgeris, and R. Singh, "Challenges of Future Aircraft Propulsion: A Review of Distributed Propulsion Technology and its Potential Application for the All Electric Commercial Aircraft," *Progress in Aerospace Sciences*, vol. 47, pp. 369–391, 2011.

[13] R. Glassock, M. Galea, W. Williams, and T. Glesk, "Hybrid Electric Aircraft Propulsion Case Study for Skydiving Mission," *Aerospace*, vol. 4, no. 45, pp. 1–22, 2017.

[14] M. Voskuijl, J. van Bogaert, and A. Rao, "Analysis and Design of Hybrid Electric Regional Turboprop Aircraft," *CEAS Aeronautical Journal*, vol. 9, pp. 15–25, 2018.

[15] F. Khan, P. Krammer, and D. Scholz, "Preliminary Aerodynamic Investigation of Box-Wing Configurations Using Low Fidelity Codes," *Deutscher Luft- und Raumfahrtkongress, DocumentID: 161308*, pp. 313–327, 2010.

[16] A. Frediani, "The Prandtl Wing," *VKI lecture series on Innovative Configurations and Advanced Concepts for Future Civil Aircraft*, pp. 1–23, 2005.

[17] I. Kroo, "Nonplanar Wing Concepts For Increased Aircraft Efficiency," *VKI lecture series on Innovative Configurations and Advanced Concepts for Future Civil Aircraft*, pp. 1–29, 2005.

[18] W. Schneider, "The Importance of Aerodynamics in the Development of Commercially Successful Transport Aircraft," in *Notes on Numerical Fluids Mechanics: Aerodynamic Drag Reduction Technologies* (P. Thiede, ed.), Springer, 2000.

[19] S. Morrison, "An Economic Analysis of Aircraft Design," *Journal of Transport Economics*, pp. 123–143, 1984.

[20] G. Kennedy, G. Kenway, and J. Martins, "High Aspect Ratio Wing Design: Optimal Aerostructural Tradeoffs for the Next Generation of Materials," in *52nd Aerospace Sciences Meeting*, pp. 1–24, 2014.

[21] R. Whitcomb, "A Design Approach and Selected Wind-Tunnel Results At High Subsonic Speeds For Wing-Tip Mounted Winglets," *NASA Technical Note: TN D-8260*, 1976.

[22] G. Kenway and J. Martins, "Multipoint High-Fidelity Aerostructural Optimization of a Transport Aircraft Configuration," *Journal of Aircraft*, vol. 51, no. 1, pp. 144–160, 2014.

[23] T. Wunderlich, "Multidisciplinary Wing Optimization of Commercial Aircraft with Consideration of Static Aeroelasticity," *CEAS Aeronautical Journal*, vol. 6, pp. 407–427, 2015.

[24] G. Kenway and J. Martins, "Aerodynamic Shape Optimization of the CRM Configuration Including Buffet-Onset Conditions," in *54th AIAA Aerospace Sciences Meeting, AIAA 2016-1294*, (San Diego, California), pp. 1–23, 2016.

[25] J. Penner, D. Lister, D. Griggs, D. Dokken, and M. McFarland, "Aviation and the Gobal Atmosphere; A special report of IPCC working groups I and III," tech. rep., 1999.

[26] P. Peeters, J. Middel, and A. Hoolhorts, "Fuel Efficiency of Commercial Aircraft: An overview of historical and future trends," *National Aerospace Laboratory NLR-CR-2005-669*, pp. 1–37, 2005.

[27] J. Lee, S. Lukachko, I. Waitz, and A. Schafer, "Historical and Future Trends in Aircraft Performance, Cost and Emissions," *Annual Review Energy Environment*, vol. 26, pp. 167–200, 2001.

[28] I. Kroo, "Innovations in Aeronautics: 2004 AIAA Dryden Lecture," *42nd AIAA Aerospace Sciences Meeting, AIAA 2004-0001*, pp. 1–11, 2004.

[29] J. Lee and J. Mo, "Analysis of Technological Innovation and Environmental Performance Improvement in Aviation Sector," *International Journal of Environmental Research and Public Health*, vol. 8, pp. 3777–3795, 2011.

[30] R. Liebeck, M. Page, and B. Rawdon, "Blended-Wing-Body Subsonic Commercial Transport," *AIAA Paper 90-0438*, 1998.

[31] A. Jameson, L. Martinelli, and J. Vassberg, "Using Computational Fluid Dynamics for Aerodynamics - A Critical Assessment," in *23rd International Congress of Aeronautical Sciences: Proceedings of ICAS*, (Toronto, Canada), 2002.

[32] R. Walker, "Final Report of the Commission on the Future of the United States Aerospace Industry," *US Government Aerospace Commission*, 2002.

[33] X. Sun, Y. Zhang, and S. Wandelt, "Air Transport vs . High Speed Rail: An Overview and Research Agenda," *Journal of Advanced Transportation*, vol. 2017, pp. 1–18, 2017.

[34] SpaceX, "Hyperloop Alpha," in *http://www.spacex.com/ sites/ spacex/ files/ hyperloop_ alpha.pdf*, 2013.

[35] KPMG, "Pre-Feasability Study Stockhold-Helsinki Using Hyperloop One Technology - Short Summary," in *https://home.kpmg.com/content/dam/kpmg/pdf/2016/07/fs-links-pre-feasibility-study-summary. pdf*, 2016.

[36] J. Braun, J. Sousa, and C. Pekardan, "Aerodynamic Design and Analysis of the Hyperloop," *AIAA Journal*, vol. 55, no. 12, pp. 4053–4060, 2017.

[37] R. Shinde, V. Raijade, A. Lahare, and V. Sarode, "Hyperloop Transportation System," *International Research Journal of Engineering and Technology*, vol. 4, no. 4, pp. 763–766, 2017.

[38] V. Vyshinsky, "Aircraft Vortex Wake and Airport Capacity," *Air and Space Europe*, vol. 3, no. 3/4, pp. 206–208, 2001.

[39] G. van Baren, L. Speijker, and A. de Bruin, "Wake Vortex Safety Evaluation of Single Runway Approaches Under Different Weather and Operational Conditions," *National Aerospace Laboratory: NRL-TP-2002-077*, 2002.

[40] J. Hallock, C. Tung, and S. Sampath, "Capacity and Wake Vorticies," *ICAS 2002 Congress*, pp. 1–10, 2002.

[41] R. Dougherty, F. Wang, E. Booth, M. Watts, N. Fenichel, and R. D'Errico, "Aircraft Wake Vortex Measurements at Denver International Airport," in *10th AIAA/CEAS Aeroacoustics Conference*, pp. 1–13, 2004.

[42] J. Hallock and F. Holzäpfel, "A Review of Recent Wake Vortex Research For Increasing Airport Capacity," *Progress in Aerospace Sciences*, vol. 98, pp. 27–36, 2018.

[43] "Aircraft Accident Report: NTSB-AAR-81-1," *United States National Transport Safety Board*, 1981.

[44] "Wake Turbulence Encounter - Collision with Terrain," *Transport Safety Board of Canada Aviation Investigation Report: A09P0187*, 2009.

[45] T. Gerz, F. Holzäpfel, and D. Darracq, "Commercial Aircraft Wake Vortices," *Progress in Aerospace Sciences*, vol. 38, pp. 181–208, 2002.

[46] C. Cone, "The Theory of Induced Lift and Minimum Induced Drag of Nonplanar Lifting Systems," *NASA Technical Report: TR R-139*, 1962.

[47] J. DeYoung, "Induced Drag Ideal Efficiency Factor of Arbitrary Lateral-Vertical Wing Forms," *NASA Contractor Report: CR-3357*, 1980.

[48] L. Demasi, A. Dipace, G. Monegato, and R. Cavallaro, "Invariant Formulation for the Minimum Induced Drag Conditions of Nonplanar Wing Systems," *AIAA Journal*, vol. 52, no. 10, pp. 2223–2240, 2014.

[49] R. Liebeck, "Design of the Blended Wing Body Subsonic Transport," *Journal of Aircraft*, vol. 41, no. 1, pp. 10–25, 2004.

[50] Z. Lyu and J. Martins, "Aerodynamic Design Optimization Studies of a Blended-Wing-Body Aircraft," *Journal of Aircraft*, vol. 51, no. 5, pp. 1604–1617, 2014.

[51] J. McMasters, D. Paisley, R. Hubert, I. Kroo, K. Bofah, J. Sullivan, and M. Drela, "Advanced Subsonic Configurations for Very Transport Airplanes Large," *NASA Contractor Report: 198351*, 1996.

[52] J. Terry, "Aerodynamic Charactaristics of Ring Wings: A Bibliography," *Redstone Scientific Information Center, Report RSIC-285*, 1964.

[53] L. Miranda, "Boxplane Configuration for Conceptual Analysis and Initial Experimental Verification," *Lockheed California Co., Report LR 25180*, 1972.

[54] J. Wolkovitch, "The Joined Wing: An Overview," *Journal of Aircraft*, vol. 23, no. 3, pp. 161–178, 1986.

[55] H. Lee, Y. Kim, G. Park, R. Kolonay, M. Blair, and R. Canfield, "Structural Optimization of a Joined Wing Using Equivalent Loads," *AIAA Journal*, vol. 44, no. 4, pp. 1302–1308, 2007.

[56] R. Cavallaro and L. Demasi, "Challenges, Ideas, and Innovations of Joined-Wing Configurations: A Concept from the Past, an Opportunity for the Future," *Progress in Aerospace Sciences*, vol. 87, pp. 1–93, 2016.

[57] M. Bhatia and R. Kapania, "Structural and Aeroelastic Characteristics of Truss-Braced Wings : A Parametric Study," *Journal of Aircraft*, vol. 49, no. 1, pp. 302–310, 2012.

[58] I. Chakraborty, T. Nam, J. Gross, D. Mavris, J. Schetz, and K. Kapania, "Comparative Assessment of Strut-Braced and Truss-Braced Wing Configurations Using Multidisciplinary Design Optimization," *Journal of Aircraft*, vol. 52, no. 6, pp. 2009–2020, 2015.

[59] W. Mallik, R. Kapania, and J. Schetz, "Effect of Flutter on the Multidisciplinary Design Optimization of Truss-Braced-Wing Aircraft," *Journal of Aircraft*, vol. 52, no. 6, pp. 1858–1872, 2015.

[60] K. Seywald, F. Hellmundt, A. Wildschek, and F. Holzapfel, "Airworthiness Investigation of a Highly Nonplanar Flexible Wing Concept," in *29th Congress of the International Council of the Aerospace Sciences*, (St. Peterspurg, Russia), pp. 1–10, 2014.

[61] W. Somerville, "US Patent Application for: "Flying Machine," No. 1,154,214, filed 4 Nov. 1910."

[62] P. Hemke, "Drag of Wings with End Plates," *NACA Technical Report: TR-267*, 1928.

[63] W. Mangler, "The Lift Distribution of Wings with End Plates," *NACA Technical Memorandum: TM-856*, vol. 14, no. 11, 1937.

[64] J. Riebe and J. Watson, "The Effect of End Plates on Swept Wings at Low Speed," *NACA Technical Report: TN-2229*, 1950.

[65] H. Heyson, G. Riebe, and C. Fulton, "Theoretical Parametric Study of the Relative Advantages of Winglets and Wing-Tip Extensions," *NASA Technical Paper 1020*, 1977.

[66] R. Jones and T. Lasinski, "Effect of Winglets on the Induced Drag of Ideal Wing Shapes," *NASA Techical Memorandum: TM-81230*, 1980.

[67] I. Kroo, "Design and Analysis of Optimally-Loaded Lifting Systems," *AIAA Paper 84-2507*, 1984.

[68] K. Asai, "Theoretical Considerations in The Aerodyanmic Effectivness of Winglets," *Journal of Aircraft: Engineering Notes*, vol. 22, no. 7, pp. 635–637, 1985.

[69] C. van Dam, "Induced-Drag Charactaristics of Crescent-Moon-Shaped Wings," *Journal of Aircraft*, vol. 24, no. 2, pp. 115–119, 1987.

[70] S. Smith and I. Kroo, "Computation of Induced Drag for Elliptical and Crescent-Shaped Wings," *Journal of Aircraft*, vol. 30, no. 4, pp. 446–452, 1993.

[71] S. Smith, "A Computational and Experimental Study of Nonlinear Aspects of Induced Drag," *NASA Technical Paper 3598*, 1996.

[72] P. Gerontakon and T. Lee, "Effect of Winglet Dihedral on a Tip Vortex," *Journal of Aircraft*, vol. 43, no. 1, pp. 117–124, 2006.

[73] S. Yen and Y. Fei, "Winglet Dihedral Effect on Flow Behavior and Aerodynamic Performance of NACA 0012 Wings," *Journal of Fluids Engineering*, vol. 133, pp. 1–9, 2011.

[74] H. Céron-Muñoz, R. Cosin, R. Coimbra, L. Correa, and F. Catalano, "Experimental Investigation of Wing-Tip Devices on the Reduction of Induced Drag," *Journal of Aircraft*, vol. 50, no. 2, pp. 441–449, 2013.

[75] D. Gueraiche and S. Popov, "Winglet Geometry Impact on DLR-F4 Aerodynamics and an Analysis of a Hyperbolic Winglet Concept," *Aerospace*, vol. 4, no. 60, 2017.

[76] S. Mostafa, S. Bose, A. Nair, M. Raheem, T. Majeed, A. Mohammed, and Y. Kim, "A Parametric Investigation of Non-Circular Spiroid Winglets," *EPJ Web of Conferences*, vol. 67, pp. 1–6, 2014.

[77] A. Mann and I. Elsholz, "The M-DAW Project - Investigations in Novel Wing Tip Device Design," in *43rd AIAA Aerospace Sciences Meeting and Exhibit, AIAA 2005-461*, (Reno, Nevada), 2005.

[78] M. Giuni, *Formation and Early Development of Wingtip Vortices*. PhD thesis, University of Glasgow, 2013.

[79] J. Spillman and J. Allen, "The Use of Wing Tip Sails To Reduce Vortex Drag," *Cranfield Institute of Technology Report*, 1977.

[80] J. Hackett, "US Patent: "Vortex Diffuser," No. 4,190,219, filed 17 May. 1977."

[81] J. Jupp and P. Rees, "US Patent: "Aircraft Wing and Winglet Arrangment," No. 4,714,215, filed 12 Jun. 1986."

[82] I. Whitehouse, "Wing Tip Fences to Sharks: The Development of Airbus Winglets," *Wing Aerodynamic Design, Airbus Operations Ltd.*, pp. 1–8, 2014.

[83] G. Heller, M. Maisel, and P. Kreuzer, "US Patent: "Wing Tip Extension For A Wing," No. 6,772,615 B2, filed 5 Apr. 2002."

[84] L. Gratzer, “US Patent: "Spiriod-Tipped Wing," No. 5,102,068, filed 25 Feb. 1991.”

[85] L. Gratzer, “US Patent: "Split Spiriod," No. 9,434,470 B2, filed 22 May. 2015,” (Seattle, Washington), United States.

[86] U. La Roche and S. Palffy, “Wing-Grid, A Novel Device for Reduction of Induced Drag on Wings,” in *AIAA\ICAS International Air and Space Symposium and Exposition*, pp. 2303–2309, 1996.

[87] U. La Roche, “US Patent: "Wing with a Wing Grid as the End Section," No. 5,823,480, filed 1 Feb. 1996.”

[88] J. Patterson, “US Patent: "Wingtip Vortex Turbine," No. 4,917,332, filed 28 Oct. 1988.”

[89] J. Haider, “Design of Wingtip Vortex Turbine,” *ICAS 2000 Congress*, pp. 1–2, 2000.

[90] D. Roman, J. Vassber, D. Friedman, A. Malachowski, and C. Vegter, “US Patent: "Performance-Enhancing Winglet System and Method," No. 8,936,219 B2, filed 30th March. 2012.”

[91] D. Roman, J. Vassberg, D. Friedman, A. Malachowski, and C. Vegter, “US Patent: "Split Winglet" No. US 2017/0203830 A1, filed 3 Apr. 2017.”

[92] K. Takenaka, K. Hatanaka, W. Yamazaki, and K. Nakahashi, “Multidisciplinary Design Exploration for a Winglet,” *Journal of Aircraft*, vol. 45, no. 5, pp. 1601–1611, 2008.

[93] J. Himisch, “Winglet Shape and Load Optimisation with a Numerically Supported Lifting Line Method; AIAA 2008-5902,” in *12th AIAA/ISSMO Multidisciplinary Analysis and Optimisation Conference, Victoria, British Columbia, Canada*, 2008.

[94] S. Ning and I. Kroo, “Multidisciplinary Considerations in the Design of Wings and Wing Tip Devices,” *Journal of Aircraft*, vol. 47, no. 2, pp. 534–543, 2010.

[95] T. Streit, R. Heinrich, B. Nagel, K. Horstmann, and C. Liersch, “Design of a Retrofit Winglet for a Transport Aircraft with Assessment of Cruise and Ultimate Structural Loads,” in *In New Results in Numerical and Experimental Fluid Mechanics VI*, pp. 61–69, Berlin, Germany: Springer, 2007.

[96] J. Hicken and D. Zingg, “Induced-Drag Minimization of Nonplanar Geometries Based on the Euler Equations,” *AIAA Journal*, vol. 48, no. 11, pp. 2564–2575, 2010.

[97] S. Khosravi and D. Zingg, “A Numerical Optimization Study on Winglets,” *15th AIAA/ISSMO Multidisciplinary Analysis and Optimization Conference*, pp. 1–14, 2014.

[98] S. Skinner and H. Zare-Behtash, "Aerodynamic Optimisation of Non-Planar Lifting Surfaces," in *57th AIAA/ASCE/AHS/ASC Structures, Structural Dynamics, and Materials Conference, AIAA 2016-0164*, (San Diego, California), pp. 1–21, 2016.

[99] M. Nemec, D. Zingg, and T. Pulliam, "Multi-Point and Multi-Objective Aerodynamic Shape Optimisation," in *9th AIAA/ISSMO Symposium on Multidisciplinary Analysis and Optimisation Conference, AIAA Paper 2002-5548*, (Atlanta, Georgia), 2002.

[100] D. Burdette, G. Kenway, and J. Martins, "Performance Evaluation of a Morphing Trailing Edge Using Multipoint Aerostructural Design Optimization," in *57th AIAA/ASCE/AHS/ASC Structures, Structural Dynamics, and Materials Conference, AIAA 2016-0159*, (San Diego, California), pp. 1–14, 2016.

[101] A. Allen and C. Breitsamter, "Transport Aircraft Wake Influenced by a Large Winglet and Winglet Flaps," *Journal of Aircraft*, vol. 45, no. 2, pp. 686–699, 2008.

[102] A. Gomes, L. Falcao, and A. Suleman, "Study of an Articulated Winglet Mechanism," in *54th AIAA/ASME/ASCE/AHS/ASC Structures, Structural Dynamics, and Materials Conference; AIAA 2013-1452*, (Boston, MA), 2013.

[103] F. Alfonso, J. Vale, F. Lau, and A. Suleman, "Multidisciplinary Performance Based Optimization of Morphing Aircraft," in *22nd AIAA/ASME/AHS Adaptive Structures Conference, AIAA SciTech Forum; AIAA 2014-0761*, (National Harbor, Maryland), 2014.

[104] J. Mills and R. Ajaj, "Flight Dynamics and Control Using Folding Wingtips: An Experimental Study," *Aerospace*, vol. 4, no. 19, 2017.

[105] R. Hornschemeyer, C. Rixen, S. Kauertz, G. Neuwerth, and R. Henke, "Active Manipulation of a Rectangular Wing Vortex Wake with Oscillating Ailerons and Winglet-Integrated Rudders," in *In New Results in Numerical and Experimental Fluid Mechanics VI*, pp. 44–51, Berlin, Germany: Springer, 2006.

[106] T. Guha and R. Kumar, "Active Control of Wingtip Vortices Using Piezoelectric Actuated Winglets," in *54th AIAA Aerospace Sciences Meeting; AIAA 2016-0323*, (San Diego, California), 2016.

[107] T. Guha and R. Kumar, "Characteristics of a Wingtip Vortex From an Oscillating Winglet," *Experiments in Fluids*, vol. 58, no. 8, pp. 1–18, 2017.

[108] K. Ramakumar and J. Jacob, "Flow Control and Lift Enhancement Using Plasma Actuators," in *35th AIAA Fluid Dynamics Conference; AIAA 2005-4635*, (Toronto, Canada), pp. 1–11, 2005.

[109] A. Mukut, H. Mizunuma, O. Hiromichi, and T. Segawa, "Winglet Type Dielectric Barrier Discharge Plasma Actuators: Performance Characterization and Numerical Comparison," *Procedia Engineering*, vol. 105, pp. 250–257, 2015.

[110] S. Popov, G. Djahid, and A. Kuznetsov, "Experimental Study of the Aerodynamics of a Wing with Various Configurations of Wingtip Triangular Extension," *Russian Aeronautics*, vol. 59, no. 3, pp. 376–380, 2016.

[111] U. La Roche and H. La Roche, "Induced Drag Reduction Using Multiple Winglets, Looking Beyond the Prandtl-Munk Linear Model," in *2nd AIAA Flow Control Conference; AIAA 2004-2120*, pp. 1–21, 2004.

[112] T. Krebs and G. Bramesfeld, "An Optimization Approach to Split-Winglet Design for Sailplanes," in *54th AIAA Aerospace Sciences Meeting; AIAA 2016-0297*, pp. 1–8, 2016.

[113] I. Kroo, J. McMasters, and S. Smith, "Highly Nonplanar Lifting Systems," *Transportation Beyond 2000: Technologies Needed for Engineering Design*, 1995.

[114] L. Demasi, G. Monegato, A. Dipace, and R. Cavallaro, "Minimum Induced Drag Theorems for Joined Wings, Closed Systems, and Generic Biwings: Theory," *Journal of Optimization Theory and Applications*, vol. 169, no. 1, pp. 200–235, 2016.

[115] P. Gage, *New Approaches to Optimisation in Aerospace Conceptual Design*. Phd. thesis, University of Stanford, 1994.

[116] L. Demasi, G. Monegato, E. Rizzo, R. Cavallaro, and A. Dipace, "Minimum Induced Drag Theorems for Joined Wings, Closed Systems, and Generic Biwings: Applications," *Journal of Optimization Theory and Applications*, vol. 169, no. 1, pp. 236–261, 2016.

[117] L. Demasi, "Investigation on the Conditions of Minimum Induced Drag of Closed Wing Systems and C-Wings," *Journal of Aircraft*, vol. 44, no. 1, pp. 81–99, 2007.

[118] L. Prandtl, "Induced Drag of Multiplanes," *NACA Technical Report TN 182, Reproduction of Der induzierte Wilderstands von Mehreckern. technische Bar*, vol. 3, no. 7, pp. 309–315, 1924.

[119] M. Munk, *Isoperimetrische Aufgaben aus der Theorie des Fluges*. PhD thesis, Universitäts-Buchdruckerei, 1919.

[120] S. Skinner and H. Zare-Behtash, "Study of a C-wing Configuration for Passive Drag and Load Alleviation," *Journal of Fluids and Structures*, vol. 78, pp. 175–196, 2018.

[121] R. Slingerland and J. Verstraeten, "Drag Characteristics for Optimally Span-Loaded Planar, Wingletted, and C-Wings," *Journal of Aircraft*, vol. 46, no. 3, pp. 962–971, 2009.

[122] H. Gagnon and D. Zingg, "High-Fidelity Aerodynamic Shape Optimization of Unconventional Aircraft through Axial Deformation," in *52nd Aerospace Sciences Meeting, AIAA 2014-0908*, (National Harbor, Maryland), pp. 1–18, 2014.

[123] M. Trapani, M. PleiBner, A. Isikveren, and K. Weiczorek, "Preliminary Investigation of a Self-Trimming Non-Planar Wing using Adaptive Utilities," *German Congress of Aeronautical Sciences*, 2012.

[124] A. Isikveren, A. Seitz, P. Vratny, C. Pornet, K. Plotner, and M. Hornung, "Conceptual Studies of Universally-Electric Systems Architectures Suitable for Transport Aircraft," *German Congress of Aeronautical Sciences*, 2012.

[125] U. Kling, C. Gologan, A. Isikveren, and M. Hornung, "Aeroelastic Investigations of a Self-Trimming Non-Planar Wing," *German Congress of Aeronautical Sciences*, pp. 1–9, 2013.

[126] C. Suresh, K. Ramesh, and V. Paramaguru, "Aerodynamic Performance Analysis of a Non-Planar C-wing Using CFD," *Aerospace Science and Technology*, vol. 40, pp. 56–61, 2015.

[127] M. Gobpinaath, K. Sivajira, C. Suresh, and K. Ramesh, "Design and Analysis of Non Planar Wing in Commercial Aircraft," *International Journal of Innovations in Engineering and Technology (IJIET)*, vol. 7, no. 3, pp. 472–485, 2016.

[128] S. Wakayama and I. Kroo, "Subsonic Wing Planform Design Using Multidisciplinary Optimization," *Journal of Aircraft*, vol. 32, no. 4, pp. 746–753, 1995.

[129] D. Zingg, M. Nemec, and T. Pulliam, "A Comparative Evaluation of Genetic and Gradient-Based Algorithms Applied to Aerodynamic Optimization," *European Journal of Computational Mechanics*, vol. 17, pp. 103–126, 2008.

[130] G. Vanderplaats, *Numerical Optimization Techniques for Engineering Design: With Applications*. McGraw-Hill Book Company, 1999.

[131] S. Skinner and H. Zare-Behtash, "State-of-The-Art in Aerodynamic Shape Optimisation Methods," *Applied Soft Computing Journal*, vol. 62, pp. 933–962, 2018.

[132] A. Oyama, S. Obayashi, and K. Nakahashi, "Real-Coded Adaptive Range Genetic Algorithm and Its Application to Aerodynamic Design.," *JSME International Journal Series A*, vol. 43, no. 2, pp. 124–129, 2002.

[133] K. Chiba, S. Obayashi, and K. Nakahashi, "High-Fidelity Multidisciplinary Design Optimization of Aerostructural Wing Shape for Regional Jet," in *23rd AIAA Applied Aerodynamics Conference, AIAA 2005-5080*, (Toronto, Canada), pp. 621–635, 2005.

[134] Z. Jinhuan and Z. Zhenggui, "An Improved Genetic Algorithm and its Applications to the Optimisation Design of an Aspirated Compressor Profile," *International Journal for Numerical Methods in Fluids*, 2015.

[135] Y. Zhang, Z. Han, L. Shi, and W. Song, "Multi-Round Surrogate-based Optimization for Benchmark Aerodynamic Design Problems," in *54th AIAA Aerospace Sciences Meeting, AIAA 2016-1545*, (San Diego, California), pp. 1–17, 2016.

[136] J. Sobieszczanski-Sobieski, "A Linear Decomposition Method For Large Optimisation Problems - Blueprint For Development," *NASA TM-83248*, pp. 51–78, 1982.

[137] J. Sobieszczanski-Sobieski, "Optimisation by Decomposition: A Step from Hierarchic to Non-Hierarchic Systems," *NASA Technical Report: N89-25149*, pp. 51–78, 1988.

[138] G. Anderson and M. Aftosmis, "Adaptive Shape Parameterization for Aerodynamic Design," *NASA Technical Report: NAS-2015-02*, 2015.

[139] S. Peigin and B. Epstein, "Multiconstrained Aerodynamic Design of Business Jet by CFD Driven Optimization Tool," *Aerospace Science and Technology*, vol. 12, pp. 125–134, 2007.

[140] S. Koziel, Y. Tesfahunegn, A. Amrit, and L. Leifsson, "Rapid Multi-Objective Aerodynamic Design Using Co-Kriging and Space Mapping," in *57th AIAA/ASCE/AHS/ASC Structures, Structural Dynamics, and Materials Conference, AIAA 2016-0418*, (San Antonio, TX, USA), pp. 1–10, 2016.

[141] P. Vecchia and F. Nicolosi, "Aerodynamic Guidelines in The Design and Optimization of New Regional Turboprop Aircraft," *Aerospace Science and Technology*, vol. 38, pp. 88–104, 2014.

[142] A. Hashimoto, S. Jeong, and S. Obayashi, "Aerodynamic Optimization of Near-Future High-Wing Aircraft," *Transactions of The Japan Society for Aeronautical and Space Sciences*, vol. 58, no. 2, pp. 73–82, 2015.

[143] M. Athanasopoulos, H. Ugail, and G. Castro, "Parametric Design of Aircraft Geometry Using Partial Differential Equations," *Advances in Engineering Software*, vol. 40, no. 7, pp. 479–486, 2009.

[144] N. Sevant, M. Bloor, and M. Wilson, "Aerodynamic Design of a Flying Wing Using Response Surface Methodology," *Journal of Aircraft*, vol. 37, no. 4, pp. 562–569, 2000.

[145] A. Jameson, L. Martinelli, and N. Pierce, "Optimum Aerodynamic Design Using the Navier-Stokes Equations," *Theoretical and Computational Fluid Dynamics*, vol. 10, pp. 213–237, 1998.

[146] G. Kenway, G. Kennedy, and J. Martins, "A CAD-Free Approach to High-Fidelity Aerostructural Optimization," in *Proceedings of the 13th AIAA/ISSMO Multidisciplinary Analysis Optimization Conference, AIAA 2010-9231*, (Fort Worth, TX), pp. 1–18, 2010.

[147] J. Fincham and M. Friswell, "Aerodynamic Optimisation of a Camber Morphing Aerofoil," *Aerospace Science and Technology*, vol. 43, pp. 245–255, 2015.

[148] J. Hall, D. Poole, T. Rendall, and C. Allen, "Volumetric Shape Parameterisation for Combined Aerodynamic Geometry and Topology Optimisation," in *16th AIAA/ISSMO Multidisciplinary Analysis and Optimization Conference, AIAA 2015-3354*, (Dallas, TX), pp. 1–29, 2015.

[149] O. Castillo, P. Melin, and J. Kacprzyk, *Soft Computing for Hybrid Intelligent Systems*. Springer, Berlin, Germany, 2008.

[150] J. Holland, "Genetic Algorithms," *Scientific American*, pp. 66–72, 1992.

[151] K. Khoo and P. Suganthan, "Evaluation of Genetic Operators and Solution Representations for Shape Recognition by Genetic Algorithms," *Pattern Recognition Letters*, vol. 23, no. 13, pp. 1589–1597, 2002.

[152] J. Holland, *Adaption in Natural and Artificial Systems*. The University of Michigan Press, 1975.

[153] E. McGookin, *Optimisation of Sliding Mode Controllers for Marine Applications : A Study of Methods and Implementation Issues*. PhD thesis, University of Glasgow, 1997.

[154] S. Sivanandam and S. Deepa, *Introduction to Genetic Algorithms*. Springer, 2008.

[155] M. Mitchell, *An Introduction to Genetic Algorithms*. MIT Press, first ed., 1998.

[156] K. Rafferty, *A Comparison Study of Search Heuristics for an Autonomous Multi-Vehicle Air-Sea Rescue System*. PhD thesis, University of Glasgow, 2014.

[157] A. Kumar, "Encoding Schemes in Genetic Algorithm," *International Journal of Advanced Research in IT and Engineering*, vol. 2, no. 3, pp. 1–7, 2013.

[158] G. Guglieri, "Using of Particle Swarm for Performance Optimization of Helicopter Rotor Blades," *Appied Mathematics*, vol. 3, pp. 1403–1408, 2012.

[159] Z. Michalewicz, *Genetic Algorithms + Data Structures = Evolution Programs*. Springer, 3rd ed., 1995.

[160] K. Deb, *Multi-Objective Optimization Using Evolutionary Algorithms*. Wiley & Sons Ltd., 2001.

[161] R. Poli, W. Langdon, and N. Mcphee, *A Field Guide to Genetic Programming*. No. March, 2008.

[162] M. Gen and R. Cheng, *Genetic Algorithms and Engineering Optimisation*. John Wiley & Sons, Inc., 2000.

[163] T. Lim, "Structured Population Genetic Algorithms: A Literature Survey," *Artificial Intelligence Review*, vol. 41, pp. 385–399, 2012.

[164] D. Popvic, "Retaining Diversity of Search Point Distrobution Through a Breeder Genetic Algorithm For Neural Network Learning," *IEEE Int. Conf. Neural Netw.*, pp. 495–498, 1997.

[165] C. Fernandes and A. Rosa, "A Study On Non-Random Mating and Varying Population Size in Genetic Algorithms Using a Royal Road Function," *Proceedings of the 2001 Congress on Evolutionary Computation (IEEE Cat. No.01TH8546)*, vol. 1, pp. 60–66, 2001.

[166] A. Massaro and E. Benini, "A Surrogate-Assisted Evolutionary Algorithm Based on the Genetic Diversity Objective," *Applied Soft Computing*, vol. 36, pp. 87–100, 2015.

[167] L. Eshelman and J. Schaffer, "Real-Coded Genetic Algorithms and Interval-Schemata," in *Foundations of Genetic Algorithms*, vol. 2, pp. 187–202, 1993.

[168] W. McCormick, P. Schweitzer, T. White, and W. Mccormick, "Problem Decomposition and Data Reorganization by a Clustering Technique," *Operations Research*, vol. 20, no. 5, pp. 993–1009, 1972.

[169] G. Walters and D. Smith, "Evolutionary Design Algorithm for Optimal Layout of Tree Networks," *Engineering Optimisation*, vol. 24, pp. 261–281, 1995.

[170] J. Badyrka, R. Jenkins, and R. Hartfield, "Aerospace Design : A Comparative Study of Optimizers," in *48th AIAA Aerospace Sciences Meeting Including the New Horizons Forum and Aerospace Exposition, AIAA 2010-1311*, (Orlando, Florida), 2010.

[171] A. Oyama and M. Liou, "Transonic Axial-Flow Blade Optimization: Evolutionary Algorithms/Three-Dimensional Navier-Stokes Solver," *Journal of Propulsion and Power*, vol. 20, no. 4, pp. 612–619, 2004.

[172] D. Dasgupta and D. Mcgregor, "sGA : A Structured Genetic Algorithm," *Technical Report No. IKBS-2-91*, pp. 1–16, 1991.

[173] C. Reeves, "Using Genetic Algorithms with Small Populations," in *Proceedings of the 5th International Conference on Genetic Algorithms*, (San Mateo, CA), pp. 92–99, 1993.

[174] O. Roeva, "Improvement of Genetic Algorithm Performance for Identification of Cultivation Process Models," in *9th WSEAS International Conference on Evolutionary Computing*, (Sofia, Bulgaria), pp. 34–39, 2008.

[175] O. Roeva, S. Fidanova, and M. Paprzycki, "Influence of the Population Size on the Genetic Algorithm Performance In Case of Cultivation Process Modelling," in *Proceedings of the 2013 Federated Conference on Computer Science and Information Systems*, pp. 371–376, 2013.

[176] H. Pandey, A. Chaudhary, and D. Mehrotra, "A Comparative Review Of Approaches To Prevent Premature Convergence In GA," *Applied Soft Computing Journal*, vol. 24, pp. 1047–1077, 2014.

[177] S. Miller, *Adaptive Wing Structures For Aeroelastic Drag Reduction and Loads Alleviation*. PhD thesis, University of Manchester, 2010.

[178] R. Haupt and S. Haupt, *Practical Genetic Algorithms*. Wiley-Interscience, 2nd ed., 2004.

[179] M. Alfaro Cid, *Optimisation of Time Domain Controllers For Supply Ships Using Genetic Algorithms and Genetic Programming*. PhD thesis, University of Glasgow, 2003.

[180] B. Miller and D. Goldberg, "Genetic Algorithms, Tournament Selection, and the Effect of Noise," in *Complex Systems 9*, pp. 193–212, 1995.

[181] G. Rudolph, "Evolutionary Search Under Partially Ordered Fitness Sets: Tech. Rep. CI-67/99," in *Technical Report CI-67/99*, University of Dortmund, Germany, 1999.

[182] E. Zitzler, K. Deb, and L. Thiele, "Comparison of Multiobjective Evolutionary Algorithms: Empirical Results," *Evolutionary Computation*, vol. 8, no. 2, pp. 173–195, 2000.

[183] D. Goldberg, *Genetic Algorithms in Searching Optimisation and Machine Learning*. Addison-Wesley, Reading, MA, 1989.

[184] K. Worrall, *Guidance and Search Algorithms for Mobile Robots: Application and Analysis Within the Context of Urban Search and Rescue*. PhD thesis, University of Glasgow, 2008.

[185] N. Srinivas and K. Deb, "Muiltiobjective Optimization Using Nondominated Sorting in Genetic Algorithms," *Evolutionary Computation*, vol. 2, no. 3, pp. 221–248, 1995.

[186] K. Deb, A. Pratap, S. Agarwal, and T. Meyarivan, "A Fast and Elitist Multiobjective Genetic Algorithm: NSGA-II," *IEEE Transactions on Evolutionary Computation*, vol. 6, no. 2, pp. 182–197, 2002.

[187] K. Deb, "Multi-Objective Genetic Algorithms: Problem Difficulties and Construction of Test Problems," *Evolutionary Computation*, vol. 7, no. 3, pp. 205–230, 1999.

[188] K. DeJong and W. Spears, "A Formal Analysis of the Role of Multi-Point Crossover in Genetic Algorithms," *Annals of Mathematics and Artificial Intelligence*, vol. 5, no. 1, pp. 1–26, 1992.

[189] L. Schmitt, "Theory of Genetic Algorithms II: Models for Genetic Operators Over the String-Tensor Representation of Populations and Convergence to Global Optima for Arbitrary Fitness Function Under Scaling," *Theoretical Computer Science*, vol. 310, pp. 181–231, 2004.

[190] D. Sasaki, M. Morikawa, S. Obayashi, and K. Nakahashi, "Aerodynamic Shape Optimization of Supersonic Wings by Adaptive Range Multiobjective Genetic Algorithms," in *First International Conference on Evolutionary Multi-Criterion Optimization*, pp. 639–652, 2001.

[191] A. Oyama and M. Liou, "Multiobjective Optimization of Rocket Engine Pumps Using Evolutionary Algorithm," *Journal of Propulsion and Power*, vol. 18, no. 3, 2002.

[192] K. DeJong, *An Analysis of the Behavior of a Class of Genetic Adaptive Systems*. PhD thesis, University of Michigan, 1975.

[193] D. Goldberg, "Real-Coded Genetic Algorithms, Virtual Alphabets, and Blocking," *Complex Systems*, vol. 5, pp. 139–167, 1991.

[194] F. Yaman and A. Yõlmaz, "Investigation of Fixed and Variable Mutation Rate Performances in Real Coded Genetic Algorithm for Uniform Circular Antenna Array Pattern Synthesis Problem," in *IEEE 18th Signal Processing and Communication and Applications Conference*, pp. 594–597, 2010.

[195] S. Koziel and Z. Michalewicz, "Evolutionary Algorithms, Homomorphous Mappings, and Constrained Parameter Optimization," *Evolutionary Computation*, vol. 7, no. 1, pp. 19–44, 1999.

[196] J. Siens and M. Innocente, "Particle Swarm Optimisation: Fundamental Study and its Application to Optimisation and to Jetty Scheduling Problems," *Trends in Engineering Computational Technology*, pp. 103–126, 2008.

[197] K. Deb, L. Thiele, M. Laumanns, and E. Zitzler, "Scalable Multi-Objective Optimization Test Problems," *IEEE*, vol. 2, pp. 825–830, 2002.

[198] T. Kato, K. Shimoyama, and S. Obayashi, "Evolutionary Algorithm with Parallel Evaluation Strategy of Feasible and Infeasible Solutions Considering Total Constraint Violation," *IEEE*, vol. 1, pp. 986–993, 2015.

[199] T. Robinson, K. Willcox, M. Eldred, and R. Haimes, "Multifidelity Optimization for Variable-Complexity Design," in *Proceedings of the 11th AIAA/ISSMO Multidisciplinary Analysis and Optimization Conference, AIAA 2006-7114*, (Portsmouth, VA), pp. 1–18, 2006.

[200] S. Gemma and F. Mastroddi, "Multi-Disciplinary and Multi-Objective Optimization of an Unconventional Aircraft Concept," in *16th AIAA/ISSMO Multidisciplinary Analysis and Optimization Conference, AIAA 2015-2327*, (Dallas, TX), pp. 1–20, 2015.

[201] M. Mitchell, *An Introduction to Genetic Algorithms*. MIT Press, first edit ed., 1998.

[202] J. Katz and A. Plotkin, *Low-Speed Aerodynamics: From Wing Theory to Panel Methods*. Cambridge UK: Cambridge University Press, 2nd ed., 2001.

[203] C. Liersch and T. Wunderlich, "A Fast Aerodynamic Tool For Preliminary Aircraft Design," in *12th AIAA/ISSMO Multidisciplinary Analysis and Optimisation Conference, AIAA 2008-5901*, (Victoria, British Columbia, Canada), 2008.

[204] P. Jansen, *Aerostructural Optimization of Non-Planar Lifting Surfaces*. PhD thesis, University of Toronto, 2009.

[205] M. Drela, *Flight Vehicle Aerodynamics*. Cambridge, MA: The MIT Press, 2014.

[206] T. Krebs and G. Bramesfeld, "An Optimization Approach to Split-Winglet Design for Sailplanes," in *54th AIAA Aerospace Sciences Meeting; AIAA 2016-0297*, pp. 1–8, 2016.

[207] S. Haghighat, J. Martins, and H. Lui, "Aeroservoelastic Design Optimization of a Flexible Wing," *Journal of Aircraft*, vol. 49, no. 2, pp. 432–443, 2012.

[208] T. Karman and J. Burgers, "General Aerodynamic Theory-Perfect Fluids," in *Aerodynamic Theory*, vol. 11, 1934.

[209] M. Drela and D. Youngeren, "XFOIL_documentation.pdf XFOIL version 6.96 documentation," 2001.

[210] M. Drela, "XFOIL: An Analysis and Design System for Low Reynolds Number Aerofoils," in *Low Reynolds Number Aerodynamics*, pp. 1–12, 1989.

[211] J. Tseng and C. Lan, "Calculation of Aerodynamic Characteristics of Airplane Configurations at High Angles of Attack," *NASA-CR-4182*, 1988.

[212] I. Tani, "A Simple Method of Calculating the Induced Velocity of a Monoplane Wing," *Tokyo Imperial University Report No. 111*, vol. IX, 3, 1934.

[213] J. Sivells and R. Neely, "Method for Calculating Wing Charactaristics By Lifting-Line Theory Using Nonlinear Section Lift Data," *NACA Report No. 865*, 1947.

[214] R. Mukherjee and A. Gopalarathnam, "Poststall Prediction of Multiple-Lifting-Surface Configurations Using a Decambering Approach," *Journal of Aircraft*, vol. 43, no. 3, pp. 660–668, 2006.

[215] S. Ning and I. Kroo, "Tip Extensions, Winglets, and C-wings: Conceptual Design and Optimization," *26th AIAA Applied Aerodynamics Conference*, 2008.

[216] P. Anderle, L. Smrdek, and F. Coton, "Aerodynamic Design and Experimental Investigation of the Sailplane Wing Tip Device," *Acta Polytechnica*, vol. 43, no. 3, pp. 3–9, 2003.

[217] P. Anderle, F. Coton, L. Smreck, and V. Brov, "A Wind Tunnel-Based Study of the Flowfield Behind Sailplane Winglets," in *24th International Congress of the Aerospace Sciences*, 2004.

[218] J. Wright, "Introduction to Flutter of Winged Aircraft," in *Introduction to Aircraft Aeroelasticity and Loads*, pp. 475–480, Wiley & Sons Ltd., 2nd ed., 2015.

[219] L. Cao and D. Zhang, "Aerodynamic Configuration Optimization for Hypersonic Gliding Vehicle Based on Improved Hybrid Multi-Objective PSO Algorithm," *IEEE*, vol. 15, pp. 1–5, 2015.

[220] K. Ishimitsu, N. VanDevender, and R. Dodson, "Design and Analysis of Winglets for Military Aircraft," *Boeing Technical Reoport AFFDL-TR-76-6*, 1976.

[221] P. Gage, I. Kroo, and P. Sobieski, "Variable-Complexity Genetic Algorithm for Topological Design," *AIAA Journal*, vol. 33, no. 11, pp. 2212–2217, 1995.

[222] I. Kroo, "Drag Due to Lift: Concepts for Prediction and Reduction," *Annual Review of Fluid Mechanics*, vol. 33, pp. 587–617, 2001.

[223] D. McLean, *Understanding Aerodynamics: Arguing from the Real Physics*. Wiley & Sons Ltd., 1st ed., 2013.

[224] T. Takahashi and S. Donovan, "Non Planar Span Loads for Minimum Induced Drag," in *49h AIAA Aerospace Sciences Meeting including the New Horizons Forum and Aerospace Exposition, AIAA Paper 2011-639*, no. January, 2011.

[225] J. Schirra, J. Watmuff, and J. Bauschat, "Accurate Induced Drag Prediction for Highly Non-Planar Lifting Systems," in *19th Australian Fluid Mechanics Conference*, (Melbourne, Australia), 2014.

[226] M. Nita and D. Scholz, "Estimating the Oswald Factor from Basic Aircraft Geometrical Parameters," *Deutscher Luft-und Raumfahrtkongress*, vol. 281424, pp. 1–19, 2012.

[227] J. Barlow, W. Rae, and A. Pope, *Low-Speed Wind Tunnel Testing*. John Wiley & Sons, 3rd ed., 1999.

[228] L. De Chant, "The Venerable 1/7th Power Law Turbulent Velocity Profile: A Classical Nonlinear Boundary Value Problem Solution and its Relationship to Stochastic Processes," *Applied Mathematics and Computation*, vol. 161, no. 2, pp. 463–474, 2005.

[229] N. Afzal, "Power Law and Log Law Velocity Profiles in Fully Developed Turbulent Pipe Flow: Equivalent Relations at Large Reynolds Numbers," *Acta Mechanica*, vol. 151, pp. 195–216, 2001.

[230] M. Buschmann and M. Gad-el Hak, "Debate Concerning the Mean-Velocity Profile of a Turbulent Boundary Layer," *AIAA Journal*, vol. 41, no. 4, 2003.

[231] G. Batchelor, *An Introduction of Fluid Dyanmics*. Cambridge University Press., 1967.

[232] F. Lynch, "Experimental Necessities for Subsonic Transport Configuration Development," *AIAA Paper 92-0158*, 1992.

[233] G. Viehweger and B. Ewald, "Half Model Testing in Cologne Cryogenic Tunnel (KK)," *AIAA Paper 94-2511*, 1994.

[234] W. Silva, B. Perry, J. Florance, M. Sanetrik, C. Wieseman, W. Stevens, C. Funk, J. Hur, D. Christhilf, and D. Coulson, "An Overview of the Semi-Span Super-Sonic Transport (S4T) Wind-Tunnel Model Program," in *53rd AIAA/ASME/ASCE/ASC Structures, Structural Dynamics and Materials Conference, AIAA 2012-1552*, 2012.

[235] N. Nguyen, E. Ting, and S. Lebofsky, "Aeroelastic Analysis of a Flexible Wing Wind Tunnel Model With Variable Camber Continuous Trailing Edge Flap Design," *56th AIAA/ASCE/AHS/ASC Structures, Structural Dynamics, and Materials Conference*, pp. 1–28, 2015.

[236] W. Millholen II and N. Chokani, "Effect of Side Boundary Layer on Transonic Flow Over a Wing," *Journal of Aircraft*, vol. 33, no. 6, pp. 1115–1122, 1996.

[237] P. Doerffer and O. Szulc, "High-Lift Behaviour of Half-Models at Flight Reynolds Numbers," *Task Quarterly*, vol. 10, no. 2, pp. 191–206, 2006.

[238] J. Anderson, *Fundmentals of Aerodynamics*. New York: McGraw-Hill, 3rd ed., 2001.

[239] S. Skinner and H. Zare-Behtash, "Semi-Span Wind Tunnel Testing Without Conventional Peniche," *Experiments in Fluids*, p. IN PRESS, 2017.

[240] F. Riegels, *Aerofoil Sections: Results From Wind-Tunnel Investigations Theortical Foundations*. London Butterworths, 1961.

[241] M. Shirk, T. Hertz, and T. Weisshaar, "Aeroelastic Tailoring- Theory, Practice, and Promise," *Journal of Aircraft*, vol. 23, no. 1, pp. 6–18, 1986.

[242] O. Stodieck, J. Cooper, P. Weaver, and P. Kealy, "Improved Aeroelastic Tailoring Using Tow-Steered Composites," *Composite Structures*, vol. 106, pp. 703–715, 2013.

[243] Y. Fung, *An Introduction of The Theory of Aeroelasticity*. New York: Dover Publications, 1st ed., 1993.

[244] T. Megson, "Elementary Aeroelasticity," in *Aircraft Structures for Engineering Students*, pp. 540–551, Elsevier, 5th ed., 2013.

[245] E. Dowell, "Static Aeroelasticity," in *A Modern Course in Aeroelasticity*, 5th ed., 2014.

[246] R. Bisplinghoff, H. Ashley, and R. Halfman, *Aeroelasticity*. NewYork: Dover Publications, 2013.

[247] F. Diederich and B. Budianski, "Divergence of Swept Wings," *NACA Report No. 2369*, 1948.

[248] E. Broadbent and O. Mansfield, "Aileron Reversal and Wing Divergence of Swept Wings," *Aeronautical Research Council Reports and Memoranda, Report No. 2817*, vol. 9, 1954.

[249] C. Junior, D. Rebolho, E. Belo, and F. Marques, "Identification of Flutter Parameters for a Wing Model," *Journal of the Brazillian Society of Mechanics, Science, and Engineering*, vol. XXVIII, no. 3, pp. 339–346, 2006.

[250] D. Hodges and G. Pierce, *Introduction to Structural Dynamics and Aeroelasticity*. Cambridge University Press, 2nd ed., 2011.

[251] D. Seal, "A Survey of Buffeting Loads," *Ministry of Aviation, Report No. 584*, 1962.

[252] Z. Zhang, T. Qiu, R. Song, and Y. Sun, "Nonlinear Finite Element Analysis of the Fluted Corrugated Sheet in the Corrugated Cardboard," *Advanced in Materials Science and Engineering*, vol. 2014, pp. 1–8, 2014.

[253] F. Ferroudji, T. Outtas, and C. Khélifi, "Large - Scale Dual Axis Sun Tracking System Modeling and Static Analysis by FEM," *International Journal of Mechanical and Mechatronics Engineering*, vol. 14, no. 4, pp. 92–97, 2014.

[254] M. Rashid, M. Latif, M. Othman, and M. Sulaiman, "Design and Simulation Study of Small Four Wheel Vehicle Chassis for Single Driver," *Modern Applied Science*, vol. 9, no. 9, pp. 240–250, 2015.

[255] E. Wilson, *Three-Dimensional Static and Dynamic Analysis of Structures*. 3rd ed., 2002.

[256] Sika Deutschland GmbH, "Product Data Sheet: SikaBlock M945," 2016.

[257] Glemco Inc., "6061 Aluminium Material Notes," 2016.

[258] Y. Yamamoto and N. Tokudo, "A Note on Convergence of Finite Element Solutions," *International Journal for Numerical Methods in Engineering*, vol. 3, pp. 485–493, 1971.

[259] S. Zhang, S. Li, M. Jia, F. Prima, L. Chen, Y. Hao, and R. Yang, "Low-Cycle Fatigue Properties of a Titanium Alloy Exhibiting Nonlinear Elastic Deformation Behavior," *Acta Materialia*, vol. 59, pp. 4690–4699, 2011.

[260] M. Ujang, S. Mat, K. Perumal, and M. Mohd-Nasir, "Experimental Study of UTM-LST Generic Half Model Transport Aircraft," *AEROTECH VI - Innovation in Aerospace Engineering and Technology*, vol. 152, 2016.

[261] H. Glauert, "Wind Tunnel Interference on Wings, Bodies and Airscrews," *Aeronautical Research Committee Reports and Memoranda, Report No. 1566*, 1933.

[262] E. Maskell, "A Theory of Blockage Effects on Bluff Bodies and Stalled Wings in a Closed Wind Tunnel," *Ministry of Aviation, Report No. 3400*, 1963.

[263] L. Stafford, "A Streamline Wind Tunnel Working Section For Testing At High Blockage Ratios," *Jounral of Wind Engineering and Inductrial Aerodynamics*, vol. 9, pp. 23–31, 1981.

[264] P. Gerontakon and T. Lee, "Near-Field Tip Vortex Behind a Swept Wing Model," *Experiments in Fluids*, vol. 40, pp. 141–155, 2006.

[265] B. Ramaprian and Y. Zheng, "Measurements in Rollup Region of the Tip Vortex from a Rectangular Wing," *AIAA Journal*, vol. 35, no. 12, pp. 1837–1843, 1997.

[266] R. Adrian, "Particle-Imaging Techniques for Experimental Fluid Mechnics," *Annual Review of Fluid Mechanics*, vol. 23, pp. 261–304, 1991.

[267] M. Raffel, C. Willert, S. Wereley, and J. Kompenhans, *Particle Image Velocimetry: A Practical Guide*. Springer, 2nd ed., 2007.

[268] K. Hinsch, "Three-Dimensional Particle Velocimetry," *Measurment Science and Technology*, vol. 6, pp. 742–753, 1995.

[269] N. Lawson and J. Wu, "Three-Dimensional Particle Image Velocimetry: Error Analysis of Stereoscopic Techniques," *Measurement Science and Technology*, vol. 8, pp. 894–800, 1997.

[270] A. Melling, "Tracer Particles and Seeding for Particle Image Velocimetry," *Measurement Science and Technology*, vol. 8, pp. 1406–1416, 1997.

[271] PIVTECH-GmbH, "User Manual: Aerosol Generator PivPart160 series," *Technology for Particles, Imaging and Velocimetry*, 2009.

[272] E. Ribeiro, T. Polachini, G. Carvalho, J. Romero, and R. Cabral, "Thermophysical Properties of Different Olive Oils : Evaluating Density and Rheology Through a Fluid Dynamic Approach," *European Journal of Lipid Science and Technology*, vol. 119, pp. 1–10, 2017.

[273] M. Samimy and S. Lele, "Motion of Particles with Inertia in a Compressible Free Shear Layer," *Phisics of Fluids A: Fluid Dynamics*, vol. 3, no. 8, pp. 1915–1923, 1991.

[274] F. Scarano, *Particle Image Velocimetry: New Developments and Recent Applications*. Springer, 2008.

[275] R. Keane and R. Adrian, "Optimization of Particle Image Velocimters. Part 1 : Double Pulsed Systems," *Measurement Science and Technology*, vol. 1, pp. 1202–1215, 1990.

[276] A. Prasad, "Stereoscopic Particle Image Velocimetry," *Experiments in Fluids*, vol. 29, pp. 103–116, 2000.

[277] LaVision, *DaVis 8 software - Product Manual*. 2012.

[278] R. Keane and R. Adrian, "Theory of Cross-Correlation Analysis of PIV Images," *Applied Scientific Research*, vol. 49, pp. 191–215, 1992.

[279] A. Boillot and A. Prasad, "Optimization Procedure for Pulse Separation in Cross-Correlation PIV," *Experiments in Fluids*, vol. 21, pp. 87–93, 1996.

[280] R. Adrian, "Double Exposure , Multiple-Field Particle Image Velocimetry for Turbulent Probability Density," *Optics and Lasers in Engineering*, vol. 9, pp. 211–228, 1988.

[281] M. Merzkirch, *Flow Visualisation*. Academic Press, 2nd ed., 1987.

[282] S. Ristic, "Flow Visualisation Techniques in Wind Tunnels Part I - Non Optical Methods," *Scientific Technical Review*, vol. 57, no. 1, pp. 39–50, 2007.

[283] T. Liu, "Extraction of Skin Friction Fields From Surface Flow Visualizations as an Inverse Problem," *Measurement Science and Technology*, vol. 24, pp. 1–18, 2013.

[284] D. Kenwright, "Automatic Detection of Open and Closed Separation and Attachment Lines," *Proceedings of the IEEE Visualization*, vol. 98, pp. 151–158, 1998.

[285] Polytec, *User Manual: Portable Digital Vibrometer PDV 100*. 2015.

[286] M. Johansmann, G. Siegmund, and M. Pineda, "Targeting the Limits of Laser Doppler Vibrometry," *Polytec Technical Report*, 2005.

[287] G. Rossi, R. Marsili, V. Gusella, and M. Gioffre, "Comparison Between Accelerometer and Laser Vibrometer to Measure Traffic Excited Vibrations on Bridges," *Shock and Vibration*, vol. 9, pp. 11–18, 2002.

[288] V. Yanchich and O. Kramarov, "Piezoelectric Accelerometer: Theory and Application," *Metra Mess-und Frequenztechnik*, 2001.

[289] W. Millholen II, N. Chokani, and R. McGhee, "Development of Semispan Model Test Techniques," *Journal of Aircraft*, vol. 33, no. 6, pp. 1115–1122, 1996.

[290] G. Gatlin, W. Tomek, F. Payne, and R. Griffiths, "Recent improvements in semispan testing at the National Transonic Facility (invited)," *14th AIAA Aerospace Sciences Meeting 2006*, no. NASA-TM-111454, 1996.

[291] G. Gatlin, P. Parker, and L. Owens, "Development of a Semi-Span Test Capability at the National Transonic Facility," in *39th AIAA Aerospace Sciences Meeting and Exhibit, AIAA Paper 2001-0759*, (Reno, Nevada), 2001.

[292] P. Eliasson, "Investigation of a Half-Model High-Lift Configuration in a Wind Tunnel," *Journal of Aircraft*, vol. 45, no. 1, pp. 29–37, 2008.

[293] A. Malik and P. Render, "Use of Wall Suction in Half Model Wind Tunnel Testing," in *28th Applied Aerodynamics Conference*, (Chilcago, Ill, USA), 2010.

[294] Y. Yokokawa, M. Murayama, H. Uchida, and K. Tanaka, "Aerodynamic Influence of a Half-Span Model Installation for High-Lift Configuration Experiment," in *48th AIAA Aerospace Sciences Meeting Including the New Horizons Forum and Aerospace Exposition, AIAA 2010-684*, (Orlando, Florida), 2010.

[295] F. Kafyeke, F. Pépin, and C. Kho, "Development of High-Lift Systems for the Bombardier CRJ-700," in *ICAS 2002 Congress*, pp. 1–10, 2002.

[296] H. Kuo, C and D. Lin, "Non-Uniform Recovery of Vortex Breakdown Over Delta Wing in Response to Blowing Along Vortex Core," *Experiments in Fluids*, vol. 22, pp. 33–44, 1996.

[297] T. Lee and Y. Su, "Aerodynamic Performance of a Wing with a Deflected Tip-Mounted Reverse Half-Delta Wing," *Experiments in Fluids*, vol. 53, pp. 1221–1232, 2012.

[298] S. Eder, K. Hufnagel, and C. Tropea, "Semi-Span Testing in Wind Tunnels," in *25th International Congress of the Aeronautical Sciences*, pp. 1–9, 2006.

[299] R. Wallis, "Wind Tunnel Studies of Leading Edge Separation Phenomena on a Quarter Scale Model of the Outer Panel of the Handley Page 'Victor' Wing, with and without Nose Droop," *Ministry of Aviation, Report No. 3455*, 1967.

[300] P. Lissaman, "Low-Reynolds-Number Airfoils," *Annual Review of Fluid Mechanics*, vol. 15, pp. 223–239, 1983.

[301] A. Webster and R. Vaicaitis, "Application of Tuned Mass Dampers to Control Vibrations of Composite Floor Systems," *Engineering Journal of the American Institute of Steel Construction*, vol. 29, no. 3, pp. 116–124, 2003.

[302] A. Groh, "The Dynamic Vibration Absorber Principle Applied to a High-Quality Phonograph Pickup," *Journal of The Audio Engineering Society*, vol. 25, no. 6, pp. 385–390, 1977.

[303] N. Jalili and N. Olgac, "A Sensitivity Study on Optimum Delyed Feedback Vibration Absorber," *Journal of Vibration and Acoustics*, vol. 122, no. 2, pp. 1–8, 2000.

[304] S. Ali and S. Adhikari, "Energy Harvesting Dynamic Vibration Absorbers," *Journal of Applied Mechanics*, vol. 80, no. 4, pp. 1–9, 2013.

[305] M. Tursun and E. Eskinat, "H2 Optimization of Damped-Vibration Absorbers for Suppressing Vibrations in Beams With Constrained Minimization," *Journal of Vibration and Acoustics*, vol. 136, no. 2, pp. 1–14, 2014.

[306] Y. Bobrovnitskii, K. Morozov, and T. Tomilina, "Impedance Approach to Designing Efficient Vibration Energy Absorbers," *Acoustical Physics*, vol. 63, no. 2, pp. 141–147, 2017.

[307] J. Hall and J. Grose, "Some Effects of Auditory Grouping Factors on Modulation Detection Interference (MDI)," *Journal of the Acoustical Society of America*, vol. 90, no. 6, pp. 3028–3035, 1991.

[308] R. Pastel, J. Caruthers, and W. Frost, "Airplane Wing Vibration Due to Atmospheric Turbulence," *NASA Contractor Report 3431*, 1982.

[309] L. Flore and A. Cubillo, "Dynamic Mechanical Analysis of an Aircraft Wing With Emphasis on Vibration Modes Change With Loading," in *International Conference of Scientific Paper AFASES*, (Brasov), 2015.

[310] R. Whalley and M. Ebrahimi, "Vibration and Control of Aircraft Wings," *Proceedings of the Institution of Mechanical Engineers, Part G: Journal of Aerospace Engineering*, vol. 212, no. 5, pp. 353–365, 1998.

[311] P. Molton, J. Dandois, A. Lepage, V. Brunet, and R. Bur, "Control of Buffet Phenomenon on a Transonic Swept Wing," *AIAA Journal*, vol. 51, no. 4, pp. 761–772, 2013.

[312] R. Destuynder, J. Bouttes, and P. Poisson-Quinton, "US Patent: "Active Method and Installation for the Reduction of Buffetting of the Wings of an Aircraft," No. 4,706,902, filed 6 May 1985."

[313] A. Ali and M. Saeed, "Active Vibration Suppression of Aerobatic Aircraft Wing by Acceleration Feedback Controller," *International Journal of Computer Applications*, vol. 157, no. 10, pp. 30–36, 2017.

[314] H. Jo and H. Yabuno, "Amplitude Reduction of Primary Resonance of Nonlinear Oscillator by a Dynamic Vibration Absorber Using Nonlinear Coupling," *Nonlinear Dynamics*, vol. 55, pp. 67–78, 2009.

[315] S. Skinner and H. Zare-Behtash, "Study of a C-wing Configuration for Passive Drag and Load Alleviation," *Journal of Fluids and Structures*, vol. 78, pp. 175–196, 2018.

[316] M. Ramasamy, B. Johnson, T. Huismann, and J. Leishman, "Digital Particle Image Velocimetry Measurements of Tip Vortex Characteristics Using an Improved Aperiodicity Correction," *Journal of the American Helicopter Society*, vol. 54, no. 1, 2009.

[317] D. Birch, "Self-Similarity of Trailing Vortices," *Physics of Fluids*, vol. 24, no. 2, 2012.

[318] J. Sousa and J. Pereira, "Rollup Region of a Turbulent Trailing Vortex Issued from a Blade with Flow Separation," *Experimental Thermal and Fluid Science*, vol. 20, pp. 150–161, 2000.

[319] W. Devenport, M. Rife, S. Liapis, and G. Follin, "The Structure and Development of a Wing-Tip Vortex," *Journal of Fluid Mechanics*, vol. 312, pp. 67–106, 1996.

[320] M. Ramasamy, B. Johnson, T. Huismann, and J. Leishman, "Procedures for Measuring the Turbulence Characteristics of Rotor Blade Tip Vortices," *Journal of the American Helicopter Society*, vol. 54, 2009.

[321] F. Albano, F. De Gregorio, and A. Ragni, "Trailing Vortex Detection and Quantitative Evaluation of Vortex Characteristics by PIV Technique," *IEEE*, vol. 3, pp. 31–43, 2003.

[322] S. Beresh, J. Henfling, and R. Spillers, "Meander of a Fin Trailing Vortex and the Origin of its Turbulence," *Experiments in Fluids*, vol. 49, pp. 599–611, 2010.

[323] B. van der Wall and H. Richard, "Analysis Methodology for 3C-PIV Data of Rotary Wing Vortices," *Experiments in Fluids*, vol. 40, pp. 798–812, 2006.

[324] M. Ramasamy, R. Paetzel, and M. Bhagwat, "Aperiodicity Correction of Rotor Wip Vortex Measurements," in *In American Helicopter Society 67th Annual Forum*, (Virginia Beach, VA), 2011.

[325] F. Durst, A. Melling, and J. Whitelaw, "Principles and Practice of Laser-Doppler Anemometry," *Journal of Fluid Mechanics*, vol. 80, no. 1, pp. 204–206, 1977.

[326] J. Jeong and F. Hussain, "On the Identification of a Vortex," *Journal of Fluid Mechanics*, vol. 285, pp. 69–94, 1995.

[327] B. van der Wall, B. Junker, C. Burley, T. Brooks, Y. Yu, C. Tung, M. Raffel, H. Richard, W. Wagner, E. Mercker, K. Pengel, H. Holthusen, P. Beaumier, and Y. Delrieux, "The HART II Test in the LLF of the DNW - A Major Step Towards Rotor Wake Understanding," in *Proceedings of the 28th European Rotorcraft Forum*, (Bristol, UK), 2002.

[328] M. Jiang, R. Machiraju, and D. Thompson, "Detection and Visualization of Vortices," *Visualization Handbook*, pp. 295–309, 2005.

[329] A. Berson, M. Michard, and P. Blanc-Benon, "Vortex Identification and Tracking in Unsteady Flows," *Comptes Rendus - Mecanique*, vol. 337, pp. 61–67, 2009.

[330] C. Morgan, H. Babinsky, and J. Harvey, "Vortex Detection Methods for Use with PIV and CFD Data," in *47th AIAA Aerospace Sciences Meeting including The New Horizons Forum and Aerospace Exposition; AIAA-2009-74*, (Orlando, Florida), 2009.

[331] J. Llobet, J. Barth, and I. Jahn, "Vortex Tracking Algorithm for Hypersonic Flow in Scramjets," in *19th Australian Fluid Mechanics Conference*, (Melbourne, Australia), 2014.

[332] Y. Huang and M. Green, "Detection and Tracking of Vortex Phenomena Using Lagrangian Coherent Structures," *Experiments in Fluids*, vol. 56, no. 7, 2015.

[333] P. Spalart, "Airplane Trailing Vortices," *Annual Review of Fluid Mechanics*, vol. 30, pp. 107–138, 1998.

[334] S. Bailey, S. Tavoularis, and B. Lee, "Effects of Free-Stream Turbulence on Wing-Tip Vortex Formation and Near Field," *Journal of Aircraft*, vol. 43, no. 5, pp. 1282–1291, 2006.

[335] S. Gunasekaran and A. Altman, "Is There a Relationship Between the Wingtip Vortex and the Shear Layer?," *54th AIAA Aerospace Sciences Meeting, AIAA 2016-1068*, 2016.

[336] W. Phillips, "The Turbulent Trailing Vortex During Roll-Up," *Journal of Fluid Mechanics*, vol. 105, pp. 451–467, 1981.

[337] J. Chow, G. Zilliac, and P. Bradshaw, "Mean and Turbulence Measurements in the Near Field of a Wingtip Vortex," *AIAA Journal*, vol. 35, no. 10, pp. 1561–1567, 1997.

[338] Y. Han, J. Leishman, and A. Coyne, "Measurements of the Velocity and Turbulence Structure of a Rotor Tip Vortex," *AIAA Journal*, vol. 35, no. 3, pp. 477–485, 1997.

[339] M. Engel, *A Wind Tunnel Investgation of a Wing-Tip Trailing Vortex*. PhD thesis, Virginia Polytechnic Institute, 1995.

[340] D. Birch, T. Lee, F. Mokhtarian, and F. Kafyeke, "Structure and Induced Drag of a Tip Vortex," *Journal of Aircraft*, vol. 41, no. 5, pp. 1138–1145, 2004.

[341] P. Singh and M. Uberoi, "Experiments on Vortex Stability," *The Physics of Fluids*, vol. 19, no. 12, 1976.

[342] G. Batchelor, "Axial Flow in Trailing Line Vortices," *Journal of Fluid Mechanics*, vol. 26, no. 4, pp. 645–658, 1964.

[343] W. Phillips and J. Graham, "Reynolds Stress Measurements in a Turbulent Trailing Vortex," *Journal of Fluid Mechanics*, vol. 147, pp. 353–371, 1984.

[344] D. Dosanjh, E. Gasparek, and S. Eskinazi, "Decay of a Viscous Trailing Vortex," *The Aeronautical Journal*, vol. 13, no. 2, pp. 167–188, 1962.

[345] S. Green and A. Acosta, "Unsteady Flow in Trailing Vortices," *Journal of Fluid Mechanics*, vol. 227, pp. 107–134, 1991.

[346] K. Yang and S. Xu, "Wing Tip Vortex Structure Behind an Airfoil with Flaps at the Tip," *Science China: Physics, Mechanics and Astronomy*, vol. 54, no. 4, pp. 743–747, 2011.

[347] A. Cotel, "Turbulence Inside a Vortex: Take Two," *Physics of Fluids*, vol. 14, no. 8, pp. 2933–2934, 2002.

[348] A. Cotel and R. Breidenthal, "Turbulence Inside a Vortex," *Physics of Fluids*, vol. 11, no. 10, pp. 3026–3029, 1999.

[349] R. Narasimha and K. Sreenivasan, "Laminarization of Fluid Flows," *Advances in Applied Mechanics*, vol. 19, pp. 221–309, 1979.

[350] P. Martin and J. Leishman, "Trailing Vortex Measurements in the Wake of a Hovering Rotor Blade With Various Tip Shapes," in *58th Annual Forum of the AHS International*, (Montréal, Canada), pp. 2058–2080, 2002.

[351] P. Martin, G. Pugliese, and J. Leishman, "High Resolution Trailing Vortex Measurements in the Wake of a Hovering Rotor," *Journal of the American Helicopter Society*, vol. 48, no. 1, pp. 39–52, 2003.

[352] O. Zeman, "The Persistence of Trailing Vortices: A Modeling Study," *Physics of Fluids*, vol. 7, no. 1, pp. 135–143, 1995.

[353] P. Bradshaw, "The Analogy Between Streamline Curvation and Buoyancy in Turbulent Shear Flow," *Journal of Fluid Mechanics*, vol. 36, no. 1, pp. 177–191, 1969.

[354] A. Cotel, J. A. Gjestvang, N. Ramkhelawan, and R. Breidenthal, "Laboratory Experiments of a Jet Impinging on a Stratified Interface," *Experiments in Fluids*, vol. 23, pp. 155–160, 1997.

[355] M. Churchfield and G. Blaisdell, "Numerical Simulations of a Wingtip Vortex in the Near Field," *Journal of Aircraft*, vol. 46, no. 1, pp. 230–243, 2009.

[356] K. Duraisamy and G. Iaccarino, "Curvature Correction and Application of the v2-f Turbulence Model to Tip Vortex Flows," *Center for Turbulence Research Annual Research Briefs*, pp. 157–168, 2005.

[357] E. Hoffmann and P. Joubert, "Turbulent Line Vortices," *Journal of Fluid Mechanics*, vol. 16, no. 3, pp. 395–411, 1963.

[358] P. Panagiotou, G. Ioannidis, I. Tzivinikos, and K. Yakinthos, "Experimental Investigation of the Wake and the Wingtip Vortices of a UAV Model," *Aerospace*, vol. 4, no. 53, pp. 1–17, 2017.

[359] C. Breitsamter, "Wake Vortex Characteristics of Transport Aircraft," *Progress in Aerospace Sciences*, vol. 47, pp. 89–134, 2011.

[360] V. Corsiglia and R. Dunham, "Aircraft Wake-Vortex Minimization by Use of Flaps," in *Proceedings of the NASA symposium on wake vortex minimization, NASA SP-409*, pp. 305–338, 1976.

[361] V. Corsiglia, V. Rossow, and D. Cliffone, "Experimental Study of the Effect of Span Loading on Aircraft Wakes," *Journal of Aircraft*, vol. 13, no. 12, pp. 968–973, 1976.

[362] J. Crouch, G. Miller, and P. Spalart, "Active-Control System of Breakup of Airplane Trailing Vorticies," *AIAA Journal*, vol. 39, no. 12, pp. 2374–2381, 2001.

[363] D. Greenblatt, S. Vey, O. Paschereit, and R. Meyer, "Flap Vortex Management Using Active Gurney Flaps," *AIAA Journal*, vol. 47, no. 12, pp. 2845–2856, 2009.

[364] C. Breitsamter and A. Allen, "Transport Aircraft Wake Influenced by a Large Winglet and Winglet Flaps," *Journal of Aircraft*, vol. 46, no. 1, pp. 175–188, 2009.

[365] I. Gursul and E. Vardaki, "Control of Wing Vortices," in *In Active Flow Control*, pp. 137–151, Springer, 2007.

[366] F. Marchman, H. Faery, and D. Manor, "Whitcomb Winglet Applications to General Aviation Aircraft," in *Aircraft Systems and Technology Conference, AIAA Paper 78-1478*, (Los Angeles, CA), 1978.

[367] J. Guerrero, D. Maestro, and A. Bottaro, "Biomimetic Spiroid Winglets for Lift and Drag Control," *Comptes Rendus - Mecanique*, vol. 340, pp. 67–80, 2012.

[368] R. White, "US Patent: "Vortex Dissipator," No. 3,845,918, filed 7 Dec. 1972," (Rochester, NY), United States.

[369] Boeing, "Boeing's New Winglets Reduce Fuel Burn: Noise and Vibration World Wide," *SAGE Journals, Aircraft Noise*, 2001.

[370] L. Gratzer, "US Patent: "Blended Winglet," No. 5,348,253, filed 1 Feb 1993," (Seattle, Washington), United States.

[371] M. Ramasamy and J. Leishman, "Benchmarking Particle Image Velocimetry with Laser Doppler Velocimetry for Rotor Wake Measurements," *AIAA Journal*, vol. 45, no. 11, pp. 2622–2633, 2007.

[372] N. Nathan, *The Rotor Wake in Ground Effect and its Investigation in a Wind Tunnel*. PhD thesis, University of Glasgow, 2010.

[373] R. Green, "Optical methods," in *In Experimental Aerodynamic 5 - Lectures Notes.*

[374] A. Prasad, R. Adrian, C. Landreth, and P. Offutt, "Effect of Resolution on the Speed and Accuracy of Particle Image Velocimetry Interrogation," *Experiments in Fluids*, vol. 13, pp. 105–116, 1992.

[375] D. Hart, "PIV Error Correction," *Experiments in Fluids*, vol. 29, no. 1, pp. 13–22, 2000.

[376] E. Hopkins, "Charts for Predicting Turbulent Skin Friction from the Van Driest Method (II)," *NASA Technical Note: TN D-6945*, 1972.

[377] K. McAlister and R. Takahashi, "NACA 0015 Wing Pressure and Trailing Vortex Measurements," *NASA Technical Paper: TP-3151*, 1991.

[378] H. Ghimire and S. Bailey, "An Experimental Investigation of Wing-Tip Vortex Decay in Turbulence," *Physics of Fluids*, vol. 29, no. 3, 2017.

APPENDICES

A: VORTEX RING METHOD CONVERGENCE ANALYSIS

Utilising the first experimental validation case for the vortex ring analysis model in Section 2.4.7, a convergence analysis is conducted here considering spanwise and chordwise wing discretisation. The purpose of doing so considers the minimisation of round-off and discretionary errors by refining geometry discretisation.

Discretisation errors are directly related to the discretisation quality. These errors occur from the representation of governing equations and the wing physical geometric description as algebraic expressions in a discrete spatial domain. A consistent numerical method to approach the continuum representation of the equations and zero discretisation error is to systematically increase the number of surface mesh panels to reduced the size of the finite vortex elements; thereby increasing the number of elements (vortex rings) in the discretisation. This process is illustrated in figure A.1, where the lift and drag coefficient of the wing at $\alpha = +7.48^\circ$ is modelled. The experimental data is also shown.

The spatial discretisation of aerodynamic surfaces is also important to consider from the point of balancing accuracy and computational time. Clearly spanwise vortex rings (N_p) alone do not provide sufficient accuracy for the prediction of wing lift

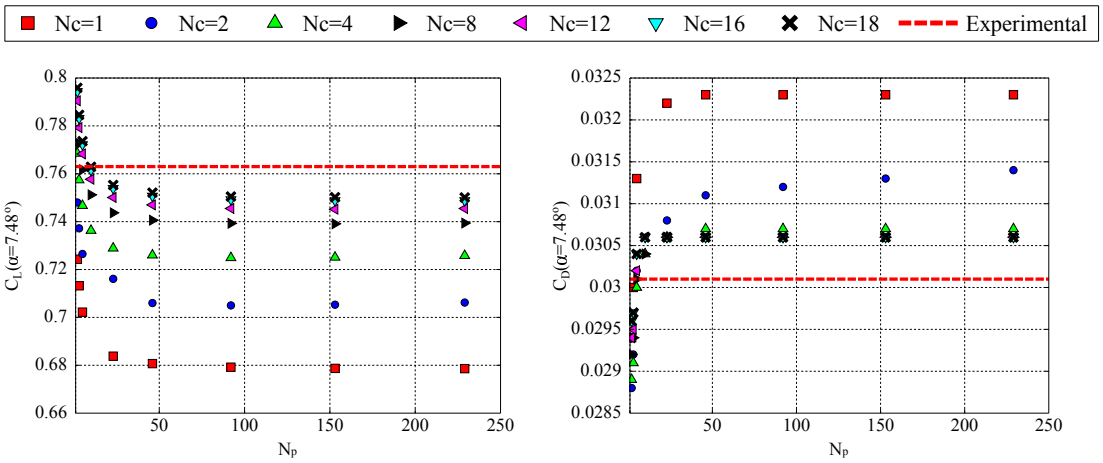

(a) Variation of C_L.

(b) Variation of C_D.

FIGURE A.1: VRM spatial discretisation convergence analysis using validation case 1 at $\alpha = 7.48^\circ$.

or induced drag, however all solutions converge with $N_p = 46$ (spanwise spatial resolution of $\approx 0.05m$).

A fundamental statement within thin aerofoil theory is that the camber line is considered a streamline of the flow over which the vortex strength varies. The nature of the panel method is devised to conceptually obtain values for vortex strength which make the modelled wing a streamline of the flow and also satisfy the Kutta condition. Increasing the number of spanwise panels serves to better resolve vortex strength per unit length across the span (more precisely evaluating lift), but it does not sufficiently resolve the induced velocities (*i.e.* downwash). Hence, increasing the number of chordwise panels serves to distribute more control points along the camber line at which boundary conditions are applied; that is, at each control point the normal component of the velocity is zero. This velocity is the superposition of the uniform flow velocity and the velocity induced by the vortex panels. As a result, the induced velocity distribution over the wing is more accurately modelled (leading to a more accurate computation of the induced drag), and the Kutta condition is applied more precisely. Chord-wise panels are also necessary to resolve the effects of geometric twist, affecting the predicted lift-curve-slope.

Figure A.2 illustrates the corresponding variations in computational time with spatial resolution. The need for compromise and accuracy become obvious; for a single of analyses it may be acceptable to run higher fidelity meshes with an associated computation time of several minutes. However, for parametric studies and optimisation algorithms where many planform evaluations are necessary, a lower number of panels (chordwise in particular) should be used. This would lead to fairly accurate solutions with faster computations of the order of a few seconds. On average, the genetic algorithm is required to analyse $90,000$ wing geometries in a single optimisation.

It has been found that regardless of wing geometry 8 chordwise vortex rings are sufficient to model aerofoil camber and twist. Spanwise discretisation of geometries

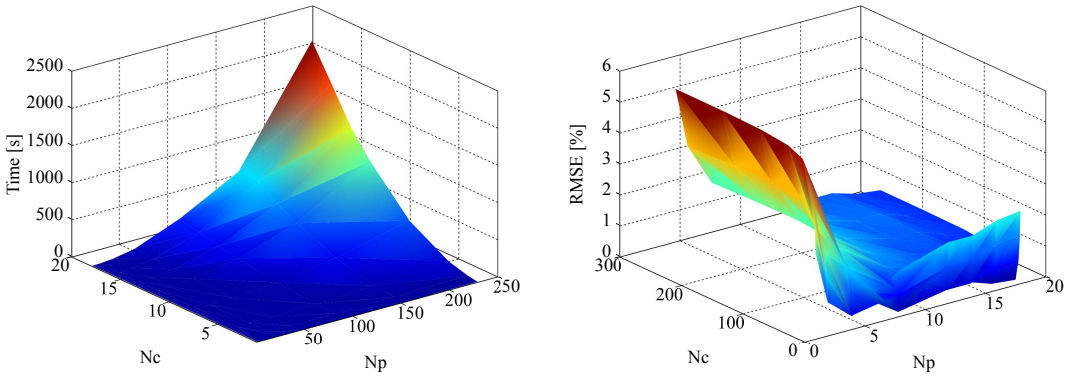

(a) Computation time with discretisation.

(b) RMSE with discretisation.

FIGURE A.2: VRM accuarcy Vs. speed.

into $\approx 0.05m$ wide vortex rings provide good accuracy and computation times. For optimisations, due to the range of geometries involved, spanwise discretisation of $\approx 0.01m$ wide vortex rings was used to accommodate more complex shapes. This is found to have a maximum analysis time of ≈ 15 seconds per wing, translating to a maximum optimisation time of ≈ 25 hours using a genetic algorithm population of 150 candidate solutions over 600 generations using.

B: CONSIDERATIONS OF SPIV MEASUREMENT ERROR

Errors in the velocity information derived from SPIV come from a variety of sources including the optical system, experimental set-up, image reconstruction method, image digitisation, seeding quality, correlation process and post-processing of the images [267, 371, 372]. Some of these errors can be rectified with the implementation of post-processing algorithms and by following guidelines from similar experiments [267].

The set-up of the camera position and angular displacement, the choice and positioning of the calibration plate, the focusing of the image, the calibration procedure and the calculation of the mapping function were accomplished following the guidelines of the PIV system manufacturer [277] and adopting the DaVis 8 software. The quality of the calibration process was given by the software in terms of average deviation of the de-warped marker positions of the calibration plate to the ideal regular grid. A value consistently lower than 0.3 pixels was calculated, which ensured accurate calibration of the system [277].

The digitisation of the smoke tracer particles can be one of the most significant sources of error in the accurate determination of the velocity information [372]. Digitisation effects in PIV occur when the imaged flow tracer particles are too small to be adequately defined as a distinctive image, which is an effect of the limited spatial resolution of the CCD/CMOS sensor chip used in digital cameras. The limited pixel size of these cameras result in reduced resolution for a given magnification. The small tracer particles in the flow field are thus imaged without an accurate profile and the displacements derived from the correlation processes tend to be biased to integer values resulting in clusters of vectors in the derived velocity maps to have block like appearances [373]. This phenomenon is known as *peak-locking* which the probability density function (PDF) histograms relating to the velocity field computation will show biased peaks toward integer velocity values [267]. In other words, if the experimental arrangement is such that the seeding particles are seen on the CCD/CMOS sensor chip with definition of less than one pixel in diameter, peak-locking can occur.

The camera lenses and the position of the cameras during the experiments were chosen to minimise the peak-locking effects and the particle size on the image plane was between 1 and 2 pixels [374]. Additionally, errors from an improper seeding

density of the flow field were minimised ensuring sufficiently populated interrogation windows [278, 375]; in certain experimental conditions (vortex core) pre-processing of the raw data using a particle intensity normalisation filter was applied to increase particle population within interrogation windows. The time delay between the two laser pulses was also accurately calculated (see Section 3.9).

The peak-locking effect in the velocity maps was monitored within the DaVis 8 software to have an average value within the acceptable range [277]. Histograms, such as that presented in figure B.1, of all corresponding velocity components for all values from minimum to maximum were monitored. Based on this, DaVis 8 calculates a 'score' for the peak locking where: a score of 0 indicates no peak-locking; a score of ≤ 0.1 indicates negligible peak-locking effects; and a score ≥ 0.1 indicated strong peak-locking. For all of the data sets collected the peak-locking score from DaVis 8 was not logged to exceed 0.015 for any velocity component.

Figure B.1 presents examples of the in- and out-of-plane histogram for an instantaneous realisation of the planar wing vortex at $\alpha = 0°$, from which peak-locking to

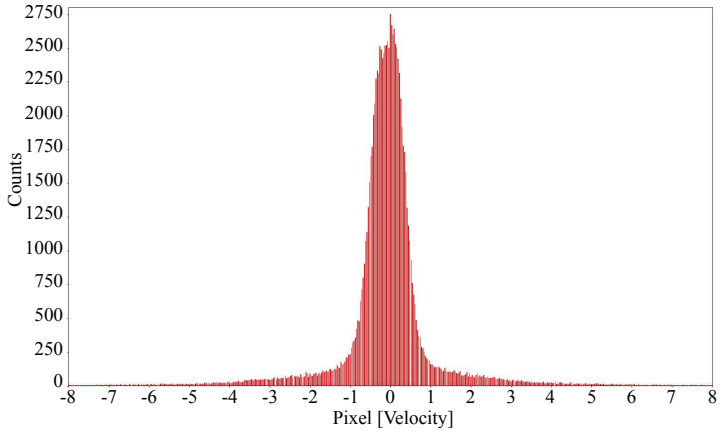

(a) In-plane velocity PDF histogram.

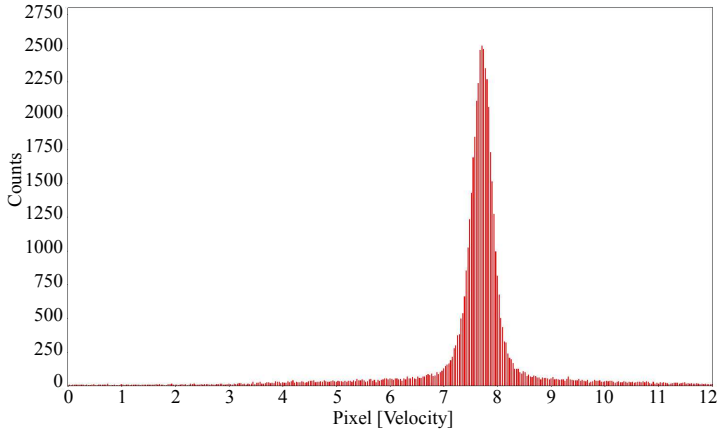

(b) Out-of-plane PDF histogram.

FIGURE B.1: Probability density function (PDF) histogram of velocity components for instantaneous vector grid realisation for the planar wing for $Re = 1.5 \times 10^6$, at $\alpha = 0°$ at $x/\bar{c} = 2.5$.

integer values is not observed.

The image processing procedure can also be a source of large errors in the velocity vector evaluation. An appropriate choice of interrogation window size, overlap and processing procedure is fundamental in the accuracy of the calculated velocity vector field [266]. Giuni [78] provides a detailed analysis for the selection of the interrogation window size and overlap.

C: STATISTICAL CONVERGENCE OF TIME-AVERAGED VORTEX

The assessment of the statistical convergence for selected vortex flow properties is performed, adopting the helicity centring method with up to 1800 velocity vector fields of the planar wing reference case. The effects of varying the number of instantaneous velocity vector fields enables the determination of the minimum number of samples that are required to achieve statistical convergence. Furthermore, when averaging over a range of data samples, the random uncertainty characterising the dispersion of values of the measurand, based on a confidence interval/margin of error, can be obtained. Since the SPIV hardware used during the experiments limits the number of samples recorded (at $200Hz$) in a single experimental run to 600, the errors incurred by time-averaging over this number of vector fields is presented.

Quantities such as swirl velocity, axial velocity, vorticity, Reynolds shear stress, and shear strain rate are reported as peak averaged for an increasing number of samples, N, of instantaneous vector realisations. The physical distribution of such quantities is as important as the peak values; the comparison of different states of convergence are likely to show different distributions and structure of the vortex flow properties. For the flow property contours, the reaching of convergence is observed as a smooth and distinct shape forms.

The swirl velocity contour shows a distinct shape with only 25 samples, as shown in figure C.1a. With 250 samples (figure C.1c) the vector field is smooth, and is deemed converged. Averaging over additional samples smooths the velocity gradients and thus provides a slightly better definition of the core shape.

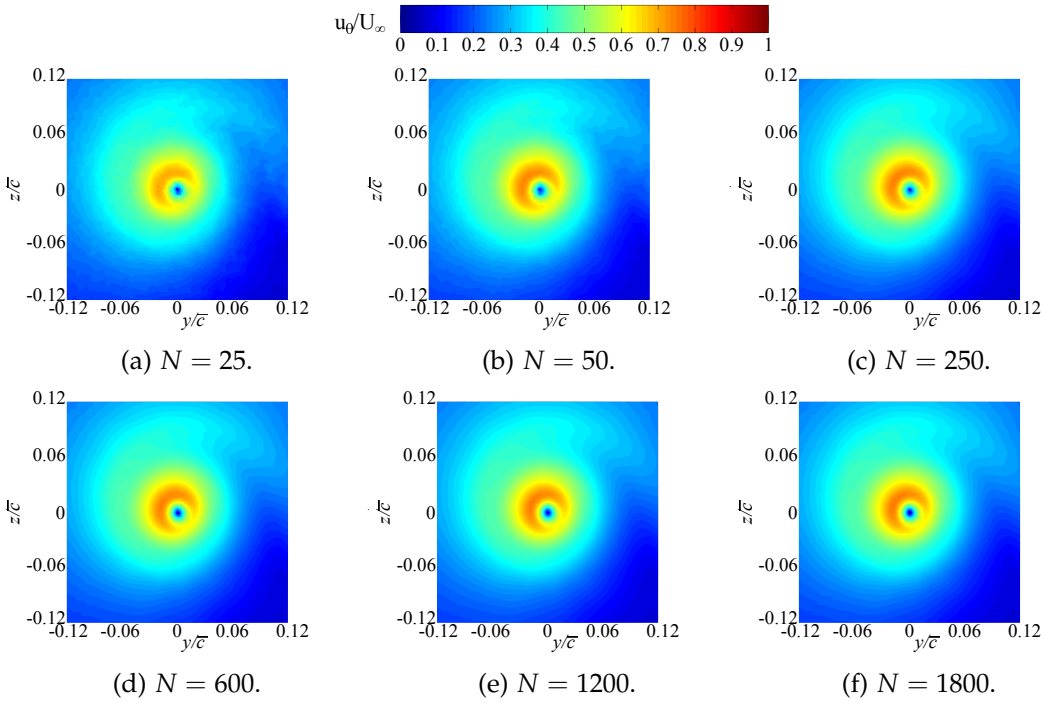

(a) $N = 25$. (b) $N = 50$. (c) $N = 250$.

(d) $N = 600$. (e) $N = 1200$. (f) $N = 1800$.

FIGURE C.1: Swirl velocity at $x/\bar{c} = 2.5$, $Re = 1.5 \times 10^6$, and $\alpha = 8^\circ$ for the planar wing.

Figure C.2 illustrates the in-plane uncertainty in the spatial region of the vortex, showing that the peak errors are found inside the vortex core. With only 50 samples (figure C.2a) the uncertainties within the core exceed 20% due to the presence of turbulent velocity fluctuations. Thus, even though a formed swirl velocity profile is found, the errors associated with the vector field is not acceptable. Increasing the sample ranges to $N = 600$ brings the uncertainty down to $\approx 6\%$, where sampling over the full sample range available $N = 1800$ lowers the uncertainty within the core to $\approx 3\%$. Notice that for sample ranges ≥ 600, shown in figures C.2b and C.2c, the in-plane flow outside of the vortex core indicates a random uncertainty $< 1\%$.

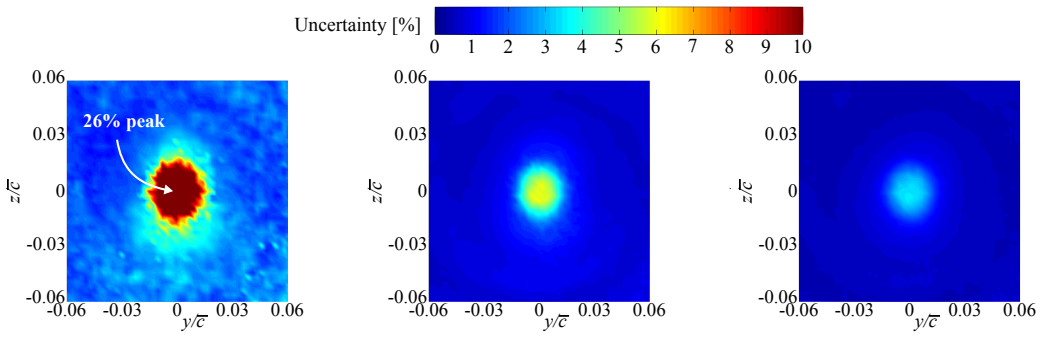

(a) $N = 50$. (b) $N = 600$. (c) $N = 1800$.

FIGURE C.2: Uncertainty for a confidence level of 95% for the helicity centred swirl velocity with different sample sizes of N instantaneous vortex realisations.

The uncertainties associated axial velocity vector field, presented as contours are shown in figure C.2. Maximum error is again found within the vortex core. Similar to the in-plane vector field uncertainties, high uncertainty is recorded within the vortex core with only 50 samples (figure C.2a), where increasing the sampled range to $N = 600$ brings the uncertainty down to $\approx 6\%$, and then sampling over $N = 1800$ lowers the uncertainty within the core to $\approx 3\%$. Outside of the vortex core the surrounding axial flow field is found to have a random uncertainty $\leq 1\%$ for all sample ranges shown in figure C.3.

Convergence curves are presented in figure C.4, illustrating how the peak swirl velocity, vortex core radius, peak axial deficit, and peak vorticity vary with N samples. The uncertainties shown in the convergence plots are the maximum uncertainty identified within the vector field for a given sample range N, hence the spatial location of the peak error may change. It is observed that regardless of flow property monitored the peak uncertainty is always identified within the vortex core.

Previously mentioned, the in-plane and out-of-plane velocity vector fields show a distinct and converged shape with only 25 samples, however, many more samples (≈ 250) are required to bring the uncertainty error within the core down to $\approx 10\%$ and reach a smooth, fully converged state. This is observed in figures C.4a and C.4c where the uncertainty is inversely proportional to the number of samples N.

A cubic interpolation of 36 equispaced radii around the vortex centre is performed to evaluate the circumferential mean of the vortex core radius; the value and associated uncertainty, as a function of N, is given in figure C.4b. There is no distinct trend observed for the variation in the vortex radius with sample range N. This is due to the observational systematic error of the vector field grid dominating errors associated with measuring the vortex core radius ($r_c \pm 0.7mm$). The variation in the mean core radius observed with number of samples N ($0.0168 r_c/\bar{c}$ to $0.0192 r_c/\bar{c}$) equates to a change in the mean radius of $\approx 0.66mm$. The uncertainty of the vortex measurement does not exceed 6% for any range of N, where for $N \geq 1000$ the maximum uncertainty is approximately constant at 4%.

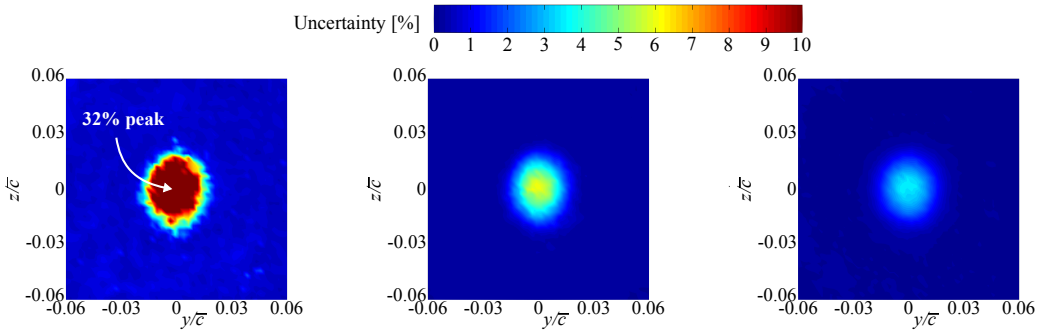

(a) $N = 50$. (b) $N = 600$. (c) $N = 1800$.

FIGURE C.3: Uncertainty for a confidence level of 95% for the helicity centred axial velocity with different sample sizes of N instantaneous vortex realisations.

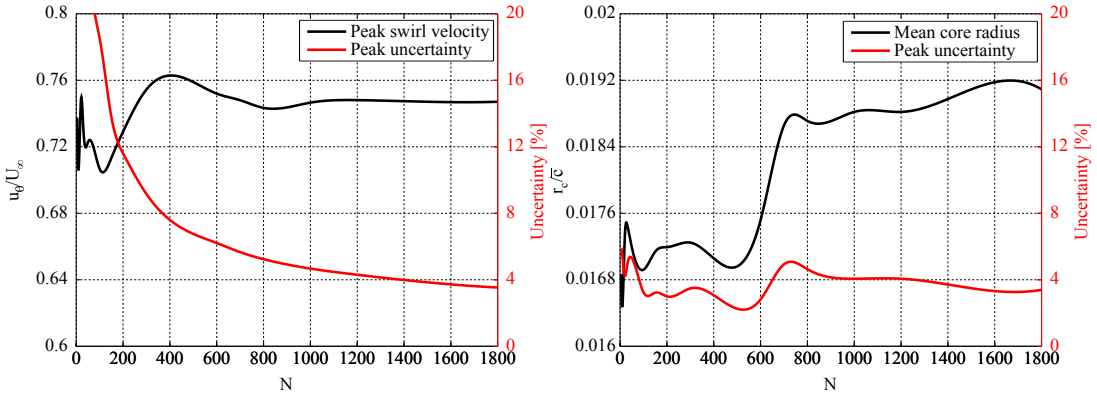

(a) Swirl velocity.

(b) Vortex core radius.

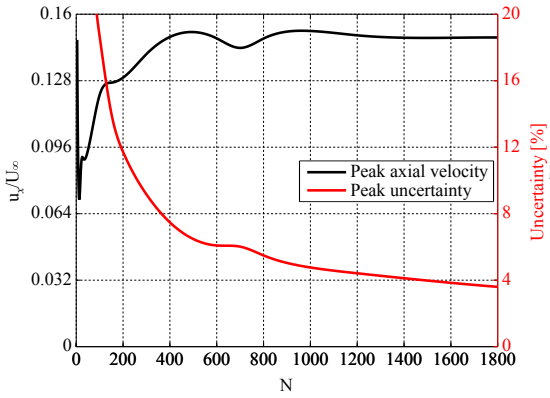

(c) Axial velocity.

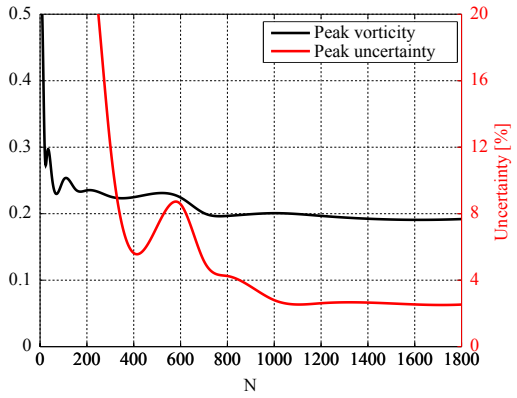

(d) Vorticity.

FIGURE C.4: Convergence of the vortex peak swirl velocity, core radius, axial deficit, and vorticity, with maximum uncertainty for a confidence level of 95% for wingtip vortex of the planar wing at $\alpha = 8°$, $x/\bar{c} = 2.5$.

Convergence of the streamwise vorticity distribution, which involves derivatives of the in-plane velocity field, requires a higher number of samples for convergence. Figure C.4d presents the peak vorticity convergence and maximum uncertainty identified. With 250 samples the vorticity distribution within the core is fully defined, however averaging over $N = 600$ samples is required for full definition of the vortex sheet and roll-up structure. More samples are required for the definition of the vortex sheet due to the lower signal-to-noise ratio. For $N \geq 1000$ the maximum uncertainty in the vorticity field is $< 3\%$.

The convergence and associated random uncertainty for first order turbulent quantities show a trend similar to the convergence of the velocity fields, shown in figures C.4a and C.4c. Second order turbulent quantities, such as the Reynolds shear stress and shear strain rates are expected to require a higher number of images to converge. Figure C.5 presents the contour convergence of the shear strain rate. Averaging over 250 samples, the peak magnitudes have converged and the distribution seems to have reached a moderately converged level although, averaging over 1200 samples achieves smoother gradients within the core and heighten structure definition. The Reynolds stresses demonstrate this same rate of convergence. As the Reynolds

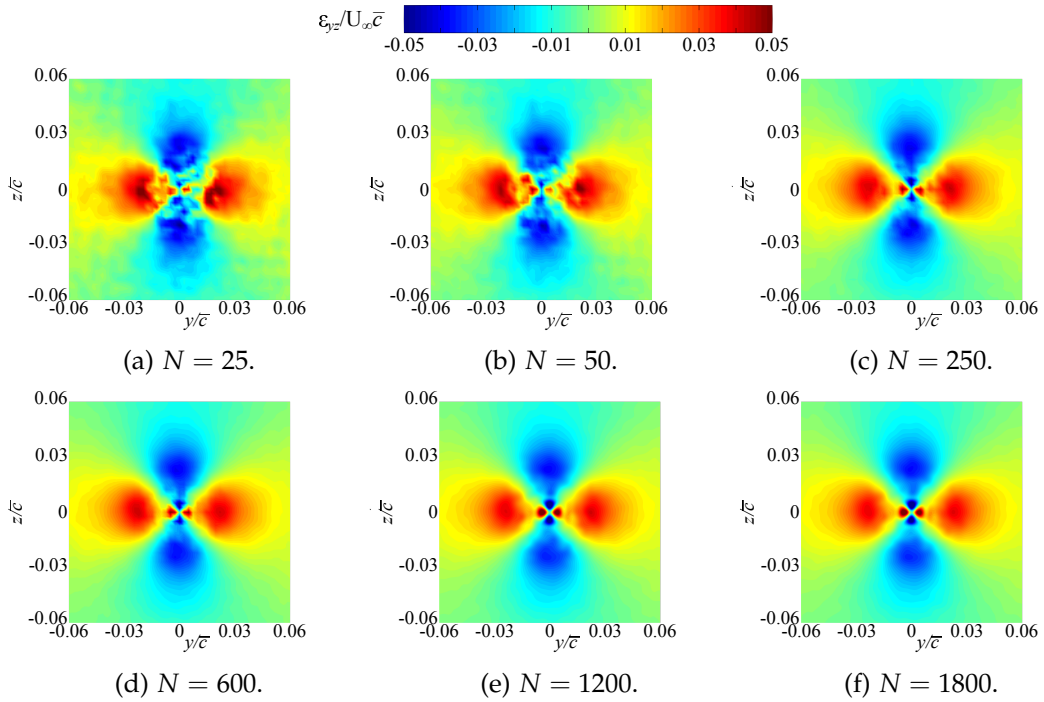

(a) $N = 25$. (b) $N = 50$. (c) $N = 250$.

(d) $N = 600$. (e) $N = 1200$. (f) $N = 1800$.

FIGURE C.5: Shear strain rate convergence at $x/\bar{c} = 2.5$, $Re = 1.5 \times 10^6$, and $\alpha = 8°$ for the planar wing.

shear stresses and the shear strain rates each show a four-lobed pattern of alternatively positive and negative values, the convergence curve of these properties are presented for the average of the absolute values of those peaks in figure C.6.

With 250 samples, the maximum uncertainty in the evaluation of the Reynolds stress and shear strain is 11% and 23% respectively. Increasing the samples to $N >$ 1200, the random uncertainty falls to $\approx$ 5.5% for the shear stresses, and $\approx$ 8% for the shear strain rate. A similar evaluation of the statistical convergence of these turbulent properties was performed on rotor wingtip vortices by Ramasamy et al. [320] who

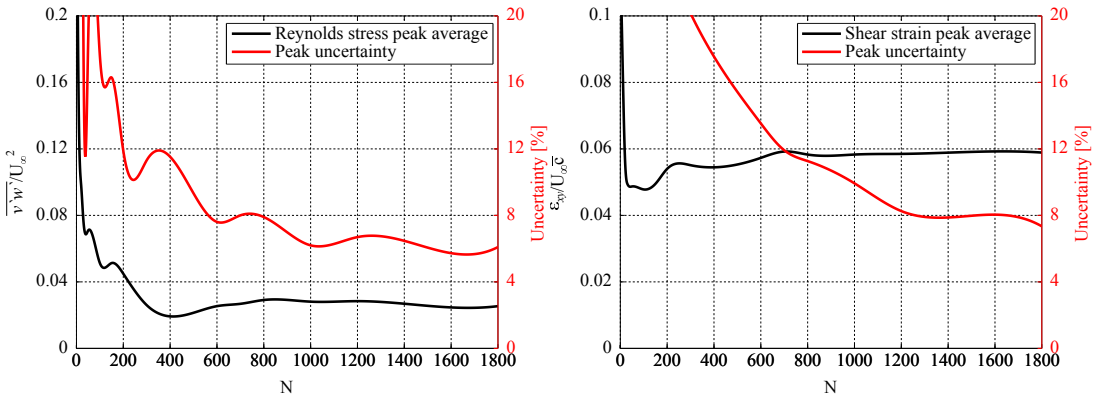

(a) Reynolds shear stress (in-plane). (b) Shear strain rate.

FIGURE C.6: Convergence and peak uncertainty for the in-plane Reynolds shear stress, and shear strain rate for a confidence level of 95% for wingtip vortex of the planar wing at $\alpha = 8°$, $x/\bar{c} = 2.5$.

observed convergence of the first order flow properties with 250 samples, with more than 750 samples required to evaluate second order characteristics.

As a result of this convergence analysis, a minimum of 1200 samples has been deemed adequate for convergence however, the full available data range of 1800 samples is utilised to minimise the random uncertainty. The evaluation of the uncertainties presented in this section are to be taken as an overestimation of the global measurement as they only represent peak values. The uncertainty outside of the vortex core for all flow properties is recoded to be $< 1\%$ when more than 600 samples are used for averaging, as shown in figures C.2 and C.3.

D: VORTEX RING METHOD PLANAR WING AND C-WING VALIDATION

Variation in lift and drag coefficients as a function of angle of attack evaluated from the vortex ring method (VRM) and wind tunnel force platform experiments are presented in figure D.1. All wind tunnel measurements presented here (adapted from figure 5.1) have been corrected for solid-body blockage (Planar wing: 4.9% at $\alpha = 14°$; C-wing: 5.2% at $\alpha = 14°$), wake blockage, and horizontal buoyancy using methods presented by Barlow et al. [227].

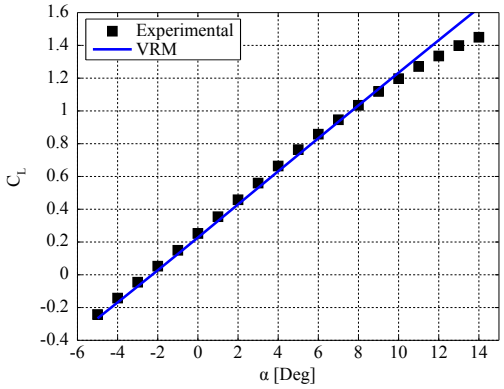

(a) Planar wing: C_L vs. α

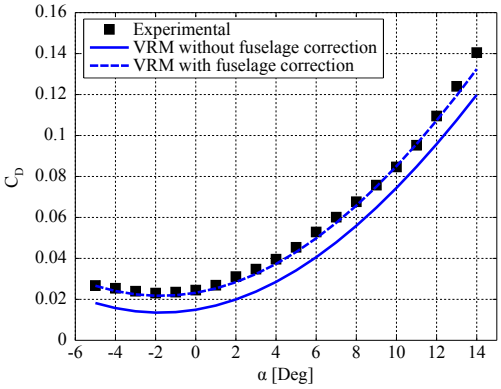

(b) Planar wing: C_D vs. α

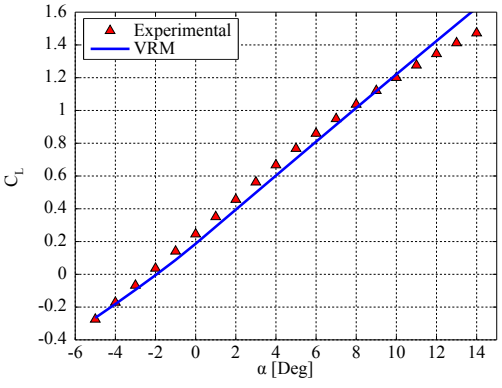

(c) C-wing: C_L vs . α

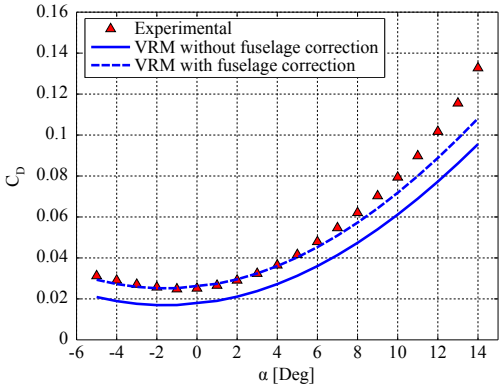

(d) C-wing: C_D vs. α

FIGURE D.1: Numerically predicted VRM and experimentally evaluated lift and drag coefficients for the planar wing and the C-wing.

Each wing has been discretised into spanwise vortex rings approximately $0.01m$ in width, with 8 chordwise vortex rings. The computational time for each wing is approximately 15 seconds per angle of attack. In agreement with the experimental validation cases presented in Section 2.4.7, the VRM predications here are observed to be able capable to adequately capturing the pre-stall performance trends of the planar wing and C-wing configurations.

Figures D.1a and D.1c present the lift-curve-slope of the planar and C-wing respectively. Over the range $-5^\circ \leq \alpha \leq +7^\circ$, the root mean square error (RMSE) for the VRM prediction is less than 1% for the planar wing and $\approx 1.3\%$ for the C-wing. A summary of the zero-lift angle of attack, α_0, the lift gradient, C_{L_α}, and the angle of attack at which stall onset is detected, $\alpha_{Stall\ Onset}$, from both experimental and VRM prediction is provided in table D.1. It is highlight that $\alpha_{Stall\ Onset}$ is not the stall angle of attack, is it the angle of attack at which stalled regions over the wing surface begin to develop.

	Planar (EXP)	Planar (VRM)	C-wing (EXP)	C-wing (VRM)
α_0	-2.56°	-2.28	-2.36°	-2.02
C_{L_α}	0.100	0.100	0.104	0.102
$\alpha_{Stall\ Onset}$	$\approx +7$	$+8.5$	$\approx +7$	$+8.9$

TABLE D.1: Summary of numerically predicted (VRM) and experimentally evaluated (EXP) lift-curve-slope data.

The drag polars for the two wing arrangement presented in figures D.1b and D.1d, for the planar and C-wing respectively, indicate that fuselage drag corrections improve the drag accuracy of the VRM. In the optimisation routine no fuselage drag correction was used. This is not consequential as the drag from the fuselage is primarily due to viscous effects, dictating an approximate constant drag increase over the angle do attack range. For both the planar and C-wing arrangements the drag offset between the experimental data and VRM prediction without the fuselage correction is approximately $\Delta C_D = +0.0116$.

The fuselage drag, which contributes to the wind tunnel model total drag, is not computed by the VRM model directly. Instead an empirical correction has been developed to predict the fuselage drag contribution as a function of Reynolds number and angle of attack. To achieve and accurate fuselage drag prediction, wind tunnel data of the semi-span model at $4\delta^*$ with the wing removed was used to calibrate a viscous drag estimate based on the van Driest II method [376]. This method has been frequently adopted to provide viscous drag predictions of the fuselage and wing in Euler and potential flow simulations [20, 22, 128].

The van Driest II method [376] is used to estimate the turbulent skin friction coefficient, C_f. This method uses a flat-plate turbulent skin friction estimate with form factor corrections to account for the added pressure drag due to viscous effects. For

fuselage-like bodies the following form factor correction is described by the empirical function equation D.1 [22] :

$$K_{form} = 1 + 1.5\left(\frac{d}{l}\right)^{1.5} + 50\left(\frac{d}{l}\right)^{3} \tag{D.1}$$

where d/l is the ratio of diameter to length. The contribution of an axisymmetric fuselage component is then:

$$C_D = K_{form} C_f \tag{D.2}$$

From equation D.2, half of the drag contribution has been added to the VRM perdition of the wing arrangement as shown figures D.1b and D.1d. Over the range $-5^\circ \leq \alpha \leq +7^\circ$, the RMSE for C_D between with experimental and the VRM prediction with empirical fuselage correction is less than 2% for both arrangements.

The wing arrangements are not forced into a completely stalled condition for any of the the tests considered in this work. Figure D.1b illustrating the planar wing drag polar shows that the VRM model adequately captures the drag coefficient for $\alpha > 7^\circ$ despite lightly stalled regions over the wing. The same accuracy is not observed for the C-wing VRM model. Discrepancies occur for $\alpha > 7^\circ$ as the C-wing begins to enter a condition analogous of a T-tail aircraft approaching deep stall. In this condition, the main-wing's wake begins to impinge in the top-wing reducing it's effectiveness for induced drag reduction. The VRM does not capture the flow physics of this interaction.

E: UNIVERSAL BEHAVIOUR OF THE PLANAR WING VORTEX CORE

With the planar wing vortex fully developed and axisymmetric, the self-similar behaviour of the vortex core warrants investigation. The radial distribution of the circulation, Γ, of the trailing vortex, normalised by the circulation of the vortex core, Γ_c, plotted against $log(r/r_c)$ for $\alpha = 8^\circ$ over $1.35 \leq x/\bar{c} \leq 5.418$, is presented in figure E.1a. Additionally, figure E.1b shows the variation of the scaled circulation profiles for various α at $x/\bar{c} = 2.5$. The distribution of the vortex circulation is calculated by integrating the swirl velocity (circulation is the macroscopic measure of fluid swirl, and is a precise measure of the average flow of fluid along a given closed curve).

From the distributions shown in figures E.1a and E.1b, the scaled circulation within the tip vortex core follows a $\Gamma \propto r^2$ profile for $r/r_c < 0.4$, and varies logarithmically for $0.5 \leq r/r_c \leq 1.4$. This phenomenon has been observed in trailing vortices for both rectangular [265, 340] and swept/tapered wing sections [264]. For $r/r_c > 1.4$, Γ continued to vary with x/c and α, suggesting that for $r > 1.4r_c$, the roll-up of the vortex is not complete and therefore there is still a slow addition of vorticity to the outermost layers of the vortex from the shear-layer arriving from the inboard regions [377]. The observed self-similar universal circulation behaviour of the core region of the axisymmetric tip vortex in the near-wake region is of particular interest, as it generally takes several tens or even hundreds of wing chords downstream for the vortex to become fully developed and attain the characteristics of asymptotic trailing vortices [340].

Based on dimensional arguments alone, Hoffman and Joubert [357] demonstrated that turbulent vortices should be expected to exhibit a universal inner-scaled circulation profile. Their work presents empirical curve-fit relationships that describe the inner core region, and the region where the Γ/Γ_c distribution is logarithmic as:

$$\Gamma/\Gamma_c = A(r/r_c)^2 \quad for \quad r/r_c < 0.4 \tag{E.1}$$

$$\Gamma/\Gamma_c = Blog(r/r_c) + C \quad for \quad 0.5 < r/r_c < 1.4 \tag{E.2}$$

where A, B, and C are empirical curve-fit constants.

Furthermore, for $1.35 \leq x/\bar{c} \leq 5.418$, all data profiles within $0 \leq r/r_c \leq 1.2$ collapse together onto a sixth-order polynomial (similar to that reported by Ramaprian and Zheng [265] and Birch and Lee [340]) with a self-correlation coefficient of 0.998:

$$\Gamma/\Gamma_c = 1.756(r/r_c)^2 - 1.044(r/r_c)^4 + 0.263(r/r_c)^6 \tag{E.3}$$

Figure E.1c compares the self-similar (or universal) core flow structure of the tip vortex of the planar wing at $\alpha = 8^\circ$ at $x/\bar{c} = 2.5$ with the empirical relationships (curve-fit constants used: $A = 1.666$ in equation E.1; $B = 2.010$ and $C = 0.972$ in equation E.2). Results are consistent with those presented by Hoffman and Joubert [357], Phillips [336], Ramaprian and Zheng [265], Birch and Lee [340], Gerontakos and Lee [264], and Ghimire and Bailey [378]. A direct comparison of the levels and radial growth of the vortex strength, $\Gamma/U_\infty\bar{c}$, of the tip vortex at different α at $x/c = 2.5$ is summarised in figure E.1d. This shows the increased level of circulation within the core with angle of attack from $\alpha = 0^\circ$ to 8°, after which for $\alpha = 10^\circ$ the circulation is noticed to reduced slightly due to weaker vortex formation driven by the wingtip stall progression.

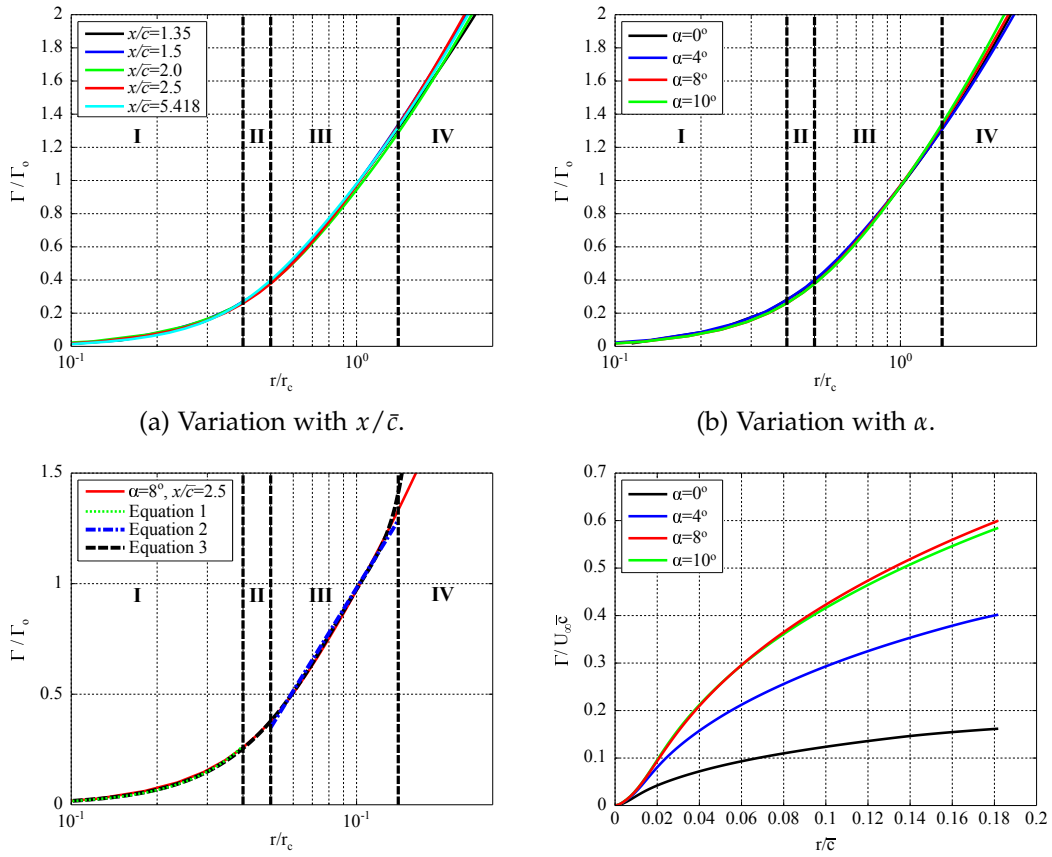

(a) Variation with $x/\bar{c}$.

(b) Variation with α.

(c) Universal circulation profile.

(d) Radial circulation distribution at $x/\bar{c} = 2.5$.

FIGURE E.1: Radial distribution of circulation: **I**, inner-core region; **II**, buffer region; **III**, logarithmic region; **IV**, outer region.